Ferrocene-Phenol Conjugates – Secondary Structures and Reactivity

Dissertation
zur Erlangung des Grades
„Doktor der Naturwissenschaften“
im Promotionsfach Chemie

am Fachbereich Chemie, Pharmazie und Geowissenschaften
der Johannes Gutenberg-Universität Mainz

vorgelegt von
Andreas Neidlinger
geboren in Worms
Mainz, 2016

Die vorliegende Arbeit wurde unter Betreuung von [redacted] in der Zeit von Mai 2011 bis Januar 2016 am Institut für Anorganische Chemie und Analytische Chemie der Johannes Gutenberg-Universität Mainz angefertigt.

Mainz, Januar 2016

Dekan: [redacted]

1. Berichterstatter: [redacted]

2. Berichterstatter: [redacted]

Tag der mündlichen Prüfung: 29. Januar 2016

Ich, Andreas Neidlinger, Matrikelnummer [redacted] versichere, dass ich meine Promotionsarbeit selbstständig verfasst und keine anderen als die angegebenen schriftlichen und elektronischen Quellen, sowie andere Hilfsmittel benutzt habe. Alle Ausführungen, die anderen Schriften wörtlich oder sinngemäß entnommen wurden, habe ich kenntlich gemacht.

Datum _____________ Unterschrift ___________________

Short abstract

The investigation of electron transfer reactions, especially in combination with proton transfers − so called proton coupled electron transfers − is of considerable interest from a chemical and biological perspective. For example, in photosystem II, the electron transfer from the oxygen evolving complex is achieved via a proton coupled electron transfer to a tyrosyl residue. Successful operation of photosynthesis is influenced by many factors. The presence of highly reactive intermediates and the complicated environment, however, render the investigation of such processes in vitro quite difficult, despite of their utmost importance. Accordingly, especially proton coupled electron transfer reactions between organic and organometallic redox centers lack experimental studies.

The successful syntheses of several amide-linked conjugates of ferrocene and phenol moieties allows a facile insight into the influences of intramolecular hydrogen bonding on the redox potentials of both redox centers (ferrocene vs. phenol(ate)) and the stability of the respective valence isomers and tautomers. Intramolecular proton coupled electron transfer via light excitation is evidenced by the presence of a characteristic NIR intervalence charge transfer band for a mixed-valent ferrocenium-phenolate involving proton movement in the intramolecular hydrogen bond according to DFT calculations. The influence of the lack of intramolecular hydrogen bonds is illustrated by an appropriate ferrocene-phenol conjugate, showing rapid follow-up reactions under alkaline and oxidative conditions. Cooperative hydrogen bonding is furthermore presented for a series of conjugates varying in substitution pattern and hydrogen bond donating/accepting capabilities, respectively. The mutual influence of one or more intramolecular hydrogen bonds on the stability of secondary structures and on the redox behavior is presented.

In a second project, the general behavior of ferrocenium compounds in an alkaline medium is investigated. Possible degradation pathways of ferrocenyl compounds are in focus of pharmaceutical research, due to the high efficiency of ferrocene-containing (pro-)drugs in the treatment of malaria and some types of cancer. The increased efficiency of such pharmaceuticals in comparison with similar ferrocene-free compounds is at least partially assigned to the enhanced redox behavior of ferrocene and its derivatives in contrast to purely organic substrates. Besides the formation of reactive oxygen species, the presence of carbon-centered ferrocenyl radicals was proposed for some ferrocene-containing drugs. Experimental evidence of such highly reactive species for simple ferrocene derivatives is illustrated in this work by rapid-freeze EPR and spin-trapping techniques, providing references for the effectiveness of ferrocene-containing drugs.

The last project deals with the investigation of the influence of dipole moments on electron transfer reactions via a hopping mechanism. In this theoretical approach, synthetic access to immobilizable wires, available from literature known ferrocenyl precursors by established amide coupling procedures, is presented. The formation of stable macrodipole moments of oligoferrocenyl amides is evidenced by literature references. DFT calculations corroborate these results for the wires. Therefore, these wires could act as a first test system for the investigation of intramolecular electron transfer rates with respect to a macrodipole moment within the wire.

Mein Dank gilt

[redacted]

für die Möglichkeit, an diesem vielfältigen Thema zu arbeiten, die wissenschaftliche Betreuung und stete Diskussionsbereitschaft sowie die gewährten Freiheiten bei der Bearbeitung meines Forschungsthemas.

Diese Arbeit widme ich meiner Familie.

There is no subject, however complex, which, if studied with patience and intelligence will not become more complex.

D. Gordon Rohman

oder auch

Ebbes is fer Ebbes gut!

Lebensweisheit von der linken (richtigen) Rheinseite

CONTENTS

ABBREVIATIONS

δ	chemical shift in NMR spectroscopy or isomeric shift in Mößbauer spectrometry
ε	molarer Extinktionskoeffizient (M^{-1} cm^{-1})
λ	wavelength in UV/Vis spectroscopy,
$\tilde{\nu}$	wavenumber
A	hyperfine coupling constant in EPR spectroscopy
Ac	acetyl
Ar	aryl
a.u.	arbitrary units
B	magnetic field
Boc	*tert*-butyloxycarbonyl
^{t}Bu	*tert*-butyl
°C	degree Celsius
calcd.	calculated
cat.	catalyst
Cp	cyclopentadienyl (η^5-C_5H_5)
Cp*	pentamethylcyclopentadienyl (η^5-C_5Me_5)
CV	cyclic voltammetry
CW	continuous wave
d	day
d	doublet signal in NMR spectroscopy
dq	doublet of quartets signal in NMR spectroscopy
DCM	dichloromethane
DFT	density functional theory
DIPEA	di-*iso*-propylethyl amine
DMF	dimethylformamide
dpph	2,2-diphenyl-1-picrylhydrazyl
$E_{1/2}$	half wave potential
eq.	equivalent
EPR	electron paramagnetic resonance
Et	ethyl

ET	electron transfer
exp	experimental
Fc	ferrocenyl
Fca	1-aminoferrocene-1′-carboxylic acid
FD(-MS)	field desorption (mass spectrometry)
G	Gauss
Ghosez’ reagent	1-chloro-*N*,*N*,2-trimethyl-1-propenylamine
H	hour
HT	hole transfer
HOMO	highest occupied molecular orbital
I	nuclear spin
IHB	intramolecular hydrogen bond
IR	infrared
IVCT	inter valence charge transfer
^{n}J	coupling constant in NMR spectroscopy
K	Kelvin
LUMO	lowest unoccupied molecular orbital
M	molar (mol L^{-1})
Me	methyl
Min	minute
m.p.	melting point
mT	Millitesla (= 10 Gauss)
NIR	near infrared
NMR	nuclear magnetic resonance
NOESY	nuclear Overhauser effect spectroscopy
P1^{t}Bu	*tert*-butylimino-tris(dimethylamino)phophorane
PCET	proton coupled electron transfer
Ph	phenyl
pt	pseudo triplet signal in NMR spectroscopy (doublet of an unresolved doublet)
ppm	parts per million
q	quartet signal in NMR spectroscopy
r.t.	room temperature

S	electron spin
s	singlet signal in NMR spectroscopy
SOMO	singly occupied molecular orbital
SWV	square wave voltammetry
T	temperature
t	triplet signal in NMR spectroscopy
TFA	trifluoracetic acid
THF	tetrahydrofuran
UV/Vis	ultraviolet-visible
V	volt
X-band	frequency range in EPR measurements ($\nu \approx 9.4$ GHz)

1 INTRODUCTION

In bioinorganic chemistry, a scientific field located between chemistry and biology, a lot of effort is put into the design, synthesis, and analysis of model complexes to investigate modes of action of biologically active molecules.[1–12] In many of these compounds, a central role is played by metal ions, which have a large variability of coordinational properties and oxidation states. Thus, facile tuning of properties is possible. A principal point in those investigations are electron transfer (ET) reactions due to their high importance in a plethora of chemical and biological processes.[13–19] Mixed-valent and mixed-metal compounds are powerful tools to study ET processes, straight-forwardly allowing the tuning of properties. ET has been thoroughly studied, e.g. on the symmetric mixed-valent Creutz-Taube ion and similar complexes.[17,19–26] Suitable organic redox couples have also been amply investigated.[27,28] ET reactions of compounds built up of different building blocks (organic and organometallic) are, however, less well explored.

The coupling with proton transfer (PT) reactions facilitates the ET in combined mechanisms (proton coupled electron transfer, PCET).[21,29–37] In nature, a very prominent example for PCET between chemically different moieties from is photosystem II, in which a tyrosyl residue (phenoxyl radical) is reduced to the phenol(ate) by the oxygen evolving complex (OEC; Mn_4CaO_4 cluster). The reaction is assisted by a nearby histidine base as proton shuttle. This is a key process in the ET from the OEC allowing water oxidation to release oxygen.[38–44] The immense importance of this reaction becomes clear by a look at the annual production of oxygen by photosynthesis, which equals approximately $8.4\ 10^{13}$ mol.[45] Furthermore, carbon fixation is directly linked to oxygen production in photosynthesis with an annually carbon fixation of $1.05\ 10^{14}$ kg of carbon.[46] Hence, in a world with limited resources and dramatically increasing pollution of the environment by burning fossil fuels, it is crucial to exploit sustainable, environmentally friendly energy sources.

The abundancy of iron in nature and its biocompatibility allows its application as part of molecular structures in living organisms. Iron is in fact the most abundant transition metal in the human body. It is, for example, relevant for oxygen transport in hemoglobin and myoglobin,[47–51] and is furthermore part of ET reactions in cytochromes,[52,53] and iron sulfur proteins.[54–56] As simple, yet stable organometallic redox center, bis(η^5-cyclopentadienyl)-iron(II), or ferrocene, and its derivatives are easily accessible, due to simple C−C or amide coupling reactions for example. Since its discovery in 1951 by Pauson and Kealy,[57] ferrocene has been the center of many research activities.[58–61] Firstly, it is was starting point for a new class of organometallic compounds, generally called metallocenes or sandwich complexes. Many other metallocenes, e.g. chromocene,[62] cobaltocene,[63] and nickelocene,[63] have also been explored. Yet, ferrocene is still a prominent compound in current research due to its high stability and reversible redox behavior originating from the stable 18 valence electron configuration. It is used in pharmaceutical substances, such as antibiotics,[64] antimalaria medication,[65–67] and antitumor medication.[68–76] In the latter, the ferrocene containing drugs ferrocifen and ferrociphenol show high levels of cytotoxicity against breast cancer cells.[69,71,73,77,78] They are even more effective compared to the respective ferrocene free drugs like tamoxifen, but cause less oxidative stress.[72,79] Hence, another mode of action is assumed, which is not based on the formation of reactive oxygen species, but possibly on carbon based radicals.[71] These carbon based radicals are in equilibrium with the respective ferrocenium radicals under alkaline conditions, a property missing in purely organic compounds like tamoxifen. Accordingly, the better targeting and fewer side reactions of ferrocifen etc. can be explained by the redox chemistry of the ferrocene units.

Furthermore, the development of electronic devices demands continuation of miniaturization and is therefore in need of molecular electronics and molecular wires as smallest possible designs.[80,81] Organic structures like oligophenylene ethynylenes (OPEs) have been widely investigated for their electronic conductivity of the π conjugated systems.[82–86] While these systems are straightforwardly synthesized,[87–89] the high rigidity of the resulting wires are often unable to face the geometrical requirements of their surroundings. π-π stacking of neighboring wires furthermore may induce short-circuits, which justifies the need for further research on flexible wires, which are not prone to π-π stacking. Ferrocenyl derivatives are able to overcome both drawbacks, e.g. with 1,n'-ferrocenylene moieties. Firstly, their pseudo-C_5 axis gives potential wires a higher flexibility and, secondly, they are less prone to form coagulates, thus, no short-circuiting is expected.[90]

As stated above, iron is one of the central elements in a plethora of chemical reactions in nature and in the laboratory. The combination of iron's abundance with facile synthetic procedures makes this element a great tool for future challenges.

1.1 Electron Transfer

Electron transfer (ET) reactions are one of the most important and fundamental chemical reactions.[91] The detailed understanding of mechanisms and kinetics of ET reactions is essential for the development of molecular wires, i.e. wire-like molecules that show electronic conductivity. Simple systems for the investigation of such intramolecular ET reactions are mixed-valent bimetallic complexes, which are described in theory in chapter 1.1.1. Different mechanisms of ET like superexchange and electron hopping are illustrated in chapters 1.1.2 – 1.1.4.

1.1.1 Intramolecular Electron Transfer

A simple system containing two redoxactive centers connected by a bridging group can perform ET thermally or upon excitation. Bimetallic systems are defined as complexes with two metal atoms, which are connected by a spacer or a bridging ligand. There are basically two different kinds of bimetallic metal complexes. First, homobimetallic complexes, in which the same metal is in the same chemical environment and second, heterobimetallic complexes, in which either the same metal atom is in different chemical surroundings or two different metals are used. Mixed-valent bimetallic complexes are powerful systems for the investigation of intramolecular ET, since tuning of properties is easily possible by variation of the bridging ligand and the complex environment of the metal atoms. A prominent example for a homobimetallic, mixed-valent complex is the Creutz-Taube ion (Figure 1), with two identically coordinated ruthenium atoms bridged by a pyrazine ligand. Assignment of redox states ($2^+/3^+$ vs. $2.5^+/2.5^+$) varies depending on the spectroscopic method.[19,92] However, both ruthenium centers are strongly electronically coupled.

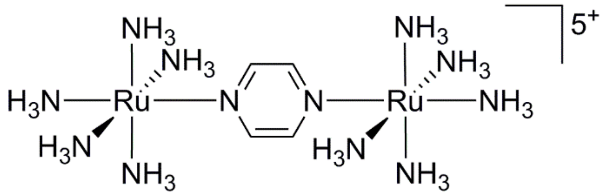

Figure 1. Lewis structure of the Creutz-Taube ion.

In principle, ET can occur via a thermal and a photochemical way for the reaction from M-M$^+$ → M$^+$-M (Figure 2). According to the Franck-Condon principle, the ET is much faster than the reorganization of single atoms (complex and solvent molecules). The reorganization upon ET occurs due to different bond distances and angles between metal atoms and ligand as well as different solvation of the redox centers in different oxidation states (inner/outer-sphere reorganization). Hence, the ET always occurs in a fixed environment. This leads to a different treatment of thermal and optical ET as explained by Marcus theory.[93–96] For thermal ET, the metal-ligand bonds and the solvation of both metal centers needs to be changed to allow ET under constant geometries (Figure 2, bottom). In photochemical ET, however, the electronic interaction of both redox centers occurs from relaxed geometries by excitation, leading to an ET within the complex and solvation geometry of the initial complex. Afterwards, the environment of the complex changes accordingly (Figure 2, top). Due to the symmetry in homobimetallic systems, the two mixed-valent states M-M$^+$ and M$^+$-M are degenerate, resulting in $\Delta G_0 = 0$. However, the reorganization is the reason for the activation energy $\Delta G^{\neq}$ of such processes.[97]

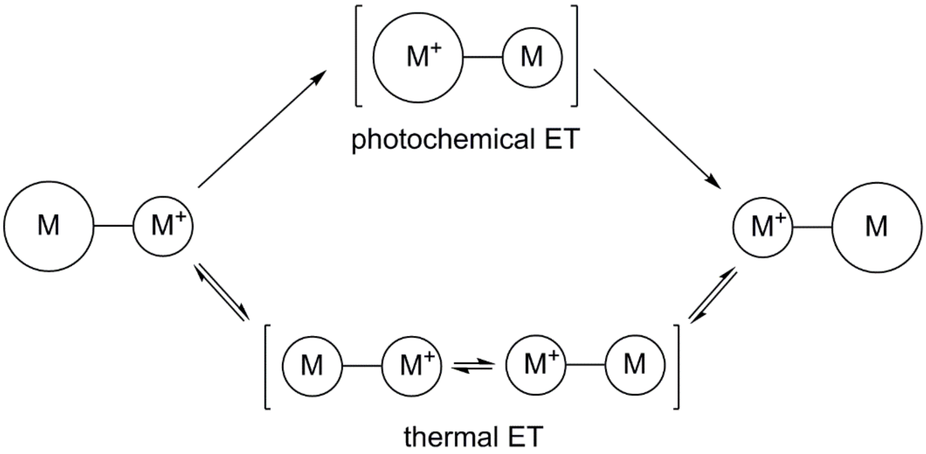

Figure 2. Illustration of photochemical (top) and thermal ET (bottom) in a homobimetallic complex.

In a first approximation, both potential curves of M-M$^+$ and M$^+$-M are described as parabolas, at different position of the reaction coordinate due to the dissimilar nuclear coordinates. In Figure 3, the energy profile for an ET reaction, projected on a one-dimensional reaction coordinate, is depicted. At the crossing of both parabolas, the dotted region represents electronic coupling of both valence isomers, which allows thermal ET. At this point, all nuclear coordinates and the solvation are arranged to allow ET at fixed environment (Franck-Condon principle) leading to the transition states in Figure 2, bottom.

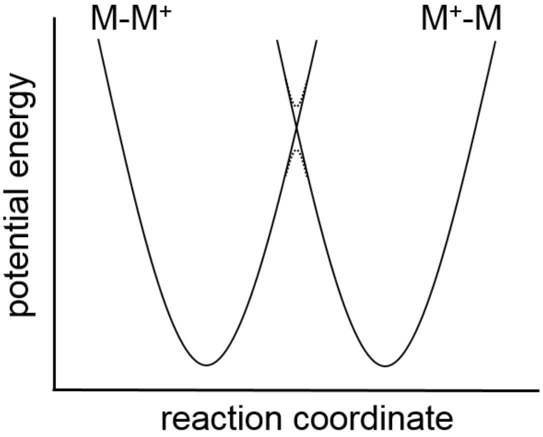

Figure 3. Energy profile for ET reaction M-M$^+$ → M$^+$-M including nuclear coordinates and solvation. Dotted lines indicate electronic interaction at the equilibrium conformation.[13]

The parameter H_{AB}, introduced by Hush, is a measure for the electronic coupling between the two redox centers.[98] With data from optical spectroscopy (IVCT band), this electronic coupling is accessible by equation (1).[98]

$$H_{AB} = \frac{2.06\ 10^{-2}}{r}\sqrt{\varepsilon_{max}\ \tilde{\nu}_{max}\ FWHM}\ \text{(in cm}^{-1}\text{)} \qquad (1)$$

with r = distance of the redox centers (in Å), ε_{max} = absorption coefficient of IVCT band (in M^{-1} cm^{-1}), $\tilde{\nu}_{max}$ = wavenumber of excitation (in cm^{-1}), and FWHM = full-width-at-half-maximum (in cm^{-1})

Robin and Day classified the strength of electronic communication between redox centers in three classes.[99] In systems with an "insulating" bridge, no interaction of the metal atoms is observed and accordingly, the redox centers are more or less independent of each other (Figure 4a).[99,100] Such systems are classified as Class I according to Robin and Day. If electronic interaction increases (due a better suited bridging ligand or smaller metal-metal distance), the mixed-valent state is characterized as a hypersurface with two minima for the M-M$^+$ and M$^+$-M states , which represents a bonding state, while the upper curve represents an excited state (Figure 4b).[99,100] In this Class II case, the reorganization energy λ – a measure for structural adjustment of the different redox sites and the solvent shell upon ET – is larger than $2H_{AB}$, resulting in a double minimum potential surface. In these cases intervalence charge transfer (IVCT) bands can be observed, which arise from photochemical ET between the two redox centers. Furthermore, thermal ET can take place, with an activation energy of one-fourth of the optical transition according to the harmonic approximation.[99,100] If the electronic coupling increases, this reorganization energy becomes smaller than $2H_{AB}$, leading to a Class III system characterized by a hypersurface with complete delocalization and thus, only one minimum (Figure 4c). In this case, optical excitation does not lead to ET, but merely populates an electronically excited state of the delocalized minimum structure.[100] Accordingly, Class I systems act as if composed of two individual complexes, while Class II systems show the characteristics of the single redox centers, but also feature additional properties like the IVCT band. In Class III compounds, however, the two redox centers show complete delocalization of the electron and no detection of single valence-isomers is possible, yielding entirely new properties with respect to its components.

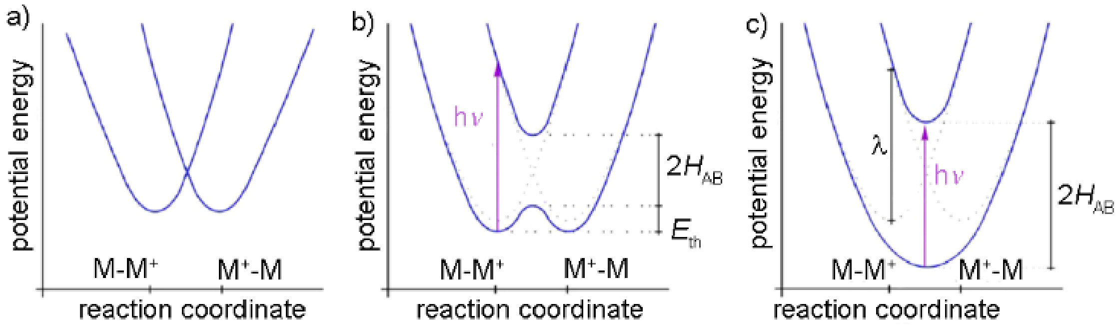

Figure 4.[1] **Energy profiles for ET reaction according to Robin and Day for a) Class I, b) Class II, and c) Class III systems.**[100]

Furthermore, disproportionation of the mixed valent-state like in equation (2) has to be taken into account.

$$2\ \text{M-M}^+ \rightleftharpoons \text{M-M} + \text{M}^+\text{-M}^+ \qquad (2)$$

Only if the equilibrium lies on the left side of equation (2), an investigation of a mixed valent complex is possible. By electrochemical methods, an approximation of the comproportionation constant K_c is possible by the difference of half-wave potentials $\Delta E_{1/2}$ for both redox events.[99,101] A large separation of redox potentials indicates a higher comproportionation constant K_c and a smaller disproportionation constant K_d, respectively. K_c can be obtained by equation (3).

$$\Delta G = -zF\,\Delta E_{1/2}$$
$$\Delta G = -\mathrm{R}T\ln(K_c)$$

---

[1] Adapted with permission from R. F. Winter, *Organometallics* **2014**, *33*, 4517–4536. Copyright 2014 American Chemical Society.

$$K_c = exp\left(\frac{zF\ \Delta E_{1/2}}{RT}\right) \tag{3}$$

with z = number of transferred electrons, F = 96485 C mol^{-1}, R = 8.314472 J mol^{-1} K^{-1}, $\Delta E_{1/2}$ in V, and T in K

1.1.2 Thermal Electron Transfer

As mentioned above, ET can in principle occur via two different mechanisms. In donor-bridge-acceptor (D-B-A) systems with non-redox active or small bridges (with high lying HOMOs (highest occupied molecular orbitals) and low lying LUMOs (lowest unoccupied molecular orbitals)), respectively, the ET occurs by a superexchange mechanism.[102] If the bridge is redox active (thermally accessible redox states of the bridge), e.g. in a longer conjugated OPEs, the ET can be performed by electron hopping as described in chapter 1.1.4. Superexchange makes use of virtual states including the bridge's frontier orbitals, which are not thermally accessible, but allow mixing of donor and acceptor orbitals in a single step (Figure 5).[102] Therefore, formally one electron from the bridge's low lying HOMO is transferred to the higher lying LUMO of the acceptor ($D\text{-}B^{+}\text{-}A^{-}$) and the resulting electron hole is formally filled by the donor ($D^{+}\text{-}B\text{-}A^{-}$) → hole transfer (HT) / reductive ET. Alternatively, an ET from donor to bridge's LUMO can occur ($D^{+}\text{-}B^{-}\text{-}A$), which, after formally transferring this electron to the LUMO of the acceptor, finally leads to the same result → oxidative ET.[102]

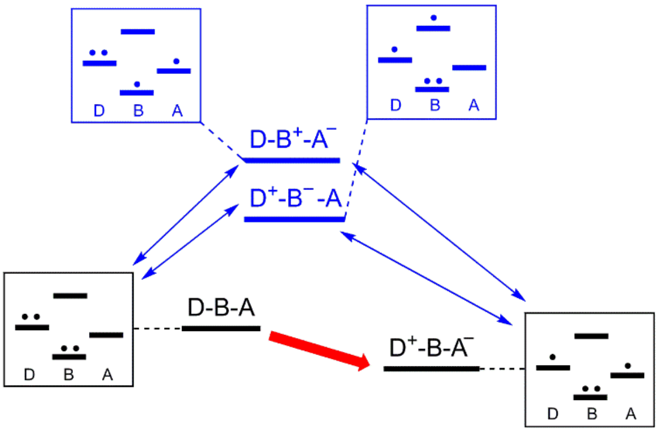

Figure 5. Schematic representation of ET via superexchange in a D-B-A dyad. The blue boxes represent virtual states in terms of the one-electron configuration. Couplings are shown by blue double arrows, while the single-step, exothermic ET is represented by the red arrow.[102]

The above schematic illustrations and explanations dealt with D-B-A systems with single bridging groups. In systems where donor and acceptor are connected via modular bridges of weakly interacting repeating units, these schemes need to be extended. Superexchange in these systems again make use of various virtual states, in which the electron is transferred via all HOMOs or LUMOs of the bridge, respectively.[102] The illustration in Figure 6 shows oxidative ET in a system with a bridge consisting of three similar, weakly interacting bridge units (D-B-B-B-A). Similar as for simple bridges (Figure 5), oxidative ET takes place by a single step involving mixing with virtual states $D^{+}\text{-}B_1^{-}\text{-}B_2\text{-}B_3\text{-}A$ → $D^{+}\text{-}B_1\text{-}B_2^{-}\text{-}B_3\text{-}A$ → $D^{+}\text{-}B_1\text{-}B_2\text{-}B_3^{-}\text{-}A$

→ D^+-B_1-B_2-B_3-A^-. The respective reductive ET (HT) similarly works by D-B_1-B_2-B_3^+-A^- → D-B_1-B_2^+-B_3-A^- → D-B_1^+-B_2-B_3-A^- → D^+-B_1-B_2-B_3-A^- (not shown in Figure 5). Therefore, in this simple picture, with weak interaction between the bridge units, the energy difference of the bridge's frontier orbitals is considered to be constant independent of the bridge length. This is however not always true, especially for longer conjugated π-systems, where HOMO and LUMO levels vary with elongation. In cases where these bridge orbitals are thermally accessible, ET is no longer described as superexchange, but takes place by a hopping mechanisms.[102] This is explained in detail in chapter 1.1.4.

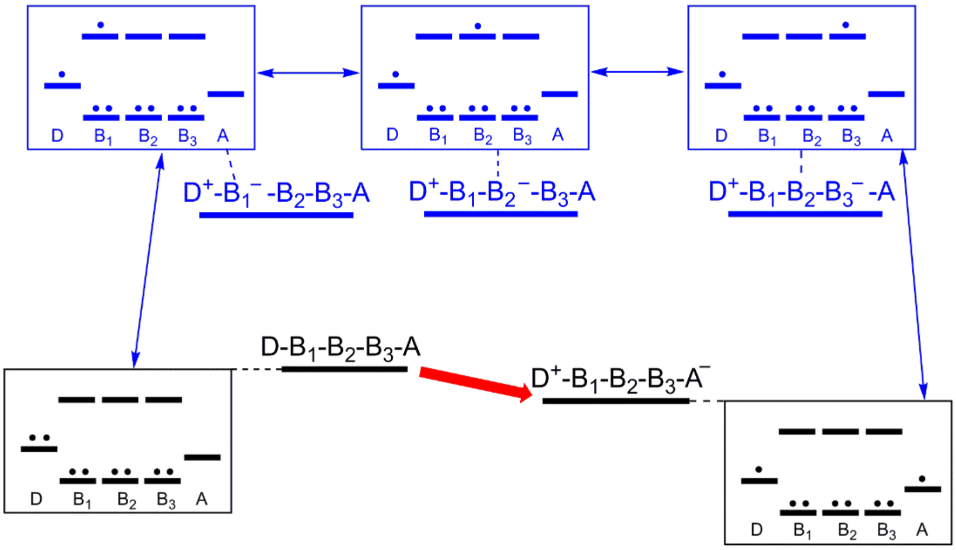

Figure 6. Schematic representation of oxidative ET via superexchange in a D-B-B-B-A system. The blue boxes represent virtual states in terms of the one-electron configuration. Couplings are shown by blue double arrows, while the single-step, exothermic ET is represented by the red normal arrow.[102]

1.1.3 Photoinduced Electron Transfer

In the previous chapter, thermal ET was discussed. Photoinduced ET (PET) can occur in two ways, either in an oxidative or in a reductive manner. Both processes can be explained as a reaction of the type D-B-A + hν → D^+-B-A^-. The differences between those two modes are illustrated in this chapter.

In oxidative PET (OPET) the excitation of the donor (D*-B-A) leads to an ET from the excited donor's SOMO (singly occupied molecular orbital) to the LUMO (D^+-B-A^-) of the acceptor via a virtual state LUMO of the bridge (Figure 7, left half) → oxidation of the donor by ET.[102] For reductive PET (RPET), on the other hand, excitation of the acceptor (D-B-A*) leads to a ET from a virtual HOMO of the bridge to the acceptor (D-B^+-A^-) and this hole is filled by the HOMO of the donor → reduction of the acceptor by HT (Figure 7, right half). The final charge separated state is the same as obtained by OPET (D^+-B-A^-).

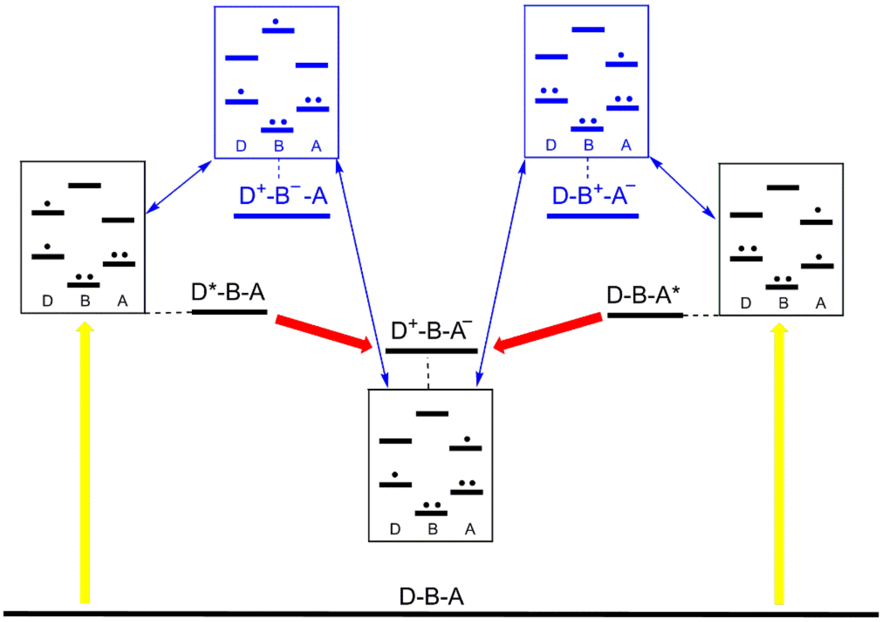

Figure 7. Schematic representation of PET via superexchange in a D-B-A dyad. Excitations (yellow arrows) of the donor following ET (OPET, left half) and of the acceptor and HT (RPET, right half). The blue boxes represent virtual states in terms of the one-electron configuration. Couplings are shown by blue double arrows, while the single-step, exothermic ET is represented by the red arrows.[102]

1.1.4 Electron Hopping

As mentioned above, not all ETs work via superexchange. In compounds with elongated conjugated or redox active bridges (such as oligoferrocene amides), the transfer of charge is mediated by a hopping mechanism involving MOs of the ferrocenyl units that are thermally accessible for the excited donor or acceptor, respectively. This multi-step mechanism is illustrated in Figure 8 for a simple D-B-A system. If the LUMO of the bridge is thermally accessible, the incoherent two-step CT utilizes this orbital for the interaction of donor and acceptor, by the real D^+-B^--A state (Figure 8, left half). If, on the other hand, the HOMOs of the bridge are accessible, ET is facilitated by a hole transport (HT) process involving the real D-B^+-A^- state (Figure 8, right half).[102]

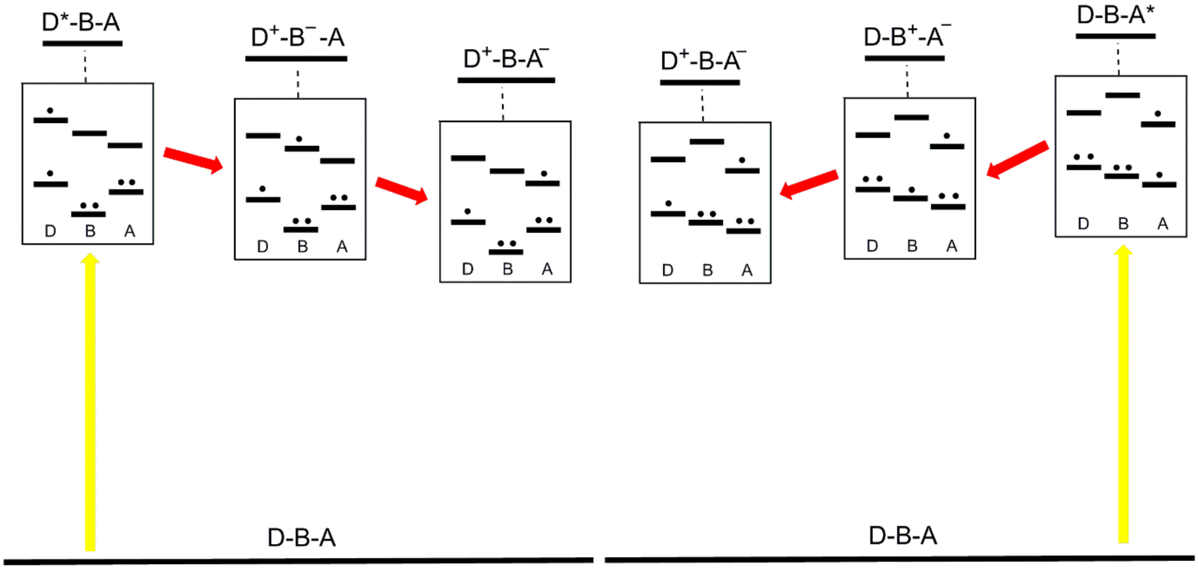

Figure 8. Schematic representation of PET via a hopping mechanism in a D-B-A dyad for oxidative ET with low lying LUMOs mediating ET (left half) and for reductive ET involving high lying HOMOs for ET (right half). Single-steps of the exothermic ET are represented by red arrows.[102]

In cases of modular bridges as discussed in chapter 1.1.2, all involved MOs of the bridge have to be accounted for. If these orbitals are thermally accessible for the excited donor or acceptor, respectively, ET or HT takes place by a random, reversible hopping between the degenerate bridge orbitals as illustrated for an oxidative hopping-mechanism in Figure 9. The respective reductive HT by a hopping-mechanism can be derived from this figure with higher lying bridge HOMOs by picturing the donor in the ground state, while the acceptor is excited. Such systems are well suited for long range CT and can thus be considered as real molecular wires.[102]

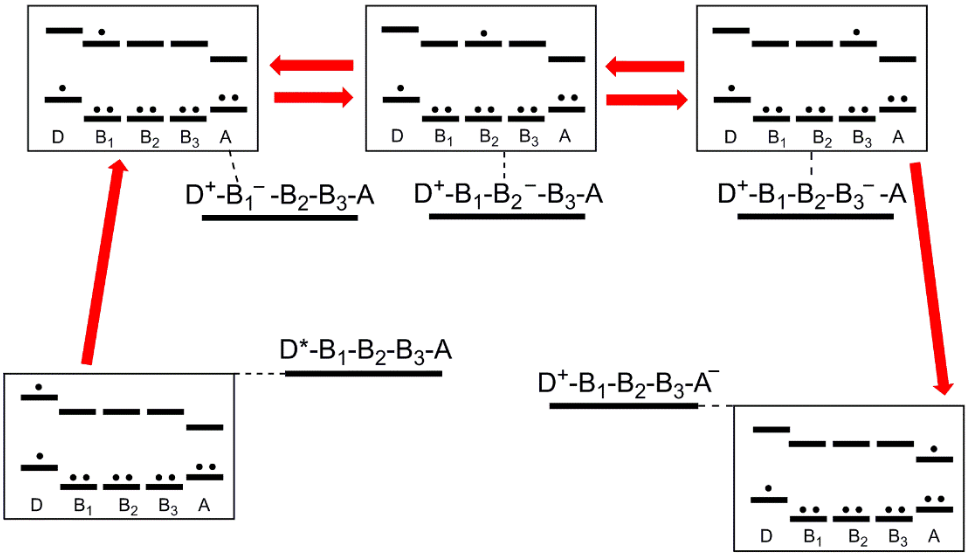

Figure 9. Schematic representation of PET via a hopping mechanism in a D-B-B-B-A system for oxidative ET with low lying LUMOs mediating ET. Single-steps of the exothermic ET and random electron hopping in the bridge are represented by red arrows.[102]

1.1.5 Electron Transfer in Oligogerrocenes

As illustrated in chapter 1.1.1, the electronic interaction of bimetallic complexes can be obtained by $\Delta E_{1/2}$ from electrochemical experiments[99,101] in combination with IVCT bands from UV/Vis/NIR spectroscopy.[13] Compounds with more than one ferrocenyl unit accordingly allow a facile insight into the effects of bridging ligands on the electronic communication of the redox centers. In a compound with n non-interacting, identical redox centers, a separation of redox events of $\Delta E_{1/2} = (\mathrm{R}T/\mathrm{F})\ln(2^n)$ is expected in the statistical limit.[103] In a bimetallic system ($n = 2$) this leads to a minimal theoretical separation of $\Delta E_{1/2} = 36$ mV at 298 K, which is, however, not observable by cyclic voltammetry.

The intensity of electronic coupling depends on the distance of the redox centers and the coupling capabilities of the bridging ligand. The simplest diferrocenyl compound is biferrocene (**I⁰**; Figure 10), in which the iron centers are bridged by a dicyclopentadienediyl bridging ligand. Cyclic voltammetry measurements of **I⁰** show a separation of redox processes of $\Delta E_{1/2} = 350$ mV, showing intensive interaction of the two iron centers.[104] The presence of an NIR absorption for the mixed-valent complex **[I⁰]⁺** at ca $\lambda = 1800$ nm arises from the intramolecular ET between the two redox centers.[105,106] Therefore, **[I⁰]⁺** is classified as Class II system according to Robin and Day.[99] The insertion of an alkyl group between the Cp rings of **I⁰** leads to decreased electronic interaction of the redox centers. In the methylene bridged derivative **I¹**, $\Delta E_{1/2} = 120$ mV is recorded, while already for **I²**, no separation of redox processes is detected and only a single redox event is recorded, in which both ferrocenyl moieties are oxidized.[107] The alkyl bridge, however, does not include any π orbitals, which are able to support electronic coupling. Yet, the observation of separate redox potentials for the homobimetallic complexes **I¹** and **I²** alone is no evidence of the presence or absence of electronic coupling of the redox centers, since mere electrostatic interaction also leads to the separation of redox waves.[100] Therefore, also data from optical spectroscopy (IVCT bands) has to be taken into account. Already for **[I¹]⁺**, no NIR band is detected, indicating that, despite the separation of redox waves, no intramolecular ET is observed.[108]

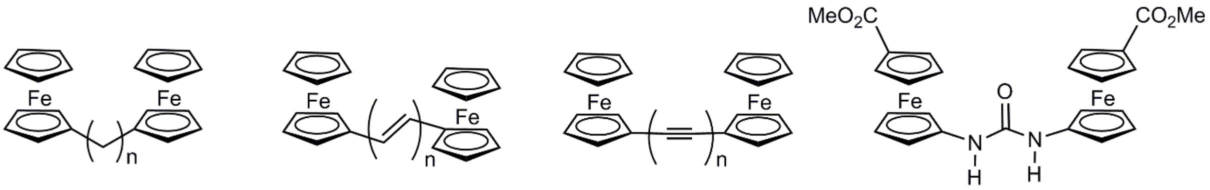

Iⁿ

I⁰: $\Delta E_{1/2} = 350$ mV
I¹: $\Delta E_{1/2} = 120$ mV
I²: $\Delta E_{1/2}$ = n.o.

IIⁿ

II¹: $\Delta E_{1/2} = 160$ mV
II²: $\Delta E_{1/2} = 130$ mV
II³: $\Delta E_{1/2} = 100$ mV
II⁴⁻⁶: $\Delta E_{1/2}$ = n.o.

IIIⁿ

III¹: $\Delta E_{1/2} = 140$ mV
III²: $\Delta E_{1/2} = 100$ mV

IV

$\Delta E_{1/2} = 137$ mV

Figure 10. Difference in redox behavior of various oligoferrocenes with respect to the bridging ligand.

Derivatives with alkenyl bridges like **IIⁿ** (Figure 10) show larger redox separations, even with longer bridges. For the compound with the shortest bridge **II¹** an even larger redox-splitting

($\Delta E_{1/2} = 160$ mV) as for **I^{1}** with the shorter methylene bridge is detected.[107] This result is, however, not very surprising, since the alkyl bridge is not very supporting for the electronic communication as stated above. Again, further elongation of the bridge results in smaller separations. **II$^{2\text{-}6}$** show separations of $\Delta E_{1/2} = 130$ (**II^{2}**), 100 (**II^{3}**), and <60 mV (**II$^{4-6}$**), respectively.[109] In the optical spectra of the mixed-valent complexes **[II$^{1\text{-}6}$]$^{+}$**, however, NIR absorptions resulting from IVCT are not only detected for **II$^{1-2}$**, which show separate redox waves, but also for the compounds with longer bridges.[109] Accordingly, electronic coupling between the ferrocenyl moieties is detected for all mixed-valent complexes **[II$^{1\text{-}6}$]$^{+}$** with decreasing intensity for increasing bridge length. The ethylene bridge allows two conformers (*E* and *Z*). While for these bridges an all-*E* conformation is expected, the orientation of the terminal ferrocenyl moieties can also adapt two positions (*syn* and *anti*), which has an influence on the metal-metal distance and hence on the ET.[109] However, the detection of NIR absorptions for all mixed-valent complexes **[II$^{1\text{-}6}$]$^{+}$**, is an illustrative example for the erroneous assumption that electronic coupling can be obtained only by separate redox waves for homobimetallic complexes as it was also presented by Winter in a recent review.[100]

A similar trend in redox-separation is observed for alkynyl bridged ferrocenes **III^{n}** (Figure 10). While for **III^{1}** $\Delta E_{1/2} = 140$ mV is detected,[104] the longer bridge in **III^{2}** reduces the separation to $\Delta E_{1/2} = 100$ mV.[105] Again, both mixed-valent compounds display NIR bands representing IVCT transitions with decreasing intensity for increased bridge length.[105] Another bimetallic system with identical redox systems showing electronic interaction is a diferrocenyl urea compound **IV** (Figure 10) with $\Delta E_{1/2} = 137$ mV.[110] For the mixed-valent complex **[IV]$^{+}$** a weak NIR band is detected.[110] Hence, the ureylene bridge is also able to mediate intramolecular ET reactions, as **[IV]$^{+}$** displays Class II behavior according to Robin and Day.[99]

When using 1,n'-ferrocendiyl complexes with different substitution patterns as redox active building blocks in oligonuclear arrays, the single redox events are of course shifted due to the dissimilar substituent effect, but ET over an asymmetric bridging unit can still be obtained depending on the electronic dissimilarity. Oligomers of 1,1'-ferrocenedicarboxylic acid and 1,1'-diaminoferrocene (**V^{n}**; Figure 11) by Kraatz *et al.* show two redox events. The one at lower potential is straight-forwardly assigned to the diamino substituted ferrocenediyl units, while the other one represents the dicarboxylic acid substituted units. However, a comparison of the compounds **V$^{1-3}$** in electrochemical investigations ($\Delta E_{1/2} = 681$, 675, and 662 mV for **V^{1}**, **V^{2}**, and **V^{3}**, respectively) as well as the absence of NIR absorptions for the mixed-valent compounds **[V$^{1-3}$]$^{+}$** shows essentially no electronic communication between the chemically very different redox centers.[111] Accordingly, the separation observed in the cyclic voltammetry measurements results merely from the different substitution patterns and partly electrostatic interaction.

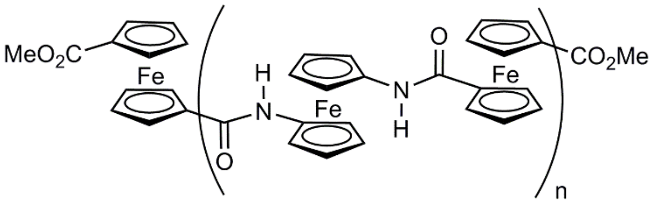

V^{n}

V^{1}: $\Delta E_{1/2}$ = 681 mV
V^{2}: $\Delta E_{1/2}$ = 675 mV
V^{3}: $\Delta E_{1/2}$ = 662 mV

Figure 11. Difference in electronic communication of various oligoferrocenes of 1,1'-ferrocenedicarboxylic acid and 1,1'-diaminoferrocene with respect to the chain length.

Oligomers of 1-amino-1'-carboxylic acid **VI**^{n} (Figure 12), however, show electronic interaction of the identically substituted ferrocendiyl units. A separation of the first and second redox event of $\Delta E_{1/2}$ = 160, 85, 75, and 75 mV is recorded for **VI**^{1}, **V**^{2}, **V**^{3}, and **V**^{4}, respectively.[26] This observation is even more remarkable, since upon second oxidation of compounds **V**$^{2-4}$, the second oxidation does not occur on neighboring ferrocenediyl units, but on other metal centers, which are further away in the peptide chain. This is due to electrostatic interaction,[112] but also influenced by electronic communication over the hydrogen bond network (see chapter 1.2). For all mixed-valent complexes **[VI**$^{1-4}$**]**$^{+}$, IVCT transitions were recorded around $\lambda = 1100 - 1200$ nm.[26]

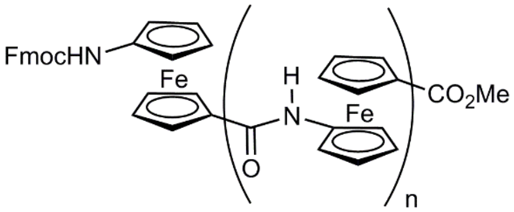

VI^{n}

VI^{1}: $\Delta E_{1/2}$ = 160 mV
VI^{2}: $\Delta E_{1/2}$ = 85 mV
VI^{3}: $\Delta E_{1/2}$ = 75 mV
VI^{4}: $\Delta E_{1/2}$ = 75 mV

Figure 12. Difference in electronic communication of various oligoferrocenes of 1-amino-1'-ferrocenecarboxylic acid with respect to the chain length.

1.1.6 Proton Coupled Electron Transfer

Combined proton transfer (PT) and ET reactions play an essential role in many biological systems and are are in the focus of many research activities.[21,29–34,37,39–41,113–120] In sequential PT and ET, the proton and the electron are transferred to different orbitals/molecules in subsequent steps, while in proton coupled electron transfers (PCET), proton and electron are transferred in a concerted manner to different substrates.[21] PCET reactions are the basis in a plethora of crucial redox centers in organisms, like cytochrome *c* oxidase[121,122] and reductase[123,124] and in photosynthesis.[34,39–41,113,117,125] In the latter, a very prominent example is found in photosystem II (PS II). The electron hole produced upon excitation of P680 is filled via a PCET reaction by a tyrosyl residue, which is coordinated by a nearby histidine base as proton shuttle (Scheme 1). The resulting tyrosyl radical is subsequently reduced by the oxygen evolving complex (OEC), which finally fills the electron hole by the oxidation of water, releasing oxygen.[40,41,44,117,126]

Scheme 1. PCET of a tyrosyl residue in photosystem II.[127]

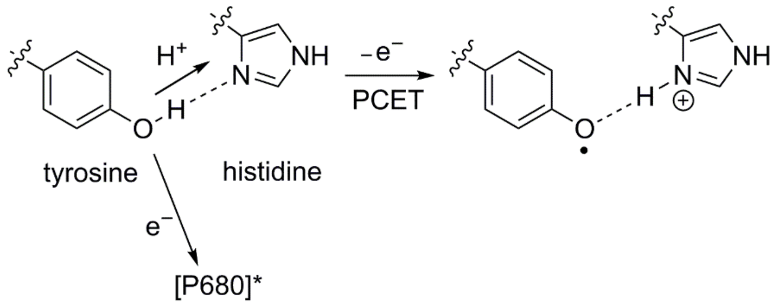

The reason for this complicated mechanism is of energetic nature. A simple example is a stepwise PT and ET reaction from phenol yielding the respective phenoxyl radical (Scheme 2). When performing these processes in subsequent steps, one process is often energetically unfavored. Deprotonation of phenol for instance requires a strong base to form the phenolate anion (Scheme 2, top). The oxidation of the phenolate, however, is achieved at a very low electrochemical potential (Scheme 2, right). On the other hand, oxidation of phenol requires a much higher potential than the phenolate (Scheme 2, left), while deprotonation of the obtained radical cation is performed with a weak base (Scheme 2, bottom). The combination of both processes in a single coupled mechanism eliminates high energy intermediates, thus it is easily executed in biological systems (Scheme 2, diagonal pathway).[115]

Scheme 2. PT and ET reactions from phenol to yield a phenoxyl radical in single steps and as coupled process.[115]

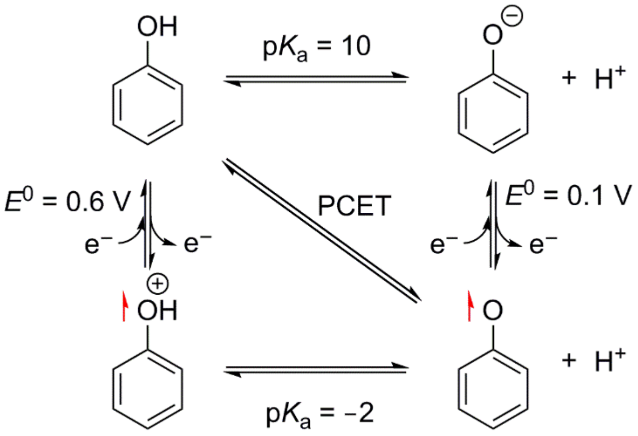

Accordingly, the combination of PT and ET reactions allows avoiding thermodynamically unfavored reactions. In oligomers of 1-amino-1'-ferrocenecarboxylic acid (see chapter 1.2), the intimate coupling of PT and ET processes is further illustrated. While the monoferrocenyl amide *N*-acteylaminoferrocene (**VII**) is reversibly oxidized at a potential of ($E_{1/2}$ = −75 mV vs. FcH/FcH$^+$ in CH_3CN/[^{n}Bu$_4$N][PF$_6$]) (Scheme 3a),[128,129] the diferrocenyl amide **VIII** shows its first oxidation at the terminal ferrocenylamine moiety at $E_{1/2}$ = −115 mV vs. FcH/FcH$^+$ in CH_3CN/[^{n}Bu$_4$N][PF$_6$] (Scheme 3b).[128,129]

Scheme 3 Lewis structures and hydrogen bonds in a) mono and b) diferrocenyl amides and their influence on redox behavior.

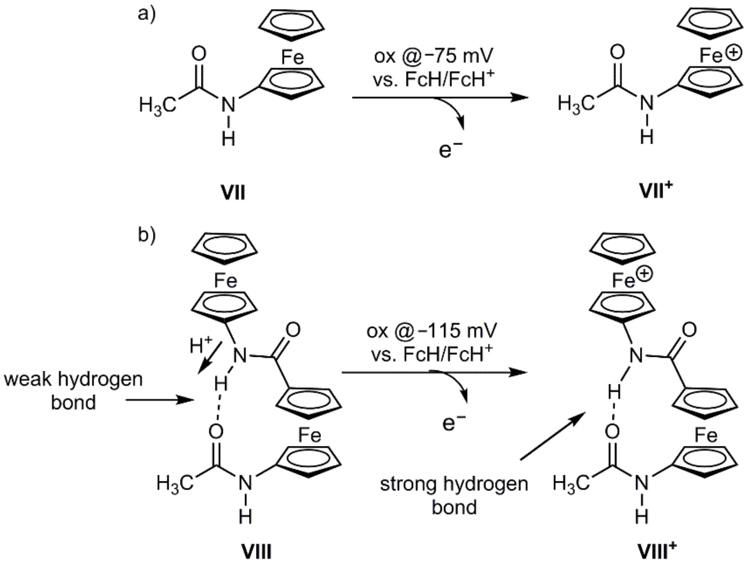

Since in both compounds, the same mono-substituted ferrocenyl moiety is oxidized, this difference in redox chemistry is attributed to the intermolecular hydrogen bond in **VIII**, in which the amide proton of the terminal ferrocenyl amide group is coordinated by the oxygen atom of the other amide group. Due to the increased hydrogen bond donating abilities of ferrocenium amides,[130] this coordination decreases the redox potential of the terminal ferrocenyl group, while the intramolecular hydrogen bond becomes stronger upon oxidation. This effect is even further enhanced in longer oligomers.[25,26]

1.2 Ferrocene Foldamers

Peptides built up from natural amino acids form secondary structures in solution and in the solid state due to the interaction of the amide bonds. The most prominent structures are α-helices and β-sheets.[131] These secondary structures enable the proteins to fulfill a plethora of functions in biological systems. Hence, they receive a lot of attention from researchers around the world. For better understanding of the secondary structures and to tune molecular properties, respectively, the introduction of artificial building blocks is a promising tool. In this respect, a lot of research has been conducted with peptides containing ferrocenediyl moieties like 1,1'-ferrocenedicarboxylic acid, 1,1'-diaminoferrocene, and 1-amino-1'-ferrocenecarboxylic acid (**Fca**) (Figure 13).

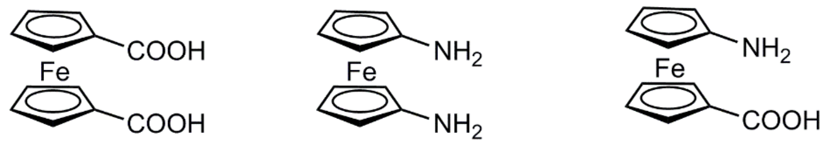

1,1'-ferrocene-dicarboxylic acid

1,1'-diaminoferrocene

1-amino-1'-ferrocene-carboxylic acid (Fca)

Figure 13. Ferrocene derivatives used in peptides.

The ferrocene moieties show conformational freedom by rotation around the pseudo-C_5 axis. However, very stable secondary structures are formed in the solid state and in solution for peptides of the building blocks shown in Figure 13. Therefore, a stereochemical nomenclature is needed to clarify the relative position of the single substituents. This is illustrated in Figure 14 for ferrocene derivatives featuring a single substituent at each Cp ring. If both substituents are attached at C-atoms aligned on top of each other, the conformation is called 1,1'. Substitution on neighboring C-atoms or in an opposite orientation, are called 1,2'- or 1,3'-conformation, respectively.[132]

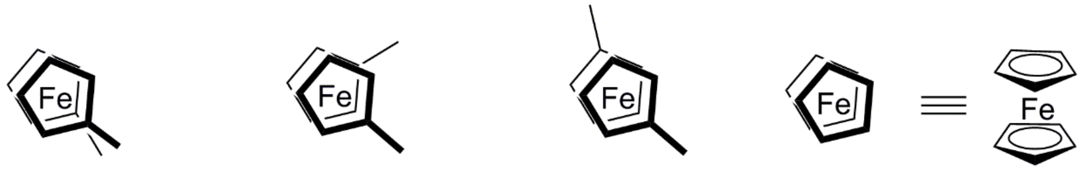

1,1' conformation

1,2' conformation

1,3' conformation

Figure 14. Stereochemical description of substitution pattern utilized in ferrocene peptides

7 – 14-membered rings (iron atom not counted) in a 1,2’-conformation are found for peptides of 1,1-ferrocenedicarboxylic acid, 1,1’-diaminoferrocene, and 1-amino-1’-ferrocenecarboxylic acid with natural α-amino acids as intensely studied by Barišić,[133] Hirao,[134–137] Kraatz,[138] Metzler-Nolte,[139,140] as well as Heinze and Rapić.[141–147] The helices formed by those peptides are classified as “Herrick” conformation, which is detected in solution and in the solid state. Some examples are illustrated in Figure 15.

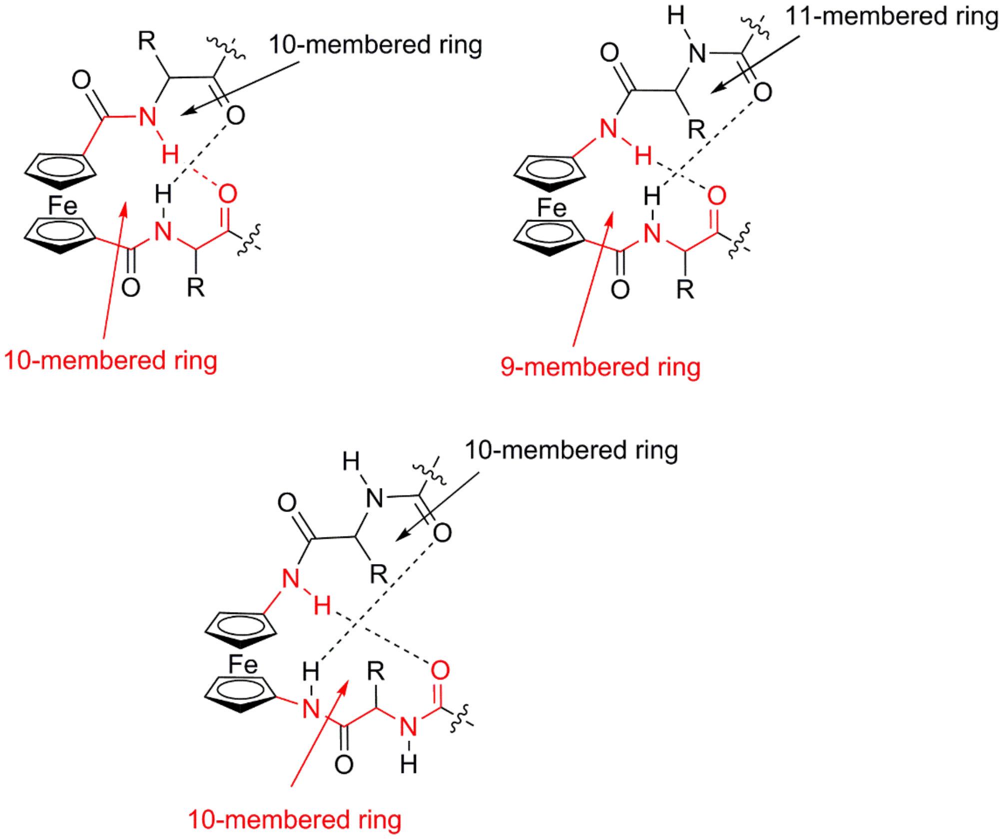

Figure 15. 8 – 11-membered rings of 1,1’-disubstituted ferrocene containing peptides.

Oligomers of **Fca**, however, display a different behavior. As deeply investigated by Heinze *et al.*, these compounds form 8-membered rings in a 1,2’ conformation (Figure 16a).[25,26,112] This structure is even retained upon oxidation due to increased hydrogen bond donating abilities of ferrocenium amides in spite of repulsive interaction resulting from charge accumulation in the peptide wires. Only upon full oxidation, the splitting of all intramolecular hydrogen bonds resulting in an extended structure was predicted by DFT methods (Figure 16b).[25,26]

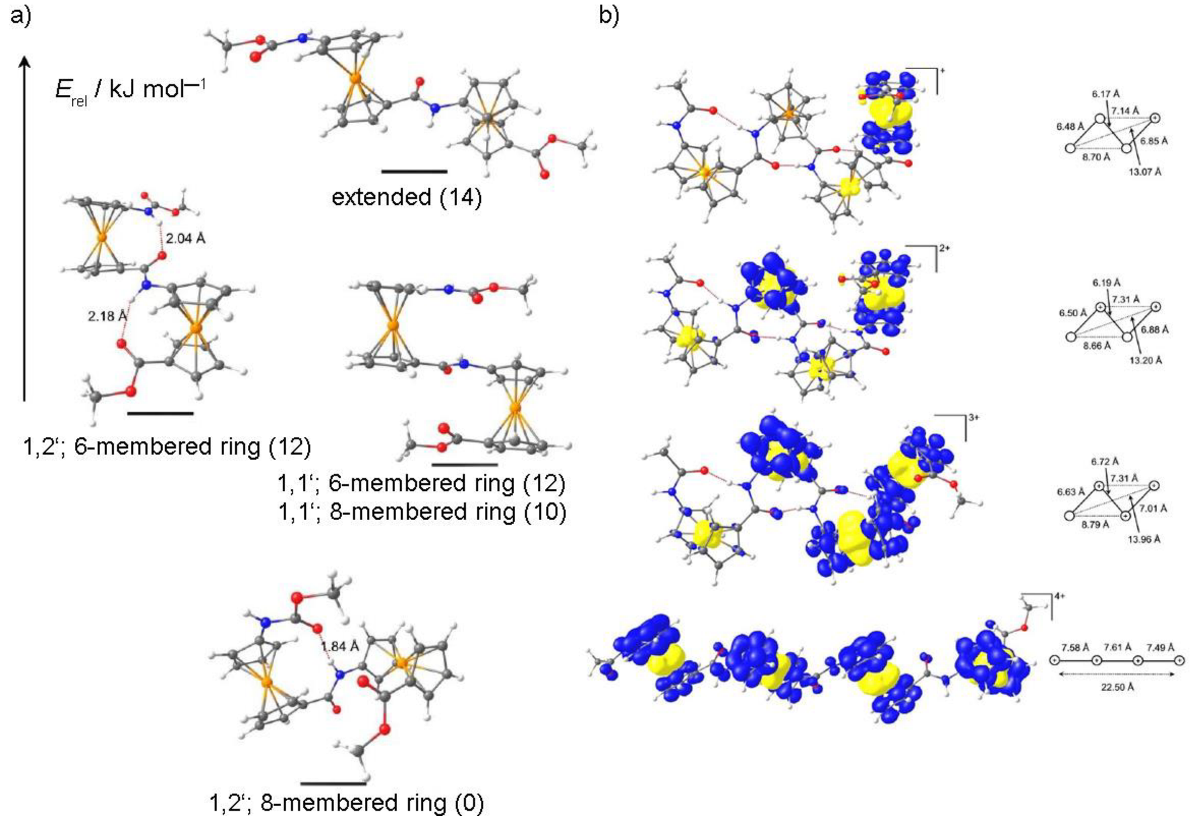

Figure 16.[2] DFT optimized geometries (LANL2DZ, B3LYP) of a) possible conformers of a neutral diferrocenyl amide showing relative energies and b) behavior of a tetraferrocenyl amide upon stepwise oxidation (top to bottom) with Fe-Fe distances and spin densities (isosurface 0.001 a.u.).[148]

1.3 Elucidation of Secondary Structures of Ferroceneamides

As illustrated in chapter 1.2, oligoferrocene amides of 1-amino-1’-ferrocenecarboxylic acid are able to form several secondary structures, which differ in the conformation of intramolecular hydrogen bonds (6-membered vs. 8-membered ring). For the assignment of all chemical shifts in ^{1}H and ^{13}C NMR spectroscopy, 2D methods like HMBC and HSQC are insufficient, since no couplings are observed over the iron centers. Thus, only individual fragments can be determined by these methods. For unambiguous elucidation of all signals, and importantly, of the secondary structures in solution, utilization of another 2D NMR spectroscopy method is required. Nuclear Overhauser effect spectroscopy (NOESY) allows to get information about the spatial proximity of different protons through space (NOE contacts). In oligoferrocenyl amides, NOESY allows detection of contacts between the amide protons and α-Cp protons as well as protons from other substituents in close proximity. Therefore, NOE contacts allow the assignment of all resonances and provide information about the secondary structure. DFT calculations, on the other hand, provide relative energies for the various conformers.

---

[2] Figures adapted from D. Siebler, *Dissertation*, Johannes Gutenberg-University, **2010**.

Accordingly, theoretical calculations are an essential tool to get insight into the secondary structure of such peptides and partly overcome the drawbacks of NMR spectroscopy in that field. This was intensively studied by Heinze *et al*. on oligoferrocenyl amides.[25,26] For a diferrocenyl amide, the NOE contacts of the amide protons are exemplarily depicted in Figure 17. The respective relative energies of the possible conformers are shown in Figure 16. Contacts of an NH proton from a bridging amide group (NH^z) to the α-protons of the adjacent amino substituted Cp ring ($H^{2z/5z}$) and to the α protons of the adjacent carbonyl substituted Cp ring ($H^{7a/10a}$) are always detected for single fragments. The essential contact for the corroboration of the 1,2'-8-membered ring geometry is the one from the amide proton (NH^z) to the α-protons of the next amino substituted Cp ring ($H^{2a/5a}$) over the iron atom.[26]

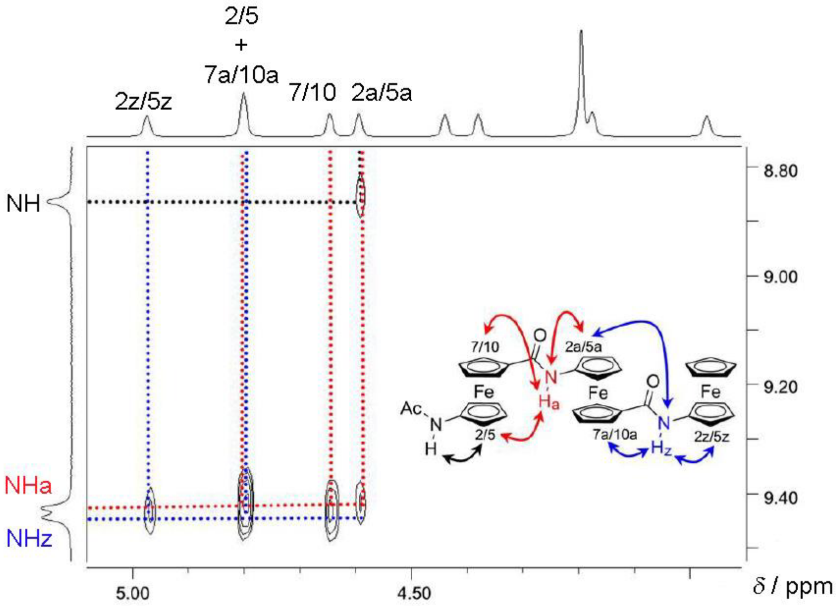

Figure 17.[3] **Partial NOESY spectrum of a triferrocenyl amide showing contacts between amide protons and α-Cp protons in THF-d8.**[148]

1.4 Ferrocene-Containing (Pro-)Drugs

Ferrocene derivatives are used as (pro-)drugs e.g. in antitumor and antimalaria medication.[65–67,69,71,73,77,78,149] While ferrocene itself does not show any pharmaceutical activity and is non-toxic, the derivatives described in this chapter show an even greater activity than the corresponding ferrocene-free drugs.[72,79] Chloroquine (**IX**) is a renowned ferrocene-free antimalaria drug, which prevents biocrystallization of hemozoin – a metabolic product formed by the malaria parasites from heme – thus the parasite-infested cells "drown" in their own products.[150] Increased effectiveness is achieved by incorporation of a ferrocenyl residue,

---

[3] Figure adapted from D. Siebler, *Dissertation*, Johannes Gutenberg-University, **2010**.

yielding ferroquine (**X**, Figure 18). The additional mode of action in comparison to **IX** is the generation of reactive oxygen species in **X**.[65–67]

Mohkir *et al*. presented a class of aminoferrocene- and diaminoferrocene-based prodrugs (**XI** and **XII**, Figure 18), which are activated in cancer cells due to higher amounts of reactive oxygen species, which are not found in normal cells, but show high concentration in cancer cells. Accordingly, **XI** and **XII** show an increased targeting. The ferrocenium moieties are oxidized to the corresponding ferrocenium ions **XI**$^+$ and even further decomposed to iron(II) compounds in cancer cells, where they appear to catalyze the additional production of reactive oxygen species leading to the death of the cancer cells. [68,70,76]

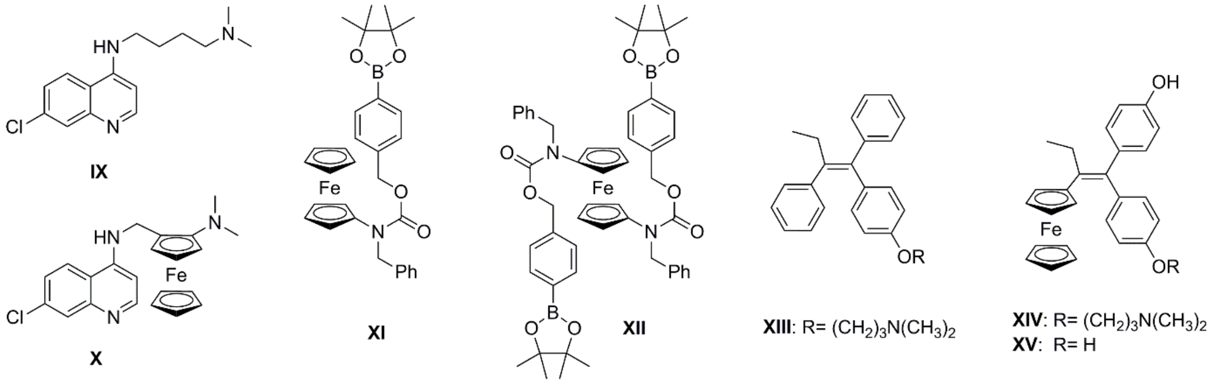

Figure 18 Lewis structures of ferrocene-free drugs chloroquine IX and tamoxifen XIII and ferrocene-based drugs ferroquine X, ferrocifen XIV, ferrociphenol XV, and ferrocene-based prodrugs by Mokhir *et al.* XI and XII.

A prominent ferrocene-free compound in the treatment of breast-cancer is tamoxifen (**XIII**; Figure 18), which works as selective estrogen-receptor modulator, i.e. it regulates cell growth and proliferation, which is, when malfunctioning, a main reason for hormonal induced breast-cancer.[151] It furthermore induces oxidative stress and apoptosis via mitochondria-dependent nitric oxide pathways.[152,153] Ferrocifen (**XIV**) and ferrociphenol (**XV**), which are also used in the treatment of breast-cancer, however, show less oxidative stress, while simultaneously resulting in higher rates of senescence on cancer cells.[72,79] This is attributed to the higher versatility of the redox active ferrocenium moiety in comparison with purely organic pharmaceuticals like **XIII**. A proposed mode of action next to the generation of reactive oxygen species as for **XI**, **X**, and **XII**, is the formation of carbon-centered ferrocenyl radicals as anticipated to be formed upon oxidation and deprotonation of **XIV** and **XV**.[71]

The reaction of ferrocenium ions with nucleophiles have been amply studied,[154–160] revealing cleavage of one or both Cp rings by the attack of nucleophiles like chloride or bromide, yielding FeX_4^- (X = Cl, Br), as evidenced by identical EPR spectra as genuine FcX_4^-.[154,158,160] In presence of hydroxide, $Fe(OH)_3$ is formed analogously by decomposition of ferrocenium.[159] Other experiments dealt with the formation of carbon-centered ferrocenyl radicals, which are obtained by photolysis and thermolysis of ferrocenyl azide as illustrated by Sutherland *et al.*[161] as well as by Jackson and Zarkadis *et al.* from methylferrocene by *γ*-

irradiation.[162] These ferrocenyl radicals are able to stabilize themselves by spin delocalization onto the iron atom, leading to higher persistence of such species compared to highly reactive organic radicals.[163,164] Spin-trapping (see chapter 1.6.3) allows the analysis of the radical compounds by transforming them into stable radical adducts, as presented by Ashkenazi and Cais on ferrocenylmethylium cations by the trapping reaction with nitrosobenzene.[165] Accordingly, the investigation of ferrocenyl-based radicals is essential to understand additional modes of action of pharmaceutically potent ferrocene derivatives.

1.5 Stable Phenoxyl Radicals

As illustrated in chapter 1.1.6, PCET reactions are a key elemental reaction in nature and chemistry. The investigation of many organic redox couples in the laboratory is nonetheless difficult, since the highly reactive radical intermediates are not stabilized by protein environments in simple model systems. The essential phenoxide (tyrosyl radical; Tyr$_Z$) in photosystem II[126] for example is not easily studied. Unsubstituted phenoxyl radicals undergo rapid follow-up reactions by recombination processes or H-atom abstraction from the solvent or other molecules (Scheme 4).[118,166,167] The radicals can however be stabilized by two ways: kinetically by substitution at the positions with high spin density (*o* and *p* positions of the aromatic ring) and thermodynamically by hydrogen bonding to the oxygen atom. Several examples of stabilized phenoxyl radicals are found in the literature.[116,120,127,168–170] A widely used sterically demanding substituent for the aromatic ring is the *tert*-butyl group, while hydrogen bonding is achieved by *o*-substitution with nitrogen containing residues. These either contain an imine group (similar to Scheme 1), which allows hydrogen bonding of the phenol proton, or an amide function, allowing hydrogen bonding of the phenolate/phenoxyl oxygen atom by the amide proton (Scheme 5). In the phenol/phenoxyl pairs in Scheme 5 a/b an actual PCET is detected, since deprotonation and oxidation of the phenol is intimately coupled by the intramolecular hydrogen bonds (IHBs).

Scheme 4. Resonance structures and *ortho*-coupling of unsubstituted phenoxyl radicals.

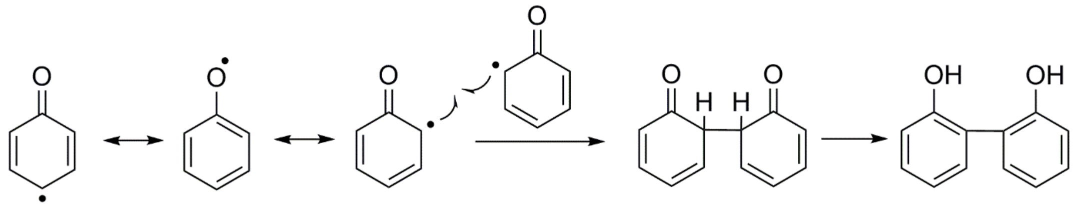

Scheme 5. Phenoxyl radicals stabilized by IHBs to a) an iminium group,[116,168,169] b) an ammonium group,[127] and c) an amide group.[120]

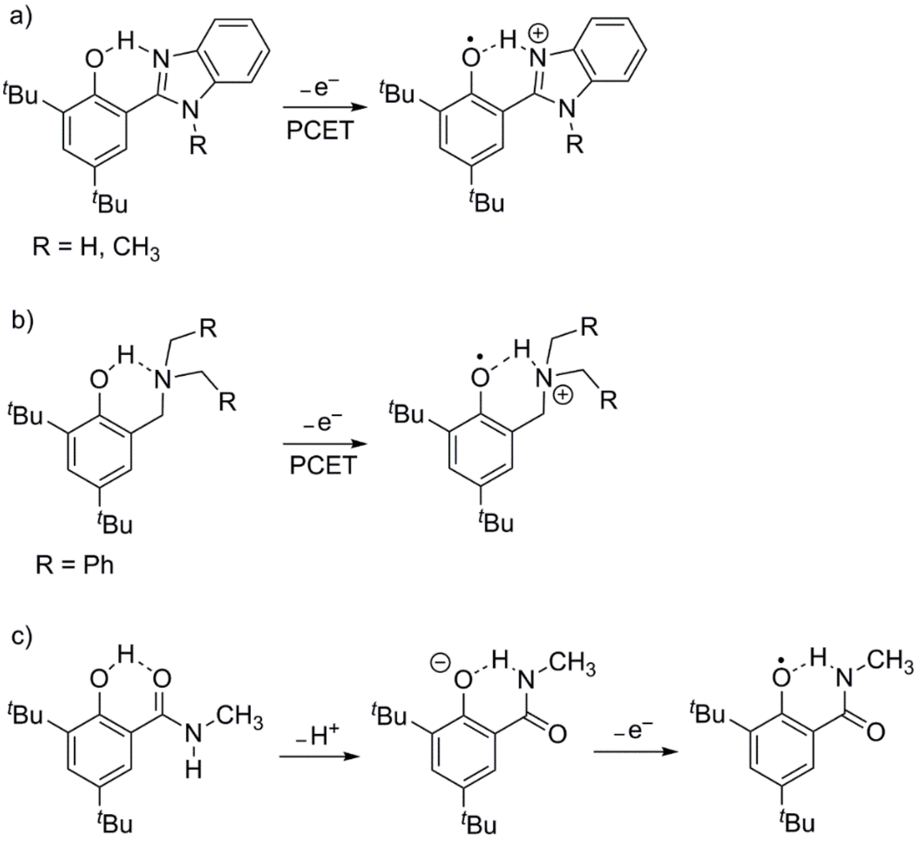

These stabilized phenoxyl radicals are suitable structures for the investigation of inter- and intramolecular PCET reactions, since redox potentials and stability are directly tunable by the hydrogen bond, while dimerizations are suppressed. Wenger *et al.* presented a bimolecular reductive quenching of an excited rhenium(I)-phenanthroline complex by PCET from an intramolecularly hydrogen bonded phenol (Scheme 6 a)[171] and monomolecular reductive quenching of an excited tris(bipyridine)-ruthenium(II) complex in combination with an external base (Scheme 6b).[172] Another example showing PCET to an unstabilized phenoxyl radical is shown in Scheme 6c, where intermolecular PCET from 4-cyanophenol to tris(bipyrazine)-ruthenium(II) upon excitation is described.[173]

Scheme 6. Photoexcited inter- and intramolecular PCET reactions forming phenoxyl radicals from phenols.[171–173]

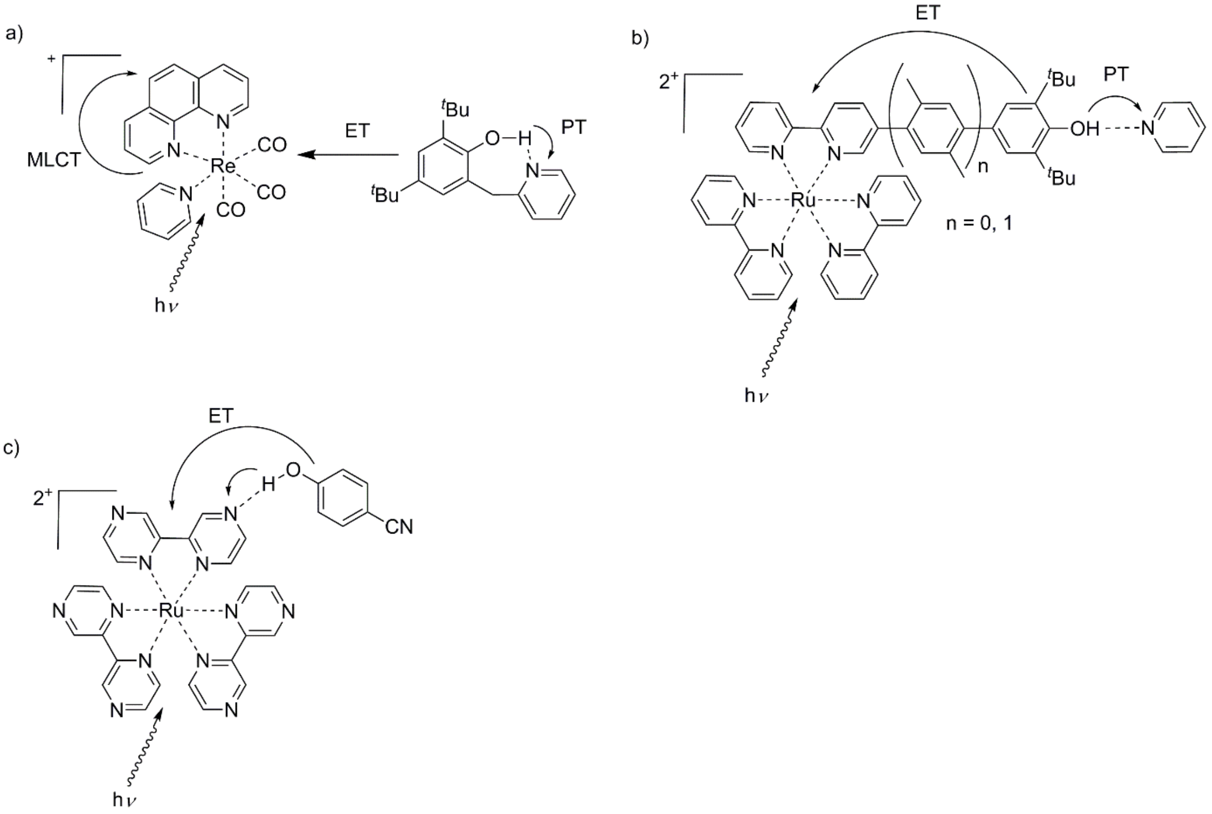

1.6 EPR Spectroscopy

Paramagnetic compounds, such as phenoxyl radicals and ferrocenium derivatives, can be studied by Electron Paramagnetic Resonance (EPR) spectroscopy, which makes use of the magnetic moment of unpaired electrons. Accordingly, EPR spectroscopy is a great addition to NMR spectroscopy, which makes use of the nuclear spin and is often not applicable to paramagnetic compounds. The measurement principle is the same for EPR and NMR spectroscopy, but EPR is much more sensitive than NMR so that even small amounts of a paramagnetic substance can be detected.[174] As the chemical shift and coupling patterns in NMR spectroscopy reveal the environment of the examined nuclei, EPR also shows a shift of the signal (g-value) and displays couplings with nuclei with $I \neq 0$. Hence, electronic and geometric structure information about the environment of the unpaired electron is received.

1.6.1 General Aspects

The unpaired electron has a spin of $s = ½$. Upon application of an external magnetic field, the degenerate levels of the electron spin m_S (intrinsic angular momentum) are separated. This is called the Zeeman effect and results in an increasing energy difference between parallel and antiparallel orientation of the spin with increasing magnetic field (Figure 19, top). An EPR transition is allowed, when the resulting change of intrinsic angular momentum Δm_S equals ±1. The absorption is detected, when the energy of the microwave irradiation equals the energy difference ΔE of those two spin states (Figure 19, top).[174,175] The resonance absorption in EPR spectroscopy has a relatively high line width, hence detection of the absorption of radiation, as in NMR spectroscopy, is unfavorable. The first derivative is used instead for the analysis (Figure 19, bottom).

During the measurement, the sample is placed in a cavity with microwave irradiation of constant frequency (continuous wave, CW), while the magnetic field is swept. The EPR spectra in this work were recorded at a microwave frequency of $\nu = 9.4$ GHz (X-band). To fulfil the resonance conditions shown in equation (4) for the X-band, the magnetic field needs to be at $B \approx 100-400$ mT (1000−4000 G).

$$\Delta E = \mathrm{h}\ \nu = g\ \mu_B\ B \qquad (4)$$

(g = g-value; μ_B = Bohr magneton; B = magnetic field)

Similar to the chemical shift δ in NMR spectroscopy, the g-value or Landé factor represents a substance specific parameter. For the free electron, the g-value is $g_e = 2.0023$.

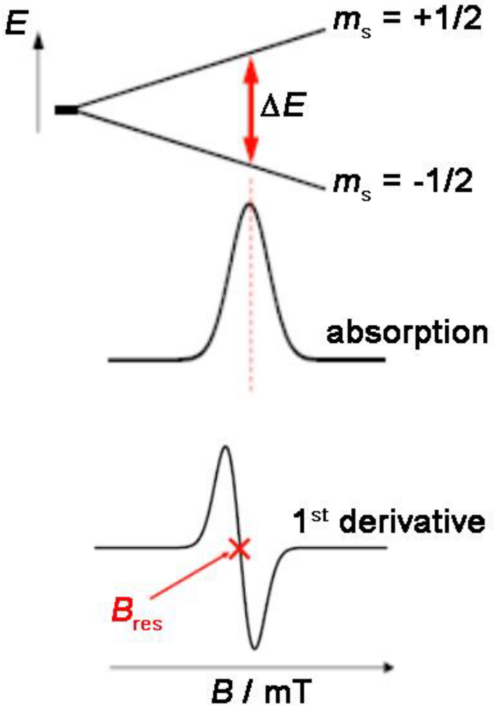

Figure 19: Example for $S = 1/2$; resonance conditions and splitting of m_s states (top), absorption spectrum (middle), first derivative of the absorption spectrum (bottom).[175]

The g-value is determined by the zero crossing of the first derivative of the resonance with equation (5).

$$g = h\,\nu / m_B\, B = 714.5\ \nu / B_{res} \qquad (5)$$

(ν = applied frequency in GHz; B_{res} = resonance B field in Gauss (Figure 19, bottom))

For simple radicals, in which no nuclei with $I \neq 0$ are nearby, a singlet resonance is recorded. If the atom on which the unpaired electron is located has a nuclear spin $I \neq 0$, the resonance of the unpaired electron is split by magnetic interaction between the electron spin and the nuclear spin. This is based on additional spin states as determined by equation (6). Furthermore, only transitions following the resonance conditions as in equation (7) are allowed (see Figure 20).

$$m_I = 2n\,I + 1 \qquad (6)$$

(n = number of equivalent nuclei, I = nuclear spin)

$$\Delta m_S = \pm 1 \text{ and } \Delta m_I = \pm 0 \qquad (7)$$

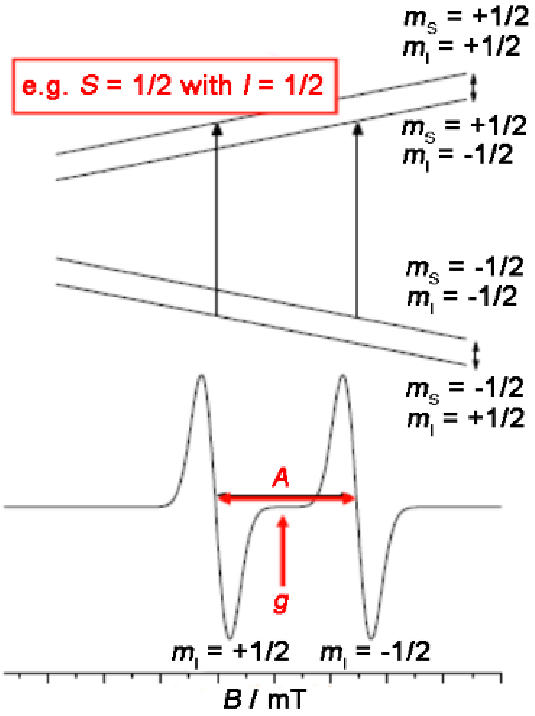

Figure 20: Example of hyperfine coupling for S = 1/2 and I = 1/2 with the allowed transitions (top) and the recorded signal (bottom).[175]

The splitting of the EPR resonance is called hyperfine coupling, when the unpaired electron is located on the nucleus with $I \neq 0$, whereas it is called superhyperfine coupling, when the nucleus is in close proximity. The resulting coupling constants A provide information about the radical environment, since they are nucleus specific and distance dependent. Similar to NMR spectroscopy, stick spectra can be used to determine the relative intensities of the signals. 2,2-Diphenyl-1-picrylhydrazyl (DPPH; Figure 21, bottom right), a stable organic radical often used for *g*-value calibration, has one unpaired electron, which is located at the two nitrogen atoms of the hydrazyl group. Both ^{14}N atoms have an accidentally identical coupling constant of $A^{14}N = 9.1$ G and according to equation (6) a pentet signal is recorded (Figure 21, bottom left) with signal intensities of 1:2:3:2:1 as derived from the stick spectrum (Figure 21, top left).

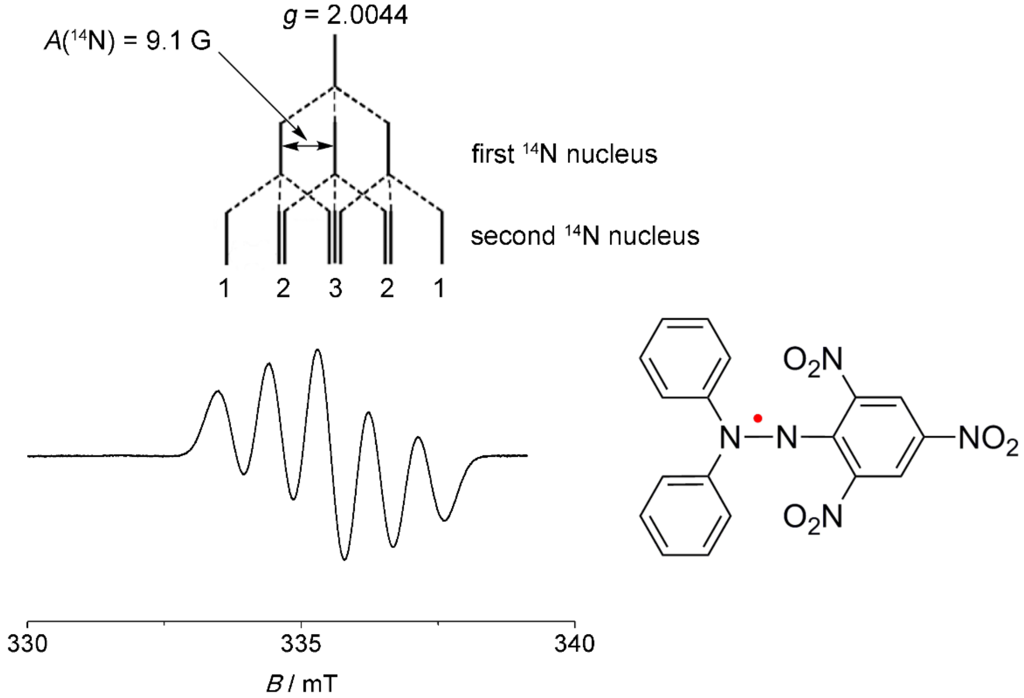

Figure 21: X-band EPR spectrum of 2,2-diphenyl-1-picrylhydrazyl (DPPH) in CH_2Cl_2 at 298 K (bottom left), stick spectrum explaining signal intensities (top left), and molecular structure of DPPH (bottom right).

Measurements in solution at room temperature usually allow rapid tumbling of the molecules on the EPR timescale. Thus, only an average signal of the molecule's resonance is recorded, resulting in the isotropic spectrum shown in Figure 21. Since paramagnetic compounds, especially metal complexes, usually are not spherically symmetric, they "look differently" from the x, y, and z direction. The *g*- and *A*-values are tensors, which depend on the orientation. In fluid solution, only an average value over the three directions is recorded as shown in equation (8).[174]

$$g_{\mathrm{iso}} = (g_{\mathrm{x}} + g_{\mathrm{y}} + g_{\mathrm{z}}) / 3 \text{ and } A_{\mathrm{iso}} = (A_{\mathrm{x}} + A_{\mathrm{y}} + A_{\mathrm{z}}) / 3 \qquad (8)$$

Measuring paramagnetic samples in frozen solution or as powder allows detection of anisotropic spectra, in which different *g*- and *A*-values can be determined for the x, y, and z, directions. This is discussed exemplarily for ferrocenium compounds in chapter 1.6.2. While the detection of anisotropic *g*- and *A*-values from measurements in the solid state even gives greater insight into the surrounding of the unpaired electron, especially small hyperfine and superhyperfine couplings are usually not detected due to the greater line width in such spectra resulting from overlapping of couplings.

In addition, if the unpaired electron is located in an orbital with non-zero orbital angular momentum, the unpaired electron interacts with the orbital angular momentum by spin-orbit coupling (SOC). This leads to a direction-dependent shift of the g-value with respect to g_e, as calculated by equation (9). This g-shift represents the difference of the detected g-value and g_e. In general, this can be imagined as mixing of the unpaired electron, located in a singly occupied molecular orbital (SOMO), into neighboring occupied or unoccupied orbitals of similar energy, as illustrated in Figure 22 for mixings into the highest occupied molecular orbital (HOMO) or into the lowest unoccupied molecular orbital (LUMO).[175] If mixing of the SOMO with an unoccupied orbital takes place, a magnetic field in the opposite direction of the local field is induced, resulting in $g < g_e$, while mixing with an occupied orbital leads to the opposite results $g > g_e$ by inducing a field parallel to the local one.[175]

$$g = g_e \pm (a^2\, n\, \lambda \,/\, \Delta E) \qquad (9)$$

(a^2 = covalency parameter, n = quantum mechanical coefficient,
λ = SOC constant, ΔE_{orb} = energy difference between involved orbitals)

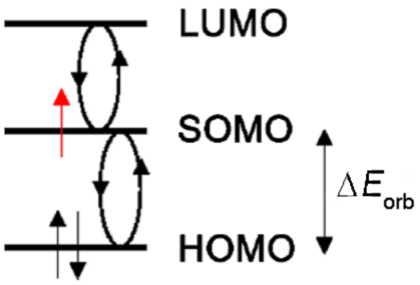

Figure 22: EPR transitions (mixing) of an unpaired electron (red arrow) into the HOMO or the LUMO.[175]

For organic radicals, the HOMO-LUMO gap or ΔE_{orb}, respectively, is usually large, which is also oberservable by the absence of optical absorptions in the visible part of the spectrum, while SOC can be neglected. Such radicals usually show g-values of $g \approx 2.002 - 2.003$, (hydrocarbon radicals), $g \approx 2.003 - 2.006$, (N/O-based radicals), and $g \approx 2.007 - 2.010$, (sulfur-based radicals).[175] On the other hand, radicals of heavier elements, e.g. of transition metals, have small ΔE_{orb}, due to the ligand field splitting of the d orbitals. Furthermore, the SOC constant is larger for heavier elements. Thus, their g-values strongly differ from g_e. This is discussed in detail for ferrocenium compounds in chapter 1.6.2

1.6.2 EPR Spectroscopy of Ferrocenium Compounds

As mentioned above, the g-value of transition metal radicals differs from g_e, due to small ΔE_{orb} (ligand field splitting) and increasing SOC. Unsubstituted ferrocenium does not display any EPR resonances above temperatures of 77 K due to short relaxation time originating from degenerate MOs (d_{xy} and d_{x2-y2}) carrying the spin density. The fast spin-lattice relaxation results in very broad signals that are usually not detectable at temperatures above 77 K.[160] At lower temperatures, however, a very broad, highly anisotropic signal was recorded at $g_z = 4.35$ and $g_{x,y} = 1.26$.[160] The broad resonance in combination with the fast relaxation makes higher concentrations, normally unsuitable for the highly sensitive EPR spectroscopy, of 10 – 20 mM necessary. Substitution of ferrocenium salts, e.g. in 1-amino-1'-ferrocenecarboxylic acid, decreases the symmetry of the system and thus lifts the degeneracy of the orbitals, which allows detection of EPR resonances already at 77 K. A derivative of 1-amino-1'-ferroceniumcarboxylic acid for instance delivers a detectable signal at 77 K at $g_z = 3.022$ and $g_{x,y} = 1.940$ (Figure 23, left).[148]

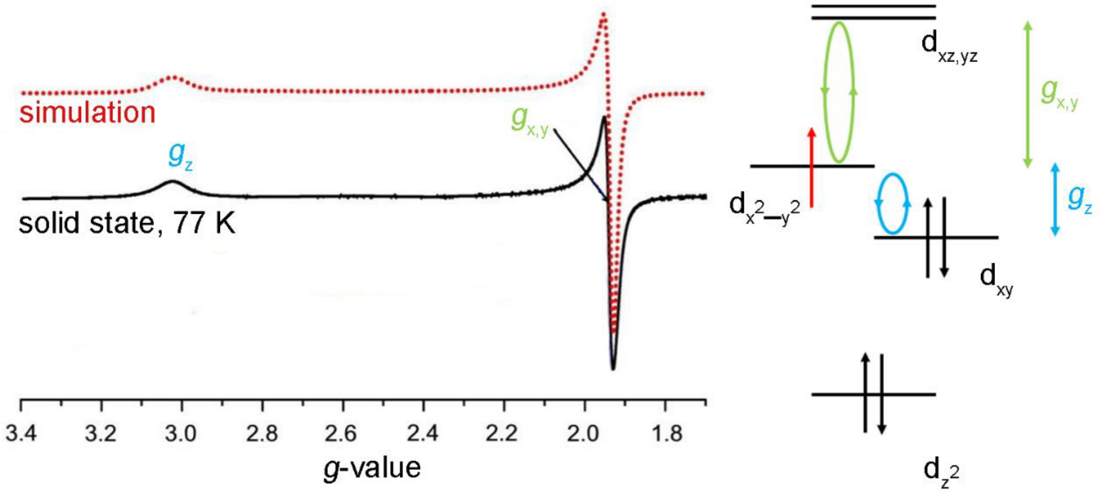

Figure 23.[4] **X-band EPR spectra of a 1-amino-1'-ferroceniumcarboxylic acid derivative at 77 K (bottom left, straight black line) and simulation of the spectrum (top left, dotted red line)**[148] **and molecular orbitals of ferrocenium illustrating the *g*-shift (right).**

As stated in chapter 1.6.1, EPR measurement in the solid state or in frozen solution allows to determine g_x, g_y, and g_z, while in fluid solution only an averaged g_{iso} can be obtained. The g-values of ferrocenium are explained by the possible mixings of the unpaired electron derived from the d orbitals (Figure 23, right). Rotation of the unpaired electron located in the d_{x2-y2} orbital in z direction leads to mixing with the d_{xy} orbital. Since this orbital is unoccupied, the resulting g-value is $g_z > g_e$. On the other hand, rotation along the x or y axis mixes the unpaired electron with the unoccupied d_{xz} and d_{yz} orbitals, respectively. Accordingly, both g-values are smaller than for the free electron (axial symmetry). In the illustration in Figure 23, a negligible influence of the substituent on the symmetry was assumed. However, degeneracy of d_{xz} and d_{yz} can be eliminated, depending on the substitution pattern of the ferrocenium moiety so that slightly different values for g_x and g_y can be obtained (rhombic symmetry). Due to the broadness of the resonance of ferrocenium compounds, usually no hyperfine couplings are resolved. Yet,

---

[4] EPR spectrum adapted from D. Siebler, *Dissertation*, Johannes Gutenberg-University, **2010**.

differences in *g*-value can be used for assignment of compounds as extensively illustrated in this dissertation.

1.6.3 Spin-Trapping

In the previous chapters, the detection of stable paramagnetic compounds by EPR spectroscopy was described. However, especially for organic radicals, this detection is rendered difficult due to the their transient nature because of their high reactivity. Thus, the slow measurement of EPR spectra due to the time consuming single sweeps is not sufficient to detect highly reactive species, e.g. unstabilized phenoxyl radicals (see chapter 1.4). An alternative method to detect such compounds is rapid freezing, i.e. the in situ formation of the paramagnetic species in the EPR tube and immediate freezing in liquid nitrogen to 77 K. Nevertheless, this method has two disadvantages. Firstly, very fast follow-up reactions of the radicals can still result in the detection of follow-up products and secondly, as described in chapter 1.6.1, especially in organic radicals with many small hyperfine and superhyperfine couplings, the lines of couplings and *g*-values can overlap in measurements in frozen solution at 77 K so that information is "lost". Thus, measurement in liquid solution is necessary. The high reactivity of organic radicals is used in that matter by the addition of spin-trapping agents, which are attacked by the initial paramagnetic species to form a stable radical that can be identified by EPR spectroscopy at room temperature. Typical spin-trapping compounds are *N*-*tert*-butyl-nitrone (PBN; **XVI**), 5,5,-dimethyl-1-pyrroline-*N*-oxide (DMPO; **XVII**), nitrosobenzene (NOB; **XVIII**), and 2-methyl-2-nitrosopropane (MNP; **XIX**) (Figure 24).

N-*tert*-butyl nitrone (PBN)
XVI

5,5-dimethyl-1-pyrrolidine-N-oxide (DMPO)
XVII

nitrosobenzene (NOB)
XVIII

2-methyl-2-nitroso-propane (MNP)
XIX

Figure 24: Lewis structures of typical spin-trapping agents.

The concept of trapping transient radical species was first reported by Janzen *et al.* in 1968.[176] Afterwards, al lot of investigations in this field have been conducted,[165,177–184] especially in biological systems as a means to trap transient species in reaction cycles.[43,76,125,149,185,186] In all spin-trapping reactions, the transient radical attacks the spin-trapping agent to form a covalent bond leading to a stable radical adduct (Scheme 7). After assignment of characteristic hyperfine couplings of the spin-trapping agent, conclusions about the initial radical by additional coupling patterns is possible. Furthermore, in spin-trapping reaction with high yield, the reduction of the spin-trapped compound allows even further characterization and structure elucidation (NMR, MS, etc.).[163,165]

Scheme 7. Illustration of radical addition of a transient paramagnetic species to XVIII yielding a stable radical suitable for EPR spectroscopy.

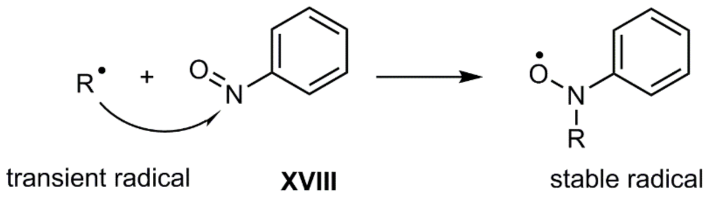

In Figure 25 some examples of EPR spectra for NOB and DMPO spin-trapped radicals are depicted. The influence of hyperfine and superhyperfine coupling is clearly visible. While both radicals feature a strong ^{14}N hyperfine coupling, the DMPO-trapped compound (Figure 25b) shows less ^{1}H superhyperfine couplings than the NOB-trapped phenoxyl radical (Figure 25a).

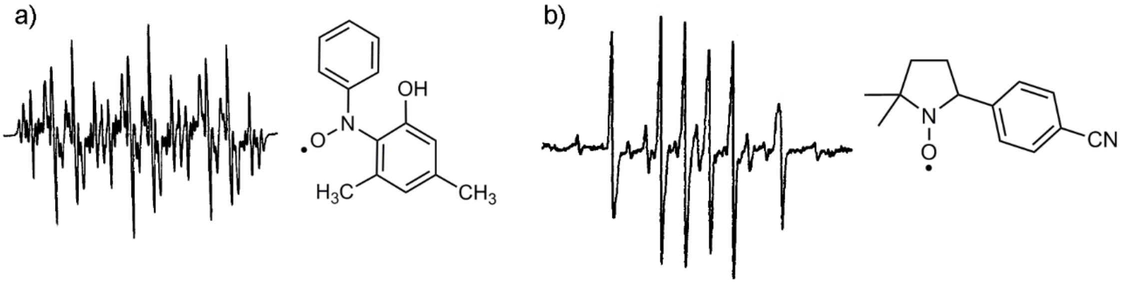

Figure 25: Examples of transient radicals trapped with a) NOB[182] 5 and b) DMPO.[187] 6

1.6.4 Quantitative EPR Spectroscopy

The quantification of EPR experiments is an interesting, yet challenging task. In reactions leading to paramagnetic compounds from diamagnetic starting materials, the conversion/yield remains uncertain, since the starting materials do not deliver any resonances in EPR spectroscopy. The application of an internal standard is not useful for EPR spectroscopy, due to the almost certain overlapping of resonances of the sample and the standard because of similar *g*-values and various line widths (see chapters 1.6.1 and 1.6.2) as well as reactivity. Therefore, quantification is achieved via an external standard.[188] The recording of EPR resonances is affected by many factors, such as dielectric constant of the solvent, temperature, magnetic field, microwave frequency, sweep, width of the EPR tube, position/depth of the EPR tube in the spectrometer, etc. It is crucial to keep these factors identical for the measurement of the calibration curve and the recording of the samples. Furthermore, all spectrometer settings and parameters described above need to be kept constant for the preparation of the calibration

---

[5] EPR spectrum adapted from L. Omelka, J. Kováčová, *Magn. Reson. Chem.* **1994**, *32*, 525–531. Copyright 1994 John Wiley and Sons.

[6] EPR spectrum adapted from P. Rapta, L. Omelka, A. Staško, J. Dauth, B. Deubzer, J. Weis, *J. Chem. Soc. Perkin Trans. 2* **1996**, 255–261. Copyright 1996 Royal Society of Chemisty.

curve and the sample measurements.[188] Stable radicals like DPPH (see Figure 21) can be used as an external standard. A calibration curve needs to be prepared by measuring DPPH samples in different concentrations. As described in chapter 1.6.1, EPR spectra are recorded as first derivative of the microwave absorption. Thus, the obtained standard spectra need to be integrated twice on to get the correct integral values applicable for quantification.[188]

1.7 References

[1] R. R. Schrock, *Acc. Chem. Res.* **2005**, *38*, 955–962.

[2] S. Kliegman, K. McNeill, *Dalton Trans.* **2008**, 4191–4201.

[3] A. B. McQuarters, N. E. Wirgau, N. Lehnert, *Curr. Opin. Chem. Biol.* **2014**, *19*, 82–89.

[4] B. A. MacKay, M. D. Fryzuk, *Chem. Rev.* **2004**, *104*, 385–401.

[5] J. Leppin, C. Förster, K. Heinze, *Inorg. Chem.* **2014**, *53*, 12416–12427.

[6] J. M. Berg, R. H. Holm, *J. Am. Chem. Soc.* **1985**, *107*, 917–925.

[7] Y.-Y. P. Tsao, C. J. Fritchie, H. A. Levy, *J. Am. Chem. Soc.* **1978**, *100*, 4089–4095.

[8] A. Wünsche von Leupoldt, C. Förster, T. J. Fiedler, N. H. Bings, K. Heinze, *Eur. J. Inorg. Chem.* **2013**, 6079–6090.

[9] W. W. Weare, X. Dai, M. J. Byrnes, J. M. Chin, R. R. Schrock, P. Müller, *Proc. Natl. Acad. Sci.* **2006**, *103*, 17099–17106.

[10] R. R. Schrock, *Angew. Chem.* **2008**, *120*, 5594–5605; *Angew. Chem. Int. Ed.* **2008**, *47*, 5512–5522.

[11] C. Schulzke, *Eur. J. Inorg. Chem.* **2011**, 1189–1199.

[12] S. P. de Visser, M. G. Quesne, B. Martin, P. Comba, U. Ryde, *Chem. Commun.* **2014**, *50*, 262–282.

[13] R. A. Marcus, N. Sutin, *Biochim. Biophys. Acta* **1985**, *811*, 265–322.

[14] G. L. Closs, J. R. Miller, *Science* **1988**, *240*, 440–447.

[15] J. R. Winkler, H. B. Gray, *Annu. Rev. Biochem.* **1996**, *65*, 537–561.

[16] P. F. Barbara, T. J. Meyer, M. A. Ratner, *J. Phys. Chem.* **1996**, *100*, 13148–13168.

[17] T. Kienz, C. Förster, K. Heinze, *Organometallics* **2014**, *33*, 4803–4812.

[18] M. A. Fox, *Chem. Rev.* **1992**, *92*, 365–368.

[19] C. Creutz, H. Taube, *J. Am. Chem. Soc.* **1969**, *91*, 3988–3989.

[20] M. B. Robin, P. Day, *Adv. Inorg. Chem. Radiochem.* **1968**, *10*, 247–422.

[21] M. H. V Huynh, T. J. Meyer, *Chem. Rev.* **2007**, *107*, 5004–5064.

[22] W. Kaim, A. Klein, M. Glöckle, *Acc. Chem. Res.* **2000**, *33*, 755–763.

[23] W. Kaim, B. Sarkar, *Coord. Chem. Rev.* **2007**, *251*, 584–594.

[24] W. Kaim, G. K. Lahiri, *Angew. Chem.* **2007**, *119*, 1808–1828; *Angew. Chem. Int. Ed.*

2007, *46*, 1778–1796.

[25] D. Siebler, M. Linseis, T. Gasi, L. M. Carrella, R. F. Winter, C. Förster, K. Heinze, *Chem. Eur. J.* **2011**, *17*, 4540–4551.

[26] D. Siebler, C. Förster, K. Heinze, *Dalton Trans.* **2011**, *40*, 3558–3575.

[27] A. Heckmann, C. Lambert, *Angew. Chem.* **2012**, *124*, 334–404; *Angew. Chem. Int. Ed.* **2012**, *51*, 326–392.

[28] J. Hankache, O. S. Wenger, *Chem. Rev.* **2011**, *111*, 5138–5178.

[29] T. F. Markle, J. M. Mayer, *Angew. Chem.* **2008**, *120*, 750–752; *Angew. Chem. Int. Ed.* **2008**, *47*, 738–740.

[30] J. J. Warren, T. A. Tronic, J. M. Mayer, *Chem. Rev.* **2010**, *110*, 6961–7001.

[31] J.-M. Savéant, *Energy Environ. Sci.* **2012**, *5*, 7718–7731.

[32] I. J. Rhile, T. F. Markle, H. Nagao, A. G. DiPasquale, O. P. Lam, M. A. Lockwood, K. Rotter, J. M. Mayer, *J. Am. Chem. Soc.* **2006**, *128*, 6075–6088.

[33] C. Costentin, M. Robert, J.-M. Savéant, *Phys. Chem. Chem. Phys.* **2010**, *12*, 11179–11190.

[34] D. R. Weinberg, C. J. Gagliardi, J. F. Hull, C. F. Murphy, C. A. Kent, B. C. Westlake, A. Paul, D. H. Ess, D. G. McCafferty, T. J. Meyer, *Chem. Rev.* **2012**, *112*, 4016–4093.

[35] C. Costentin, M. Robert, J.-M. Savéant, *J. Am. Chem. Soc.* **2006**, *128*, 4552–4553.

[36] A. Neidlinger, V. Ksenofontov, K. Heinze, *Organometallics* **2013**, *32*, 5955–5965.

[37] J. L. Dempsey, J. R. Winkler, H. B. Gray, *Chem. Rev.* **2010**, *110*, 7024–7039.

[38] F. Lachaud, A. Quaranta, Y. Pellegrin, P. Dorlet, M.-F. Charlot, S. Un, W. Leibl, A. Aukauloo, *Angew. Chem.* **2005**, *117*, 1560–1564; *Angew. Chem. Int. Ed.* **2005**, *44*, 1536–1540.

[39] J. Bonin, M. Robert, *Photochem. Photobiol.* **2011**, *87*, 1190–1203.

[40] L. Hammarström, S. Styring, *Energy Environ. Sci.* **2011**, *4*, 2379–2388.

[41] C. J. Gagliardi, A. K. Vannucci, J. J. Concepcion, Z. Chen, T. J. Meyer, *Energy Environ. Sci.* **2012**, *5*, 7704–7717.

[42] E. Reisner, *Chem. Soc. Rev.* **2014**, *43*, 6485–6497.

[43] M. Sugiura, S. Ogami, M. Kusumi, S. Un, F. Rappaport, A. Boussac, *J. Biol. Chem.* **2012**, *287*, 13336–13347.

[44] V. P. Shinkarev, *Biophys. J.* **2003**, *85*, 435–441.

[45] J. C. G. Walker, in *The Natural Environment and the Biogeochemical Cycles* (Ed.: O. Hutzinger), Springer, Berlin, Heidelberg, **1980**, pp. 87–104.

[46] C. B. Field, *Science* **1998**, *281*, 237–240.

[47] J. Wyman, *Adv. Protein Chem.* **1948**, *4*, 407–531.

[48] R. Abrams, A. M. Altschul, T. R. Hogness, *J. Biol. Chem.* **1942**, *143*, 303–316.

[49] B. B. Ríos-González, E. M. Román-Morales, R. Pietri, J. López-Garriga, *J. Inorg. Biochem.* **2014**, *133*, 78–86.

[50] J. C. Kendrew, R. E. Dickerson, B. E. Strandberg, R. G. Hart, D. R. Davies, D. C. Phillips, V. C. Shore, *Nature* **1960**, *185*, 422–427.

[51] K. L. Bren, R. Eisenberg, H. B. Gray, *Proc. Natl. Acad. Sci.* **2015**, *112*, 13123–13127.

[52] P. R. Ortiz de Montellano, *Cytochrome P450*, Springer International Publishing, Cham, **2015**.

[53] S. Rasool, R. Mohamed, *Protoplasma* **2015**, 1–13.

[54] T. A. Rouault, W. H. Tong, *Trends Genet.* **2008**, *24*, 398–407.

[55] F. Bonomi, T. A. Rouault, in *Iron-Sulfur Clusters in Chemistry and Biology* (Ed.: T. Rouault), De Gruyter, Berlin, Boston, **2014**, pp. 1–10.

[56] T. A. Rouault, *Nat. Chem. Biol.* **2015**, *11*, 442–445.

[57] T. J. Kealy, P. L. Pauson, *Nature* **1951**, *168*, 1039–1040.

[58] G. Jaouen, A. Vessieres, I. S. Butler, *Acc. Chem. Res.* **1993**, *26*, 361–369.

[59] Š. Toma, R. Šebesta, *Synthesis* **2015**, *47*, 1683–1695.

[60] D. R. van Staveren, N. Metzler-Nolte, *Chem. Rev.* **2004**, 5931–5985.

[61] R. H. Fish, G. Jaouen, *Organometallics* **2003**, *22*, 2166–2177.

[62] E. O. Fischer, W. Hafner, *Z. Naturforsch.* **1953**, 444–445.

[63] J. F. Cordes, *Chem. Ber.* **1962**, *95*, 3084–3085.

[64] J. T. Chantson, M. V. V. Falzacappa, S. Crovella, N. Metzler-Nolte, *ChemMedChem* **2006**, *1*, 1268–1274.

[65] C. Biot, G. Glorian, L. A. Maciejewski, J. S. Brocard, O. Domarle, G. Blampain, P. Millet, A. J. Georges, H. Abessolo, D. Dive, J. Lebibi, *J. Med. Chem.* **1997**, *40*, 3715–3718.

[66] C. Biot, F. Nosten, L. Fraisse, D. Ter-Minassian, J. Khalife, D. Dive, *Parasite* **2011**, *18*, 207–214.

[67] F. Dubar, C. Slomianny, J. Khalife, D. Dive, H. Kalamou, Y. Guérardel, P. Grellier, C. Biot, *Angew. Chem.* **2013**, *125*, 7844–7847; *Angew. Chem. Int. Ed.* **2013**, *52*, 7690–7693.

[68] H. Hagen, P. Marzenell, E. Jentzsch, F. Wenz, M. R. Veldwijk, A. Mokhir, *J. Med. Chem.* **2012**, *55*, 924–934.

[69] D. Hamels, P. M. Dansette, E. A. Hillard, S. Top, A. Vessières, P. Herson, G. Jaouen, D. Mansuy, *Angew. Chem.* **2009**, *121*, 9288–9290; *Angew. Chem. Int. Ed.* **2009**, *48*, 9124–9126.

[70] P. Marzenell, H. Hagen, L. Sellner, T. Zenz, R. Grinyte, V. Pavlov, S. Daum, A. Mokhir, *J. Med. Chem.* **2013**, *56*, 6935–6944.

[71] E. Hillard, A. Vessières, L. Thouin, G. Jaouen, C. Amatore, *Angew. Chem.* **2005**, *118*, 291–296; *Angew. Chem. Int. Ed.* **2005**, *45*, 285–290.

[72] Q. Michard, G. Jaouen, A. Vessieres, B. A. Bernard, *J. Inorg. Biochem.* **2008**, *102*, 1980–1985.

[73] I. Zanellato, J.-M. Heldt, A. Vessières, G. Jaouen, D. Osella, *Inorg. Chim. Acta* **2009**, *362*, 4037–4042.

[74] C. Ornelas, *New J. Chem.* **2011**, *35*, 1973–1985.

[75] G. Gasser, I. Ott, N. Metzler-Nolte, *J. Med. Chem.* **2011**, *54*, 3–25.

[76] D. Osella, M. Ferrali, P. Zanello, F. Laschi, M. Fontani, C. Nervi, G. Cavigiolio, *Inorg. Chim. Acta* **2000**, *306*, 42–48.

[77] G. Jaouen, S. Top, A. Vessieres, G. Leclercq, M. McGlinchey, *Curr. Med. Chem.* **2004**, *11*, 2505–2517.

[78] A. Nguyen, S. Top, P. Pigeon, A. Vessières, E. A. Hillard, M.-A. Plamont, M. Huché, C. Rigamonti, G. Jaouen, *Chem. Eur. J.* **2009**, *15*, 684–696.

[79] D. Osella, H. Mahboobi, D. Colangelo, G. Cavigiolio, A. Vessières, G. Jaouen, *Inorg. Chim. Acta* **2005**, *358*, 1993–1998.

[80] R. L. Carroll, C. B. Gorman, *Angew. Chem.* **2002**, *114*, 4556–4579; *Angew. Chem. Int. Ed.* **2002**, *41*, 4378–4400.

[81] J. M. Tour, *Molecular Electronics: Commercial Insights, Chemistry, Devices, Architecture and Programming*, World Scientific, Singapore, **2003**.

[82] D. K. James, J. M. Tour, *Top. Curr. Chem.* **2005**, *257*, 33–62.

[83] C. Thiele, L. Gerhard, T. R. Eaton, D. M. Torres, M. Mayor, W. Wulfhekel, H. V. Löhneysen, M. Lukas, *New J. Phys.* **2015**, *17*, 053043.

[84] V. Kaliginedi, A. V. Rudnev, P. Moreno-García, M. Baghernejad, C. Huang, W. Hong, T. Wandlowski, *Phys. Chem. Chem. Phys.* **2014**, *16*, 23529–23539.

[85] A. M. Moore, B. A. Mantooth, A. A. Dameron, Z. J. Donhauser, P. A. Lewis, R. K. Smith, D. J. Fuchs, P. S. Weiss, *Front. Mater. Res.* **2008**, *10*, 29–47.

[86] J. M. Seminario, *Nat. Mater.* **2005**, *4*, 111–113.

[87] J. M. Tour, *Acc. Chem. Res.* **2000**, *33*, 791–804.

[88] J.-J. Hwang, J. M. Tour, *Tetrahedron* **2002**, *58*, 10387–10405.

[89] D. L. Pearson, J. M. Tour, *J. Org. Chem.* **1997**, *62*, 1376–1387.

[90] J. Ma, N. Krauße, H. Butenschön, *Eur. J. Org. Chem.* **2015**, 4510–4518.

[91] V. Balzani, Ed. , *Electron Transfer in Chemistry*, Wiley-VCH Verlag GmbH, Weinheim, Germany, **2001**.

[92] C. Creutz, H. Taube, *J. Am. Chem. Soc.* **1973**, *320*, 1086–1094.

[93] R. A. Marcus, *J. Chem. Phys.* **1956**, *24*, 966–978.

[94] R. A. Marcus, *J. Chem. Phys.* **1965**, *43*, 679–701.

[95] R. A. Marcus, *Discuss. Faraday Soc.* **1960**, *29*, 21–31.

[96] R. A. Marcus, *J. Electroanal. Chem.* **1996**, *437*, 251–259.

[97] L. H. Gade, in *Koordinationschemie*, Wiley-VCH, Weinheim, New York, Chichester, **1998**, pp. 405–501.

[98] N. S. Hush, *Prog. Inorg. Chem.* **1967**, *8*, 391–444.

[99] M. B. Robin, P. Day, *Adv. Inorg. Chem. Radiochem.* **1967**, *10*, 247–422.

[100] R. F. Winter, *Organometallics* **2014**, *33*, 4517–4536.

[101] J. Heinze, *Angew. Chem.* **1984**, *96*, 823–840; *Angew. Chem. Int. Ed.* **1983**, *23*, 831–847.

[102] M. Natali, S. Campagna, F. Scandola, *Chem. Soc. Rev.* **2014**, *43*, 4005–4018.

[103] J. Flanagan, S. Margel, A. J. Bard, F. C. Anson, *J. Am. Chem. Soc.* **1978**, *100*, 4248–4253.

[104] J. Kotz, G. Neyhart, W. Vining, M. Rausch, *Organometallics* **1983**, *2*, 79–82.

[105] C. Levanda, K. Bechgaard, D. O. Cowan, *J. Org. Chem.* **1976**, *41*, 2700–2704.

[106] D. O. Cowan, C. LeVanda, J. Park, F. Kaufman, *Acc. Chem. Res.* **1973**, *6*, 1–7.

[107] G. Ferguson, C. Glidewell, G. Opromolla, C. M. Zakaria, P. Zanello, *J. Organomet. Chem.* **1996**, *517*, 183–190.

[108] F. Delgado-Pena, D. R. Talham, D. O. Cowan, *J. Organomet. Chem.* **1983**, *253*, C43–C46.

[109] A.-C. Ribou, J.-P. Launay, M. L. Sachtleben, H. Li, C. W. Spangler, *Inorg. Chem.* **1996**, *35*, 3735–3740.

[110] K. A. Mahmoud, Y.-T. Long, G. Schatte, H.-B. Kraatz, *J. Organomet. Chem.* **2004**, *689*, 2250–2255.

[111] K. A. Mahmoud, H.-B. Kraatz, *J. Inorg. Organomet. Polym. Mater.* **2006**, *16*, 201–210.

[112] K. Heinze, D. Siebler, *Z. Anorg. Allg. Chem.* **2007**, *633*, 2223–2233.

[113] S. Hammes-Schiffer, A. Stuchebrukhov, *Chem. Rev.* **2010**, *110*, 6939–6960.

[114] I. J. Rhile, J. M. Mayer, *J. Am. Chem. Soc.* **2004**, *126*, 12718–12719.

[115] B. A. Barry, J. Chen, J. Keough, D. Jenson, A. Offenbacher, C. Pagba, *J. Phys. Chem. Lett.* **2012**, *3*, 543–554.

[116] L. Benisvy, E. Bill, A. J. Blake, D. Collison, E. S. Davies, C. D. Garner, G. McArdle, E. J. L. McInnes, J. McMaster, S. H. K. Ross, C. Wilson, *Dalton Trans.* **2006**, 258–267.

[117] C. Tommos, G. T. Babcock, *Biochim. Biophys. Acta* **2000**, *1458*, 199–219.

[118] N. I. Belaya, A. V. Belyi, A. I. Pomeshchenko, K. V. Glushchenko, *Russ. J. Appl. Chem.* **2015**, *88*, 1178–1185.

[119] A. L. Maniero, V. Chis, A. Zoleo, M. Brustolon, A. Mezzetti, *J. Phys. Chem. B* **2008**, *112*, 3812–3820.

[120] R. Wanke, L. Benisvy, M. L. Kuznetsov, M. F. C. Guedes Da Silva, A. J. L. Pombeiro, *Chem. Eur. J.* **2011**, *17*, 11882–11892.

[121] H. Michel, *Biochemistry* **1999**, *38*, 15129–15140.

[122] M. Wikström, *Curr. Opin. Struct. Biol.* **1998**, *8*, 480–488.

[123] E. A. Berry, M. Guergova-Kuras, L. Huang, A. R. Crofts, *Annu. Rev. Biochem.* **2006**, *69*, 1005–1075.

[124] A. R. Crofts, S. Lhee, S. B. Crofts, J. Cheng, S. Rose, *Biochim. Biophys. Acta* **2006**, *1757*, 1019–1034.

[125] P. Faller, C. Goussias, A. W. Rutherford, S. Un, *Proc. Natl. Acad. Sci. U. S. A.* **2003**, *100*, 8732–8735.

[126] K. N. Ferreira, T. M. Iverson, K. Maghlaoui, *Science* **2004**, *303*, 1831–1838.

[127] M. Orio, O. Jarjayes, B. Baptiste, C. Philouze, C. Duboc, J.-L. Mathias, L. Benisvy, F. Thomas, *Chem. Eur. J.* **2012**, *18*, 5416–5429.

[128] K. Heinze, M. Schlenker, *Eur. J. Inorg. Chem.* **2004**, 2974–2988.

[129] N. G. Connelly, W. E. Geiger, *Chem. Rev.* **1996**, *96*, 877–910.

[130] H. Huesmann, C. Förster, D. Siebler, T. Gasi, K. Heinze, *Organometallics* **2012**, *31*, 413–427.

[131] G. A. Petsko, D. Ringe, in *Protein Structure and Function* (Eds.: E. Lawrence, M. Robertson), New Science Press Ltd., London, **2004**, pp. 12–21.

[132] S. I. Kirin, H.-B. Kraatz, N. Metzler-Nolte, *Chem. Soc. Rev.* **2006**, *35*, 348–354.

[133] M. Kovačević, I. Kodrin, M. Cetina, I. Kmetič, T. Murati, M. Č. Semenčić, S. Roca, L. Barišić, *Dalton Trans.* **2015**, *44*, 16405–16420.

[134] T. Moriuchi, A. Nomoto, K. Yoshida, A. Ogawa, T. Hirao, *J. Am. Chem. Soc.* **2001**, *123*, 68–75.

[135] T. Moriuchi, A. Nomoto, K. Yoshida, T. Hirao, *J. Organomet. Chem.* **1999**, *589*, 50 – 58.

[136] A. Nomoto, T. Moriuchi, S. Yamazaki, A. Ogawa, T. Hirao, *Chem. Commun.* **1998**, 1963–1964.

[137] T. Moriuchi, T. Hirao, *Acc. Chem. Res.* **2010**, *43*, 1040–1051.

[138] S. Chowdhury, K. A. Mahmoud, G. Schatte, H.-B. Kraatz, *Org. Biomol. Chem.* **2005**, *3*, 3018–3023.

[139] S. I. Kirin, D. Wissenbach, N. Metzler-Nolte, *New J. Chem.* **2005**, *29*, 1168–1179.

[140] L. Barisić, M. Dropucić, V. Rapić, H. Pritzkow, S. I. Kirin, N. Metzler-Nolte, *Chem. Commun.* **2004**, 2004–2005.

[141] J. Lapić, S. Djaković, M. Cetina, K. Heinze, V. Rapić, *Eur. J. Inorg. Chem.* **2010**, 106–114.

[142] J. Lapić, G. Pavlovic, D. Siebler, K. Heinze, V. Rapić, *Organometallics* **2008**, *27*, 726–735.

[143] D. Siebler, C. Mojca, V. Rapić, *Organometallics* **2008**, *27*, 1447–1453.

[144] M. C. Semenčič, D. Siebler, K. Heinze, V. Rapić, *Organometallics* **2009**, *28*, 2028–2037.

[145] M. C. Semenčić, K. Heinze, C. Förster, V. Rapić, *Eur. J. Inorg. Chem.* **2010**, 1089–1097.

[146] V. Kovač, K. Radolović, I. Habuš, D. Siebler, K. Heinze, V. Rapić, *Eur. J. Inorg. Chem.* **2009**, 389–399.

[147] J. Lapić, D. Siebler, K. Heinze, V. Rapić, *Eur. J. Inorg. Chem.* **2007**, 2014–2024.

[148] D. Siebler, Amidverknüpfte Ferrocene, *Dissertation*, Johannes Gutenberg-University Mainz, **2010**.

[149] G. Tabbì, C. Cassino, G. Cavigiolio, D. Colangelo, A. Ghiglia, I. Viano, D. Osella, *J. Med. Chem.* **2002**, *45*, 5786–5796.

[150] E. Hempelmann, *Parasitol. Res.* **2007**, *100*, 671–676.

[151] Y. Shang, *Nat. Rev. Cancer* **2006**, *6*, 360–368.

[152] A. Brüning, K. Friese, A. Burges, I. Mylonas, *Breast Cancer Res.* **2010**, *12*, R45.

[153] R. R. Nazarewicz, W. J. Zenebe, A. Parihar, S. K. Larson, E. Alidema, J. Choi, P. Ghafourifar, *Cancer Res.* **2007**, *67*, 1282–1290.

[154] R. M. Golding, L. E. Orgel, *J. Chem. Soc.* **1962**, 363–364.

[155] J. P. Hurvois, C. Moinet, *J. Organomet. Chem.* **2005**, *690*, 1829–1839.

[156] P. Lemoine, *J. Organomet. Chem.* **1989**, *359*, 61–69.

[157] R. Prins, A. R. Korswagen, A. G. T. G. Kortbeek, *J. Organomet. Chem.* **1972**, *39*, 335–344.

[158] I. J. Spilners, *J. Organomet. Chem.* **1968**, *11*, 381–384.

[159] J. Holeček, K. Handlíř, J. Klikorka, N. D. Bang, *Collect. Czechoslov. Chem. Commun.* **1979**, *44*, 1379–1387.

[160] R. Prins, *Mol. Phys.* **1970**, *19*, 603–620.

[161] R. A. Abramovitch, C. I. Azogu, R. G. Sutherland, *J. Chem. Soc. D Chem. Commun.* **1971**, 134.

[162] R. A. Jackson, M. Scarmoutsosb, A. K. Zarkadis, *J. Chem. Soc. Perkin Trans. 2* **1991**, 809–810.

[163] M. Cais, P. Ashkenazi, S. Dani, J. Gottlieb, *J. Organomet. Chem.* **1977**, *124*, 49–58.

[164] X. Creary, *Org. Lett.* **2000**, *2*, 2069–2072.

[165] P. Ashkenazi, M. Cais, *Angew. Chem.* **1972**, *84*, 1106–1107; *Angew. Chem. Int. Ed.* **1972**, *11*, 1027–1028.

[166] R. A. Manderville, in *Radical and Radical Ion Reactivity in Nucleic Acid Chemistry* (Ed.: M.M. Greenberg), John Wiley & Sons, Inc., Hoboken, NJ, USA, **2009**, pp. 421–443.

[167] K. Gonter, E. Takács, L. Wojnárovits, *Radiat. Phys. Chem.* **2012**, *81*, 1495–1498.

[168] F. Thomas, O. Jarjayes, H. Jamet, S. Hamman, E. Saint-Aman, C. Duboc, J.-L. Pierre, *Angew. Chem.* **2004**, *116*, 604–607; *Angew. Chem. Int. Ed.* **2004**, *43*, 594–597.

[169] L. Benisvy, R. Bittl, E. Bothe, C. D. Garner, J. McMaster, S. Ross, C. Teutloff, F. Neese, *Angew. Chem.* **2005**, *117*, 5448–5451; *Angew. Chem. Int. Ed.* **2005**, *44*, 5314–5317.

[170] F. G. Bordwell, J. Cheng, *J. Am. Chem. Soc.* **1991**, *113*, 1736–1743.

[171] W. Herzog, C. Bronner, S. Löffler, B. He, D. Kratzert, D. Stalke, A. Hauser, O. S. Wenger, *ChemPhysChem* **2013**, *14*, 1168–1176.

[172] M. Kuss-Petermann, O. S. Wenger, *J. Phys. Chem. A* **2013**, *117*, 5726–5733.

[173] C. Bronner, O. S. Wenger, *J. Phys. Chem. Lett.* **2012**, *3*, 70–74.

[174] G. Jeschke, *Einführung In Die ESR-Spektroskopie*, Vorlesungsskript, Universität Konstanz, **2007**.

[175] D. Collison, *Introductory Workshop on the Theory and Practice of EPR Spectroscopy*, Lecture Notes and References Reported Therein, **2013**.

[176] E. G. Janzen, B. J. Blackburn, *J. Am. Chem. Soc.* **1968**, *90*, 5909–5910.

[177] E. G. Janzen, J. L. Gerlock, *J. Am. Chem. Soc.* **1969**, *91*, 3108–3109.

[178] P. Organolead, E. G. Janzen, B. J. Blackburn, *J. Am. Chem. Soc.* **1969**, *97*, 4481–4490.

[179] W. He, Y. Liu, W. G. Wamer, J.-J. Yin, *Nanomater. - Toxicol. Med. Appl.* **2014**, *22*, 49–63.

[180] O. Ouari, M. Hardy, H. Karoui, P. Tordo, *Electron Paramagn. Reson.* **2011**, *22*, 1–40.

[181] A. Hudson, M. F. Lappert, P. W. Lednor, B. K. Nicholson, *J. Chem. Soc. D Chem. Commun.* **1974**, 966–967.

[182] L. Omelka, J. Kováčová, *Magn. Reson. Chem.* **1994**, *32*, 525–531.

[183] S. Terabe, R. Konaka, *J. Chem. Soc. Perkin Trans. 2* **1972**, 2163–2172.

[184] L. R. C. Barclay, J. M. Dust, *Can. J. Chem.* **1982**, *60*, 607–615.

[185] J. Stubbe, W. A. Van Der Donk, *Chem. Rev.* **1998**, *98*, 705–762.

[186] J. W. Whittaker, *Chem. Rev.* **2003**, *103*, 2347–2364.

[187] P. Rapta, L. Omelka, A. Staško, J. Dauth, B. Deubzer, J. Weis, *J. Chem. Soc. Perkin Trans. 2* **1996**, 255–261.

[188] G. R. Eaton, S. S. Eaton, D. P. Barr, T. Weber, Ralph, *Quantitative EPR*, Springer Wien, New York, **2010**.

[189] I. Noviandri, K. N. Brown, D. S. Fleming, P. T. Gulyas, P. A. Lay, A. F. Masters, L. Phillips, *J. Phys. Chem. B* **1999**, *103*, 6713–6722.

2 AIM OF WORK

The main objective of this work is the combination of organometallic (ferrocene) and organic (phenol(ate)) redox centers to understand the influence of intramolecular hydrogen bonding on the stability of secondary structures under proton transfer as well as electron transfer reactions. Different substitution patterns on the ferrocenyl moieties allow tuning of redox potentials as well as hydrogen bond acceptor and donor capabilities. Furthermore, the investigation of intervalence charge transfer reaction between metal-based and organic redox centers in mixed-valent compounds is supposed to give an insight into elementary proton coupled electron transfer reactions of biologically relevant systems, e.g. between the oxygen evolving complex and the tyrosyl / tyrosyl radical redox couple of photosystem II. The investigation of mixed-valent compounds is performed by a combination of analytic methods, like UV/Vis/NIR, IR, and EPR spectroscopy as well as electrochemical methods and is furthermore supported by DFT studies.

Another part of this work deals with the reactivity of ferrocenium compounds under alkaline conditions in the absence of nucleophiles. These investigations on ferrocenyl radicals are expected to give insight into alternative/additional modes of action of ferrocene-based drugs, e.g. ferrocifen and ferroquine in the literature. The expected reaction pathways of these pharmaceutical substances have been proposed, but lack experimental evidence. The investigation of the reactivity is performed by spin-trapping techniques for EPR spectroscopic analyses in this dissertation.

Another subject of this work is the design of potentially immobilizable molecular wires consisting of 1-amino-1’-ferrocenecarboxylic acid building blocks, which form a stable secondary structure, inducing a constant macrodipole moment by parallel alignment of the single amide groups. In self assembled monolayers, these wires allow the investigation of electron transfer reactions via a hopping mechanism over the single ferrocenediyl units with respect to dipole moment orientation.

3 RESULTS AND DISCUSSION

In the following section, the results of this work are presented as a collection of publications and a manuscript.

The first chapter presents the publication on “Proton Coupled Electron Transfer in Ferrocenium-Phenolate Conjugates”. The Mößbauer measurements reported therein were performed by [redacted] and the data were analyzed by him as well. This paper, which was published in Organometallics, was written by Andreas Neidlinger (50 %) and [redacted] (50 %). All preparative work and analytics as well as DFT calculations were performed by Andreas Neidlinger. The succeful preparation of a ferrocene-phenol conjugate with a single, switchable intramolecular hydrogen bond is presented. After deprotonation and oxidation, this compound allows detection of a PCET reaction between a thermodynamically stalbilized, intramolecularly hydrogen bonded ferrocenium-phenolate and the valence isomeric phenoxyl-ferrocene. Furthermore, the high influence of hydrogen bonding on redox potentials on the ferrocene/ferrocenium and the phenolate/phenoxyl redox pairs is illustrated.

In the second chapter, the publication on “Spin Trapping of Carbon-Centered Ferrocenyl Radicals with Nitrosobenzene” is presented. EPR spectra of the thioamide were performed by [redacted], while the other EPR data were collected by Andreas Neidlinger. The simulation of EPR spectra was done by both authors: Andreas Neidlinger 40 % and [redacted] 60 %. Electrochemical measurements were performed by Andreas Neidinger. DFT calculations of the thioamide were performed by [redacted], while the remaining calculations were performed by Andreas Neidlinger. The manuscript which was published in Organometallics, was written by Andreas Neidlinger (40 %), [redacted] (40 %), and [redacted] (20 %). A deep insight into the decomposition pathways of ferrocenium compounds under alkaline conditions, facilitating the formation of highly reactive carbon-centered ferrocenyl radicals is presented. The stabilizing influence of a valence-tautomeric iminolate is furthermore illustrated, which is expected to play an important role in the activity of ferrocene-containing (pro-)drugs.

The third chapter shows the publication on “How Hydrogen Bonds Affect Reactivity and Intervalence Charge Transfer in Ferrocenium-Phenolate Radicals”. This paper was written by Andreas Neidlinger (70 %) and [redacted] (30 %). The X-ray crystal structure was solved by [redacted]. All syntheses, analyses, and DFT calculations were performed by Andreas Neidlinger. The effects of hydrogen bonding in valence-isomeric/-tautomeric ferrocene-phenol conjugates is explored further by succesful synthesis and analysis of a ferrocene-phenol compound without intramolecular hydrogen bonds. The high influence of hydrogen bonds on redox potentials and the stability of the ferrocene/ferrocenium and the phenolate/phenoxyl redox pairs is illustrated by spectroscopic data from UV/Vis, IR, and EPR spectroscopy as well as electrochemical analyses. DFT calcuation were performed to support the experimental data.

The fourth chapter concludes the work on hydrogen bonded ferrocene-phenol conjugates and presents the publication on “Conformational Switching of Multi-Responsive Ferrocenyl-

Phenol Conjugates”. This work was written by Andreas Neidlinger (60 %) and [redacted] (40 %). The X-ray crystal structure was solved by [redacted]. All syntheses and analyses as well as DFT calculations were performed by Andreas Neidlinger. The paper illustrates the effects of variations of the redox potentials and hydrogen bond donor/acceptor capabilities of the ferrocenyl amides. The length of the intramolecular hydrogen bond network (cooperative hydrogen bonding) is varied to gain insight on the stability of the singly oxidized and deprotonated compounds (acid/base vs. redox switching). Furthermore, the influence of the different substitution patterns under PCET conditions is presented. Conclusions are allowed by spectroscopic data from UV/Vis, IR, and EPR spectroscopy as well as electrochemical analyses. DFT calcuation were performed to support the experimental data.

The last chapter includes the manuscript about “Attempts to Study the Effects of Internal Dipole Moment on Electron Transfer Rates Within Peptides of 1-Amino-1‘-Ferrocenecarboxylic Acid”. This theoretical study and retrosynthetic approach on immobilizable peptide wires delivers a foundation for the investigation of the influence of the accumulated dipole moments of the amide bonds in the secondary structure on ET rates along the wires.

CONTENTS

3.1 Proton Coupled Electron Transfer in Ferrocenium-Phenolate Conjugates
Andreas Neidlinger, Vadim Ksenofontov, Katja Heinze
Published in: *Organometallics* **2013**, *32*, 5955–5965.
[DOI: 10.1021/om400498h]
http://pubs.acs.org/doi/pdf/10.1021/om400498h

"Adapted with permission from A. Neidlinger, V. Ksenofontov, K. Heinze, *Organometallics* **2013**, *32*, 5955–5965. Copyright 2013 American Chemical Society."

3.2 Spin Trapping of Carbon-Centered Ferrocenyl Radicals with Nitrosobenzene
Andreas Neidlinger, Torben Kienz, Katja Heinze
Published in: *Organometallics **2015**, 34, 5310−5320.*
[DOI: 10.1021/acs.organomet.5b00778]
http://pubs.acs.org/doi/pdf/10.1021/acs.organomet.5b00778

"This is an unofficial adaptation of an article that appeared in an ACS publication. ACS has not endorsed the content of this adaptation or the context of its use. Copyright 2015 American Chemical Society."

3.3 How Hydrogen Bonds Affect Reactivity and Intervalence Charge Transfer in Ferrocenium-Phenolate Radicals
Andreas Neidlinger, Christoph Förster, Katja Heinze
European Journal of Inorganic Chemistry **2016**, in print.

3.4 Ferrocenyl-Phenolate Conjugates – A deep, yet fascinating insight
Andreas Neidlinger, Christoph Förster, Katja Heinze
To be Submitted.

3.5 Attempts to Study the Effects of Internal Dipole Moment on Electron Transfer Rates Within Peptides of 1-Amino-1'-Ferrocenecarboxylic Acid
Andreas Neidlinger, Katja Heinze

3.1 Proton Coupled Electron Transfer in Ferrocenium-Phenolate Conjugates

Andreas Neidlinger, Vadim Ksenofontov, and Katja Heinze

Organometallics **2013**, *32*, 5955–5965.

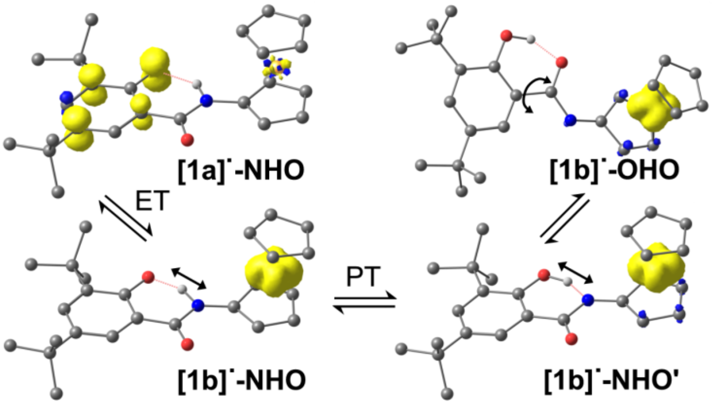

Abstract

Electron and proton transfer (ET, PT) can be intimately coupled provided suitable redox and acid/base sites are available. Amide-linked ferrocene-phenol **H-1** is deprotonated to the phenolate **[1]**$^-$ by phosphazene bases and oxidized to the ferrocenium ion **[H-1]**$^+$ by silver hexafluoroantimonate. Concomitant oxidation and deprotonation yields the radical **[1]**$^\bullet$ featuring a characteristic NIR absorption band. The ground state of **[1]**$^\bullet$ is best described as a ferrocenium-phenolate zwitterion **[1b]**$^\bullet$ with a dynamic dissymmetric N···H···O hydrogen bond (PT). The ferrocenium-iminolate N···H-O tautomer **[1b]**$^\bullet$**-NHO’** can undergo a thermal structural rearrangement to a high energy OH···O tautomer **[1b]**$^\bullet$**-OHO** while the amide-phenolate N-H···O tautomer **[1b]**$^\bullet$**-NHO** is poised to optical electron transfer to yield the ferrocene-phenoxyl valence isomer **[1a]**$^\bullet$**-NHO** (E_{op} = 1.18 – 1.19 eV).

Supporting information for this article (without Cartesian coordinates from DFT calculations) is found at pp. 186. For full supporting information, refer to:

http://pubs.acs.org/doi/suppl/10.1021/om400498h/suppl_file/om400498h_si_001.pdf.

Adapted with permission from A. Neidlinger, V. Ksenofontov, K. Heinze, Organometallics 2013, 32, 5955−5965.

3.1.1 INTRODUCTION

Electron transfer (ET) is one of the fundamental and most important phenomena in chemistry and biology.[1-3] To study thermally and optically driven ET processes mixed-valent and mixed-metal compounds are highly suitable systems. ET between chemically similar moieties has been amply studied, e.g. based on the famous symmetric mixed-valent Creutz-Taube ion and related complexes[4-10] as well as on suitable organic redox couples.[11] ET processes between chemically different building blocks which feature similar redox potentials are less well explored. Such systems are in principle suited to display bistability based on ET processes (valence isomers) which can also be coupled to structural rearrangements such as proton transfer (PT).

In this context we have designed redoxactive oligopeptides **A**[12-15] built from 1-aminoferrocene-1'-carboxylic acid[12,16,17] (Scheme 1). These organometallic peptides form well defined hydrogen bonded secondary zigzag structures in solution and they can be oxidized stepwise to mixed-valent ferrocene/ferrocenium peptides **[A]$^{n+}$** featuring intervalence charge transfer (IVCT; $\lambda \approx 1030 - 1180$ nm) between adjacent ferrocene and ferrocenium units.[14,15] In the mixed-valent peptides **[A]$^{n+}$** the positive charges are largely localized at those [Fc-NH]$^+$ units (Robin Day class II[4]) which form the strongest intramolecular hydrogen bonds in the zigzag chain.[14,15] Oxidation to the all-Fe^{III} peptide switches the zigzag structure into an extended one lacking hydrogen bonds.[14,15] Replacing a ferrocene unit by the electron accepting cobaltocenium moiety (**B**) allows light-induced electron transfer between the different metallocenes (MM'CT, $\lambda = 620$ nm) resulting in the excited cobaltocene ferrocenium species **B'** (Scheme 1).[18] The electrochemically derived driving-force for the back electron transfer **B'** → **B** was estimated as $\Delta G^0 = 1.135$ eV.[18] Similarly, electronic spectra of amide-linked ferrocenyl terpyridine ruthenium conjugates [FcCONH-(tpy)Ru(tpy-R)]$^{2+}$ (Scheme 1, **C**) feature an absorption band ($\lambda \approx 494$ nm) in addition to the MLCT of the ruthenium(II) complex which is absent in the individual components and hence assigned to a charge transfer from the ferrocenyl moiety to the electron deficient terpyridine ligands.[19]

Proton loss following oxidation has been observed for hydroxyferrocifen (Scheme 1, **D-H** → **[D-H]$^+$** → **[D']**). The final carbon-centered radical **[D]$^\bullet$** is believed to be formed via intramolecular ET (IET) of the initially formed zwitterionic ferrocenium-phenolate **[D']**.[20] ET can also induce formation of charge-assisted hydrogen bonds which stabilize the ET product. For example the amide-linked ferrocenyl-quinone **E** is reduced to the semiquinonate **[E]$^{\bullet-}$** with a strong intramolecular charge-assisted NH···O$^-$ hydrogen bond (Scheme 1). Similarly, photo-induced charge separation by a 388 nm pulse yields the NH···O$^-$ hydrogen bond stabilized zwitterion **[E']** with a lifetime of 4 ns at ambient temperature (Scheme 1). The corresponding *N*-methylated species does not show long-lived photo-induced charge separation as hydrogen bonding is impossible.[21,22] A zwitterionic ferrocenium-semiquinonate state can be further stabilized to become even the ground state by addition of Lewis acids as shown by the charge separation occurring in **F** upon addition of $Sc(OTf)_3$ to give **[F'(Sc^{3+})]** (Scheme 1).[23]

Scheme 1. Thermal and photoinduced ET and PCET in ferrocenyl conjugates with dissymmetric redox centers and in salicylamides

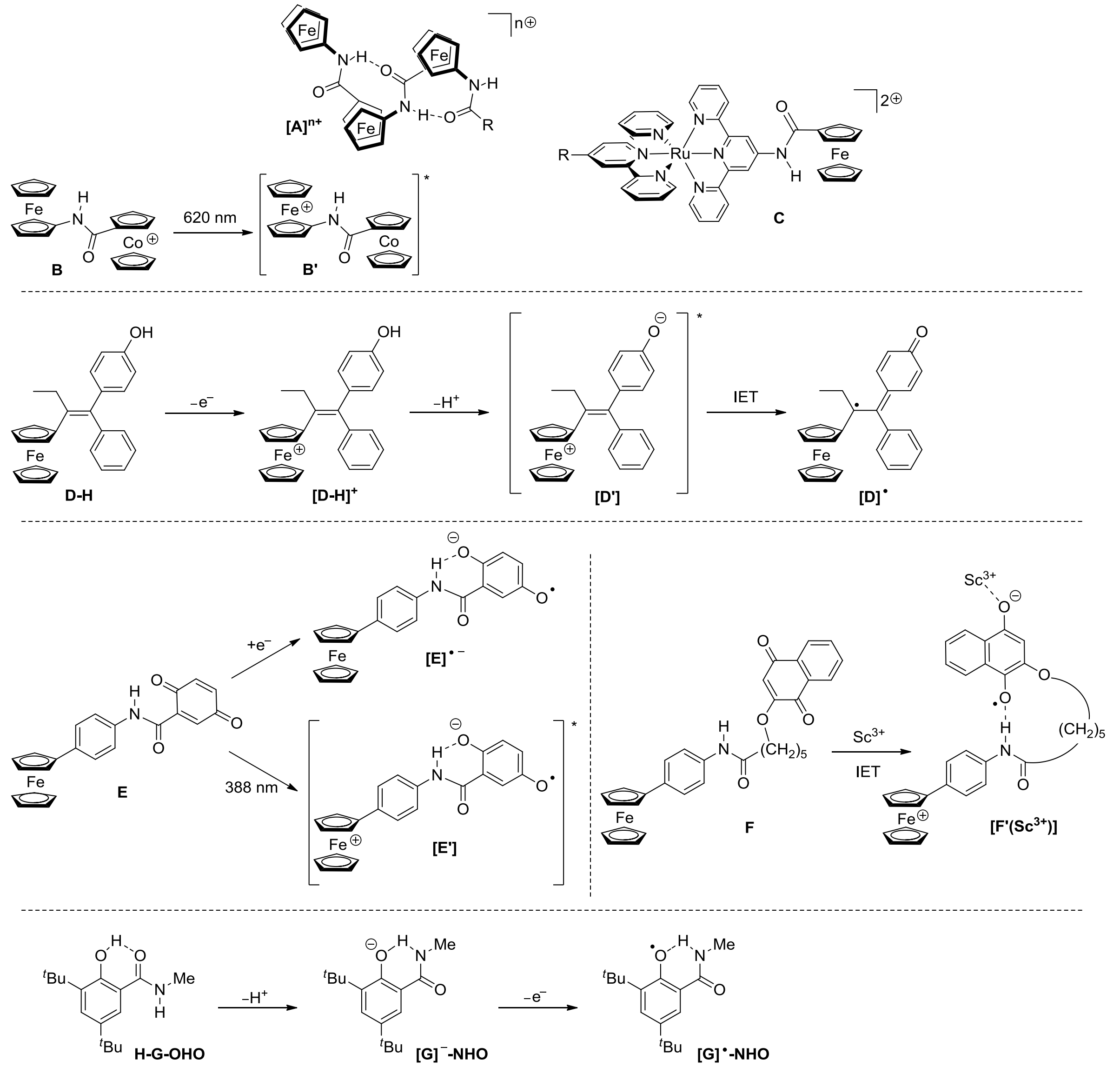

The phenolate/phenoxyl redox couple is an important redox mediator in biology, e.g. shuttling electrons between P680 and the oxygen evolving complex in photosystem II.[1,2,24] Oxidation of tyrosine to the tyrosyl radical is only possible with the assistance of a nearby base (histidine) to deprotonate the phenolic OH group.[25-34] Thus ET is synchronized to PT and several important artificial model systems have been devised to study the proton-coupled electron transfer (PCET[35-44]) process. Intramolecular hydrogen bonds contribute to the pK_a value and the oxidation potential of a phenol in salicylamide model systems.[45-47] Persistent phenoxyl radicals **[G]**$^{\bullet}$ have been electrochemically prepared after deprotonation of salicylamide **H-G** to the phenolate **[G]**$^{-}$ ($E_{1/2}$ = −160 mV vs. FcH/FcH^{+} in MeCN/[$^{n}Bu_4N$][BF_4]) and analyzed by EPR spectroscopy (Scheme 1).[47] For a successful deprotonation of a salicylamide a “pre-located NH group” (**H-G-OHO** → **H-G-NHO**; OH···O → NH···O switch[45]) is required to lower the pK_a value of the phenol (Scheme 1).[46]

Scheme 2. ET and PT as well as H-bond conformations in H-1, [H-1]$^+$, [1]$^-$ and [1]$^•$ (atom numbering used for NMR assignment)

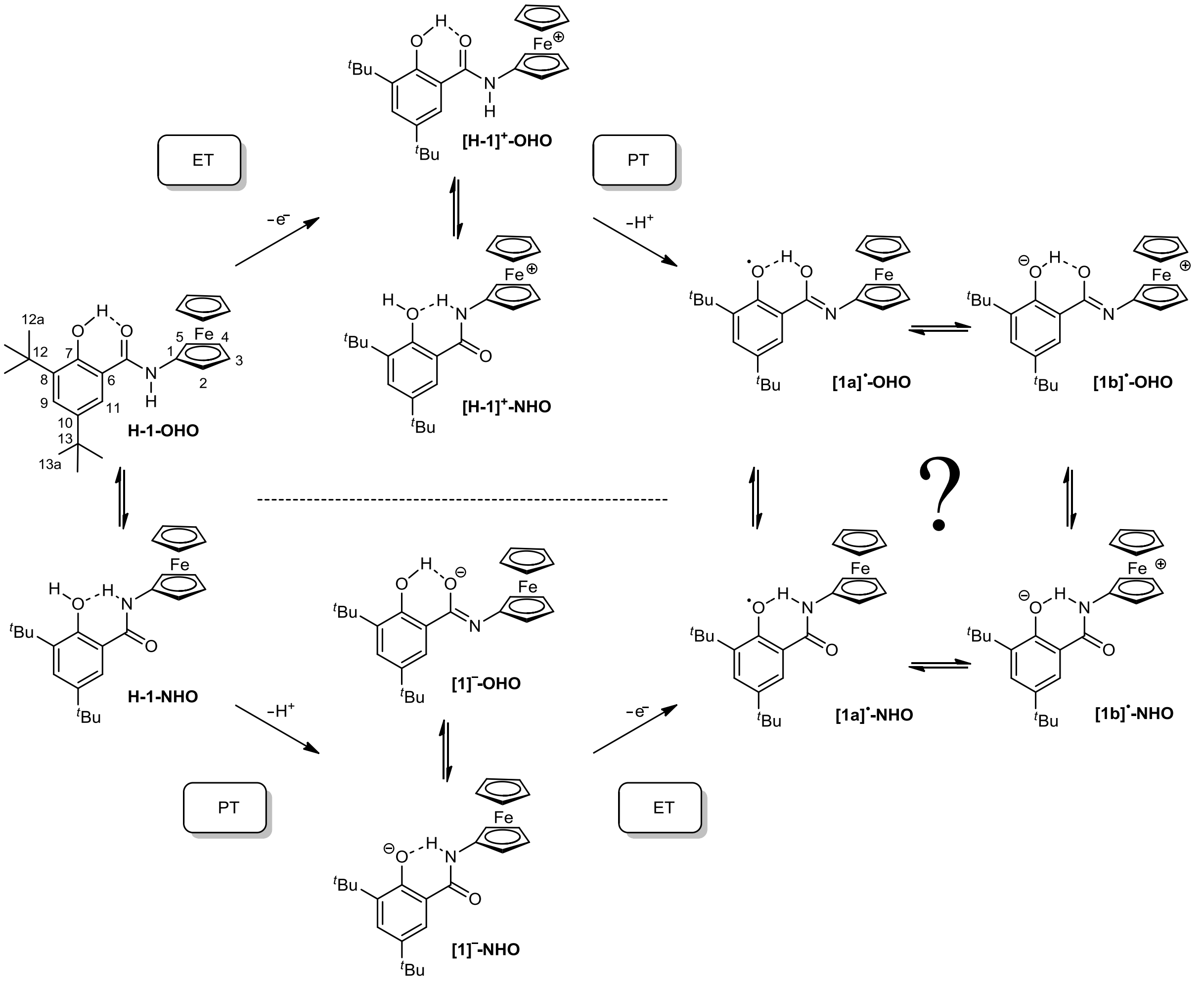

On the other hand, the metallocene *N*-acetylaminoferrocene **H-J** is easily oxidized to the corresponding ferrocenium cation **[H-J]$^+$** ($E_{1/2}$ = −75 mV vs. FcH/FcH$^+$ in MeCN/[^{n}Bu$_4$N][PF$_6$]).[12-14] The cation is a stronger acid and a stronger hydrogen atom donor in hydrogen bonds due to the electron withdrawing effect of the adjacent ferrocenium moiety.[14,15] Formal merging of phenol **H-G** with ferrocene **H-J** yields the novel amide-linked ferrocene-phenol **H-1** (Scheme 2) featuring two different redox sites (ferrocene and phenol(ate)) and two different acidic protons (phenol/amide).

The phenolic site can be oxidized to the phenoxyl radical only after or synchronous to deprotonation of the OH group to give **[1]$^-$** while the amide proton NH is acidic after oxidation of the ferrocene moiety **[H-1]$^+$**. Thus, electron and proton transfer is expected to be intimately coupled in the species **H-1**/**[H-1]$^+$**/**[1]$^-$**. The final product **[1]$^•$** after ET and PT can in principle be described as a phenoxyl radical **[1a]**$^{\bullet}$ or a ferrocenium-phenolate zwitterion **[1b]**$^{\bullet}$ (Scheme 2). In addition to this valence ambiguity, the stability of the intramolecular hydrogen bonds $OH\cdots O_{amide}$ or $NH\cdots O_{phenol(ate)}$ should be reflected by the pK_a values of OH and NH groups, with the latter one being tuned by the oxidation state of the iron center.[15,48,49] Thus, the conformation and the most stable hydrogen bonding motif $OH\cdots O_{amide}$ or $NH\cdots O_{phenol(ate)}$ are expected to be modulated by the oxidation and protonation state of **H-1**.

In the following we describe our attempts to elucidate the most stable hydrogen bonding motif (OH···O, NH···O) and charge distribution (zwitterion or phenoxyl radical) in radical **[1]**$^{\bullet}$, as well as hydrogen bonds and oxidation sites in the intermediates **[H-1]**$^{+}$ and **[1]**$^{-}$ on the way to radical **[1]**$^{\bullet}$ (Scheme 2). The hydrogen bonding motifs OH···O/NH···O are probed by IR spectroscopy, the oxidation states and redox communication by (spectro)electrochemical measurements, UV/Vis/NIR, EPR and Mößbauer spectroscopy. Relevant conformational and electronic issues will be discussed on the basis of DFT/PCM and TD-DFT/PCM calculations.

3.1.2 RESULTS AND DISCUSSION

Synthesis of H-1: The multifunctional compound **H-1** is readily synthesized by condensation of aminoferrocene[12,50] with the activated salicylic acid derivative 2,5-dioxopyrrolidine-1-yl-3,5-di-*tert*-butyl-2-hydroxybenzoate[47] similar to the preparation of the methyl derivative **H-G**.[120] **H-1** is fully characterized by NMR and IR spectroscopy as well as by mass spectrometry and elemental analysis. The molecular ion peak is found at $m/z = 433$ in the mass spectrum of **H-1**. The ^{1}H NMR spectra display the expected number of resonances with correct integral ratios. In CD_2Cl_2 the OH proton resonates at $\delta = 12.69$ ppm and the NH proton at $\delta = 7.36$ ppm suggesting a hydrogen bond of the OH group to the amide oxygen atom[45-47] and an essentially non-bonded NH group (Scheme 2, **H-1-OHO**).[51,52] In THF-d_8 the corresponding resonances are shifted to $\delta = 13.37$ ppm and $\delta = 9.01$ ppm suggesting the presence of H-bonds involving OH and NH groups. For *N*-acetylaminoferrocene **H-J**[12] the corresponding NH resonances are found at $\delta = 6.59$ ppm and $\delta = 8.28$ ppm in CD_2Cl_2 and THF-d_8, respectively, showing the same trend as **H-1**. NOESY data of **H-1** further suggest that H^{11} of the phenol is close to the amide NH group in both solvents confirming that the OH···O bridge is indeed present in both solvents (Scheme 2; see Supporting Information, Figure S1). In THF the OH proton shows an additional cross peak to a methyl proton of the *tert*-butyl substituent suggesting the presence of some additional **H-1-NHO** isomer in THF possibly further coordinated by THF. The IR spectra of **H-1** fully corroborate this assignment. In CH_2Cl_2 the NH group is not involved in H-bonding ($\tilde{\nu}(NH) = 3450\ cm^{-1}$; cf. **H-J**[12]: $\tilde{\nu}(NH) = 3435\ cm^{-1}$) while in THF hydrogen bonds are formed to the solvent and to some extend to the phenol ($\tilde{\nu}(NH) = 3320\ cm^{-1}$; cf. **H-J**: $\tilde{\nu}(NH) = 3315\ cm^{-1}$). The combined data suggest that the OH···O bridged conformer **H-1-OHO** is more stable than the NH···O bridged one (**H-1-NHO**) in both solvents similar to known salicylamides[45-47], although the presence of some **H-1-NHO** in the equilibrium especially in THF is possible.

The transformations of **H-1** investigated are compiled in Scheme 2. Chemical oxidations are performed using silver hexafluoroantimonate ($AgSbF_6$) as oxidant ($E_{1/2}(CH_2Cl_2) = 650$ mV; $E_{1/2}(THF) = 410$ mV vs. FcH/FcH^+)[53] which is competent to oxidize ferrocene or phenolate units. Proton transfer reactions are performed using the phosphazene bases $P_1{}^t$Bu (*tert*-butylimino-tris(dimethylamino)phosphorane, pK_a(MeCN) = 26.98)[54] or $P_4{}^t$Bu (1-*tert*-butyl-4,4,4-tris(dimethylamino)-2,2-bis[tris(dimethylamino)-phosphoranylidenamino]-2λ^5,4λ^5-catena-di(phosphazene), pK_a(MeCN) = 42.7)[54] as non-nucleophilic and non-coordinating proton acceptors. After filtration the resulting solutions are immediately subjected to spectroscopic analyses.

Oxidation of H-1: Cyclic voltammograms and square wave voltammograms of the ferrocene-phenol **H-1** recorded at 298 K in CH_2Cl_2 and THF are shown in Figure 1. To suppress interference of counterions tetra(*n*-butyl)ammonium tetrakis(pentafluorophenyl)borate ($[^n Bu_4N][B(C_6F_5)_4]$) is used as weakly coordinating electrolyte.[55,56] **H-1** shows a single reversible one-electron redox process at $E_{1/2} = -150/-85$ mV vs. FcH/FcH^+ (CH_2Cl_2/THF). This process is readily assigned to the ferrocene/ferrocenium couple (cf. **H-J**: $E_{1/2}(MeCN/[^n Bu_4N][PF_6]) = -75$ mV vs. FcH/FcH^+).[12,57] The phenol typically has a more than 1 V higher redox potential than its conjugate base[46] and hence the phenol unit of **H-1** is not oxidized to a phenoxyl radical in the potential range investigated in spite of the presence of the intramolecular OH···O hydrogen bond (Scheme 2). Obviously, the proton affinity of the amide oxygen atom is not sufficient to deprotonate the phenol. A simple ET process is hence observed to give the ferrocenium cation **[H-1]$^+$**.

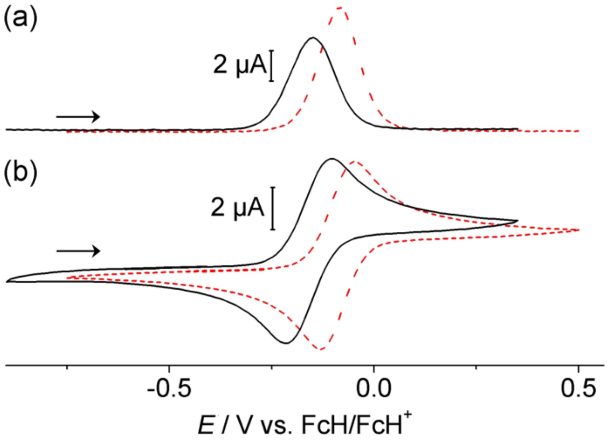

Figure 1. (a) Square wave and (b) cyclic voltammograms of H-1 in CH_2Cl_2 (full black line) and in THF (dashed red line) at 298 K.

Formation of the ferrocenium cation is proven by Mößbauer and EPR spectra of the chemically generated species **[H-1]$^+$** in frozen solution at $T < 90$ K. The Mößbauer parameters $\delta = 0.46(3)/0.34(3)$ mm s^{-1} and $\Delta E_Q = 0.33(5)$/n.d. mm s^{-1} (CH_2Cl_2/THF) clearly indicate the presence of ferrocenium ions in both solvents (see Supporting Information, Figure S2).[15,18,58] The EPR spectra of **[H-1]$^+$** in CH_2Cl_2 and in THF at 77 K are depicted in Figure 2. In both solvents nearly axial spectra typical of ferrocenium ions[15,18,58,59] are obtained with *g*-values of

$g_{1,2,3}$ = 3.4200, 1.8552, 1.7550 (Δg = 1.6650; CH_2Cl_2) and $g_{1,2,3}$ = 3.4200, 1.8880, 1.7700 (96%; Δg = 1.6500; THF). In THF solution a second minor species is observed with $g_{1,2,3}$ ≈ (n.d.), 1.9633, 1.8990 (≈4%). A similar picture is obtained for the *N*-acetylaminoferrocenium ion **[H-J]**$^+$ (CH_2Cl_2: $g_{1,2,3}$ = 3.3500, 1.8750, 1.7870; Δg = 1.5630; THF: $g_{1,2,3}$ = 3.3000, 1.9169, 1.7900; Δg = 1.5100 (70%); $g_{1,2,3}$ = 3.3000, 1.8850, 1.8300; Δg = 1.4700 (30%); see Supporting Information, Figure S3). The presence of the minor species is thus associated with the THF solvent and not with different intramolecular hydrogen bonds which are obviously impossible in **[H-J]**$^+$ (OH···O, NH···O; Scheme 2). We tentatively assign the major ferrocenium species (CH_2Cl_2 and THF) to contact ions pairs **[H-1]**$^+$ and **[H-J]**$^+$ with the SbF_6^- counterion hydrogen bonded to the NH group and the minor ferrocenium species to solvent separated ion pairs with THF hydrogen bonded to the NH group.[58,60]

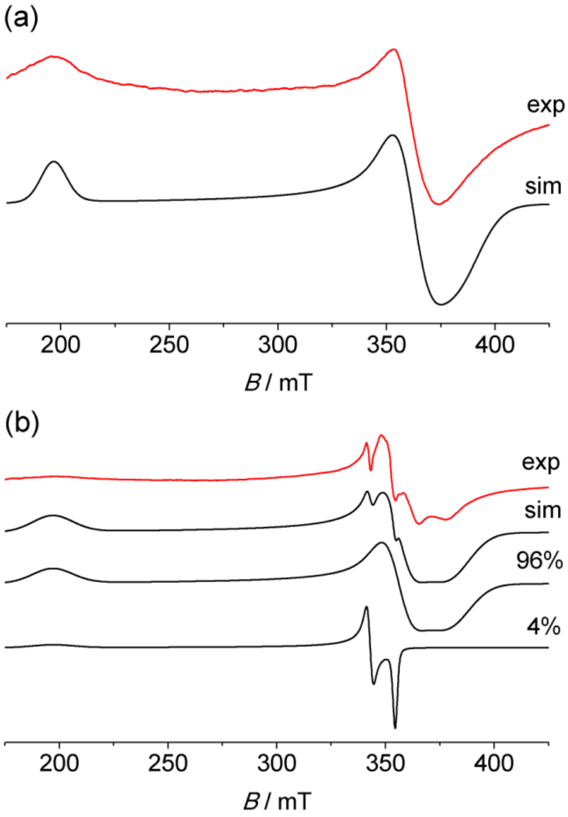

Figure 2: (a) X-band EPR spectrum of [H-1]$^+$ in CH_2Cl_2 at 77 K and simulated spectrum and (b) X-band EPR spectrum of [H-1]$^+$ in THF at 77 K and simulated spectrum including subspectra with their fractional contribution.

Concerning the conformation of **[H-1]**$^+$ this interpretation implies that the intramolecular OH···O hydrogen bond is still present in **[H-1]**$^+$ (Scheme 2, **[H-1]$^+$-OHO** conformer) while the NH group is coordinated to the counterion or to the solvent. This assignment is further supported by the very similar NH stretching vibrations of **[H-1]**$^+$ and **[H-J]**$^+$ in CH_2Cl_2 and THF, respectively (CH_2Cl_2: $\tilde{\nu}$(NH) = 3370 cm^{-1} (**[H-1]**$^+$), $\tilde{\nu}$(NH) = 3360 cm^{-1} (**[H-J]**$^+$); THF: $\tilde{\nu}$(NH) = 3350, 3240 cm^{-1} (**[H-1]**$^+$), $\tilde{\nu}$(NH) = 3340, 3210 cm^{-1} (**[H-J]**$^+$)). The optical spectra of

[H-1]$^+$ show the characteristic ferrocenium absorption band at λ_{max} = 770/745 nm (CH_2Cl_2/THF), respectively (see Supporting Information, Figure S4).[14,15]

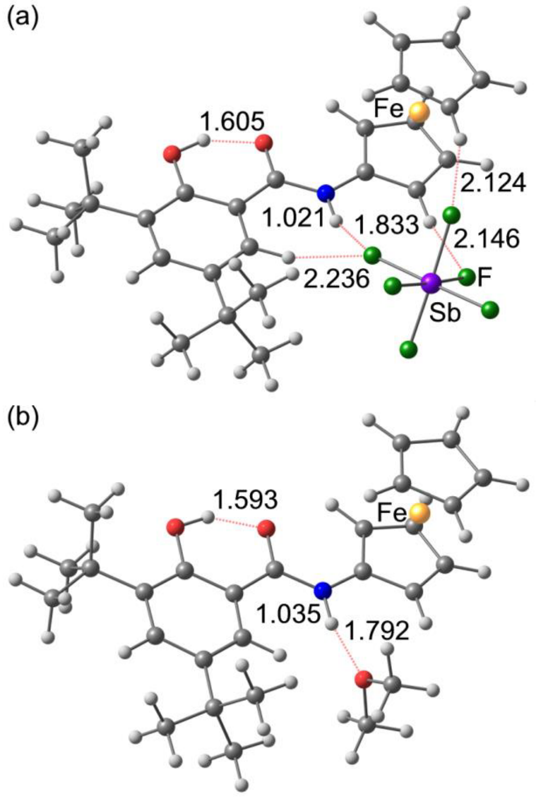

Figure 3: DFT optimized geometries of (a) [H-1]$^+$-OHO(SbF_6^-) and (b) [H-1]$^+$-OHO(OMe_2) in THF (distances in Å).

DFT/PCM models of **[H-1]$^+$-OHO** with explicit coordination of SbF_6^- to the NH group yield harmonic NH stretching frequencies $\tilde{\nu}$ = 3509/3507 cm^{-1} (CH_2Cl_2/THF; unscaled) essentially independent of the continuum solvent type (Figure 3a). Explicit coordination of OMe_2 to the NH group in THF instead of the counterion (Figure 3b) yields a significantly lower stretching energy $\tilde{\nu}$ = 3252 cm^{-1} which nicely reproduces the experimental trend and further supports our assignment of the major species [**H-1**]$^+$ as **[H-1]$^+$-OHO(SbF_6^-)** and the minor component as **[H-1]$^+$-OHO(thf)** in THF.

Addition of approximately equimolar amounts of $P_1{}^t$Bu to the **H-1**/electrolyte solution resulted in the appearance of two new one-electron redox processes at the expense of the original one in both solvents (see Supporting Information, Figure S5). The potentials of these new redox processes depend weakly on the solvent ($E_{1/2} = -535$, $E_p = +100$ mV (CH_2Cl_2); $E_{1/2} = -555$, $E_p = +75$ mV (THF)). The first oxidation is quasireversible while the second one is irreversible under these conditions. The processes are assigned to the phenolate and ferrocene units of the generated phenolate **[1]**$^-$. The geometric and electronic description of the resulting one-electron oxidized species **[1]**$^\bullet$ will be disclosed by spectroscopic means. First, we discuss the proton transfer step **H-1** → **[1]**$^-$.

Deprotonation of H-1: In CH_2Cl_2 **H-1** is easily deprotonated by $P_1{}^t$Bu to **[1]**$^-$ as shown by the characteristic shift of the UV absorption band from 320 nm (π-π* phenol) to 365 nm (π-π* phenolate) and an unaffected ferrocene absorption band at 440 nm (Figure 4).[61,62] In THF, however, the UV/Vis spectra remain unchanged and hence the acid-base reaction of **H-1** is not observed with $P_1{}^t$Bu. The same result is found for amidophenol **H-G** and $P_1{}^t$Bu in THF (see Supporting Information, Figure S6). In the presence of $[{}^nBu_4N][B(C_6F_5)_4]$ (as in the electrochemical experiments) proton transfer from **H-1** to $P_1{}^t$Bu is however successful as judged by the observed 320 nm → 365 nm shift of the phenol/phenolate absorption band (Figure 4). Deprotonation of **H-1** in THF is also successful using $P_4{}^t$Bu as base. Thus, $P_1{}^t$Bu alone in THF is obviously incompetent to deprotonate the phenol which could possibly be a microsolvation effect.[63]

The successfully generated phenolate **[1]**$^-$ shows its NH stretching vibration at $\tilde{\nu}(NH) = 3380\ cm^{-1}$ (CH_2Cl_2, $P_1{}^t$Bu) and at $\tilde{\nu}(NH) = 3220\ cm^{-1}$ (THF, $[{}^nBu_4N][B(C_6F_5)_4]$, $P_1{}^t$Bu) both indicative for hydrogen bonds involving the NH group. Hence, we propose the intramolecular NH···O hydrogen bond being dominant in the phenolate **[1]**$^-$ (**[1]$^-$-NHO**). No evidence for a hydrogen bonded iminolate **[1]$^-$-OHO** could be found which is expected from the different pK_a values of phenol and amide.[46] The higher stability of the NH···O phenolate tautomer is also reproduced by DFT calculations in both solvents (by 37/31 kJ mol^{-1} in CH_2Cl_2/THF; see Supporting Information, Figure S7).

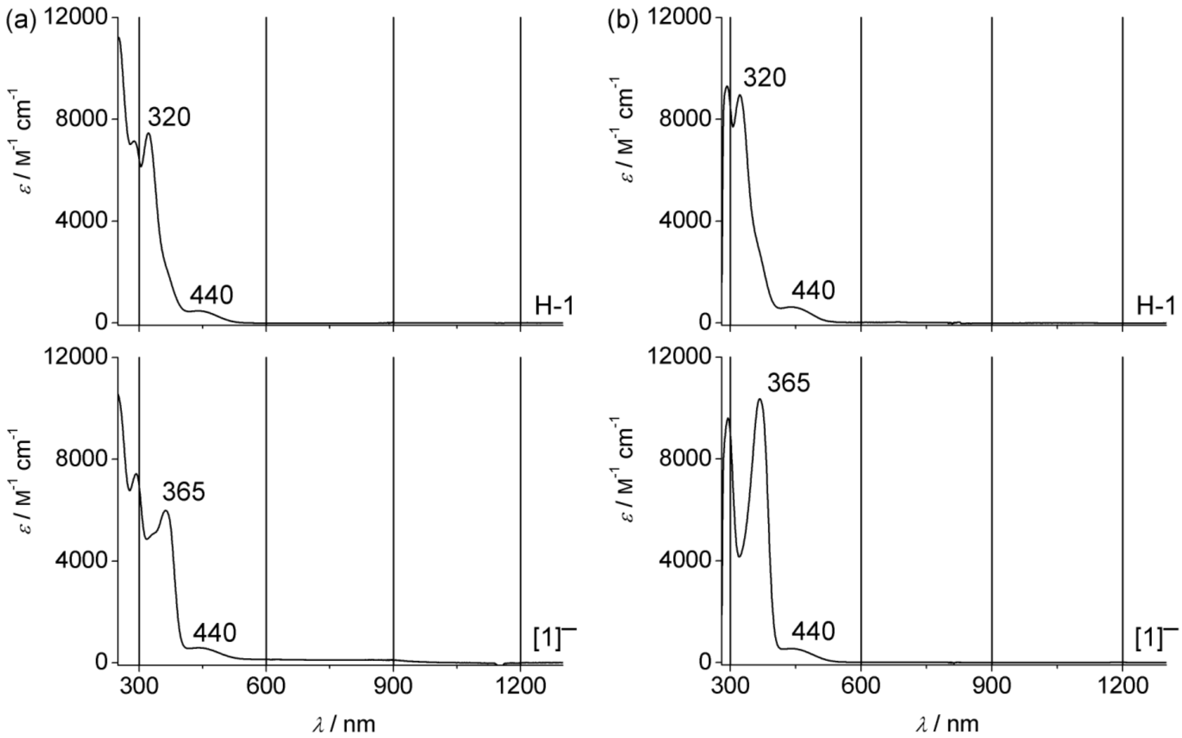

Figure 4. UV/Vis/NIR spectra of H-1 (top) and [1]$^-$ (bottom) (a) in CH_2Cl_2 and (b) in THF ($[{}^nBu_4N][B(C_6F_5)_4]$, $P_1{}^t$Bu) at 298 K.

Oxidation of $[1]^-$-NHO and deprotonation of $[H\text{-}1]^+$-OHO: Treating **$[1]^-$-NHO** with $AgSbF_6$ yields EPR-active (frozen) solutions ($g_{1,2,3} = 3.0400, 1.9490, 1.9030$; $\Delta g = 1.1370$ (CH_2Cl_2+$P_1{}^t$Bu); $g_{1,2,3} = 3.1500, 1.9740, 1.9579$; $\Delta g = 1.1921$ (THF+$P_4{}^t$Bu)) clearly indicating the presence of ferrocenium species different from **$[H\text{-}1]^+$** (Figure 5a,b).[58,59] The presence of phenoxyl radicals is definitively excluded as under similar conditions **$[G]^-$**/$AgSbF_6$/CH_2Cl_2 gives a sharp intense EPR resonance at $g_{1,2,3} = 2.0067, 2.0060, 2.0043$ ($\Delta g = 0.0024$) for the phenoxyl radical **$[G]^•$** at 77 K (Figure 5c).[47,64-66]

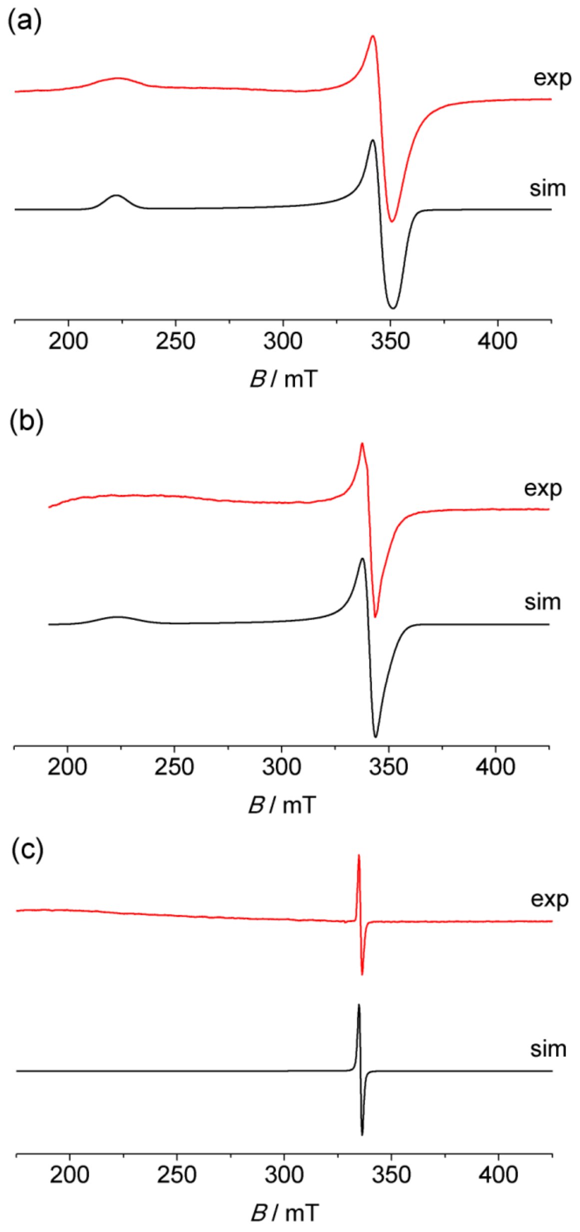

Figure 5. (a) X-band EPR spectrum of $[1]^•$ in CH_2Cl_2 at 77 K and simulation, (b) X-band EPR spectrum of $[1]^•$ in THF at 77 K and simulation, and (c) X-band EPR spectrum of $[G]^•$ in CH_2Cl_2 at 77 K and simulation.

In the optical spectra (Figure 6) of thus generated **[1]$^•$** a weak NIR absorption band is observed at 1040/1050 nm (CH_2Cl_2+$P_1{}^t$Bu/THF+$P_4{}^t$Bu) in addition to the still present π-π* phenolate band at 365/370 nm (CH_2Cl_2+$P_1{}^t$Bu/THF+$P_4{}^t$Bu). Absorption bands of a side product (possibly decomposed phenoxyl radicals formed under these conditions) are found at 410 and 420 nm in CH_2Cl_2 and in THF, respectively (Figure 6, top). The reverse reaction sequence (oxidation, deprotonation) results in a cleaner and more complete transformation without any side products (Figure 6, bottom). Similar clean results are obtained by spectroelectrochemical methods using an OTTLE cell (CH_2Cl_2, [^{n}Bu$_4$N][B(C_6F_5)$_4$], $P_1{}^t$Bu or THF, [^{n}Bu$_4$N][B(C_6F_5)$_4$], $P_1{}^t$Bu; see Supporting Information, Figure S8).

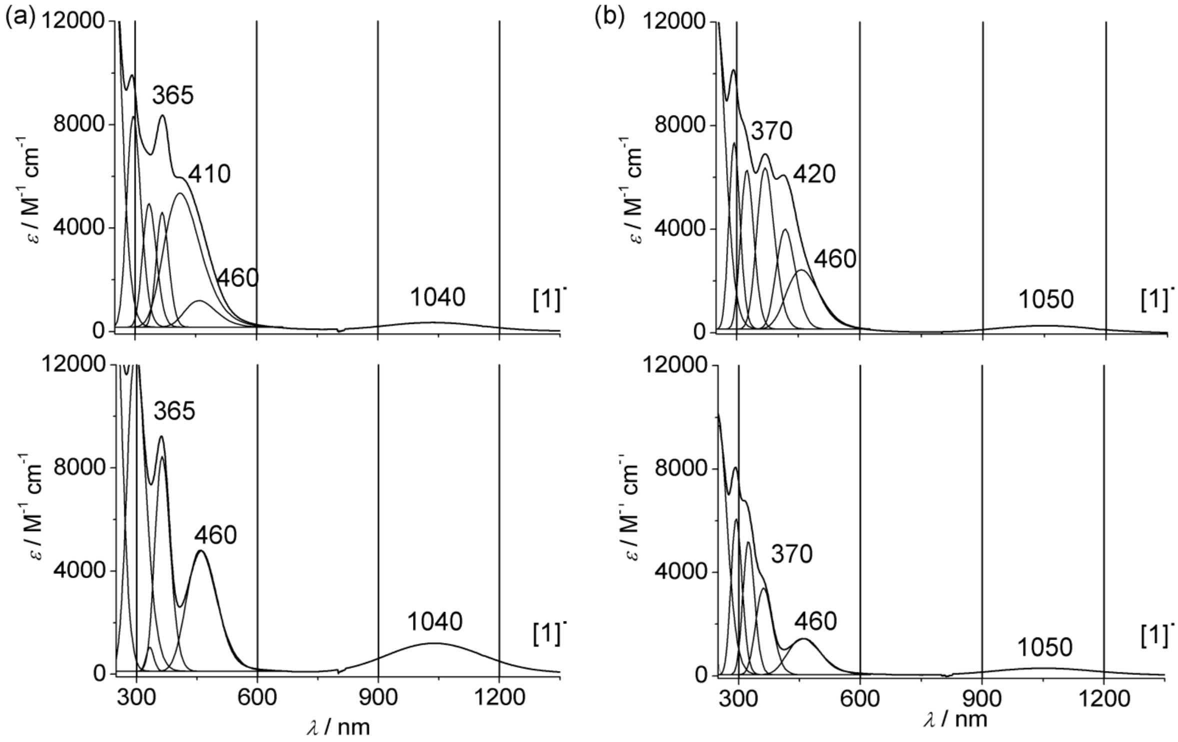

Figure 6. UV/Vis/NIR spectra of [1]$^•$ (a) in CH_2Cl_2 generated from [1]$^-$-NHO/$P_1{}^t$BuH$^+$ by addition of $AgSbF_6$ (top), generated from [H-1]$^+$-NHO by addition of $P_1{}^t$Bu (bottom), and (b) in THF generated from [1]$^-$-NHO/$P_4{}^t$BuH$^+$ by addition of $AgSbF_6$ (top), and generated from [H-1]$^+$-NHO by addition of $P_4{}^t$Bu (bottom) at 298 K. A Gaussian band shape analysis is included to demonstrate the formation of a side product (410/420 nm) in the deprotonation/oxidation sequence (top) but not in the oxidation/deprotonation sequence (bottom).

The presence of several isosbestic points in the UV/Vis/NIR spectra indicate a clean oxidation of **[1]$^-$-NHO** in both solvents under these conditions (CH_2Cl_2: 338, 389 nm; THF: 339, 394 nm; see Supporting Information, Figure S8). In the electrochemically derived radical **[1]$^•$** the NIR band is slightly shifted to higher energies (1025/1035 nm in CH_2Cl_2 and THF) which can be ascribed to the higher ionic strength of the solution. The observed solvatochromic and ionochromic effects clearly argue against an assignment of the NIR band as a metal centered transition but rather points to some charge transfer character. The combined EPR and optical spectroscopic data clearly support a ferrocenium-phenolate zwitterionic description of **[1]$^•$** in both solvents (**[1b]$^•$**). The NIR absorption band is hence assigned to a phenolate → ferrocenium charge transfer. Band shape analyses of the electrochemically derived NIR bands yield the following parameters $\tilde{\nu}_{max}$ = 9738/9638 cm^{-1}, $\Delta\tilde{\nu}_{1/2}$ = 2550/2575 cm^{-1} and ε = 749/255 M^{-1} cm^{-1} in CH_2Cl_2 and THF, respectively. If we estimate the electron transfer distance from the Fe center to the phenolate oxygen atom as 5.3 Å electronic coupling constants can be derived from Hush's formula as H_{AB} = 530/310 cm^{-1} in CH_2Cl_2 and THF, respectively. The values demonstrate a moderate electronic communication of the redox sites in **[1b]$^•$** in both solvents.

To probe the H-bonding motif in **[1b]$^•$** IR spectra of **[1b]$^•$** are recorded in solution (see Supporting Information, Figure S9). Both in CH_2Cl_2 and in THF two absorptions assignable to NH stretching vibrations are reproducibly observed ($\tilde{\nu}$(NH) = 3380, 3340 cm^{-1} (CH_2Cl_2); $\tilde{\nu}$(NH) = 3320, 3220 cm^{-1} (THF)). This finding points to two different NH hydrogen bonded zwitterions **[1b]$^•$-NHO** in solution on the IR time scale (vide infra). Reversing the reaction sequence to oxidation followed by deprotonation (**H-1-OHO → [H-1]$^+$-OHO → [1b]$^•$**) gives essentially the same spectral data of **[1b]$^•$-NHO** (EPR, UV/Vis/NIR, IR), however, with slightly higher yields of **[1b]$^•$** as judged by the UV/Vis/NIR spectra (vide supra).

To corroborate these assignments and to get deeper insight into the nature of the species present in solution DFT optimizations of phenoxyl radicals **[1a]$^•$-OHO** and **[1a]$^•$-NHO** and the zwitterions **[1b]$^•$-OHO** and **[1b]$^•$-NHO** were performed in CH_2Cl_2 and THF (continuum) solvents (Scheme 2). The optimized geometries, relative energies and spin density plots are summarized in Figure 7. Minimum structures could be located for all valence isomers/tautomers, except for the phenoxyl radical **[1a]$^•$-OHO** which converges to the zwitterion **[1b]$^•$-OHO**. The valence state in each case is easily deduced from the spin density plots (Figure 7). For **[1b]$^•$-NHO** we were able to locate two essentially degenerate tautomers with the proton of the charge-assisted NHO hydrogen bond residing near to the nitrogen (**[1b]$^•$-NHO**) or close to the phenolic oxygen atom (**[1b]$^•$-NHO'**).

Obviously, the acidity of a phenol and a ferrocenium-substituted amide [FcNHCO]$^+$ is very similar and an (accidentally nearly symmetric) double minimum potential is found. These two zwitterions with the intramolecular N···H···O hydrogen bond **[1b]$^•$-NHO** and **[1b]$^•$-NHO'** are calculated as the most stable valence isomeric and tautomeric forms (Figure 7). This fits to the proposed NH···O intramolecular hydrogen bond in **[1]$^•$**. The barrier between these tautomers is believed to be very low and all spectroscopic techniques with a slower time scale will not be able to distinguish these. Indeed, DFT/PCM(CH_2Cl_2) calculations of a simplified model (^{t}Bu groups were replaced by H atoms as the methyl rotations are detrimental to location of the correct transition state) yield a transition state structure with one imaginary frequency corresponding to the movement of the proton in the N···H···O hydrogen bond. Its electronic energy (without zero-point correction) is only 4 kJ mol^{-1} higher than the energy of the minimum structure. IR spectroscopy, however, might be fast enough two detect both chemically different tautomers of the real system and indeed two absorptions assigned to NH stretching vibrations are observed experimentally (vide supra). Accordingly, the DFT calculated tautomers feature different NH/OH vibrations for the tautomers (**[1b]$^•$-NHO/[1b]$^•$-NHO'** 2312/2129 cm^{-1} in

CH_2Cl_2; **[1b]$^\bullet$-NHO**/**[1b]$^\bullet$-NHO'** 2436/2046 cm^{-1} in THF; unscaled). Hence, we tentatively assign the most stable geometries of **[1]$^\bullet$** to a double minimum situation connected by a simple proton movement (Figure 7, PT).

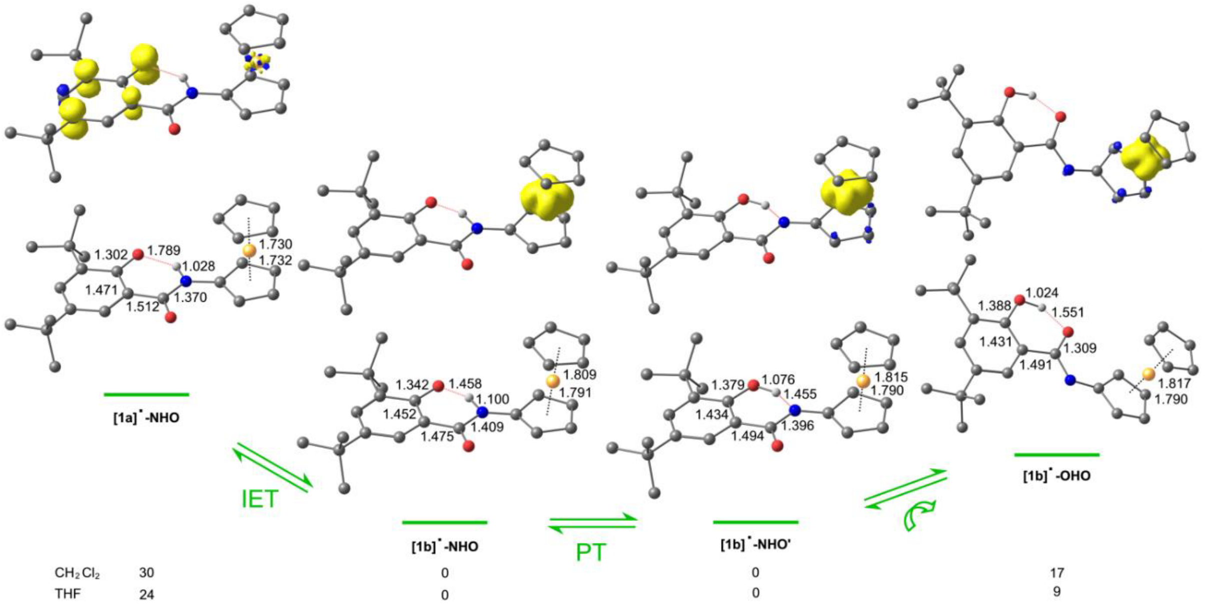

Figure 7. DFT calculated energy profiles (CH_2Cl_2, THF; free energies in kJ mol^{-1}), geometries (CH_2Cl_2, distances in Å, CH hydrogen atoms omitted) and spin densities (yellow, CH_2Cl_2, isosurface value 0.01 a.u.) of the valence isomers and tautomers of [1]$^\bullet$ in CH_2Cl_2.

The geometry with the next higher energy is represented by the OH···O hydrogen bonded zwitterion **[1b]$^\bullet$-OHO** (17/9 kJ mol^{-1}; CH_2Cl_2/THF) while the phenoxyl radical **[1a]$^\bullet$-NHO** is calculated at even higher energy (30/24 kJ mol^{-1}; CH_2Cl_2/THF). The zwitterion **[1b]$^\bullet$-OHO** might be accessible via the **[1b]$^\bullet$-NHO'** tautomer as the N···H distance is already elongated to 1.455 Å in the iminolate **[1b]$^\bullet$-NHO'** (Figure 7). This would allow breaking the OH···N hydrogen bond and rotation around the C–C(=O) bond to yield the **[1b]$^\bullet$-OHO** isomer with phenol/iminolate geometry (Figure 7). As we do not observe **[1b]$^\bullet$-OHO** experimentally the equilibrium concentration of **[1b]$^\bullet$-OHO** is obviously below our experimental detection limit.

The phenoxyl valence isomer **[1a]$^\bullet$-NHO** might be thermally accessible via IET within the **[1b]$^\bullet$-NHO** tautomer (Figure 7). The spin density shifts from the iron atom to the phenolate/phenoxyl unit paralleling the IET from phenolate to ferrocenium (Figure 7). The geometric differences between **[1b]$^\bullet$-NHO** and its higher energy valence isomer **[1a]$^\bullet$-NHO** (in their relaxed geometries) are relatively small leading to a small inner-sphere reorganization energy for the thermal IET. The Fe-Cp(centroid) distances are reduced from 1.80 Å (ferrocenium) to 1.73 Å (ferrocene). The C-O$_{\text{phenol}}$ distances also decrease from 1.342 Å to 1.302 Å reflecting the increased C-O bond order in the phenoxyl radical. Furthermore, the NH bond is shortened from 1.100/1.088 Å to 1.028/1.027 Å (CH_2Cl_2/THF) due to the reduced acidity of the ferrocene unit [Fc-NH]. Concomitantly, the O···H distances increase from 1.458/1.491 Å to 1.789/1.795 Å (CH_2Cl_2/THF) due to the lost charge assistance in the hydrogen bond. In other words the inner-sphere ET reaction coordinate **[1b]$^\bullet$-NHO** → **[1a]$^\bullet$-NHO** involves the ferrocenium/ferrocene moiety, the phenolate/phenoxyl site (ET) and the hydrogen atom in the hydrogen bond (partial PT).

To elucidate possible optical electron transfer pathways and to assign the experimental NIR absorption band TD-DFT calculations were performed for the optimized isomers **[1a]$^\bullet$-NHO**, **[1b]$^\bullet$-OHO** and **[1b]$^\bullet$-NHO**/**[1b]$^\bullet$-NHO'** with CH_2Cl_2 and THF continuum solvent models. All species display NIR transitions. Most of them are weak forbidden transitions of the ferrocenium unit (**[1b]$^\bullet$**; $d_{z2} \rightarrow d_{x2-y2}$; $\lambda = 1075 - 1095$ nm; $f < 0.0045$) or the ferrocene unit (**[1a]$^\bullet$**; $d_{x2-y2} \rightarrow d_{xz}/d_{yz}$; $\lambda = 1079 - 1084$ nm; $f < 0.0011$). The phenoxyl radical **[1a]$^\bullet$-NHO** additionally shows a transition at 971/986 nm (CH_2Cl_2/THF) which is assigned to a charge transfer from the electron-rich Fe(CpNHCO) unit to the phenoxyl moiety ($f = 0.0118/0.0126$; CH_2Cl_2/THF) and the expected ferrocene $d_{x2-y2} \rightarrow$ phenoxyl charge transfer at 2583/2789 nm ($f = 0.0147/0.0174$; CH_2Cl_2/THF) (Figure 8a). The zwitterion **[1b]$^\bullet$-NHO** shows a low-energy band at 1016/1044 nm ($f = 0.0145/0.0130$; CH_2Cl_2/THF) with high phenolate → d_{xz} charge transfer character (84/86%; CH_2Cl_2/THF; Figure 8b).[67] This excellently fits to the experimental values of 1040/1050 nm (CH_2Cl_2/THF; Figure 6) even reproducing the small solvatochromic effect.

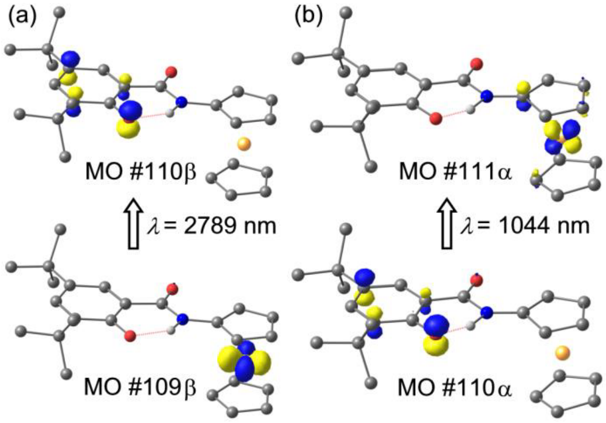

Figure 8. Relevant Kohn-Sham molecular orbitals involved in the NIR charge transfer transition of (a) [1a]$^\bullet$-NHO and (b) [1b]$^\bullet$-NHO (CH_2Cl_2, isosurface value 0.1 a.u., CH hydrogen atoms omitted).[67]

According to the TD-DFT calculations the tautomeric zwitterion **[1b]$^\bullet$-NHO'** (Figure 7) lacks this charge transfer transition further supporting the view that (thermal and optical) ET occurs via the **[1b]$^\bullet$-NHO** tautomer and proton movement prior to ET is necessarily involved. The **[1b]$^\bullet$-OHO** isomer shows a calculated transition at 813/826 nm ($f = 0.0113/0.0117$; CH_2Cl_2/THF) which has iminolate → d_{xz}/d_{x2-y2} character consistent with the absence of an electron-rich phenolate unit and the presence of an electron-rich iminolate substituent (Figure 7). Such an absorption is clearly absent in the experimental spectrum excluding the presence of significant amounts of **[1b]$^\bullet$-OHO** (Figure 6). In summary the TD-DFT data support the view that the zwitterions **[1b]$^\bullet$-NHO**/**[1b]$^\bullet$-NHO'** represent the ground state of **[1]$^\bullet$**. The former tautomer can be excited to the valence isomeric phenoxyl radical **[1a]$^•$-NHO** by IR-A light (≈1000 nm) and back by IR-B light (≈2600 nm) according to the calculations.

3.1.3 CONCLUSIONS

The multifunctional amide-linked ferrocene-phenol **H-1** prefers an OH···O hydrogen bond in CH_2Cl_2 and THF solution (**H-1-OHO**). This hydrogen bond motif is retained upon oxidation to the cation **[H-1]$^+$-OHO** in both solvents. The counterion $SbF_6^–$ coordinates to the NH group of the cation in CH_2Cl_2 resulting in a contact ion pair while in THF solution the solvent competes to some extent for this binding site giving solvent separated ion pairs. Mößbauer, EPR and UV/Vis spectroscopic data clearly demonstrate that **[H-1]$^+$-OHO** is a genuine ferrocenium ion in both solvents. Deprotonation of **H-1** to **[1]$^–$** by $P_1{}^t$Bu is straightforward in CH_2Cl_2 but hampered in THF. In THF deprotonation is achieved by $P_4{}^t$Bu or by $P_1{}^t$Bu/[^{n}Bu$_4$N][B(C_6F_5)$_4$]. IR spectroscopy and DFT calculations reveal the presence of the NH···O phenolate tautomer **[1]$^–$-NHO** (OH···O to NH···O switch). Oxidation of the phenolate **[1]$^–$-NHO** gives the radical **[1]$^•$**. This neutral radical is best described as ferrocenium-phenolate zwitterion with a dynamic NH···O/N···HO hydrogen bond **[1b]$^•$-NHO** (EPR, UV/Vis/NIR spectroscopy) with the proton bonded either to nitrogen or to oxygen (IR spectroscopy, DFT calculations; flat double minimum). The valence isomeric phenoxyl radical **[1a]$^•$-NHO** is calculated higher in energy by 30/24 kJ mol$^{–1}$ (CH_2Cl_2/THF). The phenoxyl radical state **[1a]$^•$-NHO** can be optically populated by exciting the 1040/1050 nm (CH_2Cl_2/THF) phenolate → ferrocenium charge transfer band of **[1b]$^•$-NHO**. In this respect zwitterionic **[1b]$^•$** and its valence isomer **[1a]$^•$** represent the inverse electronic situation of ferrocene-quinone conjugate **E** and its zwitterionic ferrocenium-semiquinonate excited state **E'**.[21]

Future investigations will probe the lifetime of valence isomer **[1a]$^•$-NHO** and analogous systems by pump-probe spectroscopy. The application of systems based on amide-linked ferrocenium/phenolate zwitterions as light-triggered molecular switches is currently investigated in more detail in our laboratory.

3.1.4 EXPERIMENTAL SECTION

General Considerations: All reactions were performed under argon atmosphere unless otherwise noted. Dichloromethane was dried over CaH_2 and distilled prior to use; THF was distilled from potassium. Absolute DMF was used as received from Acros. $P_1{}^t$Bu and $P_4{}^t$Bu (2 M in hexanes) were commercially available from Sigma-Aldrich. Aminoferrocene[12,50], 2,5-dioxopyrrolidine-1-yl-3,5-di-*tert*-butyl-2-hydroxybenzoate[47], **H-G**[47], and [^{n}Bu$_4$N][B(C_6F_5)$_4$][55] were prepared according to literature procedures. Filtrations from precipitated silver after oxidation were performed with syringe filters (Rotilabo-Spritzenfilter, Ø = 25 mm, pore size = 0.20 µm; Carl Roth GmbH + Co. KG, Germany). NMR spectra were recorded on a Bruker Avance DRX 400 spectrometer at 400.13 MHz (^{1}H) and 100.03 MHz (^{13}C{^{1}H}) at 25 °C. All resonances are reported in ppm versus the solvent signal as internal standard. CD_2Cl_2 (^{1}H: δ = 5.32 ppm; ^{13}C: δ = 54.0 ppm), THF-d_8 (^{1}H: δ = 3.58 ppm; ^{13}C: δ = 67.6 ppm). (s) = singlet, (d) = doublet, (pt) = pseudo triplet (unresolved doublet of doublets). Coupling constants $^nJ_{XY}$

are reported in Hertz (Hz). IR spectra were recorded with a Varian Excalibur Series 3100 FT-IR spectrometer using KBr cells in CH_2Cl_2 and THF, and as KBr disks. (s) = strong, (m) = medium, (w) = weak. Electrochemical experiments were carried out on a BioLogic SP-50 voltammetric analyzer using a platinum working electrode, a platinum wire as counter electrode, and a 0.01 M $Ag/AgNO_3$ electrode as reference electrode. The measurements were carried out at a scan rate of 100 mV s^{-1} for cyclic voltammetry experiments and for square wave voltammetry experiments using 0.1 M $[^nBu_4N][B(C_6F_5)_4]$ as supporting electrolyte and 0.001 M of the sample in CH_2Cl_2 or THF, respectively. Potentials are given relative to the ferrocene/ferrocenium couple. Referencing was achieved by addition of decamethylcobaltocene ($E_{1/2} = -2.04/-1.94$ V vs. FcH/FcH^+ (CH_2Cl_2/THF; $[^nBu_4N][B(C_6F_5)_4]$)) to the sample. The latter data were converted to the respective ferrocene/ferrocenium values according to the literature.[68] Spectroelectrochemical experiments were performed using a thin layer quartz glass (path length 1 mm) cell kit (GAMEC Analysentechnik, Illingen, Germany) equipped with a Pt gauze working electrode, a Pt counter electrode and a $Ag/AgNO_3$ reference electrode (0.3 mM solutions of **[1]**$^-$ in $CH_2Cl_2/P_1{}^tBu$ or in $THF/P_1{}^tBu$, containing 0.1 M $[^nBu_4N][B(C_6F_5)_4]$). UV/Vis/NIR spectra were recorded on a Varian Cary 5000 spectrometer using 1.0 cm cells (Hellma, suprasil). ESI mass spectra were recorded on a Micromass Q-TOF-Ultima spectrometer. CW EPR spectra (X-band; ca. 9.4 GHz) were measured on a Miniscope MS 300 at 77 K cooled by liquid nitrogen in a finger dewar (Magnettech GmbH, Berlin, Germany). Settings were as follows: center field: 2499.01 G; modulation amplitude: 2000 mG; receiver gain: 0.5; microwave attenuation: 10 dB; sweep time: 60 s. g-values are referenced to external Mn^{2+} in ZnS ($g = 2.118, 2.066, 2.027, 1.986, 1.946, 1.906$). Simulations of EPR spectra were performed with EasySpin (v 4.0.0)[69] for MatLab (R2007b). ^{57}Fe Mößbauer measurements of samples dissolved and frozen in a sample holder made of PMMA (18 mm external diameter; 4.5 mm thickness; 16 mm effective sample diameter; 1.5 mm pathlength; sealed with 2 mm natural rubber) were performed in transmission geometry using a constant-acceleration spectrometer and the source ^{57}Co(Rh). The Recoil 1.03 Mössbauer Analysis Software was used to fit the experimental spectra with Lorentzian peaks.[70] Isomer shift values are quoted relative to α-Fe at 295 K. Melting points were determined using a Gallenkamp capillary melting point apparatus MFB 595 010M and were not corrected. Elemental analyses were performed by the microanalytical laboratory of the chemical institutes of the University of Mainz.

Density functional calculations were carried out with the Gaussian09/DFT series[71] of programs. The B3LYP formulation of density functional theory was used employing the LANL2DZ basis set. No symmetry constraints were imposed on the molecules. The presence of energy minima of the ground states was checked by analytical frequency calculations. Solvent modeling was done employing the integral equation formalism polarizable continuum model (IEFPCM, dichloromethane and THF). In some instances coordination of solvent (OMe_2) or counterions (SbF_6^-) was explicitly included. The approximate free energies at 298 K were obtained through thermochemical analysis of the frequency calculation, using the thermal correction to Gibbs free energy as reported by Gaussian09.

Synthesis of 2,4-di-*tert*-butyl-6-(2-ferrocenylcarbamoyl)phenol (H-1): Aminoferrocene (149 mg, 0.74 mmol; 1.2 eq.) and 2,5-dioxopyrrolidine-1-yl-3,5-di-*tert*-butyl-2-hydroxybenzoate (215 mg, 0.62 mmol; 1.0 eq.) were dissolved in absolute DMF (5 ml). Absolute triethylamine (87 mg, 120 µl; 0.86 mmol; 1.4 eq.) was added and the mixture was stirred at room temperature for 18 hours. Water (15 ml) was added and the product was extracted with CH_2Cl_2 (4 × 30 ml). The organic phase was washed with water and brine and dried over $MgSO_4$. After filtration the solvent was removed under reduced pressure. The raw product was purified by column chromatography (SiO_2, petroleum ether (boiling point 40 – 60 °C) and CH_2Cl_2 (1:0 → 1:1) resulting in an orange colored solid. Yield: 48% (128 mg, 0.30 mmol). ^{1}H NMR (CD_2Cl_2): δ (ppm) = 12.69 (s, 1H, OH), 7.51 (s, 1H, H^9), 7.36 (s, 1H, NH), 7.21 (s, 1H, H^{11}), 4.72 (s, 2H, H$^{2/5}$), 4.22 (s, 5H, CpH), 4.12 (s, 2H, H$^{3/4}$), 1.44 (s, 9H, H^{12a}), 1.35 (s, 9H, H^{13a}). ^{1}H NMR (THF-d$_8$): δ (ppm) = 13.37 (s, 1H, OH), 9.01 (s, 1H, NH), 7.55 (d, 1H, $^4J_{HH}$ = 2.32 Hz, H^{11}), 7.48 (d, 1H, $^4J_{HH}$ = 2.28 Hz, H^9), 4.74 (pt, 2H, H$^{2/5}$), 4.15 (s, 5H, CpH), 4.01 (pt, 2H, H$^{3/4}$), 1.44 (s, 9H, H^{12a}), 1.32 (s, 9H, H^{13a}). ^{13}C NMR (CD_2Cl_2): δ(ppm) = 170.3 (C=O), 159.3 (C^7), 140.8 (C^{10}), 138.8 (C^8), 129.7 (C^9), 119.7 (C^{11}), 114.1 (C^6), 94.4 (C^1), 70.0 (Cp), 65.6 (C$^{3/4}$), 62.8 (C$^{2/5}$), 35.7 (C^{12}), 34.8 (C^{13}), 31.8 (C^{13a}), 29.7 (C^{12a}). ^{13}C NMR (THF-d$_8$): δ(ppm) = 171.3 (C=O), 160.4 (C^7), 140.5 (C^{10}), 138.4 (C^8), 129.2 (C^9), 121.5.7 (C^{11}), 115.1 (C^6), 96.4 (C^1), 70.0 (Cp), 65.3 (C$^{3/4}$), 62.4 (C$^{2/5}$), 36.1 (C^{12}), 35.2 (C^{13}), 32.0 (C^{13a}), 30.0 (C^{12a}). ESI-MS: *m/z* (%) = 433.17 (100) [M]$^+$. UV/Vis/NIR (CH_2Cl_2): λ (ε) = 250 (11205), 290 (7140), 320 (7140), 440 nm (475 M^{-1} cm^{-1}). UV/Vis/NIR (THF): λ (ε) = 250 (7460), 290 (5775), 320 (5620), 440 nm (405 M^{-1} cm^{-1}). IR (KBr): $\tilde{\nu}$ = 3358 (m, NH), 1624 (m, CO) cm^{-1}. IR (CH_2Cl_2): $\tilde{\nu}$ = 3450 cm^{-1} (m, NH), 1641 (m, CO) cm^{-1}. IR (THF): $\tilde{\nu}$ = 3320 cm^{-1} (m, NH), 1638 (m, CO) cm^{-1}. R_f (CH_2Cl_2) = 0.93. M.p. 213 °C (decomp.). Elemental analysis calcd (%) for $C_{25}H_{31}FeNO_2$ (433.17): C 69.29, H 7.21, N 3.23; found C 69.09, H 6.52, N 3.39.

Deprotonation and oxidation: The samples were prepared from stock solutions of **H-1** in CH_2Cl_2 or in THF. After addition of one equivalent base ($P_1{}^t$Bu or $P_4{}^t$Bu) to the solution of **H-1** the mixture was shaken for a few seconds. Oxidation was achieved by addition of one equivalent $AgSbF_6$ dissolved in the same solvent, allowing the mixture to react for 30 seconds and filtration from precipitated silver using syringe filters. Final concentrations of **H-1**, **[1]**$^-$, **[H-1]**$^+$, and **[1]**$^\bullet$ were 0.15 mM (UV/Vis/NIR), 5 mM (IR), 25 mM (EPR) and 25 – 70 mM (Mößbauer). For the latter two methods samples were frozen by cooling to $T < 90$ K.

3.1.5 ASSOCIATE CONTENT

Supporting Information

NOESY spectra of **H-1** in CD_2Cl_2 and in THF-d$_8$ at 298 K; Mößbauer spectra of **[H-1]**$^+$ in CH_2Cl_2 and in THF at 77 K; EPR spectra of **[H-J]**$^+$ in CH_2Cl_2 and in THF at 77 K; UV/Vis/NIR spectra of **H-1** and **[H-1]**$^+$ in CH_2Cl_2 and in THF at 298 K; square wave and cyclic voltammograms of **[1]**$^-$ in CH_2Cl_2 and in THF at 298 K; UV/Vis/NIR spectra of **H-1** and **H-G** in THF at 298 K in the absence and presence of $P_1{}^t$Bu; DFT optimized geometries of **[1]$^-$-NHO** and **[1]$^-$-OHO** in CH_2Cl_2 and in THF; spectroelectrochemical oxidation of **[1]$^-$** in CH_2Cl_2/[^{n}Bu_4N][$B(C_6F_5)_4$] and in THF/[^{n}Bu_4N][$B(C_6F_5)_4$] at 298 K; IR spectra of **H-1**, **[1]$^-$**, **[H-1]$^+$** and **[1]$^•$** in CH_2Cl_2 and in THF at 298 K. Cartesian coordinates of optimized structures. This material is available free of charge via the Internet at http://pubs.acs.org.

AUTHOR INFORMATION

Corresponding Author

*E-mail: katja.heinze@uni-mainz.de

Present Address

Institute of Inorganic and Analytical Chemistry, Johannes Gutenberg-University of Mainz, Duesbergweg 10-14, 55128 Mainz, Germany

Notes

The authors declare no competing financial interest.

3.1.6 ACKNOWLEDGMENT

We are grateful to Dr. Dariush Hinderberger and Dipl.-Chem. Anica Wünsche von Leupoldt for helpful discussions of the EPR spectra, Dipl.-Chem. Teuta Gasi for measuring a Mößbauer spectrum and Dipl.-Chem. Torben Kienz, Benedikt Dahms, Maximilian Lauck, and Thorsten Prechtl for preparative assistance.

3.1.7 REFERENCES

(1) Ferreira, K. N.; Iverson, T. M.; Maghlaoui, K. Barber, J.; Iwata, S. *Science* **2004**, *303*, 1831–1838.
(2) Wasielewski, M. R. *Chem. Rev.* **1992**, *92*, 435–461.
(3) Fox, M. A. *Chem. Rev.* **1992**, *92*, 365–368.
(4) Robin, M. B.; Day, P. *Adv. Inorg. Chem. Radiochem.* **1967**, *10*, 247–422.
(5) Creutz, C.; Taube, H. *J. Am. Chem. Soc.* **1969**, *91*, 3988–3989.
(6) Huynh, M. H. V; Meyer, T. J. *Chem. Rev.* **2007**, *107*, 5004–5064.
(7) Kaim, W.; Klein, A.; Glöckle, M. *Acc. Chem. Res.* **2000**, *33*, 755–763.
(8) Kaim, W.; Sarkar, B. *Coord. Chem. Rev.* **2007**, *251*, 584–594.
(9) Kaim, W.; Lahiri, G. K. *Angew. Chem.* **2007**, *119*, 1808–1828; *Angew. Chem. Int. Ed.* **2007**, *46*, 1778–1796.
(10) Kaim, W. *Coord. Chem. Rev.* **2011**, *255*, 2503–2513.
(11) a) Heckmann, A.; Lambert, C. *Angew. Chem.* **2012**, *124*, 334–404; *Angew. Chem. Int. Ed.* **2012**, *51*, 326–392; b) Hankache, J.; Wenger, O. S. *Chem. Rev.* **2011**, *111*, 5138–5178.
(12) Heinze, K.; Schlenker, M. *Eur. J. Inorg. Chem.* **2004**, 2974–2988.
(13) Heinze, K.; Siebler, D. *Z. Anorg. Allg. Chem.* **2007**, *633*, 2223–2233.
(14) Siebler, D.; Förster, C.; Heinze, K. *Dalton Trans.* **2011**, *40*, 3558–3575.
(15) Siebler, D.; Linseis, M.; Gasi, T.; Carrella, L. M.; Winter, R. F.; Förster, C.; Heinze, K. *Chem. Eur. J.* **2011**, *17*, 4540–4551.

(16) Okamura, T.; Sakauye, K.; Ueyama, N.; Nakamura, A. *Inorg. Chem.* **1998**, *37*, 6731–6736.
(17) Barišić, L.; Rapić, V.;Kovač, V. *Croat. Chem. Acta* **2002**, *75*, 199–210.
(18) Huesmann, H.; Förster, C.; Siebler, D.; Gasi, T.; Heinze, K. *Organometallics* **2012**, *31*, 413–427.
(19) Heinze, K.; Hempel, K.; Beckmann, M. *Eur. J. Inorg. Chem.* **2006**, 2040–2050.
(20) Hillard, E.; Vessières, A.; Thouin, L.; Jaouen, G.; Amatore, C. *Angew. Chem.* **2006**, *118*, 291–296; *Angew. Chem. Int. Ed.* **2006**, *45*, 285–290.
(21) Fukuzumi, S.; Yoshida, Y.; Okamoto, K.; Imahori, H.; Araki, Y.; Ito, O. *J. Am. Chem. Soc.* **2002**, *124*, 6794–6795.
(22) Fukuzumi, S.; Okamoto, K.; Yoshida, Y.; Imahori, H.; Araki, Y.; Ito, O. *J. Am. Chem. Soc.* **2003**, *125*, 1007–1013.
(23) Fukuzumi, S.; Okamoto, K.; Imahori, H. *Angew. Chem.* **2002**, *114*, 642–644; *Angew. Chem. Int. Ed.* **2002**, *41*, 620–622.
(24) Stubbe, J.; Donk, W. A. van der *Chem. Rev.* **1998**, *98*, 705–762.
(25) Orio, M.; Jarjayes, O.; Baptiste, B.; Philouze, C.; Duboc, C.; Mathias, J.-L.; Benisvy, L.; Thomas, F. *Chem. Eur. J.* **2012**, *18*, 5416–5429.
(26) Maki, T.; Araki, Y.; Ishida, Y. *J. Am. Chem. Soc.* **2001**, *123*, 3371–3372.
(27) Rhile, I. J.; Mayer, J. M. *J. Am. Chem. Soc.* **2004**, *126*, 12718–12719.
(28) Thomas, F.; Jarjayes, O.; Jamet, H.; Hamman, S.; Saint-Aman, E.; Duboc, C.; Pierre, J.-L. *Angew. Chem.* **2004**, *116*, 604–607; *Angew. Chem. Int. Ed.* **2004**, *43*, 594–597.
(29) Rhile, I. J.; Mayer, J. M. *Angew. Chem.* **2005**, *117*, 1624–1625; *Angew. Chem. Int. Ed.* **2005**, *44*, 1598–1599.
(30) Benisvy, L.; Bill, E.; Blake, A. J.; Collison, D.; Davies, E. S.; Garner, C. D.; McArdle, G.; McInnes, E. J. L.; McMaster, J.; Ross, S. H. K.; Wilson, C. *Dalton Trans.* **2006**, 258–267.
(31) Costentin, C.; Robert, M.; Savéant, J.-M. *J. Am. Chem. Soc.* **2006**, *128*, 4552–4553.
(32) Markle, T. F.; Mayer, J. M. *Angew. Chem.* **2008**, *120*, 750–752; *Angew. Chem. Int. Ed.* **2008**, *47*, 738–740.
(33) Rhile, I. J.; Markle, T. F.; Nagao, H.; DiPasquale, A. G.; Lam, O. P.; Lockwood, M. A.; Rotter, K.; Mayer, J. M. *J. Am. Chem. Soc.* **2006**, *128*, 6075–6088.
(34) Faller, P.; Goussias, C.; Rutherford, A. W.; Un, S. *Proc. Natl. Acad. Sci. U. S. A.* **2003**, *100*, 8732–8735.
(35) Dempsey, J. L.; Winkler, J. R.; Gray, H. B. *Chem. Rev.* **2010**, *110*, 7024–7039.
(36) a) Hammes-Schiffer, S. *Chem. Rev.* **2010**, *110*, 6937–6938; b) Hammes-Schiffer, S.; Stuchebrukhov, A. *Chem. Rev.* **2010**, *110*, 6939–6960.
(37) a) Wenger, O. S. *Chem. Eur. J.* **2011**, *17*, 11692–11702; b) Herzog, W.; Bronner, C.; Löffler, S.; He, B.; Kratzert, D.; Stalke, D.; Hauser, A.; Wenger, O. S. *ChemPhysChem* **2012**, *14*, 1168-1176.
(38) Warren, J. J.; Tronic, T. A.; Mayer, J. M. *Chem. Rev.* **2010**, *110*, 6961–7001.
(39) Weinberg, D. R.; Gagliardi, C. J.; Hull, J. F.; Murphy, C. F.; Kent, C. A.; Westlake, B. C.; Paul, A.; Ess, D. H.; McCafferty, D. G.; Meyer, T. J. *Chem. Rev.* **2012**, *112*, 4016–4093.
(40) Bonin, J.; Robert, M. *Photochem. Photobiol.* **2011**, *87*, 1190–1203.
(41) Savéant, J.-M. *Energy Environ. Sci.* **2012**, *5*, 7718–7731.
(42) Gagliardi, C. J.; Vannucci, A. K.; Concepcion, J. J.; Chen, Z.; Meyer, T. J. *Energy Environ. Sci.* **2012**, *5*, 7704–7717.
(43) Hammarström, L.; Styring, S. *Energy Environ. Sci.* **2011**, *4*, 2379–2388.

(44) Costentin, C.; Robert, M.; Savéant, J.-M. *Phys. Chem. Chem. Phys.* **2010**, *12*, 11179–11190.

(45) Kanamori, D.; Okamura, T.; Yamamoto, H.; Ueyama, N. *Angew. Chem.* **2005**, *117*, 991–994; *Angew. Chem. Int. Ed.* **2005**, *44*, 969–672.

(46). a) Kanamori, D.; Furukawa, A.; Okamura, T.; Yamamoto, H.; Ueyama, N. *Org. Biomol. Chem.* **2005**, *3*, 1453–1459; b) Mock, W. L.; Chua, D. C. Y. *J. Chem. Soc. Perkin Trans. 2* **1995**, 2069–2072.

(47) Wanke, R.; Benisvy, L.; Kuznetsov, M. L.; Guedes Da Silva, M. F. C.; Pombeiro, A. J. L. *Chem. Eur. J.* **2011**, *17*, 11882–11892.

(48) Kütt, A.; Movchun, V.; Rodima, T.; Dansauer, T.; Rusanov, E. B.; Leito, I.; Kaljurand, I.; Koppel, J.; Pihl, V.; Koppel, I.; Ovsjannikov, G.; Toom, L.; Mishima, M.; Medebielle, M.; Lork, E.; Röschenthaler, G.-V. Koppel, I. A.; Kolomeitsev, A. A. *J. Org. Chem.* **2008**, *73*, 2607–2620.

(49) Bordwell, F. G.; Ji, G. *J. Am. Chem. Soc.* **1991**, *113*, 8398–8401.

(50) Bildstein, B.; Malaun, M.; Kopacka, H.; Wurst, K.; Ongania, Mitterböck, M.; K.-H.; Opromolla, G. Zanello, P. *Organometallics* **1999**, *18*, 4325–4336.

(51) Heinze, K.; Hüttinger, K.; Siebler, D. In *Modeling of Molecular Properties*; Comba, P., Ed.; Wiley-VCH Weinheim, Germany, **2011**; pp. 325–346.

(52) Siebler, D.; Förster, C.; Heinze, K. *Eur. J. Inorg. Chem.* **2010**, 523-527

(53) Connelly, N. G.; Geiger, W. E. *Chem. Rev.* **1996**, *96*, 877–910.

(54) Kondo, Y. In *Supberbases for Organic Synthesis*; Ishikawa, T., Ed.; John Wiley & Sons, Ltd: Chichester, UK, **2009**; pp. 145–185.

(55) LeSuer, R. J.; Buttolph, C.; Geiger, W. E. *J. Organomet. Chem.* **2004**, *76*, 6395–6401.

(56) Camire, N.; Mueller-Westerhoff, U. T.; Geiger, W. E. *J. Organomet. Chem.* **2001**, *639*, 823–826.

(57) Smith, T. J.; Stevenson, K. J. In *Handbook of Electrochemistry*; Zoski, C. G., Ed.; Elsevier: Oxford, UK, **2007**; pp. 100–102.

(58) Siebler, D.; Förster, C.; Gasi, T.; Heinze, K. *Organometallics* **2011**, *30*, 313–327.

(59) Prins, R. *Mol. Phys.* **1970**, *19*, 603–620.

(60) Dietrich, J.; Thorenz, U.; Förster, C.; Heinze, K. *Inorg. Chem.* **2013**, *52*, 1248–1264.

(61) Disinger, J.; Manahan, S. E. *Anal. Lett.* **1982**, *15*, 1017–1029.

(62) Tolstoy, P. M.; Koeppe, B.; Denisov, G. S.; Limbach, H.-H. *Angew. Chem.* **2009**, *121*, 5855–5858; *Angew. Chem. Int. Ed.* **2009**, *48*, 5745–5747.

(63) Doi, K.; Togano, E.; Xantheas, S. S.; Nakanishi, R.; Nagata, T.; Ebata, T.; Inokuchi, Y. *Angew. Chem.* **2013**, *125*, 4476–4479; *Angew. Chem. Int. Ed.* **2013**, *52*, 4380–4383.

(64) Benisvy, L.; Bittl, R.; Bothe, E.; Garner, C. D.; McMaster, J.; Ross, S.; Teutloff, C.; Neese, F. *Angew. Chem.* **2005**, *117*, 5448–5451; *Angew. Chem. Int. Ed.* **2005**, *44*, 5314–5317.

(65) Benisvy, L.; Hammond, D.; Parker, D. J.; Davies, E. S.; Garner, C. D.; McMaster, J.; Wilson, C.; Neese, F.; Bothe, E.; Bittl, R.; Teutloff, C. *J. Inorg. Biochem.* **2007**, *101*, 1859–64.

(66) Lachaud, F.; Quaranta, A.; Pellegrin, Y.; Dorlet, P.; Charlot, M.-F.; Un, S.; Leibl, W.; Aukauloo, A. *Angew. Chem.* **2005**, *117*, 1560–1564; *Angew. Chem. Int. Ed.* **2005**, *44*, 1536–1540.

(67) Please note the different symmetry of the metal d orbitals involved in the ferrocene → phenoxyl transition and the phenolate → ferrocenium transition which might a consequence of the non-validity of Koopman's theorem for the ionization of ferrocene: Coutière, M.-M.; Demuynck, J.; Veillard, A. *Theoret. Chim. Acta (Berl.)* **1972**, *27*, 281–287.

(68) Noviandri, I.; Brown, K. N.; Fleming, D. S.; Gulyas, P. T.; Lay, P. A.; Masters, A. F.; Phillips, L. *J. Phys. Chem. B* **1999**, *103*, 6713–6722.

(69) Stoll, S.; Schweiger, A. *J. Magn. Reson.* **2006**, *178*, 42–55.

(70) Lagarec, K.; Rancourt, D. G. *Nucl. Instrum. Methods Phys. Res. B* **1997**, *129*, 266–280.

(71) Frisch, M. J.; Trucks, G. W.; Schlegel, H. B.; Scuseria, G. E.; Robb, M. A.; Cheeseman, J. R.; Scalmani, G.; Barone, V.; Mennucci, B.; Petersson, G. A.; Nakatsuji, H.; Caricato, M.; Li, X.; Hratchian, H. P.; Izmaylov, A. F.; Bloino, J.; Zheng, G.; Sonnenberg, J. L.; Hada, M.; Ehara, M.; Toyota, K.; Fukuda, R.; Hasegawa, J.; Ishida, M.; Nakajima, T.; Honda, Y.; Kitao, O.; Nakai, H.; Vreven, T.; Montgomery, Jr., J. A.; Peralta, J. E.; Ogliaro, F.; Bearpark, M.; Heyd, J. J.; Brothers, E.; Kudin, K. N.; Staroverov, V. N.; Kobayashi, R.; Normand, J.; Raghavachari, K.; Rendell, A.; Burant, J. C.; Iyengar, S. S.; Tomasi, J.; Cossi, M.; Rega, N.; Millam, J. M.; Klene, M.; Knox, J. E.; Cross, J. B.; Bakken, V.; Adamo, C.; Jaramillo, J.; Gomperts, R.; Stratmann, R. E.; Yazyev, O.; Austin, A. J.; Cammi, R.; Pomelli, C.; Ochterski, J. W.; Martin, R. L.; Morokuma, K.; Zakrzewski, V. G.; Voth, G. A.; Salvador, P.; Dannenberg, J. J.; Dapprich, S.; Daniels, A. D.; Farkas, Ö.; Foresman, J. B.; Ortiz, J. V.; Cioslowski, J.; Fox, D. J. *Gaussian 09,* **2009**, Revision A.02; Gaussian, Inc., Wallingford, CT.

3.2 Spin Trapping of Carbon-Centered Ferrocenyl Radicals with Nitrosobenzene

Andreas Neidlinger,[‡] Torben Kienz,[‡] and Katja Heinze[*]

Organometallics **2015**, *34*, 5310−5320.

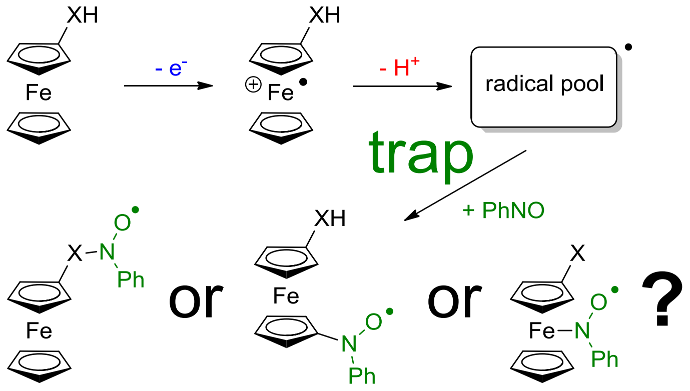

Abstract

In contrast to metal centered 17 valence electron radicals, such as $[Mn(CO)_5]^•$, ferrocenium ions $[Fe(C_5H_5)_2]^+$ (**1**$^+$), $[Fe(C_5Me_5)_2]^+$ (**2**$^+$), $[Fe(C_5H_5)(C_5H_4Et)]^+$ (**3**$^+$), $[Fe(C_5H_5)(C_5H_4NHC(O)Me)]^+$ (**4**$^+$), and $[Fe(C_5H_5)(C_5H_4NHC(S)Me)]^+$ (**5**$^+$) do not add to nitrosobenzene PhNO to give metal-coordinated stable nitroxyl radicals. In the presence of the strong and oxidatively stable phosphazene base *tert*-butylimino-tris(dimethylamino)phosphorene, the quite acidic ferrocenium ions **1**$^+$ – **5**$^+$ are deprotonated to give a pool of transient and persistent radicals with different deprotonation sites **[1−H^x]**$^•$ – **[5−H^x]**$^•$. One rather persistent iron-centered radical **[4−H^N]**$^•$, deprotonated at the nitrogen atom, has been detected by rapid-freeze EPR spectroscopy at 77 K. This iron-centered radical **[4−H^N]**$^•$ is also inert toward PhNO. The transient carbon-centered radicals **[1−H^x]**$^•$ – **[5−H^x]**$^•$ appear to rapidly abstract hydrogen atoms from the adjacent base or the solvent to regenerate the corresponding ferrocenes **1** – **5**. These transient radicals are only present in trace amounts (< 1 %). However, some of the transient carbon-centered radicals in the radical pool can be trapped by 1 – 1.2 equivalents of PhNO, even at room temperature. The corresponding resulting stable nitroxyl radicals **[6]**$^•$ – **[10]**$^•$ were studied by EPR spectroscopy at room temperature and at 77 K. The hyperfine coupling pattern to protons close to the spin center allows one to assign the site of PhNO attack in radicals **[6]$^\bullet$** – **[10]$^\bullet$**, namely, at the C_5H_5 ring in **[6]$^\bullet$**, **[9^{Cp}]$^\bullet$**, and **[10^{Cp}]$^\bullet$**, at a methyl group in **[7]$^\bullet$**, and at the methylene group in **[8^1]$^\bullet$**. These studies give a deeper insight into the stability and reactivity of radicals derived from ferrocene derivatives which might also be relevant for the biological activity of high-potent antitumor and antimalaria ferrocene-based drugs and prodrugs such as ferrocifen or ferroquine.

Supporting information for this article (without Cartesian coordinates from DFT calculations) is found at pp. 194. For full supporting information, refer to:

http://pubs.acs.org/doi/suppl/10.1021/acs.organomet.5b00778/suppl_file/om5b00778_si_001.pdf.

Adapted with permission from A. Neidlinger, T. Kienz, and K. Heinze, *Organometallics* **2015**, *34*, 5310−5320.

3.2.1 INTRODUCTION

Ferrocene and its derivatives have been found useful for a variety of applications in fundamental research, especially electron transfer, in biology and catalysis, as well as in material and pharmaceutical science.[1–5] While many of these applications rely on the reversible oxidation chemistry of the ferrocenyl moiety, investigation of the reactivity and possible degradation pathways of the resulting ferrocenium cations is worthwhile.

For instance, ferrocene itself displays no antitumor activity, while ferrocenium derivatives show in vitro cytotoxicity due to oxidative damage of DNA.[6] This has been further exploited using amino ferrocene based selective prodrugs **A** by Mohkir *et al.* (Scheme 1). In tumor cells, ferrocenes **A** are oxidized to the corresponding ferrocenium ions **A**$^+$. The ferrocenium cations **A**$^+$, as well as their degradation products, iron(II) ions, appear to catalyze the generation of reactive oxygen species. This increases the oxidative stress in cancer cells and finally leads to apoptosis.[7,8] This concept has been further explored with a variety of amino ferrocene and diamino ferrocene based prodrugs (**B**; Scheme 1a). The degradation products of **B**/**B**$^+$ again act as catalysts for generating reactive oxygen species.[9] In fact, first in vivo experiments show promising results for further pharmaceutical applications.[10]

The effectiveness of the antimalarial drug chloroquine **C** has been drastically improved by incorporation of a ferrocenyl moiety giving the potent drug ferroquine **D** (Scheme 1b). This adds the generation of reactive oxygen species as a further mode of action to the drug and takes effect in all stages of the life cycle of the parasites, thus inhibiting merozoites reinvasion.[11–13]

Scheme 1. a) Aminoferrocene Based Prodrugs A, B; b) Chloroquine C and Ferroquine D; and c) Tamoxifen E, Ferrocifen F and Ferrociphenol G.

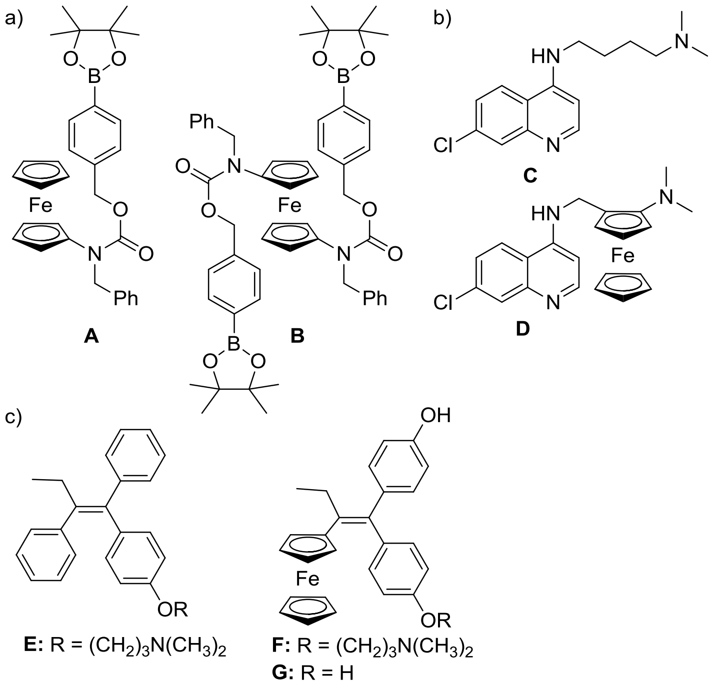

While the generation of reactive oxygen species is a valuable mechanism for amino ferrocene based prodrugs **A** and **B** and ferroquine **D**, other antitumor agents appear to follow a different mode of action. The ferrocene derivatives of tamoxifen **E**, ferrocifen **F**, and ferrociphenol **G** (Scheme 1c) show high levels of cytotoxicity against breast cancer cells. Ferrocifen **F** is even more cytotoxic than *cis*-platin.[14–18] Both ferrocifen **F** and hydroxyferrocifen **G** cause less oxidative stress compared to that of tamoxifen **E**.[19,20] Yet, in cells treated with ferrocifen derivatives a higher rate of senescence has been found. As this is unlikely to be related to oxidative stress, a further mode of action is assumed showing the versatility of ferrocenium ions. Indeed, carbon-centered radicals have been proposed to be generated after oxidation and deprotonation of ferrocifens **F**.[16]

Various experiments have been reported which focus on the ability of ferrocene to form radicals itself. First hints to the existence of ferrocenyl radicals were obtained by photo- and thermolysis of ferrocenyl azide by Sutherland *et al.*[21] γ-Irradiation of methylferrocene led to the ferrocenyl methylradical.[22] Later, it was found that ferrocenyl substituted radicals are stabilized due to spin delocalization to the iron atom.[23] This can even be exploited to generate polymetallocenylenes[24] or in stereoselective pinacol coupling reactions.[25]

Scheme 2. a) Oxidation and Deprotonation of a [4]ferrocenophane; b) Spin Trapping of a Ferrocenylmethylium Ion with Nitrosobenzene and c) Spin Trapping of Metal Centered 17 Valence Electron Radicals.

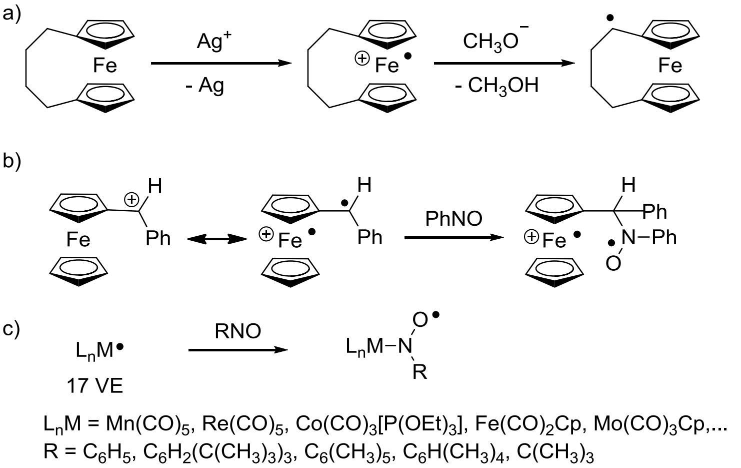

The radical reactivity of ferrocenium ions has been demonstrated by the oxidation of ferrocenophanes with silver salts in the presence of sodium methoxide. As reported by Hisatome *et al.*, this procedure results in the intermediate formation of a carbon-centered radical in the aliphatic bridge (Scheme 2a). Ferrocenylmethylium cations, as shown by Ashkenazi and Cais, react as biradicals with nitrosobenzene PhNO as spin trap (Scheme 2b).[26]

Obviously, spin trapping is a valuable tool for the investigation of transient radicals. Indeed, various manganese centered 17 valence electron radicals prepared by homolysis of carbonyl complexes could be spin trapped with nitrosodurene as spin trapping agent by Hudson and

Lappert[27] as well as with 2,4,6-tri(*tert*-butyl)nitrosobenzene by Simpson *et al.*[28] and with the aid of nitroso-*tert*-butane by Benner and Balch.[29] Later on, Re, Co, Fe, and Mo centered 17 valence electron radicals could be trapped with 2,3,5,6-tetramethyl-1-nitrosobenzene as spin trapping agent and identified by EPR spectroscopy (Scheme 2c).[30]

With the versatile and not yet fully understood reaction pathways of ferrocenium ions in mind, we were interested to generate and trap radical species of different ferrocenium ions under neutral and strongly basic conditions using the spin trapping technique. The starting iron(III) complexes ferrocenium (**1**$^+$), decamethylferrocenium (**2**$^+$), ethylferrocenium (**3**$^+$), *N*-acetylaminoferrocenium (**4**$^+$), and *N*-thioacetylaminoferrocenium (**5**$^+$) were prepared by oxidation of the corresponding ferrocenes **1** – **5** with silver hexafluoroantimonate. Spin trapping of radicals was attempted with nitrosobenzene (PhNO) in the absence and presence of the strong, non-nucleophilic, noncoordinating, and oxidatively stable phosphazene base $P_1{}^t$Bu (*tert*-butylimino-tris(dimethylamino)phosphorane (Scheme 3). In the presence of $P_1{}^t$Bu, **1**$^+$ – **5**$^+$ are expected to yield the corresponding radicals or radical pools **[1−H]**$^\bullet$ – **[5−H]**$^\bullet$. In order to address the question as to whether radicals are formed at all and to identify the site of the generated radicals (carbon, iron, nitrogen centered), the conceivable spin trapped nitroxide radical adducts of **1**$^+$ – **5**$^+$ and **[1−H]**$^\bullet$ – **[5−H]**$^\bullet$ were probed by EPR spectroscopy (Scheme 3).

While ferrocenyl nitroxide radicals have been prepared via autoxidation of ferrocenyl hydrazine and investigated by EPR spectroscopy by Forrester and Hepburn, the present approach offers a different and more general access to ferrocenyl nitroxyl radicals.[31a] Elschenbroich has reported the electrochemical generation and EPR spectroscopic study of isoelectronic radical anions of ferrocenyl arylketones.[31b] Similarly, ferrocenoylsilanes have been reduced to the corresponding radical anions by Grignard reagents.[31c]

Reactions of ferrocenium **1**$^+$ with nitrogen bases (pyrazolide, 3,5-dimethyl pyrazolide, imidazolide, and benzotriazolide) have been reported in the literature.[32] Yet, these bases are oxidized by the ferrocenium cation **1**$^+$ to the corresponding azolide radicals while **1**$^+$ is reduced to **1**. The azolide radicals are suggested to attack **1**$^+$ to give *N*-ferrocenyl azoles after proton loss (Scheme 4). No ferrocenyl radicals were reported. Clearly, such a reactivity is not expected with the base $P_1{}^t$Bu employed in this study.

Scheme 3. Spin Trapping Reactions of Ferrocenium Derivatives in the Absence and Presence of $P_1{}^tBu$ for a) 1^+, b) 2^+, c) 3^+, and d) 4^+ and 5^+ Investigated in This Study. Relevant Atom Numbering is Given. Possible Acidic Hydrogen Atoms are Marked in Red.

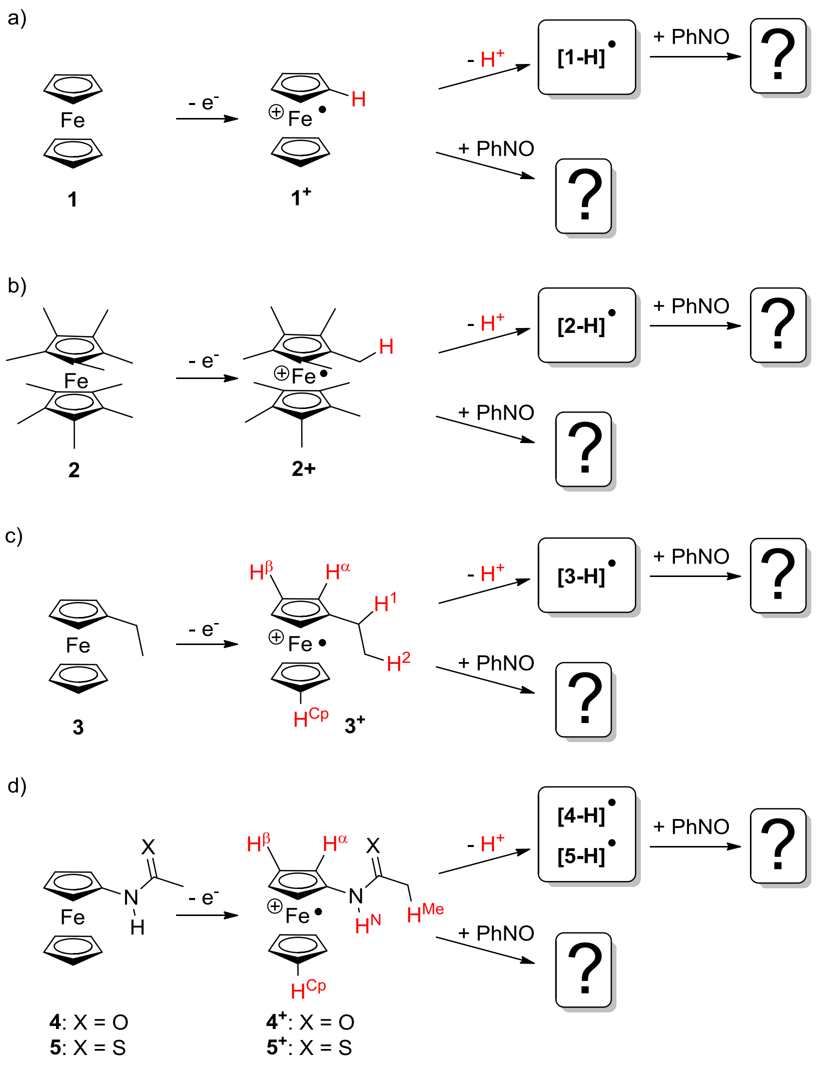

Scheme 4. Suggested Mechanism of the Formation of *N*-Ferrocenylpyrazole from Ferrocenium Radical Cations and Pyrazolide Anions.[32]

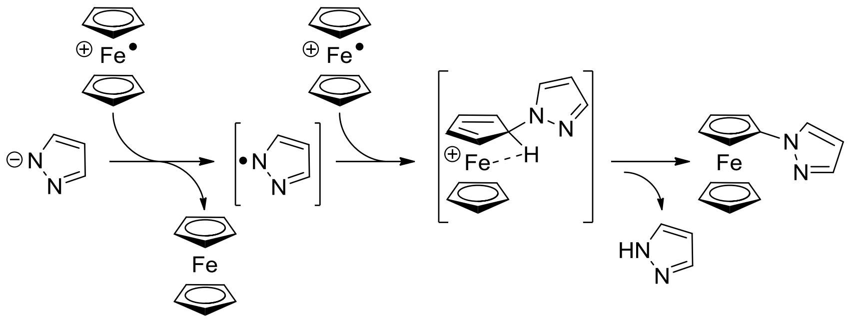

3.2.2 RESULTS AND DISCUSSION

Spin Trapping of Ferrocenium Ions: The oxidations of ferrocenes **1** – **5** to their respective cations **1**$^+$ – **5**$^+$ (Scheme 3) are performed in CH_2Cl_2 under inert conditions using one equivalent of silver hexafluoroantimonate $AgSbF_6$ as oxidant as its oxidation potential [$E_{1/2}(CH_2Cl_2)$ = 650 mV vs. FcH/FcH$^+$][33a] is sufficient for this purpose [$E_{1/2}(CH_2Cl_2)$ = 0, –480, –55, –50, –20 mV for **1** – **5**, respectively].[33] Furthermore, the coproduct silver is easily removed by filtration.

The presence of 1 – 1.2 equivalents of PhNO does not influence the EPR spectra of the ferrocenium ions. Indeed, **1**$^+$ is EPR silent both at 298 K and at 77 K as its EPR spectrum has been observed only below 20 K due to fast spin-lattice relaxation.[34] No EPR resonances are observed in the presence of PhNO as well. Obviously, the iron-centered 17 valence electron radical **1**$^+$ does not add to PhNO to give the conceivable nitroxide adduct **[1-PhNO]**$^+$, in contrast to what has been reported for $[Mn(CO)_5]^\bullet$ radicals for example (Scheme 2c). DFT calculations for **1**$^+$, PhNO, and **[1-PhNO]**$^+$ account for this lack of reactivity as the formation of **[1-PhNO]**$^+$ is endergonic by 49 kJ mol^{-1} (Supporting Information, Figure S1).

Similarly, **4**$^+$ gives a nearly axial EPR resonance at 77 K in frozen solution[35] which remains unchanged in the presence of PhNO. At room temperature, **4**$^+$ and the **4**$^+$/PhNO mixture are EPR-silent. Obviously, iron-centered ferrocenium radical ions are unable to react with PhNO to give the nitroxyl radicals. This behavior contrasts the reactivity of other organometallic 17 valence electron complexes (Scheme 2c).[27–30]

Spin Trapping of Ferrocenium Ions in the Presence of a Base: The ferrocenium ions **1**$^+$ – **5**$^+$ were treated with one equivalent of the non-nucleophilic and noncoordinating phosphazene base $P_1{}^t$Bu (*tert*-butylimino-tris(dimethylamino)phosphorane, (pK_a (MeCN) = 26.98)[36] as proton acceptor. To ensure that the ferrocenium salts **1**$^+$ – **5**$^+$ are unable to oxidize the employed $P_1{}^t$Bu base, its redox potential has been determined by cyclic voltammetry. Indeed, $P_1{}^t$Bu is irreversibly oxidized at E_p = 400 mV vs. FcH/FcH$^+$ ($[^nBu_4N][B(C_6F_5)_4]/CH_2Cl_2$), significantly higher than the redox potentials of the **1**/**1**$^+$ – **5**/**5**$^+$ redox couples (Supporting Information, Figure S2). A mechanistic scenario as shown in Scheme 4 for heterocyclic nitrogen bases is possible in principle due to the irreversible nature of the $P_1{}^t$Bu / $P_1{}^t$Bu$^+$ oxidation, although it is not very likely. Hence, a simple deprotonation of **1**$^+$ – **5**$^+$ to give the radicals and radical pools **[1−H]**$^\bullet$ – **[5−H]**$^\bullet$ should be achieved (Scheme 3). As illustrated in Scheme 3, deprotonation of **1**$^+$ and **2**$^+$ should yield the radicals **[1−H]**$^\bullet$ and **[2−H]**$^\bullet$, respectively. As **3**$^+$, **4**$^+$, and **5**$^+$ possess five chemically different protons which might be abstracted, radical pools consisting of up to five radical species might be present. The different radicals will be designated by the location of the abstracted proton as **[3−H^{Cp}]**$^\bullet$, **[3−H$^\alpha$]**$^\bullet$, **[3−H$^\beta$]**$^\bullet$, **[3−H^1]**$^\bullet$, and **[3−H^2]**$^\bullet$ for the radical pool **[3−H]**$^\bullet$; **[4−H^{Cp}]**$^\bullet$, **[4−H$^\alpha$]**$^\bullet$, **[4−H$^\beta$]**$^\bullet$, **[4−H^N]**$^\bullet$, and **[4−H^{Me}]**$^\bullet$ for the radical pool **[4−H]**$^\bullet$; and **[5−H^{Cp}]**$^\bullet$, **[5−H$^\alpha$]**$^\bullet$, **[5−H$^\beta$]**$^\bullet$, **[5−H^N]**$^\bullet$, and **[5−H^{Me}]**$^\bullet$ for the radical pool **[5−H]**$^\bullet$ (Scheme 3). Trapping of these radicals or some of these radicals by the spin trapping technique using nitrosobenzene PhNO is attempted. We will start with the simple ferrocene and decamethylferrocene derivatives **[1−H]$^•$** and **[2−H]$^•$** and then describe the more diverse reactivity of **[3−H]$^•$** − **[5−H]$^•$**. DFT calculations were employed both for the radical species **[1−H]$^•$** − **[5−H]$^•$** as well as for the conceivable corresponding PhNO adducts **[6]$^•$** − **[10]$^•$**.

For the **1**$^+$/PhNO/P$_1{}^t$Bu mixture, an EPR triplet resonance at $g_{\mathrm{iso}} = 2.0063$ with nitrogen hyperfine coupling (hfc) $A(^{14}\mathrm{N}) = 11.1$ G was recorded (Figure 1), similar to typical nitroxyl radicals.[37–40] Furthermore, hyperfine couplings to hydrogen nuclei of the phenyl moiety and the substituted cyclopentadienyl ring are extracted from the simulation of the EPR resonance (Table 1). $\mathrm{H^o}$, $\mathrm{H^m}$, and $\mathrm{H^p}$ denote the *ortho*, *meta*, and *para* protons of the phenyl substituent, respectively, while H^{α} and H^{β} are the *alpha* and *beta* protons of the substituted Cp ring. The observed coupling pattern allows a clear assignment to the ferrocenyl phenyl nitroxide radical **[6]$^•$** (*N*-oxyl-*N*-phenyl-ferrocenylamine). The hfc to ^{14}N in **[6]$^•$** is close to the observed hfc in the reported nitroxide radical [Fc-N(O)-tBu]$^•$ [$A(^{14}\mathrm{N}) = 11.75$ G].[31a] Some phenyl hydrogen hfc's of **[6]$^•$** are similar to those obtained for the isoelectronic radical anion [Fc-C(O)-Ph]$^{•-}$.[31b] At 77 K, a slightly anisotropic signal at $g_{\mathrm{av}} \approx 2.0071$ with a large nitrogen hyperfine coupling of $A(^{14}\mathrm{N}) = 26$ G in the high field region is recorded (Table 2; Supporting Information, Figure S4a). Hyperfine couplings to hydrogen atoms are not resolved in the frozen solution spectrum, and hence, a larger line width was applied in the simulation instead.

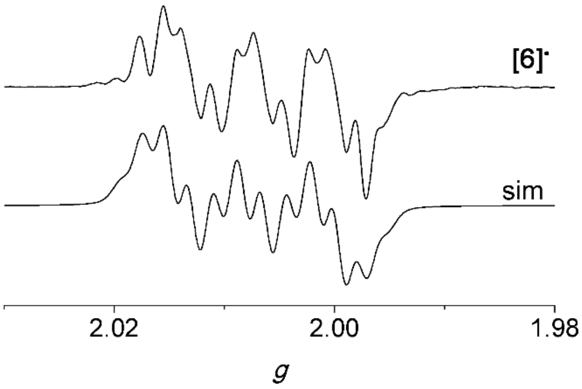

Figure 1. X-band EPR spectrum (top) and simulated spectrum (bottom) of [6]$^•$ (20 mm 1 in CH_2Cl_2) at the following experimental parameters: temperature = 298 K, field = 3358.98 G, sweep = 298.72 G, sweep time = 120 s, modulation = 1000 mG, and MW attenuation = 9 db.

Table 1. EPR parameters obtained by simulation of experimental spectra (298 K).

radical	g_{iso}	$A(^{14}N)$ / G	$A(^{1}H^{o})$ / G (2 ×)	$A(^{1}H^{m})$ / G (2 ×)	$A(^{1}H^{p})$ / G	$A(^{1}H^{\alpha})$ / G	$A(^{1}H^{\beta})$ / G	$A(^{1}H^{1})$ / G	Gauss pp linewidth / MHz	Lorentz pp linewidth / MHz
[6]$^{\bullet}$	2.0063	11.10	2.90	0.80	2.70	3.80 (2 ×)	0.60 (2 ×)		0.15	0.08
[7]$^{\bullet}$	2.0068	11.07	2.77	0.95	2.64			8.64 (2 ×)	0.02	0.015
[8^{1}]$^{\bullet}$	2.0072	11.16	2.77	1.00	2.65			2.10	0.035	0.065
[9^{Cp}]$^{\bullet}$	2.0072	10.90	2.77	0.90	2.64	1.20 / 1.10	0.70 (2 ×)		0.06	0.02
[10^{Cp}]$^{\bullet}$	2.0068	11.09	2.77	0.91	2.64	2.55 / 2.10	1.82 / 1.08		0.085	0.005

Table 2. EPR parameters obtained by simulation of experimental spectra (77 K).

radical (mixture)	$g_{1,2,3}$	$A(^{14}N)$ / G	fraction / %	Gauss pp linewidth / MHz	Lorentz pp linewidth / MHz
[6]$^{\bullet}$	2.0104, 2.0068, 2.0040	4.0, 4.0, 26.0		0.90	0.30
[7]$^{\bullet}$	2.0094, 2.0067, 2.0048	4.0, 4.0, 26.0		1.50	0.60
[8^{1}]$^{\bullet}$	2.0095, 2.0073, 2.0045	3.0, 3.0, 27.5		0.90	0.40
[9^{Cp}]$^{\bullet}$	2.0105, 2.0060, 2.0045	3.5, 3.5, 28.0	17	0.30	0.40
[4−H^{N}]$^{\bullet}$	N/A^{a}, 1.9620, 1.9450	N/A	83	0.50	0.20
[4−H^{x}]$^{\bullet}$(x = α,β,Cp,Me)	2.0095, 2.0065, 2.0030		0.8	0.30	0.2
[4−H^{N}]$^{\bullet}$	N/A^{a}, 1.9650, 1.9400		99.2	0.1	0.1
[10^{Cp}]$^{\bullet}$	2.0105, 2.0060, 2.0020	3.5, 3.5, 28.0	5	0.60	0.60
[11a]$^{\bullet}$	2.3100, 2.0695, 1.9990		48	0.50	0.50
[11b]$^{\bullet}$	2.2250, 2.0565, 2.0095		47	0.50	0.50

Obviously, the increased acidity of the positively charged ferrocenium ion **1**$^{+}$ [35,41] allows C-H deprotonation by P$_1{}^{t}$Bu. The initially formed *C*-deprotonated zwitterionic ferrocenium species corresponds to an electronically excited state and relaxes to the carbon centered radical **[1−H]**$^{\bullet}$ by internal electron transfer (Supporting Information, Figure S3a; Mulliken spin density at C 0.787; Mulliken spin density at Fe 0.212). The *C*-centered radical **[1−H]**$^{\bullet}$ attacks the nitrogen atom of PhNO leading to the spin trapped nitroxyl radical *N*-oxyl-*N*-phenyl-ferrocenylamine **[6]**$^{\bullet}$ (Figure 2a). DFT calculations revealed that the nitroxyl radical **[6]**$^{\bullet}$ is lower in energy than the starting materials **[1−H]**$^{\bullet}$ and PhNO by 208 kJ mol^{-1} (Supporting Information, Figure S3a), explaining the facile formation of **[6]**$^{\bullet}$.

Successful deprotonation of **1**$^{+}$ with P$_1{}^{t}$Bu was further evidenced by cyclic voltammetry of **1** in the absence and presence of the base using tetra(*n*-butyl)ammonium tetrakis(pentafluorophenyl)borate ([^{n}Bu$_4$N][B(C$_6$F$_5$)$_4$]) as weakly coordinating electrolyte.[42,43] Expectedly, ferrocene **1** shows a reversible one-electron redox process at a potential of

$E_{1/2}$ = 0 V vs. FcH/FcH$^+$ per definition (Supporting Information, Figure S5a). Addition of a stoichiometric amount of $P_1{}^t$Bu renders this oxidation irreversible, due to the deprotonation of **1**$^+$ to **[1−H]**$^\bullet$ and follow up reactions of the highly reactive *C*-centered radical **[1−H]**$^\bullet$ (Supporting Information, Figure S5b). As the oxidation process occurs at essentially the same potential (against the Ag/AgNO$_3$ reference electrode) in the presence of $P_1{}^t$Bu, deprotonation of **1** to **[1−H]**$^-$ by $P_1{}^t$Bu prior to oxidation is unlikely. Deprotonation of ferrocene **1**, however, is achieved using alkyl lithium bases as a well-known starting point for the rich ferrocene substitution chemistry.[44–47]

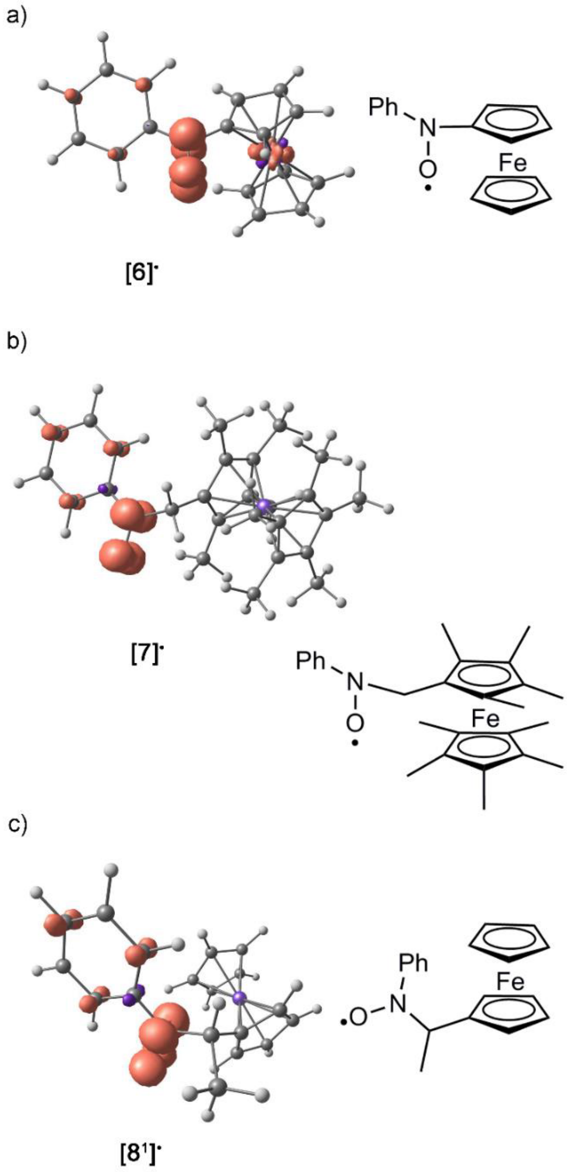

Figure 2: DFT optimized geometries with spin densities (0.01 a.u. isosurface value) in CH_2Cl_2 continuum solvent as well as Lewis structures of nitroxide radicals (a) [6]$^\bullet$, (b) [7]$^\bullet$, and (c) [8^1]$^\bullet$.

Despite the lack of aromatic C-H atoms, decamethylferrocenium $\mathbf{2}^+$ reacts with PhNO as well in the presence of P$_1{}^t$Bu (Scheme 3b). Obviously, the methyl groups become sufficiently acidic upon oxidation of **2** to $\mathbf{2}^+$ due to the increased electron deficiency. Hence, the *C*-centered radical **[2−H]**$^\bullet$ is generated from $\mathbf{2}^+$ by deprotonation of a CH_3 group (Supporting Information, Figure S3b, Mulliken spin density at C 0.650; Mulliken spin density at Fe 0.513). Similar to **[1−H]**$^\bullet$, **[2−H]**$^\bullet$ is trapped by PhNO resulting in the formation of the nitroxide radical **[7]**$^\bullet$ 1-[(*N*-oxyl-*N*-phenylamino)methyl]-1',2,2',3,3',4,4',5,5'-nonamethylferrocene (Figure 2b). The driving force for formation of **[7]**$^\bullet$ from the starting materials **[2−H]**$^\bullet$ and PhNO (Supporting Information, Figure S3b) is calculated as 80 kJ mol^{-1} by DFT methods. At 298 K, **[7]**$^\bullet$ gives an EPR resonance with parameters summarized in Table 1 (Figure 3). The nitrogen and hydrogen hyperfine couplings for the PhNO moiety of **[7]**$^\bullet$ are very similar to those of **[6]**$^\bullet$. The two large hydrogen hyperfine couplings of **[7]**$^\bullet$ ($A(^1H) = 8.64$ G), obtained by simulation, are assigned to the protons of the methylene group. The large hfc's nicely fit to the reported hfc's for the ferrocenylmethyl radical prepared from methylferrocene by γ-irradiation ($A(^1H) = 14.71$ G).[22] At 77 K in frozen solution, the nitroxide radical **[7]**$^\bullet$ displays a slightly anisotropic resonance similar to that of **[6]**$^\bullet$ (Supporting Information, Figure S4b) with one large nitrogen hyperfine coupling component (Table 2). Again, hydrogen hyperfine couplings are not resolved under these conditions.

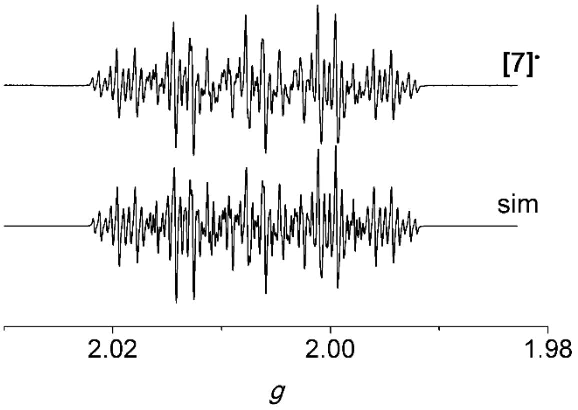

Figure 3: X-band EPR spectrum (top) and simulated spectrum (bottom) of [7]$^\bullet$ (25 mm 2 in CH_2Cl_2) at the following experimental parameters: temperature = 298 K, field = 3346.20 G, sweep = 94.79 G, sweep time = 90 s, modulation = 250 mG, and MW attenuation = 5 db.

In contrast to **1** and **2**, ethylferrocene **3** has five chemically different protons resulting in five conceivable *C*-centered radicals **[3−H^{Cp}]**$^\bullet$, **[3−H$^{\alpha}$]**$^\bullet$, **[3−H$^{\beta}$]**$^\bullet$, **[3−H^1]**$^\bullet$, and **[3−H^2]**$^\bullet$ (Scheme 3c). Consequently, five distinct nitroxyl radicals can in principle be obtained from this radical pool by reaction with PhNO, namely, **[8^{Cp}]**$^\bullet$, **[8$^{\alpha}$]**$^\bullet$, **[8$^{\beta}$]**$^\bullet$, **[8^1]**$^\bullet$, and **[8^2]**$^\bullet$. Despite the possible mixture of products, the room temperature EPR spectrum of **[8]**$^\bullet$ is well resolved, suggesting the presence of only a single nitroxide radical. The EPR pattern of **[8]**$^\bullet$ is well reproduced by assuming the typical ^{14}N and ^1H hfc's of the PhNO unit in addition to a further hfc to a single hydrogen atom (Table 1, Figure 4). This perfectly fits to the **[8^1]**$^\bullet$ nitroxide radical with the

PhNO substituent attached to the C^1 atom of the ethyl substituent. For all other nitroxide radicals **[8^{Cp}]•**, **[8^α]•**, **[8^β]•**, and **[8²]•**, more than one chemically different hydrogen atom would have been expected to display hfc's. At 77 K, a similar spectrum as that for **[6]•** is recorded for **[8¹]•** (Table 2; Supporting Information, Figure S4c).

The presence of only a single product **[8¹]•** derived from **[3−H¹]•** is straightforwardly explained by the pronounced stability of the secondary *C*-centered radical **[3−H¹]•** by more than 60 kJ mol^{-1} with respect to all other radicals **[3−H^{Cp}]•**, **[3−H^α]•**, **[3−H^β]•**, and **[3−H²]•** according to DFT calculations (Supporting Information, Figure S6, Mulliken spin density at C^1 0.757; Mulliken spin density at Fe 0.341). However, all five conceivable nitroxide radicals **[8^{Cp}]•**, **[8^α]•**, **[8^β]•**, **[8¹]•**, and **[8²]•** are quite similar in energy (Supporting Information, Figure S7). The driving force for the formation of **[8¹]•** from **[3−H¹]•** and PhNO amounts to 81 kJ mol^{-1} (Supporting Information, Figure S7). Hence, the product distribution is controlled by the relative stability of the *C*-centered radical **[3−H¹]•** but not by the relative stability of the product nitroxide radical **[8¹]•**.

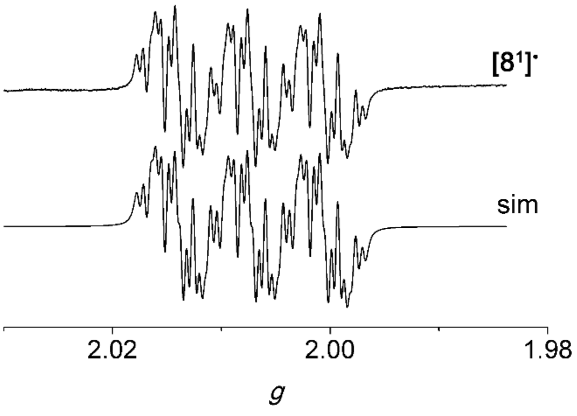

Figure 4. X-band EPR spectrum (top) and simulated spectrum (bottom) of [8^1]• (25 mm 3 in CH_2Cl_2) at the following experimental parameters: temperature = 298 K, field = 3346.20 G, sweep = 94.79 G, sweep time = 90 s, modulation = 250 mG, and MW attenuation = 0 db.

In order to gain insight into the reactivity of NH-containing ferrocenyl compounds, which are substructures of cytotoxic prodrugs **A** and **B** and antimalarial drugs **D** (Scheme 1),[7,9–13,48] we investigated the reactivity of the simple oxo- and thioamides, namely, *N*-acetylaminoferrocenium **4**$^+$ (Scheme 3d), and *N*-thioacetylaminoferrocenium **5**$^+$ in the presence of the $P_1{}^t$Bu base.

Because of the presence of five chemically different protons in **4**, five distinct radicals **[4−H^{Cp}]•**, **[4−H^α]•**, **[4−H^β]•**, **[4−H^N]•**, and **[4−H^{Me}]•** can be conceived in the radical pool **[4−H]•** (Scheme 3d). The same holds analogously for **5**. This translates to the corresponding nitroxide radicals **[9^{Cp}]•**, **[9^α]•**, **[9^β]•**, **[9^N]•**, and **[9^{Me}]•** derived from **4**$^+$ and PhNO and **[10^{Cp}]•**, **[10^α]•**, **[10^β]•**, **[10^N]•**, and **[10^{Me}]•** derived from the thioanalogue **5**$^+$ and PhNO. Similar to the situation observed for **[8^1]$^•$**, the room temperature EPR spectrum of **[9]$^•$** is rather well resolved, suggesting that only one or two nitroxide radical species are present (Figure 5). The main features of the experimental EPR resonance of **[9]$^•$** can be simulated by the expected hfc's to the PhNO moiety (^{14}N, H^o, H^m, H^p, Table 1) and coupling to four protons of 1.2 G (1H), 1.1 G (1H) and 0.70 G (2H). Further, small differences between the simulated and the experimental spectrum are associated with the presence of a second nitroxide radical with rather similar parameters. However, simulation of a full second parameter set would lead to severe overparametrization of the simulation. Hence, we note, that the hfc's to ferrocene protons are less well defined for **[9]$^•$** than that for **[6]$^•$**, **[7]$^•$**, and **[8^1]$^•$**. The presence of four protons close to the radical center suggest the **[9^{Cp}]$^•$** nitroxide radical derived from **[4−H^{Cp}]$^•$** as the major trapped species (Figure 6). In **[9^{Cp}]$^•$**, the hfc to H$^\alpha$ is smaller than that in **[6]$^•$** and furthermore, two slightly different hfc's to chemically different H$^\alpha$ atoms are found for **[9^{Cp}]$^•$** (Table 1). The larger hfc to H$^\alpha$ in **[6]$^•$** is easily traced back to the favorable coplanar orientation of the NO unit with the C_5H_4 ring (O-N-C^{ipso}-C$^\alpha$ = –23.0°) as compared to the corresponding torsion angle in **[9^{Cp}]$^•$** (O-N-C^{ipso}-C$^\alpha$ = –31.4°). The larger twist in **[9^{Cp}]$^•$** arises from an intramolecular NH(amide)···O(nitroxyl) hydrogen bond (Figure 6). Similar intramolecular hydrogen bonds have been amply observed in ferrocenyl polyamides.[49–51] This hydrogen bond furthermore provides a straightforward explanation for the chemically different H$^\alpha$/H$^{\alpha}$' protons.

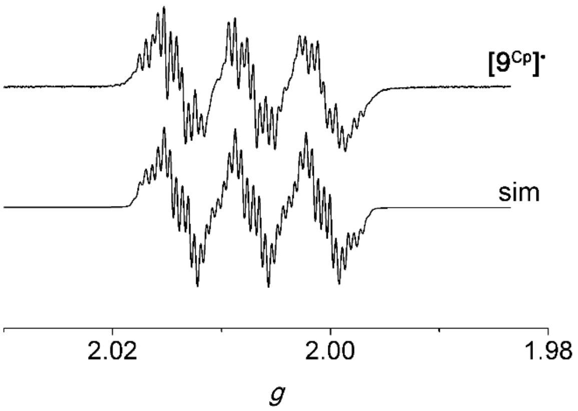

Figure 5. X-band EPR spectrum (top) and simulated spectrum (bottom) of [9^{Cp}]$^•$ (25 mm 4 in CH_2Cl_2) at the following experimental parameters: temperature = 298 K, field = 3346.20 G, sweep = 94.79 G, sweep time = 90 s, modulation = 1000 mG, and MW attenuation = 10 db.

Expectedly, in the radical pool **[4−H]$^•$** the nitrogen-deprotonated radical **[4−H^N]$^•$** is the most stable one (Supporting Information, Figure S9). However, this radical is essentially iron-centered with a Mulliken spin density at iron of 1.248 with some small contribution of the nitrogen atom (Mulliken spin density at N 0.016). Attack of PhNO at iron is excluded based on the general lack of reactivity of ferrocenium ions toward PhNO. Attack of PhNO at the nitrogen atom of **[4−H^N]$^•$** to give **[9^N]$^•$** is calculated to be disfavored by 37 kJ mol^{-1} relative to the starting materials **[4−H^N]$^•$** and PhNO (Figure 6). A ring-slipped isomer **[4−H^{N}']$^•$** has been calculated as well, yet its spin density is also localized at the iron atom (Mulliken spin density at Fe 1.268), precluding the reaction of **[4−H$^{N'}$]$^{\bullet}$** with PhNO (Supporting Information, Figure S9). The calculated ring-slipped structure of **[4−H$^{N'}$]$^{\bullet}$** suggests a viable decomposition pathway of radicals **[4−H]$^{\bullet}$** releasing the substituted cyclopentadienyl ligand as *N*-acetyl-2,4-cyclopentadien-1-imine. Indeed, the formation of di(cyclopentadiene) and di(aminocyclopentadiene) has been observed in the reaction of prodrugs **A** with H_2O_2 (Scheme 1).[7]

In addition to these PhNO-resistant iron-centered radicals **[4−H^{N}]$^{\bullet}$** and **[4−H$^{N'}$]$^{\bullet}$**, the radicals **[4−H^{Cp}]$^{\bullet}$**, **[4−H$^{\alpha}$]$^{\bullet}$**, **[4−H$^{\beta}$]$^{\bullet}$**, and **[4−H^{Me}]$^{\bullet}$** deprotonated at carbon atoms were calculated by DFT (Supporting Information, Figure S9). The reactions of **[4−H^{Cp}]$^{\bullet}$**, **[4−H$^{\alpha}$]$^{\bullet}$**, **[4−H$^{\beta}$]$^{\bullet}$**, and **[4−H^{Me}]$^{\bullet}$** and PhNO to **[9^{Cp}]$^{\bullet}$**, **[9$^{\alpha}$]$^{\bullet}$**, **[9$^{\beta}$]$^{\bullet}$**, and **[9^{Me}]$^{\bullet}$**, respectively, are thermodynamically feasible (Figure 6). Interestingly, **[4−H$^{\alpha}$]$^{\bullet}$** mainly features spin density at the iron center (Mulliken spin density at Fe 1.251) and is hence considered unreactive towards PhNO, so **[9$^{\alpha}$]$^{\bullet}$** should not be observed. In **[4−H^{Me}]$^{\bullet}$**, the spin density is smeared over the nitrogen, oxygen, and CH_2 units of the substituent. This spin delocalization reduces the probability of PhNO attack, and hence, **[9^{Me}]$^{\bullet}$** is not particularly favored as well. The remaining two highly reactive radicals **[4−H^{Cp}]$^{\bullet}$** and **[4−H$^{\beta}$]$^{\bullet}$**, although high in energy, might account for the observed EPR pattern with **[9^{Cp}]$^{\bullet}$** derived from **[4−H^{Cp}]$^{\bullet}$** being the major and **[9$^{\beta}$]$^{\bullet}$** derived from **[4−H$^{\beta}$]$^{\bullet}$** being the minor species based on simple statistical arguments. This interpretation agrees with the EPR spectral data. While the radicals **[4−H^{Cp}]$^{\bullet}$** and **[4−H$^{\beta}$]$^{\bullet}$** of the radical pool can be trapped by PhNO, **[4−H^{N}]$^{\bullet}$** and **[4−H$^{N'}$]$^{\bullet}$** are inert toward PhNO. In order to possibly detect the rather persistent and PhNO-resistant Fe-centered radical **[4−H^{N}]$^{\bullet}$** rapid-freeze EPR techniques have been employed.

The EPR spectrum recorded at 77 K rapidly after deprotonation of **4^{+}** in the presence of PhNO shows a characteristic broad ferrocenium-based resonance (83 %) in addition to the slightly anisotropic nitrogen-split triplet resonance of a nitroxide radical with one large hfc to ^{14}N (17 %) (Figure 7, Table 2). The latter EPR resonance is very similar to the corresponding resonance of **[6]$^{\bullet}$** and is hence safely assigned to already formed nitroxide radicals **[9$^{Cp/\beta}$]$^{\bullet}$**. The broad ferrocenium resonance ($g_{1,2,3}$ = N/A, 1.9650, 1.9400, Table 2), however, clearly differs from the EPR resonance of the ferrocenium ion **4^{+}** ($g_{1,2,3}$ = 3.3500, 1.8750, 1.7870).[35] Hence, the resonance is assigned to **[4−H^{N}]$^{\bullet}$**. This iron-centered radical is unable to react with PhNO itself, but equilibrates with radical species deprotonated at carbon atoms **[4−H^{x}]$^{\bullet}$** (x = α, β, Cp, Me). After annealing the sample to room temperature for five minutes and refreezing to 77 K, the ferrocenium resonance of **[4−H^{N}]$^{\bullet}$** has vanished and only the resonance of the nitroxide radicals **[9$^{Cp/\beta}$]$^{\bullet}$** remained.

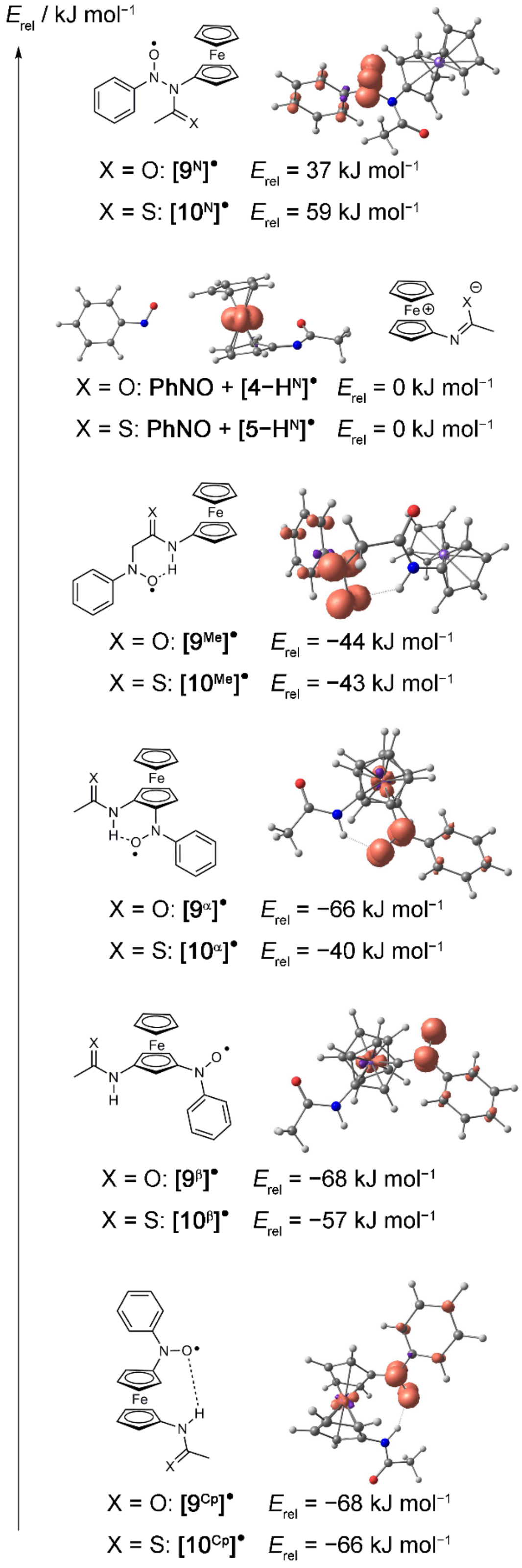

Figure 6. DFT optimized geometries with spin densities for $[9^x]^•$ (x = □, □, Cp, N, and Me) (0.01 a.u. isosurface value) and energies in CH_2Cl_2 continuum solvent for $[9^x]^•$ and $[10^x]^•$ (x = □, □, Cp, N, and Me) as well as Lewis structures.

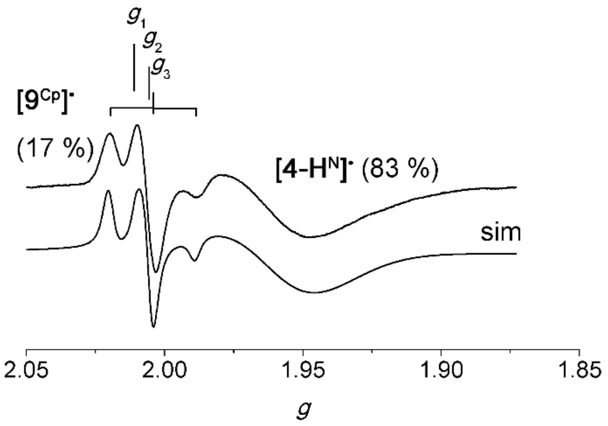

Figure 7. X-band EPR spectrum (top) and simulated spectrum (bottom) of [9^{Cp}]• / [4−H^N]• (25 mm 4 in CH_2Cl_2) at the following experimental parameters: temperature = 77 K, field = 3346.20 G, sweep = 499.77 G, sweep time = 90 s, modulation = 5000 mG, and MW attenuation = 10 db.

In the absence of PhNO, rapid-freeze EPR spectroscopy of the **4**$^+$/P$_1{}^t$Bu mixture yields an EPR spectrum displaying the resonance assigned to **[4−H^N]•** (99.2 %) (Supporting Information, Figure S8a). This finding supports the above assignment. Furthermore, a weak, but significant, slightly anisotropic resonance at g = 2.0 without resolved hyperfine couplings is detected (0.8 %) (Table 2, Supporting Information, Figure S8a). This resonance is assigned to traces of the carbon-centered radicals **[4−H^x]•** (x = α, β, Cp, Me) of the radical pool **[4−H]•** (Table 2). At room temperature, this sample exhibits a transient EPR resonance without discernible hfc's at g_{iso} = 2.0078 (Supporting Information, Figure S8b) which is assigned to the *C*-centered radicals **[4−H^x]•** (x = α, β, Cp, Me) as well. The proposed reactivity of **4**$^+$ in the presence of a base is summarized in Scheme 5. Deprotonation of **4**$^+$ gives the radical pool **[4−H]•** with **[4−H^N]•** being the most stable and abundant radical (99.2 %). Neither **4**$^+$ nor **[4−H^N]•** react with PhNO. Less than one percent of the observed radicals are carbon-centered radicals **[4−H^x]•** (x = α, β, Cp, Me). However, two of these, namely, **[4−H^{Cp}]•** and **[4−H^β]•**, can be trapped by PhNO to give the respective nitroxide radicals **[9^{Cp}]•** and **[9^β]•**. Quantification[52] of the nitroxide radical species **[9^{Cp}]•** and **[9^β]•** with respect to external calibration with DPPH reveals that indeed less than 1 % of the original ferrocenium radical **4**$^+$ is transformed into the nitroxides **[9^{Cp}]•** and **[9^β]•**. One possible decomposition pathway of the radicals via the ring-slipped isomer **[4−H$^{N'}$]•** is proposed on the basis of DFT calculations of **[4−H$^{N'}$]•**. Further radical reactivity might be hydrogen atom abstraction from the solvent or the base to give the starting material **4**. Indeed, quenching the radical pool **[4−H]•** by hydrazine hydrate essentially quantitatively recovers ferrocene **4** as shown by ^{1}H NMR spectroscopy.

Scheme 5. Suggested Radical Reactivity of 4^+ in the Presence of a Base and PhNO; EPR Data (77 K) of Identified Intermediates Given.

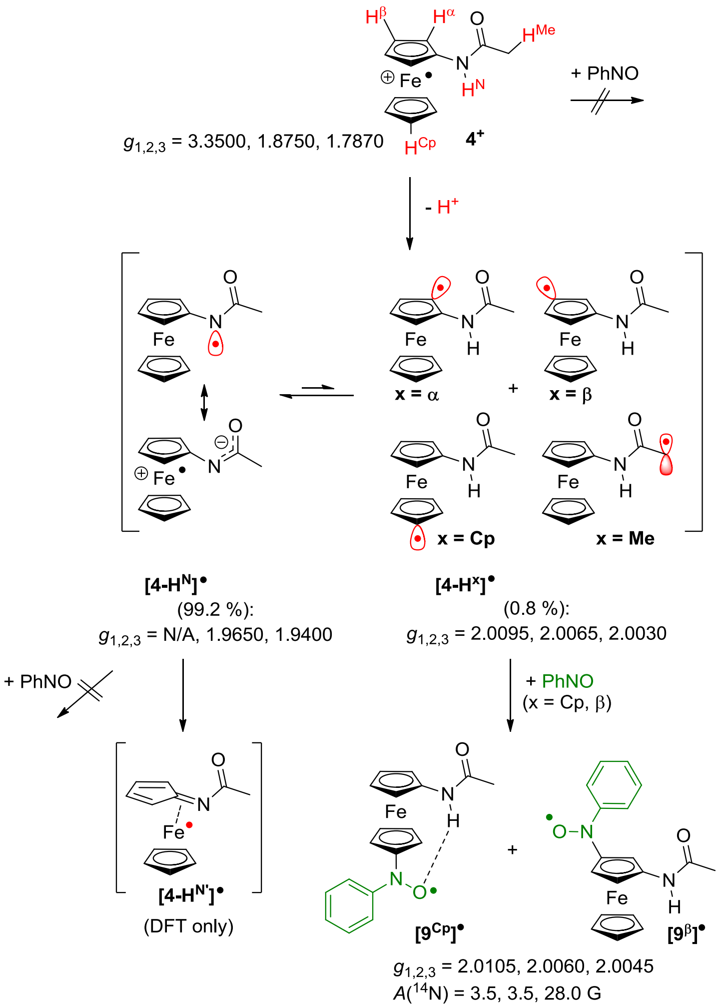

The successful deprotonation of $\mathbf{4}^+$ to the radical pool **[4−H]**$^{\bullet}$ is furthermore evidenced by cyclic voltammetry. At 298 K in $CH_2Cl_2/[^{n}Bu_4N][B(C_6F_5)_4]$, a reversible one-electron process is observed at $E_{1/2} = -50$ mV vs. FcH/FcH$^+$ and assigned to the **4**/$\mathbf{4}^+$ couple (Supporting Information, Figure S10a). After the addition of stoichiometric amounts of $P_1{}^{t}Bu$, this process is replaced by an irreversible oxidation at $E_p = -175$ mV vs. FcH/FcH$^+$ (Supporting Information, Figure S10b). The lower potential of the **4**/$\mathbf{4}^+$ couple in the presence of $P_1{}^{t}Bu$ is ascribed to coordination of the base to the amide unit of **4** via a hydrogen bond. Oxidation to $\mathbf{4}^+$ acidifies this NH proton and the proton is transferred to the base giving the radicals **[4−H]**$^{\bullet}$, with **[4−H^{N}]**$^{\bullet}$ being the major product. Reduction of the rather persistent radical **[4−H^{N}]**$^{\bullet}$ occurs at E_p’ = −890 mV vs. FcH/FcH$^+$ (Supporting Information, Figure S10b). These results reflect the intimate coupling of proton transfer and electron transfer reactions in ferrocenium amides as reported in the literature.[35,49–51]

In order to investigate the effect of O→S exchange in the amide for the spin trapping experiments in the presence of $P_1{}^{t}Bu$, we employed thioamide **5** as the sulfur analogue of **4**.[51]

Similar to **4**$^+$, a radical pool **[5−H^{Cp}]$^•$**, **[5−H$^{\alpha}$]$^•$**, **[5−H$^{\beta}$]$^•$**, **[5−H^{N}]$^•$**, and **[5−H^{Me}]$^•$** is established after deprotonation of **5**$^+$ (Scheme 5) Fully paralleling the energies of the corresponding radicals **[4−H]$^•$** , the most stable one is the iron-centered radical **[5−H^{N}]$^•$** (Supporting Information, Figure S9) while the ring and side chain radicals **[5−H^{Cp}]$^•$**, **[5−H$^{\alpha}$]$^•$**, **[5−H$^{\beta}$]$^•$**, and **[5−H^{Me}]$^•$** are higher in energy.

The EPR spectrum obtained from the **5**$^+$/PhNO/P$_1{}^t$Bu mixture at room temperature is very well simulated by a single set of parameters (Figure 8, Table 1). The hfc's are consistent with the nitroxide radical **[10^{Cp}]$^•$**. Similar to **[9^{Cp}]$^•$**, hyperfine coupling to the H$^{\alpha}$ atoms is split due to the chemical dissimilarity of H$^{\alpha}$ and H$^{\alpha}$' in **[10^{Cp}]$^•$** featuring an intramolecular NH(thioamide)···O(nitroxide) hydrogen bond (Figure 6). According to the DFT calculations this hydrogen bond is shorter in **[10^{Cp}]$^•$** (NH···O 1.885 Å) than that in **[9^{Cp}]$^•$** (NH···O 1.984 Å), suggesting a stronger bond in **[10^{Cp}]$^•$** in agreement with the increased acidity of thioamides.[51] The stronger intramolecular hydrogen bond might also lead to a more pronounced differentiation between H$^{\alpha}$ and H$^{\alpha}$'. In fact, even the β-hydrogen atoms become chemically inequivalent and yield different hfc's in **[10^{Cp}]$^•$** (Table 1). The larger hfc to H$^{\alpha}$/H$^{\alpha}$' in **[10^{Cp}]$^•$** than in **[9^{Cp}]$^•$** might be associated with the smaller torsion angle O-N-C^{ipso}-C$^{\alpha}$ = –25.1° in **[10^{Cp}]$^•$**.

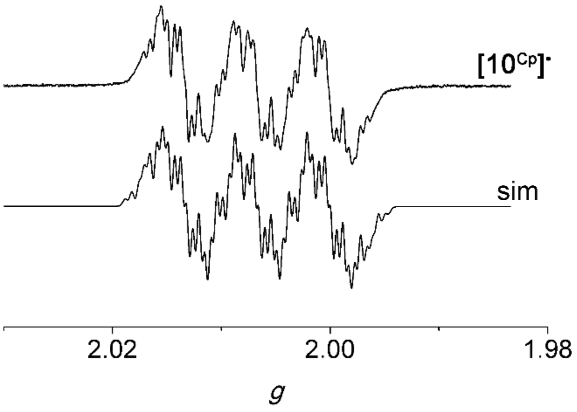

Figure 8. X-band EPR spectrum (top) and simulated spectrum (bottom) of [10^{Cp}]$^•$ (25 mm 5 in CH_2Cl_2) at the following experimental parameters: temperature = 298 K, field = 3346.20 G, sweep = 94.79 G, sweep time = 90 s, modulation = 1000 mG, and MW attenuation = 10 db.

In order to observe iron-centered radicals, the **5**$^+$/PhNO/P$_1{}^t$Bu reaction mixture was subjected to EPR spectroscopy at 77 K (Figure 9). The EPR spectrum displays three discernible resonances. One resonance originates from the spin trapped product **[10^{Cp}]$^•$** (5 %) bearing close resemblance to the resonance of the amide nitroxide radical **[9^{Cp}]$^•$** (Table 2). The other two rhombic resonances, present in nearly equal intensities (48 %; 47 %; Table 2), appear to correlate to follow-up products **[11a]$^•$** and **[11b]$^•$** of the initially formed radicals **[5−H]$^•$**. The identity of these follow-up products is as yet unknown. In the absence of PhNO, the resonances of these follow-up products **[11a]$^•$** and **[11b]$^•$** are observed as well (Figure 10). This finding eliminates a reaction with PhNO as being responsible for the formation of **[11a]**$^{\bullet}$ and **[11b]**$^{\bullet}$. In the absence of PhNO, the resonance of the **5**$^{+}$ cation[51] is observed additionally (Table 2, Figure 10). Hence, **[11a]**$^{\bullet}$ and **[11b]**$^{\bullet}$ seem to be associated with follow-up products of the sulfur substituent **[5−H]**$^{\bullet}$, independent of the presence of PhNO.

While it has been reported previously that the chemical reactivity and properties of ferrocenyl thioamides can differ from the chemistry of the corresponding amides,[51] *C*-radical reactivity in the presented spin trapping reaction results in the analogous product(s) **[9$^{Cp/β}$]**$^{\bullet}$ and **[10^{Cp}]**$^{\bullet}$. Yet, the sulfur atom appears to open further reaction pathways yielding radicals **[11a]**$^{\bullet}$ and **[11b]**$^{\bullet}$. Their investigation is beyond the scope of the present study and will be reported elsewhere.

Obviously, oxidized ferrocenyl amides and thioamides **4**$^{+}$ and **5**$^{+}$ can be easily deprotonated at their respective nitrogen atoms yielding the metal-centered radicals **[4−H^{N}]**$^{\bullet}$ (observed by rapid-freeze EPR) and **[5−H^{N}]**$^{\bullet}$. These iron-centered radicals are even resistant towards reaction with PhNO. Yet, the *N*-deprotonated tautomers **[4−H^{N}]**$^{\bullet}$ and **[5−H^{N}]**$^{\bullet}$ can isomerize to reactive *C*-deprotonated species **[4−H^{x}]**$^{\bullet}$ and **[5−H^{x}]**$^{\bullet}$ to a small extent ($x = \alpha$, β, Cp, Me). Some of these *C*-centered radicals **[4−H^{x}]**$^{\bullet}$ and **[5−H^{x}]**$^{\bullet}$ can be trapped by PhNO (<1%) to give the stable nitroxyl radicals **[9$^{Cp/β}$]**$^{\bullet}$ and **[10^{Cp}]**$^{\bullet}$. In the presence of a base even two more radical species **[11a]**$^{\bullet}$ and **[11b]**$^{\bullet}$ are detected for the sulfur derivative **5**$^{+}$ by EPR in the reaction mixture. **[11a]**$^{\bullet}$ and **[11b]**$^{\bullet}$ are inert towards PhNO, similar to other ferrocenium radicals **1**$^{+}$ – **5**$^{+}$. It appears that Fc-NHC(X)R can be oxidized to the rather stable conjugate acid/base pair [Fc-NHC(X)R]$^{+}$ / [Fc-NC(X)R]$^{\bullet}$ (X = O, S). *C*-centered reactive radicals are then slowly formed via intramolecular proton-coupled electron transfer (PCET) or hydrogen atom transfer (Scheme 5).[53–64]

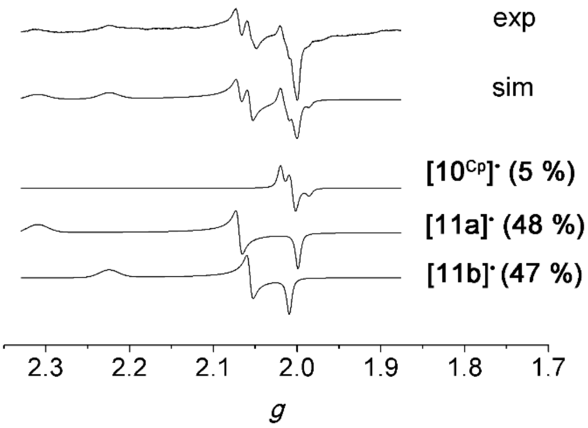

Figure 9. X-band EPR spectrum (exp) and simulated spectrum (sim) of [10^{Cp}]$^{\bullet}$ consisting of three components [10^{Cp}]$^{\bullet}$, [11a]$^{\bullet}$, and [11b]$^{\bullet}$; (5 mm 5 in CH_2Cl_2) at the following experimental parameters: temperature = 77 K, field = 3245.45 G, sweep = 697.96 G, sweep time = 90 s, modulation = 5000 mG, and MW attenuation = 10 db.

In the PCET reaction, a proton is transferred from a cyclopentadienyl carbon atom to the nitrogen atom, while an electron from the original CH bond is transferred to the iron(III) center. Hence, **4^+/[4−H^N]$^•$** and **5^+/[5−H^N]$^•$** might act as a reservoir for reactive *C*-centered radicals (maybe even under physiological conditions). This might also explain some of the enhanced biological reactivity patterns observed for amino ferrocene based drugs and prodrugs such as **A**, **B**, or **D** (Scheme 1). *C*-Centered radicals have also been proposed for the active species derived from ferrocifen **F** (Scheme 1). Hence, a common feature of such biologically active ferrocene/ferrocenium species might be the presence of some ionizable NH/OH group close to the ferrocenium site, suggesting an intimate coupling of electron and proton transfer to generate metastable iron-centered radicals. Highly reactive carbon-centered radicals might then be formed from these species in small amounts via intramolecular proton-coupled electron transfer reactions. These might account for further biological effects.

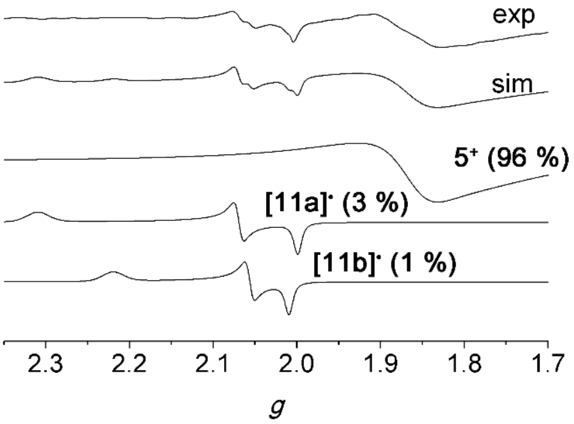

Figure 10. X-band EPR spectrum (exp) and simulated spectrum (sim) of 5^+/P$_1$^{t}Bu consisting of three components 5^+, [11a]$^•$, and [11b]$^•$; (5 mm 5 in CH_2Cl_2) at the following experimental parameters: temperature = 77 K, field = 2499.01 G, sweep = 3989.53 G, sweep time = 120 s, modulation = 3000 mG, and MW attenuation = 10 db.

3.2.3 CONCLUSIONS

In contrast to other 17 valence electron metal centered radicals, such as $[Mn(CO)_5]^•$, ferrocenium ions are inert toward the reaction with the spin trapping agent nitrosobenzene. However, in the presence of a suitable base, small amounts of carbon-centered radicals are generated. Some of these reactive radicals add to nitrosobenzene giving the respective stable nitroxide radicals. EPR spectra of the corresponding stable ferrocenyl phenyl nitroxide radicals clearly reveal the position of the original radical site, namely, C_5H_5 for ferrocene, CH_3 for decamethylferrocene, and CH_2 for ethylferrocene. The most acidic site in NHC(X)CH_3 substituted ferrocene/ferrocenium couples (X = O, S) is the NH group, and iron-centered radicals are formed according to EPR studies. Again, these iron-centered radicals do not add to nitrosobenzene. Yet, small amounts of *C*-deprotonated tautomers generated from the *N*-

deprotonated, iron-centered radicals are trapped by attack of nitrosobenzene at the Cp rings. Hence, these stable and inert NHC(X)CH_3 substituted ferrocene/ferrocenium couples slowly release reactive *C*-centered radicals and can thus be considered as a reservoir for reactive radicals. This reactivity might also be of importance in the biological mode of action of OH/NH-substituted ferrocene-based drugs and prodrugs, such as ferrocifen, ferroquine, and related compounds.

3.2.4 EXPERIMENTAL SECTION

General Considerations: All reactions were performed under argon atmosphere unless otherwise noted. Dichloromethane was dried over CaH_2 and distilled prior to use. Ferrocene (**1**) was commercially available from Acros. Decamethylferrocene (**2**) was used as received from ABCR. Ethylferrocene (**3**), $P_1{}^tBu$, 2,2-diphenyl-1-picrylhydrazyl (DPPH), and nitrosobenzene (PhNO) were commercially available from Sigma-Aldrich. *N*-Acetylaminoferrocene (**4**),[65] *N*-thioacetylaminoferrocene (**5**),[51] and $[^nBu_4N][B(C_6F_5)_4]$[42,43] were prepared according to literature procedures. Filtrations from precipitated silver after oxidation were performed with syringe filters (Rotilabo-Spritzenfilter, *Ø* = 15 mm, pore size = 0.20 µm; Carl Roth GmbH + Co. KG, Germany). Electrochemical experiments were carried out on a BioLogic SP-50 voltammetric analyzer using a platinum working electrode, a platinum wire as counter electrode, and a 0.01 M $Ag/AgNO_3$ electrode as reference electrode. The measurements were carried out at a scan rate of 100 mV s^{-1} for cyclic voltammetry experiments and for square wave voltammetry experiments unless noted otherwise using 0.1 M $[^nBu_4N][B(C_6F_5)_4]$ as supporting electrolyte and 0.001 M solution of the sample in CH_2Cl_2. Potentials are given relative to the ferrocene/ferrocenium couple. Referencing was achieved by addition of ferrocence or decamethylcobaltocene ($E_{1/2} = -2.04$ V vs. FcH/FcH^+ (CH_2Cl_2; $[^nBu_4N][B(C_6F_5)_4]$)) to the sample.[42,43] CW EPR spectra (X-band; ca. 9.4 GHz) were measured on a Miniscope MS 300 at 298 K and at 77 K cooled by liquid nitrogen in a finger dewar (Magnettech GmbH, Berlin, Germany). Settings are given at the respective displayed spectra. *g*-Values are referenced to external Mn^{2+} in ZnS ($g = 2.118$, 2.066, 2.027, 1.986, 1.946, and 1.906). Simulations of EPR spectra were performed with EasySpin (v 5.0.0)[66] for MatLab (R2015a). For quantification measurements, EPR tubes with an internal diameter of 2.0 mm were used. The calibration curve was determined using commercially available 2,2-diphenyl-1-picrylhydrazyl (DPPH) as standard. The samples were prepared in a glovebox under argon, and the EPR tubes were filled with 400 µl of the solution and sealed with Critoseal®. They were inserted 10.4 cm (measured at the Teflon holder) into the EPR spectrometer. Three concentrations (0.03, 0.01, and 0.005 mM) in CH_2Cl_2 were used for the calibration. The settings for the calibration curve and the sample EPR spectra were as follows: temperature = 298 K, field = 3346.20 G, sweep = 94.79 G, sweep time = 90 s, modulation = 5000 mG, MW attenuation = 10 db, and number of passes = 3. For an estimation of the error at the insertion of the EPR tube into the spectrometer cavity, the sample with 0.03 mM concentration was inserted, measured, reinserted, and measured three times. For the $c = 0.03$ mM sample a variation of 13 % between highest and lowest value of the three measurements after double integration is obtained. Baseline correction was achieved with EasySpin[66] for MatLab with normalization turned off. The obtained spectra were integrated twice with Origin Pro 8.0 and the double integral values were plotted against the concentration (Supporting Information, Figures S11 and S12).

Density Functional Calculations: These were carried out with the ORCA 3.0.2 / DFT series[67] of programs. For geometry optimizations and energy calculations, the B3LYP formulation of density functional theory was used employing the SV(P)[68,69] basis set, the RIJCOSX approximation, approximate Second Order SCF (SOSCF),[70,71] the zeroth order regular approximation (ZORA),[72–74] and the KDIIS algorithm, at GRIDX4. No symmetry constraints were imposed on the molecules. The presence of energy minima of the ground states was checked by numerical frequency calculations. Solvent modeling was done employing the conductor like screening model (COSMO, CH_2Cl_2).[75] The approximate free energies at 298 K were obtained through thermochemical analysis of the frequency calculation, using the thermal correction to Gibbs free energy as reported by ORCA 3.0.2.

3.2.5 ASSOCIATE CONTENT

Supporting Information

Square wave and cyclic voltammograms of $P_1{}^t$Bu, **1**, **1**/$P_1{}^t$Bu, **4**, and **4**/$P_1{}^t$Bu in CH_2Cl_2/[^{n}Bu$_4$N][B(C_6F_5)$_4$] at 298 K, DFT optimized geometry and spin density in CH_2Cl_2 for **[1-PhNO]**$^+$, **[1−H]**$^{\bullet}$, **[2−H]**$^{\bullet}$, **[3−H^x]**$^{\bullet}$ (x = α, β, Cp, 1, 2), **[8^x]**$^{\bullet}$ (x = α, β, Cp, 1, 2), **[4−H^x]**$^{\bullet}$ and **[5−H^x]**$^{\bullet}$ (x = α, β, Cp, N, Me), and **[4−H$^{N'}$]**$^{\bullet}$, and EPR spectra and simulations in CH_2Cl_2 at 77 K of **[6]**$^{\bullet}$, **[7]**$^{\bullet}$, **[8^1]**$^{\bullet}$, **[4−H^N]**$^{\bullet}$ and **[4−H^x]**$^{\bullet}$ (x = α, β, Cp, Me), and at 298 K of **[4−H^x]**$^{\bullet}$ (x = α, β, Cp, Me), and EPR spectra of quantification experiments in CH_2Cl_2 at 298 K of **[6]**$^{\bullet}$, **[7]**$^{\bullet}$, **[8^1]**$^{\bullet}$, **[9$^{Cp/\beta}$]**$^{\bullet}$, **[10^{Cp}]**$^{\bullet}$, and DPPH in 0.03 mM, 0.01 mM, and 0.005 mM concentration, and Cartesian coordinates of optimized structures. This material is available free of charge via the Internet at http://pubs.acs.org.

AUTHOR INFORMATION

Corresponding Author

*E-mail: katja.heinze@uni-mainz.de

Present Address

Institute of Inorganic and Analytical Chemistry, Johannes Gutenberg-University of Mainz, Duesbergweg 10-14, 55128 Mainz, Germany

Notes

[‡]A.N. and T.K. contributed equally to the manuscript. The authors declare no competing financial interest.

3.2.6 ACKNOWLEDGMENT

We are grateful to Dipl.-Chem. Christoph Kreitner for his helpful remarks concerning DFT calculations. Parts of this research were conducted using the supercomputer Mogon and advisory services offered by Johannes Gutenberg University Mainz (www.hpc.uni-mainz.de), which is a member of the AHRP and the Gauss Alliance e. V.

3.2.7 REFERENCES

(1) Special issue on ferrocene chemistry: Heinze, K.; Lang, H. *Organometallics* **2013**, *32*, 5623–5625.

(2) Special issue on ferrocene chemistry: Adams, R. D. *J. Organomet. Chem.* **2001**, *637-639*, 1.

(3) a) Togni, A.; Hayashi, T. *Ferrocenes*; Togni, A., Hayashi, T., Eds.; VCH: Weinheim, 1995; b) Stepnicka, P., Ed., *Ferrocenes: Ligands, Materials and Biomolecules*, VCH Weinheim, 2008.

(4) Ornelas, C. *New J. Chem.* **2011**, *35*, 1973–1985.

(5) Gasser, G.; Ott, I.; Metzler-Nolte, N. *J. Med. Chem.* **2011**, *54*, 3–25.

(6) Tabbì, G.; Cassino, C.; Cavigiolio, G.; Colangelo, D.; Ghiglia, A.; Viano, I.; Osella, D. *J. Med. Chem.* **2002**, *45*, 5786–5796.

(7) Hagen, H.; Marzenell, P.; Jentzsch, E.; Wenz, F.; Veldwijk, M. R.; Mokhir, A. *J. Med. Chem.* **2012**, *55*, 924–934.

(8) Osella, D.; Ferrali, M.; Zanello, P.; Laschi, F.; Fontani, M.; Nervi, C.; Cavigiolio, G. *Inorg. Chim. Acta* **2000**, *306*, 42–48.

(9) Marzenell, P.; Hagen, H.; Sellner, L.; Zenz, T.; Grinyte, R.; Pavlov, V.; Daum, S.; Mokhir, A. *J. Med. Chem.* **2013**, *56*, 6935–6944.

(10) Daum, S.; Chekhun, V. F.; Todor, I. N.; Lukianova, N. Y.; Shvets, Y. V.; Sellner, L.; Putzker, K.; Lewis, J.; Zenz, T.; de Graaf, I. A. M.; Groothuis, G. M. M.; Casini, A.; Zozulia, O.; Hampel, F.; Mokhir, A. *J. Med. Chem.* **2015**, *58*, 2015–2024.

(11) Dubar, F.; Slomianny, C.; Khalife, J.; Dive, D.; Kalamou, H.; Guérardel, Y.; Grellier, P.; Biot, C. *Angew. Chem.* **2013**, *125*, 7844−7847; *Angew. Chem. Int. Ed.* **2013**, *52*, 7690–7693.

(12) Biot, C.; Nosten, F.; Fraisse, L.; Ter-Minassian, D.; Khalife, J.; Dive, D. *Parasite* **2011**, *18*, 207–214.

(13) Biot, C.; Glorian, G.; Maciejewski, L. A.; Brocard, J. S.; Domaire, O.; Blampain, G.; Millet, P.; Georges, A. J.; Abessolo, H.; Dive, D.; Lebibi, J. *J. Med. Chem.* **1997**, *40*, 3715–3718.

(14) Zanellato, I.; Heldt, J.-M.; Vessières, A.; Jaouen, G.; Osella, D. *Inorg. Chim. Acta* **2009**, *362*, 4037–4042.

(15) Hamels, D.; Dansette, P. M.; Hillard, E. A.; Top, S.; Vessières, A.; Herson, P.; Jaouen, G.; Mansuy, D. *Angew. Chem.* **2009**, *121*, 9288−9290; *Angew. Chem. Int. Ed.* **2009**, *48*, 9124–9126.

(16) Hillard, E.; Vessières, A.; Thouin, L.; Jaouen, G.; Amatore, C. *Angew. Chem.* **2006**, *118*, 291−296; *Angew. Chem. Int. Ed.* **2006**, *45*, 285–290.

(17) Jaouen, G.; Top, S.; Vessieres, A.; Leclercq, G.; McGlinchey, M. *Curr. Med. Chem.* **2004**, *11*, 2505–2517.

(18) Nguyen, A.; Top, S.; Pigeon, P.; Vessières, A.; Hillard, E. a.; Plamont, M. A.; Huché, M.; Rigamonti, C.; Jaouen, G. *Chem. Eur. J.* **2009**, *15*, 684–696.

(19) Michard, Q.; Jaouen, G.; Vessieres, A.; Bernard, B. A. *J. Inorg. Biochem.* **2008**, *102*, 1980–1985.

(20) Osella, D.; Mahboobi, H.; Colangelo, D.; Cavigiolio, G.; Vessières, A.; Jaouen, G. *Inorg. Chim. Acta* **2005**, *358*, 1993–1998.

(21) Abramovitch, R. A.; Azogu, C. I.; Sutherland, R. G. *J. Chem. Soc., Chem. Commun.* **1971**, 134–135.

(22) Jackson, R. A.; Scarmoutsos, M.; Zarkadis, A. K. *J. Chem. Soc. Perkin Trans.* **1991**, *2*, 809–810.

(23) a) Cais, M.; Ashkenazi, P.; Dane, S.; Gottlieb, J. *J. Organomet. Chem.* **1976**, *122*, 403–411; b) Creary, X. *Org. Lett.* **2000**, *2*, 2069–2072.

(24) Neuse, E. W. *J. Macromol. Sci. Part A - Chem.* **1981**, *16*, 3–72.

(25) Taniguchi, N.; Uemura, M. *Tetrahedron Lett.* **1998**, *39*, 5385–5388.

(26) Ashkenazi, P.; Cais, M. *Angew. Chem.* **1972**, *84*, 1106−1107; *Angew. Chem. Int. Ed.* **1972**, *11*, 1027–1028.

(27) Hudson, A.; Lappert, M. F.; Lednor, P. W.; Nicholson, B. K. *J. Chem. Soc. D Chem. Commun.* **1974**, 966–967.

(28) Huffadine, A. S.; Dawson, P. A.; Peake, B. M.; Robinson, B. H.; Simpson, J. *J. Organomet. Chem.* **1976**, *121*, 391–403.

(29) Bennar, L. S.; Balch, A. L. *J. Organomet. Chem.* **1977**, *134*, 121–130.

(30) Hudson, A.; Lappert, M. F.; Nicholson, B. K. *J. Chem. Soc. Dalt. Trans.* **1977**, 551–554.

(31) a) Forrester, A. R.; Hepburn, P.; Dunlop, R. S.; Mills, H. H. *J. Chem. Soc., Chem. Commun.* **1969**, 698–699; b) Elschenbroich, C.; Cais, M. *J. Organomet. Chem.* **1969**, *18*, 135–143; c) Alberti, A.; Benaglia, M.; Bonini, B. F.; Fochi, M.; Macciantelli, D.; Marcaccio, Paolucci, F.; Roffia, S. *J. Phys. Org. Chem.* **2004**, *17*, 1084–1090.

(32) Babin, V. N.; Belousov, Y. A.; Belousova, T. A.; Borisov, Y. A.; Gumenyuk, V. V.; Nekrasov, Y. S. *Russ. Chem. Bull. Int. Ed.* **2011**, *60*, 2081–2087.

(33) a) Connelly, N. G.; Geiger, W. E. *Chem. Rev.* **1996**, *96*, 877–910; b) Fujita, E.; Gordon, B.; Hillman, M.; Nagy, A. G. *J. Organomet. Chem.* **1981**, *218*, 105–114.

(34) Prins, R. *Mol. Phys.* **1970**, *19*, 603–620.

(35) Neidlinger, A.; Ksenofontov, V.; Heinze, K. *Organometallics* **2013**, *32*, 5955–5965.

(36) Kondo, Y. In *Supberbases for Organic Synthesis*; Ishikawa, T., Ed.; John Wiley & Sons, Ltd: Chichester, UK, 2009; pp 145–185.

(37) Barclay, L. R. C.; Dust, J. M. *Can. J. Chem.* **1982**, *60*, 607–615.

(38) Omelka, L.; Kováčová, J. *Magn. Reson. Chem.* **1994**, *32*, 525–531.

(39) Cais, M.; Ashkenazi, P.; Dani, S.; Gottlieb, J. *J. Organomet. Chem.* **1977**, *124*, 49–58.

(40) Buettner, G. R. *Free Radic. Biol. Med.* **1987**, *3*, 259–303.

(41) Huesmann, H.; Förster, C.; Siebler, D.; Gasi, T.; Heinze, K. *Organometallics* **2012**, *31*, 413–427.

(42) LeSuer, R. J.; Buttolph, C.; Geiger, W. E. *J. Organomet. Chem.* **2004**, *76*, 6395–6401.

(43) Camire, N.; Mueller-Westerhoff, U. T.; Geiger, W. E. *J. Organomet. Chem.* **2001**, *639*, 823–826.

(44) Bildstein, B.; Malaun, M.; Kopacka, H.; Wurst, K.; Ongania, K.-H.; Opromolla, G. *Organometallics* **1999**, *18*, 4325–4336.

(45) Sanders, R.; Mueller-Westerhoff, U. T. *J. Organomet. Chem.* **1996**, *512*, 219–224.

(46) Guillaneux, D.; Kagan, H. B. *J. Org. Chem.* **1995**, *60*, 2502–2505.

(47) Förster, C.; Heinze, K. *Z. Anorg. Allg. Chem.* **2015**, *641*, 517–520.

(48) Plazuk, D.; Vessières, A.; Hillard, E. A.; Buriez, O.; Labbé, E.; Pigeon, P.; Plamont, M. A.; Amatore, C.; Zakrzewski, J.; Jaouen, G. *J. Med. Chem.* **2009**, *52*, 4964–4967.

(49) a) Heinze, K.; Siebler, D. *Z. Anorg. Allg. Chem.* **2007**, *633*, 2223-2233; b) Siebler, D.; Linseis, M.; Gasi, T.; Carrella, L. M.; Winter, R. F.; Förster, C.; Heinze, K. *Chem. Eur. J.* **2011**, *17*, 4540–4551; c) Siebler, D.; Förster, C.; Heinze, K. *Dalton Trans.* **2011**, *40*, 3558–3575.

(50) Heinze, K.; Hüttinger, K.; Siebler, D. in *Modeling of Molecular Properties* (Ed. P. Comba), Wiley-VCH: Weinheim, Germany, 2011.

(51) Kienz, T.; Förster, C.; Heinze, K. *Organometallics* **2014**, *33*, 4803–4812.

(52) Eaton, G. R.; Eaton, S. S.; Barr, D. P.; Weber, Ralph, T. *Quantitative EPR*; Springer Wien, New York, 2010.

(53) Dempsey, J. L.; Winkler, J. R.; Gray, H. B. *Chem. Rev.* **2010**, *110*, 7024–7039.

(54) Hammes-Schiffer, S. *Chem. Rev.* **2010**, *110*, 6937–6938.

(55) Hammes-Schiffer, S.; Stuchebrukhov, A. *Chem. Rev.* **2010**, *110*, 6939–6960.

(56) Wenger, O. S. *Chem. Eur. J.* **2011**, *17*, 11692–11702.

(57) Herzog, W.; Bronner, C.; Löffler, S.; He, B.; Kratzert, D.; Stalke, D.; Hauser, A.; Wenger, O. S. *ChemPhysChem* **2013**, *14*, 1168–1176.

(58) Warren, J. J.; Tronic, T. A.; Mayer, J. M. *Chem. Rev.* **2010**, *110*, 6961–7001.

(59) Weinberg, D. R.; Gagliardi, C. J.; Hull, J. F.; Murphy, C. F.; Kent, C. A.; Westlake, B. C.; Paul, A.; Ess, D. H.; Mccafferty, D. G.; Meyer, T. J. *Chem. Rev.* **2012**, *112*, 4016–4093.

(60) Bonin, J.; Robert, M. *Photochem. Photobiol.* **2011**, *87*, 1190–1203.

(61) Savéant, J.-M. *Energy Environ. Sci.* **2012**, *5*, 7718–7731.

(62) Gagliardi, C. J.; Vannucci, A. K.; Concepcion, J. J.; Chen, Z.; Meyer, T. J. *Energy Environ. Sci.* **2012**, *5*, 7704–7717.

(63) Hammarström, L.; Styring, S. *Energy Environ. Sci.* **2011**, *4*, 2379–2388.

(64) Costentin, C.; Robert, M.; Savéant, J.-M. *Phys. Chem. Chem. Phys.* **2010**, *12*, 11179–11190.

(65) Heinze, K.; Schlenker, M. *Eur. J. Inorg. Chem.* **2004**, 2974–2988.

(66) Stoll, S.; Schweiger, A. *J. Magn. Reson.* **2006**, *178*, 42–55.

(67) Neese, F. *Wiley Interdiscip. Rev. Comput. Mol. Sci.* **2012**, *2*, 73–78.

(68) Schäfer, A.; Horn, H.; Ahlrichs, R. *J. Chem. Phys.* **1992**, *97*, 2571–2577.

(69) Weigend, F.; Ahlrichs, R. *Phys. Chem. Chem. Phys.* **2005**, *7*, 3297–3305.

(70) Neese, F. *Chem. Phys. Lett.* **2000**, *325*, 93–98.

(71) Fischer, T. H.; Almlof, J. *J. Phys. Chem.* **1992**, *96*, 9768–9774.

(72) Lenthe, E. van; Baerends, E. J.; Snijders, J. G. *J. Chem. Phys.* **1993**, *99*, 4597–4610.

(73) Van Wüllen, C. *J. Chem. Phys.* **1998**, *109*, 392.

(74) Pantazis, D. A.; Chen, X. Y.; Landis, C. R.; Neese, F. *J. Chem. Theory Comput.* **2008**, *4*, 908–919.

(75) Sinnecker, S.; Rajendran, A.; Klamt, A.; Diedenhofen, M.; Neese, F. *J. Phys. Chem. A* **2006**, *110*, 2235–2245.

3.3 How Hydrogen Bonds Affect Reactivity and Intervalence Charge Transfer in Ferrocenium-Phenolate Radicals

Andreas Neidlinger, Christoph Förster, and Katja Heinze*

European Journal of Inorganic Chemistry, in print.

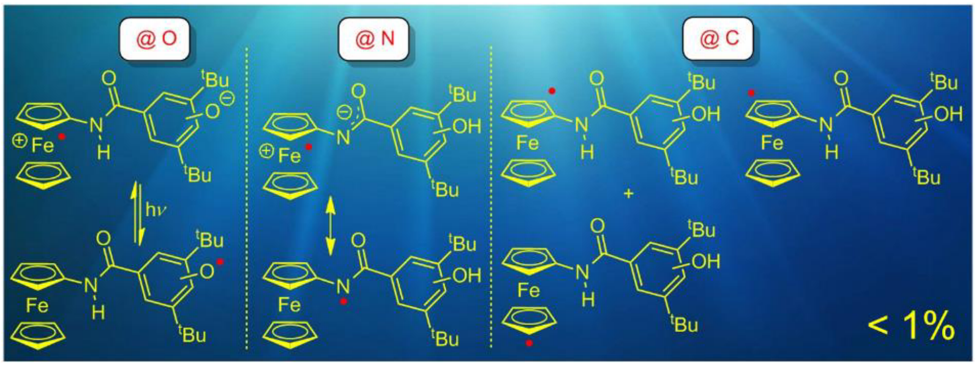

Abstract

Ferrocenyl phenol 2,4-di-*tert*-butyl-6-(2-ferrocenylcarbamoyl)phenol (**H-1**) forms intramolecular hydrogen bonds while its constitutional isomer 2,6-di-*tert*-butyl-4-(2-ferrocenylcarbamoyl)phenol (**H-2**) lacks intramolecular hydrogen bonds. Their corresponding bases **1**$^-$ and **2**$^-$ show intramolecular and intermolecular NH•••O hydrogen bonds, respectively. The phenolate **1**$^-$ is reversibly oxidized to **1**$^{\bullet}$, while **2**$^-$ only shows a quasireversible oxidation to **2**$^{\bullet}$ suggesting a higher reactivity. The radical pools **1**$^{\bullet}$ and **2**$^{\bullet}$ formed by an oxidation/deprotonation sequence of **H-1** and **H-2** are probed by (rapid-freeze) electron paramagnetic resonance spectroscopy and by spin-trapping techniques to elucidate the types of radicals present. Ferrocenium phenolate **[1a]**$^{\bullet}$ featuring an NH•••O intramolecular hydrogen bond is the most stable radical and undergoes thermal and photoinduced valence isomerization to the phenoxyl radical valence isomer **[1b]**$^{\bullet}$ with participation of the NH stretching mode (proton coupled electron transfer). A ferrocenium iminolate radical **[1c]**$^{\bullet}$ is present as well and equilibrates with carbon-centered ferrocenyl radicals **[1^{Cp}]**$^{\bullet}$ and **[1$^{\beta}$]**$^{\bullet}$. The latter radicals are intercepted by nitrobenzene to give corresponding stable nitroxyl radicals **[6^{Cp}]**$^{\bullet}$ and **[6$^{\beta}$]**$^{\bullet}$. All radicals **2**$^{\bullet}$, lacking intramolecular hydrogen bonds, are transient in nature due to rapid follow up reactions. Yet, rapid-freeze EPR spectroscopy indicated the presence of ferrocenium iminolate **[2c]**$^{\bullet}$ and phenoxyl radical **[2b]**$^{\bullet}$ and/or carbon-centered radicals **[2^{Cp}]**$^{\bullet}$ and **[2$^{\beta}$]**$^{\bullet}$. The carbon-centered radicals **[2^{Cp}]**$^{\bullet}$ and **[2$^{\beta}$]**$^{\bullet}$ are selectively trapped as corresponding nitroxide radicals **[7^{Cp}]**$^{\bullet}$ and **[7$^{\beta}$]**$^{\bullet}$. These diverse reactivity patterns are relevant for cytostatic ferrocenyl phenols such as ferrocifen.

Supporting information for this article (without Cartesian coordinates from DFT calculations) is found at pp. 206.

3.3.1 INTRODUCTION

Electron transfer (ET) reactions continue to be in the center of interest due to their importance in a plethora of chemical and biological processes.[1–7] Combination with proton transfer (PT) reactions facilitates the ET (proton coupled electron transfer, PCET).[8–18] As a prominent example, a tyrosyl residue (phenoxyl radical) is reduced to the phenol(ate) by the oxygen-evolving complex via PCET with the assistance of a nearby histidine base as proton shuttle in photosystem II.[19–24] This PCET is a key process in the stepwise oxidation of the oxygen evolving complex. This oxidation finally results in water oxidation to dioxygen at the oxygen-evolving complex, which is based on PCET processes itself.[19–24]

We have been interested in small model systems comprised of a phenoxyl radical[25] and ferrocene[26-30] (and in the corresponding ferrocenium/phenolate valence isomers) in order to investigate PCET intervalence charge transfer (IVCT)[31] reactions in redox-asymmetric systems.[16] In the parent ferrocenyl phenol conjugate **H-1**[16] an intramolecular hydrogen bond (IHB) is formed between the phenolic OH group and the carbonyl oxygen of the amide bond (OH•••O IHB, Scheme 1a), similar to ferrocene-free salicyl amide **H-4** (Scheme 1b). Deprotonation and oxidation of **H-1** yields the ferrocenium phenolate zwitterion **[1a]**$^\bullet$, the valence isomeric ferrocenyl phenoxyl radical **[1b]**$^\bullet$ and the ferrocenium iminolate tautomer **[1c]**$^\bullet$. In the latter tautomer the OH•••O IHB is retained while an NH•••O IHB is established in the valence isomers **[1a]**$^\bullet$ and **[1b]**$^\bullet$.

The IHB of the zwitterion **[1a]**$^\bullet$ is highly stabilized with respect to the IHB of the phenoxyl radical **[1b]**$^\bullet$ for two reasons: First, the phenolate is a better hydrogen atom acceptor than a phenoxyl radical which is also observed for the IHB of the ferrocene-free reference phenolate/phenoxyl pair **4**$^-$ and **4**$^\bullet$ (Scheme 1b).[25] Second, the ferrocenium-amide is a stronger hydrogen atom donor than the ferrocenyl-amide due to the positive charge.

This phenomenon has been previously observed, e.g. in oligoferrocene amides **H-A** and their mixed-valent systems **[H-A]**$^{\bullet +}$ (Scheme 2a).[28,29] Hence, the zwitterion **[1a]**$^\bullet$ is considerably stabilized with respect to **[1b]**$^\bullet$ (by 30 kJ mol^{-1} according to DFT calculations).[16] The proton in the IHB is involved in the thermal intramolecular ET between **[1a]**$^\bullet$ and **[1b]**$^\bullet$, with the proton being closer to the oxygen atom in **[1a]**$^\bullet$ and closer to the nitrogen atom in **[1b]**$^\bullet$. Optical ET (IVCT absorption band at 1040 nm) from the **[1a]**$^\bullet$ ground state to give the metastable phenoxide **[1b]**$^\bullet$ can only occur when the proton is already closer to the nitrogen atom as found in **[1b]**$^\bullet$. Hence, the ET is coupled to the NH vibrational mode of the **[1a]**$^\bullet$ / **[1b]**$^\bullet$ valence isomers.

Scheme 1. Hydrogen bonding in salicyl amides H-1, H-4 and H-4^{Me}, their corresponding phenolates 1^{-}, 4^{-} and [4^{Me}]$^{-}$ and their corresponding phenoxyl radicals 1$^{•}$, 4$^{•}$ and [4^{Me}]$^{•}$.[16,25]

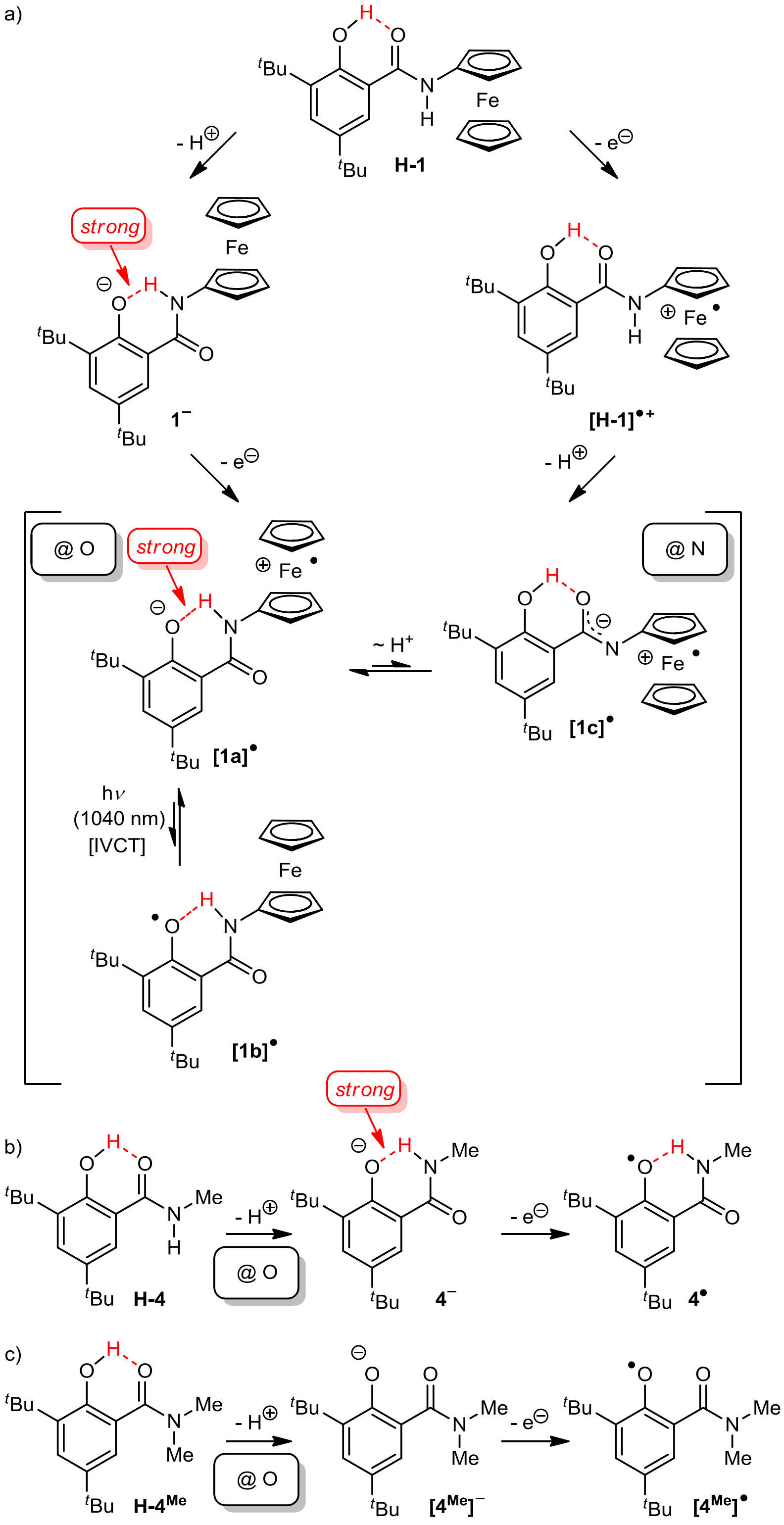

Charges stabilize the IHB and *vice versa* the hydrogen bond affects the redox potentials of the redox centers connected by the IHB. Large potential differences are observed between hydrogen bonded and non-hydrogen bonded phenolate/phenoxyl couples such as **4**$^{-}$/**4**$^{•}$ ($E_{½}$ =

−160 mV vs. FcH/FcH^+ in $CH_3CN/[^nBu_4N][BF_4]$)[25] and $[\mathbf{4^{Me}}]^-$/ $[\mathbf{4^{Me}}]^\bullet$ ($E_{½}$ = −425 mV vs. FcH/FcH^+ in $CH_3CN/[^nBu_4N][BF_4]$)[25] (Scheme 1b,c).[25] Similarly, the hydrogen-bonded ferrocenyl-NH moiety in **H-A** ($E_{½}$ = −115 mV vs. FcH/FcH^+ in $CH_3CN/[^nBu_4N][PF_6]$)[27,28] is oxidized at a lower potential than *N*-acetyl aminoferrocene **H-3** ($E_{½}$ = −50 mV vs. FcH/FcH^+ in $CH_2Cl_2/[^nBu_4N][B(C_6F_5)_4]$ [26,27,29,30]) (Scheme 2a).

Scheme 2. a), b) IHBs in ferrocene/ferrocenium amide redox couples H-A / [H-A]$^{\bullet+}$ and H-B / [H-B]$^{\bullet-}$ and c) ET and PT from the ferrocenyl phenol ferrocifen H-C.

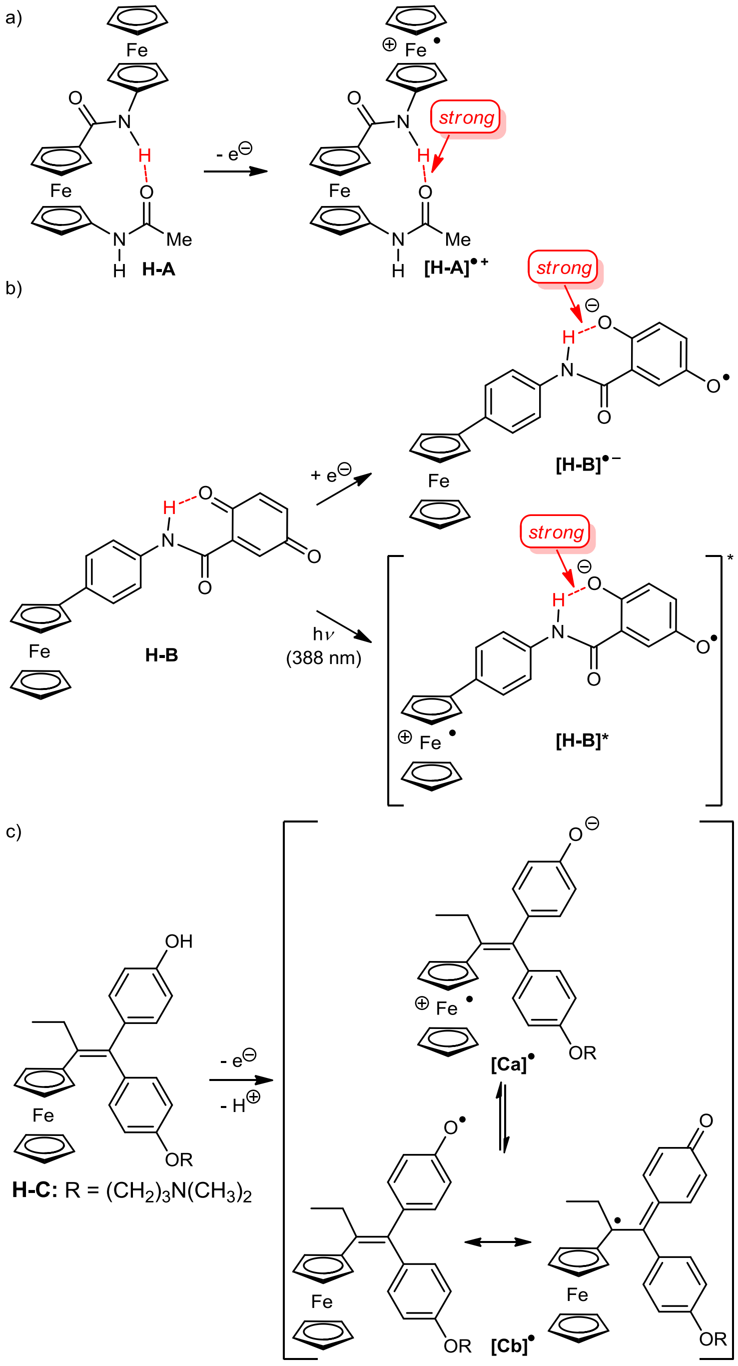

Another intriguing example of this kind of PCET with a crucial NH•••O IHB is found for the amide-linked ferrocenyl-quinone dyad **H-B** (Scheme 2b).[32] Upon reduction of the quinone to the semiquinonate **[H-B]**$^{\bullet-}$, the NH•••O IHB is strengthened and the semiquinone radical anion is stabilized. Similarly, irradiation of **H-B** at 388 nm yields the charge-separated state **[H-B]*** with ferrocenium-semiquinonate character effecting a strong NH•••O IHB. Due to the stabilizing effect of this IHB the lifetime of this zwitterionic state **[H-B]*** is quite high (Scheme 2b).[32]

Ferrocenyl phenols such as ferrocifen **H-C** (Scheme 2c) have found considerable interest as potent anti-cancer drugs.[33] Indeed, oxidation and deprotonation yields the mesomeric phenoxyl radical/*C*-centered radical **[Cb]**$^{\bullet}$ and a conceivable ferrocenium phenolate zwitterionic valence isomer **[Ca]**$^{\bullet}$, both lacking IHBs.

Scheme 3. Radical reactivity of [H-3]$^{\bullet+}$ in the presence of a base and PhNO.[26]

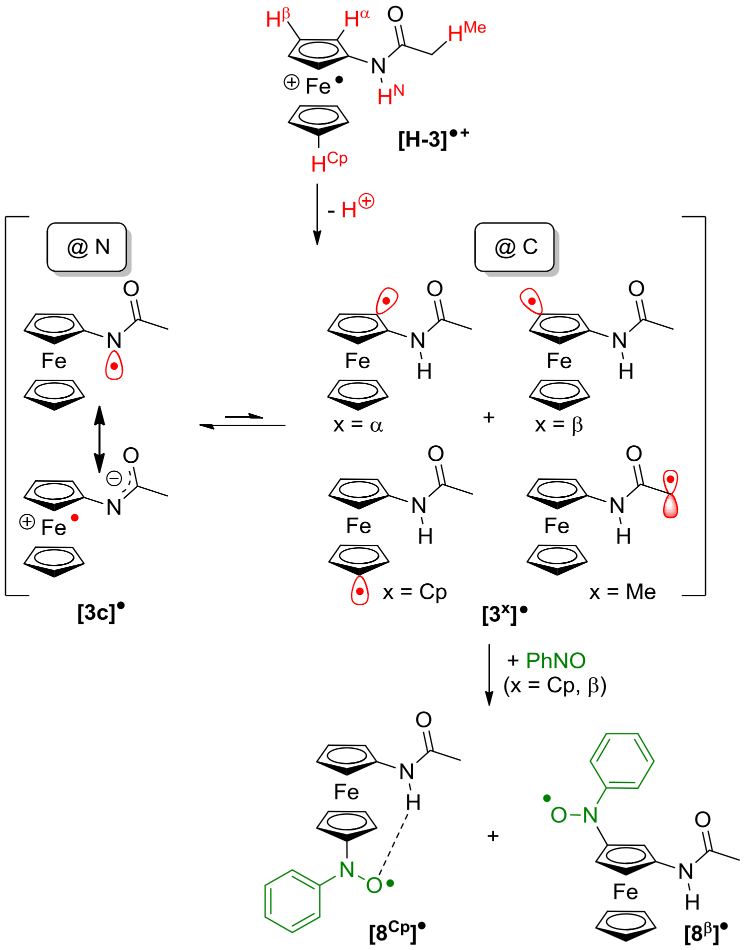

In this context, we recently succeeded in capturing transient carbon-centered ferrocenyl radicals, as proposed for **[Cb]**$^{\bullet}$, using nitrosobenzene (PhNO) as spin trap.[26] Relevant to the present study is the formation of trace amounts of *C*-centered radicals **[3^{x}]**$^{\bullet}$ derived from *N*-acetylaminoferrocene **H-3** in the presence of a base and an oxidant, in addition to the more stable ferrocenium iminolate radical **[3c]**$^{\bullet}$ (Scheme 3). EPR spectra of the nitroxyl radicals **[8^{x}]**$^{\bullet}$

resulting from the *C*-centered radicals **[3^{x}]$^{\bullet}$** and PhNO revealed the preferred site of attack, namely at the unsubstituted cyclopentadienyl ring and at the β position (**[8^{Cp}]$^{\bullet}$**, **[8$^{\beta}$]$^{\bullet}$**;Scheme 3).[26] The ferrocenium iminolate **[3c]$^{\bullet}$** does not react with PhNO, neither at the nitrogen atom nor at the metal center.[26]

In the present study, we address the effect of the NH•••O IHB in **1$^{\bullet}$** on the reactivity and the distribution of valence isomers (ferrocenium phenolate zwitterion **[1a]$^{\bullet}$** vs. phenoxyl radical **[1b]$^{\bullet}$**) and tautomers (ferrocenium iminolate **[1c]$^{\bullet}$**; *C*-centered radicals **[1^{x}]$^{\bullet}$**). To eliminate all IHBs, while essentially maintaining the overall geometry and electronic structure, the phenolic OH group is formally shifted from the 2-position in **H-1** to the 4-position in the constitutional isomer **H-2**. The properties of phenol **H-2**, its conjugate base **2^{-}**, its oxidation product **[H-2]$^{\bullet+}$** and the conceivable radical species **[2a]$^{\bullet}$**, **[2b]$^{\bullet}$**, **[2c]$^{\bullet}$** and **[2^{x}]$^{\bullet}$** will be disclosed and contrasted to the corresponding species derived from **H-1** by (rapid-freeze) EPR spectroscopy and DFT calculations. The potential presence of *C*-centered radicals **[1^{x}]$^{\bullet}$** and **[2^{x}]$^{\bullet}$** (in analogy to **[3^{x}]$^{\bullet}$**) derived from the corresponding ferrocenyl phenols **H-1** and **H-2** in the presence of base and oxidant will be probed by the spin-trapping technique. The possible presence of different radical types is relevant for the reactivity of cytostatic drugs based on the ferrocenyl phenol motif, such as ferrocifen **H-C**.

3.3.2 RESULTS AND DISCUSSION

Synthesis and characterization of ferrocenyl phenols H-1 and H-2 and reference phenols H-4 and H-5: The phenols **H-1** and **H-4** were prepared according to literature procedures[16,25] (Scheme 1). The constitutional isomer of **H-1**, 2,6-di-*tert*-butyl-4-(2-ferrocenylcarbamoyl)phenol **H-2** (Scheme 4a), is obtained by condensation of aminoferrocene[27] with the commercially available benzoic acid derivative 3,5-di-*tert*-butyl-4-hydroxybenzoic acid with HATU (1-[bis(dimethylamino)methylene]-1H-1,2,3-triazolo[4,5-b] pyridinium 3-oxide hexafluorophosphate) as coupling reagent. The ferrocene-free reference phenol **H-5** [2,6-di-*tert*-butyl-4-(2-(2,4,6-trimethylphenyl)carbamoyl)phenol, Scheme 4b] is accessible by an analogous coupling of the same benzoic acid derivative with 2,4,6-trimethyl aniline. Both phenols are fully characterized by NMR and IR spectroscopy as well as by mass spectrometry and elemental analysis.

Scheme 4. Generation of radicals a) from H-2 and b) from H-5 (atom numbering for NMR assignment given).

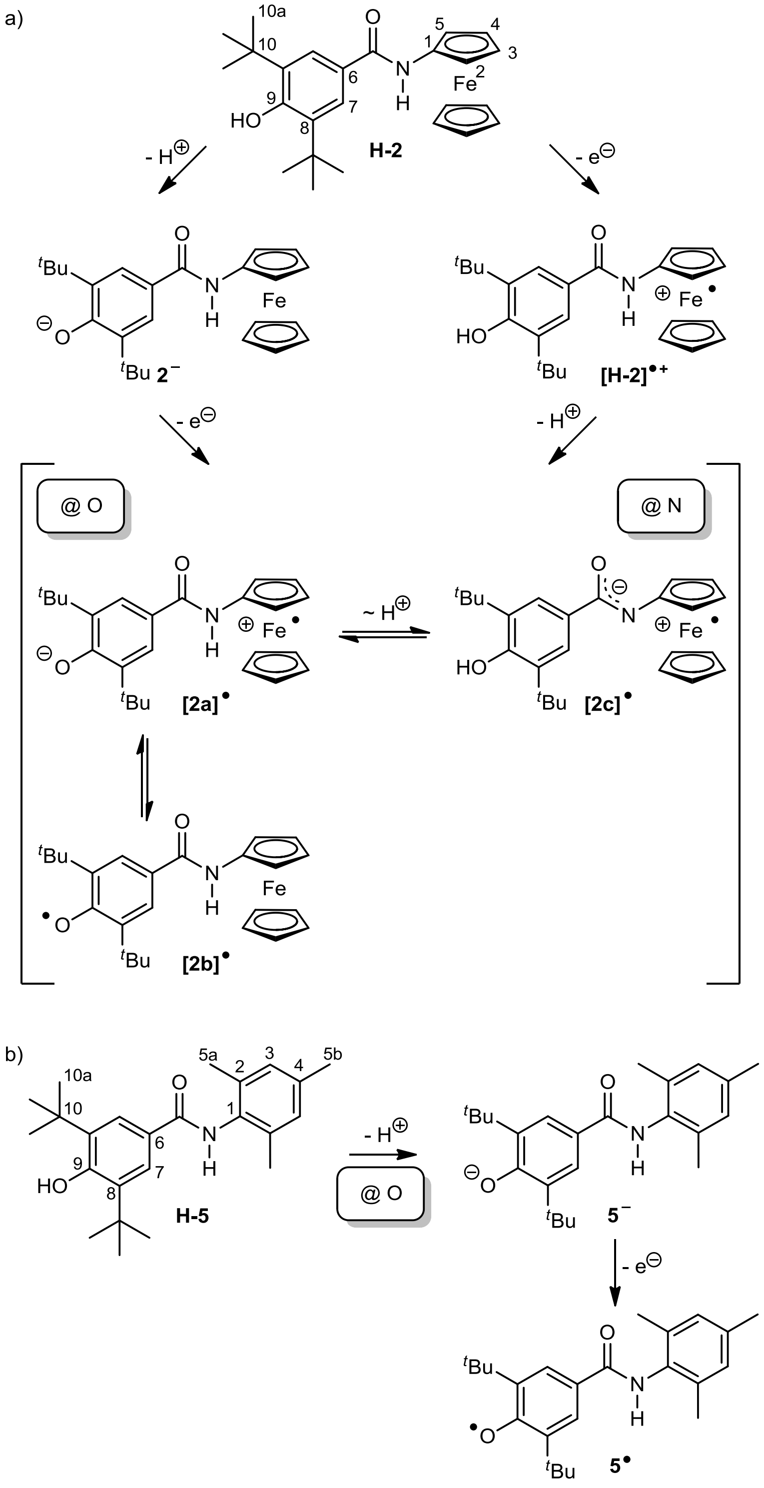

The molecular ion peak of **H-2** is found at *m*/*z* = 433 in the FD mass spectrum of **H-2**. The ^{1}H NMR spectra of **H-2** display the expected number of resonances with correct integral ratios. Due to the low solubility of **H-2** in dichloromethane, more detailed NMR studies (^{13}C NMR, 2D NMR) were also conducted in THF-d$_8$. In this coordinating solvent, the NH and OH protons resonate at δ_{NH} = 8.50 ppm and δ_{OH} = 6.59 ppm, respectively. These two resonances are unambiguously assigned by NOE spectroscopy (Supporting Information, Figure S1a). Contacts between the NH proton and the α-ferrocenyl protons $H^{2/5}$ (δ = 4.71 ppm) as well as the aromatic protons H^7 (δ = 7.73 ppm) are observed (Scheme 4). Expectedly, the OH proton shows a contact to the flanking ^{t}Bu groups (δ = 1.47 ppm). Both chemical shift values suggest the absence of hydrogen bonds in **H-2** in contrast to its constitutional isomer **H-1** featuring an OH•••O IHB (δ_{NH} = 9.01 ppm; δ_{OH} = 13.37 ppm in THF-d_8; Scheme 1).[16,35] Similarly, in CD_2Cl_2 the resonances for the NH proton and the OH proton are found at δ_{NH} = 7.09/7.36 ppm and δ_{OH} = 5.63/12.69 ppm for **H-2** and **H-1**, respectively. Hence, weak intermolecular hydrogen bonds from NH/OH to THF are likely, but IHBs of any kind are clearly absent in **H-2**.

The IR spectrum of **H-2** in CH_2Cl_2 confirms the absence of IHBs involving NH or OH groups. The absorption for the NH stretching vibration is observed at $\tilde{\nu}_{NH}$ = 3440 cm^{-1} similar to those of **H-3** ($\tilde{\nu}_{NH}$ = 3435 cm^{-1})[27] and **H-1** ($\tilde{\nu}_{NH}$ = 3450 cm^{-1}),[16] characteristic for a free NH group. The free OH group of **H-2** gives an absorption at $\tilde{\nu}_{OH}$ = 3625 cm^{-1}. In contrast, the OH stretching vibration of **H-1** is not observed in the spectral region between 3800 – 3100 cm^{-1} due to its involvement in the OH•••O IHB (Scheme 1).[16]

The reference phenol **H-5** is similarly characterized (Experimental Section, Supporting Information, Figure S1b). Expectedly, no IHBs are detected for **H-5** in $CDCl_3$ by ^{1}H NMR spectroscopy (δ_{OH} = 5.60 ppm; δ_{NH} = 7.18 ppm) as well as in CH_2Cl_2 by IR spectroscopy ($\tilde{\nu}_{OH}$ = 3625 cm^{-1}; $\tilde{\nu}_{NH}$ = 3425 cm^{-1}).

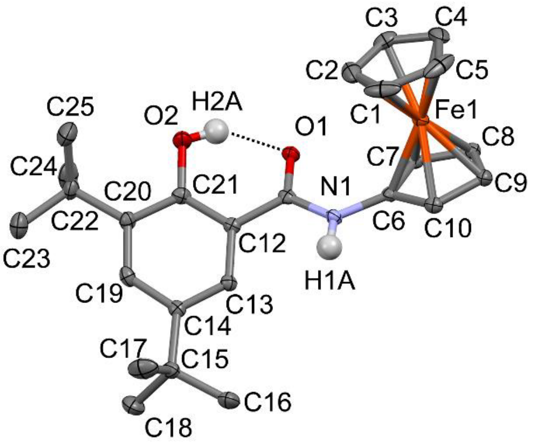

Figure 1. Molecular structure (thermal ellipsoids at 50 % probability level) of H-1 in the crystal (CH hydrogen atoms omitted).

The presence of the OH•••O IHB in **H-1**, as suggested by NMR and IR studies in solution,[16] is further corroborated by a single crystal XRD study. **H-1** crystallizes from ethyl acetate at 4 °C in the monoclinic space group $P2_1/c$ (Figure 1). The ferrocenyl moiety shows the usual structural features. The OH•••O IHB realizes an O1•••O2 distance of 2.580(3) Å. Further intermolecular hydrogen bonds between the amide proton and the carbonyl oxygen O1' of neighboring molecules of **H-1** lead to the typical hydrogen bonded chain of amides in the solid state with a N1•••O1' distance of 3.220(3) Å.[27,28] Additional crystallographic details are given in the Supporting Information (Table S1, Figure S2).

Radical formation and radical characterization: PT and ET reactions from **H-1**, **H-2** and their corresponding reference phenols **H-4**, **H-5** are depicted in Schemes 1 and 4. Chemical oxidations are performed using silver hexafluoroantimonate ($AgSbF_6$) as oxidant [$E_{1/2}(CH_2Cl_2)$ = 650 mV vs. FcH/FcH$^+$],[36] which is capable to oxidize ferrocenyl as well as phenolate units. Deprotonation is achieved using the non-nucleophilic and non-coordinating phosphazene base $P_1{}^t$Bu (*tert*-butylimino-tris(dimethylamino)phosphorane, pK_a(MeCN) = 26.98)[37] as proton acceptor. All analyses, oxidations, and deprotonations were performed under an inert atmosphere. After filtration from precipitated silver where applicable, the resulting solutions were immediately subjected to spectroscopic analyses (IR, UV/Vis and EPR spectroscopy).

Table 1. EPR parameters obtained by simulation of experimental X-band EPR spectra (298 K).[a]

radical	g_{iso}	$A(^{14}N)$ / G	$A(^1H^o)$ / G	$A(^1H^m)$ / G	$A(^1H^p)$ / G	other $A(^1H)$ / G	Gauss pp linewidth / MHz	Lorentz pp linewidth / MHz
[1b]$^\bullet$	2.0059						0.4	0.4
4$^\bullet$	2.0058					1.8 / 0.95[b]	0.1	0.07
5$^\bullet$	2.0060	1.90[c]				1.7 (2 x)[d]	0.02	0.02
[6^{Cp}]$^\bullet$	2.0071	11.10	2.80 (2 x)	0.90 (2 x)	2.60	1.20, 1.00, 0.90 (2 x) [e]	0.08	0.04
[7^{Cp}]$^\bullet$	2.0069	11.30	2.90 (2 x)	0.85 (2 x)	2.70	1.10 (2 x), 0.85 (2 x) [e]	0.15	0.05
[8^{Cp}]$^\bullet$ [26]	2.0072	10.90	2.77 (2 x)	0.90 (2 x)	2.64	1.20 / 1.10, 0.70 (2 x) [e]	0.06	0.02

[a] For atom numbering of nitroxyl radicals see Scheme 7. [b] H atoms of the 3,5-di-*tert*-butyl-2-hydroxybenzoic acid moiety. [c] Amide nitrogen atom. [d] H atoms of the 2,6-di-*tert*-butyl-4-hydroxybenzoic acid moiety. [e] H atoms of the ferrocenyl moiety.

The reference radical **4**$^\bullet$ obtained from **H-4** by PT and ET gives the expected sharp EPR resonance of a phenoxyl radical at $g_{1,2,3}$ = 2.0117, 2.0071, 2.0037; Table 2) at 77 K and at g_{iso} = 2.0058 at 298 K in CH_2Cl_2 (Figure 2, Table 1).[16] The most stable valence isomer of **1**$^\bullet$ obtained by oxidation and deprotonation of **H-1** is the zwitterionic **[1a]**$^\bullet$. The zwitterion is characterized by its 77 K EPR resonance ($g_{1,2,3}$ = 3.0400, 1.9490, 1.9030, Table 2) which significantly differs from the EPR pattern of the parent ferrocenium ion **[H-1]**$^{\bullet+}$ ($g_{1,2,3}$ = 3.4200, 1.8552, 1.7550, Table 2).[16] Attempts to observe the expected trace amounts of the phenoxyl radical valence isomer **[1b]**$^\bullet$ were recently successful delivering a very weak EPR resonance at g_{iso} = 2.0059 at 298 K (Figure 2, Table 1). At this temperature, the resonance of **[1a]**$^\bullet$ is not observed as typical for ferrocenium radicals which are EPR-silent at room temperature due to fast spin-lattice relaxation.[38] The signal of **[1b]**$^\bullet$ is broader than that of **4**$^\bullet$ possibly due to additional unresolved hyperfine couplings (hfc's) to ferrocenyl protons (Figure 2). The yield of **[1b]**$^\bullet$ with respect to initial **H-1** as obtained by double integration of the EPR resonance referenced against the DPPH radical is approximately 0.05 %.[26,39] This low yield explains the difficulty of its observation.

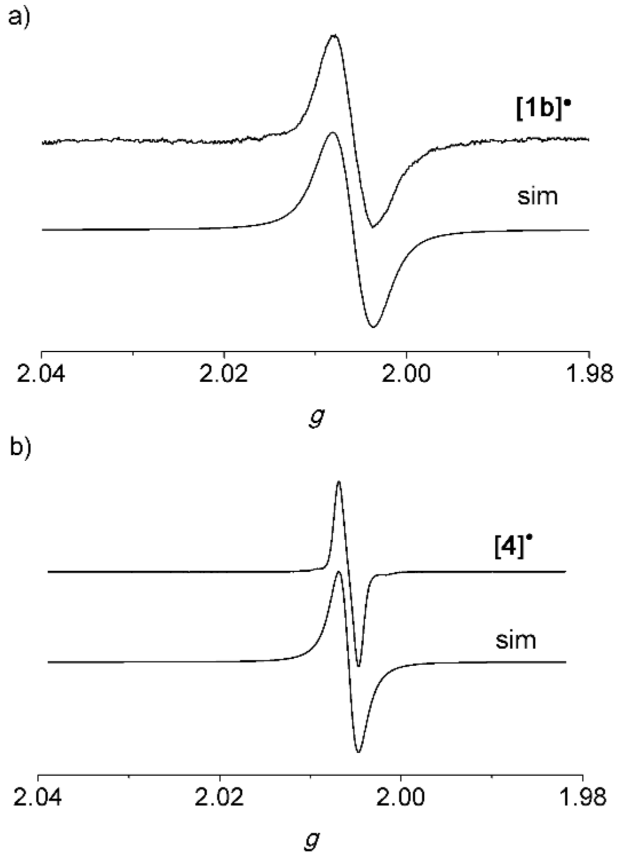

Figure 2. a) X-band EPR spectrum of $[1b]^{\bullet}$ (20 mM solution of H-1 in CH_2Cl_2) at 298 K including simulation recorded at the following parameters: field = 3346.20 G, sweep = 499.77 G, sweep time = 90 s, modulation = 5000 mG, MW attenuation = 10 dB and b) X-band EPR spectrum of $4^{\bullet}$ (5 mM solution of H-4 in CH_2Cl_2) at 298 K including simulation recorded at the following parameters: field = 3346.20 G, sweep = 94.79 G, sweep time = 90 s, modulation = 1000 mG, MW attenuation = 10 dB.[16]

Table 2. EPR parameters obtained by simulation of experimental X-band spectra (77 K).

radical (mixture)	$g_{1,2,3}$	$A(^{14}N)$ / G (nitroxyl N)	fraction / %	Gauss pp linewidth / MHz	Lorentz pp linewidth / MHz
[H-1]$^{\bullet+}$ [16]	3.4200, 1.8552, 1.7550			1.5	1.5
[1a]$^{\bullet}$ [16]	3.0400, 1.9490, 1.9030			0.5	0.5
[H-2]$^{\bullet+}$	3.4000, 1.8780, 1.7965			1.0	1.0
[H-3]$^{\bullet+}$ [16]	3.3500, 1.8750, 1.7870			1.5	1.5
[1^x]$^{\bullet}$ (x = α, β, Cp) **[1c]**$^{\bullet}$	2.0105, 2.0070, 2.0025 2.9600, 1.9530, 1.9330		1.3 98.7	0.5 0.5	0.5 0.5
[2b]$^{\bullet}$/ **[2^x]**$^{\bullet}$ (x = α, β, Cp) **[2c]**$^{\bullet}$	~2.011, 2.008, 2.005 N/A, ~1.98, ~1.96		30 70	0.3 1.7	0.3 1.7
[8^{Cp}]$^{\bullet}$ [26] **[3c]**$^{\bullet}$ [26]	2.0105, 2.0060, 2.0045 N/A, 1.9620, 1.9450	3.5, 3.5, 28.0	17 83	0.3 0.3	0.4 0.2
[3^x]$^{\bullet}$ (x = α, β, Cp, Me) [26] **[3c]**$^{\bullet}$ [26]	2.0095, 2.0065, 2.0030 N/A, 1.9650, 1.9400		0.8 99.2	0.3 0.1	0.2 0.1
4$^{\bullet}$	2.0117, 2.0071, 2.0037			0.6	0.5
5$^{\bullet}$	2.0096, 2.0065, 2.0036			0.3	0.3
[6^{Cp}]$^{\bullet}$	2.0103, 2.0069, 2.0040	3.0, 3.0, 28.0		0.5	0.5
[7^{Cp}]$^{\bullet}$	2.0094, 2.0067, 2.0048	4.0, 4.0, 26.0		0.5	0.6
[8^{Cp}]$^{\bullet}$ [26]	2.0105, 2.0060, 2.0045	3.5, 3.5, 28.0		0.3	0.4

We furthermore attempted to detect the conceivable IVCT band of **[1b]**$^{\bullet}$ in addition to the IVCT band of **[1a]**$^{\bullet}$ (1040 nm in CH_2Cl_2),[16] although **[1b]**$^{\bullet}$ is only present in trace amounts. Indeed, by close inspection of the NIR spectral region we were able to observe two further very weak NIR bands at 1970 and 1820 nm ($\tilde{\nu}_{max}$ = 5076 and 5491 cm^{-1}, $\Delta\tilde{\nu}_{1/2}$ = 548 and 815 cm^{-1}, □ = 45 and 27 m^{-1} cm^{-1}) in CH_2Cl_2 (obtained by Gaussian deconvolution; Supporting Information, Figure S3). However, the width $\Delta\tilde{\nu}_{1/2}$ of these bands is rather low and smaller than expected for IVCT transitions.[40] Those two low energy bands are fairly similar to the ones observed for NHR-substituted ferrocenium ions such as **[H-3]**$^{\bullet+}$ [41a] and also for other substituted Fc^+ ions[41b] and are attributed to Laporte-forbidden d-d transitions of the ferrocenium moiety of **[1a]**$^{\bullet}$. To further confirm this assignment, a time-dependent density functional theory (TD-DFT) calculation (B3LYP/SV(P), COSMO CH_2Cl_2) was performed for **[1a]**$^{\bullet}$ providing low-energy transitions at 2765, 2055, 1317, 1091, 997, and 771 nm (3617, 4865, 7594, 9168, 10031, and 12973 cm^{-1}), respectively (Supporting Information, Table S2). The calculated lowest-energy band corresponds to an IVCT (phenolate → d_{xy} (Fc^+), f = 0.00623) giving the ferrocenyl phenoxyl radical ground state of **[1b]**$^{\bullet}$. This band is experimentally not observed. The 1091 nm band (phenolate → d_{xz}(Fc^+), f = 0.01999) corresponds to the experimentally observed IVCT band of **[1a]**$^{\bullet}$ (1040 nm).[16] The calculated transitions at 2055 and 1317 nm are assigned to the experimentally observed weak NIR bands at 1970 and 1820 nm and are clearly ferrocenium d-d transitions (Supporting Information, Table S2, Figure S4).

Two further IVCT bands are calculated by TD-DFT at 997 and 771 nm (10031 and 12973 cm^{-1}). These represent phenolate → d_{yz}(Fc^+) and lone pair(phenolate) → d_{xy} (Fc^+) transitions. As they are close to the 1040 nm IVCT band and very weak in intensity ($f < 0.0001$) they are not distinctly observed. In essence, the relevant bands of **[1a]**$^•$ are well understood, while IVCT bands of **[1b]**$^•$ are not detectable due to the very low concentration of the phenoxyl radical **[1b]**$^•$. Obviously, **[1a]**$^•$ is significantly preferred over **[1b]**$^•$ due to the strong NH•••O IHB in the zwitterion.

The phenol amides **H-1** and **H-4** are easily deprotonated by one equivalent $P_1{}^t$Bu in CH_2Cl_2. The analogous reaction with the constitutional isomers **H-2** and **H-5** proved to be more challenging, based on UV/Vis and IR spectroscopic studies, namely an incomplete shift of the π- π* phenol/phenolate band[42,43] and incomplete decrease of the $\tilde{\nu}_{OH} = 3625$ cm^{-1} IR absorption band (Supporting Information, Figures S6a–S9a). Increasing the ionic strength of the CH_2Cl_2 solution by addition of [$^n Bu_4N$][$B(C_6F_5)_4$] (similar to the electrochemical experiments[44,45]; *vide infra*) resulted in almost complete deprotonation of **H-5** to **5**$^-$ and quantitative deprotonation of **H-2** to **2**$^-$ by one equivalent $P_1{}^t$Bu as judged from the π- π* phenolate bands and the absence of OH vibrational stretching bands (Supporting Information, Figures S6b–S9b). Obviously, the proton transfer benefits from a higher ionic strength of the solution.

The NH stretching vibrational bands of **2**$^-$ and **5**$^-$ ($\tilde{\nu}_{NH} = 3435$ cm^{-1}) are essentially unperturbed as compared to those of **H-2** and **H-5** (Supporting Information, Figures S7b and S9b). Yet, an additional NH stretching band is found at $\tilde{\nu}_{NH} = 3365$ and 3380 cm^{-1}, for **2**$^-$ and **5**$^-$, respectively. These bands are assigned to an NH group *inter*molecularly hydrogen bonded to a phenolate ion giving at least dimeric aggregates **[2$_2$]**$^{2-}$ and **[5$_2$]**$^{2-}$ in CH_2Cl_2 solution (Scheme 5a; intermolecular NH•••O hydrogen bond). Even higher aggregates of these ionic systems **2**$^-$ and **5**$^-$ might be present as well, but these are not shown for clarity. The presence of intermolecular hydrogen bonds is supported by the analogous association of **H-3** and phenolate (Scheme 5b, Supporting Information, Figure S10; $\tilde{\nu}_{NH} = 3380$ cm^{-1}). As expected from the different pK_a values of phenol and amide[35,46] and supported by DFT calculations, favoring the phenolate over the iminolate by 65 kJ mol^{-1} and 71 kJ mol^{-1} for **2**$^-$ and **5**$^-$, respectively (Supporting Information, Figure S11), no evidence for the presence of conceivable iminolate tautomers is found (Scheme 5). That the NH group of amide **2**$^-$ should be sterically accessible for hydrogen bonding is also evident from the solid state structure of **H-1** and other substituted *N*-ferrocenyl amides (Supporting Information, Figure S2). The observed *inter*molecular NH•••O hydrogen bond between an amide and a phenolate is electronically congruent with the *intra*molecular NH•••O hydrogen bond in **1**$^-$ (Scheme 1; $\tilde{\nu}_{NH} = 3380$ cm^{-1}).[16]

Scheme 5. a) Formation of $[2_2]^{2-}$ and $[5_2]^{2-}$ from 2^- and 5^- through intermolecular hydrogen bonds and b) intermolecular hydrogen bond between H-3 and phenolate in CH_2Cl_2 solution.

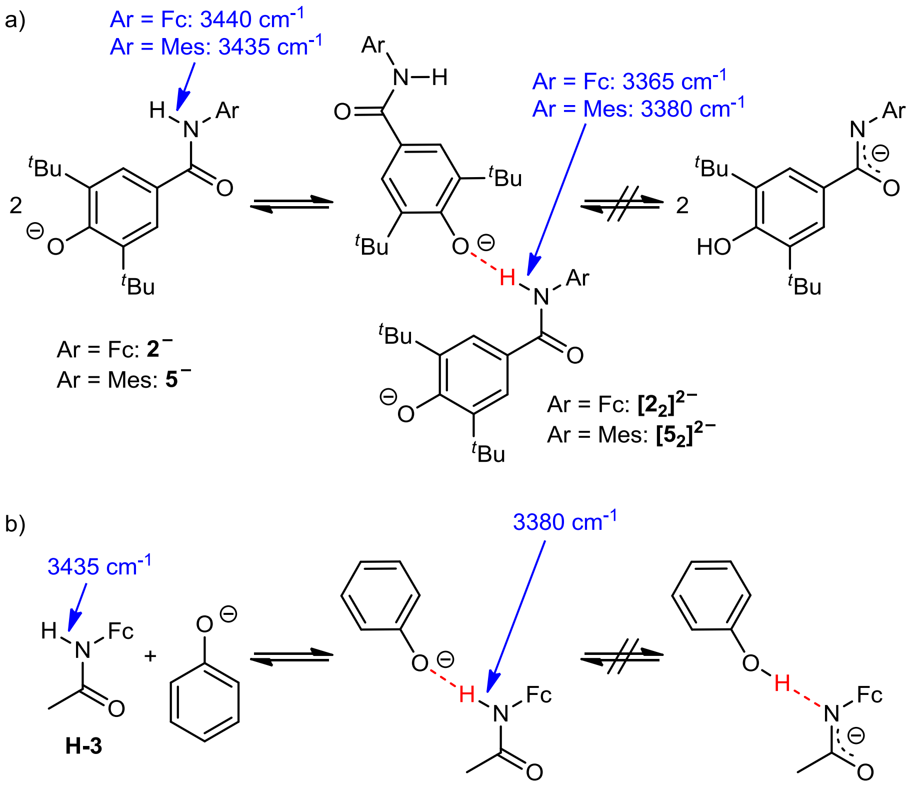

H-2 is reversibly oxidized to **[H-2]**$^{\bullet+}$ at $E_{½} = -105$ mV vs. FcH/FcH$^+$ at 298 K in $CH_2Cl_2/[^nBu_4N][B(C_6F_5)_4]$ solution (Supporting Information, Figure S12). Under the same conditions, the **H-1**/**[H-1]**$^{\bullet+}$ redox couple is observed at $E_{½} = -150$ mV.[16] The EPR spectrum of **[H-2]**$^{\bullet+}$ in frozen $CH_2Cl_2/[^nBu_4N][B(C_6F_5)_4]$ at 77 K obtained by oxidation of **H-2** with $AgSbF_6$ shows a characteristic nearly axial ferrocenium resonance (Supporting Information, Figure S13) similar to the ferrocenium ion **[H-1]**$^{\bullet+}$,[16] fully confirming the metal-centered oxidation (Table 2). The UV/Vis spectrum of **[H-2]**$^{\bullet+}$ prepared under the same conditions features the expected ferrocenium absorption band at $\lambda_{max} = 770$ nm (Supporting Information, Figure S14) similar to **[H-1]**$^{\bullet+}$.[16,28,29] The IR spectrum of **[H-2]**$^{\bullet+}$ prepared in the same fashion shows an essentially unperturbed OH vibration ($\tilde{\nu}_{OH} = 3620$ cm^{-1}) and a slightly shifted NH vibration ($\tilde{\nu}_{NH} = 3365$ cm^{-1}). This suggests a weakening of the NH bond in the cation **[H-2]**$^{\bullet+}$ and hence an acidification of the NH group due to the positive charge on the ferrocenium moiety close to the NH group, which results in coordination of the counter ion NH•••F(SbF_6).[16]

In the presence of approximately equimolar amounts of $P_1{}^tBu$ **H-2**, i.e. phenolate **2**$^-$, shows two redox processes in $CH_2Cl_2/[^nBu_4N][B(C_6F_5)_4]$ solution. An irreversible oxidation at $E_p = -500$ mV vs. FcH/FcH$^+$ is observed followed by a reversible, one-electron oxidation process at $E_{½} = -110$ mV vs. FcH/FcH$^+$ and another irreversible follow-up wave at $E_p = 70$ mV (Figure 3, bottom). The potential of the reversible wave ($E_{½} = -110$ mV) is close to that of the **H-2**/**[H-2]**$^{\bullet+}$ pair and the irreversible wave resembles the one of the reference **5**$^-$/**5**$^{\bullet}$ couple

($E_{1/2} = -490$ mV vs. FcH/FcH$^+$; Supporting Information, Figure S15b). The reversible wave is indeed assigned to the **H-2**/**[H-2]**$^{\bullet+}$ pair. As both **5**$^-$ and **2**$^-$ are present as (at least dimeric) aggregates (Scheme 5), we assign the first wave to the irreversible oxidation of the hydrogen bonded aggregate **[2$_2$]**$^{2-}$ to the hydrogen bonded radical **[2$_2$]**$^{\bullet-}$. At higher scan rates (up to 800 mV s^{-1}), the irreversible oxidation of **[2$_2$]**$^{2-}$ becomes partially reversible (Supporting Information, Figure S16). The fact that the peak area of the two high potential waves is approximately twice that of the area of the **[2$_2$]**$^{2-}$/**[2$_2$]**$^{\bullet-}$ oxidation wave (Figure 3, top), suggests, that oxidation of **[2$_2$]**$^{2-}$ releases the phenol **H-2** after proton transfer and a another species. Furthermore, the wave of the initially present aggregated phenolate **[2$_2$]**$^{2-}$ decreases upon further scanning confirming a follow-up reaction of **[2$_2$]**$^{\bullet-}$ after electron transfer. In contrast to the behavior of **[2$_2$]**$^{2-}$, monomeric **1**$^-$ displays a (quasi)reversible oxidation at $E_{½} = -535$ mV and an irreversible oxidation at $E_p = +100$ mV.[16] This reactivity difference will be discussed below.

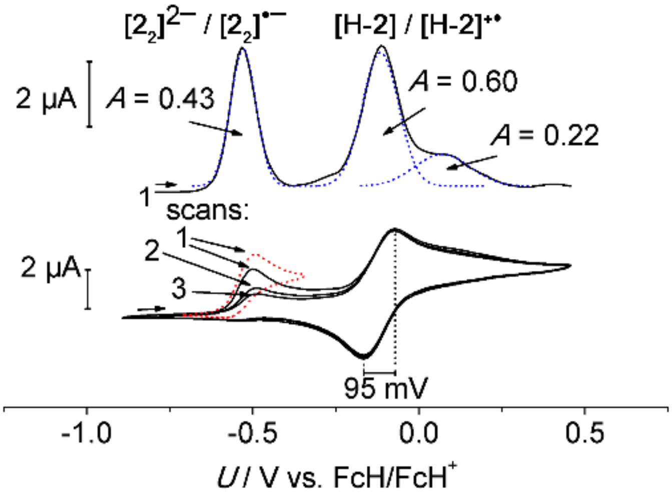

Figure 3. Square wave (top) and cyclic voltammogram (bottom) of 2$^-$ in CH$_2$Cl$_2$ containing [^{n}Bu$_4$N][B(C$_6$F$_5$)$_4$] as supporting electrolyte at 298 K. Relative peak areas *A* given.

Attempts to spectroscopically observe the radicals **2**$^\bullet$ met with limited success due to the transient nature of these radical species. Independent of the preparative pathway (oxidation/deprotonation or deprotonation/oxidation) only EPR-silent reaction mixtures were obtained. However, addition of approximately one equivalent of P$_1{}^t$Bu to a pre-cooled solution (ca. 193 K) of **[H-2]**$^{\bullet+}$ and rapidly freezing the sample to 77 K delivered an EPR spectrum displaying a sharp resonance at $g \approx 2.00$ next to a broad resonance at $g \approx 1.96$ (Supporting Information, Figure S17). Tentatively, we assign the resonance at $g \approx 2.00$ to the phenoxyl radical valence isomer **[2b]**$^\bullet$ and/or the carbon-centered radicals **[2^x]**$^\bullet$ by comparison with the resonance of phenoxyl radical **5**$^\bullet$ and radicals **[3^x]**$^\bullet$ (Supporting Information, Figure S18, Table 2, Scheme 3). The high-field resonance is assigned to the ferrocenium part of the zwitterion **[2c]**$^\bullet$ by comparison with the resonances of the ferrocenium iminolates **[1c]**$^\bullet$ and **[3c]**$^\bullet$ (Schemes 1, 3 and 4; Table 2).[16,26] Annealing this sample to room temperature for one minute and refreezing to 77 K resulted in an EPR-silent mixture. Obviously, the radicals **2**$^{\bullet}$ are much more reactive than the radicals **1**$^{\bullet}$ and their observation by UV/Vis or IR spectroscopy fails.[16]

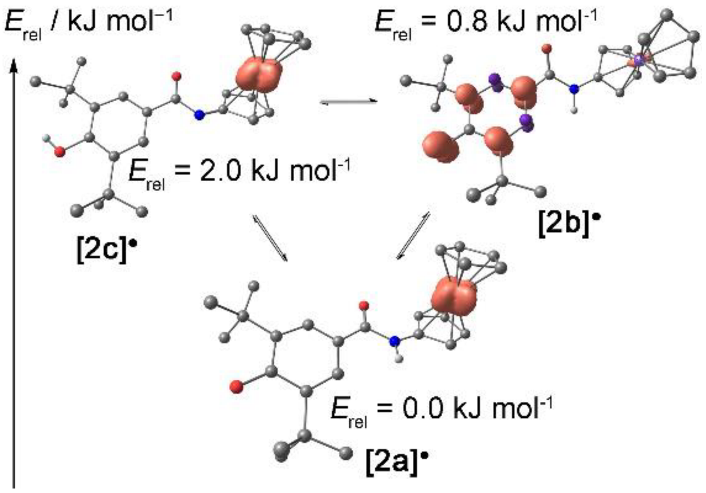

Figure 4. DFT calculated geometries and energies, and spin densities (red, isosurface value 0.01 a.u.) of the valence isomers and tautomers of 2$^{\bullet}$ (CH_2Cl_2; CH hydrogen atoms omitted).

DFT geometry optimizations of the ferrocenium phenolate zwitterion **[2a]**$^{\bullet}$, the ferrocenyl phenoxyl radical **[2b]**$^{\bullet}$ and the ferrocenium iminolate zwitterion **[2c]**$^{\bullet}$ show that these valence isomers and tautomers are very close in energy (Figure 4). The quite high stability of the ferrocenium iminolate **[2c]**$^{\bullet}$ can be accounted for by the increased acidity of the positively charged ferrocenium amides similar to the stability of **[3c]**$^{\bullet}$ (Scheme 3).[26,28-29] In contrast, zwitterion **[1a]**$^{\bullet}$ is significantly stabilized relative to **[1b]**$^{\bullet}$ and **[1c]**$^{\bullet}$ due to its strong NH•••O IHB.[16] A comparison of the charge-transfer and d-d transitions of **[1a]**$^{\bullet}$ and the elusive **[2a]**$^{\bullet}$ derived by TD-DFT calculations can be found in the Supporting Information (Table S2).

Scheme 6. Oxidation of the aggregate $[2_2]^{2-}$ to $[2_2]^{\bullet-}$ followed by proton transfer and dissociation into H-2 and $[2a\text{-}H]^{\bullet-}$ / $[2b\text{-}H]^{\bullet-}$ radical anions.

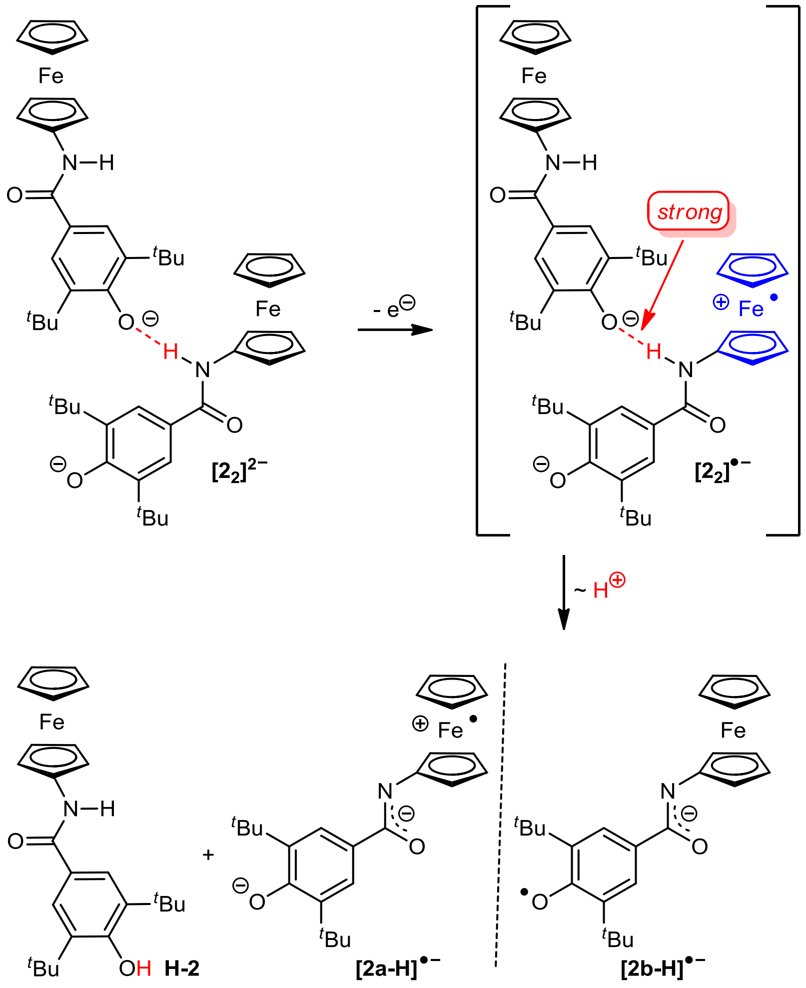

The high reactivity of **2**$^\bullet$ in comparison to **1**$^\bullet$ is not immediately obvious from the DFT calculations. All radicals **[2a]**$^\bullet$, **[2b]**$^\bullet$ and **[2c]**$^\bullet$ should be quite persistent when compared to typical phenoxyl and ferrocenium radicals, such as **4**$^\bullet$, **5**$^\bullet$ or FcH$^{\bullet+}$, **[H-2]**$^{\bullet+}$, **[3c]**$^\bullet$ (Supporting Information, Figures S18, S13 and literature data [16,26,47-52]). The main difference between **1**$^\bullet$ and **2**$^\bullet$ is the type of NH•••O hydrogen bond between amide and phenolate in their precursor phenolates **1**$^-$ and **2**$^-$, namely an intramolecular hydrogen bond in **1**$^-$ (Scheme 1) and an intermolecular hydrogen bond in **2**$^-$ (Scheme 5a). Given, that **2**$^-$ forms (at least) dimeric aggregates **[2₂]**$^{2-}$ in CH_2Cl_2/[^{n}Bu$_4$N][B(C_6F_5)$_4$] solution (Scheme 5a), oxidation of this aggregate to **[2₂]**$^{\bullet-}$ should occur at the ferrocenyl moiety which forms the NH•••O bond (Scheme 6) as this hydrogen bond increases the phenolate/phenoxyl potential but lowers the ferrocene/ferrocenium potential (*vide supra*).

In the radical aggregate **[2₂]**$^{\bullet-}$ a phenolate **2**$^-$ is coordinated to the positively charged [Fc-NH]$^{\bullet+}$ site of radical **[2a]**$^\bullet$ which could easily result in a proton transfer from the acidic [Fc-NH]$^{\bullet+}$ group to the phenolate. Dissociation furnishes **H-2** and the doubly deprotonated ferrocenium phenolate iminolate **[2a-H]**$^{\bullet-}$ or the phenoxyl iminolate species **[2b-H]**$^{\bullet-}$ (Scheme

6). The latter radical anions might be susceptible to decomposition. This mechanistic scenario perfectly fits to the electrochemical experiments (Figure 3): one electron oxidation of the dimer **[2$_2$]$^{2-}$** (E_p = −500 mV) leads to **[2$_2$]$^{\bullet-}$** followed by formation of **H-2** ($E_{½}$ = −110 mV) and follow-up products of **[2a-H]$^{\bullet-}$** / **[2b-H]$^{\bullet-}$** (−300 to +300 mV). The **[2$_2$]$^{2-}$** / **[2$_2$]$^{\bullet-}$** redox process is followed by an intermolecular proton transfer leading to dissociation (EC mechanism). Oxidation of **1**$^{-}$, however, leads to stable **[1a]**$^{\bullet}$ with the hydrogen-bonded proton simply moving between the nitrogen and oxygen atoms.[16] To conclude, the fundamental reactivity difference between **2**$^{\bullet}$ and **1**$^{\bullet}$ is based on the nature of the hydrogen bond.

Spin-trapping of carbon-centered radicals. The ferrocenium iminolate **[3c]**$^{\bullet}$ equilibrates with a pool of carbon-centered radicals **[3^{x}]**$^{\bullet}$ (x = α, β, Cp, Me) and some of these radicals can be intercepted by PhNO to give the nitroxides **[8^{Cp}]**$^{\bullet}$ and **[8$^{\square}$]**$^{\bullet}$ (Scheme 3). Carbon-centered metallocenyl radicals might also be involved in the decarboxylation of cobaltocenium carboxylate.[53] Although, PhNO has been reported to trap phenoxyl radicals[54-57], the phenoxyl reference radicals **4**$^{\bullet}$ and **5**$^{\bullet}$ are inert towards PhNO under our conditions. Furthermore, simple ferrocenium ions, such as FcH$^{\bullet+}$ or **[H-3]**$^{\bullet+}$ are resistant towards PhNO as well.[26] Hence, the formation of nitroxide radicals selectively indicates the presence of ferrocenium iminolates, which equilibrate with *C*-centered radicals.

Indeed, **[H-1]**$^{\bullet+}$ and **[H-2]**$^{\bullet+}$ are unreactive towards PhNO and only the ferrocenium resonances are observed by EPR spectroscopy at 77 K (Table 2, Scheme 7). In the presence of base, the valence isomeric radicals **[1a]**$^{\bullet}$/**[2a]**$^{\bullet}$ and **[1b]**$^{\bullet}$/**[2b]**$^{\bullet}$ are formed (O deprotonation), along with the ferrocenium iminolates **[1c]**$^{\bullet}$/**[2c]**$^{\bullet}$ (N deprotonation) (Schemes 1, 4a and 7). The latter might equilibrate with *C*-centered radicals **[1^{x}]**$^{\bullet}$/ **[2^{x}]**$^{\bullet}$ (x = α, β, Cp; C deprotonation) which should be susceptible to the spin trap reaction giving nitroxide radicals **[6^{x}]**$^{\bullet}$/ **[7^{x}]**$^{\bullet}$ (Scheme 7). Indeed, EPR triplet resonances characteristic for nitroxide radicals are observed at 298 K in both cases (Figure 5) with a spectroscopic yield of less than 1 % (by double integration of the EPR resonance referenced against the DPPH radical).[26,39] The EPR parameters obtained for **[6^{x}]**$^{\bullet}$ / **[7^{x}]**$^{\bullet}$ closely resemble those of **[8^{Cp}]**$^{\bullet}$ (Scheme 3, Table 1) suggesting the preferred substitution at the Cp ring (**[6^{Cp}]**$^{\bullet}$ / **[7^{Cp}]**$^{\bullet}$) with possibly some substitution at the β position (**[6$^{\beta}$]**$^{\bullet}$ / **[7$^{\beta}$]**$^{\bullet}$) (Scheme 7). Similar to the **[3^{x}]**$^{\bullet}$ / **[8^{x}]**$^{\bullet}$ case and in agreement with DFT calculations, substitution at the nitrogen atom (**[6^{N}]**$^{\bullet}$ / **[7^{N}]**$^{\bullet}$) is thermodynamically uphill while substitution reactions at the Cp ring and at the α/ β positions giving **[6$^{Cp,\alpha,\beta}$]**$^{\bullet}$ and **[7$^{Cp,\alpha,\beta}$]**$^{\bullet}$ are thermodynamically feasible (Figure 6). The driving forces are similar for the **[6$^{Cp,\alpha,\beta}$]**$^{\bullet}$ and **[7$^{Cp,\alpha,\beta}$]**$^{\bullet}$ nitroxides derived from the radicals **[1^{x}]**$^{\bullet}$ / **[2^{x}]**$^{\bullet}$ (Scheme 7). According to DFT calculations, the conceivable nitroxide radicals **[6b]**$^{\bullet}$ / **[7b]**$^{\bullet}$ derived from the phenoxyl radicals **[1b]**$^{\bullet}$ / **[2b]**$^{\bullet}$ are thermodynamically unfavorable with respect to the starting radical and PhNO (Supporting Information, Figures S19, S20) in agreement with the experimental observation that the phenoxyl radicals **4**$^{\bullet}$ and **5**$^{\bullet}$ are inert towards nitroxide radical formation with PhNO (*vide supra*).

Scheme 7. Suggested radical reactivity of [H-1]$^{\bullet+}$, [H-2]$^{\bullet+}$ and [H-3]$^{\bullet+}$ in the presence of a base and PhNO; EPR data (298 K, 77 K) of identified radical intermediates given..

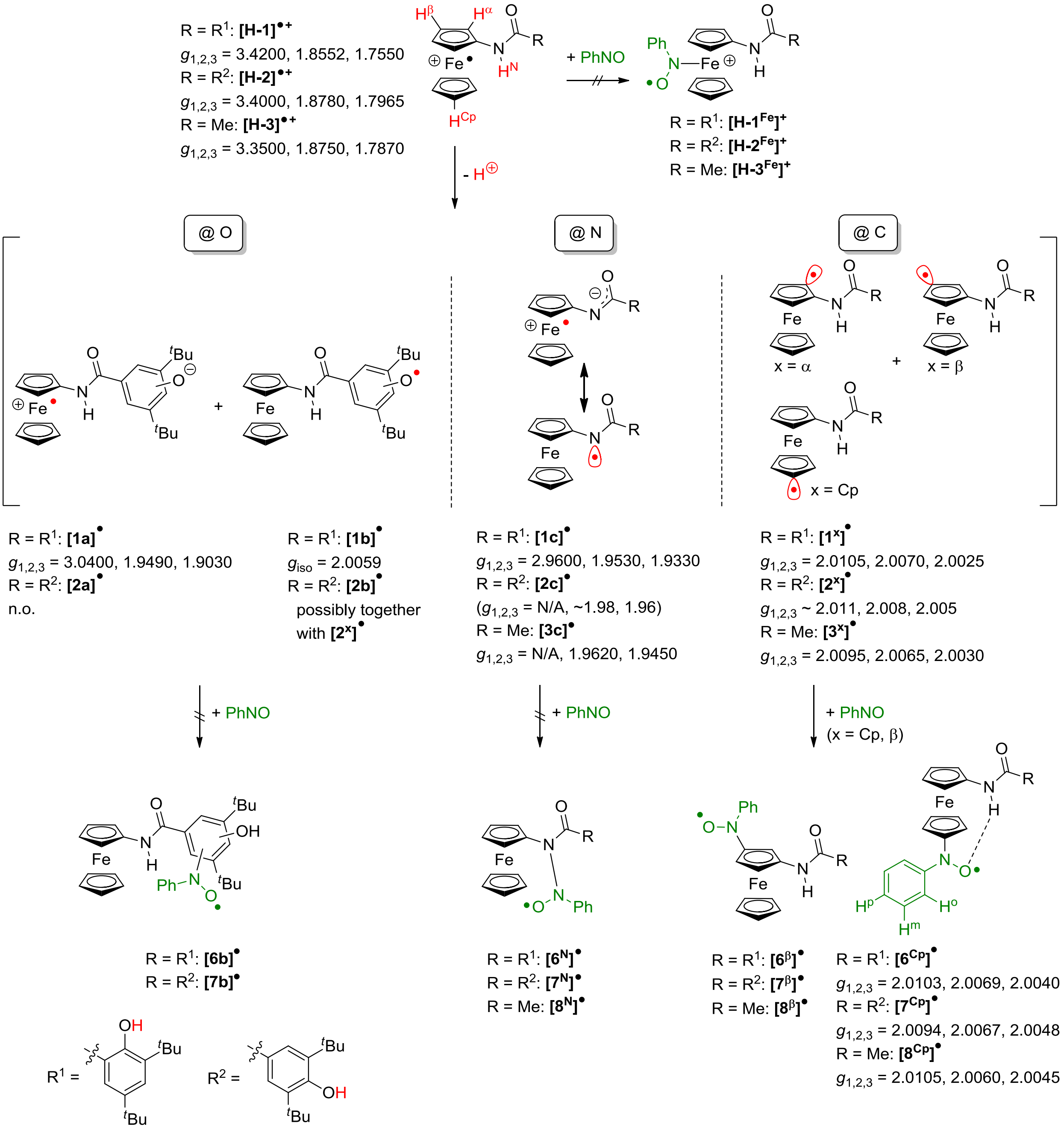

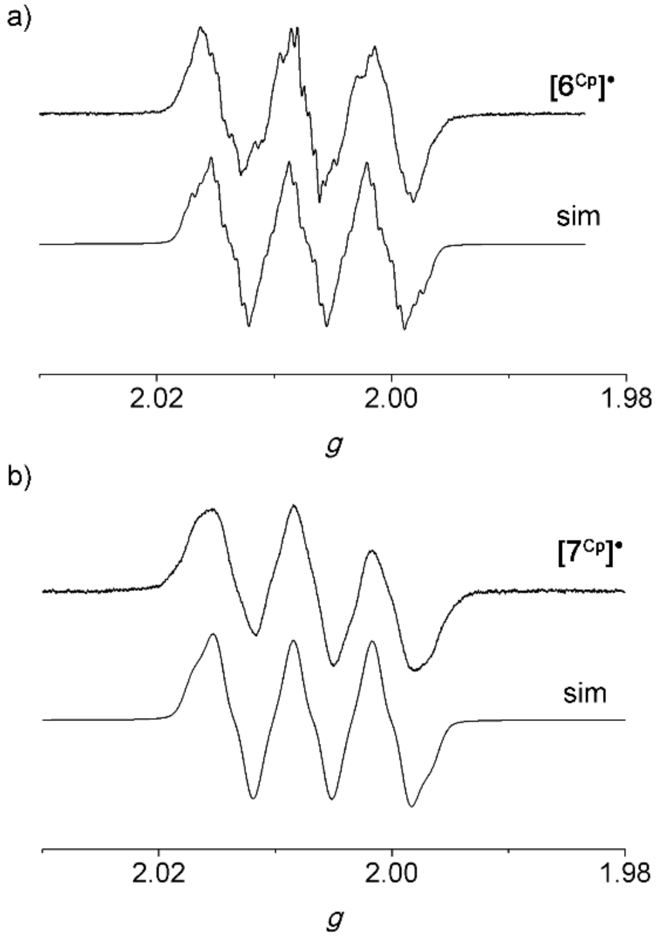

Figure 5. X-band EPR spectra (top) and simulated spectra (bottom) of a) $[6^{Cp}]^{\bullet}$ (25 mM) in CH_2Cl_2 and b) $[7^{Cp}]^{\bullet}$ (3 mM) in CH_2Cl_2 both at the following parameters: temperature = 298 K, field = 3346.20 G, sweep = 94.79 G, sweep time = 90 s, Modulation = 250 mG, MW attenuation = 5 dB ($[6^{Cp}]^{\bullet}$) and modulation = 5000 mG, MW attenuation = 10 dB ($[7^{Cp}]^{\bullet}$).

The radicals $[\mathbf{1}^{x}]^{\bullet}$ / $[\mathbf{2}^{x}]^{\bullet}$ (x = α, β, Cp) were calculated by DFT methods (Supporting Information, Figures S21, S22). Expectedly, all these radicals are high-energy species, independent of the presence or absence of NH•••O or OH•••O IHBs. The spin densities in radicals $[\mathbf{1}^{\alpha}]^{\bullet}$ and $[\mathbf{2}^{\alpha}]^{\bullet}$ are essentially localized at the iron center (Mulliken spin density at iron: 1.25/1.25) suggesting a dominant contribution of a ferrocenium carbanion resonance structure, similar to the $[\mathbf{3}^{\alpha}]^{\bullet}$ case.[26] Hence, no reaction of $[\mathbf{1}^{\alpha}]^{\bullet}$ / $[\mathbf{2}^{\alpha}]^{\bullet}$ with PhNO is expected. In contrast, $[\mathbf{1}^{Cp}]^{\bullet}$ / $[\mathbf{2}^{Cp}]^{\bullet}$ and $[\mathbf{1}^{\beta}]^{\bullet}$ / $[\mathbf{2}^{\beta}]^{\bullet}$ feature large spin densities at the respective carbon atoms with Mulliken spin densities above 0.65 and, hence, should be susceptible to attack by PhNO. This is essentially independent on the type of IHB (NH•••O, OH•••O) in radicals $[\mathbf{1}^{x}]^{\bullet}$ (Supporting Information, Figures S21, S22).

The presence of $[\mathbf{1}^{x}]^{\bullet}$ and $[\mathbf{2}^{x}]^{\bullet}$ radicals has been probed by rapid-freeze EPR techniques. Indeed, adding $P_1{}^{t}$Bu to a pre-cooled solution containing $[\mathbf{H\text{-}1}]^{\bullet+}$ and PhNO (ca. 193 K) and rapid freezing to 77 K allowed to detect a broad, anisotropic large ferrocenium resonance around g = 1.96 (98.7 %) next to a sharp resonance signal around g = 2.00 without discernable hfc's (1.3 %) (Table 2; Figure 7a). The former closely resembles the resonance of the ferrocenium iminolate **[3c]**$^{\bullet}$ while the latter is similar to that of the carbon-centered radicals **[3$^{\mathrm{Cp},\beta}$]**$^{\bullet}$ (Table 2, Schemes 3 and 7).[26] Hence, we assign the former to the ferrocenium iminolate zwitterion **[1c]**$^{\bullet}$ and the latter to traces of the radicals **[1$^{\mathrm{Cp},\beta}$]**$^{\bullet}$. Clearly, **[H-1]**$^{\bullet+}$ is deprotonated mainly at the amide nitrogen atom to give the ferrocenium iminolate **[1c]**$^{\bullet}$ and to some extent at the Cp rings to give **[1$^{\mathrm{Cp},\beta}$]**$^{\bullet}$, as the phenol OH is engaged in the OHO IHB (Scheme 1). On this time scale, the kinetic product **[1c]**$^{\bullet}$ has not yet quantitatively isomerized to radicals **[1a]**$^{\bullet}$ and **[1b]**$^{\bullet}$.

No sign for nitroxide radicals are discernible in this sample. Obviously, the following trapping reaction of **[1$^{\mathrm{Cp},\beta}$]**$^{\bullet}$ with PhNO is slow enough to allow detecting the radicals **[1$^{\mathrm{Cp},\beta}$]**$^{\bullet}$. After annealing the sample to room temperature for five minutes and refreezing to 77 K, the **[1c]**$^{\bullet}$ and **[1$^{\mathrm{Cp},\beta}$]**$^{\bullet}$ resonances vanished in favor of the nitroxide EPR resonance of **[6$^{\mathrm{Cp},\beta}$]**$^{\bullet}$ with large nitrogen hfc in the g_3 resonance, similar to nitroxide radicals **[8$^{\mathrm{Cp},\beta}$]**$^{\bullet}$ [26] (Table 2; Figure 7b).

The rapid-freeze EPR spectrum (77 K) of a mixture of **[H-2]**$^{\bullet+}$, PhNO and $\mathrm{P_1}{}^t\mathrm{Bu}$, prepared as described for **[H-1]**$^{\bullet+}$, yielded only the resonance of the nitroxide radicals **[7$^{\mathrm{Cp},\beta}$]**$^{\bullet}$ without indication of ferrocenium phenolate **[2a]**$^{\bullet}$, phenoxyl radical **[2b]**$^{\bullet}$, ferrocenium iminolate **[2c]**$^{\bullet}$ or *C*-centered radicals **[2$^{\mathrm{Cp},\beta}$]**$^{\bullet}$ (Figure 7c). Hence, under these conditions the follow-up reactions are too fast and only some **[2$^{\mathrm{Cp},\beta}$]**$^{\bullet}$ radicals have been intercepted by PhNO to yield **[7$^{\mathrm{Cp},\beta}$]**$^{\bullet}$ (Scheme 7). Again, a conceivable follow-up reaction of **[2c]**$^{\bullet}$ and its conceivable hydrogen bonded dimer **[(2c)$_2$]**$^{\bullet\bullet}$ (Scheme 8), might be *inter*molecular proton transfer from a phenol to an iminolate to give ferrocenium cation **[H-2]**$^{\bullet+}$ and the doubly deprotonated ferrocenium phenolate iminolate **[2a-H]**$^{\bullet-}$ or phenoxyl iminolate species **[2b-H]**$^{\bullet-}$ (similar to the reactivity of **[2$_2$]**$^{\bullet-}$, Scheme 6). As the ferrocenium ion **[FcH]**$^{\bullet+}$ oxidizes phenolate **5**$^{-}$ to the phenoxyl radical **5**$^{\bullet}$ (Scheme 8b) a similar reaction might occur between **[H-2]**$^{\bullet+}$ and the proposed doubly deprotonated ferrocenium phenolate iminolate **[2a-H]**$^{\bullet-}$ giving diradical **[2-H]**$^{\bullet\bullet}$ (Scheme 8a). Such a diradical might be prone to decomposition yielding only EPR-silent products.

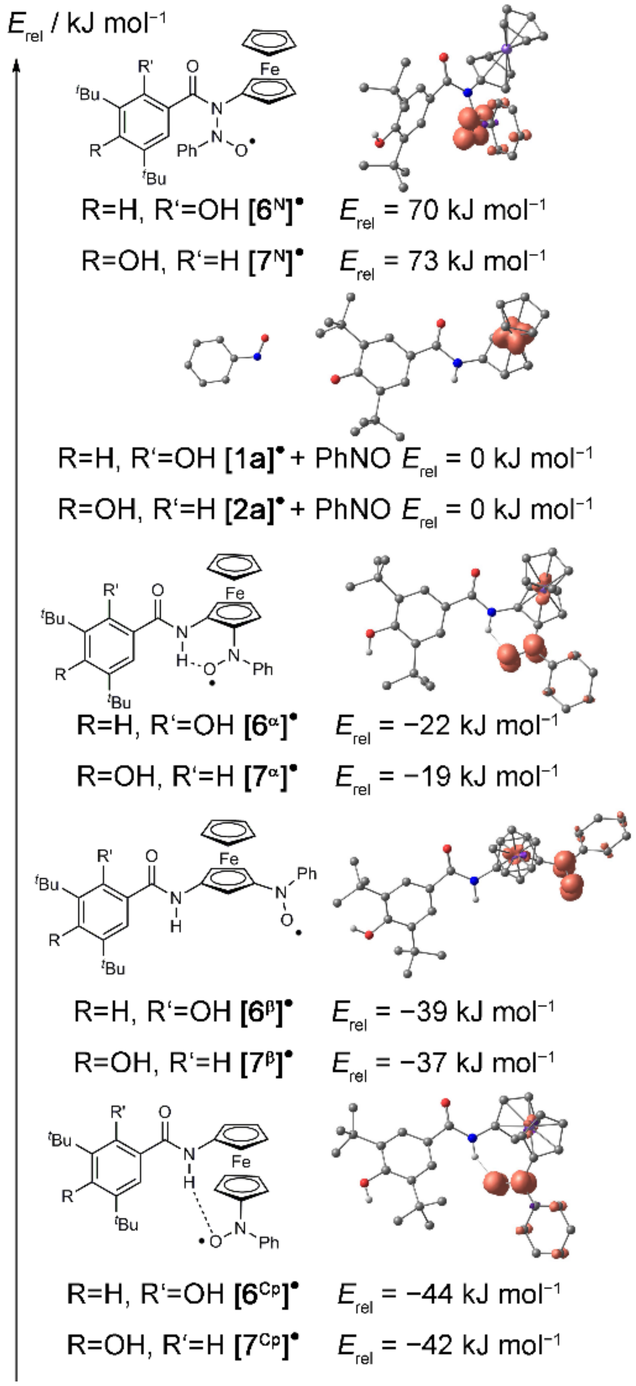

Figure 6. DFT optimized geometries with spin densities for $[7^x]^\bullet$ (x = α, β, Cp, N) (0.01 a.u. isosurface value) and energies in CH_2Cl_2 continuum solvent for $[6^x]^\bullet$ and $[7^x]^\bullet$ (x = N, α, β, Cp) as well as their Lewis structures.

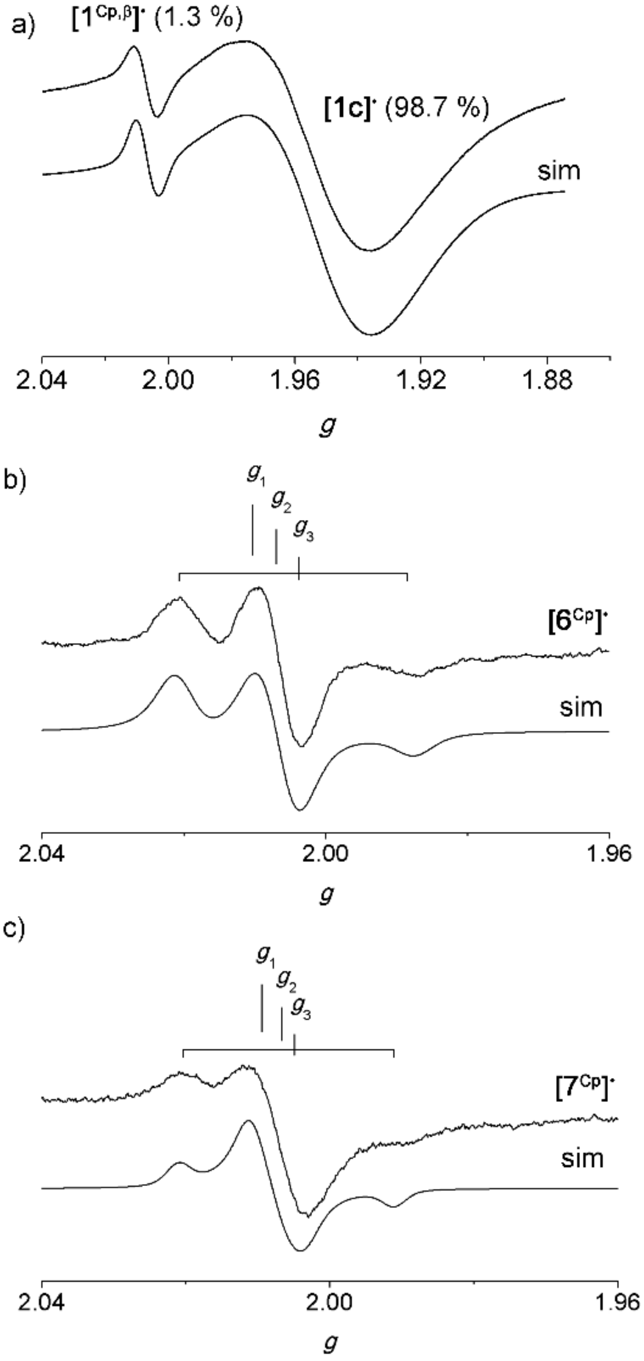

Figure 7. X-band EPR spectra (top) and simulated spectra (bottom) of (a) rapid freeze mixture of $[1^{Cp,\beta}]^\bullet$ / $[1c]^\bullet$ (25 mM H-1) in CH_2Cl_2, (b) $[6^{Cp}]^\bullet$ (25 mM H-1) in CH_2Cl_2 after room temperature annealing, and (c) $[7^{Cp}]^\bullet$ (3.0 mM H-2) in $CH_2Cl_2/[^{n}Bu_4N][B(C_6F_5)_4]$. All spectra were recorded at the following parameters: temperature = 77 K, field = 3346.20 G, sweep = 499.77 G, sweep time = 90 s, modulation = 5000 mG, MW attenuation = 20 dB ($[1^{Cp,\beta}]^\bullet$ / $[1c]^\bullet$ and $[6^{Cp}]^\bullet$) and 10 dB ($[7^{Cp}]^\bullet$).

Scheme 8. a) Possible deprotonation of ferrocenium ion $[H\text{-}2]^{\bullet+}$ giving the dimeric aggregate $[(2c)_2]^{\bullet\bullet}$, followed by proton transfer and dissociation into $[H\text{-}2]^{\bullet+}$ and $[2a\text{-}H]^{\bullet-}$ / $[2b\text{-}H]^{\bullet-}$ with subsequent electron transfer to give H-2 and diradical $[2\text{-}H]^{\bullet\bullet}$; b) oxidation of phenolate 5^- with ferrocenium $[FcH]^{\bullet+}$.

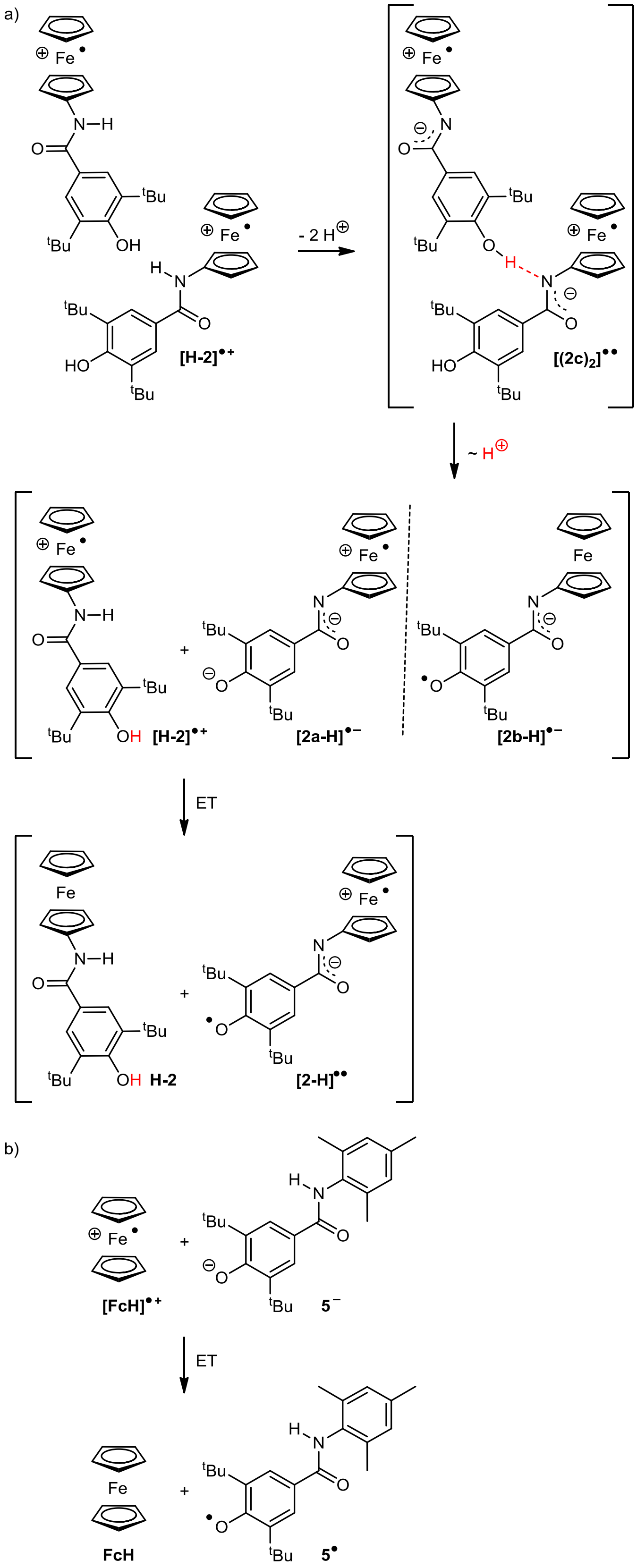

3.3.3 CONCLUSIONS

Amide-bridged ferrocenyl phenols **H-1** and **H-2** can be oxidized to the respective ferrocenium phenol radical cations **[H-1]**$^{\bullet+}$ and **[H-2]**$^{\bullet+}$, respectively. These are deprotonated at the phenol oxygen atom, the amide nitrogen atom or cyclopentadienyl carbon atoms giving the corresponding neutral radicals **[1a]**$^\bullet$ / **[2a]**$^\bullet$, **[1b]**$^\bullet$ / **[2b]**$^\bullet$ (@ O), **[1c]**$^\bullet$ / **[2c]**$^\bullet$ (@ N) and **[1^x]**$^\bullet$ / **[2^x]**$^\bullet$ (@ C) (Scheme 7). The ferrocenium iminolate **[1c]**$^\bullet$ and the carbon-centered radicals **[1$^{Cp,\beta}$]**$^\bullet$ are the kinetic products of the **[H-1]**$^{\bullet+}$ deprotonation. The latter species are intercepted by PhNO as nitroxide radicals **[6$^{Cp,\beta}$]**$^\bullet$. The NH•••O IHB in **[1a]**$^\bullet$ strongly stabilizes the ferrocenium phenolate zwitterion, yet traces of the valence isomeric phenoxyl radical **[1b]**$^\bullet$ are also observed at 298 K. The IVCT between **[1a]**$^\bullet$ and **[1b]**$^\bullet$ is coupled to the NH•••O vibration. For **[H-2]**$^{\bullet+}$ lacking IHBs, all radicals derived by deprotonation are transient. Only some of them can been observed by rapid-freeze EPR techniques (**[2b]**$^\bullet$, **[2c]**$^\bullet$) or indirectly by spin-trapping techniques (**[2$^{Cp,\beta}$]**$^\bullet$ as **[7$^{Cp,\beta}$]**$^\bullet$). Suggested follow-up reactions of these transient radicals **2**$^\bullet$ are intermolecular proton (and electron) transfer reactions in hydrogen-bonded assemblies leading finally to EPR-silent products. This is in contrast to the reversible intramolecular PCET reaction (IVCT) between **[1a]**$^\bullet$ and **[1b]**$^\bullet$. The absence of the stabilizing IHB and the resulting high reactivity precludes the observation of IVCT between the transient valence isomers **[2a]**$^\bullet$ and **[2b]**$^\bullet$. In any case, ferrocenyl phenols generate a pool of radicals under oxidative and basic conditions. This observation might be relevant for biologically active ferrocenyl phenols such as ferrocifen **H-C** as well.

3.3.4 EXPERIMENTAL SECTION

General Considerations: All reactions were performed under argon atmosphere unless otherwise noted. Dichloromethane was dried over CaH_2 and distilled prior to use. Absolute DMF was used as received from Acros. 1-[Bis(dimethylamino)methylene]-1H-1,2,3-triazolo[4,5-b]pyridinium 3-oxide hexafluorophosphate (HATU) was commercially available from Novabiochem. P$_1{}^t$Bu, sodium hydroxide, 2,6-di-*tert*-butyl-4-carboxy-phenol, *N*,*N*-diisopropylethylamine (DIPEA), 2,2-diphenyl-1-picrylhydrazyl (DPPH), nitrosobenzene (PhNO), ferrocenium hexafluorophosphate, decamethylcobaltocene, and 2,4,6-trimethylaniline were commercially available from Sigma-Aldrich. DIPEA was dried over NaOH overnight under argon and subjected to the coupling reactions by syringe. Aminoferrocene,[27,34] 2,4-di-tert-butyl-6-(2-ferrocenylcarbamoyl)phenol (**H-1**),[16] 2,4-di-tert-butyl-6-(2-methylcarbamoyl)phenol (**H-4**),[25] *N*-acetylaminoferrocene (**H-3**),[27] and [^{n}Bu$_4$N][B(C$_6$F$_5$)$_4$][44] were prepared according to literature procedures. Filtrations from precipitated silver after oxidation were performed with syringe filters (Rotilabo-Spritzenfilter, Ø = 15 mm, pore size = 0.20 µm; Carl Roth GmbH + Co. KG, Germany). NMR spectra were recorded on a Bruker Avance DRX 400 spectrometer at 400.13 MHz (^{1}H) and 100.03 MHz (^{13}C{^{1}H}) at 25 °C. All resonances are reported in ppm versus the solvent signal as internal standard. CD_2Cl_2 (^{1}H: $\delta = 5.32$ ppm; ^{13}C: $\delta = 54.0$ ppm), $CDCl_3$ (^{1}H: $\delta = 7.26$ ppm; ^{13}C: $\delta = 77.2$ ppm), THF-d$_8$ (^{1}H: $\delta = 3.58$ ppm; ^{13}C: $\delta = 67.6$ ppm). (s) = singlet. IR spectra were recorded with a Varian Excalibur Series 3100 FT-IR spectrometer using KBr cells in CH_2Cl_2, and as KBr disks. (s) = strong, (m) = medium, (w) = weak. Electrochemical experiments were carried out on a BioLogic SP-50 voltammetric analyzer using a platinum working electrode, a platinum wire as counter electrode, and a 0.01 M $Ag/AgNO_3$ electrode as reference electrode. The measurements were carried out at a scan rate of 100 mV s^{-1} for cyclic voltammetry experiments and for square wave voltammetry experiments unless noted otherwise using 0.1 M $[^nBu_4N][B(C_6F_5)_4]$ as supporting electrolyte and 0.001 M of the sample in CH_2Cl_2. Potentials are given relative to the ferrocene/ferrocenium couple. Referencing was achieved by addition of decamethylcobaltocene ($E_{1/2} = -2.04$ V vs. FcH/FcH^+ (CH_2Cl_2; $[^nBu_4N][B(C_6F_5)_4]$)) to the sample.[36] UV/Vis/NIR spectra were recorded on a Varian Cary 5000 spectrometer using 1.0 cm cells unless otherwise mentioned (Hellma, suprasil). FD mass spectra were recorded on a Thermo Fisher DFS mass spectrometer. CW EPR spectra (X-band; ca. 9.4 GHz) were measured on a Miniscope MS 300 at 298 K and at 77 K cooled by liquid nitrogen in a finger dewar (Magnettech GmbH, Berlin, Germany). Settings are given at the respective displayed spectra. g-values are referenced to external Mn^{2+} in ZnS (g = 2.118, 2.066, 2.027, 1.986, 1.946, 1.906). Simulations of EPR spectra were performed with EasySpin (v 5.0.0)[58] for MatLab (R2015a). Melting points were determined using a Gallenkamp capillary melting point apparatus MFB 595 010M and were not corrected. Elemental analyses were performed by the microanalytical laboratory of the chemical institutes of the University of Mainz.

Crystal Structure Determination: Intensity data were collected using a Bruker AXS Smart1000 CCD diffractometer equipped with an APEX II detector and an Oxford cooling system using Mo K_α radiation (λ = 0.71073 Å) at 173(2) K and corrected for absorption and other effects. The diffraction frames were integrated using the SAINT package, and most were corrected for absorption with MULABS.[59,60] The structures were solved by direct methods and refined by the full-matrix method based on F^2 using the SHELXTL software package.[61,62] All non-hydrogen atoms were refined anisotropically, while the positions of all hydrogen atoms were generated with appropriate geometric constraints and allowed to ride on their respective parent atoms with fixed isotropic thermal parameters. Crystallographic data (excluding structure factors) for the structures reported in this paper have been deposited with the Cambridge Crystallographic Data Centre as CCDC 1426154 (2,4-di-*tert*-butyl-2-(2-ferrocenylcarbamoyl)phenol). Copies of the data can be obtained free of charge upon application to CCDC, 12 Union Road, Cambridge CB2 1EZ, U.K. [fax (044) 1223-336-033; e-mail deposit@ccdc.cam.ac.uk].

Density functional calculations were carried out with the ORCA 3.0.2 / DFT series[63] of programs. For geometry optimizations and energy calculations, the B3LYP formulation of density functional theory was used employing the SV(P)[64,65] basis set, the RIJCOSX approximation, approximate Second Order SCF (SOSCF),[66,67] the zeroth order regular approximation (ZORA),[68–70] the KDIIS algorithm, at GRIDX4. No symmetry constraints were imposed on the molecules. Solvent modelling was done employing the conductor like screening model (COSMO, CH_2Cl_2).[71] The approximate free energies at 298 K were obtained through thermochemical analysis of the frequency calculation, using the thermal correction to Gibbs free energy as reported by ORCA 3.0.2. TD-DFT calculations were performed with the same basis set and functional as the geometry optimizations, calculating 50 states with MaxDim = 250. The 4-methyl group of **H-5** and all its ET and PT products was omitted in DFT calculations for convergence reasons.

Synthesis of 2,6-di-*tert*-butyl-4-(2-ferrocenylcarbamoyl)phenol (H-2): Aminoferrocene (250 mg; 1.24 mmol; 1.0 eq.) and 2,6-di-*tert*-butyl-4-carboxy-phenol (311 mg; 1.24 mmol; 1.0 eq.) were dissolved in absolute CH_2Cl_2 (10 ml). DIPEA (241 mg; 320 µl; 1.87 mmol; 1.5 eq.) was added to the mixture followed by HATU (472 mg; 1.243 mmol; 1.0 eq.). The solution was stirred at room temperature for two hours. Water (10 ml) was added and the product was extracted with CH_2Cl_2 (3 × 30 ml). The organic phase was washed with water (10 ml) and brine (10 ml) and dried over $MgSO_4$. After filtration the solvent was removed under reduced pressure. The raw product was purified by column chromatography (SiO_2, petroleum ether (boiling point 40 – 60 °C) and CH_2Cl_2 (1:0 → 1:4) resulting in a yellow colored solid. Yield: 79% (423 mg, 0.98 mmol). ^1H NMR (CD_2Cl_2): δ (ppm) = 7.60 (s, 2H, H^7), 7.09 (s, 1H, NH), 5.63 (s, 1H, OH), 4.71 (s, 2H, $H^{2/5}$), 4.18 (s, 5H, Cp), 4.05 (s, 2H, $H^{3/4}$), 1.48 (s, 18H, H^{10a}). ^1H NMR (THF-d_8): δ (ppm) = 8.50 (s, 1H, OH), 7.73 (s, 2H, H^7), 6.59 (s, 1H, NH), 4.74 (pt, 2H, $H^{2/5}$), 4.09 (s, 5H, Cp), 3.92 (pt, 2H, $H^{3/4}$), 1.47 (s, 18H, H^{10a}). ^{13}C NMR (CD_2Cl_2): δ (ppm) = 157.4 (C^9), 136.7 (C^8), 124.6 (C^7), 69.8 (Cp), 65.1 ($C^{3/4}$), 62.1 ($C^{2/5}$), 34.9 (C^{10}), 30.5 (C^{10a}). ^{13}C NMR (THF-d_8): δ (ppm) = 166.3 (C=O), 157.8 (C^9), 137.6 (C^8), 127.8 (C^6), 125.4 (C^7), 98.4 (C^1), 68.8 (Cp), 64.7 ($C^{3/4}$), 61.7 ($C^{2/5}$), 35.5 (C^{10}), 30.7 (C^{10a}). FD-MS: *m/z* (%) = 433.2 (100), 434.2 (28.7) $[M]^+$, 866.2 (11.8) $[2M]^+$. UV/Vis/NIR (CH_2Cl_2): λ (ε) = 230 (13825), 257 (16785), 325 (1815), 440 nm (325 M^{-1} cm^{-1}). IR (KBr): $\tilde{\nu}$ = 3625 (m, OH), 3285 (m, NH), 1635 (m, CO) cm^{-1}. IR (CH_2Cl_2): $\tilde{\nu}$ = 3625 cm^{-1} (m, OH), 3440 (m, NH), 1665 (m, CO) cm^{-1}. R_f (CH_2Cl_2) = 0.17. M.p. >350 °C (decomp.). $E_{1/2}$ = −105 mV. Elemental analysis calcd (%) for $C_{25}H_{31}FeNO_2$ (433.17): C 69.29, H 7.21, N 3.23; found C 69.64, H 7.48, N 3.41.

Synthesis of 2,6-di-*tert*-butyl-4-(2-(2,4,6-trimethylphenyl)carbamoyl)phenol (H-5): 2,4,6-trimethylaniline (168 mg; 174 µl; 1.24 mmol; 1.0 eq.) and 2,6-di-*tert*-butyl-4-carboxy-phenol (311 mg; 1.24 mmol; 1.0 eq.) were dissolved in CH_2Cl_2 (15 ml). DIPEA (241 mg; 320 µl; 1.87 mmol; 1.5 eq.) was added to the mixture followed by HATU (472 mg; 1.243 mmol; 1.0 eq.). The solution was stirred at room temperature for two hours. Water (15 ml) was added and the solution was extracted with CH_2Cl_2 (2 × 30 ml). The organic phase was washed with saturated aqueous sodium bicarbonate solution (15 ml) and brine (15 ml) and dried over $MgSO_4$. After filtration, the solvent was removed under reduced pressure. The raw product was purified by column chromatography (SiO_2, CH_2Cl_2/MeOH (1:0 → 95:5) resulting in a colorless solid. Yield: 72% (328 mg, 0.89 mmol). ^1H NMR ($CDCl_3$): δ (ppm) = 7.75 (s, 2H, H^7), 7.18 (s, 1H, NH), 6.93 (s, 2H, H^3), 5.60 (s, 1H, OH), 2.29 (s, 3H, H^{5b}), 2.25 (s, 6H, H^{5a}), 1.49 (s, 18H, H^{10a}). ^{13}C NMR ($CDCl_3$): δ (ppm) = 166.6 (C=O), 157.2 (C^9), 137.0 (C^4), 136.2 (C^8), 135.4 (C^2), 131.7 (C^1), 129.1 (C^3), 126.0 (C^6), 124.6 (C^7), 34.6 (C^{10}), 30.3 (C^{10a}), 21.1 (C^{5b}), 18.7 (C^{5a}). FD-MS: *m/z* (%) = 367.2 (100) $[M]^+$. UV/Vis/NIR (CH_2Cl_2): λ (ε) = 275 (15800) M^{-1} cm^{-1}. IR (KBr): $\tilde{\nu}$ = 3625 (m, OH), 3190 (m, NH), 1635 (m, CO) cm^{-1}. IR (CH_2Cl_2): $\tilde{\nu}$ = 3625 cm^{-1} (m, OH), 3425 (m, NH), 1665 (m, CO) cm^{-1}. R_f (CH_2Cl_2/MeOH

98:2) = 0.47. M.p. 301−303 °C (decomp.). Elemental analysis calcd (%) for $C_{24}H_{33}NO_2$ (367.25): C 78.43, H 9.05, N 3.81; found C 78.16, H 9.31, N 3.73.

Electron transfer between ferrocenium hexafluorophosphate [FcH][PF_6] and phenolate $\mathbf{5}^-$: To a solution of $\mathbf{5}^-$ in CH_2Cl_2/[^{n}Bu$_4$N][B(C_6F_5)$_4$] was added a stoichiometric amount of a solution of [FcH][PF_6]. An immediate color change from blue to orange (FcH) was observed. EPR spectra of a sample of this solution at 298 K and 77 K show resonances for $\mathbf{5}^\bullet$ (Supporting Information, Figure S18).

3.3.5 ACKNOWLEDGMENT

We are grateful to Regine Jung-Pothmann for the X-ray data collection, Dipl.-Chem. Torben Kienz for helpful discussions, as well as Dipl.-Chem. Mathias Enders and Dipl.-Chem. Maximilian Lauck for preparative assistance. Parts of this research were conducted using the supercomputer Mogon and advisory services offered by Johannes Gutenberg-University Mainz (www.hpc.uni-mainz.de), which is a member of the AHRP and the Gauss Alliance e. V.

Keywords: epr spectroscopy, ferrocene, hydrogen bonds, proton coupled electron transfer, radicals, spin trapping, valence isomers

3.3.6 REFERENCES

[1] R. A. Marcus, N. Sutin, *Biochim. Biophys. Acta* **1985**, *811*, 265–322.
[2] G. L. Closs, J. R. Miller, *Science* **1988**, *240*, 440–447.
[3] J. R. Winkler, H. B. Gray, *Annu. Rev. Biochem.* **1996**, *65*, 537–561.
[4] P. F. Barbara, T. J. Meyer, M. A. Ratner, *J. Phys. Chem.* **1996**, *100*, 13148–13168.
[5] T. Kienz, C. Förster, K. Heinze, *Organometallics* **2014**, *33*, 4803–4812.
[6] M. A. Fox, *Chem. Rev.* **1992**, *92*, 365–368.
[7] C. Creutz, H. Taube, *J. Am. Chem. Soc.* **1969**, *91*, 3988–3989.
[8] T. F. Markle, J. M. Mayer, *Angew. Chem.* **2008**, *120*, 750–752; *Angew. Chem. Int. Ed.* **2008**, *47*, 738–740.
[9] J. J. Warren, T. A. Tronic, J. M. Mayer, *Chem. Rev.* **2010**, *110*, 6961–7001.
[10] a) J.-M. Savéant, *Energy Environ. Sci.* **2012**, *5*, 7718–7731; b) C. Costentin, M. Robert, J.-M. Savéant, *Phys. Chem. Chem. Phys.* **2010**, *12*, 11179–11190.
[11] a) S. Hammes-Schiffer, *Chem. Rev.* **2010**, *110*, 6937–6938; b) S. Hammes-Schiffer, A. Stuchebrukhov, *Chem. Rev.* **2010**, *110*, 6939–6960; c) S. Hammes-Schiffer, *J. Am. Chem. Soc.* **2015**, *137*, 8860−8871.
[12] I. J. Rhile, T. F. Markle, H. Nagao, A. G. DiPasquale, O. P. Lam, M. A. Lockwood, K. Rotter, J. M. Mayer, *J. Am. Chem. Soc.* **2006**, *128*, 6075–6088.
[13] a) O. S. Wenger, *Chem. Eur. J.* **2011**, *17*, 11692–11702; b) W. Herzog, C. Bronner, S. Löffler, B. He, D. Kratzert, D. Stalke, A. Hauser, O. S. Wenger, *ChemPhysChem* **2013**, *14*, 1168–1176.
[14] D. R. Weinberg, C. J. Gagliardi, J. F. Hull, C. F. Murphy, C. A. Kent, B. C. Westlake, A. Paul, D. H. Ess, D. G. McCafferty, T. J. Meyer, *Chem. Rev.* **2012**, *112*, 4016–4093.

[15] C. Costentin, M. Robert, J.-M. Savéant, *J. Am. Chem. Soc.* **2006**, *128*, 4552–4553.

[16] A. Neidlinger, V. Ksenofontov, K. Heinze, *Organometallics* **2013**, *32*, 5955–5965.

[17] M. H. V Huynh, T. J. Meyer, *Chem. Rev.* **2007**, *107*, 5004–5064.

[18] J. L. Dempsey, J. R. Winkler, H. B. Gray, *Chem. Rev.* **2010**, *110*, 7024–7039.

[19] F. Lachaud, A. Quaranta, Y. Pellegrin, P. Dorlet, M.-F. Charlot, S. Un, W. Leibl, A. Aukauloo, *Angew. Chem.* **2005**, *117*, 1560–1564; *Angew. Chem. Int. Ed.* **2005**, *44*, 1536–1540.

[20] J. Bonin, M. Robert, *Photochem. Photobiol.* **2011**, *87*, 1190–1203.

[21] L. Hammarström, S. Styring, *Energy Environ. Sci.* **2011**, *4*, 2379–2388.

[22] C. J. Gagliardi, A. K. Vannucci, J. J. Concepcion, Z. Chen, T. J. Meyer, *Energy Environ. Sci.* **2012**, *5*, 7704–7717.

[23] A. Migliore, N. F. Polizzi, M. J. Therien, D. N. Beratan, *Chem. Rev.* **2014**, *114*, 3381–3465.

[24] M. Sugiura, S. Ogami, M. Kusumi, S. Un, F. Rappaport, A. Boussac, *J. Biol. Chem.* **2012**, *287*, 13336–13347.

[25] R. Wanke, L. Benisvy, M. L. Kuznetsov, M. F. C. Guedes Da Silva, A. J. L. Pombeiro, *Chem. Eur. J.* **2011**, *17*, 11882–11892.

[26] A. Neidlinger, T. Kienz, K. Heinze, *Organometallics*, *34*, 5310−5320.

[27] K. Heinze, M. Schlenker, *Eur. J. Inorg. Chem.* **2004**, 2974–2988.

[28] a) K. Heinze, D. Siebler, *Z. Anorg. Allg. Chem.* **2007**, *633*, 2223–2233; b) D. Siebler, M. Linseis, T. Gasi, L. M. Carrella, R. F. Winter, C. Förster, K. Heinze, *Chem. Eur. J.* **2011**, *17*, 4540–4551.

[29] D. Siebler, C. Förster, K. Heinze, *Dalton Trans.* **2011**, *40*, 3558–3575.

[30] H. Huesmann, C. Förster, D. Siebler, T. Gasi, K. Heinze, *Organometallics* **2012**, *31*, 413–427.

[31] M. B. Robin, P. Day, *Adv. Inorg. Chem. Radiochem.* **1968**, *10*, 247-422.

[32] a) S. Fukuzumi, K. Okamoto, Y. Yoshida, H. Imahori, Y. Araki, O. Ito, *J. Am. Chem. Soc.* **2003**, *125*, 1007–1013; b) S. Fukuzumi, Y. Yoshida, K. Okamoto, H. Imahori, Y. Araki, O. Ito, *J. Am. Chem. Soc.* **2002**, *124*, 6794–6795.

[33] a) G. Jaouen, S. Top, A. Vessieres, G. Leclercq, M. McGlinchey, *Curr. Med. Chem.* **2004**, *11*, 2505–2517; b) E. Hillard, A. Vessières, L. Thouin, G. Jaouen, C. Amatore, *Angew. Chem.* **2006**, *118*, 291−296; *Angew. Chem. Int. Ed.* **2006**, *45*, 285–290; c) A. Nguyen, S. Top, P. Pigeon, A. Vessières, E. A. Hillard, M. A. Plamont, M. Huché, C. Rigamonti, G. Jaouen, *Chem. Eur. J.* **2009**, *15*, 684–696; d) D. Hamels, P. M. Dansette, E. A. Hillard, S. Top, A. Vessières, P. Herson, G. Jaouen, D. Mansuy, *Angew. Chem.* **2009**, *121*, 9288–9290; *Angew. Chem. Int. Ed.* **2009**, *48*, 9124–9126; e) D. Plażuk, A. Vessières, E. A. Hillard, O. Buriez, E. Labbé, P. Pigeon, M.-A. Plamont, C. Amatore, J. Zakrzewski, G. Jaouen, *J. Med. Chem.* **2009**, *52*, 4964–4967.

[34] B. Bildstein, M. Malaun, H. Kopacka, K. Wurst, K.-H. Ongania, G. Opromolla, P. Zanello, *Organometallics* **1999**, *18*, 4325–4336.

[35] D. Kanamori, A. Furukawa, T. Okamura, H. Yamamoto, N. Ueyama, *Org. Biomol. Chem.* **2005**, *3*, 1453–1459.

[36] N. G. Connelly, W. E. Geiger, *Chem. Rev.* **1996**, *96*, 877–910.

[37] Y. Kondo, in *Supberbases for Organic Synthesis* (Ed.: T. Ishikawa), John Wiley & Sons, Ltd, Chichester, UK, **2009**, pp. 145–185.

[38] R. Prins, *Mol. Phys.* **1970**, *19*, 603–620.

[39] G. R. Eaton, S. S. Eaton, D. P. Barr, T. Weber, Ralph, *Quantitative EPR*, Springer Wien, New York, **2010**.

[40] B. S. Brunschwig, C. Creutz, N. Sutin, *Chem. Soc. Rev.* **2002**, *31*, 168–184.

[41] a) D. Siebler, C. Förster, K. Heinze, *Eur. J. Inorg. Chem.* **2010**, 3986–3992; b) T. Tagg, H. G. Kjaergaard, J. R. Lane, C. J. McAdam, B. H. Robinson, J. Simpson, *Organometallics* **2015**, *34*, 2662−2666.

[42] J. Disinger, S. E. Manahan, *Anal. Lett.* **1982**, *15*, 1017−1029.

[43] P. M. Tolstoy, B. Koeppe, G. S. Denisov, H.-H. Limbach, *Angew. Chem.* **2009**, *121*, 5855−5858; *Angew. Chem. Int. Ed.* **2009**, *48*, 5745−5747.

[44] R. J. LeSuer, C. Buttolph, W. E. Geiger, *J. Organomet. Chem.* **2004**, *76*, 6395–6041.

[45] N. Camire, U. T. Mueller-Westerhoff, W. E. Geiger, *J. Organomet. Chem.* **2001**, *639*, 823–826.

[46] W. L. Mock, D. C. Y. Chua, *J. Chem. Soc. Perkin Trans. 2* **1995**, 2069–2074.

[47] S. Panagiota, M. Louloudi, Y. Deligiannakis, *Chem. Phys. Lett.* **2009**, *472*, 85–89.

[48] P. Neta, R. W. Fessenden, *J. Phys. Chem.* **1974**, *78*, 523–529.

[49] L. W. Kiruri, L. Khachatryan, B. Dellinger, S. Lomnicki, *Environ. Sci. Technol.* **2014**, *48*, 2212–2217.

[50] J. W. Whittaker, *Chem. Rev.* **2003**, *103*, 2347–2363.

[51] F. Thomas, O. Jarjayes, H. Jamet, S. Hamman, E. Saint-Aman, C. Duboc, J.-L. Pierre, *Angew. Chem.* **2004**, *116*, 604–607; *Angew. Chem. Int. Ed.* **2004**, *43*, 594–597

[52] T. Maki, Y. Araki, Y. Ishida, *J. Am. Chem. Soc.* **2001**, *123*, 3371–3372.

[53] S. Vanicek, H. Kopacka, K. Wurst, S. Vergeiner, L. Oehninger, I. Ott, B. Bildstein, *Z. Anorg. Allg. Chem.* **2015**, *641*, 1282–1292.

[54] M. Breza, *J. Mol. Struct.* **2004**, *683*, 167–169.

[55] P. Pelikán, L. Omelka, K. Brudíková, M. Breza, *J. Mol. Struct. Theochem.* **2003**, *624*, 251–255.

[56] L. Omelka, J. Kováčová, *Magn. Reson. Chem.* **1994**, *32*, 525–531.

[57] S. Terabe, R. Konaka, *J. Chem. Soc. Perkin Trans. 2* **1972**, 2163–2172.

[58] S. Stoll, A. Schweiger, *J. Magn. Reson.* **2006**, *178*, 42–55.

[59] *SMART Data Collection and SAINT-Plus Data Processing Software for the SMART System*, (various Versions); Bruker Analytical X-Ray Instruments, Inc., Madison, WI, **2000**.

[60] R. H. Blessing, *Acta Crystallogr.* **1995**, *A51*, 33–38.

[61] G. M. Sheldrick, *SHELXTL*, Version 5.1; Bruker AXS, Madison, WI, **1998**.

[62] G. M. Sheldrick, *SHELXL-97*, University Göttingen, Göttingen, Germany, **1997**.

[63] F. Neese, *Wiley Interdiscip. Rev. Comput. Mol. Sci.* **2012**, *2*, 73–78.

[64] A. Schäfer, H. Horn, R. Ahlrichs, *J. Chem. Phys.* **1992**, *97*, 2571–2577.

[65] F. Weigend, R. Ahlrichs, *Phys. Chem. Chem. Phys.* **2005**, *7*, 3297–3305.

[66] F. Neese, *Chem. Phys. Lett.* **2000**, *325*, 93–98.
[67] T. H. Fischer, J. Almlof, *J. Phys. Chem.* **1992**, *96*, 9768–9774.
[68] E. van Lenthe, E. J. Baerends, J. G. Snijders, *J. Chem. Phys.* **1993**, *99*, 4597–4610.
[69] C. van Wüllen, *J. Chem. Phys.* **1998**, *109*, 392.
[70] D. A. Pantazis, X. Y. Chen, C. R. Landis, F. Neese, *J. Chem. Theory Comput.* **2008**, *4*, 908–919.
[71] S. Sinnecker, A. Rajendran, A. Klamt, M. Diedenhofen, F. Neese, *J. Phys. Chem. A* **2006**, *110*, 2235–2245.

3.4 Conformational Switching of Multi-Responsive Ferrocenyl-Phenol Conjugates

Andreas Neidlinger, Christoph Förster, and Katja Heinze*

To be Submitted.

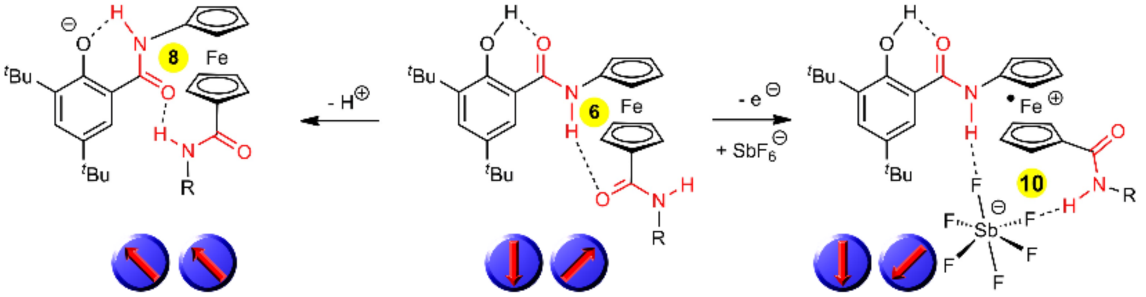

Abstract

Multifunctional conformational switches based on the ferrocenyl salicylic acid amide motif with increasing additional complexity (R = COOMe, **H-2**; R = CONHEt, **H-3**; R = CONHFc, **H-4**) have been prepared and their preferred secondary structures in solution have been determined by NMR and IR spectroscopy in combination with conformational searches based on Density Functional Theory calculations. Their conformational response to deprotonation (**[2]**$^-$ – **[4]**$^-$) as well as to oxidation (**[H-2]**$^{+\bullet}$ – **[H-4]**$^{+\bullet}$) has been revealed by IR, EPR and UV/Vis spectroscopy as well as by Density Functional Theory calculations. Deprotonation inverts all amide units (double amide twist) while oxidation flips only the terminal amide unit (single amide twist). Additionally, the combined action of deprotonation and oxidation is explored.

Supporting information for this article (without Cartesian coordinates from DFT calculations) is found at pp. 224.

3.4.1 INTRODUCTION

Conformational changes triggered by chemical stimuli, such as acids or bases (acid/base switches) are a viable tool for tuning molecular properties and geometrical architectures to achieve molecular-sized devices. Thorough studies have been devoted to structural rearrangements and molecular recognition events in the fields of rotaxanes,[1–6] calixarenes,[7] porphyrins,[8] phenol/phenolate conjugate acid/base pairs,[9,10] spiroxazines,[11] and many other structures.[12] We have been investigating the secondary structure as well as proton and electron transfer initiated rearrangements of a ferrocenyl phenol conjugate **H-A^{OHO}** featuring a ferrocenyl moiety and a salicylic acid amide residue (Scheme 1a).[13] In the parent phenol **H-A^{OHO}** the phenolic hydrogen atom forms an intramolecular hydrogen bond (IHB) with the oxygen atom of the carbonyl group (OH•••O conformation; Scheme 1a). Oxidation of **H-A^{OHO}** to the ferrocenium ion **[H-A^{OHO}]$^{+\bullet}$** leaves the OH•••O IHB intact. On the other hand, deprotonation of **H-A^{OHO}** to **[A]$^-$** switches the OH•••O bridge to the NH•••O IHB in the phenolate **[A^{NHO}]$^-$** by inversion of the amide unit providing an acid/base conformational switch (Scheme 1a).[13]

Organic secondary amides featuring a salicylic acid amide motif, e.g. **H-B^{OHO}**, form an analogous IHB between the carbonyl oxygen atom of the amide group and the phenol proton (OH•••O conformation) and undergo an analogous rearrangement to the NH•••O IHB in the phenolate **[B^{NHO}]$^-$** (Scheme 1b).[14] While oxidation of the phenolate **[B^{NHO}]$^-$** results in the expected formation of the respective phenoxyl radical **[B^{NHO}]$^\bullet$** (Scheme 1b),[14] the ferrocenyl phenolate **[A^{NHO}]$^-$** displays an even more diverse redox reactivity (Scheme 1a).[13]

In addition to the phenoxyl radical valence isomer **[Ab^{NHO}]$^\bullet$**, the ferrocenium phenolate zwitterion **[Aa^{NHO}]$^\bullet$** and the ferrocenium iminolate zwitterions **[Ac^{NHO}]$^\bullet$** and **[Ac^{OHO}]$^\bullet$** have been identified by IR and EPR spectroscopy as well as by Density Functional Theory (DFT) calculations.[13] Interestingly, the accidentally degenerate zwitterions **[Aa^{NHO}]$^\bullet$** and **[Ac^{NHO}]$^\bullet$** differ mainly by the position of the proton in the NH•••O IHB. On the other hand, the phenoxyl radical **[Ab^{NHO}]$^\bullet$** displays a very different electronic situation with respect to the zwitterion **[Aa^{NHO}]$^\bullet$**. Indeed, photochemical excitation of the phenolate **[Aa^{NHO}]$^\bullet$** with near-IR light (1040 nm) yields the phenoxyl radical **[Ab^{NHO}]$^\bullet$**.[13] The higher stability of the zwitterions can be traced back to the increased hydrogen bond strength in ionic systems.[15] Indeed, phenolates are better hydrogen acceptors than phenoxyl radicals.[14] Furthermore, ferrocenium amides such as the mixed-valent cation **[H-C]$^{+\bullet}$** are stronger hydrogen atom donors than neutral ferrocenyl amides.[16,17] In the neutral case, **H-C** prefers an NH•••O IHB forming an 8-membered ring (**H-C^{NHO-8}**) including the ferrocene backbone in the 1,2’ rotameric orientation[18] over the more strained 6-membered ring in **H-C^{NHO-6}** (Scheme 1c). The former IHB is even more favored in the **[H-C^{NHO-8}]$^{+\bullet}$** mixed-valent cation. According to DFT calculations, full oxidation of **H-C** to **[H-C]$^{2+}$** splits all IHBs due to the increased positive charge. Hence, neutral and fully charged oligopeptides incorporating 1-aminoferrocene-1’-carboxylic acid (Fca)[19] as building blocks are redox-responsive foldamers, i.e. redox switches.[16,17]

Scheme 1. Acid/base and redox switches a) ferrocenyl phenol H-A,[13] b) phenol H-B,[14] and c) oligoferrocene amide H-C.[16,17] Hydrogen bonds are colored in red. The 1,2' conformation of H-C is indicated with blue indices.

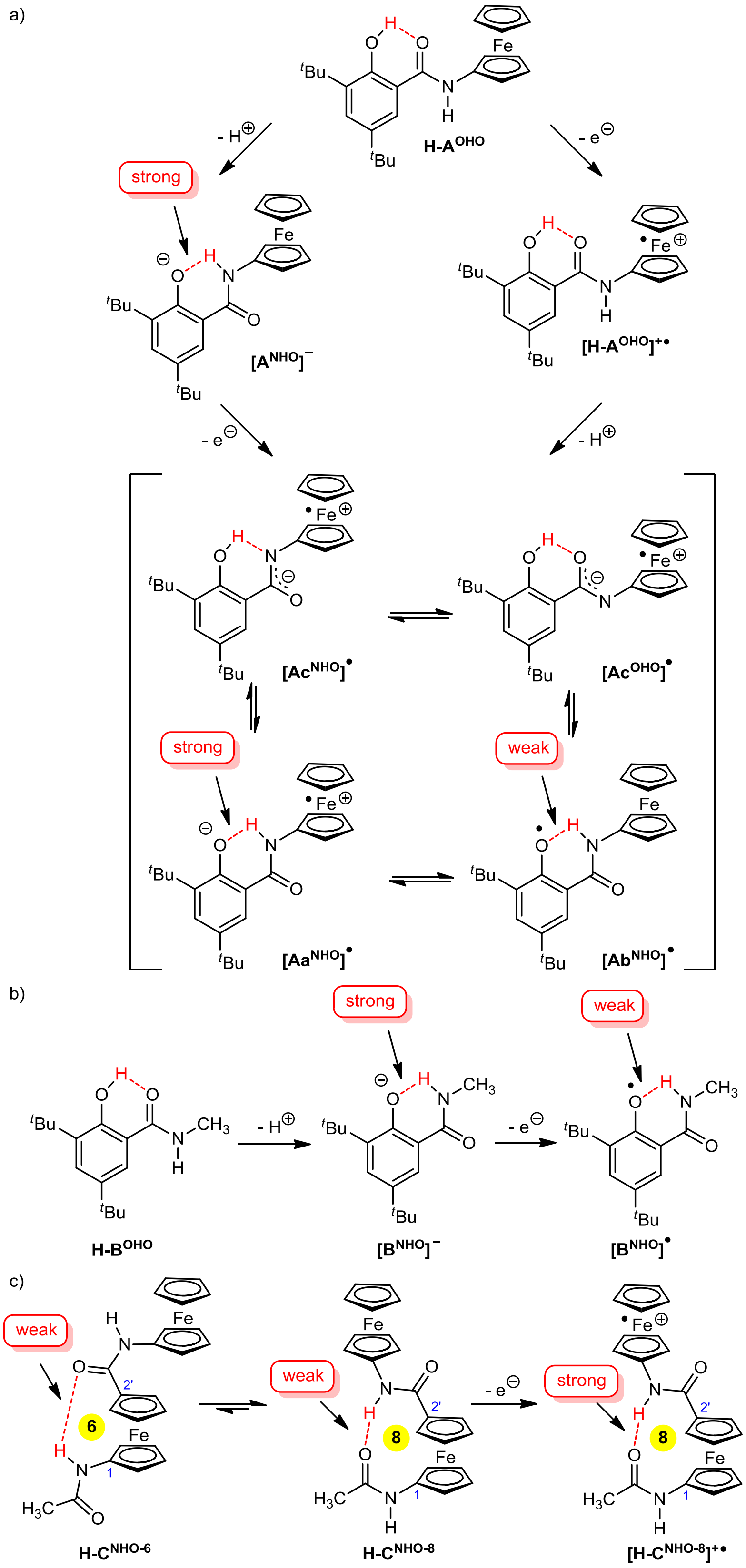

The application of redox switches has found considerable interest in molecular electronics,[20] e.g. as potential data storage devices,[21,22] in catalysts that can be switched on and off by redox reactions,[23] in dihydrogen storage,[24] as fluorescent switches,[25] in molecular recognition,[26] and as a means to modulate IHBs in hydrogen bonded foldameric architectures, respectively.[16,17,27]

In order to combine the acid/base switching capability of salicylic acid amides (e.g. **H-A** or **H-B**) with redox active ferrocenyl foldamers forming hydrogen bonded rings (e.g. **H-C**) we designed three ferrocenyl phenol conjugates with increasing complexity (Scheme 2). Formally, further substituents are attached to the unsubstituted cyclopentadienyl ring of **H-A**, namely a hydrogen atom accepting ester group (R = COOMe, **H-2**), a potential hydrogen atom accepting or hydrogen atom donating substituent (R = CONHEt, **H-3**) and a further ferrocenyl redox center via an amide bridge (R = CONHFc, **H-4**). In the diamides **H-3** and **H-4** the preferential orientations of $\mathbf{H\text{-}A^{OHO}}$ (OH•••O IHB) and $\mathbf{H\text{-}C^{NHO\text{-}8}}$ (8-membered ring) cannot be realized simultaneously without realizing bifurcated IHBs and hence potentially bistable systems are envisaged. Furthermore, the electron withdrawing capabilities of COOMe and CONHEt substituents increase the ferrocene/ferrocenium oxidation potential and hence match the energies of the zwitterionic valence isomers $\mathbf{[2a^{NHO}]^{\bullet}}$ and $\mathbf{[3a^{NHO}]^{\bullet}}$ with those of the corresponding phenoxyl radical valence isomers $\mathbf{[2b^{NHO}]^{\bullet}}$ and $\mathbf{[3b^{NHO}]^{\bullet}}$, respectively. In the diferrocene **H-4**, the terminal ferrocenyl unit is expected to be oxidized in favor of the central disubstituted ferrocenyl unit, and hence, the phenolate/ferrocene redox switching sites are held in a more distant position than in the parent amide **H-A**.

In this study, we experimentally address the stability of the secondary structures of ferrocenyl phenols **H-2**, **H-3**, and **H-4**. Furthermore, we explore the conformational switching under external perturbation, namely deprotonation (acid/base switch), oxidation (redox switch), and proton-coupled electron transfer conditions (PCET, potential valence isomeric equilibria between zwitterions and phenoxyl radicals). DFT calculations are employed to gain deeper insight into the relative energies of all conceivable tautomers, conformers and valence isomers in these complex, multifunctional systems.

3.4.2 RESULTS AND DISCUSSION

Syntheses and characterization of H-1, H-2, H-3, and H-4: Salicylic acid amides **H-2** – **H-4** are conveniently prepared from the substituted salicylic acid derivative 3,5-di-*tert*-butyl-2-hydroxy benzoic acid and an amino substituted ferrocene (Scheme 2). The amines are obtained from the corresponding Boc-protected Fca derivatives Boc-Fca-OMe,[19a] Boc-Fca-NHEt (**H-1**), and Boc-Fca-NH-Fc,[16] respectively (Boc = *tert*-butoxycarbonyl). Boc-Fca-OMe[19a] and Boc-Fca-NH-Fc[16] have been prepared according to literature procedures, while ethyl amide **H-1** is obtained from Boc-Fca-OH[19a] and ethyl amine (Experimental Section). After Boc removal by TFA, the amines are treated with the benzoic acid derivative in the presence of 1-[bis(dimethylamino)methylene]-1H-1,2,3-triazolo[4,5-b]pyridinium 3-oxide hexafluorophosphate (HATU), and *N*,*N*-diisopropylethylamine (DIPEA) in DMF to give the salicylic acid amides **H-2** – **H-4**.

Scheme 2. Syntheses of ferrocenyl phenols H-2 – H-4 from corresponding Boc-protected amino ferrocenes. Hydrogen bonds are colored in red. Atom numbering for NMR assignment given.

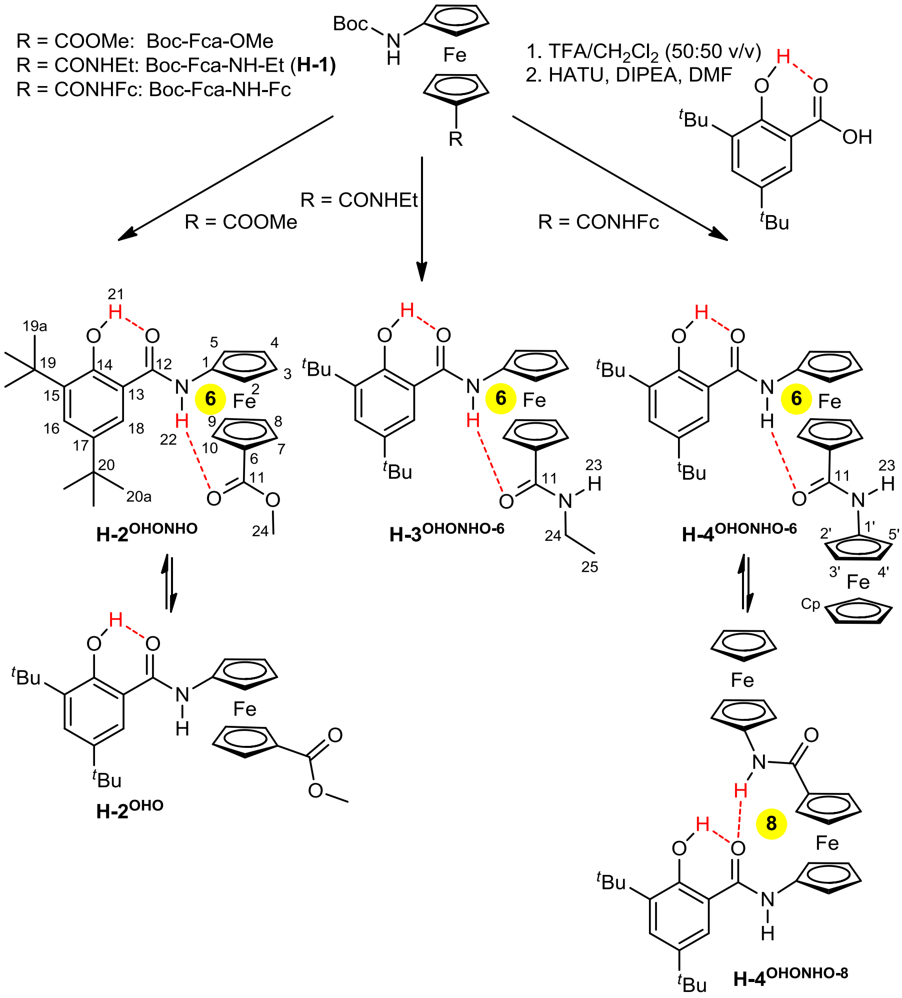

All ferrocenes **H-1** – **H-4** have been fully characterized by NMR, IR, and UV/Vis spectroscopy, as well as by mass spectrometry and voltammetric methods (Figure S1 – S7, Supporting Information, Experimental Section). The molecular ion peaks are found in the FD mass spectra at $m/z = 372.0$ for the ferrocenyl precursor **H-1**, at $m/z = 491.1$ for the methylester **H-2**, at $m/z = 504.2$ for the ethylamide **H-3**, and at $m/z = 660.2$ for the diferrocenyl phenol conjugate **H-4**, respectively. The UV/Vis spectra of **H-1** – **H-4** in CH_2Cl_2 show the characteristic d-d transitions of the ferrocenyl moieties at $\lambda = 440$ nm for **H-1** and **H-3** and at $\lambda = 445$ nm for **H-2** and **H-4**, respectively (Supporting Information, Figures S6 – S7). The three phenols **H-2** – **H-4** furthermore show several π-π* transitions of the aromatic system in the UV part of the spectra and most importantly the characteristic lowest energy transitions of the phenols around $\lambda = 320$ nm (Supporting Information, Figure S7). The ^{1}H NMR and ^{13}C NMR spectra of **H-1** – **H-4** display the expected number of resonances, with correct integral ratios in the ^{1}H NMR spectra. An X-ray crystal structure analysis reveals the secondary structure of the diamide **H-1** in the solid state (Figure 1).

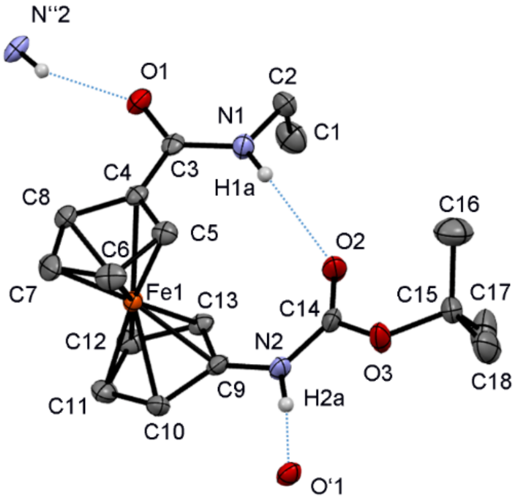

Figure 1. ORTEP representation (thermal ellipsoids at 50 % probability level) of H-1 in the crystal (CH hydrogen atoms omitted) showing inter- and intramolecular hydrogen bonds.

Single crystals of **H-1** were grown from CH_2Cl_2 solution by slow evaporation of the solvent at room temperature (Figure 1). **H-1** crystallized in the monoclinic space group $P2_1/c$. The cyclopentadienyl rings of the ferrocenyl moiety are in a nearly ecliptic conformation in a 1,2' substitution[18] pattern. This 1,2' orientation is forced by the intramolecular NH•••O hydrogen bond from the ethyl amide N1H1a to the Boc carbonyl oxygen atom O2 forming the typical 8-membered ring structure **H-1^{NHO-8}**.[16,17] The N1•••O2 distance amounts to 2.919(3) Å. An intermolecular hydrogen bond between the Boc carbamate group N2H2a and the carbonyl oxygen atom of the ethylamide group O'1 is formed with a N2••• O'1 distance of 2.835(3) Å linking the individual molecules into a hydrogen bonded chain. Further detailed crystallographic information is given in the Supporting Information (Supporting Information, Table S1). The IR spectrum of **H-1** as CsI disk displays two distinct absorptions for NH stretching vibrations at $\tilde{\nu}$ = 3330 and 3220 cm^{-1}. In view of the metrical data of the solid structure, we ascribe the absorption band at $\tilde{\nu}$ = 3330 cm^{-1} to the intramolecularly hydrogen bonded NH group within the 8-membered ring and the absorption band at $\tilde{\nu}$ = 3220 cm^{-1} to the stronger intermolecular hydrogen bond. Upon dissolution of **H-1** in CH_2Cl_2, the absorption band of the IHB is still present ($\tilde{\nu}$ = 3350 cm^{-1}), while the intermolecular hydrogen bond is disrupted resulting in an absorption band at $\tilde{\nu}$ = 3440 cm^{-1} (Supporting Information, Figure S5a). ^{1}H NMR NOE spectroscopy confirms the persistence of the IHB within the 8-membered ring in solution (**H-1^{NHO-8}**, Supporting Information, Figure S1). In addition to the expected NOE crosspeaks due to the covalent framework, contacts between the substituents are present, namely between the ethyl amide group (δ = 6.62 ppm; ethyl amide NH and δ = 3.39 ppm; methylene CH_2) and the Boc group (δ = 1.49 ppm; *tert*-butyl substituent of the Boc group). According to DFT calculations, these short H•••H contacts are only possible in the conformation with the 8-membered ring but impossible in the conceivable 6-membered ring structure (cf. Scheme 1c), similar to previously reported diamides of Fca.[16,17] The presence of IHBs in the phenols **H-2** – **H-4** is probed by a combination of spectroscopy and DFT calculations.

Secondary structures of H-2 – H-4 in solution: The ferrocenyl diamides **H-3** and **H-4** should prefer IHBs forming 8-membered rings over 6-membered rings while **H-2** can only form 6-membered rings due the lack of a second amide substituent at the ferrocene. Salicyl amides favor the OH•••O IHB over the NH•••O IHB, and this OH•••O bridge is better compatible with 6-membered rings.

Table 1. Chemical shifts of OH and NH protons in CD_2Cl_2 and energies of NH stretching vibrations in CH_2Cl_2 of ferrocenyl phenols **H-A**, **H-2**, **H-3**, and **H-4**.

	δ_{OH} / ppm	δ_{NH} / ppm	$\tilde{\nu}$ / cm^{-1}
H-A [13]	12.69	7.36	3450
H-2	12.77	7.85	3445, 3345
H-3	13.08	9.25, 5.97	3445, 3240
H-4	12.89	8.90, 7.40	3430, 3325, 3270

The presence of the OH•••O IHB is clearly advocated in all cases by the chemical shift of the OH proton around $\delta = 12 - 13$ ppm, similar to **H-A^{OHO}** (Table 1, Schemes 1 – 2).[13] Furthermore, NOE crosspeaks between the amide NH protons H^{22} and the phenol CH protons H^{18} place the NH group close to this CH group excluding an NH•••O^{phenol} IHB in all phenols **H-2** – **H-4** (Supporting Information, Figures S2 – S4). No discernible absorption band for the OH^{phenol} stretching vibration is detected in the IR spectrum as typical for strongly hydrogen bonded phenols, while the absorption band of a free phenolic OH group would be expected at around $\tilde{\nu} = 3625$ cm^{-1}.[13,28] The NH proton of **H-A^{OHO}** resonates at $\delta = 7.36$ ppm in the ^{1}H NMR spectrum.[13] Compared to that, the NH resonance of **H-2** is only slightly shifted to lower field ($\delta = 7.85$ ppm) suggesting a weak interaction of the NH group with the ester carbonyl forming a 6-membered ring. IR spectroscopy further confirms this structure assignment. **H-A^{OHO}** features merely a single NH stretching vibration at $\tilde{\nu} = 3450$ cm^{-1}, but **H-2^{OHO}** shows two NH absorptions at $\tilde{\nu} = 3445$ cm^{-1} and 3345 cm^{-1}, respectively (Supporting Information, Figure S5b). The former band is assigned to a free NH group (**H-2^{OHO}**) while the latter corresponds to an NH group interacting with the CO^{ester} substituent and thus forming a 6-membered ring (**H-2^{OHONHO}**). Hence, according to ^{1}H NMR and IR spectroscopy, an NH•••O IHB is present in **H-2**. DFT based conformational searches on **H-2** conformers prefer the OH•••O bridge in combination with the 6-membered ring (**H-2^{OHONHO}**) over all other conceivable folded structures (Supporting Information, Scheme S1). DFT harmonic frequency calculations estimate the NH stretching vibration of **H-2^{OHONHO}** with the 6-membered ring at $\tilde{\nu} = 3381$ cm^{-1} and of **H-2^{OHO}** without the NH•••O IHB at $\tilde{\nu} = 3481$ cm^{-1} in good agreement with the experiment (energies scaled by 0.9614).

H-3$^{OHONHO-6}$ and **H-4$^{OHONHO-6}$** exhibit analogous conformations, both featuring the OH•••O bridge and a 6-membered ring with NH•••O IHB (Scheme 2). Yet, the NH•••O IHBs in **H-3$^{OHONHO-6}$** and **H-4^{OHONHO}** appear to be much stronger than in **H-2^{OHONHO}** based on the significantly shifted NH resonances to $\delta = 9.25$ and 8.90 ppm, respectively (Table 1). The protons of the second NH group in **H-3$^{\mathbf{OHONHO\text{-}6}}$** and **H-4$^{\mathbf{OHONHO\text{-}6}}$** resonate at δ = 5.97 and 7.40 ppm, respectively (Table 1). For ethyl amide **H-3**, this clearly corroborates the **H-3$^{\mathbf{OHONHO\text{-}6}}$** conformation with the 6-membered ring leaving the terminal NH group essentially non-hydrogen bonded. This is also substantiated by the NH stretching absorptions of **H-3$^{\mathbf{OHONHO\text{-}6}}$** in CH_2Cl_2 solution at $\tilde{\nu}$ = 3445 cm^{-1} (free NH) and $\tilde{\nu}$ = 3240 cm^{-1} (strong NH•••O IHB). Again, DFT harmonic frequency calculations estimate the NH stretching vibrations of **H-3$^{\mathbf{OHONHO\text{-}6}}$** with the 6-membered ring at $\tilde{\nu}$ = 3279 cm^{-1} corresponding to the IHB and at $\tilde{\nu}$ = 3468 cm^{-1} assigned to the free NH group in good agreement with the experiment (energies scaled by 0.9614).

The NH proton resonance of **H-4** at δ = 7.40 ppm points to some additional hydrogen bonding interaction of the terminal NH group. In the IR spectrum, absorptions of NH stretching vibrations are found at $\tilde{\nu}$ = 3430, 3325 and 3270 cm^{-1} also suggesting the presence of weakly and strongly hydrogen bonded NH groups. Indeed, DFT calculations suggest a further low-energy **H-4$^{\mathbf{OHONHO\text{-}8}}$** structure with the OH•••O bridge and an NH•••O IHB of the terminal NH group to the salicylic acid amide carbonyl oxygen atom forming an 8-membered ring in addition to the **H-4$^{\mathbf{OHONHO\text{-}6}}$** conformation with the 6-membered ring (Scheme 2, Supporting Information, Scheme S1). DFT harmonic frequency calculations estimate the NH stretching vibrations of **H-4$^{\mathbf{OHONHO\text{-}6}}$** with the 6-membered ring at $\tilde{\nu}$ = 3306 and 3451 cm^{-1} corresponding to the IHB and the free NH group, respectively, in good agreement with the experiment (energies scaled by 0.9614). The NH stretching energies of the conformer **H-4$^{\mathbf{OHONHO\text{-}8}}$** with the 8-membered ring are estimated at somewhat higher energies with $\tilde{\nu}$ = 3326 and 3465 cm^{-1} for the IHB and the free NH group, respectively (energies scaled by 0.9614).

In conclusion, all ferrocenyl phenols **H-2** – **H-4** realize the OH•••O bridge in solution accompanied by NH•••O IHBs forming 6-membered rings as basic structural motif (Scheme 2). In **H-2**, this NH•••O IHB is not especially strong and **H-4** features a further NH•••O IHB motif forming an 8-membered ring (Scheme 2).

The conformational preferences and the possibility for conformational switching under alkaline or oxidative conditions are investigated next. Deprotonation of the phenols is accomplished using the strong, non-nucleophilic and non-coordinating phosphazene base $P_1{}^t$Bu (*tert*-butylimino-tris(dimethylamino)phosphorane, pK_a(MeCN) = 26.98) as proton acceptor.[29] Chemical oxidations of the ferrocenyl phenols and phenolates are performed using silver hexafluoroantimonate $AgSbF_6$ as oxidant ($E_{1/2}$(CH_2Cl_2) = 650 mV vs. FcH/FcH$^{+\bullet}$), which is competent to oxidize ferrocenyl as well as phenolate units.[30] All these reactions and analyses were performed in an inert atmosphere. After filtration from precipitated silver where applicable, the resulting solutions were immediately subjected to spectroscopic analyses

Proton-induced switching of H-2 – H-4: Deprotonation of the phenols **H-2** – **H-4** to the corresponding phenolates **[2]$^-$** – **[4]$^-$** by $P_1{}^t$Bu is depicted in Scheme 3. The different pK_a values of phenol vs. amide protons suggest that proton abstraction should preferentially occur from the phenol.[31,32] Indeed, no evidence for deprotonation of amide protons was found in the optical spectra of **[2]**$^-$, **[3]**$^-$, and **[4]**$^-$. The absorptions of the ferrocenyl d-d transitions in the UV/Vis spectra are unaffected by the base. On the other hand, all three phenol/phenolate pairs investigated in this study show a bathochromic shift of the π-π^* absorption bands from 320 nm to 370 nm in the presence of base (Supporting Information, Figure S7). Such a shift is expected for phenol/phenolate π-π^* transitions and has also been observed for the **H-A**/**[A]**$^-$ acid-base pair.[13]

The negatively charged phenolate group in **[2]**$^-$ is a strong hydrogen atom acceptor, and hence a NH•••O IHB is expected to be formed. This is indeed reflected in the lower energy of the NH stretching vibration of **[2]**$^-$ found at $\tilde{\nu} = 3380$ cm^{-1} as compared to that of **H-2**$^{\mathbf{OHONHO}}$ (Table 1, Supporting Information Figure S8). According to DFT calculations, the hydrogen bonded phenolate **[2**$^{\mathbf{NHO}}$**]**$^-$ is stabilized by 42 kJ mol^{-1} with respect to a conceivable iminolate tautomer **[2**$^{\mathbf{OHO}}$**]**$^-$ hydrogen bonded to a phenol (Supporting Information, Scheme S2).

Scheme 3. Deprotonation of ferrocenyl phenols H-2 – H-4 to the corresponding phenolates [2$^{\mathbf{NHO}}$**]**$^-$ **– [4**$^{\mathbf{NHO}}$**]**$^-$**. Hydrogen bonds are colored in red.**

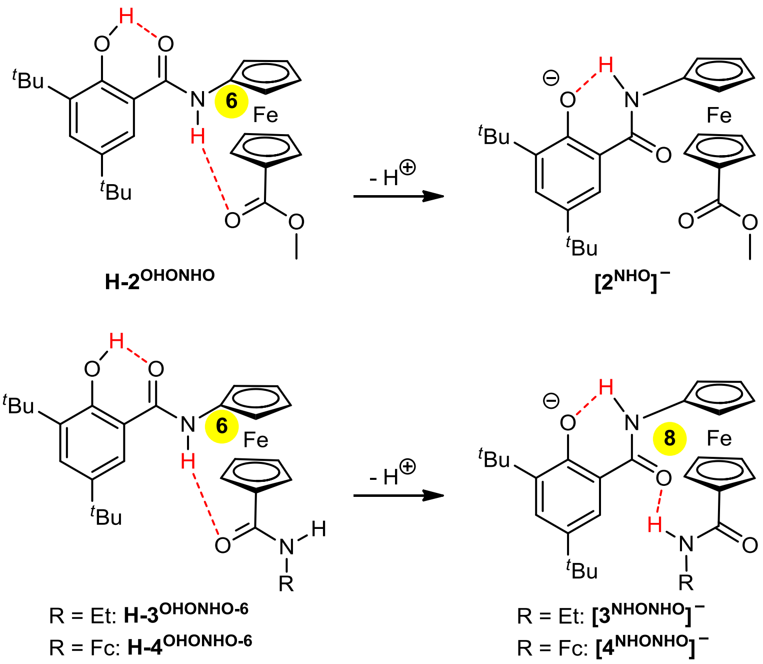

The diamides **H-3**$^{\mathbf{OHONHO\text{-}6}}$ and **H-4**$^{\mathbf{OHONHO\text{-}6}}$ feature three potentially acidic protons, namely one phenolic OH and two amide NH groups. DFT studies consistently confirm that the hydrogen bonded phenolates **[3**$^{\mathbf{NHONHO}}$**]**$^-$ and **[4**$^{\mathbf{NHONHO}}$**]**$^-$ possessing an additional NH•••O IHB within an 8-membered ring are the most stable tautomers (Scheme 3, Supporting Information, Scheme S3). Indeed, the IR spectra of **[3]**$^-$ and **[4]**$^-$ in CH_2Cl_2 substantiate that all NH groups engage in hydrogen bonding (**[3**$^{\mathbf{NHONHO}}$**]**$^-$: $\tilde{\nu} = 3375$, 3240 cm^{-1} ; **[4**$^{\mathbf{NHONHO}}$**]**$^-$: $\tilde{\nu} = 3380$, 3235 cm^{-1}; Supporting Information, Figure S8). This is fully consistent with the two NH•••O IHBs shown in Scheme 3 for **[3**$^{\mathbf{NHONHO}}$**]**$^-$ and **[4**$^{\mathbf{NHONHO}}$**]**$^-$. An additional band at 3190 cm^{-1} in the IR spectrum of **[4]**$^-$ was detected, but remains unassigned, since no other reasonable structure of similar energy as for **[4**$^{\mathbf{NHONHO}}$**]**$^-$ was obtained by DFT calculations (Supporting

Information, Figure S8). Obviously, the OH•••O to NH•••O rearrangement in the **H-3$^{\mathbf{OHONHO\text{-}6}}$/[3$^{\mathbf{NHONHO}}$]$^-$** and **H-4$^{\mathbf{OHONHO\text{-}6}}$/[4$^{\mathbf{NHONHO}}$]$^-$** pairs cooperatively switches the 6-membered ring to the preferred 8-membered ring structure. In this sense, the 6-membered ring in **H-3** and **H-4** can be viewed as an entatic state and this strain is released upon deprotonation to **[3$^{\mathbf{NHONHO}}$]$^-$** and **[4$^{\mathbf{NHONHO}}$]$^-$** at a more distant site (allosteric effect), namely at the phenol entity, allowing for the formation of the 8-membered ring.

In summary, phenol deprotonation of **H-2** – **H-4** switches the OH•••O into the NH•••O bridge and disrupts the 6-membered ring in all cases (Scheme 3). For the **H-3/[3]$^-$** and **H-4/[4]$^-$** conjugate acid/base pairs, the 6-membered ring is replaced by an 8-membered ring and all amide units invert their orientations (double amide flip). This leads to a reorientation and parallel alignment of all amide groups and concomitantly aligns the local amide dipole moments of around 3.5 D each in the same direction.[16b]

Redox-induced switching of H-2 – H-4: Voltammetric data of **H-1** – **H-4** were recorded at room temperature in CH_2Cl_2 using tetra(*n*-butyl)ammonium tetrakis(pentafluorophenyl)borate $[^nBu_4N][B(C_6F_5)_4]$ as weakly coordinating electrolyte.[34,35] The ferrocene diamide **H-1** is reversibly oxidized to **[H-1]$^{+\bullet}$** at $E_{1/2}$ = 55 mV vs. FcH/FcH$^{+\bullet}$ (Supporting Information, Figure S9). Chemical oxidation of **H-1** with $AgSbF_6$ in CH_2Cl_2 yields the ferrocenium ion **[H-1][SbF$_6$]** with a characteristic electronic absorption band of a 1-NHR,n'-COR' disubstituted ferrocenium ion centered at λ = 805 nm (Supporting Information, Figure S6a).[16,17]

As [Fc-NH]$^{+\bullet}$ entities are quite acidic and strong hydrogen atom donors,[13,16,17] ionic hydrogen bonds[15] involving this positively charged functional group are highly favorable. Negatively charged acceptors further enhance the hydrogen bond strength. Hence, coordination of the $[SbF_6]^-$ counter ion to this NH group forming a contact ion pair is likely. Coordination of anions to [Fc-NH]$^{+\bullet}$ groups has been demonstrated previously for coordinating anions such as chloride, acetate or dihydrogenphosphate in Fca-based anion sensors[36] and suggested for weakly coordinating anions such as hexafluoroantimonate or tetrafluoroborate based on EPR evidence and DFT calculations.[13,17,37] For Fca-based contact ion pairs chelating coordination modes have been suggested as well.[36] Indeed, **[H-1][SbF$_6$]** shows absorption bands for NH stretching vibrations at $\tilde{\nu}$ = 3425 and 3370 cm^{-1} (Supporting Information, Figure S5a), which can be assigned to a weak and a strong NH•••X hydrogen bond, respectively. As the monofunctional ferrocenium salt [Fc-NHAc][SbF$_6$] features an absorption band at $\tilde{\nu}$ = 3360 cm^{-1} in CH_2Cl_2, which is assigned to the contact ion pair with a strong NH•••F hydrogen bond,[13] the remaining band of **[H-1][SbF$_6$]** at $\tilde{\nu}$ = 3425 cm^{-1} is straightforwardly assigned to a weaker NH•••F hydrogen bond with the NHEt substituent. These two NH•••F hydrogen bonds result in the formation of a 10-membered ring involving the counter ion in **[H-1$^{\mathbf{NHFNHF}}$][SbF$_6$]** (Scheme 4). The EPR spectral data of a frozen CH_2Cl_2 solution of **[H-1][SbF$_6$]** (*g* = 3.300, 1.890, 1.887) are consistent with those of [Fc-NHAc][SbF$_6$] (*g* = 3.350, 1.875, 1.787)[13] (Table 2, Supporting Information, Figure S10a) further underlining the similarity of **[H-1][SbF$_6$]** and [Fc-NHAc][SbF$_6$] ion pairs. DFT calculations on further conceivable contact ion pairs and separated ion pairs **[H-1][SbF$_6$]** additionally confirm the strong preference of the

10-membered ring structure in **[H-1^{NHFNHF}][SbF$_6$]** (Supporting Information, Scheme S4). The two distinct hydrogen bond strengths are evident from the different calculated H•••F distances of 1.888 and 1.819 Å and different calculated harmonic frequencies for the NH stretches at $\tilde{\nu}$ = 3409 and 3310 cm^{-1}, respectively (energies scaled by 0.9614).

Scheme 4. Oxidation of ferrocenes H-1 – H-4 to the corresponding ferrocenium ions present as contact ion pairs [H-1][SbF$_6$] – [H-4][SbF$_6$]. Hydrogen bonds are colored in red.

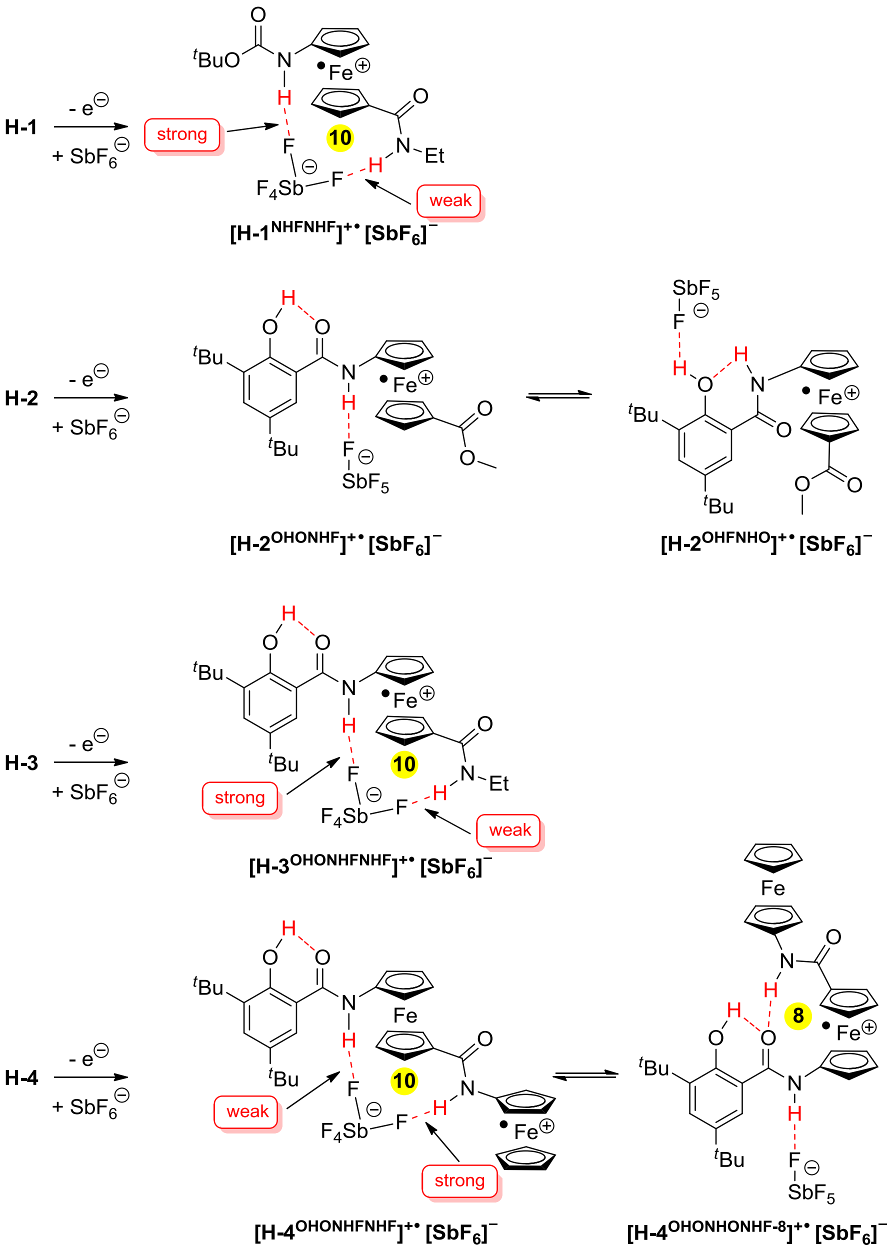

The ferrocene moieties of ferrocenyl phenols **H-2** and **H-3** are reversibly oxidized to the ferrocenium cations **[H-2]$^{+•}$** and **[H-3]$^{+•}$** at $E_{1/2}$ = 170 and 190 mV vs. FcH/FcH$^{+•}$, respectively (Figure 2). Due to the electron withdrawing effect of COOMe and CONHR substituents at the ferrocene, these redox potentials are shifted to higher values as compared to that of the **H-A/[H-A]$^{+•}$** couple ($E_{1/2}$ = −150 mV vs. FcH/FcH$^{+•}$ in CH_2Cl_2),[13] as expected.[16,19c] According to substituent effects,[16,17] diferrocene **H-4** is oxidized to **[H-4]$^{+\bullet}$** at the terminal monosubstituted ferrocene at $E_{1/2} = -120$ mV vs. FcH/FcH$^{+\bullet}$ and in a second step to **[H-4]$^{2+}$** at the central ferrocene at $E_{1/2} =$ 390 mV vs. FcH/FcH$^{+\bullet}$ (Figure 2).

Table 2. EPR parameters obtained by simulation of experimental spectra (77 K).

radical (mixture)		$g_{1,2,3}$	H strain	fraction / %	Gauss pp linewidth / MHz	Lorentz pp linewidth / MHz
[H-A][SbF$_6$] [13]		3.420, 1.855, 1.755	600, 400, 600	N/A	1.5	1.5
[Aa^{OHO}]$^\bullet$ / **[Ac^{NHO}]$^\bullet$** [13]		3.040, 1.949, 1.903	500, 150, 215	N/A	0.5	0.5
[H-A][SbF$_6$]/P$_1$^{t}Bu C-centered radical **[A^x]$^\bullet$** [28]		2.011, 2.007, 2.003	0, 0, 0	1.3	0.5	0.5
[H-A][SbF$_6$]/P$_1$^{t}Bu ferrocenium iminolate **[Ac^{OHO}]$^\bullet$** [28]		2.960, 1.953, 1.933	500, 150, 215	98.7	0.5	0.5
[Fc-NHAc][SbF$_6$] [13]		3.350, 1.875, 1.787	800, 350, 700	100	1.5	1.5
[Fc-NHAc][SbF$_6$]/P$_1$^{t}Bu C-centered radical [28]		2.010, 2.007, 2.003	0, 0, 0	0.8	0.3	0.2
[Fc-NHAc][SbF$_6$]/P$_1$^{t}Bu ferrocenium iminolate [28]		N/A, 1.965, 1.940	500, 130, 200	99.2	0.1	0.1
[H-1][SbF$_6$]		3.300, 1.890, 1.887	600, 450, 650	100	0.01	1.0
[H-1][SbF$_6$]/PhO$^-$	Fe^{III} (LS)	2.013, 2.008, 2.003	40, 10, 25	15	0.05	0.01
[H-1][SbF$_6$]/PhO$^-$	Fe^{III} (HS)	4.295, 4.295, 4.000	150, 150, 400	85	0.01	0.9
[H-1][SbF$_6$]/P$_1$^{t}Bu	Fe^{III} (LS)	2.009, 2.006, 2.000	40, 10, 25	0.5	0.05	0.01
[H-1][SbF$_6$]/P$_1$^{t}Bu	Fe^{III} (HS)	4.330, 4.290, 4.000	150, 150, 400	99.5	0.01	1.5
[Fc-COOMe][SbF$_6$]/PhO$^-$	Fe^{III} (LS)	2.008, 2.006, 2.002	40, 10, 25	100	0.01	0.01
[H-2^{OHFNHO}][SbF$_6$]		3.333, 1.912, 1.852	800, 50, 150	45	0.01	1.2
[H-2^{OHONHF}][SbF$_6$]		3.333, 1.888, 1.820	800, 40, 190	55	0.01	1.5
[H-3^{OHONHFNHF}][SbF$_6$]		3.400, 1.881, 1.800	600, 500, 450	100	0.01	1.2
[H-4$^{OHONHONHF\text{-}8}$][SbF$_6$]		3.333, 1.921, 1.825	800, 120, 280	35	0,01	1,5
[H-4^{OHONHFNHF}][SbF$_6$]		3.333, 1.882, 1.820	800, 185, 330	65	0.01	1.7
[H-2][SbF$_6$]/P$_1$^{t}Bu rapid-freeze C-centered radical **[2^x]$^\bullet$**		2.0090, 2.004, 2.000	0, 0, 0	5.0	0.2	0.5
[H-2][SbF$_6$]/P$_1$^{t}Bu rapid-freeze ferrocenium iminolate **[2c^{OHO}]$^\bullet$**		N/A, 1.980, 1.938	N/A, 150, 300	95.0	0.5	0.5
[H-3][SbF$_6$]/P$_1$^{t}Bu rapid-freeze C-centered radical **[3^x]$^\bullet$**		2.010, 2.005, 2.001	0, 0, 0	1.0	0.2	0.7
[H-3][SbF$_6$]/P$_1$^{t}Bu rapid-freeze ferrocenium iminolate **[3c^{OHO}]$^\bullet$**		3.000, 1.967, 1.913	800, 130, 270	98.9	0.5	0.5
[H-3][SbF$_6$]/P$_1$^{t}Bu rapid-freeze Fe^{III} (HS)		4.300, 4.280, 4.250	200, 300, 400	0.1	0.5	0.5
[H-4][SbF$_6$]/P$_1$^{t}Bu rapid-freeze C-centered radical **[4^x]$^\bullet$**		2.011, 2.006, 1.999	0, 0, 0	0.5	0.5	0.5
[H-4][SbF$_6$]/P$_1$^{t}Bu rapid-freeze ferrocenium iminolate **[4c$^{OHONHO\text{-}6}$]$^\bullet$**		N/A, 1.986, 1.960	N/A, 100, 130	99.2	0.5	0.5
[H-4][SbF$_6$]/P$_1$^{t}Bu rapid-freeze Fe^{III} (HS)		4.320, 4.290, 4.270	100, 300, 400	0.3	0.5	0.5
[H-2][SbF$_6$]/P$_1$^{t}Bu after RT	Fe^{III} (LS)	2.035, 2.004, 1.998	100, 10, 100	25	0.5	0.5
[H-2][SbF$_6$]/P$_1$^{t}Bu after RT	Fe^{III} (HS)	4.390, 4.300, 3.940	500 100 400	75	0.5	0.5
[H-3][SbF$_6$]/P$_1$^{t}Bu after RT	Fe^{III} (LS)	2.040, 2.004, 1.990	100, 10, 100	10	1	1
[H-3][SbF$_6$]/P$_1$^{t}Bu after RT	Fe^{III} (HS)	4.390, 4.300, 3.980	700, 100, 600	90	0.5	0.5
[H-4][SbF$_6$]/P$_1$^{t}Bu after RT	Fe^{III} (LS)	2.032, 2.004, 1.968	100, 50, 100	20	0.5	0.5
[H-4][SbF$_6$]/P$_1$^{t}Bu after RT	Fe^{III} (HS)	4.550, 4.300, 4.000	700, 100, 600	80	0.5	0.5

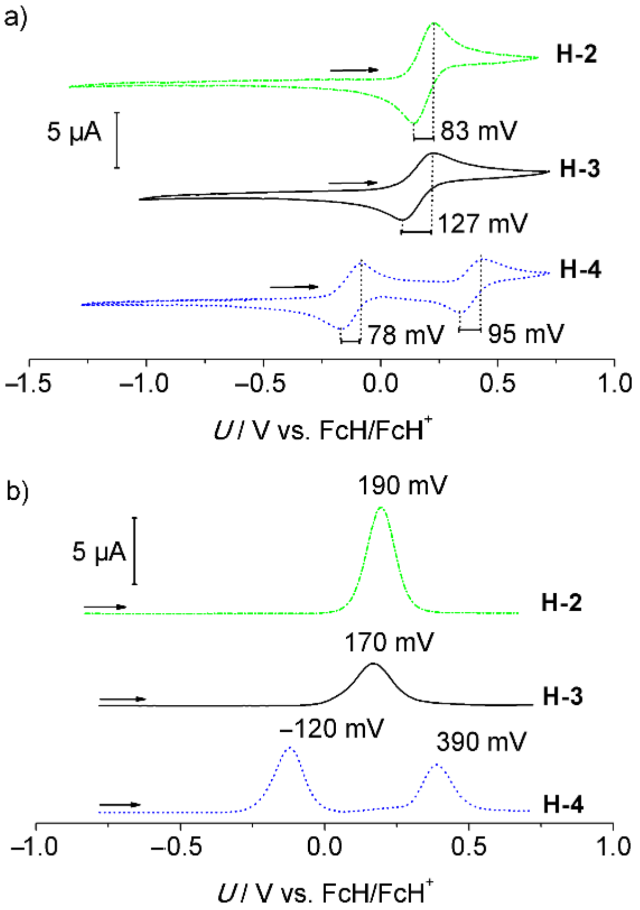

Figure 2. a) Cyclic voltammograms and b) square wave voltammograms of H-2 (green, dash-dot), H-3 (black, solid), and H-4 (blue, dotted) in CH_2Cl_2 containing [^{n}Bu_4N][$B(C_6F_5)_4$] as supporting electrolyte at room temperature.

All ferrocenium ions **[H-2][SbF$_6$]** – **[H-4][SbF$_6$]** prepared by oxidation of **H-2** – **H-4** with $AgSbF_6$ display absorption bands for an NH stretching vibration at $\tilde{\nu} = 3360$, 3365 and 3370 cm^{-1}, respectively (Supporting Information, Figure S5). These bands are assigned to a strong NH•••X hydrogen bond, e.g. a NH•••F bond within a contact ion pair, similar to **[H-1][SbF$_6$]** and [Fc-NHAc][SbF$_6$]. No evidence for a non-hydrogen bonded phenolic OH group is detected in either case.

This is consistent with two conceivable structures for **[H-2][SbF$_6$]** as shown in Scheme 4. In **[H-2^{OHONHF}][SbF$_6$]**, the OH•••O bridge of **H-2** remains intact while its weak NH•••O IHB involving the COOMe group is replaced by the strong NH•••F bond (Scheme 4). In the **[H-2^{OHFNHO}][SbF$_6$]** tautomer, the counter ion coordinates to the OH group supporting the NH•••O bridge. In both cases, the NH•••X hydrogen bond is expected to be rather strong. Indeed, DFT calculations find these two tautomers within a 3 kJ mol^{-1} energy range (Supporting Information, Scheme S5). Their NH stretching vibrations are both calculated at $\tilde{\nu} = 3293$ cm^{-1} (scaled by 0.9614; accidentally degenerate). Spectroscopic evidence for the presence of two ferrocenium species in solution is gained from the EPR spectrum of **[H-2][SbF$_6$]** in frozen solution. In fact, the experimental EPR spectrum could only be simulated by two ferrocenium resonances in a

45:55 ratio (*g* = 3.330, 1.912, 1.852; *g* = 3.330, 1.888, 1.820; Figure 3a, Table 2). By comparison with the EPR spectra of **[H-A][SbF$_6$]** and [Fc-NHAc][SbF$_6$], we tentatively assign the latter *g* value to the **[H-2$^{\mathrm{OHONHF}}$][SbF$_6$]** ion pair (Table 2). In summary, oxidation of **H-2** and counter ion coordination either stabilizes the OH•••O bridge by coordination to the NH group or the NH•••O bridge by coordination to the OH group. Both coordination modes split the weak IHB forming the 6-membered ring and release the COOMe substituent.

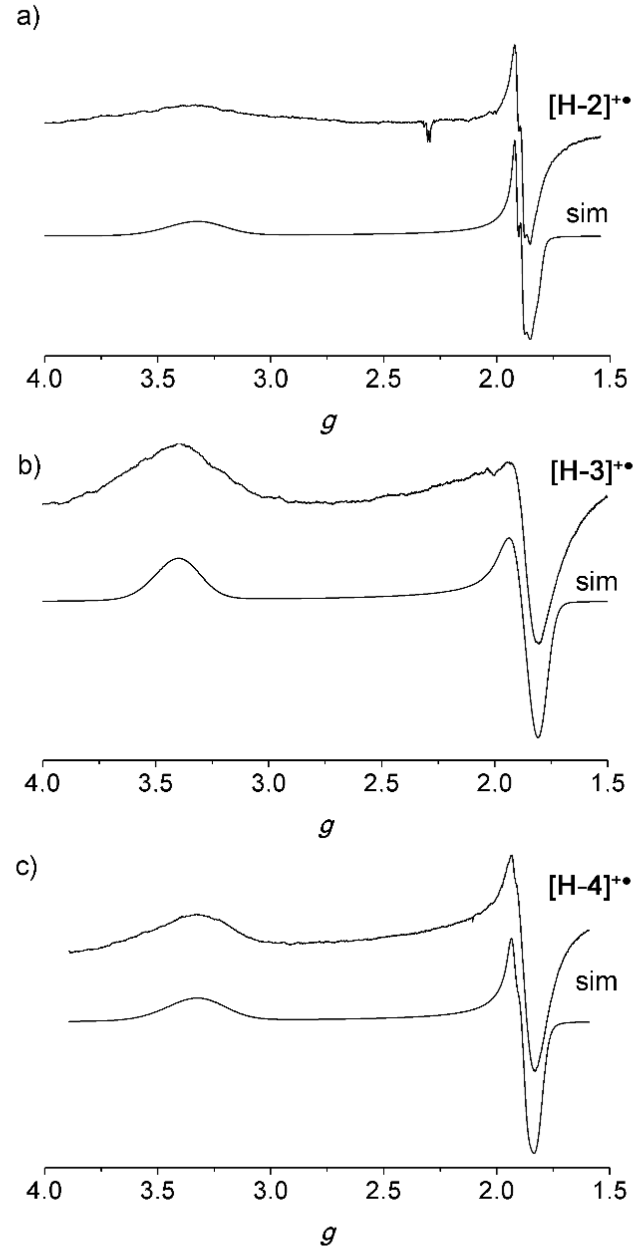

Figure 3. X-band EPR spectra and simulations of 25 mM solutions of (a) [H-2][SbF$_6$], (b) [H-3][SbF$_6$], and (c) [H-4][SbF$_6$] in CH$_2$Cl$_2$ at 77 K recorded at the following parameters: (a) field = 2999.95 G, sweep = 2998.61 G, sweep time = 90 s, modulation = 5000 mG, MW attenuation = 15 dB, (b) field = 2499.01 G, sweep = 3788.47 G, sweep time = 90 s, modulation = 2000 mG, MW attenuation = 10 dB, and (c) field = 2999.95 G, sweep = 2498.84 G, sweep time = 90 s, modulation = 2000 mG, MW attenuation = 10 dB.

The diamides **[H-3][SbF$_6$]** and **[H-4][SbF$_6$]** show further IR absorption bands at $\tilde{\nu}$ = 3420 and 3415 cm^{-1}, respectively (Supporting Information, Figure S5). These are associated with weaker NH•••F hydrogen bonds. These data are consistent with a 10-membered ring structure as found for **[H-1][SbF$_6$]** (Scheme 4, Supporting Information, Scheme S6). Hence, the OH•••O bridges of **H-3** and **H-4** are retained but the 6-membered rings are replaced by the 10-membered rings involving the counter ion in **[H-3$^{\text{OHONHFNHF}}$][SbF$_6$]** and **[H-4$^{\text{OHONHFNHF}}$][SbF$_6$]**, respectively. DFT based harmonic frequency calculations yield $\tilde{\nu}$ = 3407, 3372 cm^{-1} and $\tilde{\nu}$ = 3422, 3375 cm^{-1} (scaled by 0.9614) for **[H-3$^{\text{OHONHFNHF}}$][SbF$_6$]** and **[H-4$^{\text{OHONHFNHF}}$][SbF$_6$]**, respectively, in very good agreement with the experimental values. Importantly, the strong and weak NH•••F hydrogen bonds differ in **[H-3$^{\text{OHONHFNHF}}$][SbF$_6$]** and **[H-4$^{\text{OHONHFNHF}}$][SbF$_6$]**, as the strong hydrogen bond is formed with the positively charged [Fc-NH]$^{+\bullet}$ site in both cases. This corresponds to the disubstituted ferrocenium site in **[H-3$^{\text{OHONHFNHF}}$][SbF$_6$]** but to the terminal monosubstituted ferrocenium site in **[H-4$^{\text{OHONHFNHF}}$][SbF$_6$]** (Scheme 4).

Oxidation of the **H-4$^{\text{OHONHO-8}}$** tautomer (Scheme 2) with concomitant coordination of the counter ion at the free NH group gives the conceivable tautomeric ion pair **[H-4$^{\text{OHONHONHF-8}}$][SbF$_6$]** (Scheme 4, Supporting Information, Scheme S7). By DFT methods only an electronically excited state was obtained for **[H-4$^{\text{OHONHONHF-8}}$][SbF$_6$]**, but this OH•••O, NH•••O, NH•••F hydrogen bond network should stabilize the positive charge at the central ferrocene leading to a different valence isomeric description. This peculiar hydrogen bond network allows for strong counter ion coordination at the central or at the terminal NH group, which consequently determines the charge distribution. Indeed, EPR spectroscopy provides hints that two different ferrocenium ion pairs **[H-4][SbF$_6$]** are present in (frozen) solution in a 35:65 ratio (g = 3.330, 1.921, 1.825; g = 3.330, 1.882, 1.820), while for **[H-3][SbF$_6$]** only a resonance for a single ferrocenium ion pair is clearly discernible (g = 3.400, 1.881, 1.800; Figure 3, Table 2). The two resonances are assigned to the two ion pairs **[H-4$^{\text{OHONHFNHF}}$][SbF$_6$]** and **[H-4$^{\text{OHONHONHF-8}}$][SbF$_6$]**. In contrast to the **[H-4$^{\text{OHONHFNHF}}$][SbF$_6$]** / **[H-4$^{\text{OHONHONHF-8}}$][SbF$_6$]** valence isomeric tautomers, the **[H-3$^{\text{OHONHONHF-8}}$][SbF$_6$]** tautomer is not competitive with the more stable **[H-3$^{\text{OHONHFNHF}}$][SbF$_6$]** tautomer and DFT calculations estimate this structure being 22 kJ mol^{-1} higher in energy (Supporting Information, Scheme S6). In all these tautomers, all OH and NH groups engage in hydrogen bonding interactions.

Similar to **[H-1]**$^{+\bullet}$ and characteristic for 1-NHR,n'-COR' disubstituted ferrocenium ions, **[H-2]**$^{+\bullet}$ and **[H-3]**$^{+\bullet}$ display absorption bands at λ = 815 and 820 nm, respectively (Supporting Information, Figure S6).[16,17] On the other hand, **[H-4]**$^{+\bullet}$ features an absorption band at λ = 771 nm, characteristic for an NHR-substituted ferrocenium ion, fully analogous to **[H-A]**$^{+\bullet}$ (λ = 770 nm).[13] This suggests, that the **[H-4$^{\text{OHONHFNHF}}$][SbF$_6$]** valence isomer with a terminal NHR-substituted ferrocenium ion is predominantly present. Additionally, **[H-4]**$^{+\bullet}$ exhibits a broad absorption band at λ = 1074 nm with a full-width-at-half-maximum of 4575 cm^{-1} (Supporting Information, Figure S11). Such an absorption band is characteristic for amide bridged mixed-valent ferrocene/ferrocenium complexes and assigned to an intervalence charge transfer (IVCT) transition.[16,17] For example, the mixed-valent amide [Fmoc-Fca-NH-Fc]$^{+\bullet}$

features its IVCT band at 1036 nm in THF (Fmoc = fluorenylmethoxycarbonyl).[16b] Applying a conventional Marcus-Hush analysis[38] yields an electronic coupling constant of H_{AB} = 310±20 cm^{-1} for **[H-4]**$^{+\bullet}$, with the distance between the redox sites assumed as R_{AB} = 7.0±0.5 Å. This electronic coupling is somewhat higher than that obtained for [Ac-Fca-NH-Fc]$^{+\bullet}$ in CH_2Cl_2 (H_{AB} = 260±10 cm^{-1})[37] but still places **[H-4]**$^{+\bullet}$ in the class II regime of the Robin-Day classification,[39] similar to comparable amide and thioamide bridged ferrocene/ferrocenium systems.[16,17,37,40] In addition to the ferrocenium and the IVCT bands at λ = 771 and 1074 nm, respectively, a further weak absorption band at λ = 935 nm (ε = 30 M^{-1} cm^{-1}; FWHM = 1780 cm^{-1}) is required to satisfactorily fit the experimental UV/Vis spectrum (Supporting Information, Figure S11). This absorption is assigned either to an IVCT to the central ferrocenium or to a d-d transition within the central ferrocenium of **[H-4$^{\text{OHONHONHF-8}}$][SbF$_6$]** (Supporting Information, Scheme S7). Unambiguous assignment was impossible because DFT calculations repeatedly resulted in an electronically excited state for this structure.

In the UV/Vis spectrum of the diferrocenium salt **[H-4][SbF$_6$]$_2$**, the low energy IVCT band of **[H-4]**$^{+\bullet}$ has vanished and only narrow ferrocenium based transitions are visible at λ = 757, 788, and 873 nm, respectively (Supporting Information, Figure S11b), confirming the assignment of the band of **[H-4]**$^{+\bullet}$ at λ = 1074 nm as IVCT band. The IR spectrum of **[H-4][SbF$_6$]$_2$** displays a single absorption at $\tilde{\nu}$ = 3355 cm^{-1} in CH_2Cl_2 solution, which is characteristic for strong NH•••F hydrogen bonds. As no free phenolic OH is observed, the IR data suggest the presence of the OH•••O bridge and two NH•••F interactions with disruption of all NH•••O IHBs. Such an oxidation-induced splitting of all NH•••O IHBs has been previously suggested for small and large Fca oligomers.[16,17] This contact ion pair structure of **[H-4$^{\text{OHONHFNHF}}$][SbF$_6$]$_2$** is furthermore confirmed by DFT calculations (Supporting Information, Scheme S8).

In conclusion, all three ferrocenes **H-2** – **H-4** are oxidized to the respective ferrocenium salts **[H-2][SbF$_6$]** – **[H-4][SbF$_6$]** by AgSbF_6. IR and EPR spectroscopy in combination with DFT calculations suggest that the preferred conformations of the paramagnetic cations retain the OH•••O bridge (except for one additional conformation of **[H-2$^{\text{OHFNHO}}$][SbF$_6$]**). Importantly, the NH•••O IHBs forming the 6-membered rings in **H-3** and **H-4** are replaced by intermolecular NH•••F interactions with the counter ion, forming 10-membered ring systems **[H-3$^{\text{OHONHFNHF}}$][SbF$_6$]** and **[H-4$^{\text{OHONHFNHF}}$][SbF$_6$]**, respectively (Scheme 4). For **[H-4][SbF$_6$]** a further valence isomeric conformation **[H-4$^{\text{OHONHONHF-8}}$][SbF$_6$]** with a central ferrocenium ion is suggested, in addition to the terminal ferrocenium ion in **[H-4$^{\text{OHONHFNHF}}$][SbF$_6$]** (Scheme 4). This is valence isomeric equilibrium triggered by the location of the hydrogen bonded counter ion.

Reactivity of H-2 – H-4 under PCET conditions: The cyclic and square wave voltammograms of solutions of **[2]**$^-$ – **[4]**$^-$, prepared from **H-2** – **H-4** in the presence of one equivalent of phosphazene base $\text{P}_1{}^t\text{Bu}$ in $\text{CH}_2\text{Cl}_2/[^n\text{Bu}_4\text{N}][\text{B}(\text{C}_6\text{F}_5)_4]$, reveal only quasi-reversible or irreversible first oxidations, pointing to further reactivity of the initially formed radicals **[2]**$^\bullet$ – **[4]**$^\bullet$.

The first oxidation waves are recorded at E_p = −360, −380 and –260 mV vs. FcH/FcH$^{+\bullet}$ for **[2]**$^-$, **[3]**$^-$, and **[4]**$^-$, respectively, while **[A]**$^-$ displays a quasi-reversible oxidation at $E_{1/2}$ = −535 mV under the same conditions.[13] The initial oxidation to **[2]**$^\bullet$ – **[4]**$^\bullet$ is followed by diverse reactions and several further oxidative waves are observed in the voltammograms, which are difficult to assign to defined redox processes (Supporting Information, Figure S12).

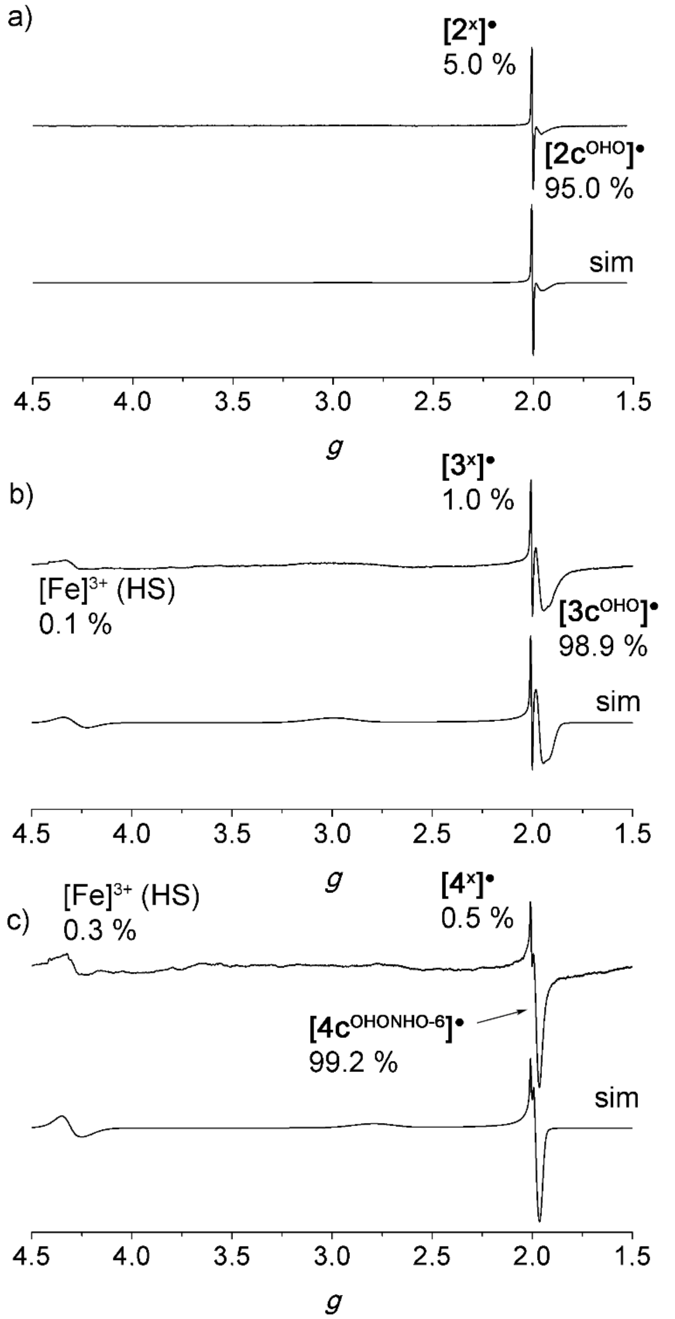

Figure 4. X-band rapid freeze EPR spectra and simulations of 25 mM solutions of (a) [H-2]$^{+\bullet}$/P$_1{}^t$Bu, (b) [H-3]$^{+\bullet}$/P$_1{}^t$Bu, and (c) [H-4]$^{+\bullet}$/P$_1{}^t$Bu in CH_2Cl_2 at 77 K recorded at the following parameters: (a) field = 2999.95 G, sweep = 2998.61 G, sweep time = 90 s, modulation = 5000 mG, MW attenuation = 15 dB, (b) field = 2799.86 G, sweep = 3199.65 G, sweep time = 90 s, modulation = 2000 mG, MW attenuation = 30 dB, and (c) field = 2999.95 G, sweep = 2998.61 G, sweep time = 90 s, modulation = 5000 mG, MW attenuation = 15 dB.

As all three initially formed radicals **[2]**$^{\bullet}$, **[3]**$^{\bullet}$, and **[4]**$^{\bullet}$ are unstable, irrespective of the pathway of their formation (oxidation of **[2]**$^{-}$ – **[4]**$^{-}$ or deprotonation of **[H-2]**$^{+\bullet}$ – **[H-4]**$^{+\bullet}$, respectively), conclusive characterization by UV/Vis or IR spectroscopy failed. Yet, rapid-freeze EPR spectroscopy allowed to detect transient radicals directly after the reaction of **[H-2]**$^{+\bullet}$ – **[H-4]**$^{+\bullet}$ with approximately equimolar amounts of $\mathrm{P}_1{}^t\mathrm{Bu}$ (Figure 4). By comparison with EPR spectra obtained from **[H-A]**$^{+\bullet}$/$\mathrm{P}_1{}^t\mathrm{Bu}$ or [FcNHAc]$^{+\bullet}$/$\mathrm{P}_1{}^t\mathrm{Bu}$,[28,41] the resonances are straightforwardly assigned to ferrocenium iminolate zwitterions with non-hydrogen bonded iminolate nitrogen atoms **[2c$^{\mathrm{OHO}}$]**$^{\bullet}$ (Scheme 5a), **[3c$^{\mathrm{OHO}}$]**$^{\bullet}$ (Scheme S9), and **[4c$^{\mathrm{OHONHO\text{-}6}}$]**$^{\bullet}$ (Scheme S10) (cf. Scheme 1; **[Ac$^{\mathrm{OHO}}$]**$^{\bullet}$) as major EPR-active species (≥95 %) and carbon-centered ferrocenyl radicals **[2$^{\mathrm{x}}$]**$^{\bullet}$ – **[4$^{\mathrm{x}}$]**$^{\bullet}$ as minor radical species[41] (≤ 5%) (Table 2, Schemes 5 and 6). Carbon-centered radical ferrocenyl species of the type [Fc$^{\mathrm{x}}$]$^{\bullet}$ have been identified previously for a range of ferrocenium cations in the presence of a base by the spin-trapping technique (Scheme 5c).[41] However, these radicals cannot be made not responsible for the rapid decomposition of **[2]**$^{\bullet}$ – **[4]**$^{\bullet}$. For the **[H-3]**$^{+\bullet}$/$\mathrm{P}_1{}^t\mathrm{Bu}$ and **[H-4]**$^{+\bullet}$/$\mathrm{P}_1{}^t\mathrm{Bu}$ mixtures, further weak resonances around $g \approx 4.3$ are noted (Table 2, Figure 4). Such resonances are characteristic for high-spin ferric complexes.[42,43]

After annealing the samples at room temperature for one minute and refreezing to 77 K, all resonances of ferrocenium iminolate zwitterions **[2c$^{\mathrm{OHO}}$]**$^{\bullet}$, **[3c$^{\mathrm{OHO}}$]**$^{\bullet}$, and **[4c$^{\mathrm{OHONHO\text{-}6}}$]**$^{\bullet}$ as well as the ferrocenyl radicals **[2$^{\mathrm{x}}$]**$^{\bullet}$ – **[4$^{\mathrm{x}}$]**$^{\bullet}$ have decayed. Instead, resonances with $g \approx 4.3$ and $g \approx 2.0$ corresponding to high-spin[42,43] and low-spin ferric ion species[44-49] are present. Obviously, the ferrocenium ions **[H-2]**$^{+\bullet}$ – **[H-4]**$^{+\bullet}$ are susceptible to nucleophilic attack under these conditions with substitution of the Cp ligands. Similar reactivity has been observed for ferrocenium ions in the presence of coordinating anions such as chloride, bromide, hydroxide or phenolate.[50-57] Hence, the phenolate or iminolate zwitterions formed from **[H-2]**$^{+\bullet}$ – **[H-4]**$^{+\bullet}$ appear to substitute Cp ligands. However, the substitution pattern of the ferrocenium ion plays a decisive role as well, as **[H-A]**$^{+\bullet}$/$\mathrm{P}_1{}^t\mathrm{Bu}$ and [FcNHAc]$^{+\bullet}$/$\mathrm{P}_1{}^t\mathrm{Bu}$ mixtures are inert toward Cp substitution in the absence of other nucleophiles.[28,41]

Scheme 5. Equilibria of radicals obtained from a) $[\text{H-2}]^{+\bullet}$ and b) $[\text{H-3}]^{+\bullet}$ in the presence of a base and c) ferrocenyl radicals $[\text{Fc}^{\text{x}}]^{\bullet}$. Relative energies obtained from by DFT calculations (B3LYP/SV(P)/COSMO:CH_2Cl_2). Hydrogen bonds are colored in red.

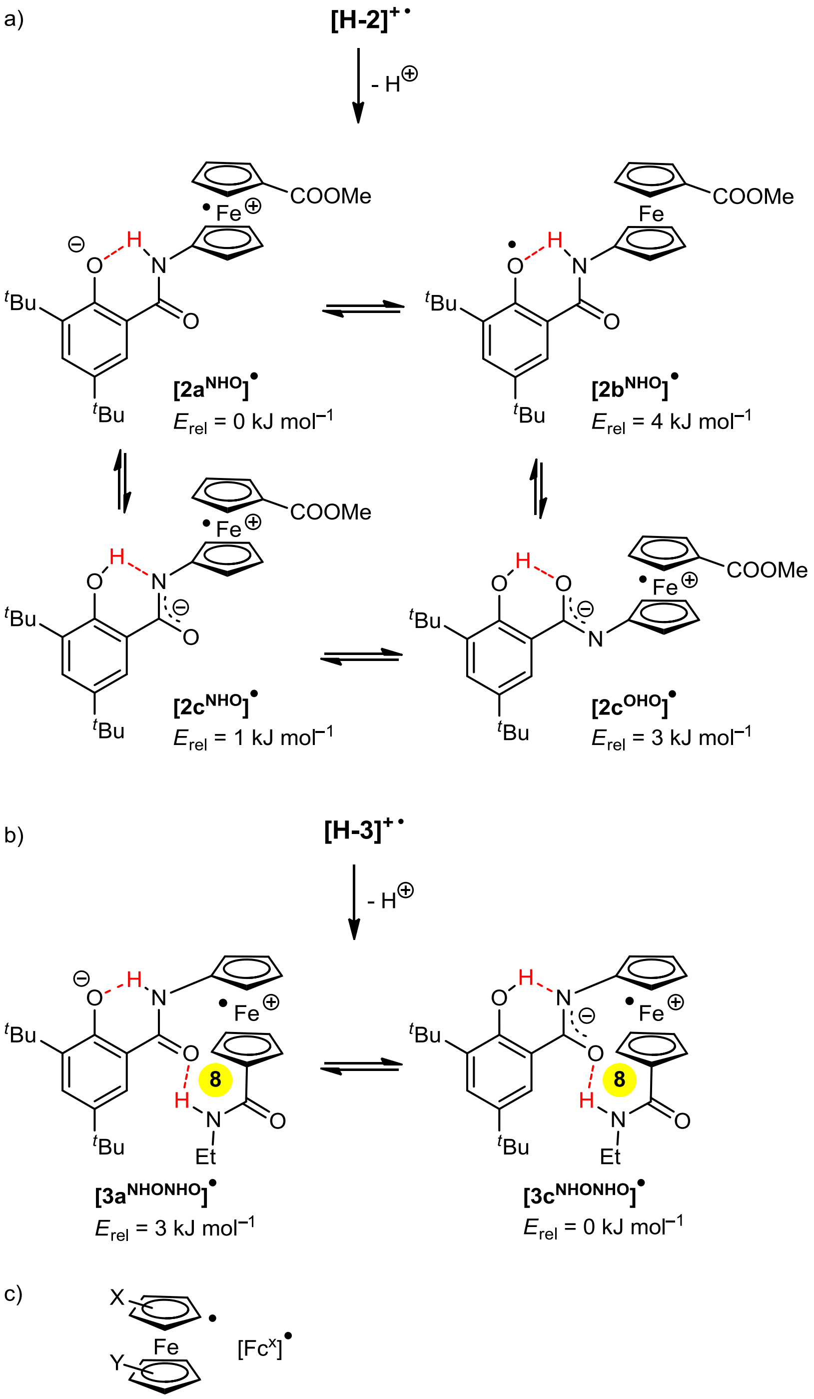

On the other hand, $[\text{FcCOOMe}]^{+\bullet}$ reacts with phenolate $[C_6H_5O]^-$ to give low-spin ferric ions ($g \approx 2.005$, Table 2, Supporting Information, Figure S13). Furthermore, **[H-1]**$^{+\bullet}$ and phenolate yields both low-spin ($g \approx 2.005$, 15 %) and high-spin ferric ions ($g \approx 4.2$, 85 %). The mixture **[H-1]**$^{+\bullet}$/$P_1{}^t$Bu yields essentially high-spin Fe^{III} species ($g \approx 4.2$, 99.5 %). These combined data suggest that monosubstituted $[\text{Fc-NHCOR}]^{+\bullet}$ complex cations are substitutionally inert while ferrocenium ions with COX substituents, such as $[\text{X(O)C-Fc-NHCOR}]^{+\bullet}$ and $[\text{X(O)C-Fc}]^{+\bullet}$, readily undergo substitution reactions either with nucleophiles such as phenolate to give essentially low-spin iron(III) or with iminolates to give essentially high-spin iron(III) species. In any case, this intrinsic reactivity of **[2]**$^\bullet$, **[3]**$^\bullet$, and **[4]**$^\bullet$ unfortunately prevents the investigation of conformational and valence isomeric preferences.

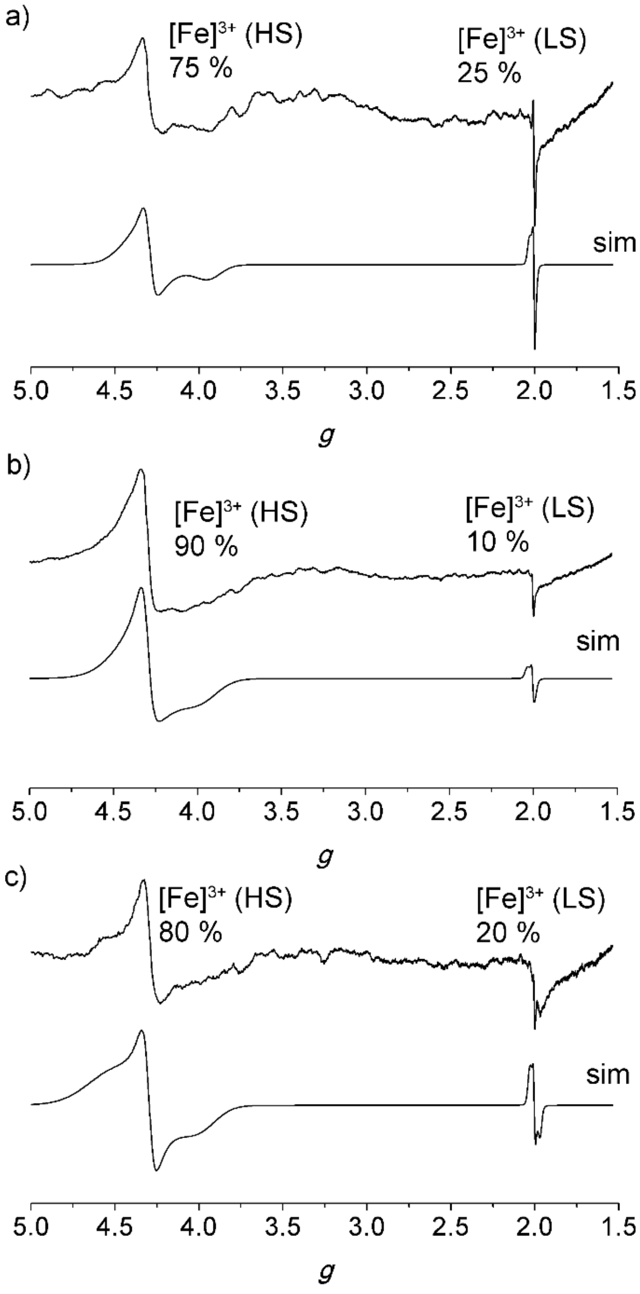

Figure 5. X-band EPR spectra and simulations of 25 mM solutions formed of (a) $[\text{H-2}]^{+\bullet}/\text{P}_1{}^t\text{Bu}$, (b) $[\text{H-3}]^{+\bullet}/\text{P}_1{}^t\text{Bu}$, and (c) $[\text{H-4}]^{+\bullet}/\text{P}_1{}^t\text{Bu}$ in CH_2Cl_2 at 77 K recorded at the following parameters: (a) field = 2799.86 G, sweep = 3199.65 G, sweep time = 90 s, modulation = 5000 mG, MW attenuation = 15 dB, (b) field = 2799.86 G, sweep = 3196.78 G, sweep time = 90 s, modulation = 5000 mG, MW attenuation = 5 dB and (c) field = 2799.86 G, sweep = 3193.92 G, sweep time = 90 s, modulation = 5000 mG, MW attenuation = 10 dB.

DFT calculations on $\mathbf{[2]^{\bullet}}$ suggest that all phenolate $\mathbf{[2a^{NHO}]^{\bullet}}$ and iminolate zwitterions $\mathbf{[2c^{NHO}]^{\bullet}}$ and $\mathbf{[2c^{OHO}]^{\bullet}}$ as well as the phenoxyl radical $\mathbf{[2b^{NHO}]^{\bullet}}$ are very close in energy, in contrast to $\mathbf{[A]^{\bullet}}$ which strongly prefers the phenolate zwitterion $\mathbf{[Aa^{NHO}]^{\bullet}}$ (Schemes 1 and 5). Similarly, for $\mathbf{[3]^{\bullet}}$ the ferrocenium phenolate and ferrocenium iminolate zwitterionic structures $\mathbf{[3a^{NHONHO}]^{\bullet}}$ and $\mathbf{[3c^{NHONHO}]^{\bullet}}$ are essentially degenerate (Scheme 5, Supporting Information, Scheme S9). Based on the above control experiments with [FcCOOMe]$^{+\bullet}$/phenolate, $\mathbf{[H\text{-}1]^{+\bullet}}$/phenolate and $\mathbf{[H\text{-}1]^{+\bullet}}$/base, we suggest, that the phenolates and the iminolates formed from $\mathbf{[H\text{-}2]^{+\bullet}}$/base and $\mathbf{[H\text{-}3]^{+\bullet}}$/base are competent to substitute the cyclopentadienyl ring with the electron withdrawing COOMe or CONHEt groups, finally yielding low-spin iron(III) and high-spin iron(III) species, respectively. A similar reactivity is conceivable for $\mathbf{[4]^{\bullet}}$, which yields two comparable reactive iminolates similar to $\mathbf{[3]^{\bullet}}$ (Scheme 5) in which the 1-amino-1'-carboxylic acid moiety is oxidized as minimum energy structure according to DFT calculations ($\mathbf{[4d^{NHONHO}]^{\bullet}}$ and $\mathbf{[4d^{NHONHO'}]^{\bullet}}$; Supporting Information, Scheme S10). On the other hand, $\mathbf{[H\text{-}A]^{+\bullet}}$ is inert in the presence of base with respect to substitution as no ferrocenium ion with an electron withdrawing COOMe or CONHR substituent is available for substitution (Scheme 1).

3.4.3 CONCLUSIONS

Three multifunctional conformational switches based on the ferrocenyl salicylic acid amide motif with increasing additional complexity (R = COOMe, **H-2**; R = CONHEt, **H-3**; R = CONHFc, **H-4**) have been prepared and their preferred conformations in solution have been determined. Typical for salicylic acid amides, all ferrocenyl phenols realize an OH•••O intramolecular hydrogen bond from the phenolic OH group to the amide carbonyl group. This hydrogen bond is further assisted by NH•••O IHBs from the amide NH to the carbonyl substituents COOMe, CONHEt and CONHFc located at the ferrocenyl moiety. This results in a 6-membered ring ($\mathbf{H\text{-}2^{OHONHO\text{-}6}}$, $\mathbf{H\text{-}3^{OHONHO\text{-}6}}$, $\mathbf{H\text{-}4^{OHONHO\text{-}6}}$) instead of the normally observed 8-membered ring system in such 1,n'-disubstituted ferrocenyl amides, as prototypically found in Boc-NH-Fc-CONHEt (**H-1**). However, the diferrocenyl phenol **H-4** equilibrates with an additional conformer featuring exactly this 8-membered ring ($\mathbf{H\text{-}4^{OHONHO\text{-}8}}$).

Deprotonation of the phenols **H-2** – **H-4** to $\mathbf{[2]^{-}}$ – $\mathbf{[4]^{-}}$ switches the OH•••O bridge to an NH•••O hydrogen bond with concomitant inversion of the amide unit (amide flip) and hence disrupts the 6-membered ring. For the $\mathbf{H\text{-}3/[3]^{-}}$ and $\mathbf{H\text{-}4/[4]^{-}}$ conjugate acid/base pairs, the 6-membered ring is replaced by an 8-membered ring and consequently the terminal amide units invert their orientations in a cooperative manner as well (double amide flip). This leads to a reorientation and parallel orientation of all amide groups and concomitantly aligns the local amide dipole moments.

Oxidation of the ferrocenyl moiety to the ferrocenium ion essentially retains the OH•••O bridge. Yet, the 6-membered ring is split and the intramolecular hydrogen bonds are replaced by intermolecular ones to the hexafluoroantimonate counter ions. This intermolecular hydrogen bonding results in the intimate contact ion pairs $\mathbf{[H\text{-}2][SbF_6]}$ – $\mathbf{[H\text{-}4][SbF_6]}$. In the ester $\mathbf{[H\text{-}2]^{+\bullet}}$, the counter ion attaches either to the amide NH or to the phenolic OH group ([**H-**

2^{OHONHF}][SbF$_6$] / **[H-2^{OHFNHO}][SbF$_6$]**). In the diamides **[H-3]$^{+\bullet}$** and **[H-4]$^{+\bullet}$**, the counter ion is chelated by the two amide NH groups resulting in a 10-membered ring (**[H-$3^{\mathrm{OHONHFNHF}}$][SbF$_6$]** and **[H-$4^{\mathrm{OHONHFNHF}}$][SbF$_6$]**) and a flipped terminal amide unit (single amide flip). In this tautomer **[H-$4^{\mathrm{OHONHFNHF}}$][SbF$_6$],** the terminal monosubstituted ferrocene unit is oxidized to the ferrocenium ion. The cationic [Fc-NH]$^{+\bullet}$ unit in the latter forms a stronger hydrogen bond to the counter ion than the uncharged [Fc-NH] unit. Yet, coordination of the counter ion to the central amide NH unit switches the oxidation site to the central ferrocene unit. This shifts the positive charge from the terminal ferrocene in the **[H-$4^{\mathrm{OHONHFNHF}}$][SbF$_6$]** valence isomer to the central ferrocene in the **[H-$4^{\mathrm{OHONHONHF\text{-}8}}$][SbF$_6$]** valence isomer. Hence, the conformation and the valence isomeric state of the ferrocenium cations **[H-2]$^{+\bullet}$** – **[H-4]$^{+\bullet}$** depends on the substituents R = COOR, CONHEt and CONHFc, as well as the counter ions.

The conformational and valence isomeric effect of the combined action of electron and proton removal, however, could not be investigated in detail as CO-substituted cyclopentadienyl ligands rings of ferrocenium ions are displaced either by the phenolates or iminolates which form by deprotonation under these conditions.

3.4.4 EXPERIMENTAL SECTION

General Considerations: All reactions were performed under argon atmosphere unless otherwise noted. Dichloromethane was dried over CaH_2 and distilled prior to use. Absolute DMF was used as received from Acros. 1-Chloro-*N*,*N*,2-trimethyl-1-propenylamine (Ghosez' reagent), *N*,*N*-diisopropylethylamine (DIPEA), $P_1{}^t$Bu, and triethylamine were available from Sigma-Aldrich, dried over CaH_2, and stored under argon at 4 °C in a Schlenk tube. 1-[Bis(dimethylamino)methylene]-1H-1,2,3-triazolo[4,5-b]pyridinium 3-oxide hexafluorophosphate (HATU) was commercially available from Novabiochem. CsI was obtained from ABCR. 3,5-Di-*tert*-butyl-2-hydroxy-benzoic acid was available as hydrate from Acros and dried prior to use according to a literature procedure.[14] Boc-Fca-NH-Fc,[16] Boc-Fca-OMe,[19a] Boc-Fca-OH,[19a] and [^{n}Bu$_4$N][B(C_6F_5)$_4$][34] were prepared according to literature procedures. Filtrations from precipitated silver after oxidation were performed with syringe filters (Rotilabo-Spritzenfilter, Ø = 15 mm, pore size = 0.20 µm; Carl Roth GmbH + Co. KG, Germany). NMR spectra were recorded on a Bruker Avance DRX 400 spectrometer at 400.13 MHz (^{1}H) and 100.03 MHz (^{13}C{^{1}H}) at 25 °C. All resonances are reported in ppm versus the solvent signal as internal standard. CD_2Cl_2 (^{1}H: $\delta = 5.32$ ppm; ^{13}C: $\delta = 54.0$ ppm). (s) = singlet, (d) = doublet, (pt) = pseudo triplet (unresolved doublet of doublets). Coupling constants $^nJ_{XY}$ are reported in Hertz (Hz). IR spectra were recorded with a Varian Excalibur Series 3100 FT-IR spectrometer using KBr cells in CH_2Cl_2, and as CsI disks. (s) = strong, (m) = medium, (w) = weak. Electrochemical experiments were carried out on a BioLogic SP-50 voltammetric analyzer using a platinum working electrode, a platinum wire as counter electrode, and a 0.01 M Ag/$AgNO_3$ electrode as reference electrode. The measurements were carried out at a scan rate of 100 mV s^{-1} for cyclic voltammetry experiments and for square wave voltammetry experiments using 0.1 M [^{n}Bu$_4$N][B(C_6F_5)$_4$] as supporting electrolyte and 0.001 M of the sample in CH_2Cl_2. Potentials are given relative to the ferrocene/ferrocenium couple.

Referencing was achieved by addition of decamethylcobaltocene ($E_{1/2}$ = −2.04 V vs. FcH/FcH$^{+•}$ in CH_2Cl_2/[^{n}Bu$_4$N][B(C_6F_5)$_4$]) to the sample.[13] UV/Vis/NIR spectra were recorded on a Varian Cary 5000 spectrometer using 1.0 cm cells (Hellma, suprasil). FD mass spectra were recorded on a FD mass spectra were recorded on a Thermo Fisher DFS mass spectrometer with a LIFDI upgrade. CW EPR spectra (X-band; ca. 9.4 GHz) were measured on a Miniscope MS 300 at 293 K and at 77 K cooled by liquid nitrogen in a finger dewar (Magnettech GmbH, Berlin, Germany). Settings are given at the respective figures. g values are referenced to external Mn$^{2+•}$ in ZnS (g = 2.118, 2.066, 2.027, 1.986, 1.946, 1.906). Simulations of EPR spectra were performed with EasySpin (v 5.0.0)[58] for MatLab (R2015a). For S = 5/2 systems, zerofield splitting parameters were arbitrarily set to D = E = 0.0001 as the resonance width precluded a more detailed analysis. Melting points were determined using a Gallenkamp capillary melting point apparatus MFB 595 010M and were not corrected. Elemental analyses were performed by the microanalytical laboratory of the chemical institutes of the University of Mainz.

Crystal Structure Determination: Intensity data were collected using a Bruker AXS Smart1000 CCD diffractometer equipped with an APEX II detector and an Oxford cooling system using Mo Kα radiation (λ = 0.71073 Å) at 173(2) K and corrected for absorption and other effects. The diffraction frames were integrated using the SAINT package, and most were corrected for absorption with MULABS.[59,60] The structure was solved by direct methods and refined by the full-matrix method based on $F2$ using the SHELXTL software package.[61,62] All non-hydrogen atoms were refined anisotropically, while the positions of all hydrogen atoms were generated with appropriate geometric constraints and allowed to ride on their respective parent atoms with fixed isotropic thermal parameters. A plot with thermal ellipsoids is displayed in Figure 1. Crystallographic data (excluding structure factors) for the structure reported in this paper has been deposited with the Cambridge Crystallographic Data Centre as CCDC 1441949 (1-(*N*-*tert*-butyloxycarbonyl)aminoferrcene-1'-carboxy-*N*'-ethylamide). Copies of the data can be obtained free of charge upon application to CCDC, 12 Union Road, Cambridge CB2 1EZ, U.K. [fax (044) 1223-336-033; e-mail deposit@ccdc.cam.ac.uk].

Density functional calculations were carried out with the ORCA 3.0.2 / DFT series[63] of programs. For geometry optimizations and energy calculations, the B3LYP formulation of density functional theory was used employing the SV(P)[64,65] basis set, the RIJCOSX approximation, approximate Second Order SCF (SOSCF),[66,67] the zeroth order regular approximation (ZORA),[68–70] the KDIIS algorithm, at GRIDX4. No symmetry constraints were imposed on the molecules. The presence of energy minima was checked by numerical frequency calculations; in a few cases, small imaginary frequencies were obtained (Supporting Information). Solvent modelling was done employing the conductor like screening model (COSMO, CH_2Cl_2).[71] The approximate free energies at room temperature were obtained through thermochemical analysis of the frequency calculation, using the thermal correction to Gibbs free energy as reported by ORCA 3.0.2. The ethyl substituents of **H-1** and **H-3** were simplified by methyl groups in all calculations for convergence reasons. Energies of vibrational modes are scaled by 0.9614 as has been suggested for the B3LYP functional.[72] The advanced spectra analysis tool provided with the ORCA program package (orca_asa)[73,74] was employed to fit the experimental UV/Vis absorption spectra of **$[H\text{-}4]^{+\bullet}$** and **$[H\text{-}4]^{2+}$** (Supporting Information, Figure S11).

Synthesis of Boc-Fca-NHEt (H-1): Boc-Fca-OH (1.50 g; 4.35 mmol; 1.0 eq.) was suspended in absolute CH_2Cl_2 (100 ml) and 1-chloro-*N*,*N*,2-trimethyl-1-propenylamine (697 mg; 690 µl; 5.21 mmol; 1.2 eq.) was added to the solution. After stirring for 30 minutes at room temperature, the mixture was added to another flask containing heat dried ethylammonium hydrochloride (886 mg; 10.86 mmol; 2.5 eq.). Triethylamine (3.32 g; 4.2 ml; 32.59 mmol; 7.5 eq.) was added to the mixture over a period of 1 h. The solution was stirred at room temperature overnight. Water (100 ml) was added and the product was extracted with CH_2Cl_2 (3 × 80 ml). The organic phase was washed with 10 % aqueous NaOH solution (3 × 100 ml) and brine (100 ml) and dried over $MgSO_4$. After filtration, the solvent was removed under reduced pressure. The raw product was purified by recrystallization by addition of petroleum ether (boiling point 40 – 60 °C) to a solution in CH_2Cl_2 yielding an orange solid. Yield: 80 % (1.3 g, 3.49 mmol). ^1H NMR (CD_2Cl_2): δ(ppm) = 6.62 (s, 1H, NH^{13}), 6.27 (s, 1H, NH^{14}), 4.56 (s, 2H, $H^{7/10}$), 4.35 – 4.30 (m, 4H, $H^{2/5/8/9}$), 4.02 (pt, 2H, $H^{3/4}$), 3.39 (dq, 2H, $^3J_{HH}$ = 7.3, 5.7 Hz, H^{15}), 1.49 (s, 9H, H^{17a}), 1.23 (t, $^3J_{HH}$ = 7.3 Hz, 3H, H^{16}). ^{13}C NMR (CD_2Cl_2): δ (ppm) = 170.0, 154.3 ($C^{11/12}$), 96.6 (C^1), 80.6 (C^{17}), 79.3 (C^6), 71.2 ($C^{3/4}$), 69.8 ($C^{7/10}$), 66.2 ($C^{8/9}$), 63.9 ($C^{2/5}$), 35.0 (C^{15}), 28.6 (C^{17a}), 15.4 (C^{16}). FD-MS: *m/z* (%) = 372.0 (100) $[M]^{+\bullet}$. UV/Vis/NIR (CH_2Cl_2): λ (ε) = 440 nm (160 M^{-1} cm^{-1}). IR (CsI): $\tilde{\nu}$ = 3330, 3220 (m, NH) cm^{-1}. IR (CH_2Cl_2): $\tilde{\nu}$ = 3440, 3350 (m, NH). $E_{1/2}$ = 55 mV vs. $FcH/FcH^{+\bullet}$ (CH_2Cl_2/[^{n}Bu_4N][$B(C_6F_5)_4$]). R_f (CH_2Cl_2/MeOH 9:1) = 0.58. M.p.: 179 °C. Elemental analysis calcd (%) for $C_{18}H_{24}FeN_2O_3$ (372.11): C 58.08, H 6.50, N 7.53; found C 58.07, H 6.63, N 7.41.

Synthesis of (H-2): Boc-Fca-OMe (295 mg; 0.82 mmol; 1.0 eq.) was dissolved in CH_2Cl_2/TFA (50:50 v/v; 20 ml) and stirred for two hours to remove the Boc group. The solvent was removed under reduced pressure. The residue was dissolved in CH_2Cl_2 (10 ml) and washed with saturated aqueous sodium bicarbonate solution (20 ml), water (20 ml), and brine (20 ml). The organic phase was dried over $MgSO_4$. After filtration, the solvent was removed under reduced pressure. The resulting amine was used without further purification by dissolving in absolute DMF (10 ml) and adding 3,5-di-*tert*-butyl-2-hydroxy benzoic acid (206 mg; 0.82 mmol; 1.0 eq.), HATU (312 mg; 0824 mmol; 1.0 eq.), and DIPEA (128 mg; 168 µl; 0.99 mmol; 1.2 eq.). The solution was stirred at room temperature overnight. Water (100 ml) was added and the product was extracted with CH_2Cl_2 (3 × 40 ml). The organic phase was washed with water (30 ml) and brine (30 ml) and dried over $MgSO_4$. After filtration, the solvent was removed under reduced pressure. The raw product was purified by column chromatography (SiO_2, CH_2Cl_2 / petroleum ether (boiling point 40 – 60 °C) 0:1 → 1:1) resulting in a red-brown solid. Yield: 75 % (304 mg, 0.62 mmol). ^1H NMR (CD_2Cl_2): δ(ppm) = 12.77 (s, 1H, OH^{21}), 7.85 (s, 1H, NH^{22}), 7.57 (d, $^4J_{HH}$ = 2.2 Hz, 1H, H^{18}), 7.52 (d, $^4J_{HH}$ = 2.2 Hz, 1H, H^{16}), 4.85 (pt, 2H, $H^{7/10}$), 4.63 (pt, 2H, $H^{2/5}$), 4.48 (pt, 2H, $H^{8/9}$), 4.17 (pt, 2H, $H^{3/4}$), 3.66 (s, 3H, H^{24}), 1.44 (s, 9H, H^{19a}), 1.39 (s, 9H, H^{20a}). ^{13}C NMR (CD_2Cl_2): δ(ppm) = 172.6 (C^{11}), 171.2 (C^{12}), 159.4 (C^{14}), 140.9 (C^{17}), 138.4 (C^{15}), 129.8 (C^{16}), 120.6 (C^{18}), 113.7 (C^{13}), 93.0 (C^1), 73.1 ($C^{8/9}$), 71.9

($C^{7/10}$), 67.7 ($C^{3/4}$), 66.3 ($C^{2/5}$), 52.4 (C^{24}), 35.7, 35.0 (C^{19}, C^{20}), 31.8 (C^{20a}), 29.7 (C^{19a}). FD-MS: *m/z* (%) = 491.1 (100) $[M]^{+\bullet}$. UV/Vis/NIR (CH_2Cl_2): λ (ε) = 250 (16140), 290 (7650), 320 (9600), 445 nm (500 M^{-1} cm^{-1}). IR (CsI): $\tilde{\nu}$ = 3360 (m, NH) cm^{-1}. IR (CH_2Cl_2): $\tilde{\nu}$ = 3445, 3345 cm^{-1} (m, NH) cm^{-1}. $E_{1/2}$ = 190 mV vs. FcH/$FcH^{+\bullet}$ (CH_2Cl_2/[$^n Bu_4N$][$B(C_6F_5)_4$]). R_f (CH_2Cl_2/petroleum ether (boiling point 40 – 60 °C) 1:1) = 0.3. M.p.: 146 °C. Elemental analysis calcd (%) for $C_{27}H_{33}FeNO_4$ (491.18): C 65.99, H 6.77, N 2.85; found C 66.12, H 7.18, N 2.98.

Synthesis of (H-3): H-1 (200 mg; 0.54 mmol; 1.0 eq.) was dissolved in CH_2Cl_2/TFA (50:50 v/v; 20 ml) and stirred for two hours to remove the Boc group. The solvent was removed under reduced pressure. The residue was dissolved in CH_2Cl_2 (10 ml) and washed with saturated aqueous sodium bicarbonate solution (20 ml), water (20 ml), and brine (20 ml). The organic phase was dried over $MgSO_4$. After filtration, the solvent was removed under reduced pressure. The resulting amine was used without further purification by dissolving in DMF (10 ml) and adding 3,5-di-*tert*-butyl-2-hydroxy benzoic acid (135 mg; 0.54 mmol; 1.0 eq.), HATU (204 mg; 0.54 mmol; 1.0 eq.), and DIPEA (84 mg; 110 µl; 0.64 mmol; 1.2 eq.). The solution was stirred at room temperature overnight. Water (100 ml) was added and the product was extracted with CH_2Cl_2 (3 × 40 ml). The organic phase was washed with water (30 ml) and brine (30 ml) and dried over $MgSO_4$. After filtration, the solvent was removed under reduced pressure. The raw product was purified by column chromatography (SiO_2, CH_2Cl_2) resulting in an orange solid. Yield: 58 % (157 mg, 0.31 mmol). ^1H NMR (CD_2Cl_2): δ(ppm) = 13.08 (s, 1H, OH^{21}), 9.25 (s, 1H, NH^{22}), 7.94 (d, $^4J_{HH}$ = 2.3 Hz, 1H, H^{18}), 7.50 ($^4J_{HH}$ = 2.2 Hz, 1H, H^{16}), 5.97 (s, 1H, NH^{23}), 4.67 (pt, 2H, $H^{7/10}$), 4.46 (pt, 2H, $H^{2/5}$), 4.40 (pt, 2H, $H^{8/9}$), 4.19 (pt, 2H, $H^{3/4}$), 3.30 (dq, 2H, $^3J_{HH}$ = 7.2, 5.8 Hz, H^{24}), 1.43 (s, 9H, H^{19a}), 1.41 (s, 9H, H^{20a}), 1.12 (t, 3H, $^3J_{HH}$ = 7.2 Hz, H^{25}). ^{13}C NMR (CD_2Cl_2): δ(ppm) = 172.3 (C^{12}), 170.7 (C^{11}), 159.5 (C^{14}), 140.7 (C^{17}), 137.9 (C^{15}), 129.3 (C^{16}), 121.9 (C^{18}), 113.8 (C^{13}), 91.7 (C^{1}), 79.2 (C^{6}), 71.9 ($C^{8/9}$), 70.1 ($C^{7/10}$), 68.2 ($C^{2/5}$), 67.9 ($C^{3/4}$), 35.6, (C^{19}), 35.5 (C^{24}), 35.1 (C^{20}), 31.9 (C^{20a}), 29.7 (C^{19a}), 15.2 (C^{25}). FD-MS: *m/z* (%) = 504.2 (100) $[M]^{+\bullet}$. UV/Vis/NIR (CH_2Cl_2): λ (ε) = 250 (14700), 320 (7720), 440 nm (250 M^{-1} cm^{-1}). IR (CsI): $\tilde{\nu}$ = 3420, 3330, 3230 (m, NH) cm^{-1}. IR (CH_2Cl_2): $\tilde{\nu}$ = 3445, 3240 (m, NH) cm^{-1}. $E_{1/2}$ = 170 mV vs. FcH/$FcH^{+\bullet}$ (CH_2Cl_2/[$^n Bu_4N$][$B(C_6F_5)_4$]). R_f (CH_2Cl_2) = 0.23. M.p.: 201 °C. Elemental analysis calcd (%) for $C_{28}H_{36}FeN_2O_3$ (504.21): C 66.67, H 7.19, N 5.55; found C 66.64, H 6.93, N 5.52.

Synthesis of (H-4): Boc-Fca-NH-Fc (497 mg; 0.94 mmol; 1.0 eq.) was dissolved in CH_2Cl_2/TFA (50:50 v/v; 20 ml) and the solution was stirred for two hours to remove the Boc group. The solvent was removed under reduced pressure. The residue was dissolved in CH_2Cl_2 (20 ml) and washed with saturated aqueous sodium bicarbonate solution (40 ml), water (40 ml), and brine (40 ml). The organic phase was dried over $MgSO_4$. After filtration, the solvent was removed under reduced pressure. The resulting amine was used without further purification by dissolving in DMF (20 ml) and adding 3,5-di-*tert*-butyl-2-hydroxy benzoic acid (267 mg; 1.10 mmol; 1.2 eq.), HATU (389 mg; 1.00 mmol; 1.1 eq.), and DIPEA (182 mg; 246 µl; 1.40 mmol; 1.5 eq.). The solution was stirred at room temperature overnight. Water (100 ml) was added and the product was extracted with CH_2Cl_2 (3 × 75 ml). An insoluble precipitate was removed by filtration of the two phase mixture over Celite and washing the solid with water and CH_2Cl_2 until the washing solution were colorless. After separation of the phases, the organic phase was washed with water (50 ml) and brine (50 ml) and dried over $MgSO_4$. After filtration, the solvent was removed under reduced pressure. The raw product was purified by column chromatography (SiO_2, CH_2Cl_2/ethyl acetate 10:1) resulting in an orange/brown solid. Yield: 82 % (510 mg, 0.77 mmol). ^{1}H NMR (CD_2Cl_2): δ(ppm) = 12.90 (s, 1H, OH^{21}), 8.91 (s, 1H, NH^{22}), 7.80 (d, $^4J_{HH}$ = 2.1 Hz, 1H, H^{18}), 7.54 (d, $^4J_{HH}$ = 2.2 Hz, 1H, H^{16}), 7.43 (s, 1H, NH^{23}), 4.71 (pt, 2H, H$^{2'/5'}$), 4.68 (s, 2H, H$^{7/10}$), 4.51 (pt, 2H, H$^{2/5}$), 4.45 (pt, 2H, H$^{3'/4'}$), 4.22 (pt, 2H, H$^{3/4}$), 4.15 (s, 5H, Cp), 3.98 (s, 2H, H$^{8/9}$), 1.45 (s, 9H, H^{19a}), 1.43 (s, 9H, H^{20a}). ^{13}C NMR (CD_2Cl_2): δ(ppm) = 171.9 (C^{12}), 169.1 (C^{11}), 159.5 (C^{14}), 140.8 (C^{17}), 138.2 (C^{15}), 129.7 (C^{16}), 121.3 (C^{18}), 113.8 (C^{13}), 95.3 (C^{6}), 92.6 (C^{1}), 79.1 (C$^{1'}$), 72.2 (C$^{3'/4'}$), 70.4 (C$^{2'/5'}$), 69.8 (Cp), 67.8 (C$^{3/4}$), 67.6 (C$^{2/5}$), 65.1 (C$^{8/9}$), 62.0 (C$^{7/10}$), 35.7 (C^{19}), 35.1 (C^{20}), 31.9 (C^{19a}), 29.7 (C^{20a}). FD-MS: m/z (%) = 660.2 (100) $[M]^{+\bullet}$. UV/Vis/NIR (CH_2Cl_2): λ (ε) = 250 (14620), 280 (12280), 320 (9740), 445 nm (920 M^{-1} cm^{-1}). IR (CsI): $\tilde{\nu}$ = 3300 (m_{br}, NH) cm^{-1}. IR (CH_2Cl_2): $\tilde{\nu}$ = 3430, 3325, 3270 (m, NH) cm^{-1}. $E_{1/2}$ = −120, 390 mV vs. FcH/FcH$^{+\bullet}$ (CH_2Cl_2/$[^nBu_4N][B(C_6F_5)_4]$). R_f (CH_2Cl_2/ethyl acetate 10:1) = 0.44. M.p.: 195 °C. Elemental analysis calcd (%) for $C_{36}H_{40}Fe_2N_2O_3$ (660.42): C 65.47, H 6.11, N 4.24; found C 65.55, H 6.42, N 4.03.

3.4.5 ACKNOWLEDGMENT

We are grateful to Dipl.-Chem. Torben Kienz for helpful discussions and donations of starting materials, Dipl.-Chem. Christoph Kreitner for assistance with DFT calculations, Tatjana Dänzer, Dipl.-Chem. Kim Garth, and Dipl.-Chem. Eduart Grune for preparative assistance, and Minh Thu Pham for analytical assistance.

Keywords: charge transfer, ferrocene, foldamers, valence isomers, epr spectroscopy, switches

3.4.6 REFERENCES

[1] M. Muraoka, H. Irie, Y. Nakatsuji, *Org. Biomol. Chem.* **2010**, *8*, 2408–2413.

[2] S.-Y. Hsueh, C.-T. Kuo, T.-W. Lu, C.-C. Lai, Y.-H. Liu, H.-F. Hsu, S.-M. Peng, C. Chen, S.-H. Chiu, *Angew. Chem.* **2010**, *122*, 9356–9359; *Angew. Chem. Int. Ed.* **2010**, *49*, 9170–9173.

[3] K.-W. Cheng, C.-C. Lai, P.-T. Chiang, S.-H. Chiu, *Chem. Commun.* **2006**, 2854–2856.

[4] C. Clavel, C. Romuald, E. Brabet, F. Coutrot, *Chem. Eur. J.* **2013**, *19*, 2982–2989.

[5] R. Arumugaperumal, V. Srinivasadesikan, M. V. Ramakrishnam Raju, M.-C. Lin, T. Shukla, R. Singh, H.-C. Lin, *ACS Appl. Mater. Interfaces* **2015**, *7*, 26491–26503.

[6] M.-L. Yen, W.-S. Li, C.-C. Lai, I. Chao, S.-H. Chiu, *Org. Lett.* **2006**, *8*, 3223–3226.

[7] O. Sénèque, M.-N. Rager, M. Giorgi, T. Prangé, A. Tomas, O. Reinaud, *J. Am. Chem. Soc.* **2005**, *127*, 14833–14840.

[8] G. A. Hembury, V. V. Borovkov, J. M. Lintuluoto, Y. Inoue, *Chem. Lett.* **2003**, *32*, 428–

429.

[9] K. A. Nielsen, S. Bähring, J. O. Jeppesen, *Chem. Eur. J.* **2011**, *17*, 11001–11007.

[10] Y. Q. Zhang, J. X. Wang, Y. L. Shang, Y. L. Song, L. Jiang, *Appl. Phys. A* **2010**, *102*, 531–536.

[11] K. Guo, Y. Chen, *J. Mater. Chem.* **2009**, *19*, 5790–5793.

[12] A. V. Samoshin, H. Joo, A. Y. Korneichuk, I. S. Veselov, G. V. Grishina, V. V. Samoshin, *Tetrahedron Lett.* **2013**, *54*, 1020–1024.

[13] A. Neidlinger, V. Ksenofontov, K. Heinze, *Organometallics* **2013**, *32*, 5955–5965.

[14] R. Wanke, L. Benisvy, M. L. Kuznetsov, M. F. C. Guedes Da Silva, A. J. L. Pombeiro, *Chem. Eur. J.* **2011**, *17*, 11882–11892.

[15] M. Meot-Ner, *Chem. Rev.* **2005**, *105*, 213–284.

[16] a) K. Heinze, D. Siebler, *Z. Anorg. Allg. Chem.* **2007**, *633*, 2223–2233; b) D. Siebler, M. Linseis, T. Gasi, L. M. Carrella, R. F. Winter, C. Förster, K. Heinze, *Chem. Eur. J.* **2011**, *17*, 4540–4551.

[17] D. Siebler, C. Förster, K. Heinze, *Dalton Trans.* **2011**, *40*, 3558–3575.

[18] S. I. Kirin, H.-B. Kraatz, N. Metzler-Nolte, *Chem. Soc. Rev.* **2006**, *35*, 348–354.

[19] a) L. Barišić, V. Rapić, V. Kovač, *Croat. Chem. Acta* **2002**, *75*, 199–210; b) T. Okamura, K. Sakauye, N. Ueyama, A. Nakamura, *Inorg. Chem.* **1998**, *37*, 6731–6736; c) K. Heinze, M. Schlenker, *Eur. J. Inorg. Chem.* **2004**, 2974–2988.

[20] E. H. van Dijk, D. J. T. Myles, M. H. van der Veen, J. C. Hummelen, *Org. Lett.* **2006**, *8*, 2333–2336.

[21] C. Simão, M. Mas-Torrent, J. Casado-Montenegro, F. Otón, J. Veciana, C. Rovira, *J. Am. Chem. Soc.* **2011**, *133*, 13256–13259.

[22] U. Darbost, V. Penin, E. Jeanneau, C. Félix, F. Vocanson, C. Bucher, G. Royal, I. Bonnamour, *Chem. Commun.* **2009**, *1*, 6774–6776.

[23] P. Neumann, H. Dib, A.-M. Caminade, E. Hey-Hawkins, *Angew. Chem.* **2015**, *127*, 316–319; *Angew. Chem. Int. Ed.* **2015**, *54*, 311–314.

[24] S. K. Brayshaw, J. C. Green, N. Hazari, J. S. McIndoe, F. Marken, P. R. Raithby, A. S. Weller, *Angew. Chem.* **2006**, *118*, 6151–6154; *Angew. Chem. Int. Ed.* **2006**, *45*, 6005–6008.

[25] T. Suzuki, A. Migita, H. Higuchi, H. Kawai, K. Fujiwara, T. Tsuji, *Tetrahedron Lett.* **2003**, *44*, 6837–6840.

[26] M. Scheibitz, R. F. Winter, M. Bolte, H.-W. Lerner, M. Wagner, *Angew. Chem.* **2003**, *115*, 954–957; *Angew. Chem. Int. Ed.* **2003**, *42*, 924–927.

[27] C. Förster, P. Veit, V. Ksenofontov, K. Heinze, *Chem. Commun.* **2015**, *51*, 1514–1516.

[28] A. Neidlinger, C. Förster, K. Heinze, *Eur. J. Inorg. Chem.* **2015**, accepted.

[29] Y. Kondo, in *Supberbases for Organic Synthesis* (Ed.: T. Ishikawa), John Wiley & Sons, Ltd, Chichester, UK, **2009**, pp. 145–185.

[30] N. G. Connelly, W. E. Geiger, *Chem. Rev.* **1996**, *96*, 877–910.

[31] D. Kanamori, A. Furukawa, T. Okamura, H. Yamamoto, N. Ueyama, *Org. Biomol. Chem.* **2005**, *3*, 1453–1459.

[32] W. L. Mock, D. C. Y. Chua, *J. Chem. Soc. Perkin Trans. 2* **1995**, 2069–2074.

[33] P. Taylor, J. Disinger, S. E. Manahan, *Anal. Lett.* **1982**, *15*, 1017–1029.

[34] R. J. LeSuer, C. Buttolph, W. E. Geiger, *J. Organomet. Chem.* **2004**, *76*, 6395–6401.

[35] N. Camire, U. T. Mueller-Westerhoff, W. E. Geiger, *J. Organomet. Chem.* **2001**, *639*, 823–826.

[36] a) K. Heinze, M, Schlenker, *Eur. J. Inorg. Chem.* **2005**, 66–71; b) D. Siebler, C. Förster, K. Heinze, *Eur. J. Inorg. Chem.* **2010**, 523–527.

[37] T. Kienz, C. Förster, K. Heinze, *Organometallics* **2014**, *33*, 4803–4812.

[38] R. A. Marcus, N. Sutin, *Biochim. Biophys. Acta* **1985**, *811*, 265–322.

[39] M. B. Robin, P. Day, *Adv. Inorg. Chem. Radiochem.* **1968**, *10*, 247–422.

[40] K. Heinze, K. Hüttinger, D. Siebler, in *Modelling of Molecular Properties* (Ed.: P. Comba), Wiley-VCH Verlag GmbH & Co. KGaA, Weinheim, **2011**, pp. 325–346.

[41] A. Neidlinger, T. Kienz, K. Heinze, *Organometallics* **2015**, *34*, 5310–5320.

[42] A. Horsfield, A. Wassermann, *J. Chem. Soc., Dalton Trans.* **1972**, 187–188.

[43] R. Aasa, *J. Chem. Phys.* **1970**, *52*, 3919–3930.

[44] D. W. Meek, R. S. Drago, *J. Am. Chem. Soc.* **1961**, *83*, 4322–4325.

[45] R. S. Drago, D. M. Hart, R. L. Carlson, *J. Am. Chem. Soc.* **1965**, *87*, 1900–1904.

[46] J. Tang, J. S. Costa, S. Smulders, G. Molnár, A. Bousseksou, S. J. Teat, Y. Li, G. A. van Albada, P. Gamez, J. Reedijk, *Inorg. Chem.* **2009**, *48*, 2128–2135.

[47] B. Djukic, P. A. Dube, F. Razavi, T. Seda, H. A. Jenkins, J. F. Britten, M. T. Lemaire, *Inorg. Chem.* **2009**, *48*, 699–707.

[48] S. A. Cotton, *Chem. Phys. Lett.* **1976**, *41*, 606–608.

[49] Y. Ting, D. Williams, *Phys. Rev.* **1951**, *82*, 507–510.

[50] R. M. Golding, L. E. Orgel, *J. Chem. Soc.* **1962**, 363–364.

[51] J. P. Hurvois, C. Moinet, *J. Organomet. Chem.* **2005**, *690*, 1829–1839.

[52] P. Lemoine, *J. Organomet. Chem.* **1989**, *359*, 61–69.

[53] R. Prins, A. R. Korswagen, A. G. T. G. Kortbeek, *J. Organomet. Chem.* **1972**, *39*, 335–344.

[54] I. J. Spilners, *J. Organomet. Chem.* **1968**, *11*, 381–384.

[55] J. Holeček, K. Handlíř, J. Klikorka, N. D. Bang, *Collect. Czechoslov. Chem. Commun.* **1979**, *44*, 1379–1387.

[56] R. Prins, *Mol. Phys.* **1970**, *19*, 603–620.

[57] M. Chahma, J. S. Lee, H.-B. Kraatz, *J. Organomet. Chem.* **2002**, *648*, 81–86

[58] S. Stoll, A. Schweiger, *J. Magn. Reson.* **2006**, *178*, 42–55.

[59] *SMART Data Collection and SAINT-Plus Data Processing Software for the SMART System*, (various Versions); Bruker Analytical X-Ray Instruments, Inc., Madison, WI, **2000**.

[60] R. H. Blessing, *Acta Crystallogr.* **1995**, *A51*, 33–38.

[61] G. M. Sheldrick, *SHELXTL*, Version 5.1; Bruker AXS, Madison, WI, **1998**.

[62] G. M. Sheldrick, *SHELXL-97*, University Göttingen, Göttingen, Germany, **1997**.

[63] F. Neese, *Wiley Interdiscip. Rev. Comput. Mol. Sci.* **2012**, *2*, 73–78.

[64] A. Schäfer, H. Horn, R. Ahlrichs, *J. Chem. Phys.* **1992**, *97*, 2571–2577.

[65] F. Weigend, R. Ahlrichs, *Phys. Chem. Chem. Phys.* **2005**, *7*, 3297–3305.

[66] F. Neese, *Chem. Phys. Lett.* **2000**, *325*, 93–98.

[67] T. H. Fischer, J. Almlof, *J. Phys. Chem.* **1992**, *96*, 9768–9774.

[68] E. van Lenthe, E. J. Baerends, J. G. Snijders, *J. Chem. Phys.* **1993**, *99*, 4597–4610.

[69] C. van Wüllen, *J. Chem. Phys.* **1998**, *109*, 392–399.

[70] D. A. Pantazis, X.-Y. Chen, C. R. Landis, F. Neese, *J. Chem. Theory Comput.* **2008**, *4*, 908–919.

[71] S. Sinnecker, A. Rajendran, A. Klamt, M. Diedenhofen, F. Neese, *J. Phys. Chem. A* **2006**, *110*, 2235–2245.

[72] W. Koch, M.C. Holthausen, A Chemist's Guide to Density Functional Theory, Wiley-VCH, Weinheim, **2001**, p. 134.

[73] T. Petrenko, F. Neese, *J. Chem. Phys.* **2007**, *127*, 164319.

[74] T. Petrenko, F. Neese, *J. Chem. Phys.* **2012**, *137*, 234107.

3.5 Attempts to Study the Effects of Internal Dipole Moment on Electron Transfer Rates Within Peptides of 1-Amino-1‘-Ferrocenecarboxylic Acid

Andreas Neidlinger and Katja Heinze*

Abstract

A synthetic approach of oligomers **1^n** and **2^n** of 1-amino-1’-ferrocenecarboxylic acid with thioether end caps by three literature known precursors is presented. The immobilization of these peptide wires allows the investigation of ET rates with respect to the macrodipole moment induced by the amide bonds in the stable secondary structure. The relative stability of diferrocenyl amides **1^2** and **2^2** in various conformations in the neutral, mixed-valent, and fully oxidized state is studied by DFT methods.

3.5.1 INTRODUCTION

The investigation of electron transfer (ET) reactions is the center of many research activities in chemistry and biology.[1–6] Much effort has been put into understanding ET in mixed-valent systems built up of different redox centers[7–11] as well as similar moieties.[12–14] The continuation of miniaturization of electronic devices is in need for molecular electronics and molecular wires, since these building blocks are the smallest possible designs for the future.[15,16] While a lot of research in this field is based on oligophenylene ethynylenes (OPEs),[17–21] these systems incorporate two large drawbacks. To gain electronic conductivity, these wire-like molecules feature highly conjugated π systems, e.g. of 1,4-phenylene rings (e.g. **A**, Figure 1), separated by ethynylene units. While the synthesis of such wires is straightforward,[22–24] their structures are highly rigid, making them incompetent to adapt to geometrical requirements of their environment. Furthermore, π-π stacking between several wires may occur, inducing short-circuits or conductivity perpendicular to the desired path. To overcome both drawbacks, ferrocenyl units come in handy, e.g. by replacing some of the 1,4-phenylene units by 1,1' ferrocenylene moieties.[25] Oligoferrocenes like **B** (Figure 1) are less prone to form π-π stacking interactions and are, in addition, more flexible by the pseudo-C_5 axis of the ferrocene moieties. However, the application of merely hydrocarbon substituted ferrocenylenes lacking further stabilization might just be too flexible to form stable molecular wire structures.

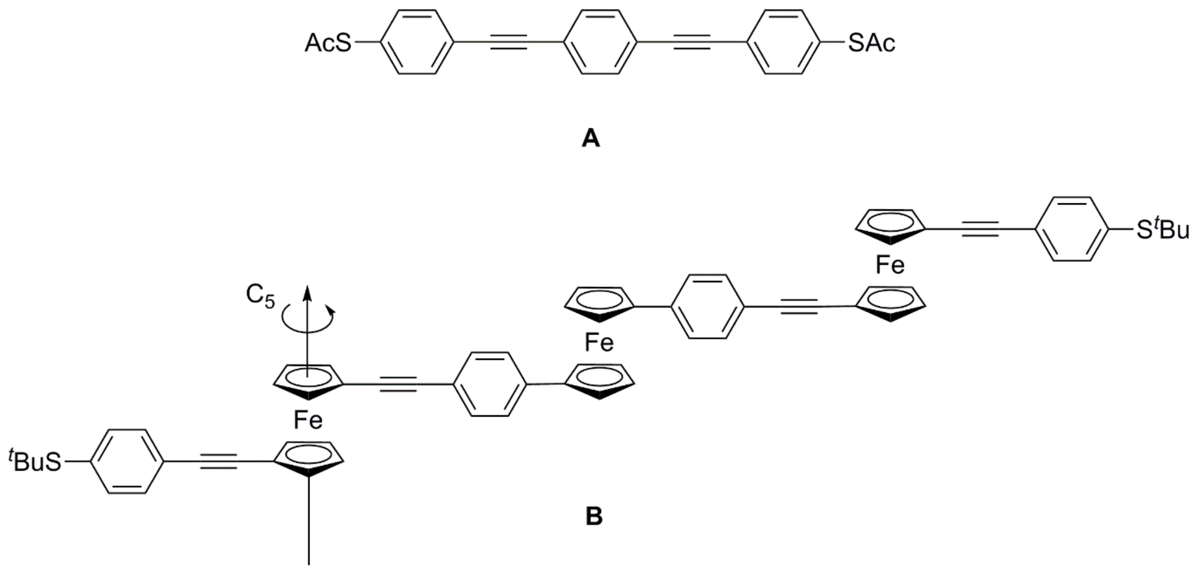

Figure 1. Structures of molecular wires A and B.

To understand the ET processes in these molecular wires, it is essential to investigate the ET mechanisms. While shorter OPEs perform ET by superexchange, utilizing virtual states of the bridging groups, to mix donor and acceptor orbitals, longer OPEs and compounds with redoxactive units (e.g. **B**) show ET by a hopping mechanism. In the superexchange mechanism, the electron is transferred via virtual orbitals of the bridge, which are not thermally accessible. These orbitals, however, allow interaction of donor and acceptor orbitals in a single step.[26] In superexchange ETs, the ET rate decreases exponentially with increasing distance between donor and acceptor group.[27] Upon elongation of the bridge, these virtual orbitals become thermally accessible due to decreasing LUMO and increasing HOMO energies and are rather defined as real orbitals allowing ET by a hopping mechanism. In this electron hopping, the transfer is no longer performed in a single step, but as a multistep charge transfer through the bridge. These ET via hopping mechanisms are usually much faster than superexchange processes. In these cases, the bridge can be considered as a real molecular wire with a linear dependence of the ET rate on the donor acceptor distance.[26,28]

We have been engaged in the synthesis of oligopeptides of 1-aminoferrocene-1‘carboxylic acid **Fca**[13,14,29] and of the respective thiocarboxylic acid **C**.[12] Both types belong to the so called foldamers[30] which realize a stable secondary structure in solution and in the solid state stabilized by intramolecular hydrogen bonds (NH•••O / NH•••S). This is similar to naturally occurring peptides forming α-helices, while oligoferrocenes form zigzag secondary structures.[31] The β-helical structure is obtained by oligomers of **Fca** and alanine for example.[32] The rotational isomers needed for naming of the secondary structures of such oligoferrocenes gives the relative conformation of the substituents (1,1' and 1,2', see Figure 2a).[33] In case of the oxoamides, the thermodynamically favored local structures for oligomers are 1,2'-8-membered rings (**D**),[13,14,29] while the respective thioamides show an increased stability of the 1,2'-6-memberd ring structure (**E**, see Figure 2b).[12]

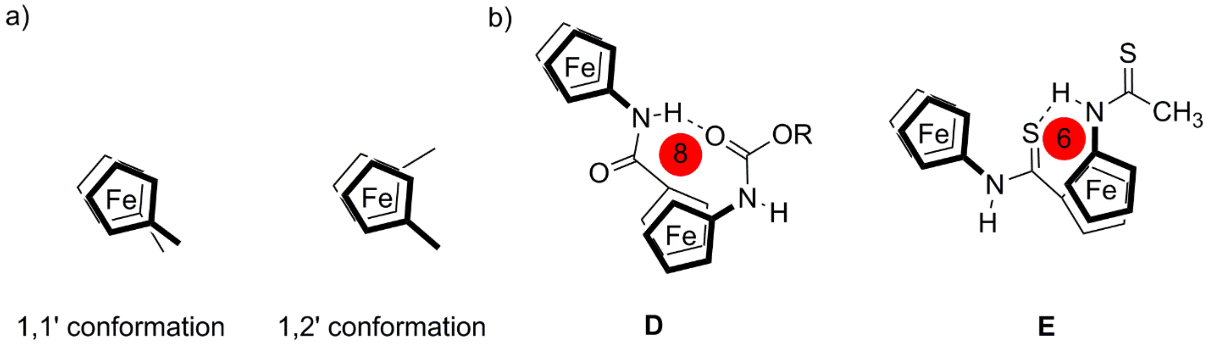

Figure 2. a) Illustration of 1,1' and 1,2' conformations of ferrocenediyl compounds and b) exemplary secondary structures of oxo and thioamides of 1-aminoferrocene-1‘carboxylic acid; R = 9-methoxylfluorenyl.

Other possible secondary structures of such amides are 1,1'-6- and 8-membered rings as well as the extended structure without and IHBs (see Figure 3). These secondary structures are, however, unfavored for oligomers of 1-amino-1'-ferrocenecarboxylic acid as evidenced by spectroscopic data and DFT calculations.[14]

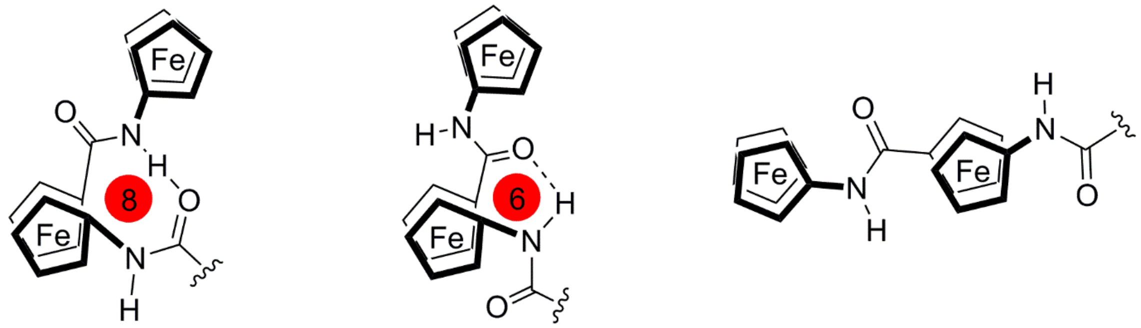

1,1'-8-membered ring 1,1'-6-membered ring extended structure

Figure 3. Illustration of 1,1'-8-membered ring (left), 1,1'-6-membered ring conformation (middle), and extended structure (right) of oligoferrocene amides.

The formation of the stable, well defined secondary structures allows the prediction of molecular properties. For example, the polarity of the amide bonds introduce a local dipole moment ($\mu \approx 3.8$ D per oxoamide bond) in these structures,[13] while the ferrocene units itself have no dipole moment.[34] The single dipoles add up to a macrodipole moment pointing from the negatively charged end to the positively charged terminus (form *C*- to *N*-terminus) in the oligopeptides, as all local amides point roughly in the same direction in the zigzag structure.[13]

In the mixed-valent state, both kinds of oligomers can be described as Robin-Day Class II systems[35] featuring moderate communication between the redox centers (H_{AB} = 140 – 260 cm^{-1}) as calculated from the respective intervalence charge transfer (IVCT) bands employing the Marcus-Hush theory[6] and ET barriers of ca. 30 – 40 kJ mol^{-1} between adjacent Fc/Fc^{+} entities.[12–14,29,36] Thus, they are possibly applicable as molecular wires in ETs with hopping mechanism. However, the influence of the dipole moment on the ET rate in these zigzag shaped oligomers has not yet been explored. Since the macrodipole adds up from the single dipoles, it is essential that the secondary structure is retained upon oxidation, because the amide groups realize an opposite orientation on the transition from 8-membered to 6-membered ring conformation.

Peptide chains of natural α-amino acids forming α-helical structures have been thoroughly investigated concerning their conducting properties.[37–41] The ET in such systems, e.g. in Ru-modified derivative of *Pseudomonas aeruginosa* copper proteins,[38] usually uses the tunneling mechanism and is thus in need of virtual bridge orbitals.[26] Hence, up to a specific limit in distance ($d < 26$ Å), the ET rate decreases exponentially with the distance of both terminal redox centers. In proteins with longer chains, however, a drastic change in ET behavior is observed, since the longer bridging networks allows multi-step electron hopping mechanisms. In this process, redox-active amino acid side chains (or amide groups) act as intermediate ET donors or acceptors, respectively.[38,42] Such electron hopping mechanisms allow for long range ET with only small energy losses. A prominent example is found in photosynthesis, where a hole, generated by excitation in the P680 pigment is transferred to the oxygen evolving complex via a tyrosylate / tyrosyl radical redox couple over ca. 20 Å.[43,44]

The secondary structure of α-helices is a good mediator of electron tunneling[45,46] compared to insulating hydrocarbon chains.[47] This is again due to a gradual change of ET mechanism from electron tunneling to electron hopping, involving the amide groups as intermediate acceptors / donors (amide oxidation). Furthermore, in the correct direction, the macrodipole of the α-helix increases the ET rate.[42,48,49] Understandably, the macrodipole induces an electrostatic field along the helix with a positively charged group at the *N*-terminus and a negatively charged end at the *C*-terminus of the chain. Thus, the respective charge separated states D^+-[α-helix]-A^- are either aligned with this electrostatic field (dipole moment oriented from acceptor to donor) or against this field (dipole moment oriented from donor to acceptor). Clearly, the potential energy of the charge separated state is higher in the latter case, promoting ET in direction of the dipole moment.[49] This is shown by numerous studies evidencing increased ET rates, when the dipole moment and the ET process point into the same direction.[42,48–52]

Molecular self-assembly, e.g. in self-assembled monolayers (SAMs) on gold surfaces, is a tool to study the behavior of suitable molecules as molecular wires,[17,20–22,24] since direct measurement of conductivity is possible e.g. by conductive tip AFM or cyclic voltammetry. Thiols and their derivatives are usually utilized for the assembly of SAMs on gold from solutions. SAMs of **Fca** derivatives have been used in molecular recognition for the detection of proteins and chemical warfare agents.[53,54] To ascertain the measurement on single molecules and close, defect-free packing, it is essential to integrate the molecular wire into an insulating environment. This is achieved by embedding the probe wire itself in insulating alkanethiols of roughly the same chain length as the molecular wire.[20–22,47] Investigations of SAMs of helical peptide chains terminated with various redox active termini have been studied in the literature.[50,55,56] Two molecular photodiodes with different redox active termini, immobilized on a gold substrate along and against the dipole moment of the α-helix has been described (Figure 4). Independent excitation of a single terminus allowed switching of the direction of the photocurrent. Excitation of the electron donating *N*-ethylcarbazolyl group resulted in an anodic photocurrent in direction of the dipole to the gold substrate. When the other terminus (tris(2,2'-bipyridine)ruthenium(II)) was exclusively excited, a cathodic photocurrent, again in direction of the dipole moment, from the gold substrate was detected.[48] Of special interest to our investigation is a study of Kimura *et al.*, which showed that SAMs of α-helical peptide wires with terminal ferrocenyl moieties allowed ET up to 100 Å chain length.[42] These compounds corroborate that electron tunneling is possible along the helices within a timescale of subseconds.[42,51,52,57,58] As mentioned above, the mechanism of ET is strongly dependent on the length of the bridge between donor and acceptor. In these long wires (30 – 110 Å) no electron tunneling but only a hopping mechanism with hole hopping over the amide groups' HOMOs is observed.[42] A graduate change of ET mechanism with elongation is also observed for immobilized oligophenylene wires with ferrocenyl end groups. While for lengths between 5 – 20 Å merely electron tunneling is observed, longer chains (20 – 50 Å) display an electron hopping mechanism.[59]

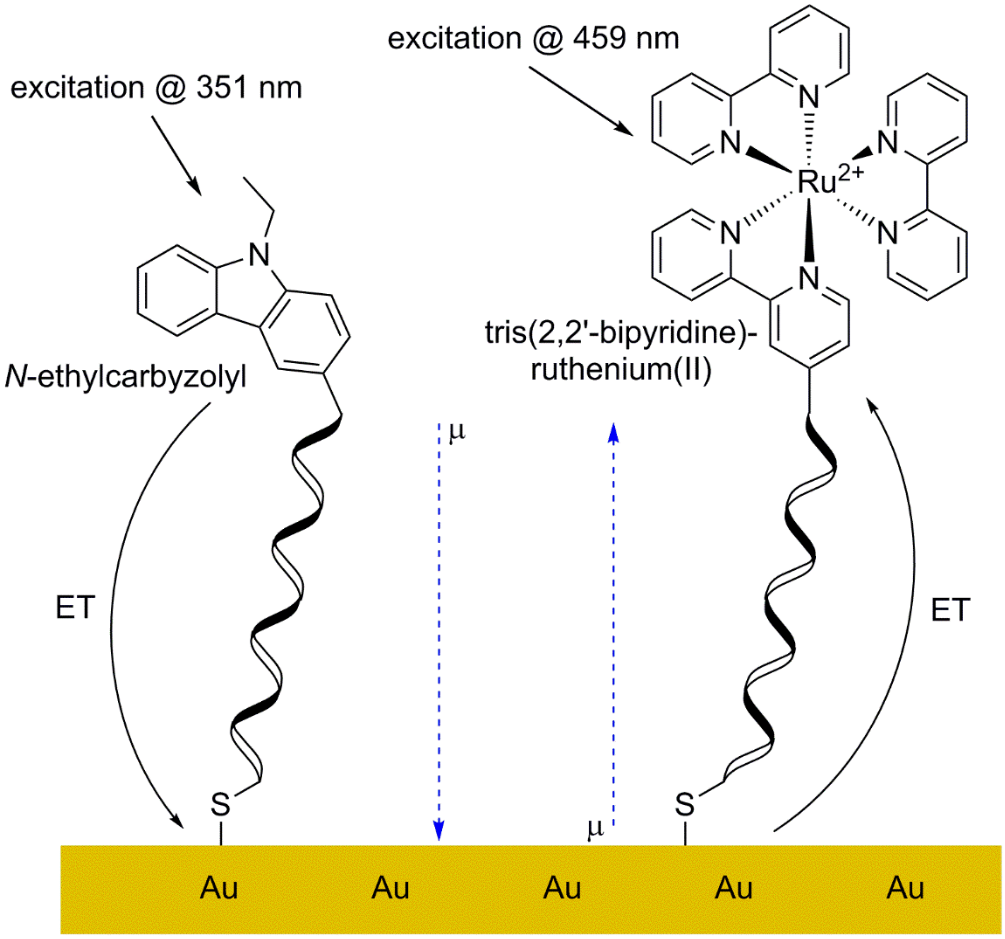

Figure 4. Illustration of molecular photodiodes showing the respective dipole moment orientations and ET directions upon excitation.

While ET along peptide wires in general is widely explored as illustrated above, including the effect of the macrodipole moment of the wires, these effects remain unknown for oligoferrocenyl amides (**D** etc.), in which not only the termini of the amide wires are redox active units, but also the wire backbone contains redox active units. Furthermore, the secondary structure of said wires would be different, since the oligomers of **Fca** form zigzag structures instead of helices, yet with the amide dipoles aligned in the chain direction as well.[13,14,29] In those wires, the bridge mediates ET in both ET mechanisms (electron tunneling and electron hopping). To gain insight into the effects of dipole moment direction in oligoferrocenyl amides, we designed modified dipeptides of **Fca** which can in principle be immobilized on a gold surface by a 4-(methylthio)phenyl unit either along their macrodipole (**1**$^{\mathbf{n}}$) and or against their dipole moment (**2**$^{\mathbf{n}}$), respectively. Other factors influencing redox potential and ET, respectively, like different chemical environments for the single redox centers were essentially eliminated as all redox units are built from 1-amino-1’-ferrocenenecarboxylic acid and thus ET along and against the macrodipole is conceivable (see Figure 4).

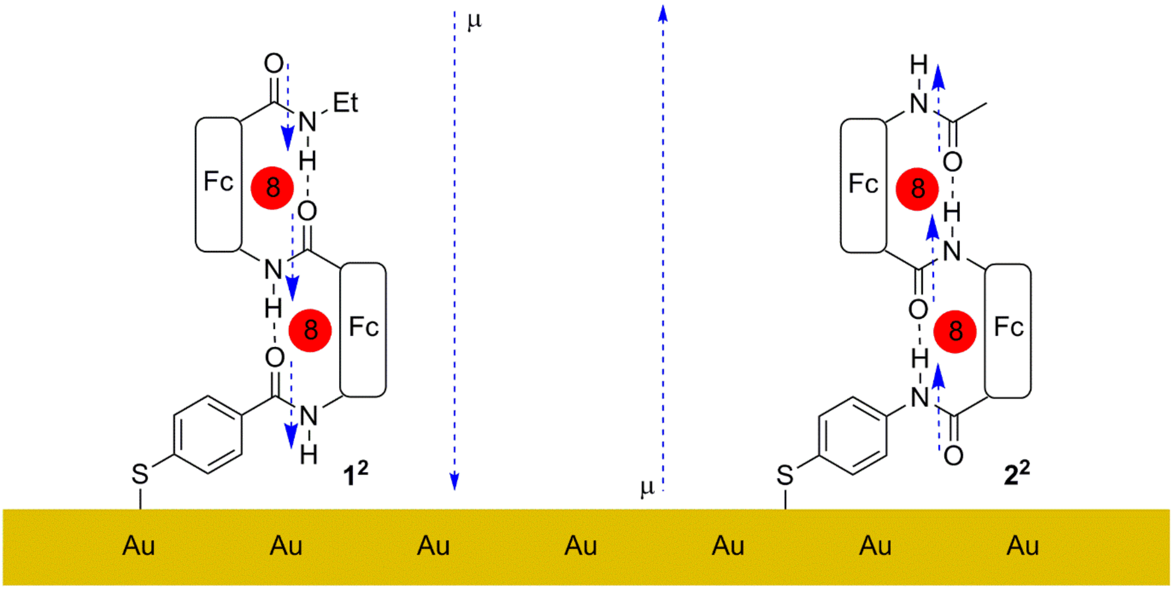

Figure 5. Structures of immobilized dyads 1^2 and 2^2 showing the respective dipole moment orientations; boxes represent ferrocendiyl moieties.

3.5.2 RESULTS AND DISCUSSION

Syntheses: A synthetic plan for both small wires **1**^{n} and **2**^{n} was developed (Scheme 1) and partly executed in the present manuscript. Only three literature known ferrocenyl building blocks (**Boc-Fca-OH**[60], **Boc-Fca-OMe**[60], and **Boc-Fca-NHEt**)[61] and two commercially available thioether end caps (**F** and **G**) are required.

Both compounds are available via standard peptide syntheses with Boc-protected ferrocenyl monomers. For oligomers **1**^{n}, immobilizable along their dipole moment, **Boc-Fca-NHEt**[61] is used as starting material. Immobilization against the macrodipole moment is achieved with oligomers **2**^{n}, when **Boc-Fca-OMe**[60] is used as starting material. The primary step is deprotection of the precursors by a TFA/CH_2Cl_2 (50:50 v/v) mixture and purification of the resulting amines by extraction with aqueous $NaHCO_3$ solution in an analogous manner to literature procedures.[61] Amide coupling is achieved by in situ activation of **Boc-Fca-OH** with 1-chloro-*N*,*N*,2-trimethyl-1-propenylamine (Ghosez'-Reagent) as acid chloride and subsequent reaction with the unprotected amines in presence of triethylamine as auxiliary base. Similar couplings of **Fca** derivatives are described in the literature.[14] This cycle can be repeated until the desired chain length is achieved.

End capping to **1**^{n} is achieved by deprotection of the Boc group (*vide supra*) and coupling of the resulting amine with commercially available 4-(methylthio)benzoylchloride (**F**) in presence of triethylamine. For the preparation of **2**^{n}, exchange of protecting groups is achieved by Boc-deprotection (*vide supra*) and coupling of the amine with acetylchloride in presence of triethylamine. After removal of the methylester group with a MeOH/H_2O mixture containing a slight excess of KOH, similar to literature procedures,[60,62] and in situ activation of the acid by

Ghosez' reagent (*vide supra*), the acid chloride is coupled with commercially available 4-(methylthio)aniline (**G**) in the presence of triethylamine.

Scheme 1. Suggested retrosynthetic pathway to the oligomers 1^n and 2^n.

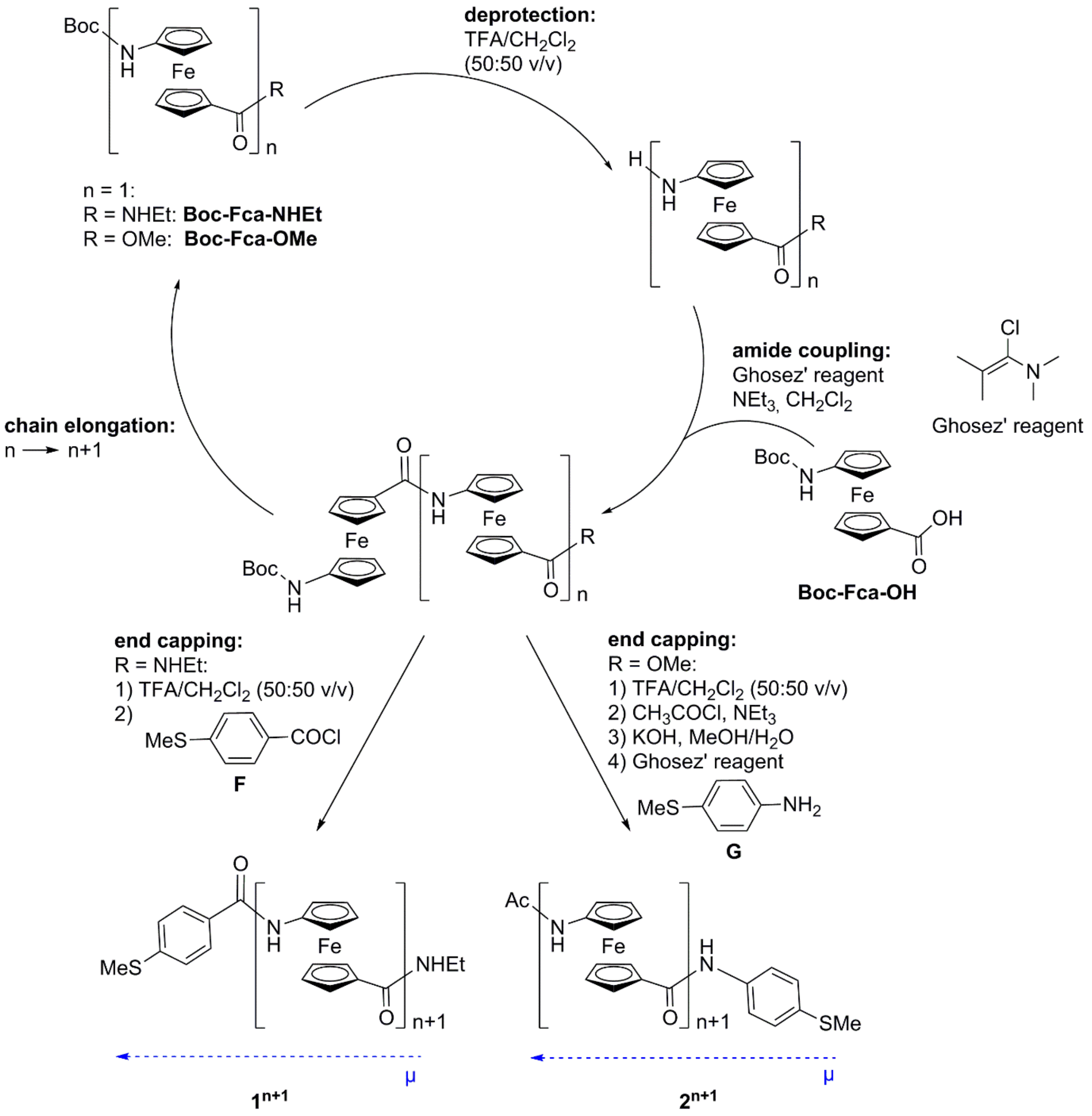

Theoretical Investigations: Dipeptides $\mathbf{1^2}$ and $\mathbf{2^2}$ were investigated in DFT studies to get some insight into the conformational properties, dipole moments, and charging properties. Similar to previous studies[13,14] two reasonable secondary structures (8-membered ring and 6-membered ring) are possible, concerning the intramolecular hydrogen bonds between the amide groups. For both compounds, the 1,2'-8-membered ring conformations ($\mathbf{1^2}$**-8** and $\mathbf{2^2}$**-8**) are the thermodynamically favored geometries, while the 1,2'-6-membered ring conformers are 5 ($\mathbf{1^2}$**-6**) and 15 kJ mol^{-1} ($\mathbf{2^2}$**-6**) higher in energy (see Figure 6).

Furthermore, the mixed-valent (**[1^2]**$^+$ / **[2^2]**$^+$)and fully oxidized (**[1^2]**$^{2+}$ / **[2^2]**$^{2+}$) structures were investigated. No interaction of counterions with the amide protons was studied, since the measurements of the resulting SAMs will be performed in a non-coordinating environment with [^{n}Bu$_4$N][B(C$_6$F$_5$)$_4$][63,64] as weakly coordinating electrolyte. For the mixed-valent form also two possible conformations (6-membered and 8-membered ring) and two valence isomers (bridging or terminal Fc oxidized) are conceivable. The terminally oxidized valence isomers will be **[1^2-6a]**$^+$, **[1^2-8a]**$^+$, **[2^2-6a]**$^+$, and **[2^2-8a]**$^+$, while the valence isomers oxidized at the bridging ferrocendiyl moiety will be named **[1^2-6b]**$^+$, **[1^2-8b]**$^+$, **[2^2-6b]**$^+$, and **[2^2-8b]**$^+$. Since both ferrocenes in the two investigated compounds share a similar electronic environment in a first approximation, both possible valence isomeric states differ only very little in energy. However, DFT results show energy differences between 11 and 28 kJ mol^{-1} between the various mixed-valent states (*vide infra*).

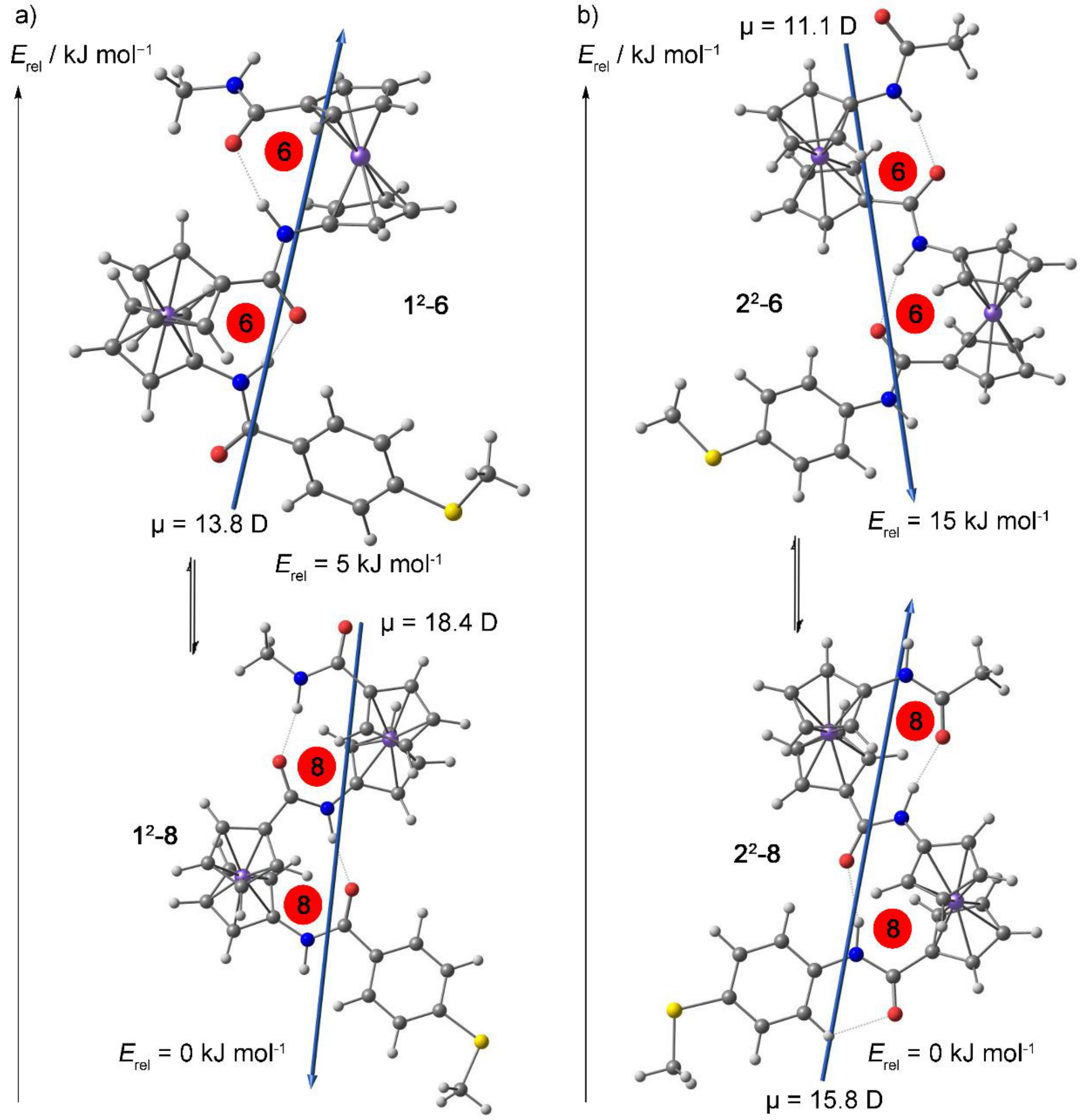

Figure 6. DFT optimized geometries and energy differences (B3LYP/SV(P)/COSMO:CH$_2$Cl$_2$) of a) 1^2-6 and 1^2-8, and b) 2^2-6 and 2^2-8. Blue vectors represent macrodipole moment.

For the mixed-valent state of peptide **1^2**, calculations were only successful for the structures in which the bridging ferrocene is oxidized (**[1^2-6b]**$^+$ and **[1^2-8b]**$^+$). Despite various attempts were made to converge to the terminally oxidized valence isomers (**[1^2-6a]**$^+$ and **[1^2-8a]**$^+$) only the valence isomers **[1^2-6b]**$^+$ and **[1^2-8b]**$^+$ were accessible. In contrast to the neutral compound, the 8-membered ring conformer **[1^2-8b]**$^+$ with two IHBs is higher in energy compared to the 6-membered ring conformer **[1^2-6b]**$^+$ (Figure 7). Furthermore, in **[1^2-6b]**$^+$ merely a single strong intramolecular hydrogen bond forms between the bridging amide proton and the terminal amide group's oxygen atom with an NH•••O distance of 1.83 Å. The oxidized Fc$^+$ moiety on the other hand prefers only a weak hydrogen bond with an NH•••O distance of 2.83 Å in **[1^2-6b]**$^+$. This is not easily explained, since ferrocenium amides are usually stronger hydrogen bond acceptors than the corresponding neutral ferrocene amides.[11,14,65] However, the weak intramolecular 6-ring hydrogen bond in **[1^2-6b]**$^+$ is still favored over the non-hydrogen bonded environment for this amide proton in **[1^2-8b]**$^+$.

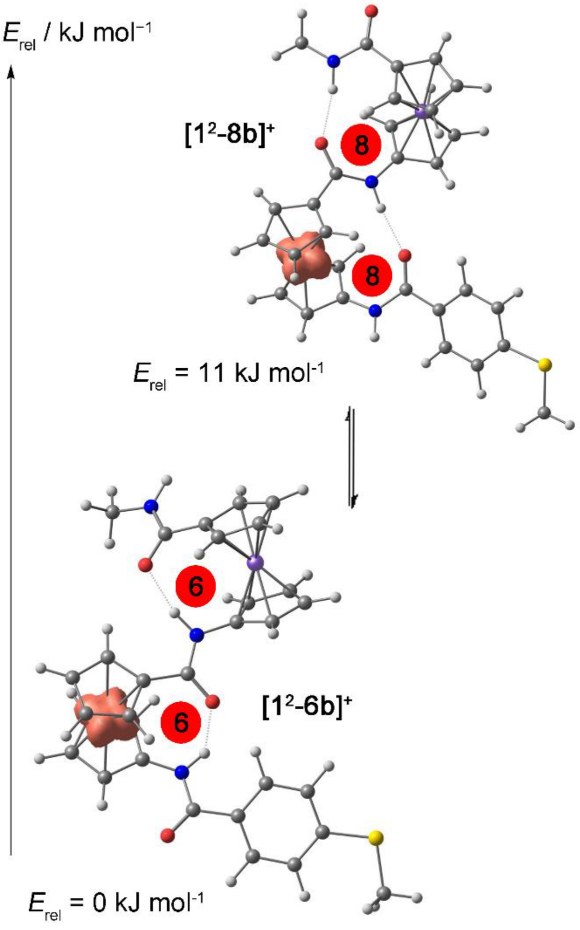

Figure 7. DFT optimized geometries and energy differences (B3LYP/SV(P)/COSMO:CH_2Cl_2) of [1^2-6b]$^+$ and [1^2-8b]$^+$.

Comparable theoretical results are found for the *N*-terminal wire **2^2** for which successful convergence was achieved for **[2^2-8b]**$^+$, **[2^2-6a]**$^+$, and **[2^2-6b]**$^+$, while terminally oxidized **[2^2-**

8a]$^+$ was not accessible by DFT calculations. The 8-ring structure **[2^2-8b]**$^+$ with two intramolecular 8-ring hydrogen bonds represents the energy minimum, followed by the terminally oxidized 6-ring **[2^2-6a]**$^+$ (+18 kJ mol^{-1}). In **[2^2-6a]**$^+$, the terminal ferrocenium moiety is not hydrogen bonded (or merely in a weak hydrogen bond). The valence isomer charged at the bridging ferrocene **[2^2-6b]**$^+$, which again features two intramolecular 6-membered ring hydrogen bonds, is even higher in energy (+28 kJ mol^{-1}) (Figure 8). Again, hydrogen bonding of the Fc$^+$-NH protons is essential and has a significant influence on the stability of the different conformers. In **[2^2-8b]**$^+$ two stable 8-ring hydrogen bonds are present, which allow the above mentioned coordination of the Fc$^+$-NH hydrogen atom. Hence, **[2^2-8b]**$^+$ is the minimum energy conformer in contrast to **[1^2-8b]**$^+$, which was disfavored over **[1^2-6b]**$^+$ do to the missing hydrogen bond at the Fc$^+$-NH moiety (*vide supra*). **[2^2-6b]**$^+$, however, is the highest energy structure, due to unfavored 6-ring hydrogen bonds, which disturb coplanar alignment of substituents containing π orbitals for Fc$^+$ compounds.[66] The remaining **[2^2-6a]**$^+$ is also disfavored over **[2^2-8b]**$^+$ because of the 6-ring conformation. It can be assumed that the middle amide group is forced in the hydrogen bond, albeit it also favors coplanar arrangement with the ferrocenyl group (*vide supra*), whereas the terminal group in **[2^2-6a]**$^+$ allows cleavage of the respective hydrogen bond. Interestingly, **[2^2-6a]**$^+$ again only forms a weak hydrogen bond at the Fc$^+$-NH group with a NH•••O distance of 3.26 Å. This is again attributed to the preferred coplanar alignment. The preference of hydrogen bonding versus coplanar alignment is just in favor of the latter for **[2^2-6a]**$^+$.

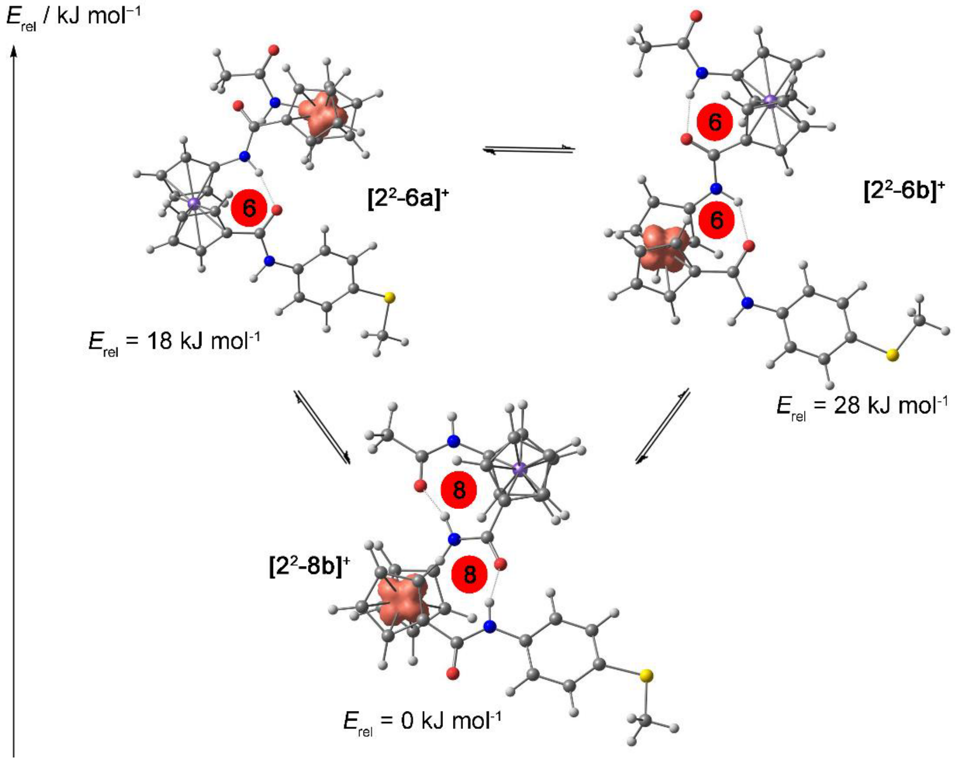

Figure 8: DFT optimized geometries and energy differences (B3LYP/SV(P)/COSMO:CH_2Cl_2) of [2^2-8b]$^+$, [2^2-6a]$^+$, and [2^2-6b]$^+$.

The fully oxidized compounds are again able to form 6-ring and 8-ring structures (**[1^2-6]$^{2+}$** and **[1^2-8]$^{2+}$** as well as **[2^2-6]$^{2+}$** and **[2^2-8]$^{2+}$**). In addition to the two conformers, also the open conformations with broken intramolecular hydrogen bonds were calculated similar to previous DFT studies, suggesting the expansion/unfolding of oligoferrocenyl amides in the fully oxidized state.[13,14] Unfortunately, the 8-ring conformers **[1^2-8]$^{2+}$**, **[2^2-8]$^{2+}$**, and the extended structure of **[1^2]$^{2+}$** are not accessible by the applied DFT methods. However, the 6-membered-ring conformer **[1^2-6]$^{2+}$** was successfully calculated. The remaining calculations show higher stability of the 6-ring conformer **[2^2-6]$^{2+}$** versus the unfolded structure **[2^2]$^{2+}$** by 8 kJ mol^{-1} (Figure 9), in contrast to previous calculations for similar compounds.[13,14]

In conclusion, stable immobilization in the desired direction of the macrodipole in the thermodynamically stable 8-membered ring conformation is expected for **1^2** and **2^2**. However, the conservation of the oriented macrodipole moment remains uncertain in the mixed-valent state of **1^2**, since a conformational change to the 6-membered ring conformer **[1^2-6b]$^+$** is expected according to DFT calculations (Figure 7). For **2^2**, however, the 8-membered ring is retained in the mixed valent state **[2^2-8b]$^+$** (Figure 8). Upon full oxidation, both peptides show increased stability of the 6-membered ring conformation, while the breakage of the intramolecular hydrogen bonds expected by comparison with the literature[13,14] is unfavored (Figure 9. Yet, reliable experimental conformational analysis is required in addition to DFT results to ascertain the conservation of the secondary structure and the macrodipole, respectively.

As mentioned above, it is furthermore necessary to dilute the analyte in an insulating environment of alkanethiols of roughly the same chain length for SAM preparation. [20–22,47] As shown in Figure 4 for the neutral compounds **1^2** and **2^2** in their most stable 8-membered ring conformations, the approximate chain length from sulfur to terminal methyl group is 14.9 and 14.5 Å for **1^2-8** and **2^2-8**, respectively. Therefore, commercially available ^{n}decyl methyl sulfide **F** can be employed as insulator. The chain length from sulfur to the terminal methyl group was calculated as 13.0 Å (Figure 10).

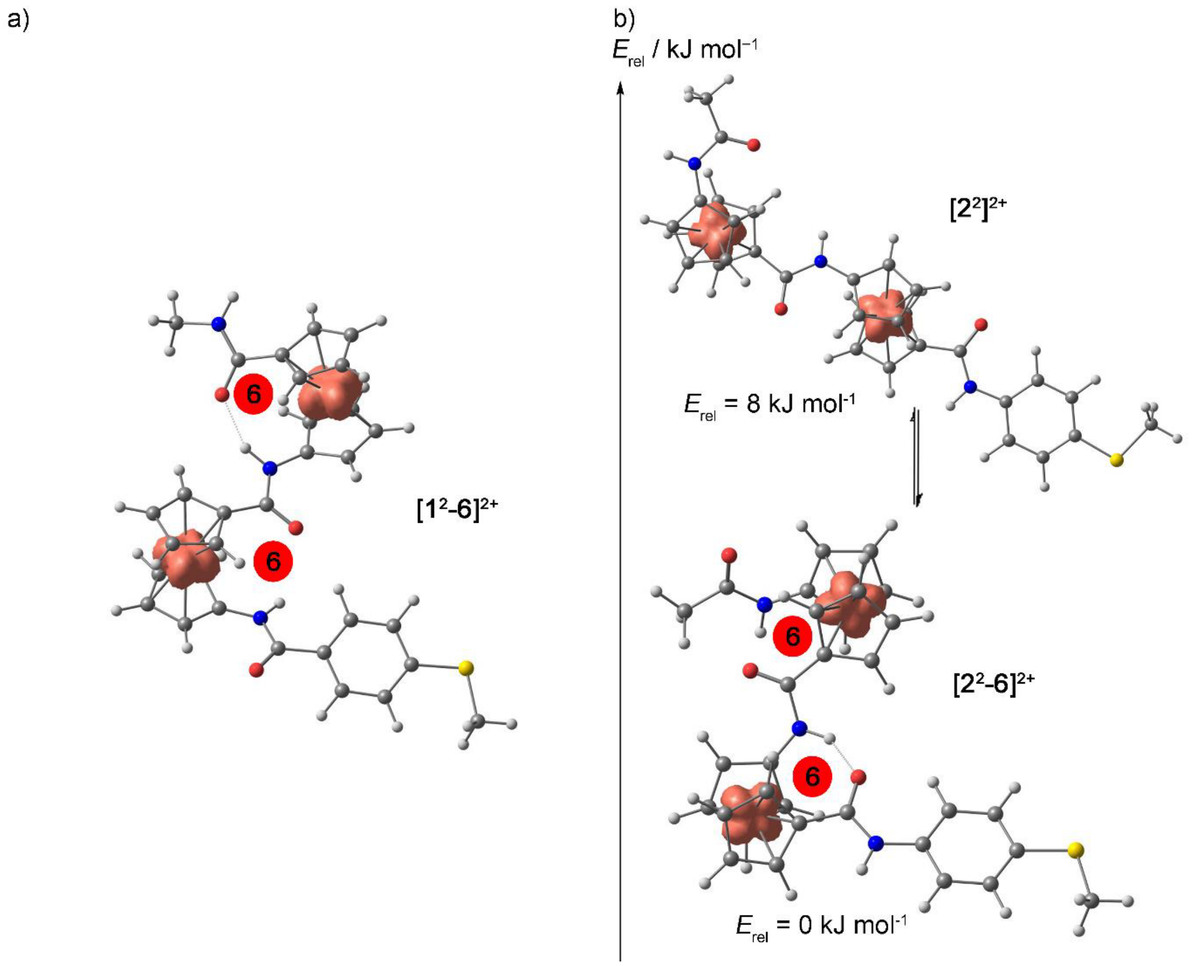

Figure 9. DFT optimized geometries and energy differences (B3LYP/SV(P)/COSMO:CH_2Cl_2) of a) $[1^2\text{-}6]^{2+}$ and b) $[2^2\text{-}6]^{2+}$ and $[2^2]^{2+}$.

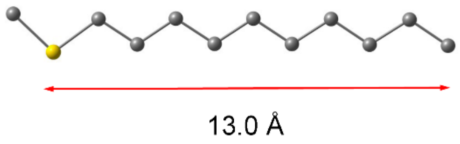

Figure 10. DFT optimized geometry of ″decyl methyl sulfide F showing the calculated chain length (B3LYP/SV(P)/COSMO:CH_2Cl_2; hydrogen atoms omitted).

3.5.3 CONCLUSIONS

Two molecular wire peptides $\mathbf{1^2}$ and $\mathbf{2^2}$ were retrosynthetically designed, which should allow formation of SAMs with the macrodipole moment pointing to the electrode surface ($\mathbf{1^2}$) or in the opposite direction ($\mathbf{2^2}$). The macrodipole moment is induced by the individual secondary zigzag structure formed by the amide groups. The conformational characteristics were calculated by DFT methods to gain insight into the stability of the secondary structures as well as the expected behavior upon single and full oxidation. Unfortunately, not all conceivable valence isomers and conformers were accessible by those calculations, but for the neutral state of both compounds, the 8-membered ring structure was calculated as most stable structure in accordance with similar peptides in the literature. Hence, SAM formation should result in the desired dipole orientation in the neutral state. However, the calculations of the mixed valent states showed different stabilities of the secondary structures. Peptide $\mathbf{2^2}$, with the macrodipole moment pointing away from the electrode surface, preserves the 8-membered ring conformation by oxidation of the bridging ferrocene unit ($\mathbf{[2^2\text{-}8b]^+}$) upon single oxidation according to DFT calculations. This conformation is expected to be unstable for compound $\mathbf{1^2}$. The isomer with the macrodipole moment pointing to the electrode surface shows increased stabilization of the 6-membered ring conformer $\mathbf{[1^2\text{-}6b]^+}$, while $\mathbf{[1^2\text{-}8b]^+}$ is less favored. Unfortunately, this conformational change will result in an inversion of the dipole moment, rendering the desired measurement of ET in dependence of the dipole moment difficult. Anyhow, a well packed SAM utilizing **F** as diluting agent might stabilize the desired 8-ring conformation during the measurements. Furthermore, ET in SAMs of 22 alone also allow the investigation of ET in both directions (with / against macrodipole moment), since an anodic and a cathodic potential can be applied on the gold substrate. Further conformational studies and stable SAMs need to be investigated experimentally. Additionally, the analysis of wires with more than two ferrocene moieties, which are also accessible by the presented retrosynthetic approach, is essential due to the higher stability of the secondary structures. Longer chains will allow the study of ET rates with respect to chain length as well.

3.5.4 EXPERIMENTAL SECTION

Density Functional Calculations: These were carried out with the ORCA 3.0.2 / DFT series[67] of programs. For geometry optimizations and energy calculations, the B3LYP formulation of density functional theory was used employing the SV(P)[68,69] basis set, the RIJCOSX approximation, approximate Second Order SCF (SOSCF),[70,71] the zeroth order regular approximation (ZORA),[72–74] the KDIIS algorithm, at GRIDX4. No symmetry constraints were imposed on the molecules. The presence of energy minima of the ground states was checked by numerical frequency calculations. Solvent modelling was done employing the conductor like screening model (COSMO, CH_2Cl_2).[75] The approximate free energies at 298 K were obtained through thermochemical analysis of the frequency calculation, using the thermal correction to Gibbs free energy as reported by ORCA 3.0.2. The ethyl group of $\mathbf{1^2}$ and all its ET products and various conformers was exchanged by a methyl group in DFT calculations for convergence reasons.

3.5.5 ACKNOWLEDGMENT

We are grateful to Dipl.-Chem. Torben Kienz for helpful discussions and Dipl.-Chem. Nils Friedrich and Minh Thu Pham for preparative assistance. Parts of this research were conducted using the supercomputer Mogon and advisory services offered by Johannes Gutenberg-University Mainz (www.hpc.uni-mainz.de), which is a member of the AHRP and the Gauss Alliance e. V.

3.5.6 REFERENCES

[1] G. L. Closs, J. R. Miller, *Science* **1988**, *240*, 440–447.

[2] R. A. Marcus, *Angew. Chem.* **1993**, *105*, 1161–1172; *Angew. Chem. Int. Ed.* **1993**, *32*, 1111–1121.

[3] P. F. Barbara, T. J. Meyer, M. A. Ratner, *J. Phys. Chem.* **1996**, *100*, 13148–13168.

[4] M. D. Newton, *Chem. Rev.* **1991**, *91*, 767–792.

[5] J. R. Winkler, H. B. Gray, *Annu. Rev. Biochem.* **1996**, *65*, 537–561.

[6] R. A. Marcus, N. Sutin, *Biochim. Biophys. Acta* **1985**, *811*, 265–322.

[7] J. Dietrich, U. Thorenz, C. Förster, K. Heinze, *Inorg. Chem.* **2013**, *52*, 1248–1264.

[8] J. Dietrich, A. Wünsche Von Leupoldt, M. Grabolle, U. Resch-Genger, K. Heinze, *Eur. J. Inorg. Chem.* **2013**, 3009–3019.

[9] A. Breivogel, S. Wooh, J. Dietrich, T. Y. Kim, Y. S. Kang, K. Char, K. Heinze, *Eur. J. Inorg. Chem.* **2014**, 2720–2734.

[10] H. Huesmann, C. Förster, D. Siebler, T. Gasi, K. Heinze, *Organometallics* **2012**, *31*, 413–427.

[11] A. Neidlinger, V. Ksenofontov, K. Heinze, *Organometallics* **2013**, *32*, 5955–5965.

[12] T. Kienz, C. Förster, K. Heinze, *Organometallics* **2014**, *33*, 4803–4812.

[13] D. Siebler, M. Linseis, T. Gasi, L. M. Carrella, R. F. Winter, C. Förster, K. Heinze, *Chem. Eur. J.* **2011**, *17*, 4540–4551.

[14] D. Siebler, C. Förster, K. Heinze, *Dalton Trans.* **2011**, *40*, 3558–3575.

[15] R. L. Carroll, C. B. Gorman, *Angew. Chem.* **2002**, *114*, 4556–4579; *Angew. Chem. Int. Ed.* **2002**, *41*, 4378–4400.

[16] J. M. Tour, *Molecular Electronics: Commercial Insights, Chemistry, Devices, Architecture and Programming*, World Scientific, Singapore, **2003**.

[17] D. K. James, J. M. Tour, *Top. Curr. Chem.* **2005**, *257*, 33–62.

[18] C. Thiele, L. Gerhard, T. R. Eaton, D. M. Torres, M. Mayor, W. Wulfhekel, H. V. Löhneysen, M. Lukas, *New J. Phys.* **2015**, *17*, 053043.

[19] V. Kaliginedi, A. V. Rudnev, P. Moreno-García, M. Baghernejad, C. Huang, W. Hong, T. Wandlowski, *Phys. Chem. Chem. Phys.* **2014**, *16*, 23529–23539.

[20] A. M. Moore, B. A. Mantooth, A. A. Dameron, Z. J. Donhauser, P. A. Lewis, R. K. Smith, D. J. Fuchs, P. S. Weiss, *Front. Mater. Res.* **2008**, *10*, 29–47.

[21] J. M. Seminario, *Nat. Mater.* **2005**, *4*, 111–113.

[22] J. M. Tour, *Acc. Chem. Res.* **2000**, *33*, 791–804.

[23] J.-J. Hwang, J. M. Tour, *Tetrahedron* **2002**, *58*, 10387–10405.

[24] D. L. Pearson, J. M. Tour, *J. Org. Chem.* **1997**, *62*, 1376–1387.

[25] J. Ma, N. Krauße, H. Butenschön, *Eur. J. Org. Chem.* **2015**, *2015*, 4510–4518.

[26] M. Natali, S. Campagna, F. Scandola, *Chem. Soc. Rev.* **2014**, *43*, 4005–4018.

[27] E. G. Petrov, Y. R. Zelinskyy, V. May, *J. Phys. Chem. B* **2002**, *106*, 3092–3102.

[28] Y.-T. Long, E. Abu-Irhayem, H.-B. Kraatz, *Chem. Eur. J.* **2005**, *11*, 5186–5194.

[29] K. Heinze, D. Siebler, *Z. Anorg. Allg. Chem.* **2007**, *633*, 2223–2233.

[30] C. Bao, B. Kauffmann, Q. Gan, K. Srinivas, H. Jiang, I. Huc, *Angew. Chem.* **2008**, *120*, 4221–4224; *Angew. Chem. Int. Ed.* **2008**, *47*, 4153–4156.

[31] G. A. Petsko, D. Ringe, *Protein Structure and Function*, New Science Press Ltd., London, **2004**.

[32] S. Chowdhury, G. Schatte, H.-B. Kraatz, *Angew. Chem.* **2006**, *118*, 7036–7038; *Angew. Chem. Int. Ed.* **2006**, *45*, 6882–6884.

[33] S. I. Kirin, H.-B. Kraatz, N. Metzler-Nolte, *Chem. Soc. Rev.* **2006**, *35*, 348–354.

[34] S. Sorriso, H. Lumbroso, *Tetrahedron* **1970**, *26*, 2695–2701.

[35] M. B. Robin, P. Day, *Adv. Inorg. Chem. Radiochem.* **1968**, *10*, 247–422.

[36] K. Heinze, K. Hüttinger, D. Siebler, in *Model. Mol. Prop.* (Ed.: P. Comba), Wiley-VCH Verlag GmbH & Co. KGaA, Weinheim, **2011**, pp. 325–346.

[37] D. S. Bendall, *Protein Electron Transfer*, BIOS Scientific Ltd., Oxford, UK, **1996**.

[38] C. Shih, A. K. Museth, M. Abrahamsson, A. M. Blanco-Rodriguez, A. J. Di Bilio, J. Sudhamsu, B. R. Crane, K. L. Ronayne, M. Towrie, A. Viček, J. H. Richards, J. R. Winkler, H. B. Gray, *Science* **2008**, *320*, 1760–1762.

[39] D. N. Beratan, J. N. Betts, J. N. Onuchic, *Science* **1991**, *252*, 1285–1288.

[40] R. Langen, J. L. Colón, D. R. Casimiro, T. B. Karpishin, J. R. Winkler, H. B. Gray, *J. Biol. Inorg. Chem.* **1996**, *1*, 221–225.

[41] H. B. Gray, J. R. Winkler, *Chem. Phys. Lett.* **2009**, *483*, 1–9.

[42] Y. Arikuma, H. Nakayama, T. Morita, S. Kimura, *Angew. Chem.* **2010**, *122*, 1844–1848; *Angew. Chem. Int. Ed.* **2010**, *49*, 1800–1804.

[43] K. N. Ferreira, T. M. Iverson, K. Maghlaoui, *Science* **2004**, *303*, 1831–1838.

[44] C. Tommos, G. T. Babcock, *Biochim. Biophys. Acta* **2000**, *1458*, 199–219.

[45] M. Sisido, S. Hoshino, H. Kusano, M. Kuragaki, M. Makino, H. Sasaki, T. A. Smith, K. P. Ghiggino, *J. Phys. Chem. B* **2001**, *105*, 10407–10415.

[46] S. Sek, A. Misicka, K. Swiatek, E. Maicka, *J. Phys. Chem. B* **2006**, *110*, 19671–19677.

[47] J. F. Smalley, H. O. Finklea, C. E. D. Chidsey, M. R. Linford, S. E. Creager, J. P. Ferraris, K. Chalfant, T. Zawodzinsk, S. W. Feldberg, M. D. Newton, *J. Am. Chem. Soc.* **2003**, *125*, 2004–2013.

[48] S. Yasutomi, T. Morita, Y. Imanishi, S. Kimura, *Science* **2004**, *304*, 1944–1947.

[49] E. Galoppini, M. A. Fox, *J. Am. Chem. Soc.* **1996**, *118*, 2299–2300.

[50] S. Sek, A. Tolak, A. Misicka, B. Palys, R. Bilewicz, *J. Phys. Chem. B* **2005**, *109*, 18433–18438.

[51] K. Takeda, T. Morita, S. Kimura, *J. Phys. Chem. B* **2008**, *112*, 12840–12850.

[52] T. Morita, S. Kimura, *J. Am. Chem. Soc.* **2003**, *125*, 8732–8733.

[53] K. A. Mahmoud, H.-B. Kraatz, *Chem. Eur. J.* **2007**, *13*, 5885–5895.

[54] M. A. K. Khan, Y.-T. Long, G. Schatte, H.-B. Kraatz, *Anal. Chem.* **2007**, *79*, 2877–2884.

[55] J. J. Wei, C. Schafmeister, G. Bird, a. Paul, R. Naaman, D. H. Waldeck, *J. Phys. Chem. B* **2006**, *110*, 1301–1308.

[56] H. B. Kraatz, I. Bediako-Amoa, S. H. Gyepi-Garbrah, T. C. Sutherland, *J. Phys. Chem. B* **2004**, *108*, 20164–20172.

[57] M. Kai, K. Takeda, T. Morita, S. Kimura, *J. Pept. Sci.* **2008**, *14*, 192–202.

[58] Y. Arikuma, K. Takeda, T. Morita, M. Ohmae, S. Kimura, *J. Phys. Chem. B* **2009**, *113*, 6256–6266.

[59] F. Li, V. M. Basile, M. J. Rose, *Langmuir* **2015**, *31*, 7712–7716.

[60] L. Barišić, V. Rapić, V. Kovač, *Croat. Chem. Acta* **2002**, *75*, 199–210.

[61] A. Neidlinger, C. Förster, K. Heinze, *Eur. J. Inorg. Chem.* **2016**, submitted.

[62] R. L. Schaaf, *J. Org. Chem.* **1962**, *27*, 107–111.

[63] R. J. LeSuer, C. Buttolph, W. E. Geiger, *J. Organomet. Chem.* **2004**, *76*, 6395–6401.

[64] N. Camire, U. T. Mueller-Westerhoff, W. E. Geiger, *J. Organomet. Chem.* **2001**, *639*, 823–826.

[65] A. Neidlinger, C. Förster, K. Heinze, *Eur. J. Inorg. Chem.* **2015**, submitted.

[66] H.-B. Kraatz, D. M. Leek, A. Houmam, G. D. Enright, J. Lusztyk, D. D. M. Wayner, *J. Organomet. Chem.* **1999**, *589*, 38–49.

[67] F. Neese, *Wiley Interdiscip. Rev. Comput. Mol. Sci.* **2012**, *2*, 73–78.

[68] A. Schäfer, H. Horn, R. Ahlrichs, *J. Chem. Phys.* **1992**, *97*, 2571–2577.

[69] F. Weigend, R. Ahlrichs, *Phys. Chem. Chem. Phys.* **2005**, *7*, 3297.

[70] F. Neese, *Chem. Phys. Lett.* **2000**, *325*, 93–98.

[71] T. H. Fischer, J. Almlof, *J. Phys. Chem.* **1992**, *96*, 9768–9774.

[72] E. van Lenthe, E. J. Baerends, J. G. Snijders, *J. Chem. Phys.* **1993**, *99*, 4597–4610.

[73] C. van Wüllen, *J. Chem. Phys.* **1998**, *109*, 392.

[74] D. A. Pantazis, X.-Y. Chen, C. R. Landis, F. Neese, *J. Chem. Theory Comput.* **2008**, *4*, 908–919.

[75] S. Sinnecker, A. Rajendran, A. Klamt, M. Diedenhofen, F. Neese, *J. Phys. Chem. A* **2006**, *110*, 2235–2245.

3.5.7 DFT optimizations with CH_2Cl_2 continuum solvent

1^2:

Cartesian coordinates of 1^2-8

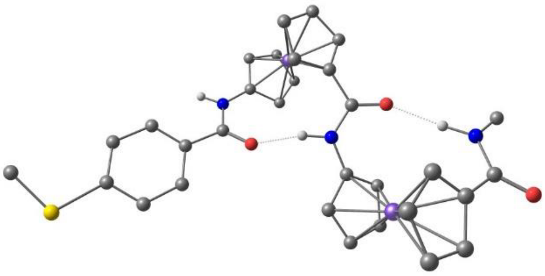

1	-0.031756000	5.664170000	1.901204000
1	1.468362000	3.749483000	3.104207000
6	-0.786331000	4.940513000	2.197472000
7	0.770342000	3.078501000	2.813206000
1	-2.714611000	6.061617000	1.945677000
6	-0.528708000	3.596887000	2.630252000
6	-2.200843000	5.147260000	2.228192000
6	1.148637000	1.772472000	2.698214000
1	-0.017514000	1.715218000	-0.304467000
6	-1.786778000	2.970481000	2.913460000
6	-2.816433000	3.932446000	2.664887000
26	-1.730812000	3.601991000	0.942579000
8	0.354443000	0.873616000	2.407807000
1	-1.925575000	1.948059000	3.242899000
1	-3.883737000	3.760052000	2.773784000
6	-0.874439000	2.363467000	-0.459322000
1	0.066077000	4.276376000	-1.157359000
6	-2.255487000	2.011348000	-0.247145000
6	-0.832372000	3.713489000	-0.920342000
6	-3.053646000	3.154455000	-0.590563000
6	-2.175883000	4.203469000	-0.994313000
1	-2.474256000	5.205944000	-1.287499000
1	-4.136627000	3.203003000	-0.524312000
6	-3.636703000	-1.843276000	1.865032000
7	-2.023136000	-0.039764000	1.012624000
6	-2.345478000	-1.298288000	1.556918000
6	-3.435382000	-3.115156000	2.490722000
6	-2.821070000	0.707692000	0.201526000
6	-1.352549000	-2.242124000	1.984752000
6	-2.028050000	-3.359322000	2.569168000
26	-2.610963000	-3.122925000	0.603131000
8	-3.945502000	0.351849000	-0.163445000
6	-3.839397000	-3.530398000	-0.997432000
6	-2.694333000	-2.766437000	-1.420778000
6	-3.357622000	-4.757745000	-0.432688000
6	-1.522055000	-3.521007000	-1.109729000
6	-1.932017000	-4.748372000	-0.494918000
1	-4.589643000	-1.382425000	1.637510000
1	-1.153498000	0.373503000	1.356998000
1	-4.220742000	-3.785104000	2.829132000
1	-0.279029000	-2.111446000	1.881402000
1	-1.552009000	-4.245153000	2.980224000
1	-3.984369000	-5.540076000	-0.015316000
1	-1.271925000	-5.527558000	-0.123702000
1	-2.719174000	-1.792371000	-1.900183000
1	-0.497241000	-3.210708000	-1.294716000
6	-5.287026000	-3.186569000	-1.137307000
7	-5.586741000	-1.864641000	-1.178163000
1	-4.888565000	-1.183054000	-0.882670000
6	-6.957571000	-1.407909000	-1.309385000
1	-7.563089000	-1.643107000	-0.418341000
1	-7.443365000	-1.881433000	-2.173265000
8	-6.145020000	-4.067016000	-1.231884000
1	-6.953732000	-0.320749000	-1.454167000
6	2.591589000	1.473283000	2.966904000
6	2.939078000	0.148019000	3.294218000
6	3.619096000	2.428531000	2.886676000
6	4.258679000	-0.203021000	3.557763000
1	2.153789000	-0.604660000	3.347097000
6	4.949707000	2.084168000	3.139326000
1	3.408027000	3.457670000	2.594804000
6	5.286010000	0.763337000	3.486202000
1	4.500496000	-1.233558000	3.820988000
1	5.713362000	2.854280000	3.055248000
16	6.927756000	0.199473000	3.841980000
6	7.967852000	1.676644000	3.611686000
1	7.700431000	2.472664000	4.317269000
1	8.991410000	1.343874000	3.822430000
1	7.919026000	2.046576000	2.580064000

Cartesian coordinates of 1^2-6

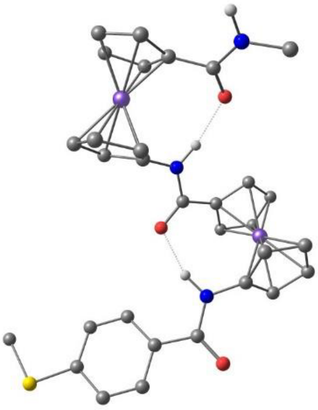

1	-0.683907000	5.086037000	0.406116000
1	-0.709235000	1.400944000	0.419755000
6	0.007324000	4.533552000	-0.221840000
7	-1.058569000	2.232559000	-0.055833000
1	1.516574000	6.079898000	-0.828949000
6	-0.083838000	3.137210000	-0.530532000
6	1.165724000	5.052933000	-0.877943000
6	-2.404108000	2.461823000	-0.147322000
1	0.581780000	2.828284000	2.914909000
6	1.024666000	2.797030000	-1.378973000
6	1.797514000	3.981045000	-1.585409000

26	1.693369000	3.530195000	0.429035000
8	-2.866793000	3.446253000	-0.719781000
1	1.239997000	1.806299000	-1.768015000
1	2.713462000	4.050232000	-2.165576000
6	1.523605000	2.974618000	2.395907000
1	2.002219000	5.133571000	2.763409000
6	2.219381000	1.966178000	1.641105000
6	2.275343000	4.183575000	2.313422000
6	3.404173000	2.573091000	1.087076000
6	3.431515000	3.936424000	1.505355000
1	4.187492000	4.668268000	1.233248000
1	4.141981000	2.083410000	0.457286000
6	2.151354000	-2.192492000	-0.717811000
7	2.566232000	-0.319324000	0.944902000
6	2.200426000	-1.647073000	0.610525000
6	1.804451000	-3.573339000	-0.609296000
6	1.678191000	0.599704000	1.408188000
6	1.869383000	-2.692575000	1.532501000
6	1.626616000	-3.880314000	0.777505000
26	3.551290000	-3.177047000	0.434050000
8	0.488839000	0.329391000	1.615352000
6	5.433901000	-2.439936000	0.084539000
6	5.259753000	-2.734964000	1.482006000
6	5.243863000	-3.666507000	-0.646644000
6	4.977792000	-4.127703000	1.606607000
6	4.964217000	-4.701196000	0.295247000
1	2.366618000	-1.646773000	-1.632124000
1	3.546738000	-0.059592000	0.795972000
1	1.708525000	-4.273293000	-1.434671000
1	1.837188000	-2.591845000	2.613168000
1	1.373006000	-4.854200000	1.186704000
1	5.267677000	-3.783191000	-1.726963000
1	4.746817000	-5.738332000	0.054573000
1	5.329110000	-2.011356000	2.288783000
1	4.779043000	-4.655613000	2.535105000
6	5.693582000	-1.074448000	-0.448371000
7	6.332195000	-1.008071000	-1.636595000
1	6.705634000	-1.859758000	-2.033164000
6	6.639446000	0.251053000	-2.293457000
1	7.474225000	0.775751000	-1.803328000
1	5.763803000	0.911673000	-2.272607000
8	5.339639000	-0.055548000	0.165470000
1	6.911260000	0.049885000	-3.335247000
6	-3.301874000	1.426974000	0.471618000
6	-4.665539000	1.461320000	0.121528000
6	-2.873612000	0.450942000	1.387260000
6	-5.568011000	0.542815000	0.648158000
1	-5.004173000	2.225408000	-0.577107000
6	-3.775972000	-0.471040000	1.928882000
1	-1.833316000	0.392813000	1.705552000
6	-5.132956000	-0.440227000	1.563130000
1	-6.617217000	0.584094000	0.352127000
1	-3.405359000	-1.207250000	2.638838000
16	-6.367964000	-1.559838000	2.172608000
6	-5.453780000	-2.652471000	3.307309000
1	-6.200906000	-3.353072000	3.699963000
1	-4.674598000	-3.218326000	2.782122000
1	-5.018385000	-2.091612000	4.143523000

Cartesian coordinates of $[1^2\text{-}8b]^+$

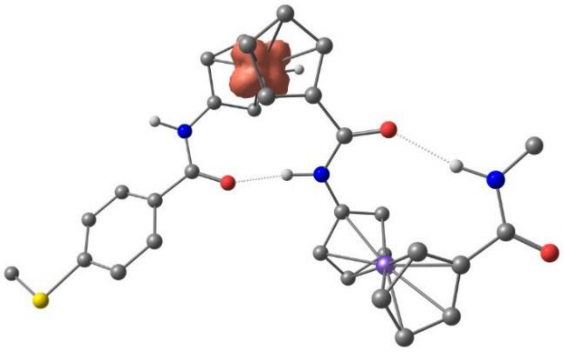

1	14.566758000	-4.766421000	3.874901000
1	12.325360000	-3.533386000	3.186269000
6	14.255524000	-5.377847000	3.032229000
7	12.027806000	-4.335993000	2.644378000
1	16.027218000	-6.711013000	2.680020000
6	13.008086000	-5.259120000	2.334357000
6	15.021202000	-6.410447000	2.404337000
6	10.662045000	-4.520213000	2.455151000
1	10.712820000	-7.257179000	4.468669000
6	12.970339000	-6.282286000	1.334740000
6	14.223902000	-6.969387000	1.356592000
26	13.309931000	-7.260051000	3.191142000
8	10.215250000	-5.611809000	2.111471000
1	12.139216000	-6.487552000	0.671203000
1	14.508516000	-7.779472000	0.691107000
6	11.630117000	-7.831408000	4.381076000
1	12.909701000	-6.960513000	6.001555000
6	11.893663000	-8.856711000	3.419668000
6	12.795619000	-7.666413000	5.183792000
6	13.219605000	-9.339947000	3.643972000
6	13.785685000	-8.598289000	4.723931000
1	14.784106000	-8.725011000	5.131720000
1	13.708560000	-10.116028000	3.063334000
6	9.184565000	-9.880917000	-0.170011000
7	10.128861000	-8.524420000	1.794123000
6	9.174762000	-8.818540000	0.794917000
6	8.045929000	-9.702287000	-1.017592000
6	10.976609000	-9.412636000	2.366249000
6	8.029237000	-7.992043000	0.542587000
6	7.337661000	-8.538907000	-0.582192000
26	7.440928000	-9.930905000	0.941587000
8	11.035114000	-10.609010000	2.090670000
6	7.212682000	-11.844633000	1.663099000
6	7.469622000	-10.926627000	2.741690000
6	6.004073000	-11.424559000	1.014567000
6	6.427847000	-9.948744000	2.745575000
6	5.526698000	-10.253560000	1.674536000
1	9.907959000	-10.685753000	-0.224740000
1	10.190546000	-7.540179000	2.058568000
1	7.763364000	-10.354465000	-1.839099000
1	7.754236000	-7.107152000	1.108285000
1	6.421085000	-8.148137000	-1.013445000
1	5.557430000	-11.911856000	0.153759000
1	4.644679000	-9.681693000	1.400295000

1	8.302084000	-10.975308000	3.438362000
1	6.343590000	-9.110404000	3.432354000
6	7.998706000	-13.049615000	1.257223000
7	9.317323000	-13.039663000	1.583985000
1	9.750574000	-12.163614000	1.864233000
6	10.199915000	-14.138473000	1.238689000
1	10.608204000	-14.042184000	0.218842000
1	9.645141000	-15.082100000	1.290384000
8	7.456685000	-13.992932000	0.680239000
1	11.037649000	-14.172015000	1.946439000
6	9.802323000	-3.342570000	2.718599000
6	8.432430000	-3.560021000	2.977185000
6	10.278358000	-2.018465000	2.689024000
6	7.576966000	-2.494988000	3.224043000
1	8.049109000	-4.579434000	2.992491000
6	9.422358000	-0.941948000	2.923530000
1	11.318976000	-1.803657000	2.445280000
6	8.060391000	-1.165775000	3.203529000
1	6.524593000	-2.685619000	3.435363000
1	9.825872000	0.066764000	2.878437000
16	6.880209000	0.104219000	3.536642000
6	7.829963000	1.652223000	3.392376000
1	8.230221000	1.782858000	2.379692000
1	7.105799000	2.450518000	3.594780000
1	8.635233000	1.701884000	4.135157000

Cartesian coordinates of $[1^2\text{-}6b]^+$

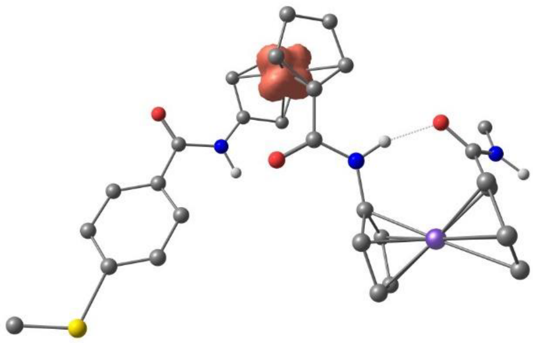

1	1.256079000	4.697090000	-0.154585000
1	1.113166000	1.028092000	1.159488000
6	0.497707000	4.294544000	0.504060000
7	1.370510000	1.938285000	0.797950000
1	-0.880239000	6.030643000	0.840056000
6	0.486652000	2.960660000	1.033960000
6	-0.638751000	4.988667000	1.029010000
6	2.585931000	2.044499000	0.114796000
1	-0.316851000	2.298336000	-2.514988000
6	-0.722870000	2.811748000	1.794940000
6	-1.391075000	4.076046000	1.830399000
26	-1.334523000	3.413385000	-0.121954000
8	3.002280000	3.124576000	-0.272072000
1	-1.045479000	1.900956000	2.291725000
1	-2.310508000	4.290878000	2.366733000
6	-1.244074000	2.604443000	-2.041161000
1	-1.497336000	4.732462000	-2.701802000
6	-2.047737000	1.781679000	-1.180488000
6	-1.874683000	3.879382000	-2.145037000
6	-3.175564000	2.571541000	-0.756891000
6	-3.064756000	3.853967000	-1.362438000
1	-3.743016000	4.688763000	-1.205540000
1	-3.975751000	2.250901000	-0.094899000
6	-2.831667000	-2.215150000	1.464570000
7	-2.651491000	-0.354770000	-0.241503000
6	-2.507195000	-1.705396000	0.161466000
6	-2.654691000	-3.631985000	1.430666000
6	-1.653374000	0.387333000	-0.778063000
6	-2.120763000	-2.807525000	-0.668807000
6	-2.211905000	-3.995242000	0.119201000
26	-4.055166000	-3.034932000	0.020556000
8	-0.497936000	0.001813000	-0.934947000
6	-5.853658000	-2.051862000	-0.003188000
6	-5.411605000	-2.328021000	-1.344940000
6	-5.998943000	-3.313961000	0.676178000
6	-5.297043000	-3.742908000	-1.487881000
6	-5.654125000	-4.349533000	-0.242026000
1	-3.171229000	-1.622666000	2.309568000
1	-3.608038000	0.021316000	-0.189169000
1	-2.839567000	-4.316390000	2.253988000
1	-1.830181000	-2.742594000	-1.712068000
1	-2.002362000	-5.003784000	-0.225610000
1	-6.282890000	-3.455273000	1.715182000
1	-5.634909000	-5.413641000	-0.023043000
1	-5.197807000	-1.580830000	-2.103012000
1	-4.967621000	-4.266918000	-2.380782000
6	-6.046171000	-0.683205000	0.550148000
7	-6.968831000	-0.561208000	1.525279000
1	-7.550530000	-1.359828000	1.741779000
6	-7.259292000	0.701533000	2.183655000
1	-7.848358000	1.372276000	1.539005000
1	-6.325420000	1.213539000	2.446722000
8	-5.392336000	0.292415000	0.139626000
1	-7.827048000	0.501170000	3.098705000
6	3.331657000	0.769443000	-0.061330000
6	2.710726000	-0.496379000	-0.117798000
6	4.726848000	0.843942000	-0.216147000
6	3.473018000	-1.646552000	-0.300164000
1	1.624249000	-0.591588000	-0.084381000
6	5.496747000	-0.306455000	-0.383973000
1	5.210563000	1.819727000	-0.192122000
6	4.877819000	-1.571568000	-0.423594000
1	2.975708000	-2.615602000	-0.358292000
1	6.575434000	-0.206292000	-0.484947000
16	5.733357000	-3.105718000	-0.629437000
6	7.486125000	-2.626320000	-0.746476000
1	8.034750000	-3.567766000	-0.867621000
1	7.671704000	-1.988900000	-1.619932000
1	7.827904000	-2.129829000	0.170014000

Cartesian coordinates of $[1^2\text{-}6]^{2+}$

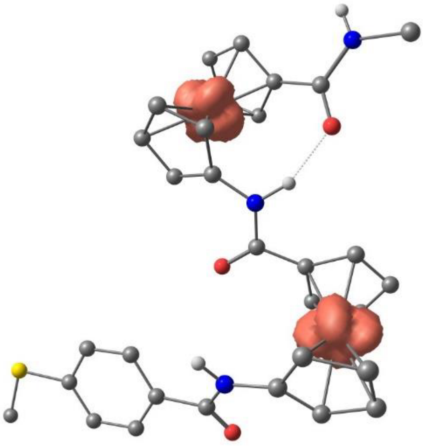

1	1.355101000	4.682481000	-0.498989000
1	1.518560000	1.252208000	1.370253000
6	0.705490000	4.369287000	0.307813000
7	1.628247000	2.055550000	0.763062000
1	-0.608663000	6.154094000	0.642485000
6	0.782421000	3.109551000	0.992381000
6	-0.339630000	5.137756000	0.914367000
6	2.662872000	2.021543000	-0.183374000
1	-0.559699000	2.122183000	-2.358739000
6	-0.303412000	3.068230000	1.934405000
6	-0.960272000	4.337447000	1.921508000
26	-1.192119000	3.462313000	0.063939000
8	2.921433000	2.998085000	-0.866358000
1	-0.545129000	2.226640000	2.578591000
1	-1.790785000	4.627343000	2.558452000
6	-1.398117000	2.495950000	-1.779051000
1	-1.704153000	4.566418000	-2.578228000
6	-2.084348000	1.773679000	-0.742376000
6	-2.012871000	3.774452000	-1.901199000
6	-3.121947000	2.633182000	-0.229315000
6	-3.075256000	3.854160000	-0.955855000
1	-3.707569000	4.720357000	-0.779114000
1	-3.826041000	2.405658000	0.565880000
6	-3.280062000	-2.149049000	1.940610000
7	-2.614372000	-0.252960000	0.470851000
6	-2.538183000	-1.588095000	0.847100000
6	-3.054484000	-3.561609000	1.949437000
6	-1.695387000	0.391256000	-0.327475000
6	-1.892089000	-2.663918000	0.157405000
6	-2.202805000	-3.875704000	0.843687000
26	-4.008147000	-3.019169000	0.192585000
8	-0.638328000	-0.109071000	-0.677612000
6	-5.817099000	-2.117217000	-0.238736000
6	-5.025517000	-2.227909000	-1.434230000
6	-6.089194000	-3.452242000	0.223259000
6	-4.820386000	-3.616827000	-1.696313000
6	-5.478316000	-4.366009000	-0.679821000
1	-3.893944000	-1.585234000	2.636676000
1	-3.535733000	0.171747000	0.625565000
1	-3.461304000	-4.264866000	2.670155000
1	-1.293140000	-2.566989000	-0.740657000
1	-1.854488000	-4.864990000	0.562819000
1	-6.633736000	-3.719218000	1.125091000
1	-5.465202000	-5.448220000	-0.576121000
1	-4.652640000	-1.399560000	-2.029523000
1	-4.239942000	-4.030797000	-2.516240000
6	-6.224491000	-0.815524000	0.399310000
7	-7.492637000	-0.766366000	0.834518000
1	-8.107398000	-1.544322000	0.628098000
6	-8.071186000	0.408327000	1.471439000
1	-8.517966000	1.087160000	0.729393000
1	-7.288094000	0.948884000	2.013418000
8	-5.428496000	0.127201000	0.503260000
1	-8.848518000	0.088322000	2.174645000
6	3.414649000	0.742084000	-0.262236000
6	2.881368000	-0.505266000	0.125090000
6	4.719861000	0.781738000	-0.785304000
6	3.640736000	-1.665383000	0.011739000
1	1.850149000	-0.593690000	0.465850000
6	5.491436000	-0.374438000	-0.888565000
1	5.133138000	1.737548000	-1.104018000
6	4.962154000	-1.616887000	-0.486078000
1	3.206949000	-2.622020000	0.304233000
1	6.501326000	-0.298290000	-1.282721000
16	5.830766000	-3.154190000	-0.564676000
6	7.459632000	-2.716312000	-1.253351000
1	8.009917000	-3.663215000	-1.310606000
1	7.369254000	-2.294958000	-2.261898000
1	8.001407000	-2.026860000	-0.594271000

2^2

Cartesian coordinates of 2^2-8

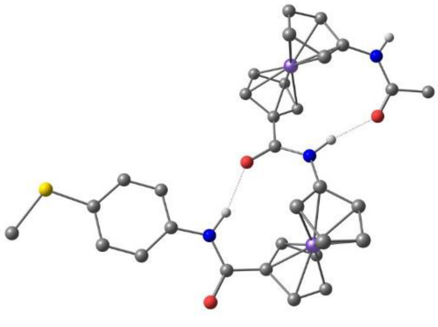

1	-4.685734000	-5.207624000	1.328153000
1	-5.939362000	-3.328672000	2.784505000
6	-3.842051000	-4.634329000	1.702075000
7	-5.142390000	-2.717577000	2.658070000
1	-2.071052000	-5.920929000	1.201997000
6	-3.923717000	-3.356531000	2.349391000
6	-2.462429000	-5.007594000	1.640618000
6	-5.352108000	-1.377345000	2.787417000
1	-4.274084000	-0.985306000	-0.226225000
6	-2.592623000	-2.934340000	2.672135000
6	-1.693482000	-3.957932000	2.234120000

26	-2.770492000	-3.234842000	0.630345000
8	-4.473405000	-0.536171000	2.598222000
1	-2.319873000	-1.999664000	3.146514000
1	-0.611015000	-3.930209000	2.324113000
6	-3.509023000	-1.697826000	-0.518710000
1	-4.695661000	-3.351881000	-1.459951000
6	-2.089385000	-1.546758000	-0.321844000
6	-3.728509000	-2.943252000	-1.180757000
6	-1.446829000	-2.704830000	-0.875601000
6	-2.457308000	-3.566940000	-1.395330000
1	-2.292103000	-4.537489000	-1.854188000
1	-0.376986000	-2.891730000	-0.867318000
6	-0.160770000	1.707350000	2.287735000
7	-2.019523000	0.252239000	1.289609000
6	-1.523583000	1.350544000	2.016238000
6	-0.173621000	2.858702000	3.137699000
6	-1.364556000	-0.399882000	0.292819000
6	-2.372473000	2.288548000	2.692993000
6	-1.535593000	3.213935000	3.391712000
26	-1.139634000	3.280395000	1.366505000
8	-0.238714000	-0.076255000	-0.102732000
6	-0.011093000	3.870362000	-0.246493000
6	-1.251067000	3.282902000	-0.687689000
6	-0.335031000	5.011908000	0.561803000
6	-2.320807000	4.056388000	-0.144970000
6	-1.755649000	5.120283000	0.630231000
1	0.714900000	1.202603000	1.899788000
1	-2.916613000	-0.119121000	1.613155000
1	0.703725000	3.379767000	3.510548000
1	-3.458488000	2.272048000	2.676148000
1	-1.878657000	4.052951000	3.990829000
1	0.390022000	5.658935000	1.045238000
1	-2.312250000	5.866373000	1.190672000
1	-1.356709000	2.412410000	-1.329174000
1	-3.380777000	3.860154000	-0.283274000
6	-6.750141000	-0.979750000	3.220222000
1	-7.049045000	-0.077817000	2.672550000
1	-7.495174000	-1.769527000	3.060293000
1	-6.732891000	-0.729284000	4.291407000
6	1.384307000	3.477866000	-0.598227000
7	1.561866000	2.154595000	-0.914753000
1	0.793887000	1.519098000	-0.691509000
8	2.281997000	4.317359000	-0.616710000
6	2.717478000	1.526660000	-1.422127000
6	3.930114000	2.189118000	-1.684660000
6	2.637228000	0.144239000	-1.700996000
6	5.021749000	1.490517000	-2.218662000
1	4.019306000	3.247851000	-1.467931000
6	3.725013000	-0.544067000	-2.231074000
1	1.706798000	-0.384439000	-1.493895000
6	4.938759000	0.119060000	-2.502538000
1	5.940038000	2.044496000	-2.405735000
1	3.628422000	-1.610578000	-2.440771000
16	6.258237000	-0.870710000	-3.181672000
6	7.611062000	0.321446000	-3.437526000
1	7.945261000	0.762713000	-2.490380000
1	8.435433000	-0.259944000	-3.868521000
1	7.325282000	1.112374000	-4.142558000

Cartesian coordinates of 2^2-6

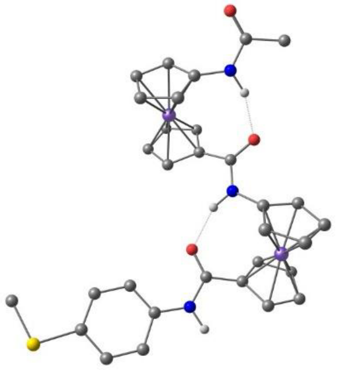

1	4.461759000	-6.424460000	0.994153000
1	4.972914000	-2.753789000	1.193239000
6	3.697344000	-5.734015000	0.654943000
7	5.071002000	-3.592406000	0.616659000
1	1.864005000	-7.019176000	0.486783000
6	3.889464000	-4.335325000	0.410627000
6	2.327606000	-6.041995000	0.383687000
6	6.317392000	-3.992954000	0.228158000
1	4.410745000	-4.184870000	3.859528000
6	2.633914000	-3.781930000	-0.014338000
6	1.670277000	-4.837664000	-0.023235000
26	2.466241000	-4.603056000	1.871300000
8	6.531471000	-5.025890000	-0.396144000
1	2.456391000	-2.738201000	-0.257164000
1	0.620246000	-4.739059000	-0.283040000
6	3.340007000	-4.210207000	3.683058000
1	2.781211000	-6.339814000	4.109051000
6	2.544289000	-3.091236000	3.251820000
6	2.477966000	-5.339516000	3.813556000
6	1.186006000	-3.551633000	3.108466000
6	1.152458000	-4.935026000	3.454391000
1	0.276182000	-5.576766000	3.423318000
1	0.340185000	-2.960873000	2.768665000
6	1.717346000	1.531906000	1.972263000
7	2.216803000	-0.720432000	2.996842000
6	2.538363000	0.628842000	2.729130000
6	2.350551000	2.813096000	1.987980000
6	3.104733000	-1.750447000	2.928384000
6	3.679317000	1.354078000	3.204167000
6	3.561951000	2.701585000	2.741664000
26	1.930350000	2.190257000	3.916204000
8	4.291197000	-1.593063000	2.616006000
6	0.234529000	1.722252000	4.960984000
6	1.407045000	1.427716000	5.742357000
6	0.249605000	3.133185000	4.665054000
6	2.125460000	2.645682000	5.932262000
6	1.416582000	3.694233000	5.264564000
1	0.773968000	1.278708000	1.497305000
1	1.286234000	-0.885661000	3.388315000
1	1.970307000	3.716065000	1.519168000
1	4.477676000	0.943644000	3.812233000
1	4.262690000	3.506081000	2.947526000
1	-0.474253000	3.672244000	4.059635000
1	1.726917000	4.733306000	5.198227000

1	1.683767000	0.445584000	6.111989000
1	3.064987000	2.750934000	6.467370000
6	7.435900000	-3.034704000	0.607892000
1	8.278576000	-3.613017000	1.008545000
1	7.791043000	-2.522881000	-0.298630000
1	7.131270000	-2.278666000	1.342993000
6	-0.747948000	0.695624000	4.515766000
7	-2.029159000	1.156740000	4.403383000
1	-2.175931000	2.115018000	4.696315000
8	-0.420959000	-0.473202000	4.285047000
6	-3.195298000	0.481151000	3.985169000
6	-3.233114000	-0.875201000	3.620790000
6	-4.391573000	1.225910000	3.938146000
6	-4.437560000	-1.464478000	3.215223000
1	-2.324798000	-1.466586000	3.660860000
6	-5.586410000	0.635699000	3.537559000
1	-4.383934000	2.279189000	4.222574000
6	-5.629056000	-0.723817000	3.166531000
1	-4.423755000	-2.516387000	2.938118000
1	-6.496375000	1.237130000	3.513883000
16	-7.212974000	-1.364757000	2.665332000
6	-6.889735000	-3.126776000	2.338786000
1	-6.527651000	-3.643000000	3.236630000
1	-7.858895000	-3.551711000	2.051012000
1	-6.181220000	-3.262438000	1.511924000

Cartesian coordinates of $[2^2\text{-8b}]^+$

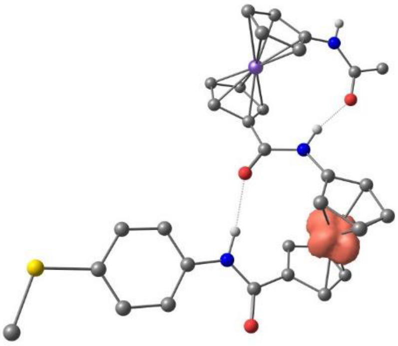

1	-5.568592000	-4.838758000	-0.261019000
1	-6.787221000	-3.000533000	1.286013000
6	-4.718116000	-4.373835000	0.229399000
7	-5.943190000	-2.442010000	1.251466000
1	-3.020505000	-5.764106000	-0.239608000
6	-4.754422000	-3.152732000	0.982046000
6	-3.374133000	-4.860191000	0.247371000
6	-6.075954000	-1.103422000	1.452849000
1	-4.726687000	-0.589190000	-1.425138000
6	-3.427971000	-2.879021000	1.450109000
6	-2.578494000	-3.936543000	0.994017000
26	-3.447339000	-2.987439000	-0.621053000
8	-5.133579000	-0.309866000	1.377572000
1	-3.124551000	-2.020463000	2.037864000
1	-1.510542000	-4.012158000	1.176614000
6	-3.982753000	-1.329192000	-1.703568000
1	-5.173778000	-2.815682000	-2.881490000
6	-2.576508000	-1.293450000	-1.375203000
6	-4.213593000	-2.498913000	-2.485370000
6	-1.957991000	-2.448068000	-1.966110000
6	-2.970313000	-3.192474000	-2.637594000
1	-2.826714000	-4.136464000	-3.155263000
1	-0.908071000	-2.712515000	-1.883266000
6	-0.763874000	1.691705000	1.552885000
7	-2.589756000	0.358135000	0.390942000
6	-2.118572000	1.354200000	1.223509000
6	-0.794063000	2.796774000	2.462110000
6	-1.859449000	-0.251443000	-0.609340000
6	-2.973371000	2.303714000	1.873379000
6	-2.159792000	3.176223000	2.658273000
26	-1.607932000	3.406515000	0.670151000
8	-0.700496000	0.077361000	-0.858054000
6	-0.313086000	4.067089000	-0.902721000
6	-1.544967000	3.610135000	-1.466687000
6	-0.614838000	5.144146000	-0.009275000
6	-2.603168000	4.384183000	-0.912986000
6	-2.030444000	5.335202000	-0.004465000
1	0.119310000	1.186139000	1.184339000
1	-3.544191000	0.025945000	0.591455000
1	0.075445000	3.261043000	2.917574000
1	-4.056378000	2.323157000	1.785684000
1	-2.520349000	3.986104000	3.285773000
1	0.117917000	5.700640000	0.566703000
1	-2.574987000	6.075511000	0.574186000
1	-1.660797000	2.794065000	-2.175329000
1	-3.659605000	4.268690000	-1.138121000
6	-7.470720000	-0.634272000	1.811648000
1	-7.686334000	0.292781000	1.266379000
1	-8.248188000	-1.376449000	1.592335000
1	-7.501941000	-0.402541000	2.886606000
6	1.095616000	3.624510000	-1.199042000
7	1.247124000	2.317765000	-1.555645000
1	0.440741000	1.702664000	-1.454026000
8	1.998086000	4.450078000	-1.124729000
6	2.430858000	1.661338000	-1.969800000
6	3.676020000	2.296581000	-2.110485000
6	2.335390000	0.285933000	-2.268995000
6	4.793406000	1.572305000	-2.545039000
1	3.775028000	3.351228000	-1.879339000
6	3.448923000	-0.427958000	-2.700656000
1	1.376832000	-0.220982000	-2.156086000
6	4.700483000	0.205143000	-2.849162000
1	5.739230000	2.101970000	-2.640977000
1	3.344675000	-1.489529000	-2.928510000
16	6.047838000	-0.809388000	-3.414071000
6	7.459897000	0.338264000	-3.486399000
1	7.699737000	0.745591000	-2.496313000
1	8.306336000	-0.265257000	-3.836546000
1	7.283055000	1.152769000	-4.199697000

Cartesian coordinates of [2^2-6a]$^+$

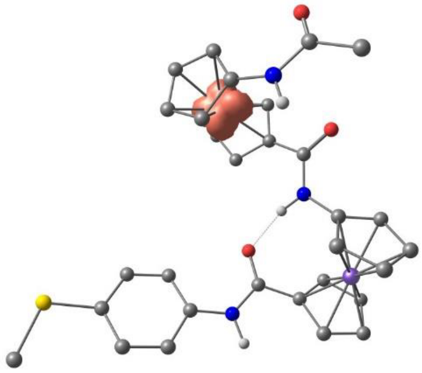

1	3.246266000	-5.503062000	-0.060640000
1	4.006118000	-2.236351000	-2.065611000
6	2.505619000	-4.845489000	-0.495630000
7	4.017360000	-3.087544000	-1.514960000
1	0.556336000	-5.846693000	-0.011980000
6	2.795575000	-3.651949000	-1.238906000
6	1.082217000	-5.011940000	-0.466040000
6	5.249927000	-3.485723000	-0.984305000
1	3.659179000	-3.159931000	2.409667000
6	1.541098000	-3.033729000	-1.564123000
6	0.487471000	-3.893985000	-1.128000000
26	1.552848000	-3.275768000	0.541186000
8	5.349686000	-4.466694000	-0.275297000
1	1.424261000	-2.088064000	-2.086744000
1	-0.574990000	-3.719019000	-1.269936000
6	2.636084000	-2.832562000	2.254214000
1	1.401852000	-4.486701000	3.140669000
6	2.246626000	-1.612428000	1.605721000
6	1.446611000	-3.523421000	2.640972000
6	0.810607000	-1.562845000	1.601625000
6	0.326688000	-2.732185000	2.246631000
1	-0.719622000	-3.000028000	2.367878000
1	0.193829000	-0.779735000	1.168119000
6	3.375049000	2.121169000	-1.277398000
7	2.739890000	0.523220000	0.587244000
6	3.533254000	1.561814000	0.036932000
6	4.301152000	3.200563000	-1.401039000
6	3.246774000	-0.662314000	1.010146000
6	4.565040000	2.289998000	0.713520000
6	5.036414000	3.301279000	-0.177653000
26	3.000043000	3.528691000	0.180833000
8	4.426717000	-0.987167000	0.921226000
6	0.981408000	3.724217000	0.468261000
6	1.675101000	3.768772000	1.729553000
6	1.471346000	4.817348000	-0.335702000
6	2.567274000	4.880180000	1.702097000
6	2.444752000	5.523444000	0.430262000
1	2.657820000	1.793632000	-2.024760000
1	1.747782000	0.742617000	0.724861000
1	4.414586000	3.845842000	-2.267523000
1	4.904432000	2.109814000	1.728381000
1	5.804832000	4.036230000	0.044997000
1	1.184920000	5.048905000	-1.357617000
1	3.017150000	6.381926000	0.091412000
1	1.532196000	3.071046000	2.549128000
1	3.244435000	5.169477000	2.500477000
6	6.395226000	-2.573553000	-1.352378000
1	6.406349000	-2.347068000	-2.427239000
1	6.282900000	-1.629312000	-0.799297000
1	7.338986000	-3.047958000	-1.064594000
6	0.008814000	2.662114000	0.098034000
7	-0.897700000	3.021494000	-0.853976000
1	-0.843077000	3.981433000	-1.172749000
8	0.036554000	1.540596000	0.625359000
6	-1.883298000	2.241138000	-1.500038000
6	-2.302139000	0.973444000	-1.052361000
6	-2.484161000	2.780205000	-2.650373000
6	-3.283472000	0.273775000	-1.755219000
1	-1.869128000	0.546953000	-0.154921000
6	-3.468703000	2.078589000	-3.349906000
1	-2.177321000	3.763184000	-3.010230000
6	-3.880248000	0.807236000	-2.914299000
1	-3.596161000	-0.704460000	-1.388318000
1	-3.900437000	2.537822000	-4.235944000
16	-5.109595000	-0.195719000	-3.720229000
6	-5.679838000	0.841964000	-5.104883000
1	-6.453830000	0.251514000	-5.610502000
1	-6.123586000	1.779617000	-4.747965000
1	-4.870215000	1.049810000	-5.815767000

Cartesian coordinates of [2^2-6b]$^+$

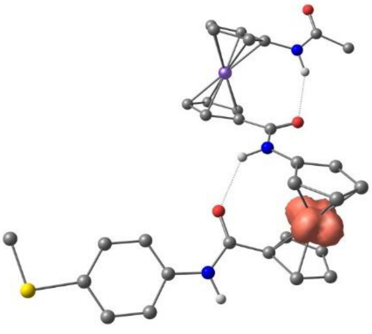

1	4.385757000	-5.347158000	0.917238000
1	5.339616000	-1.798783000	0.427416000
6	4.089798000	-4.817240000	0.018686000
7	5.578471000	-2.772312000	0.254320000
1	2.522179000	-6.145753000	-0.884385000
6	4.612298000	-3.555322000	-0.412152000
6	3.111244000	-5.234704000	-0.935150000
6	6.745359000	-3.269609000	0.770968000
1	2.959418000	-2.400946000	2.495463000
6	3.953503000	-3.197136000	-1.638471000
6	3.023442000	-4.233791000	-1.953912000
26	2.580684000	-3.407430000	-0.109814000
8	7.075419000	-4.443758000	0.667136000
1	4.128924000	-2.288528000	-2.208029000
1	2.355130000	-4.251121000	-2.810390000
6	2.232534000	-2.502964000	1.695572000
1	1.187282000	-4.426783000	2.167687000

6	2.051281000	-1.569151000	0.611388000
6	1.293950000	-3.559750000	1.521652000
6	1.002382000	-2.082719000	-0.238354000
6	0.542470000	-3.304731000	0.330417000
1	-0.226386000	-3.947982000	-0.087775000
1	0.643629000	-1.643747000	-1.164850000
6	2.451064000	2.673640000	-1.772056000
7	2.370341000	0.582094000	-0.438021000
6	2.968124000	1.778334000	-0.773682000
6	3.292267000	3.831037000	-1.813985000
6	2.904483000	-0.383315000	0.408478000
6	4.080057000	2.429915000	-0.144969000
6	4.290819000	3.680759000	-0.802368000
26	2.377164000	3.714085000	0.031972000
8	4.006558000	-0.243314000	0.931315000
6	0.393819000	3.794428000	0.599166000
6	1.195246000	3.400405000	1.725437000
6	0.810411000	5.118429000	0.215089000
6	2.083182000	4.473876000	2.028577000
6	1.845781000	5.528555000	1.102953000
1	1.585347000	2.479680000	-2.399103000
1	1.391366000	0.494080000	-0.702205000
1	3.179057000	4.671873000	-2.492407000
1	4.647913000	2.030731000	0.685545000
1	5.074675000	4.393271000	-0.561498000
1	0.425800000	5.695950000	-0.621082000
1	2.396921000	6.463163000	1.046907000
1	1.131103000	2.449891000	2.247059000
1	2.837982000	4.472060000	2.810740000
6	7.620110000	-2.246868000	1.477915000
1	8.582544000	-2.182509000	0.951974000
1	7.174465000	-1.245900000	1.531092000
1	7.828402000	-2.601549000	2.496402000
6	-0.624966000	2.908056000	-0.064447000
7	-1.758304000	3.555331000	-0.440045000
1	-1.826095000	4.530802000	-0.172682000
8	-0.407780000	1.708437000	-0.229458000
6	-2.898013000	3.044576000	-1.105215000
6	-3.017957000	1.717841000	-1.549157000
6	-3.964339000	3.937228000	-1.332688000
6	-4.179727000	1.299980000	-2.210297000
1	-2.211846000	1.013199000	-1.374871000
6	-5.117099000	3.516986000	-1.988568000
1	-3.888487000	4.970793000	-0.992061000
6	-5.244137000	2.186805000	-2.440995000
1	-4.234972000	0.264865000	-2.539966000
1	-5.926603000	4.229357000	-2.152808000
16	-6.759792000	1.767412000	-3.269521000
6	-6.544952000	0.014904000	-3.716462000
1	-7.468982000	-0.266729000	-4.236276000
1	-5.695990000	-0.125082000	-4.397298000
1	-6.429936000	-0.617903000	-2.828029000

Cartesian coordinates of $[2^2\text{-}6]^{2+}$

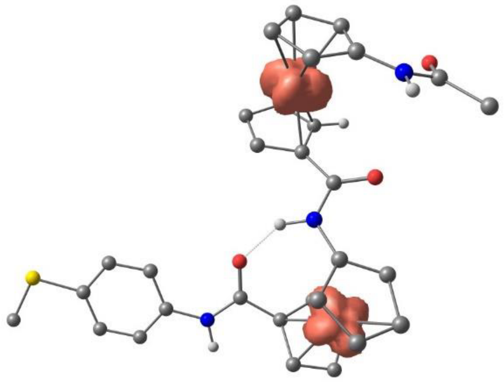

1	4.882194000	-5.234765000	-0.138887000
1	6.111106000	-2.249729000	-2.337861000
6	4.366337000	-4.834415000	-1.001369000
7	5.925136000	-2.936447000	-1.615453000
1	2.595535000	-6.192128000	-1.233206000
6	4.812155000	-3.720792000	-1.790740000
6	3.152355000	-5.327369000	-1.581671000
6	6.749038000	-2.918113000	-0.483768000
1	3.694334000	-2.550245000	1.637948000
6	3.804563000	-3.467327000	-2.782436000
6	2.807099000	-4.483599000	-2.681901000
26	2.819233000	-3.413567000	-0.900730000
8	6.550854000	-3.657669000	0.458582000
1	3.822882000	-2.655405000	-3.505318000
1	1.935292000	-4.580463000	-3.322641000
6	2.839232000	-2.512716000	0.969722000
1	1.626237000	-4.304863000	1.563198000
6	2.610229000	-1.516204000	-0.041121000
6	1.743988000	-3.427808000	0.932818000
6	1.371810000	-1.837464000	-0.696417000
6	0.841003000	-3.004135000	-0.086626000
1	-0.067468000	-3.517542000	-0.388699000
1	0.927361000	-1.314729000	-1.538579000
6	3.225427000	2.833801000	-2.199903000
7	3.025126000	0.678498000	-0.976170000
6	3.701105000	1.856703000	-1.262712000
6	4.123129000	3.947742000	-2.172017000
6	3.563576000	-0.395881000	-0.300442000
6	4.860451000	2.395983000	-0.617590000
6	5.126557000	3.676748000	-1.189903000
26	3.220824000	3.741657000	-0.320374000
8	4.726241000	-0.444716000	0.067910000
6	1.259704000	3.822740000	0.322553000
6	2.104021000	3.372474000	1.395938000
6	1.674403000	5.157358000	-0.021597000
6	3.017588000	4.423989000	1.705423000
6	2.750880000	5.519371000	0.836531000
1	2.343300000	2.726301000	-2.825007000
1	2.011310000	0.730282000	-1.097954000
1	4.045516000	4.839283000	-2.787621000
1	5.418677000	1.917904000	0.178173000
1	5.948112000	4.331254000	-0.913091000
1	1.263860000	5.771991000	-0.818217000

1	3.311298000	6.449241000	0.792550000
1	2.048196000	2.404063000	1.884583000
1	3.803684000	4.382696000	2.455017000
6	7.853902000	-1.891755000	-0.547908000
1	8.380581000	-1.919865000	-1.512071000
1	7.419590000	-0.888780000	-0.422741000
1	8.563939000	-2.077265000	0.264657000
6	0.184826000	2.985621000	-0.316989000
7	-0.969017000	3.657625000	-0.545101000
1	-0.996107000	4.617641000	-0.220351000
8	0.376163000	1.795509000	-0.579231000
6	-2.183823000	3.193180000	-1.105114000
6	-2.379678000	1.881039000	-1.576259000
6	-3.246460000	4.108678000	-1.182093000
6	-3.615597000	1.511558000	-2.106196000
1	-1.573188000	1.157852000	-1.519065000
6	-4.482042000	3.734014000	-1.713228000
1	-3.111182000	5.128767000	-0.819787000
6	-4.686573000	2.424609000	-2.183335000
1	-3.749371000	0.490257000	-2.464529000
1	-5.276382000	4.476489000	-1.752298000
16	-6.205580000	1.819480000	-2.876891000
6	-7.343712000	3.236175000	-2.747633000
1	-8.294321000	2.882275000	-3.163828000
1	-7.500710000	3.532190000	-1.703038000
1	-6.994183000	4.091422000	-3.338919000

Cartesian coordinates of $[2^2]^{2+}$

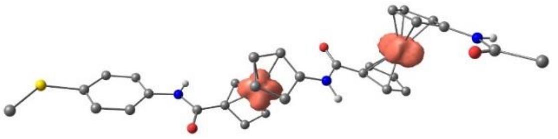

1	-3.581243000	-1.355509000	2.294047000
1	-4.185882000	-3.825576000	1.825852000
6	-4.665216000	-1.276061000	2.293879000
7	-5.175985000	-3.629626000	1.723280000
1	-5.018923000	0.846977000	2.926597000
6	-5.576461000	-2.352277000	2.022990000
6	-5.427484000	-0.113017000	2.625172000
6	-6.008001000	-4.687168000	1.337525000
1	-7.319757000	-1.627371000	-1.541057000
6	-6.904310000	-1.807821000	2.049799000
6	-6.809536000	-0.440225000	2.470081000
26	-5.842724000	-0.604865000	0.667717000
8	-7.197722000	-4.524572000	1.156710000
1	-7.809153000	-2.360014000	1.831602000
1	-7.649126000	0.229958000	2.630072000
6	-6.601396000	-0.857099000	-1.274600000
1	-4.647733000	-1.885035000	-1.654331000
6	-6.889410000	0.465599000	-0.776331000
6	-5.185550000	-0.991227000	-1.349094000
6	-5.633109000	1.122928000	-0.539072000
6	-4.594094000	0.223022000	-0.897302000
1	-3.528387000	0.412251000	-0.799698000
1	-5.513508000	2.128258000	-0.147837000
6	-11.157173000	1.984286000	-0.236942000
7	-9.274048000	0.591141000	-1.217859000
6	-10.585345000	1.026687000	-1.136308000
6	-12.558321000	2.065923000	-0.522322000
6	-8.201129000	1.138339000	-0.536834000
6	-11.616322000	0.595302000	-2.033759000
6	-12.842218000	1.206897000	-1.629037000
26	-11.538769000	2.706112000	-2.198575000
8	-8.304031000	2.113393000	0.185552000
6	-12.561405000	4.140603000	-3.411272000
6	-11.750039000	4.777513000	-2.414116000
6	-11.698473000	3.356423000	-4.236804000
6	-10.389457000	4.394904000	-2.642881000
6	-10.364449000	3.519265000	-3.773867000
1	-10.619773000	2.531723000	0.526576000
1	-9.092308000	-0.149145000	-1.886365000
1	-13.272458000	2.683465000	0.014921000
1	-11.483878000	-0.098374000	-2.859777000
1	-13.807189000	1.066650000	-2.107324000
1	-12.028221000	2.723221000	-5.054942000
1	-9.485642000	3.038104000	-4.193544000
1	-12.096092000	5.422008000	-1.610492000
1	-9.532906000	4.713012000	-2.055308000
6	-5.291857000	-6.008504000	1.185814000
1	-5.987898000	-6.744586000	0.771457000
1	-4.416707000	-5.916272000	0.527161000
1	-4.937693000	-6.360529000	2.165894000
6	-14.053592000	4.157380000	-3.592019000
7	-14.663087000	5.280825000	-3.123033000
1	-14.059053000	6.005464000	-2.753746000
8	-14.618032000	3.217159000	-4.139823000
6	-16.034415000	5.622701000	-3.155423000
6	-17.041574000	4.776571000	-3.648098000
6	-16.394651000	6.892502000	-2.660832000
6	-18.376765000	5.197362000	-3.645271000
1	-16.784372000	3.797368000	-4.035970000
6	-17.722591000	7.305933000	-2.660440000
1	-15.625372000	7.562795000	-2.274534000
6	-18.739680000	6.462442000	-3.155245000
1	-19.127598000	4.515252000	-4.037210000
1	-17.972927000	8.294333000	-2.274346000
16	-20.397296000	7.101175000	-3.108451000
6	-21.410010000	5.749188000	-3.789965000
1	-21.342720000	4.845002000	-3.172455000
1	-22.441820000	6.120950000	-3.766720000
1	-21.137098000	5.523984000	-4.828306000

Cartesian coordinates of F

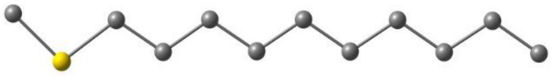

6	-2.334328000	0.248886000	0.000205000
1	-1.989219000	0.798126000	0.889207000
1	-1.991928000	0.800303000	-0.888494000
6	-1.776107000	-1.175808000	-0.002234000
1	-2.155711000	-1.716975000	0.880128000
1	-2.158152000	-1.715093000	-0.884696000
6	-0.240389000	-1.212161000	-0.004311000
1	0.136952000	-0.666417000	-0.886082000
1	0.139231000	-0.666424000	0.876483000
6	0.332532000	-2.635398000	-0.004891000
1	-0.049747000	-3.180603000	-0.885214000
1	-0.048276000	-3.180540000	0.876116000
6	1.866640000	-2.682172000	-0.006038000
1	2.247588000	-2.137530000	-0.887526000
1	2.248814000	-2.135642000	0.873742000
6	2.438788000	-4.105604000	-0.004763000
1	2.056320000	-4.651917000	-0.884567000
1	2.056779000	-4.649972000	0.876458000
6	3.972770000	-4.155922000	-0.005005000
1	4.355302000	-3.612590000	-0.886724000
1	4.355565000	-3.609121000	0.874443000
6	4.543393000	-5.579755000	-0.002188000
1	4.161187000	-6.123653000	0.879492000
1	4.161504000	-6.127148000	-0.881832000
6	6.077465000	-5.632010000	-0.001756000
1	6.459357000	-5.089137000	-0.883113000
1	6.458956000	-5.084952000	0.877171000
6	6.638345000	-7.058037000	0.001834000
1	6.303310000	-7.616278000	0.890320000
1	6.304166000	-7.620521000	-0.884291000
1	7.738832000	-7.058191000	0.002371000
16	-4.172437000	0.217035000	0.003104000
6	-4.519824000	2.008771000	0.009341000
1	-4.110554000	2.495502000	-0.886341000
1	-5.611060000	2.125988000	0.011168000
1	-4.108120000	2.489709000	0.907034000

4 SUMMARY AND OUTLOOK

In this work, the successful preparation and analyses of several amide-linked ferrocene-phenol conjugates is presented, which allow the investigation of secondary structures and redox as well as proton transfer behavior. In the simplest compound of this type with an aminoferrocene residue and a salicylic acid derivative, the intramolecularly hydrogen bonded ferrocenium-phenolate represents the thermodynamic minimum after deprotonation and oxidation. This mixed-valent compound allows the detection of intramolecular proton coupled electron transfer to the valence-isomeric phenoxyl-ferrocene upon excitation by light. The intramolecular hydrogen bond is tuning the respective redox potentials of the redox pairs (ferrocene/ferrocenium and phenolate/phenoxide), while also stabilizing the products. In an analogous compound without intramolecular hydrogen bond, this stabilizing factor is eliminated, leading to rapid follow-up reactions of the mixed-valent compounds. The outstanding importance of hydrogen bonding upon redox and proton transfer behavior is facilely illustrated.

Further studies of secondary structures and redox as well as acid/base behavior on ferrocene-phenol conjugates with elongated intramolecular hydrogen bond networks by more diverse ferrocenyl residues were conducted. The effect of cooperative hydrogen bonding is illustrated by a series of compounds. According to literature references, oligomers of 1-amino-1’-ferrocenearboxylic acid form an intramolecular 1,2’-8-membered ring by hydrogen bonds between the amide groups as stable secondary structure in the solid and in solution. The attachment of a salicylic acid moiety, featuring an OH•••O hydrogen bond, induces a change in the secondary structure, forcing the ferrocene moieties to form the usually unfavored 1,2’-6-membered ring conformation. Deprotonation of the phenol as most acidic site leads to a different hydrogen bond pattern, in which the favored 8-membered ring geometry is obtained Thus, these compounds act as acid/base switches. As evidenced in the literature, ferrocenium amides are better hydrogen bond donors. Therefore, these sites strongly favor hydrogen bonding, while hydrogen bonding in the neutral state renders the oxidation of adjacent ferrocenyl moieties easier. In conjugates with more than one amide bond, indeed a “double coordination” of the SbF_6^- counterion by both amide protons is detected by IR and EPR spectroscopy and furthermore supported by DFT studies. The OH•••O hydrogen bond of the salicylic acid residue is not affected by the oxidation. The detection of intervalence charge transfer or proton coupled electron transfer is impossible for the Cp-C(O)-R substituted ferrocenyl compounds due to rapid follow-up reactions by the electrophilic 1-amino-1’-ferrocenecarboxylic acid moieties, leading to the formation of iron(III) species in low spin and high spin states as evidenced by EPR spectroscopy.

While the decomposition of electrophilic ferrocenium compounds in alkaline medium is unfavorable for the detection of proton coupled electron transfer reactions, this behavior is of considerable interest for certain pharmaceuticals. For ferrocene-containing breast-cancer and antimalarial medication (e.g. ferrocifene and ferroquine), the presence of carbon-centered ferrocenyl radicals as additional mode of action was presumed. In this work a facile insight into the formation of such radicals is presented by a study of various ferrocenium derivatives under alkaline conditions in the absence of nucleophiles. Spin-trapping techniques allowed the detection of highly reactive ferrocenyl radicals as proposed for the above-mentioned drugs. While simple, non-stabilized ferrocenium compounds undergo rapid back-formation to the starting materials by abstraction of hydrogen atoms from the base or the solvent, compounds that are more diverse show a different behavior. The introduction of amide groups in these ferrocenyl radicals leads to an equilibration to the thermodynamically favored, metastable ferrocenium-iminolates. These act as thermodynamic reservoirs, slowly releasing the highly reactive ferrocenyl radicals, which is supposed to play an important role in aminoferrocene based (pro-)drugs. The application of similar spin-trapping techniques on such pharmaceuticals could give evidence on the modes of action of the highly targeted ferrocene drugs.

A further subject of this dissertation was the investigation of electron transfer rates with respect to the direction of a macrodipole moment. A retrosynthetic approach using simple literature known ferrocenyl precursors allows the preparation of oligoferrocene wires of variable chain length. In these wires, a macrodipole moment is induced by the stable secondary structure formed by hydrogen bonding between adjacent amide bonds. Thio ether end groups should allow the immobilization on gold substrates in the direction of the macrodipole moment or against it. Accordingly, electrochemical measurements of self assembled monolayers should allow the investigation of electron transfer rates via a hopping mechanism over the single ferrocenediyl units. DFT calculations of the shortest diferrocenyl wires are presented that corroborate the stable formation of 8-membered ring conformers for both wires in the neutral state. After successful preparation of those wires or derivatives with increased chain length, electrochemical investigations can be used to determine the electron transfer rates with respect to the macrodipole moment in the future. Indeed, the increased hydrogen bond network in longer wires should contribute to the stability of the secondary structure.

5 SUPPORTING INFORMATION

CONTENTS

To 3.1: Proton Coupled Electron Transfer in Ferrocenium-Phenolate Conjugates
Andreas Neidlinger, Vadim Ksenofontov, Katja Heinze
Published in: *Organometallics* **2013**, *32*, 5955–5965.
[DOI: 10.1021/om400498h]
http://pubs.acs.org/doi/suppl/10.1021/om400498h

To 3.2: Spin Trapping of Carbon-Centered Ferrocenyl Radicals with Nitrosobenzene
Andreas Neidlinger, Torben Kienz, Katja Heinze
Published in: *Organometallics* ***2015**, 34, 5310−5320.*
[DOI: 10.1021/acs.organomet.5b00778]
http://pubs.acs.org/doi/suppl/10.1021/acs.organomet.5b00778

To 3.3: How Hydrogen Bonds Affect Reactivity and Intervalence Charge Transfer in Ferrocenium-Phenolate Radicals
Andreas Neidlinger, Christoph Förster, Katja Heinze
Published in: *European Journal of Inorganic Chemistry* **2016**, in print.

To 3.4: Conformational Switching of Multi-Responsive Ferrocenyl-Phenol Conjugates
Andreas Neidlinger, Christoph Förster, Katja Heinze
To be submitted.

5.1 To 3.1: Proton Coupled Electron Transfer in Ferrocenium-Phenolate Conjugates

Andreas Neidlinger, Vadim Ksenofontov, and Katja Heinze

Organometallics **2013**, *32*, 5955–5965.

Figure S1. NOESY spectra of H-1 (a) in CD_2Cl_2 and (b) in THF-d_8 at 298 K; mixing time 1 s; solvent signals are marked with an asterisk.

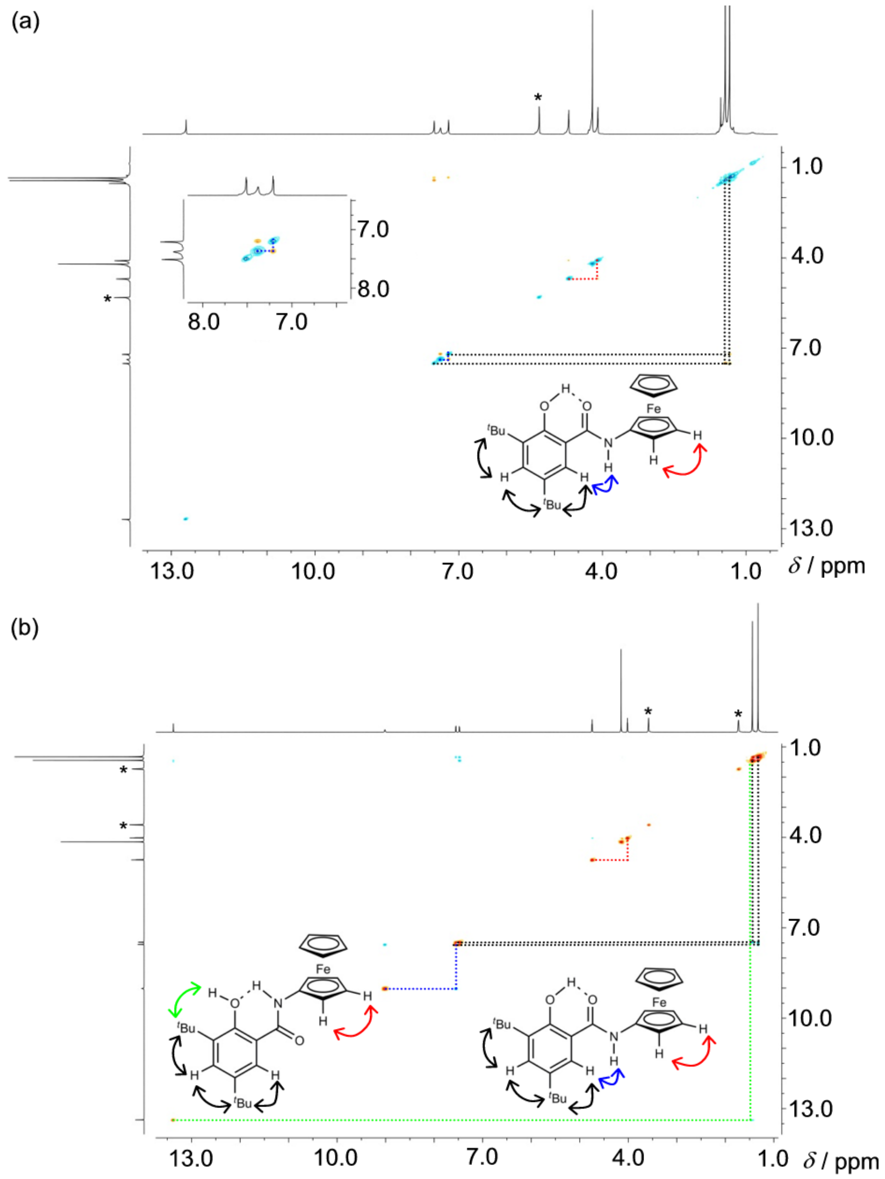

Figure S2. Mößbauer spectra of $[\mathrm{H}\text{-}1]^+$ (a) in CH_2Cl_2 at 80 K and (b) in THF at 86 K.

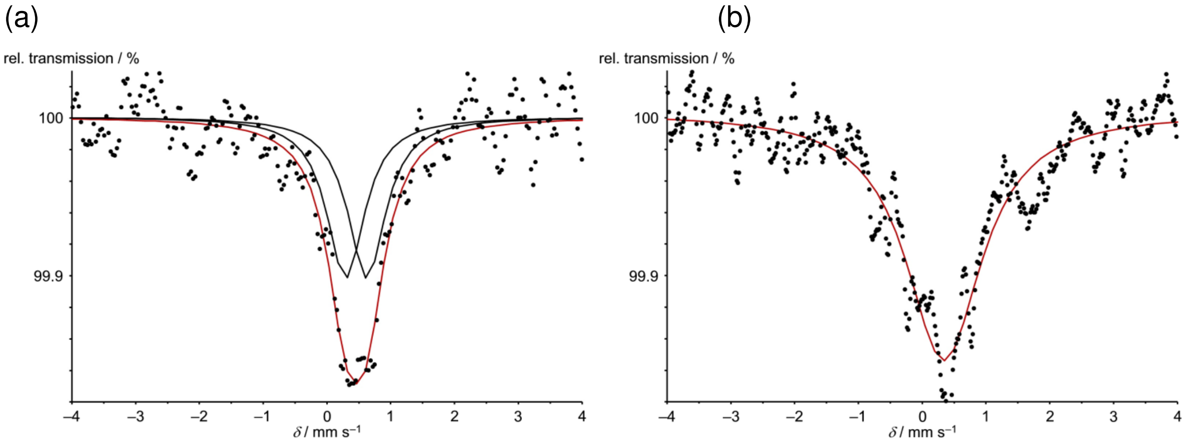

Figure S3. EPR spectra of $[\mathrm{H}\text{-}J]^+$ (a) in CH_2Cl_2 and (b) in THF including subspectra with their fractional contribution at 77 K.

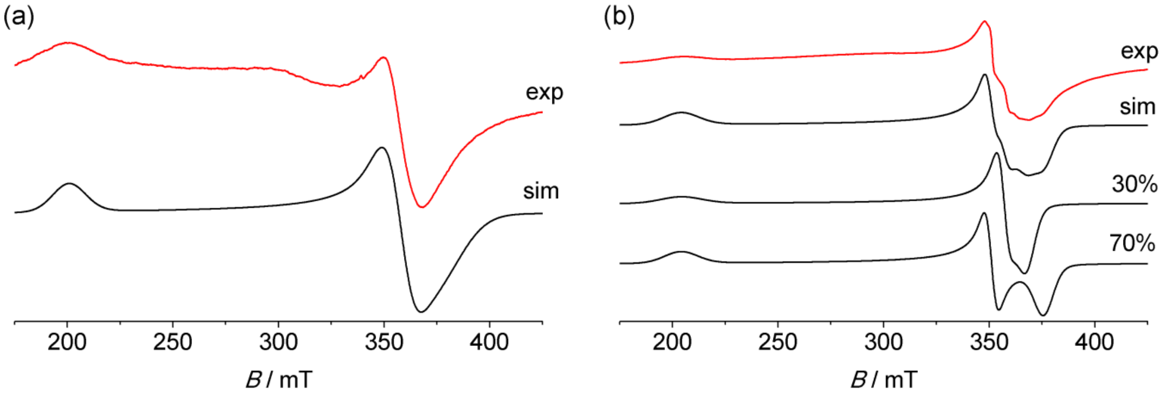

Figure S4. UV/Vis/NIR spectra of H-1 (top) and [H-1]$^+$ (bottom) (a) in CH_2Cl_2 and (b) in THF at 298 K.

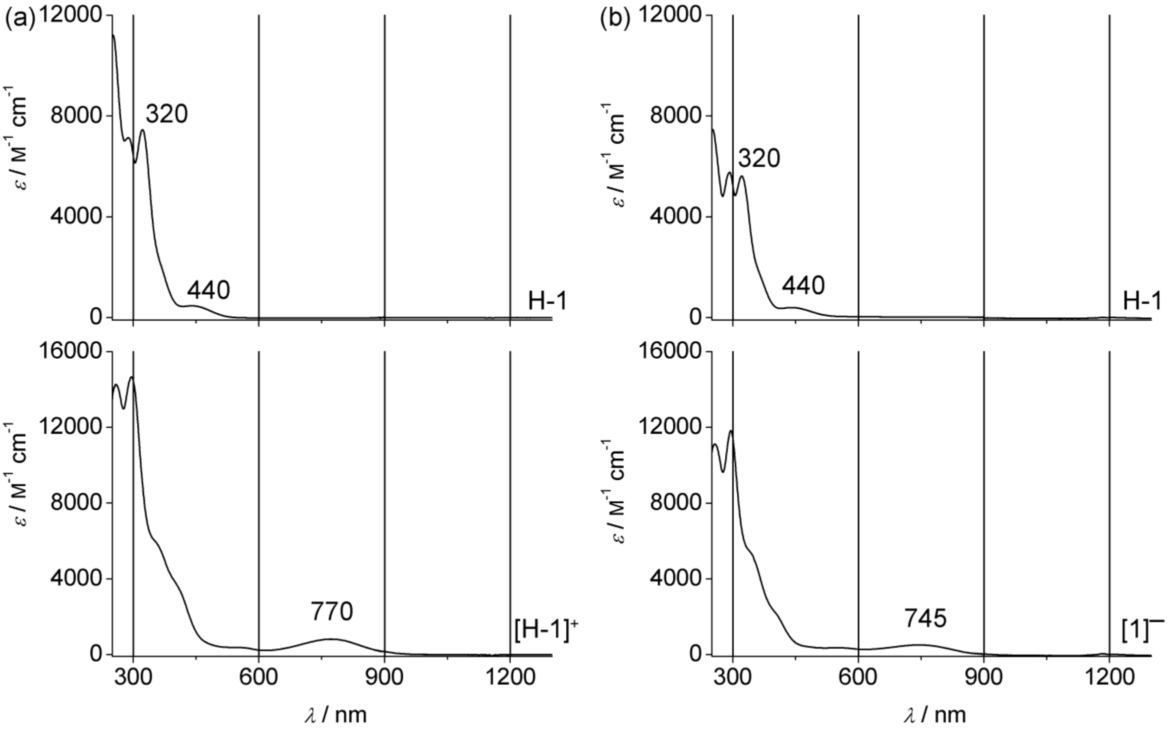

Figure S5. (a) Square wave and (b) cyclic voltammograms of [1]$^-$ in CH_2Cl_2 (full black line) and in THF (dashed red line) at 298 K.

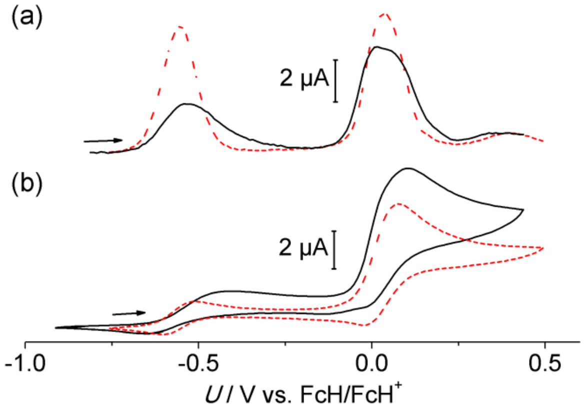

Figure S6. UV/Vis/NIR spectra of (a) H-1 and (b) H-G in THF at 298 K in the absence (top) and presence (bottom) of $P_1{}^tBu$.

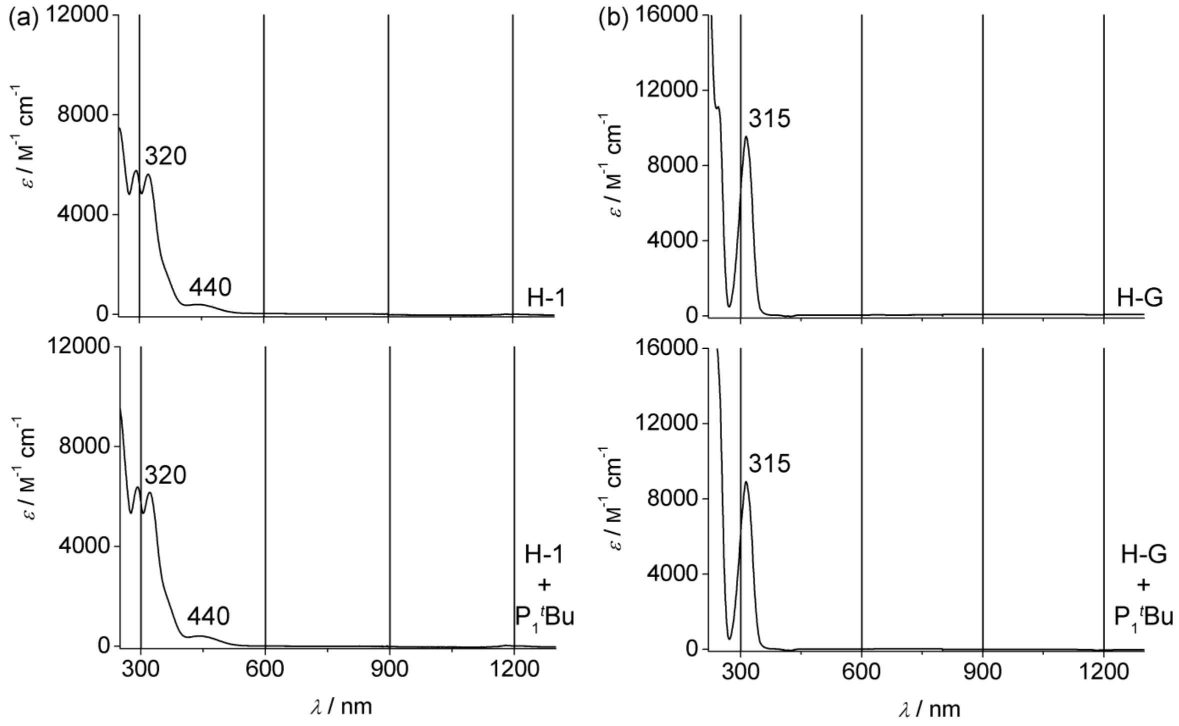

Figure S7. DFT/PCM optimized geometries of $[1]^-$-NHO and $[1]^-$-OHO (a) in CH_2Cl_2 and (b) in THF (distances in Å, CH hydrogen atoms ommited).

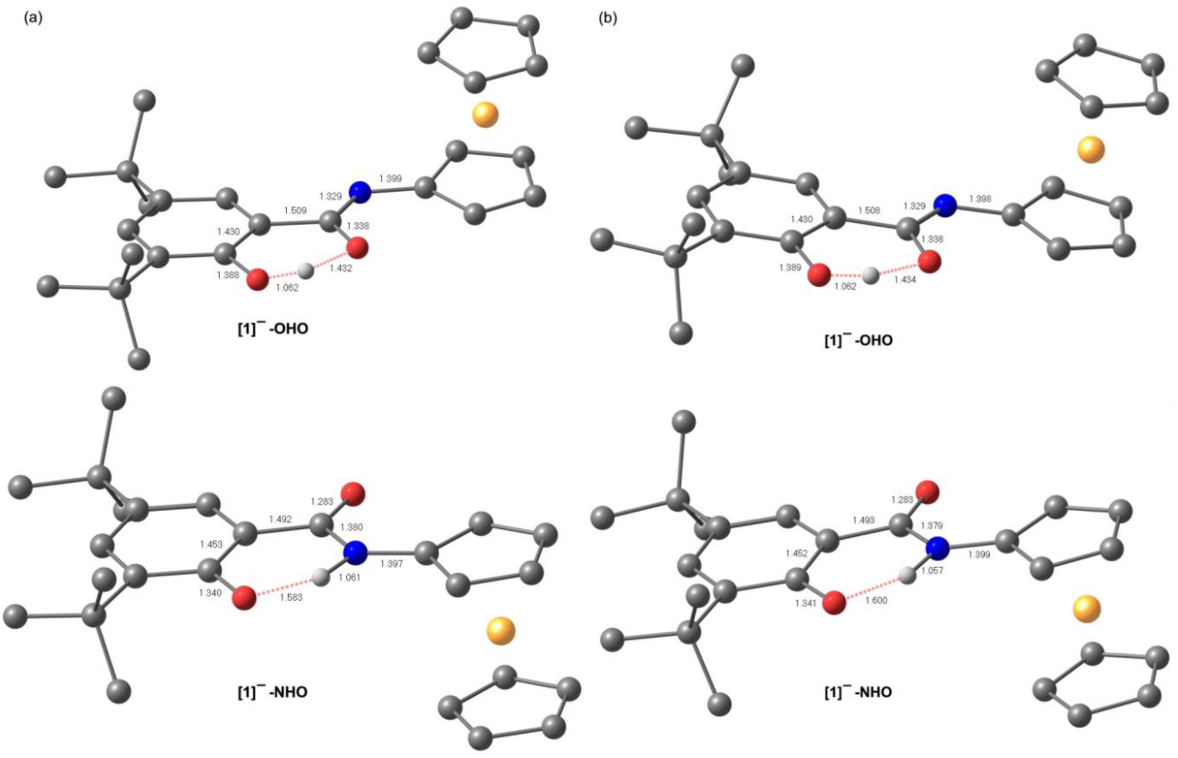

Figure S8. Spectroelectrochemical oxidation of $[1]^-$ (a) in $CH_2Cl_2/[^nBu_4N][B(C_6F_5)_4]$, $P_1{}^tBu$ and (b) in THF/$[^nBu_4N][B(C_6F_5)_4]$, $P_1{}^tBu$ at 298 K.

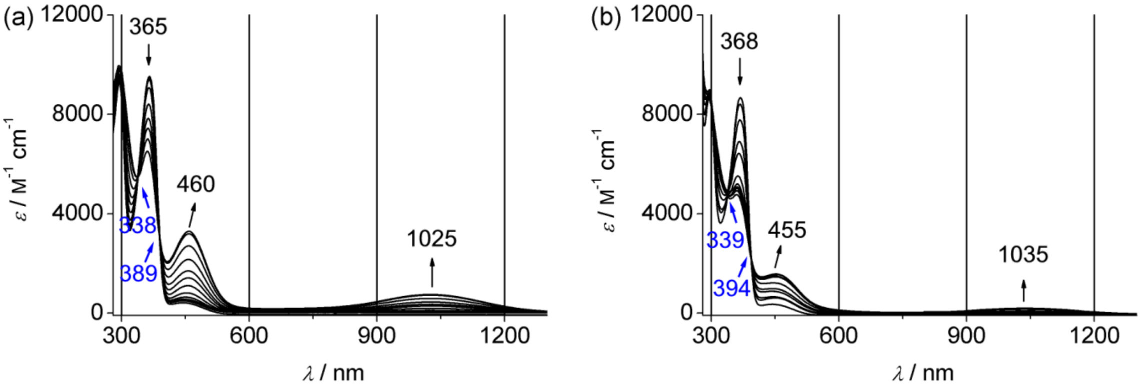

Figure S9. IR spectra of H-1, $[1]^{-}$, $[H\text{-}1]^{+}$ and $[1]^{\bullet}$ (a) in CH_2Cl_2 and (b) in THF at 298 K. $[1]^{-}$ was generated in CH_2Cl_2 or in $[^{n}Bu_4N][B(C_6F_5)_4]$/THF using $P_1{}^{t}Bu$ as base.

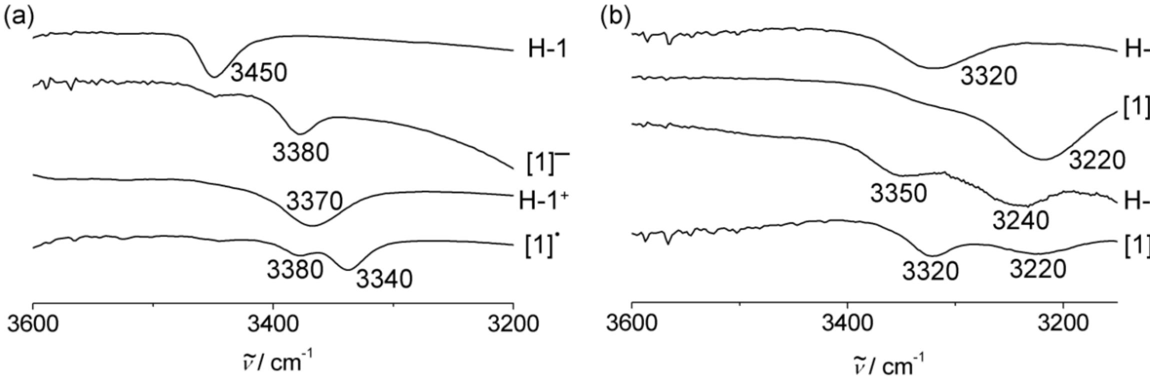

For Cartesian coordinates of **H-1-OHO**, **H-1-NHO**, **$[H\text{-}1]^{+}$-OHO(SbF_6^{-})**, **$[H\text{-}1]^{+}$-NHO(SbF_6^{-})**, **$[H\text{-}1]^{+}$-OHO**, **$[H\text{-}1]^{+}$-NHO**, **$[1]^{-}$-OHO**, **$[1]^{-}$-NHO**, **$[1a]^{\bullet}$-NHO**, **$[1b]^{\bullet}$-NHO**, **$[1b]^{\bullet}$-NHO’**, and **$[1b]^{\bullet}$-OHO** (B3LYP, LANL2DZ, PCM CH_2Cl_2) and **H-1-OHO(OMe_2)**, **H-1-NHO(OMe_2)**, **$[H\text{-}1]^{+}$-OHO(SbF_6^{-})**, **$[H\text{-}1]^{+}$-NHO(SbF_6^{-})**, **$[H\text{-}1]^{+}$-OHO(OMe_2)**, **$[H\text{-}1]^{+}$-NHO(OMe_2)**, **$[1]^{-}$-OHO(OMe_2)**, **$[1]^{-}$-NHO(OMe_2)**, **$[1a]^{\bullet}$-NHO(OMe_2)**, **$[1b]^{\bullet}$-NHO(OMe_2)**, **$[1b]^{\bullet}$-NHO’(OMe_2)**, and **$[1b]^{\bullet}$-OHO(OMe_2)** (B3LYP, LANL2DZ, PCM THF) see electronic supporting information under http://pubs.acs.org/doi/suppl/10.1021/om400498h/suppl_file/om400498h_si_001.pdf.

5.2 To 3.2: Spin Trapping of Carbon-Centered Ferrocenyl Radicals With Nitrosobenzene

Andreas Neidlinger,‡ Torben Kienz,‡ and Katja Heinze*

Organometallics **2015**, 34, 5310−5320.

Figure S1. : DFT optimized geometry with spin density (0.01 a.u. isosurface value) in CH_2Cl_2 continuum solvent for iron spin-trapped [1-PhNO]$^+$.

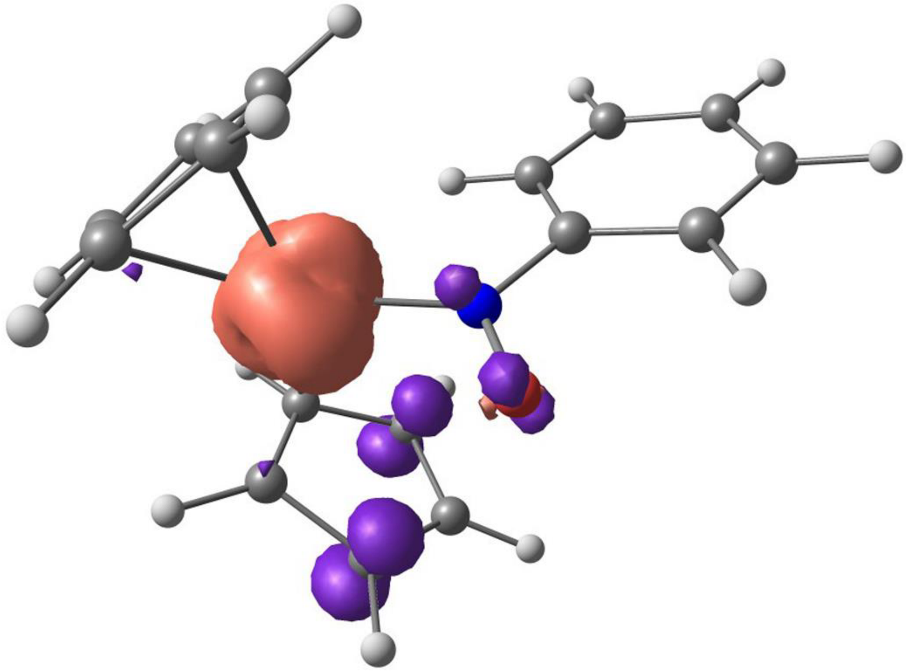

Figure S2: (top) Square wave and (bottom) cyclic voltammogram of $P_1{}^t$Bu in CH_2Cl_2 containing [^{n}Bu$_4$N][B(C_6F_5)$_4$] as supporting electrolyte at 298 K.

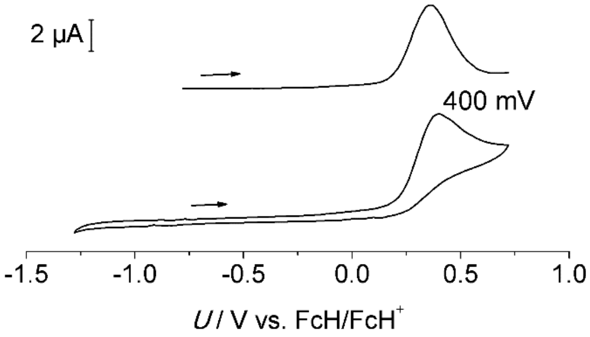

Figure S3: DFT optimized geometries with spin densities (0.01 a.u. isosurface value) in CH_2Cl_2 continuum solvent for a) ferrocenyl radical $[1{-}H]^{\bullet}$ and b) decamethylferrocenyl radical $[2{-}H]^{\bullet}$.

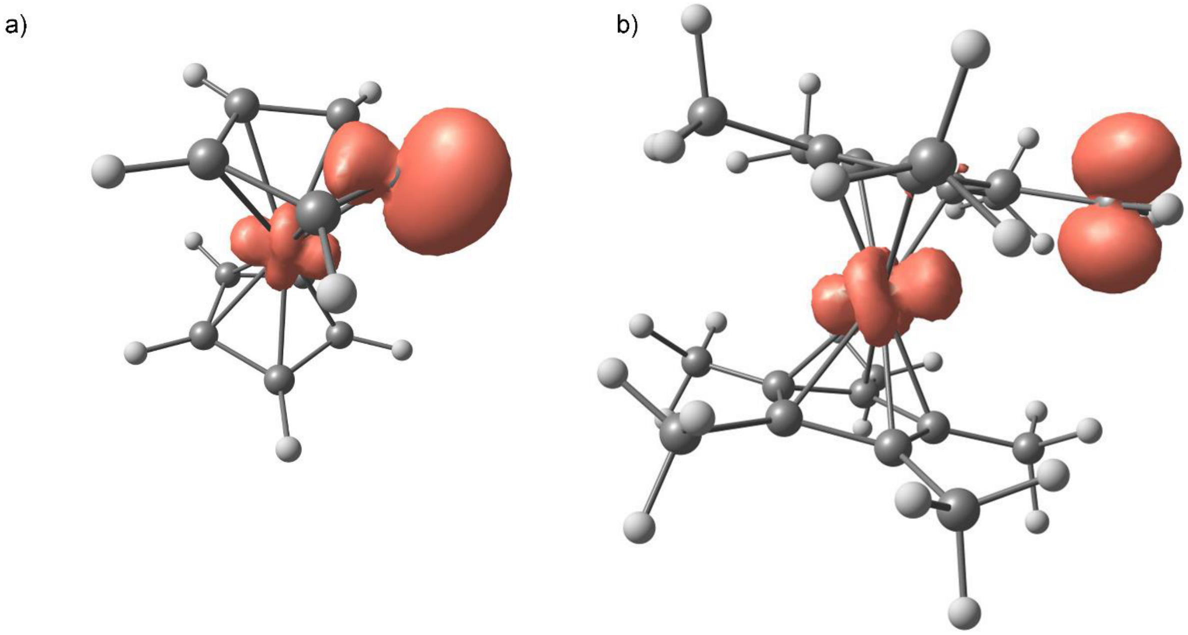

Figure S4: X-band EPR spectrum (top) and simulated spectrum (bottom) of a) $[6]^\bullet$, b) $[7]^\bullet$, and c) $[8^1]^\bullet$ (25 mM) in CH_2Cl_2 at the following parameters: a) and b) temperature = 77 K; field = 3346.20 G, sweep = 499.77 G, sweep time = 90 s, modulation = 5000 mG, MW attenuation = 10 db and c) temperature = 77 K; field = 3346.20 G, sweep = 499.77 G, sweep time = 90 s, modulation = 1000 mG, MW attenuation = 5 db.

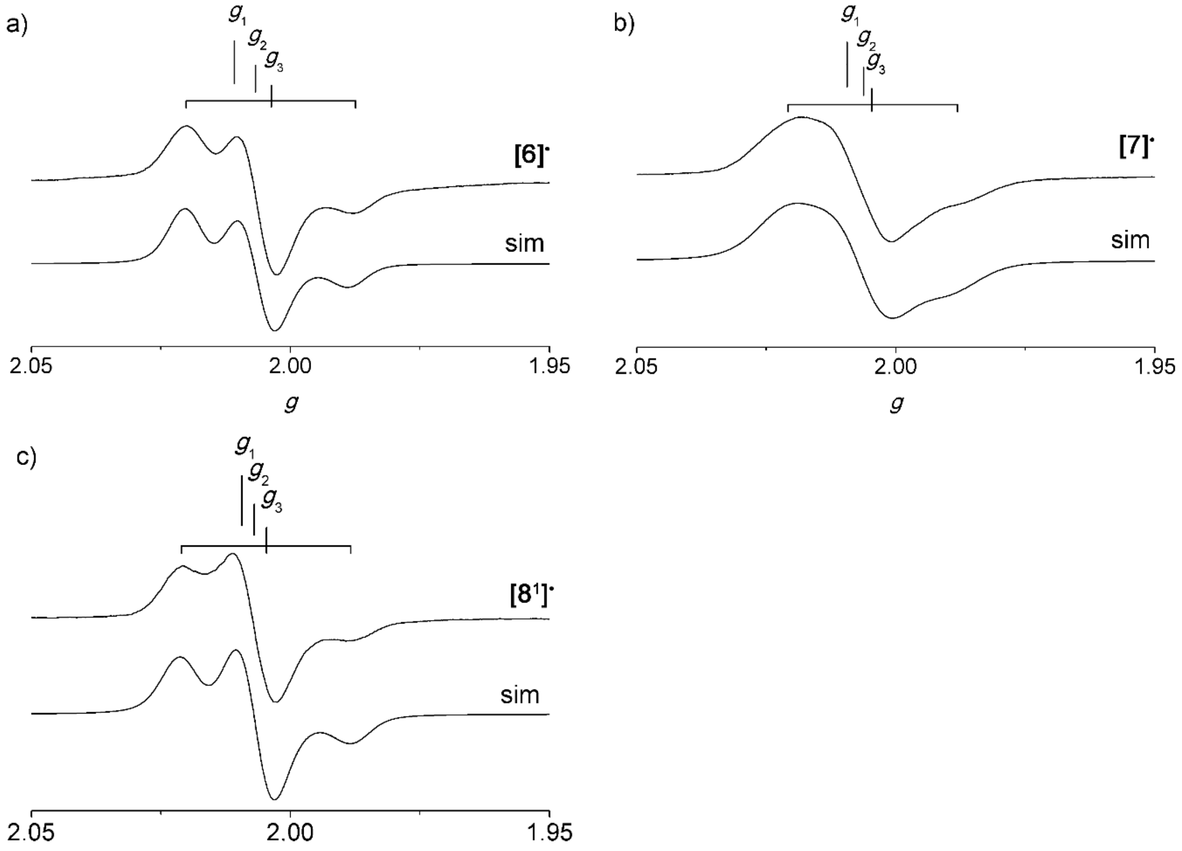

Figure S5: a) (top) Square wave and (bottom) cyclic voltammogram of 1 and b) cyclic voltammograms of a 1/$P_1{}^tBu$ mixture. All measurements performed in CH_2Cl_2 containing [$^nBu_4N$][$B(C_6F_5)_4$] as supporting electrolyte at 298 K.

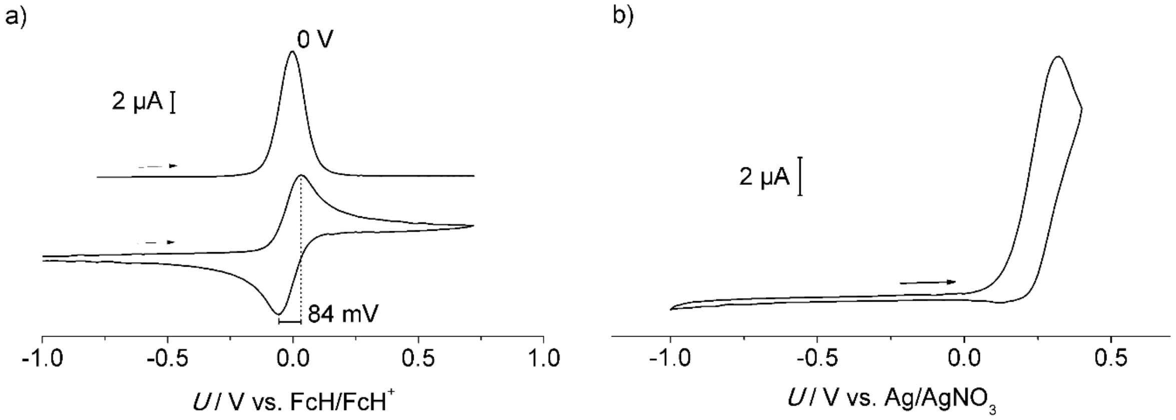

Figure S6: DFT optimized geometries with spin densities (0.01 a.u. isosurface value), chemical structures, and energies in CH_2Cl_2 continuum for ferrocenyl and alkyl radicals $[3{-}H^x]^\bullet$ (x = α, β, Cp, 1, 2).

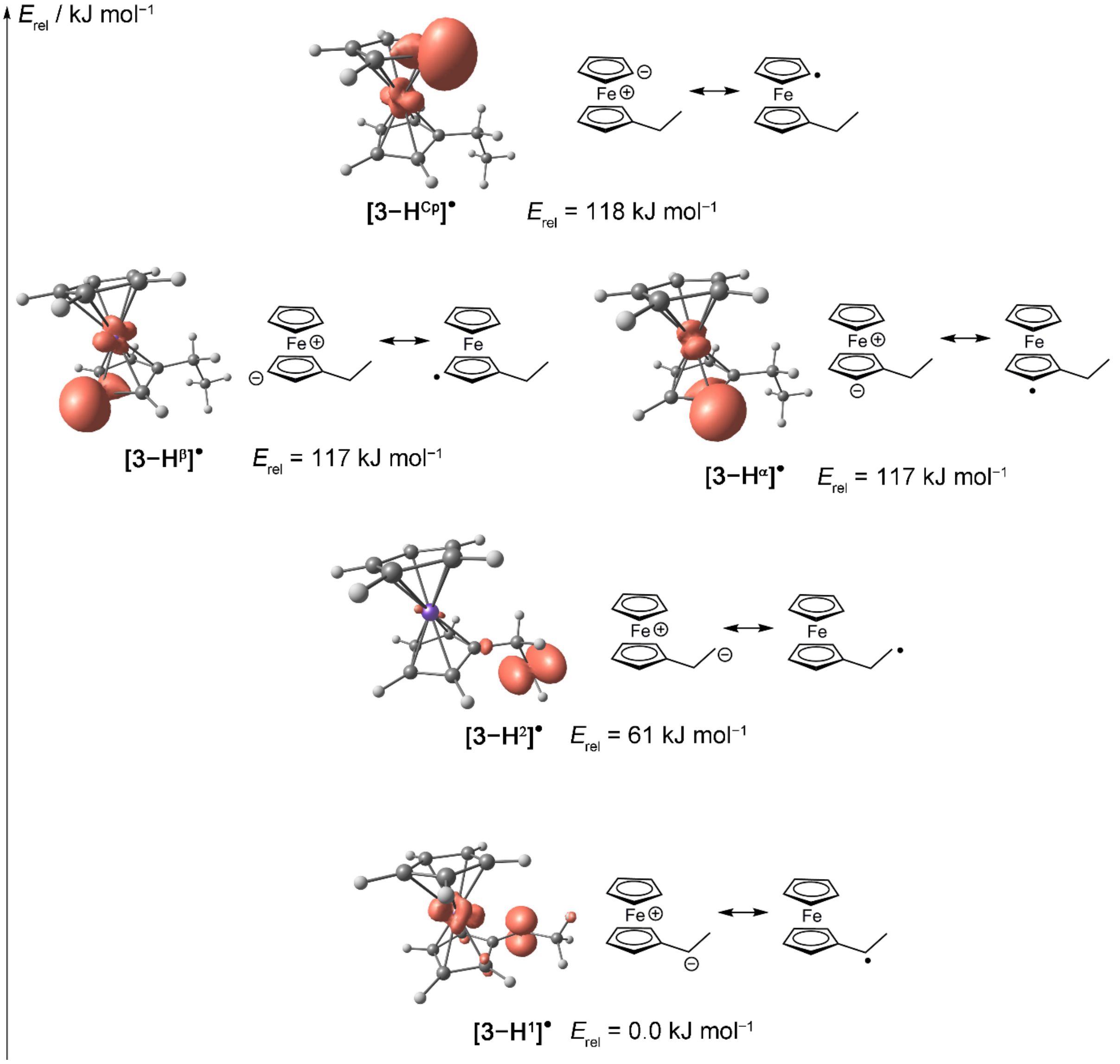

Figure S7: DFT optimized geometries with spin densities (0.01 a.u. isosurface value) and energies in CH_2Cl_2 continuum solvent as well as chemical structures for spin-trapped products of $[8^x]^\bullet$ (x = α, β, Cp, 1, 2).

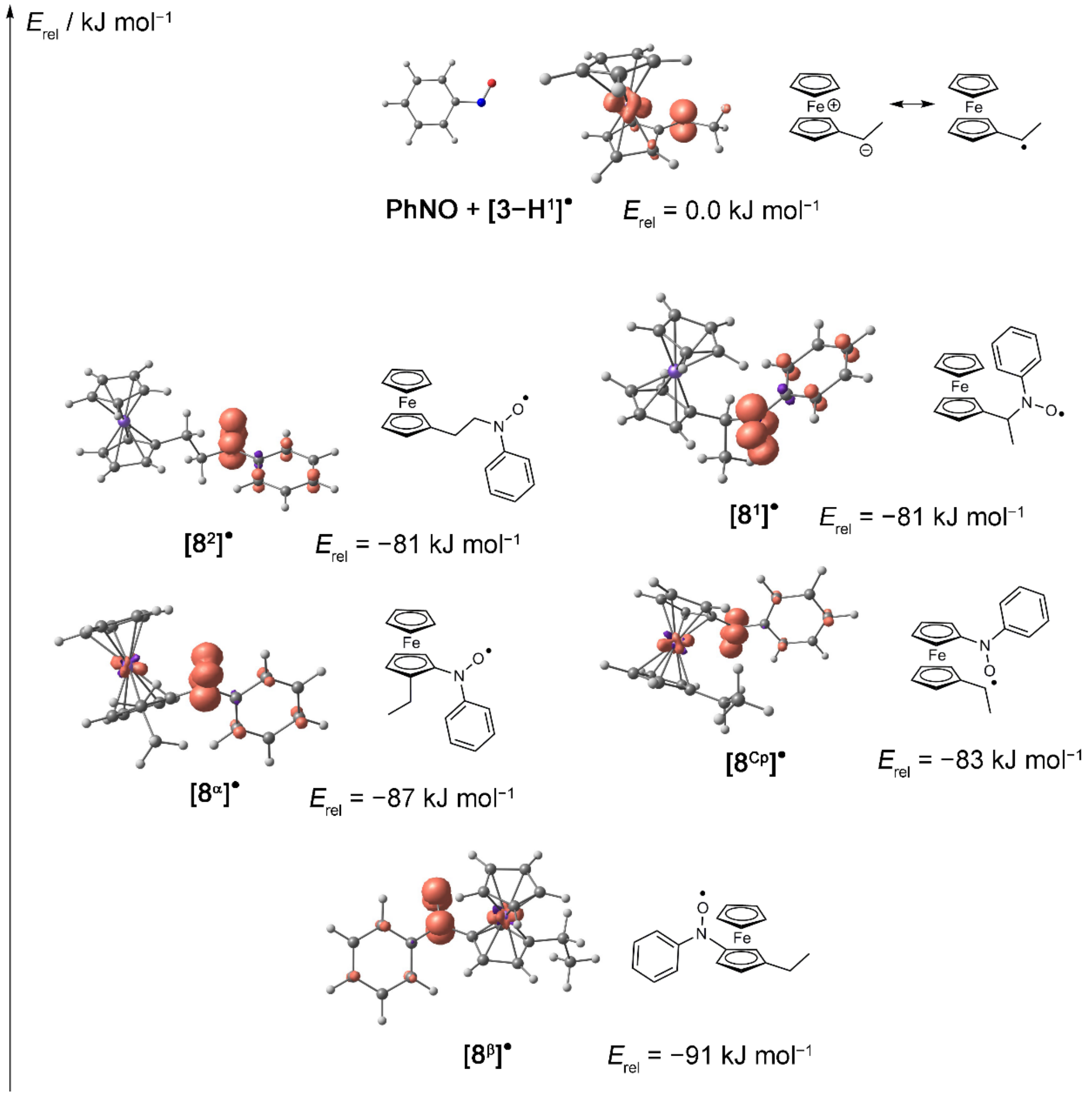

Figure S8: X-band EPR spectrum (top) and simulated spectrum (bottom) of a mixture of [4−H^{N}]$^{\bullet}$ and [4−H^{x}]$^{\bullet}$ (x = α, β, Cp) (5 mM) prepared from 4^{+} + P$_1$^{t}Bu in CH$_2$Cl$_2$ at the following parameters: a) temperature = 77 K; field = 3346.20 G, sweep = 499.77 G, sweep time = 90 s, modulation = 5000 mG, MW attenuation = 10 db and b) temperature = 298 K; field = 3346.20 G, sweep = 94.79 G, sweep time = 90 s, modulation = 1000 mG, MW attenuation = 10 db.

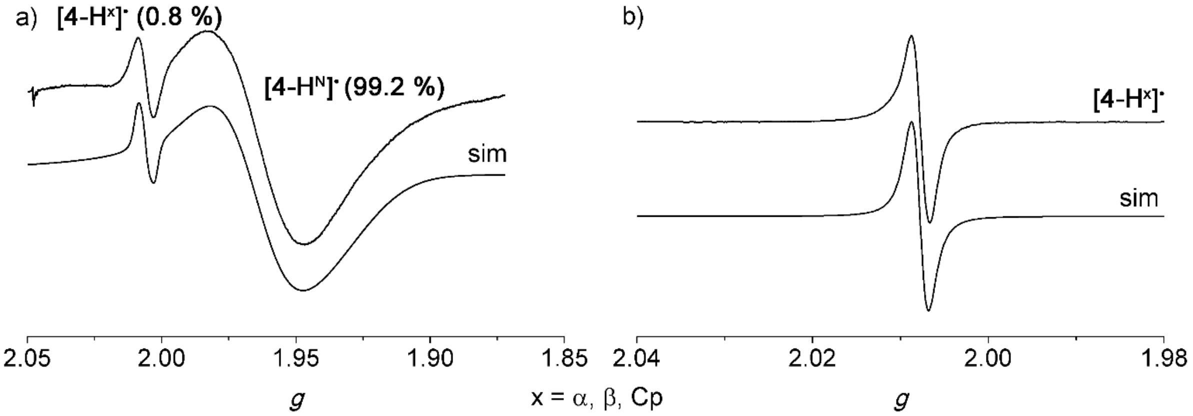

Figure S9: DFT optimized geometries with spin densities for [4−H^x]$^•$ (x = α, β, Cp, N, Me) (0.01 a.u. isosurface value) and energies in CH_2Cl_2 continuum for [4−H^x]$^•$, [5−H^x]$^•$ (x = α, β, Cp, N, Me), and [4−H$^{N'}$]$^•$ as well as chemical structures.

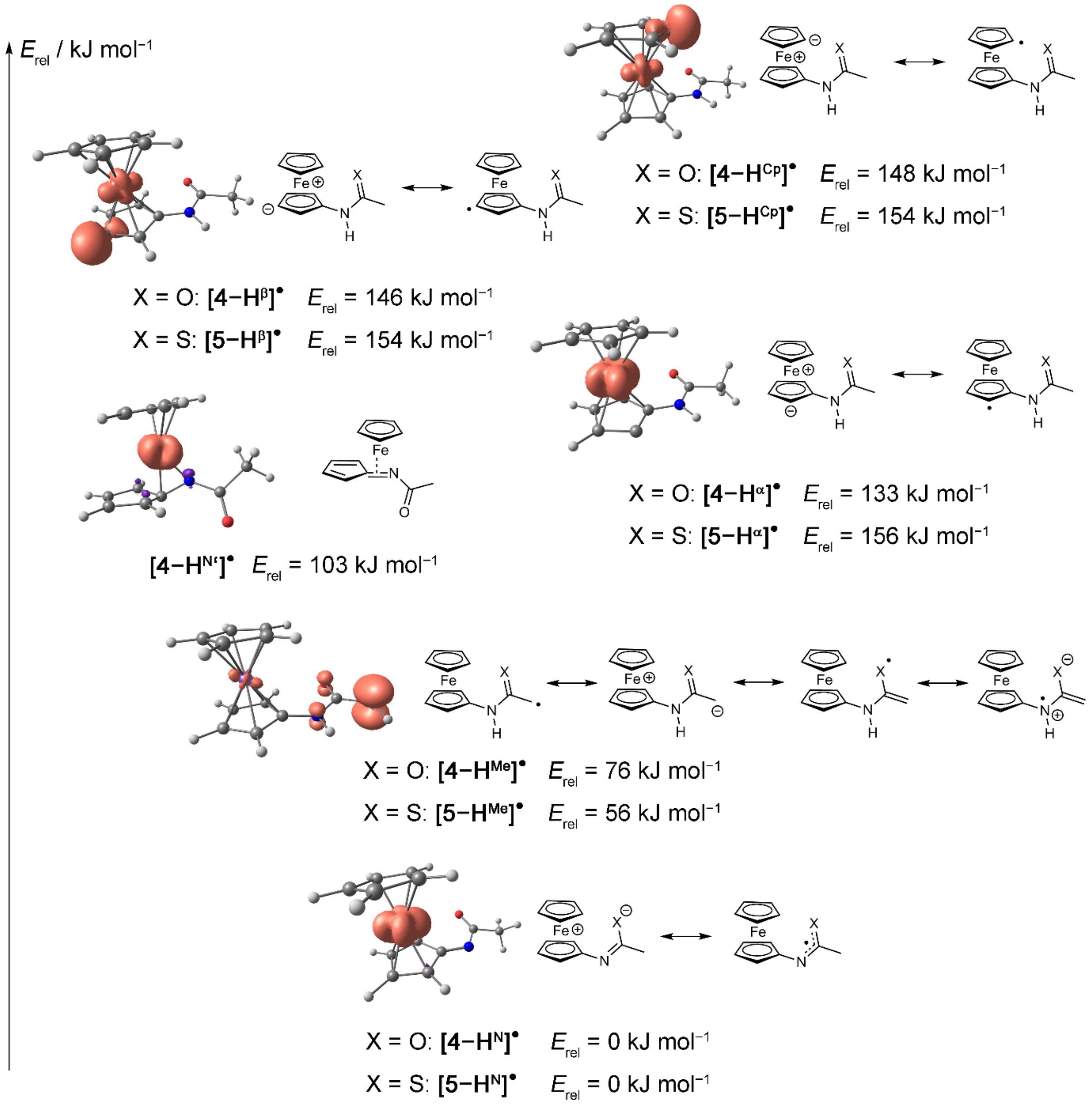

Figure S10: a) (top) Square wave and (bottom) cyclic voltammogram of 4 and b) cyclic voltammograms of a 4/P$_1{}^t$Bu mixture; red, dashed curve represents sole measurement of reduction feature. All measurements performed in CH$_2$Cl$_2$ containing [^{n}Bu$_4$N][B(C$_6$F$_5$)$_4$] as supporting electrolyte at 298 K.

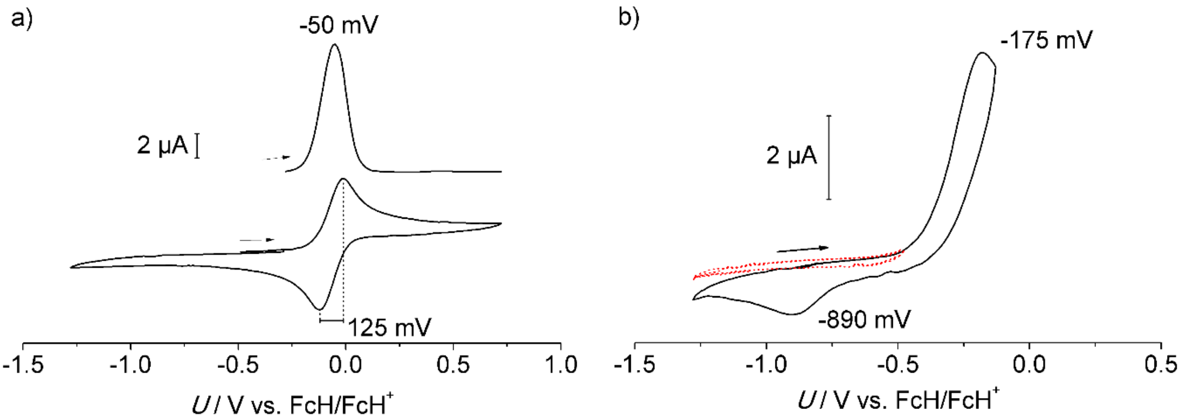

Figure S11: Experimental, baseline corrected X-band EPR spectra and values of second integration of 5 mM solutions of (a) [6]$^•$, (b) [7]$^•$, (c) [8^1]$^•$, d) [9^x]$^•$ (x = α, β, Cp), and e) [10^{Cp}]$^•$ in CH$_2$Cl$_2$ recorded at the following parameters: temperature = 298 K; field = 3346.20 G, sweep = 94.79 G, sweep time = 90 s, modulation = 1000 mG, MW attenuation = 10 db.

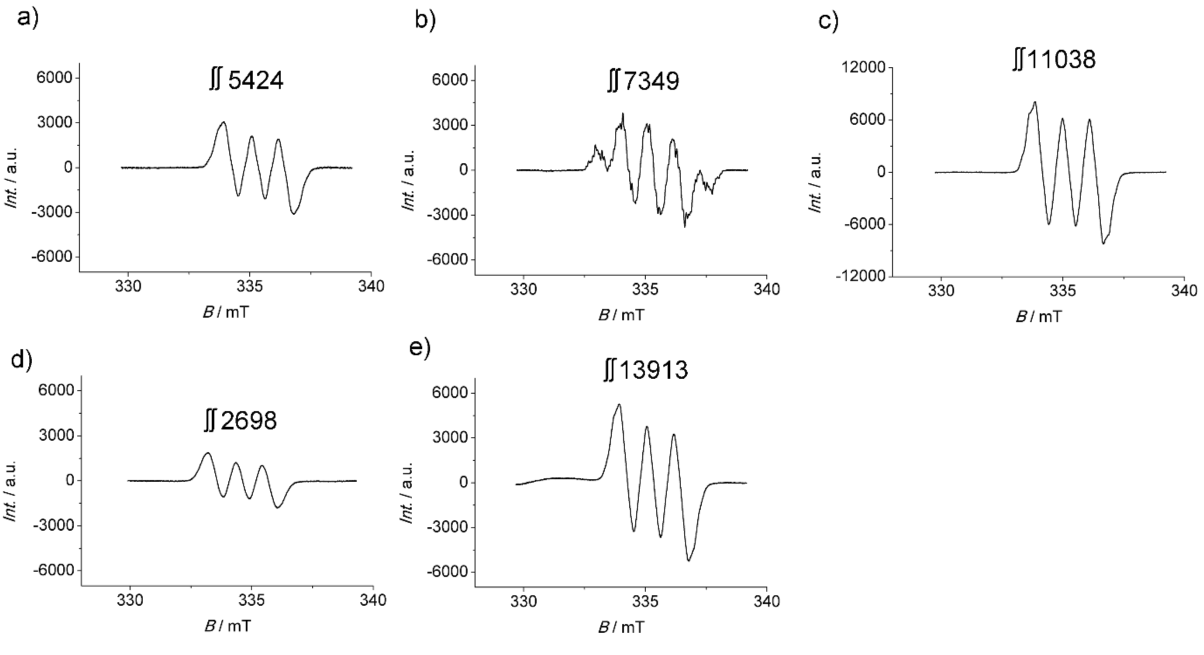

Figure S12: Experimental, baseline corrected X-band EPR spectra and values of second integration of (a) 0.03 mM, (b) 0.01 mM, and (c) 0.005 mM DPPH solutions in CH_2Cl_2 recorded at the following parameters: temperature = 298 K; field = 3346.20 G, sweep = 94.79 G, sweep time = 90 s, modulation = 1000 mG, MW attenuation = 10 db. (d) Linear regression of double integral values against concentration.

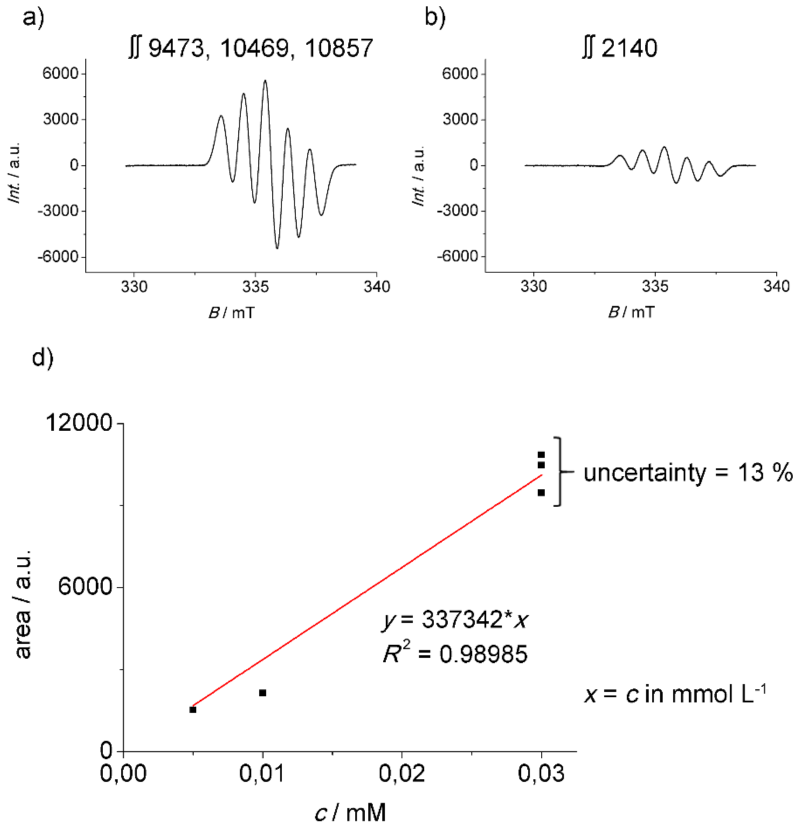

For Cartesian coordinates of **[1−H]$^\bullet$, [6]$^\bullet$, 1$^+$, [6^{Fe}]$^\bullet$, [2−H]$^\bullet$, [7]$^\bullet$, [3−H^1]$^\bullet$, [3−H^2]$^\bullet$, [3−H$^\beta$]$^\bullet$, [3−H$^\alpha$]$^\bullet$, [3−H^{Cp}]$^\bullet$, [8$^\beta$]$^\bullet$, [8$^\alpha$]$^\bullet$, [8^{Cp}]$^\bullet$, [8^2]$^\bullet$, [8^1]$^\bullet$, [4−H^N]$^\bullet$, [4−H$^\alpha$]$^\bullet$, [4−H$^\beta$]$^\bullet$, [4−H^{Cp}]$^\bullet$, [4−H$^{N'}$]$^\bullet$, [4−H^{Me}]$^\bullet$, [9^N]$^\bullet$, [9$^\beta$]$^\bullet$, [9$^\alpha$]$^\bullet$, [9^{Cp}]$^\bullet$, [9^{Me}]$^\bullet$, PhNO, [5−H^N]$^\bullet$, [5−H$^\alpha$]$^\bullet$, [5−H$^\beta$]$^\bullet$, [5−H^{Cp}]$^\bullet$, [5−H^{Me}]$^\bullet$, [10^N]$^\bullet$, [10$^\alpha$]$^\bullet$, [10$^\beta$]$^\bullet$, and [10^{Cp}]$^\bullet$.** (B3LYP, SV(P), COSMO: CH_2Cl_2) see electronic supporting information under http://pubs.acs.org/doi/suppl/10.1021/acs.organomet.5b00778/suppl_file/om5b00778_si_001.pdf.

5.3 To 3.3: How Hydrogen Bonds Affect Reactivity and Intervalence Charge Transfer in Ferrocenium-Phenolate Radicals

Andreas Neidlinger, Christoph Förster and Katja Heinze*

European Journal of Inorganic Chemistry **2016**, in print.

Figure S1. NOE spectra of (a) **H-2** in THF-d8 and (b) **H-5** in $CDCl_3$ at 298 K; mixing time 1 s; solvent signals are marked with an asterisk.

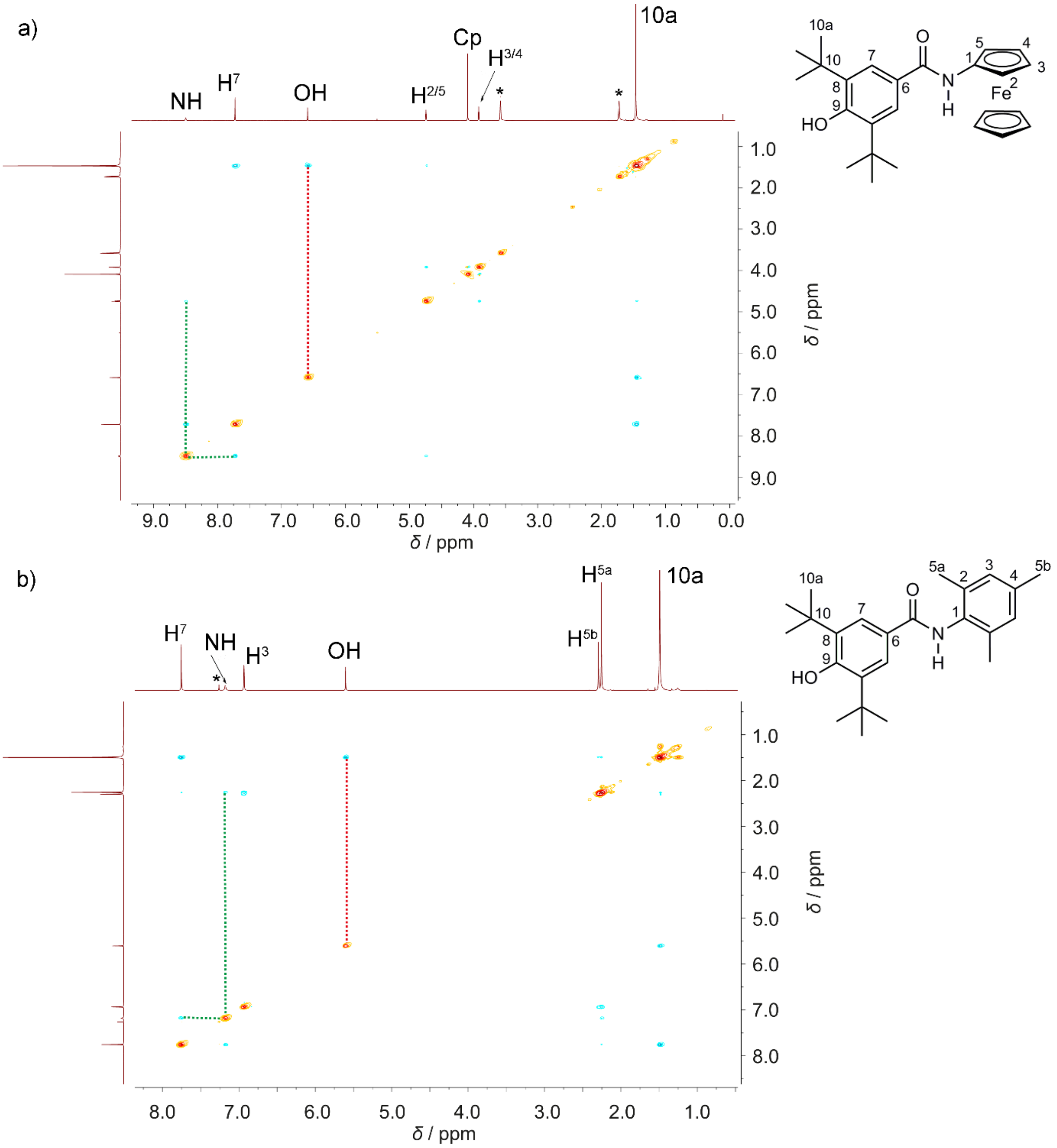

Table S1. Crystallographic data for **H-1**.

formula	$C_{25}H_{31}FeNO_2$
M	433.36
crystal system	$P2_1/c$
space group	monoclinic
a / Å	18.475(3)
b / Å	12.1652(17)
c / Å	10.0945(14)
α / °	90.0
β / °	102.921(4)
γ / °	90.0
V / Å^3	2211.3(6)
Z	4
ρ_{calcd} / g cm^{-3}	1.302
μ / mm^{-1}	0.702
F(000)	920
crystal size / mm	0.68 x 0.07 x 0.04
θ / °	2.662 – 27.924
limiting indices	$-23 \leq h \leq 24$, $-15 \leq k \leq 16$, $-13 \leq l \leq 13$
reflections collected	23624
unique reflections	5241
R_{int}	0.1581
completeness to θ = 27.92°	99.9 %
max. and min. transmission	0.9725 and 0.6467
data / restraints / parameters	5241 / 0 / 262
GOF on F^2	0.772
final R indices [$I > 2\sigma(I)$]: R_1 / wR_2	0.0487 / 0.0802
R indices (all data): R_1 / wR_2	0.1420 / 0.1021
largest difference peak and hole / e Å^{-3}	0.381 and −0.446

Figure S2. Inter- and intramolecular hydrogen bonds of three molecules **H-1** in the crystal (50 % probability level; CH hydrogen are atoms omitted).

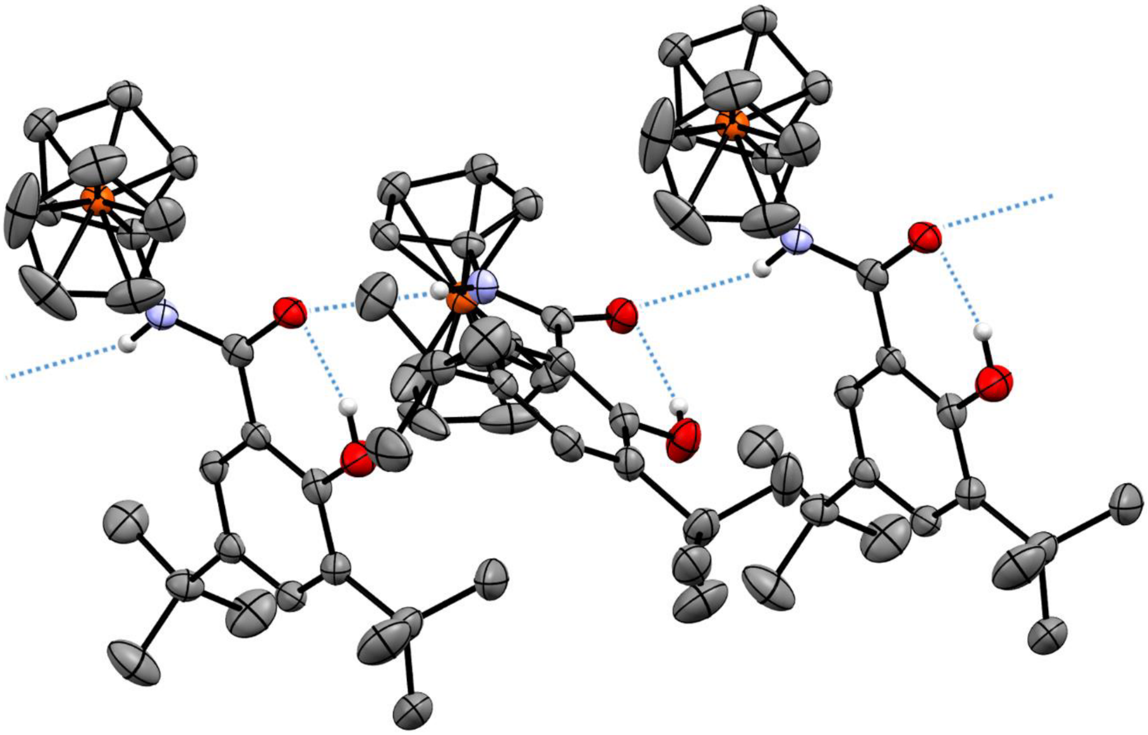

Figure S3. Gaussian deconvolution of NIR ligand field absorptions of **[1a]**$^{\bullet}$ in CH_2Cl_2 at 298 K.

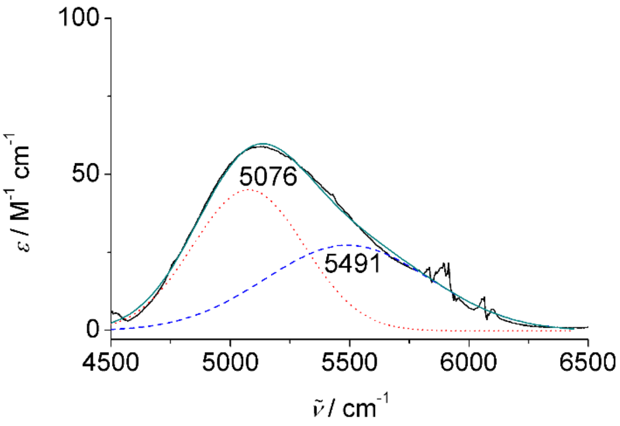

band 1: $\tilde{\nu}$ = 5076 cm^{-1}

$\tilde{\nu}_{1/2}$ = 548 cm^{-1}

ε = 45 M^{-1} cm^{-1}

band 2: $\tilde{\nu}$ = 5491 cm^{-1}

$\tilde{\nu}_{1/2}$ = 815 cm^{-1}

ε = 27 M^{-1} cm^{-1}

Table S2. TD-DFT (B3LYP/SV(P), COSMO CH$_2$Cl$_2$) calculated NIR absorption bands of **[1a]**$^{\bullet}$ and **[2a]**$^{\bullet}$

[1a]$^{\bullet}$					**[2a]**$^{\bullet}$				
$\tilde{\nu}$ / cm^{-1}	λ / nm	*f*	configurational composition	transition	$\tilde{\nu}$ / cm^{-1}	λ / nm	*f*	configurational composition	transition
3617	2765	0.006230346	114a → 115a: 0.015392 113b → 114b: 0.961161	phenolate → d_{xy} (Fc$^+$)	2467	4054	0.013587533	114a → 115a: 0.062169 110b → 114b: 0.010870 113b → 114b: 0.892706	phenolate → d_{xy} (Fc$^+$)
4865	2055	0.000010717	106b → 114b: 0.012145 107b → 114b: 0.899057 107b → 115b: 0.020630 107b → 123b: 0.024392	d_{x2-y2} → d_{xy} (Fc$^+$)	4962	2016	0.000111432	107b → 114b: 0.908660 107b → 115b: 0.021585 107b → 122b: 0.010279 107b → 123b: 0.022141	d_{x2-y2} → d_{xy} (Fc$^+$)
					5873	1703	0.000112399	112b → 114b: 0.988367	lone pair(phenolate) → d_{xy} (Fc$^+$)
7594	1317	0.000692262	108b → 114b: 0.891531 108b → 115b: 0.025944 108b → 123b: 0.018329 110b → 114b: 0.011490	d_{z2} → d_{xy} (Fc$^+$)	7724	1295	0.000028883	108b → 114b: 0.878303 108b → 115b: 0.027724 108b → 123b: 0.016214 110b → 114b: 0.021277 113b → 114b: 0.010239	d_{z2} → d_{xy} (Fc$^+$)
9168 [a]	1091	0.019990551	114a → 115a: 0.943685 113b → 114b: 0.017751 113b → 115b: 0.011013	phenolate → d_{xz} (Fc$^+$)	8089	1236	0.069745618	114a → 115a: 0.861474 113b → 114b: 0.061836 113b → 115b: 0.040878 113b → 117b: 0.012090	phenolate → d_{xz} (Fc$^+$)
10031	997	0.000025477	114a → 116a: 0.982627	phenolate → d_{yz} (Fc$^+$)	8378	1194	0.000035797	111a → 116a: 0.011021 114a → 116a: 0.979206	phenolate → d_{yz} (Fc$^+$)
12973	771	0.000118299	108b → 115b: 0.022015 112b → 114b: 0.934402	lone pair(phenolate) → d_{xy} (Fc$^+$)					

[a] Experimental IVCT $\tilde{\nu}_{exp}$ = 9615 cm^{-1} in CH$_2$Cl$_2$; calculated with B3LYP/LANL2DZ/CH$_2$Cl$_2$ at $\tilde{\nu}$ = 9843 cm^{-1}.[1]

Discussion of Table S2.

Despite the experimentally observed reactivity of ferrocenium phenolate **[2a]**$^{\bullet}$, its optical properties are accessible by theoretical calculations (TD-DFT) and can be compared to those of **[1a]**$^{\bullet}$. Charge transfer and d-d transitions, similar to **[1a]**$^{\bullet}$, are calculated for **[2a]**$^{\bullet}$ at 4054, 2016, 1703, 1295, 1236, and 1194 nm (2467, 4962, 5873, 7724, 8089, and 8378 cm^{-1}; Supporting Information, Table S2). The phenolate → d$_{xz}$(Fc^{+}) IVCT for **[2a]**$^{\bullet}$ is calculated at 1236 nm, slightly lower in energy than the corresponding IVCT for **[1a]**$^{\bullet}$ (1091 nm). This is based on the similar ground state energies of the zwitterion **[2a]**$^{\bullet}$ and the phenoxyl radical **[2b]**$^{\bullet}$ (Figure 4). All other IVCT transitions of **[2a]**$^{\bullet}$ (phenolate → d$_{yz}$(Fc^{+}) and phenolate → d$_{xy}$ (Fc^{+}); 1194 and 2016 nm) are calculated at lower energy as well. The ferrocinium d-d transitions, however, are calculated at essentially the same wavelengths as for **[1a]**$^{\bullet}$ at 2016 and 1295 nm. Obviously, hydrogen bonding within substituents barely affects these metal-centered transitions. On the other hand, the lone pair(phenolate) → d$_{xy}$ (Fc^{+}) transitions of **[1a]**$^{\bullet}$ (771 nm) and **[2a]**$^{\bullet}$ (1703 nm) differ significantly with that of **[2a]**$^{\bullet}$ being much lower in energy. This phenomenon is easily accounted for by the stabilization of the lone pair by the IHB in **[1a]**$^{\bullet}$.

Figure S4. Difference densities obtained from TD-DFT calculation of **[1a]**$^{\bullet}$ in CH$_2$Cl$_2$ continuum solvent. Purple lobes indicate electron loss and red lobes indicate increasing electron density upon excitation. CH protons are omitted for clarity.

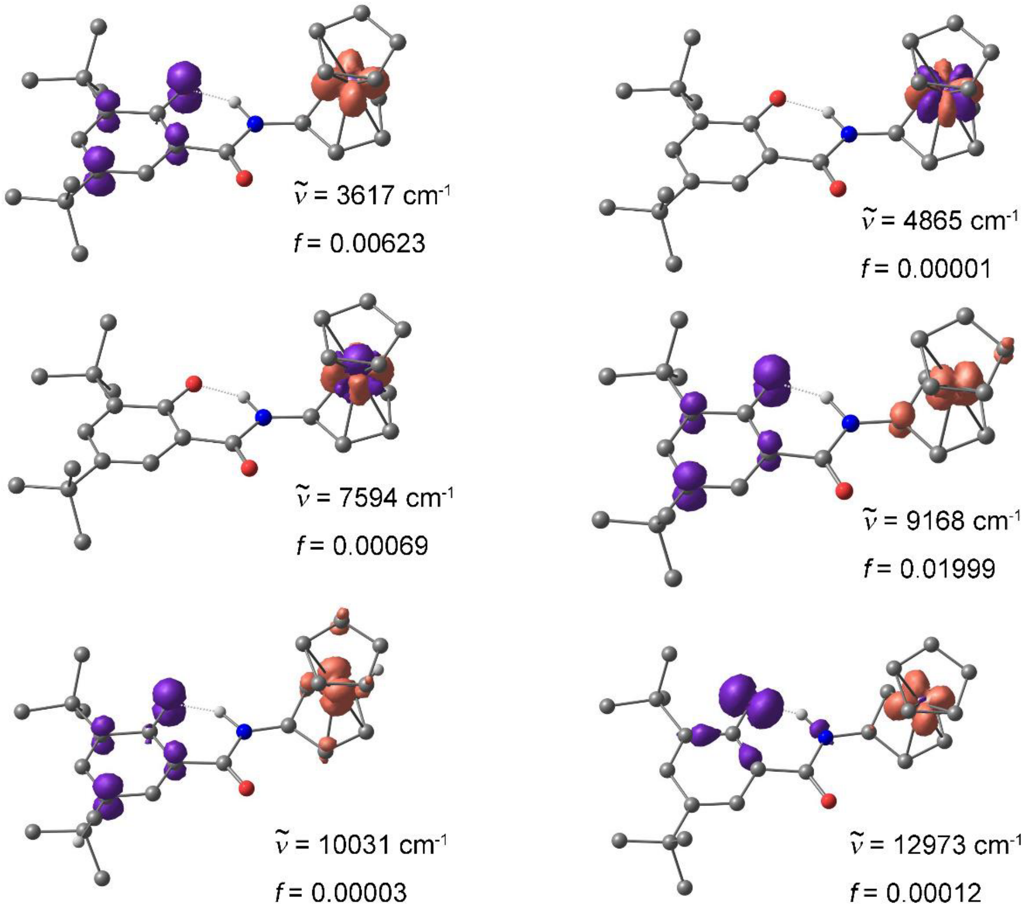

$\tilde{\nu}$ = 3617 cm^{-1}
f = 0.00623

$\tilde{\nu}$ = 4865 cm^{-1}
f = 0.00001

$\tilde{\nu}$ = 7594 cm^{-1}
f = 0.00069

$\tilde{\nu}$ = 9168 cm^{-1}
f = 0.01999

$\tilde{\nu}$ = 10031 cm^{-1}
f = 0.00003

$\tilde{\nu}$ = 12973 cm^{-1}
f = 0.00012

Figure S5. Difference densities obtained from TD-DFT calculation of **[2a]**$^\bullet$ in CH_2Cl_2 continuum solvent. Purple lobes indicate electron loss and red lobes indicate increasing electron density upon excitation. CH protons are omitted for clarity.

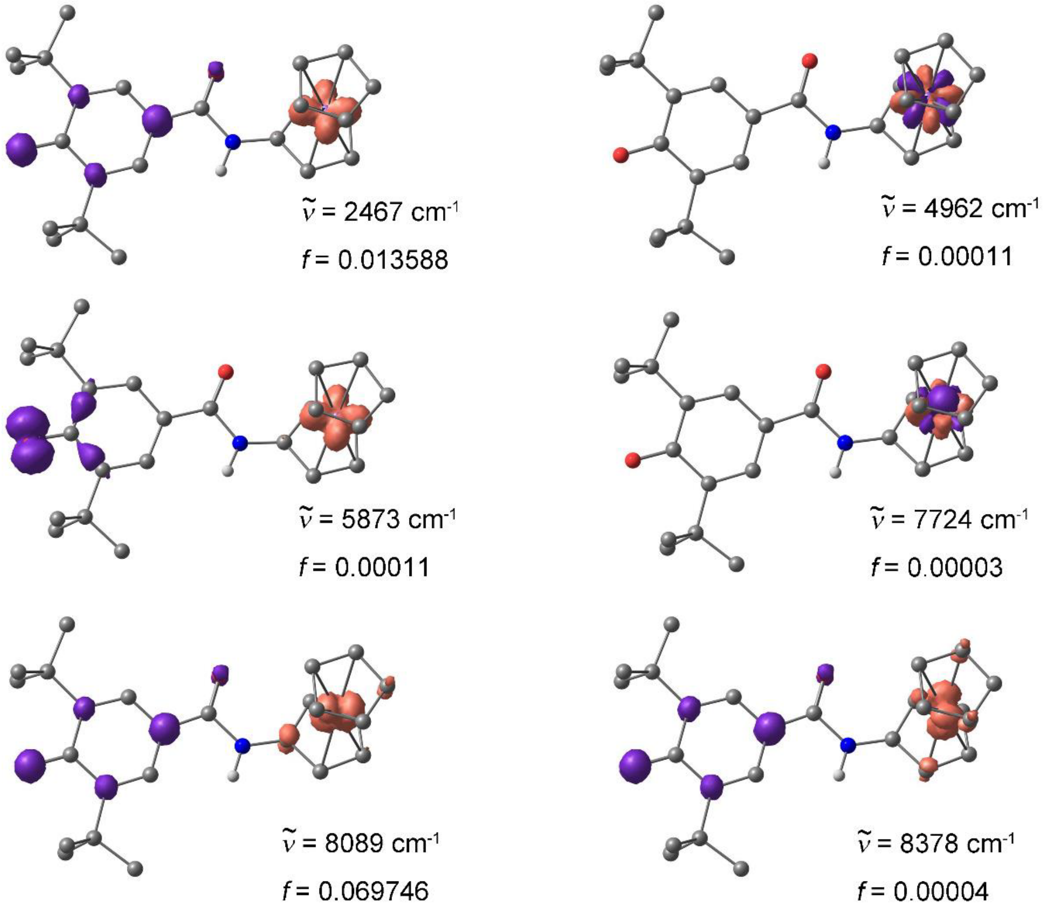

Figure S6. UV/Vis spectra of **H-2** (straight line) and **H-2**/$P_1{}^tBu$ (dotted line) in CH_2Cl_2 (a) and of **H-2** (straight line) and **2**$^-$ in CH_2Cl_2/[$^nBu_4N$][$B(C_6F_5)_4$] (dotted line) (b) at 298 K.

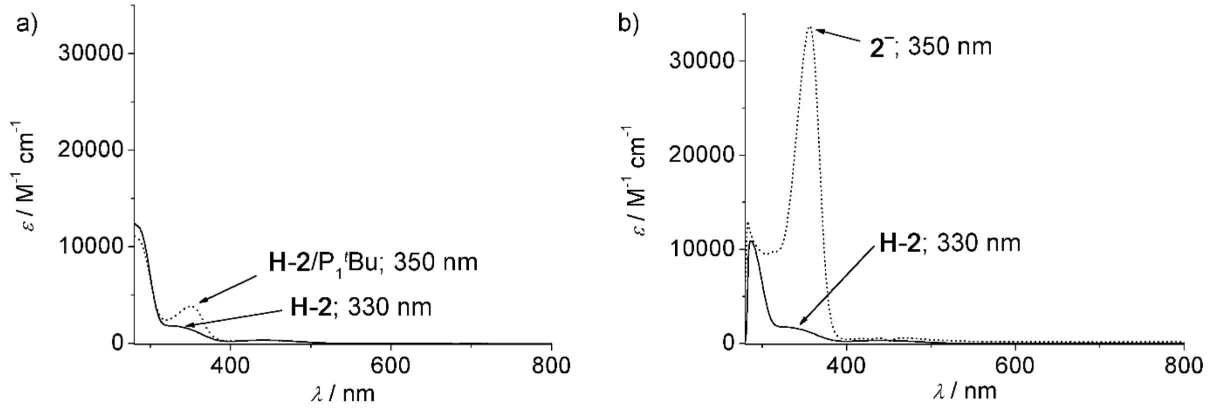

Figure S7. IR spectra of **H-2** and **H-2**/P$_1$^{t}Bu in CH_2Cl_2 (a) and of **H-2** and **2**$^-$ in CH_2Cl_2/[^{n}Bu$_4$N][B(C_6F_5)$_4$] (b) at 298 K (2 mM).

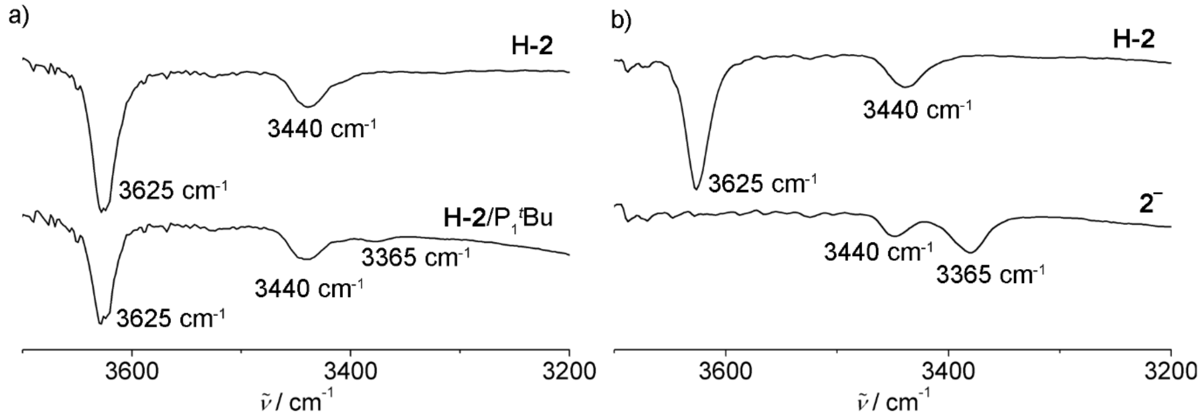

Figure S8. UV/Vis spectra of **H-5** and **H-5**/P$_1$^{t}Bu in CH_2Cl_2 (a) and of **H-5** in CH_2Cl_2 and **5**$^-$ in CH_2Cl_2/[^{n}Bu$_4$N][B(C_6F_5)$_4$] (b) at 298 K.

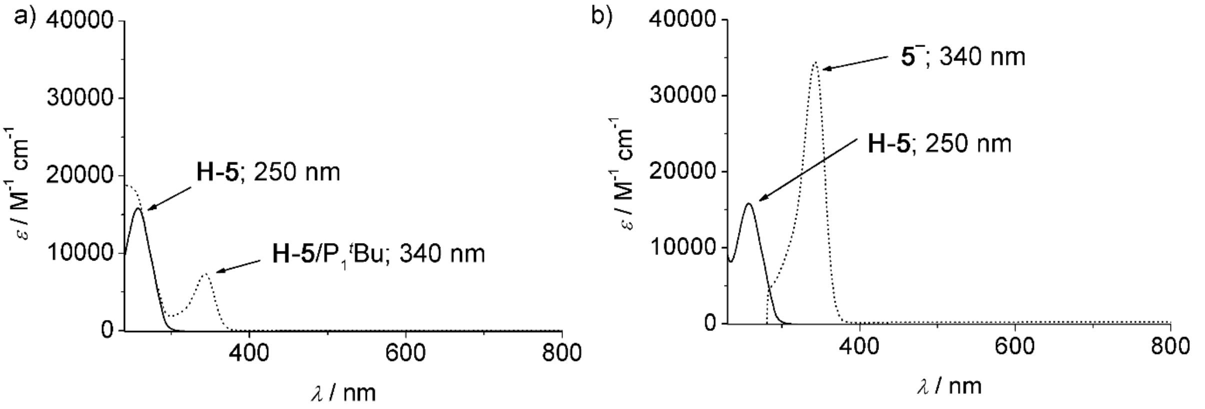

Figure S9. IR spectra of **H-5** and **H-5**/P$_1$^{t}Bu in CH_2Cl_2 (a) and of **H-5** and **5**$^-$ in CH_2Cl_2/[^{n}Bu$_4$N][B(C_6F_5)$_4$] (b) at 298 K (5 mM).

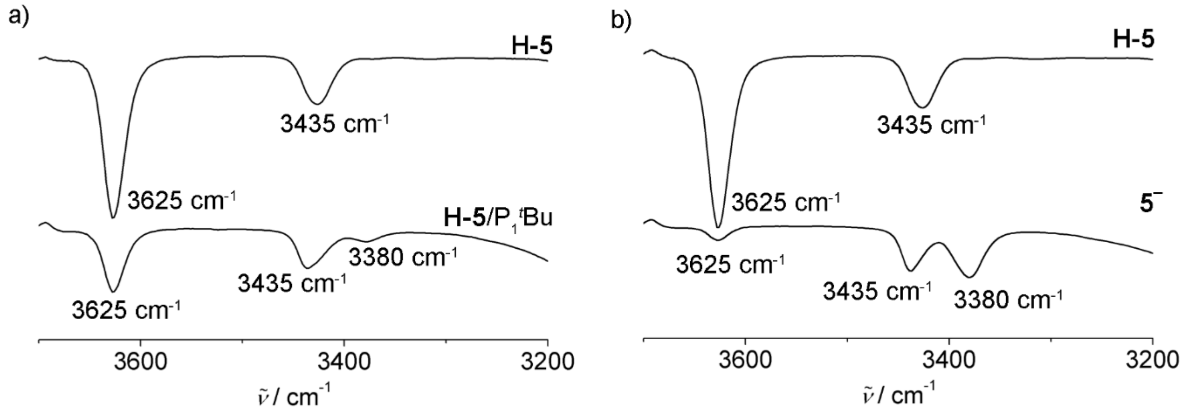

Figure S10. IR spectra of **H-3** + PhOH and **H-3** + PhOH + P$_1{}^t$Bu in CH$_2$Cl$_2$/[^{n}Bu$_4$N][B(C$_6$F$_5$)$_4$] at 298 K (5 mM).

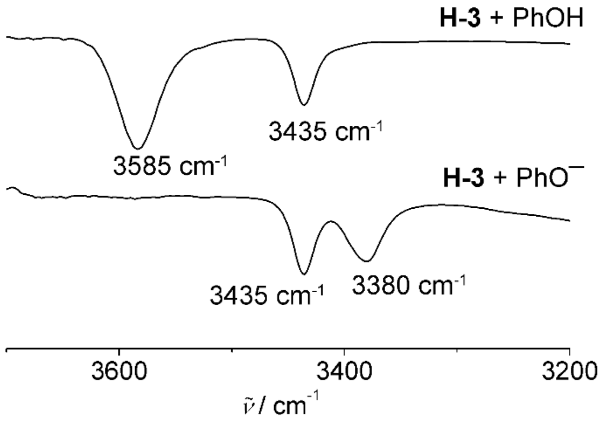

Figure S11: DFT/COSMO optimized geometries of **1**⁻ (a) and **2**⁻ (b) as phenolate (bottom) and iminolate (top) CH$_2$Cl$_2$ with energy differences. For **2**⁻ geometries, the 4-methyl substituent was omitted in DFT calculations due to difficulties in convergence. No significant influence on geometry or energy is expected.

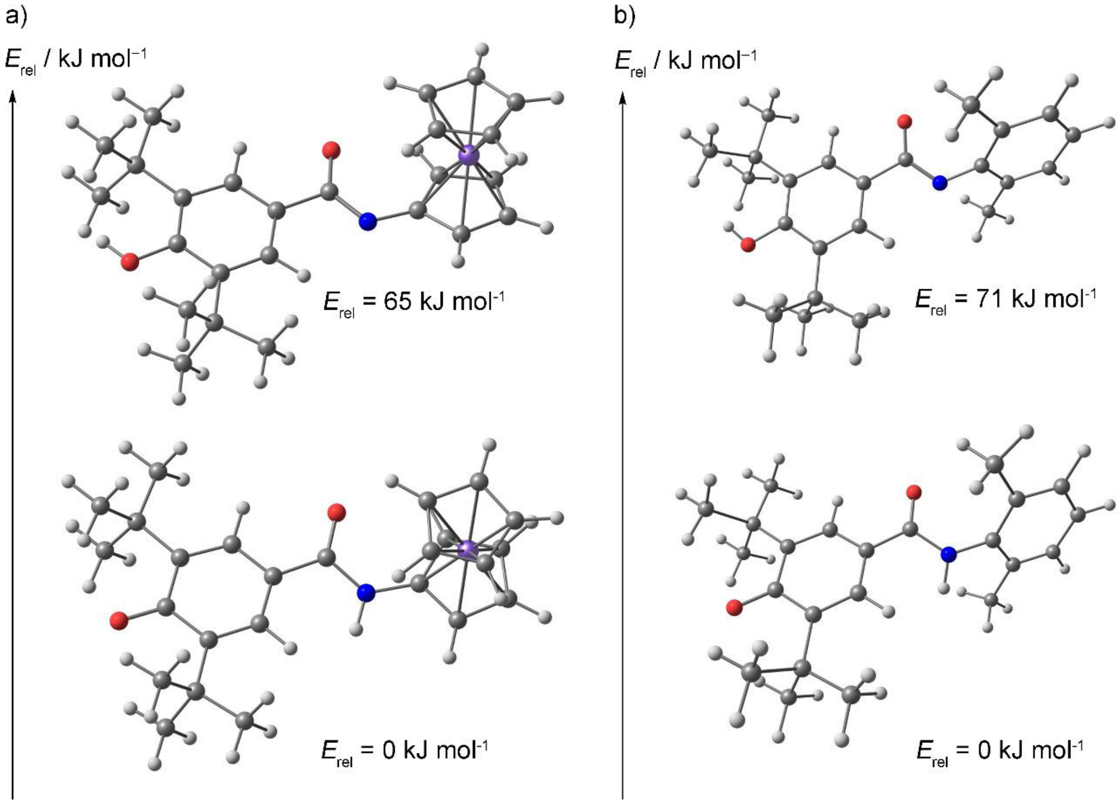

Figure S12: (top) Square wave and (bottom) cyclic voltammogram of **H-2** in CH_2Cl_2 containing [^{n}Bu$_4$N][B(C_6F_5)$_4$] as supporting electrolyte at 298 K.

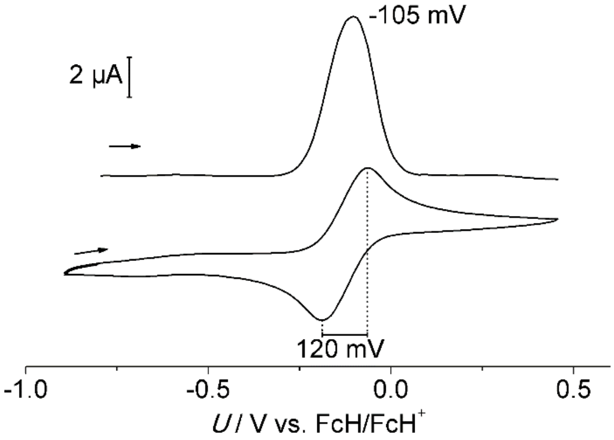

Figure S13: X-band (9.4 GHz) EPR spectrum (top) and simulated spectrum (bottom) of a 3mM solution of **[H-2]$^{\bullet+}$** in CH_2Cl_2 containing [^{n}Bu$_4$N][B(C_6F_5)$_4$] at 77 K recorded at the following parameters: field = 2499.01 G, sweep = 3788.47 G, sweep time = 90 s, modulation = 5000 mG, MW attenuation = 10 db.

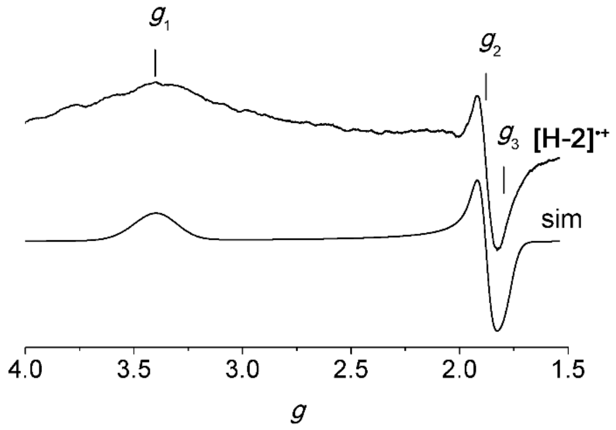

Figure S14: UV/Vis spectrum of $\mathbf{[H\text{-}2]}^{\bullet+}$ in $\mathrm{CH_2Cl_2}/[^n\mathrm{Bu_4N}][\mathrm{B(C_6F_5)_4}]$ at 298 K.

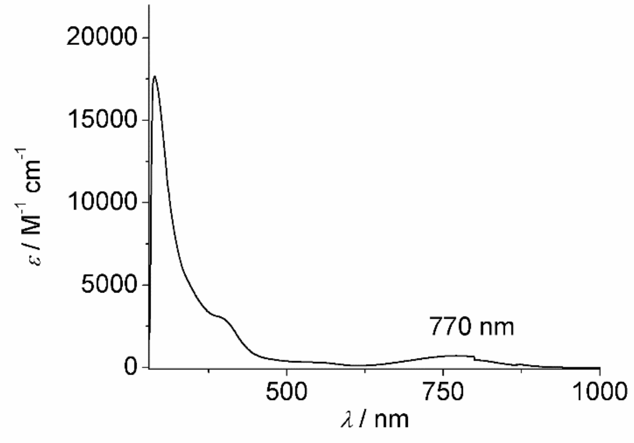

Figure S15: (top) Square wave and (bottom) cyclic voltammogram in $\mathrm{CH_2Cl_2}$ containing $[^n\mathrm{Bu_4N}][\mathrm{B(C_6F_5)_4}]$ as supporting electrolyte at 298 K of a) $\mathbf{[4]}^-$ and b) $\mathbf{[5]}^-$. The second, irreversible process at $E_\mathrm{p} = 360$ mV is assigned to the irreversible oxidation of $\mathrm{P_1}^t\mathrm{Bu}$, which was verified by previous electrochemical studies of $\mathrm{P_1}^t\mathrm{Bu}$ under the same experimental conditions, showing the irreversible process at $E_\mathrm{p} = 400$ mV.[2]

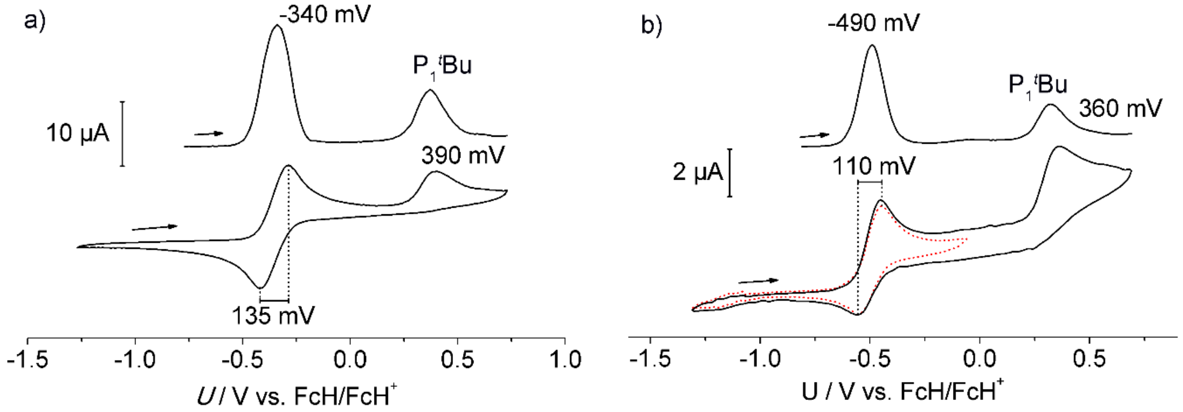

Figure S16: Cyclic voltammograms of the first oxidation of $\mathbf{[2]}^-$ in $\mathrm{CH_2Cl_2}$ containing $[^n\mathrm{Bu_4N}][\mathrm{B(C_6F_5)_4}]$ as supporting electrolyte at 298 K obtained at different scan rates.

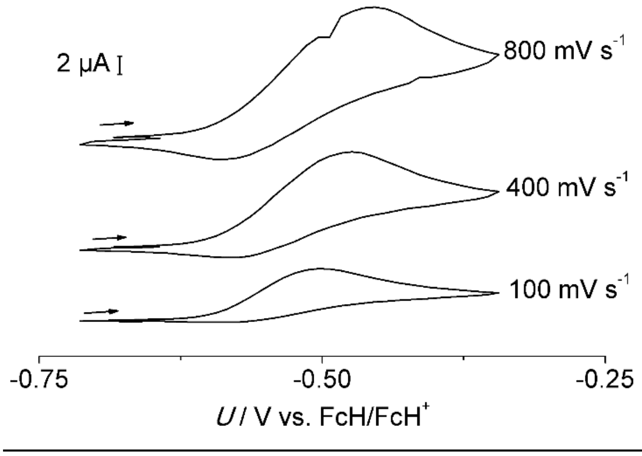

Figure S17. X-band rapid-freeze EPR spectrum of a 3 mM solution of **2$^•$** in CH$_2$Cl$_2$/[^{n}Bu$_4$N][B(C$_6$F$_5$)$_4$] at 77 K recorded at the following parameters: sweep time = 90 s, modulation = 5000 mG, MW attenuation = 10 db, (a) field = 2499.01 G, sweep = 3788.47 G, and (b) field = 3346.20 G, sweep = 499.77 G. The resonance marked with an asterisk is an artifact of the spectrometer, which is observed for highly diluted samples.

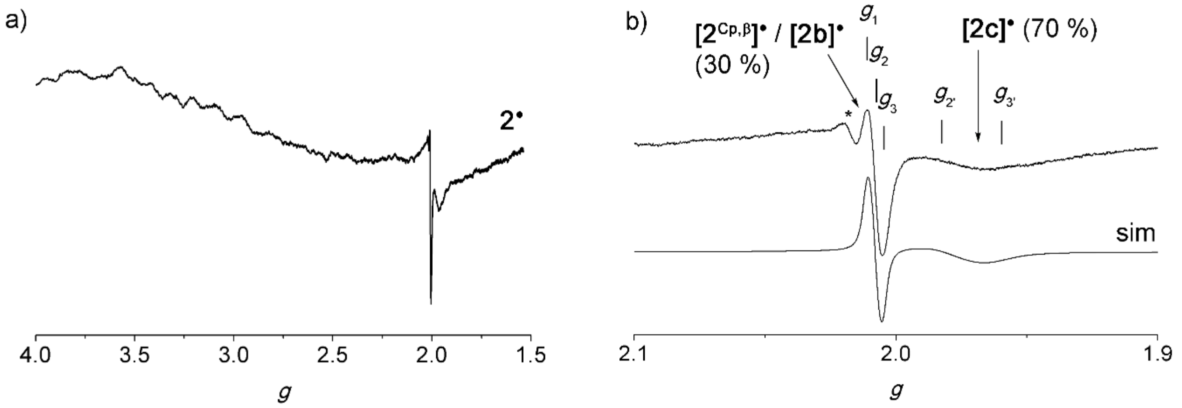

Figure S18: X-band EPR spectra and simulations of 5 mM solutions of a) **4**$^\bullet$ in CH_2Cl_2 at 298 K recorded at the following parameters: field = 3346.20 G, sweep = 94.79 G, sweep time = 90 s, modulation = 1000 mG, MW attenuation = 10 db, b) **4**$^\bullet$ in CH_2Cl_2 at 77 K recorded at the following parameters: field = 3346.20 G, sweep = 94.79 G, sweep time = 90 s, modulation = 250 mG, MW attenuation = 10 db, c) **5**$^\bullet$ in CH_2Cl_2/[^{n}Bu$_4$N][B(C_6F_5)$_4$] at 298 K recorded at the following parameters: field = 3346.20 G, sweep = 94.79 G, sweep time = 90 s, modulation = 250 mG, MW attenuation = 25 db, and d) **5**$^\bullet$ in CH_2Cl_2/[^{n}Bu$_4$N][B(C_6F_5)$_4$] at 77 K recorded at the following parameters: field = 3346.20 G, sweep = 94.79 G, sweep time = 90 s, modulation = 5000 mG, MW attenuation = 35 db.

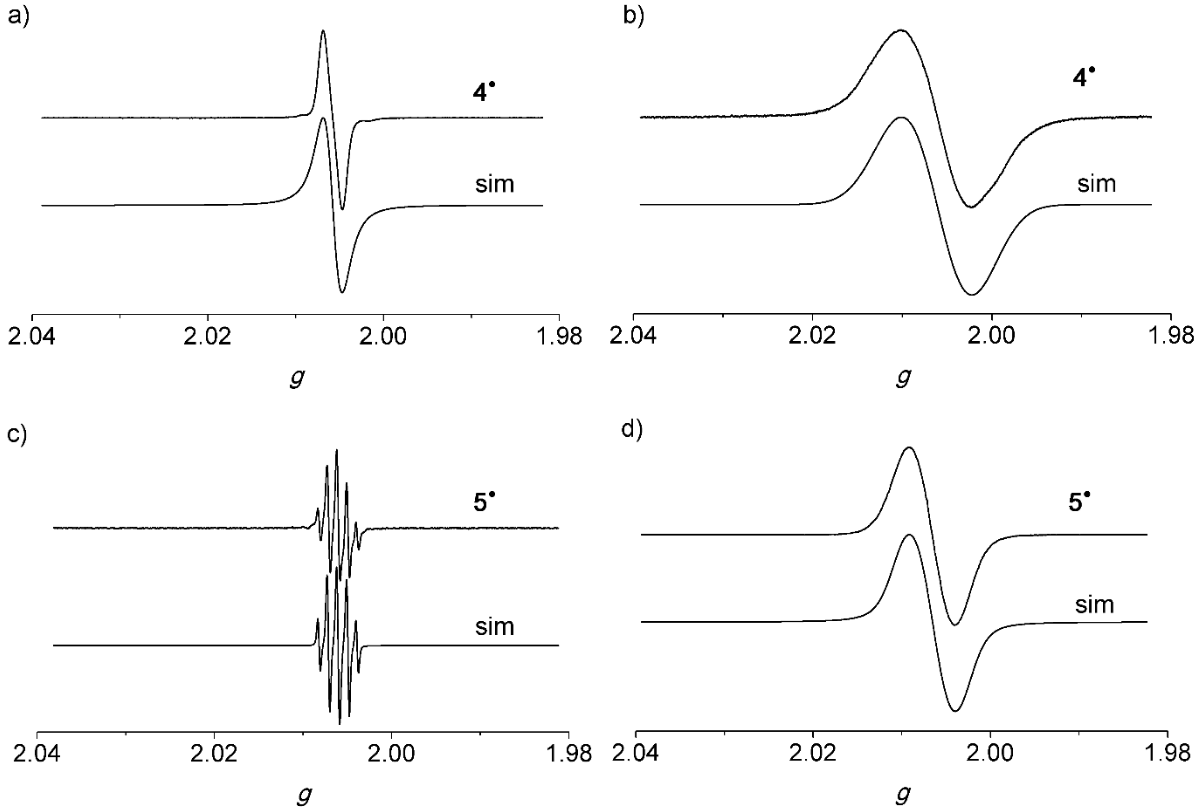

Figure S19: Lewis structures, DFT optimized geometries showing spin densities, and calculated relative energies of products spin-trapped at the phenolate / phenoxyl moiety with respect to the energy of the starting materials **[1a]**$^{\bullet}$ and PhNO in CH_2Cl_2 (red, spin densities at 0.01 a.u. isosurface value, C-H hydrogen atoms omitted).

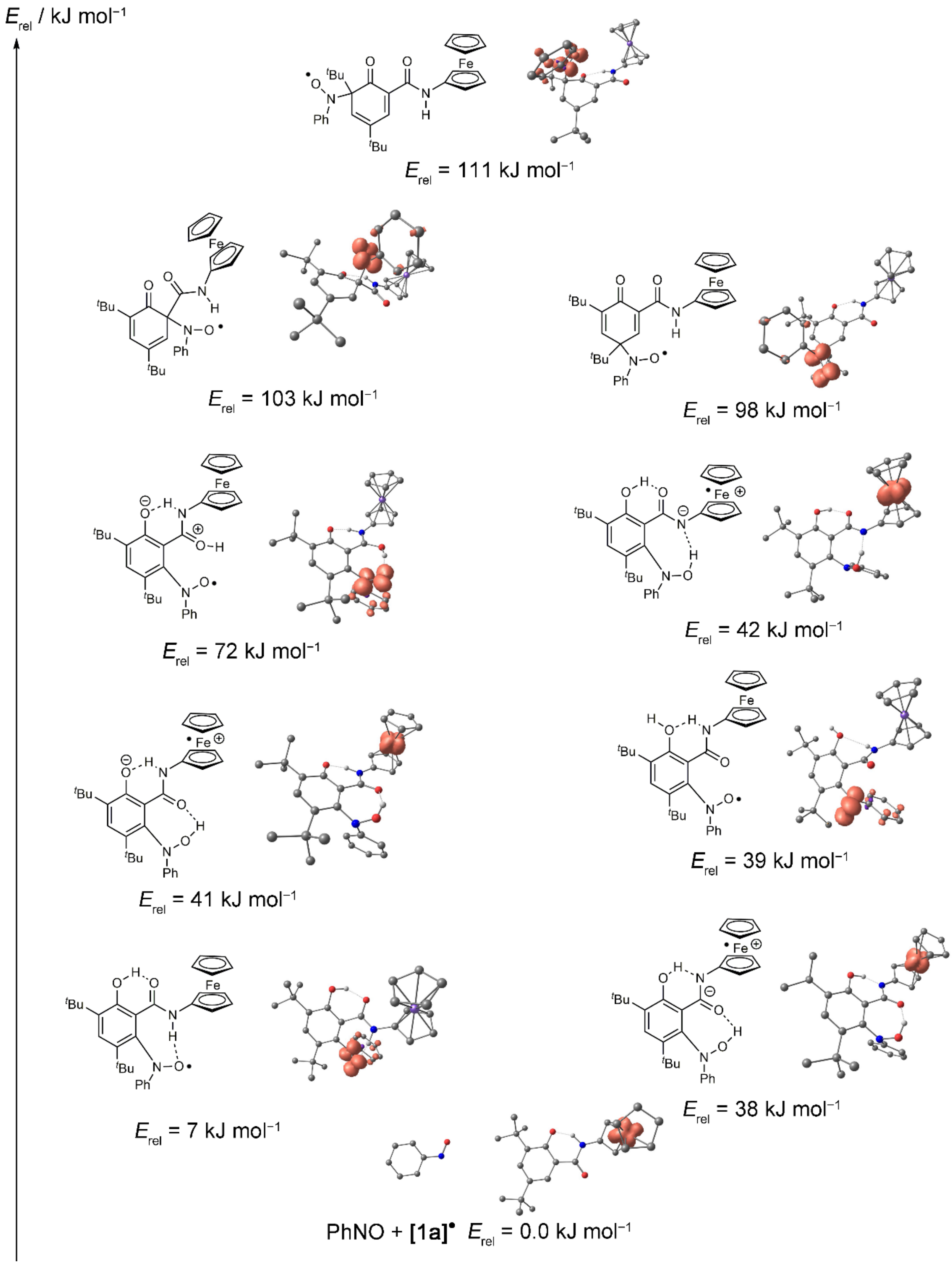

Figure S20: Lewis structures, DFT optimized geometries showing spin densities, and calculated relative energies of products spin-trapped at the phenolate / phenoxyl moiety with respect to the energy of the starting materials **[2a]**$^{\bullet}$ and PhNO in CH_2Cl_2 (red, spin densities at 0.01 a.u. isosurface value, C-H hydrogen atoms omitted).

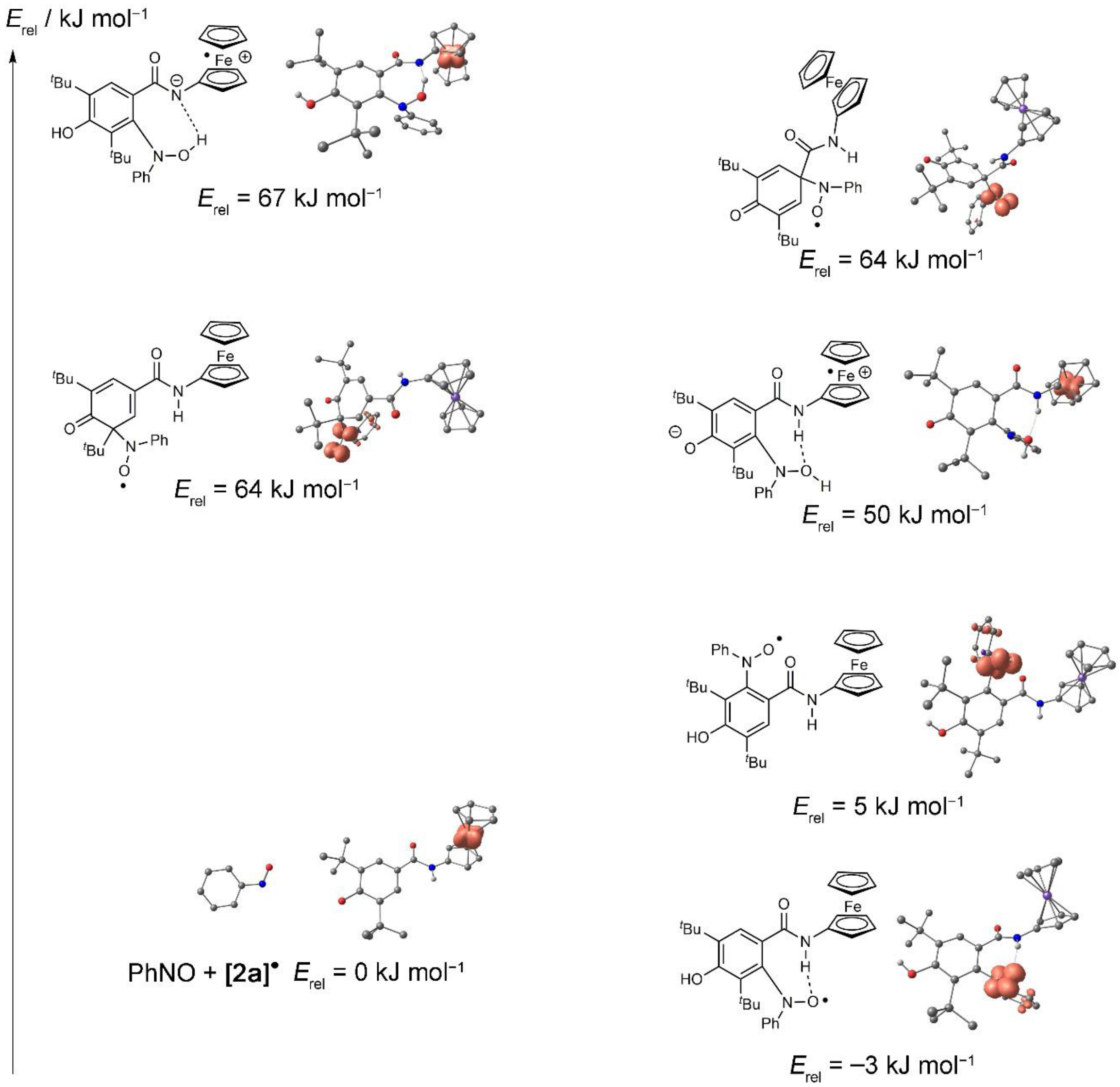

Figure S21: Lewis structures, DFT optimized geometries showing spin densities, and calculated relative energies of radical pool compounds **[1^x]$^\bullet$-OHO** and **[1^x]$^\bullet$-NHO** (x = α, β, Cp) as well as the valence isomer **[1b]$^\bullet$** and the tautomer **[1c]$^\bullet$** with respect to the energy of **[1a]$^\bullet$** in CH$_2$Cl$_2$ (red, spin densities at 0.01 a.u. isosurface value).

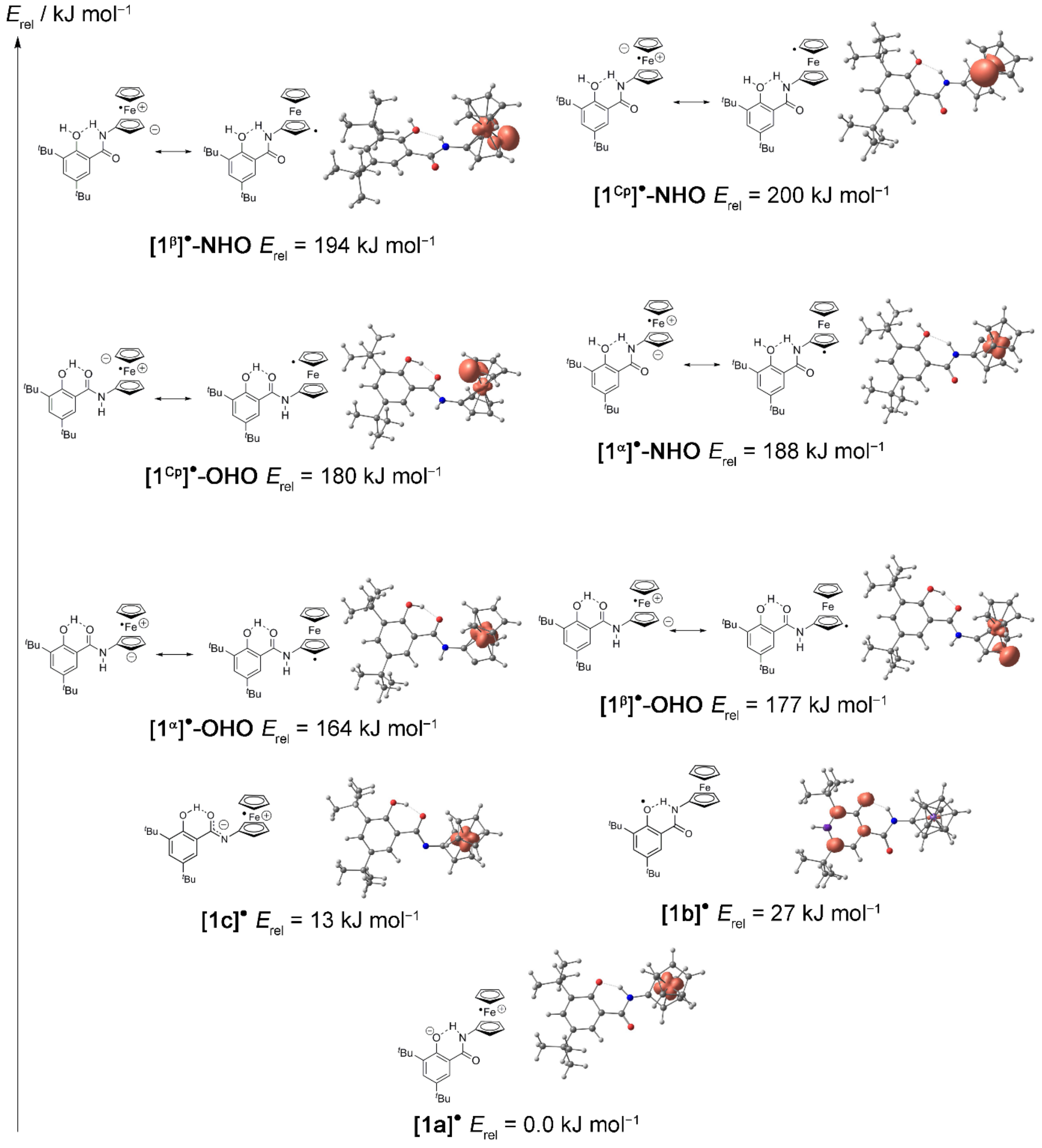

Figure S22: Lewis structures, DFT optimized geometries showing spin densities, and calculated relative energies of radical pool compounds **[2^x]•** (x = α, β, Cp) as well as the valence isomer **[2b]•** and the tautomer **[2c]•** with respect to the energy of **[2a]•** in CH_2Cl_2 (red, spin densities at 0.01 a.u. isosurface value).

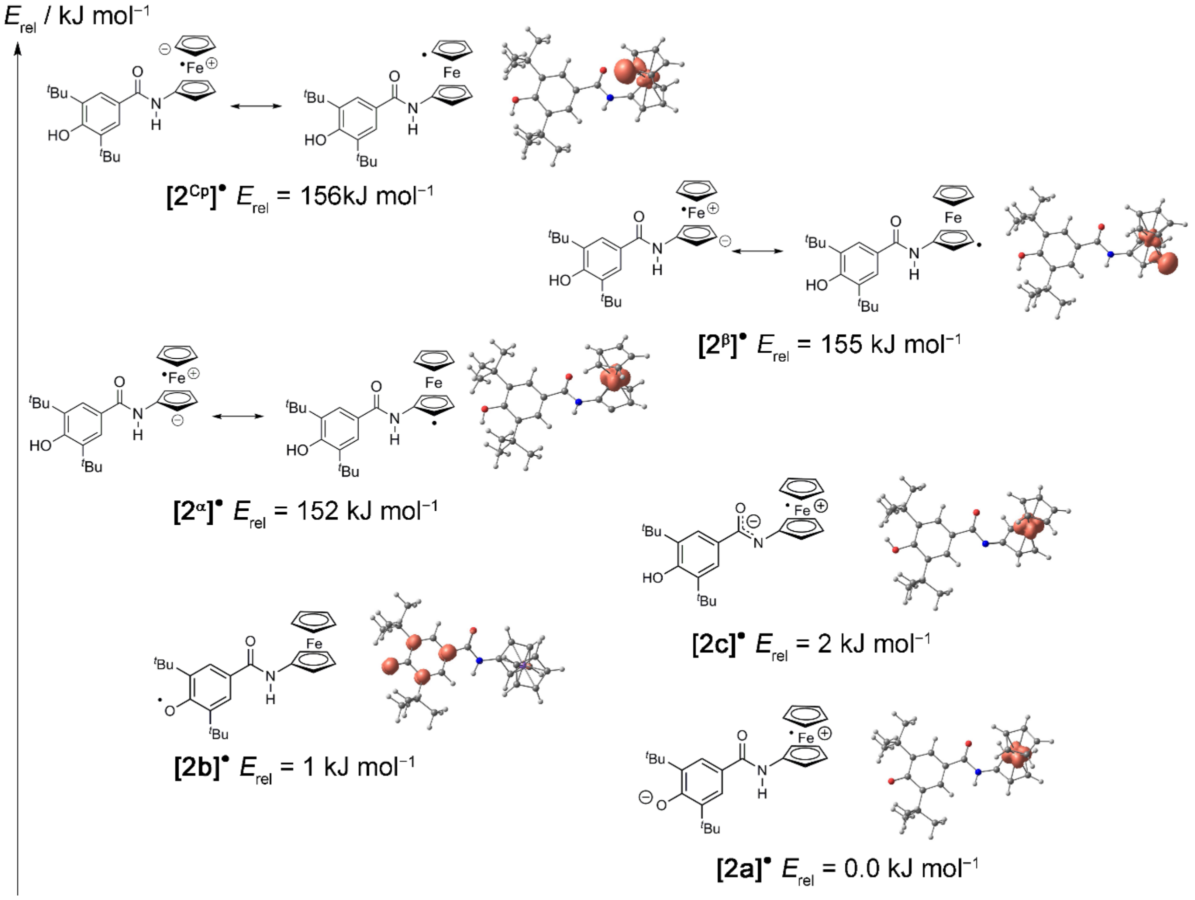

References:

[1] A. Neidlinger, V. Ksenofontov, K. Heinze, *Organometallics* **2013**, *32*, 5955–5965.

[2] A. Neidlinger, T. Kienz, K. Heinze, *Organometallics* **2015**, *34*, 5310−5320.

For Cartesian coordinates of DFT optimizations see electronic supporting information.

5.4 To 3.4: Conformational Switching of Multi-Responsive Ferrocenyl-Phenol Conjugates

Andreas Neidlinger, Christoph Förster and Katja Heinze*

To be Submitted.

Table S1. Crystallographic data for **H-1**.

formula	$C_{18}H_{24}FeN_2O_3$
M	372.24
crystal system	monoclinic
space group	$P2_1/c$
a / Å	12.9288(7)
b / Å	9.8943(6)
c / Å	14.6578(9)
α / °	90.0
β / °	110.508(3)
γ / °	90.0
V / Å^3	1756.21(18)
Z	4
ρ_{calcd} / g cm^{-3}	1.408
μ / mm^{-1}	0.877
F(000)	784
crystal size / mm	0.51 x 0.09 x 0.08
θ **/ °**	2.54 – 27.97
limiting indices	$-17 \leq h \leq 16$, $-12 \leq k \leq 13$, $-19 \leq l \leq 19$
reflections collected	15144
unique reflections	4225
R_{int}	0.0968
completeness to $\theta = 27.92°$	99.8 %
max. and min. transmission	0.9332 and 0.6634
data / restraints / parameters	4225 / 0 / 217
GOF on F^2	0.874
final R indices [$I > 2\sigma(I)$]: $R1$ / w$R2$	0.0444/ 0.0687
R indices (all data): $R1$ / w$R2$	0.0874 / 0.0799
largest difference peak and hole / e Å^{-3}	0.473 and −0.563

Figure S1. NOESY spectrum of **H-1$^{NHO\text{-}8}$** in CD_2Cl_2 at room temperature; mixing time 1 s; solvent signal marked with an asterisk.

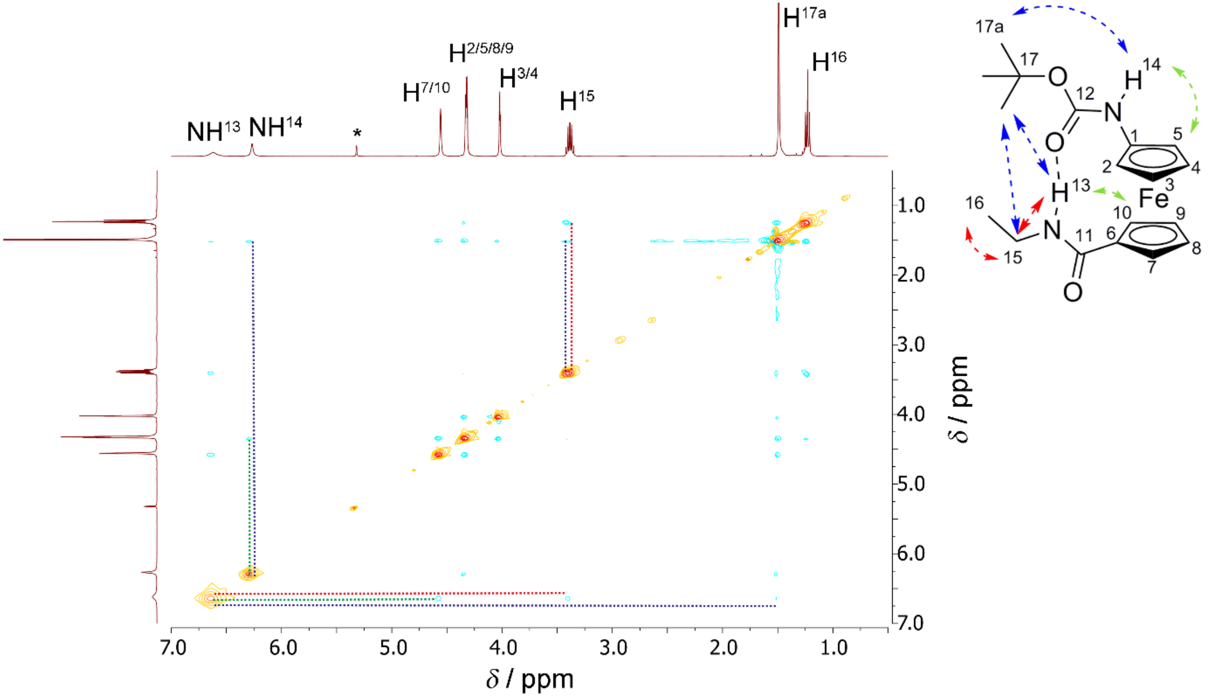

Figure S2. NOESY spectrum of **H-2^{OHONHO}** in CD_2Cl_2 at room temperature; mixing time 1 s; solvent signal marked with an asterisk.

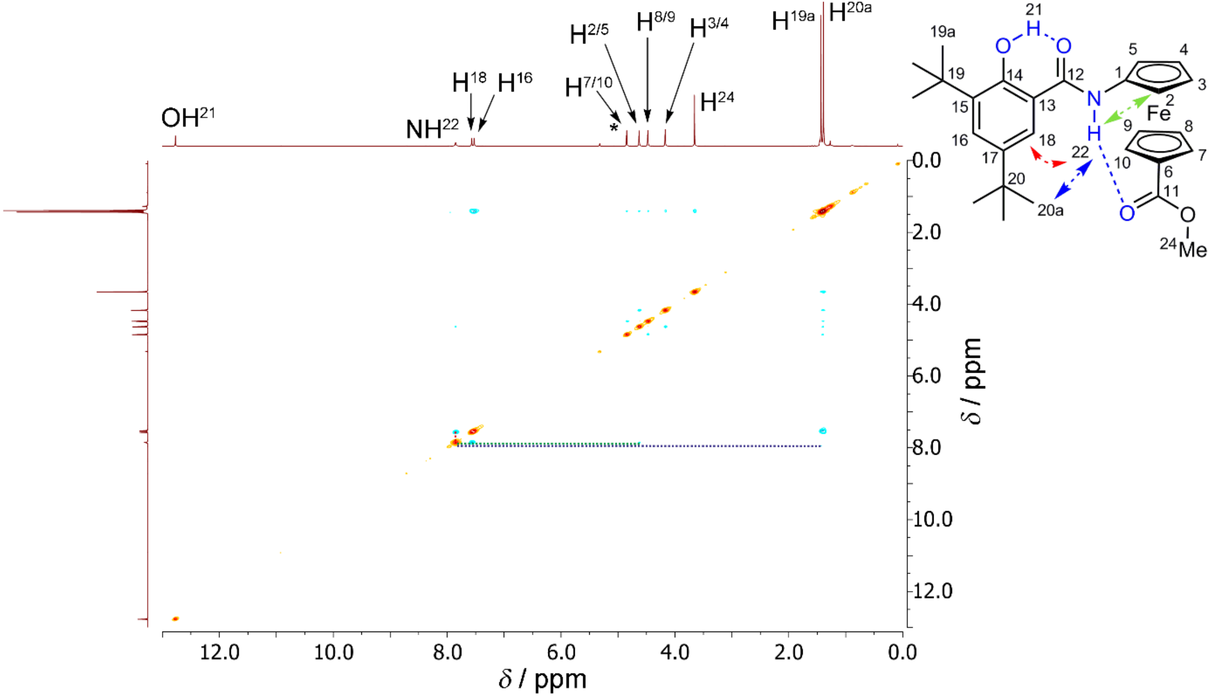

Figure S3. NOESY spectrum of $\mathbf{H\text{-}3}^{\mathbf{OHONHO\text{-}6}}$ in CD_2Cl_2 at room temperature; mixing time 1 s; solvent signal marked with an asterisk.

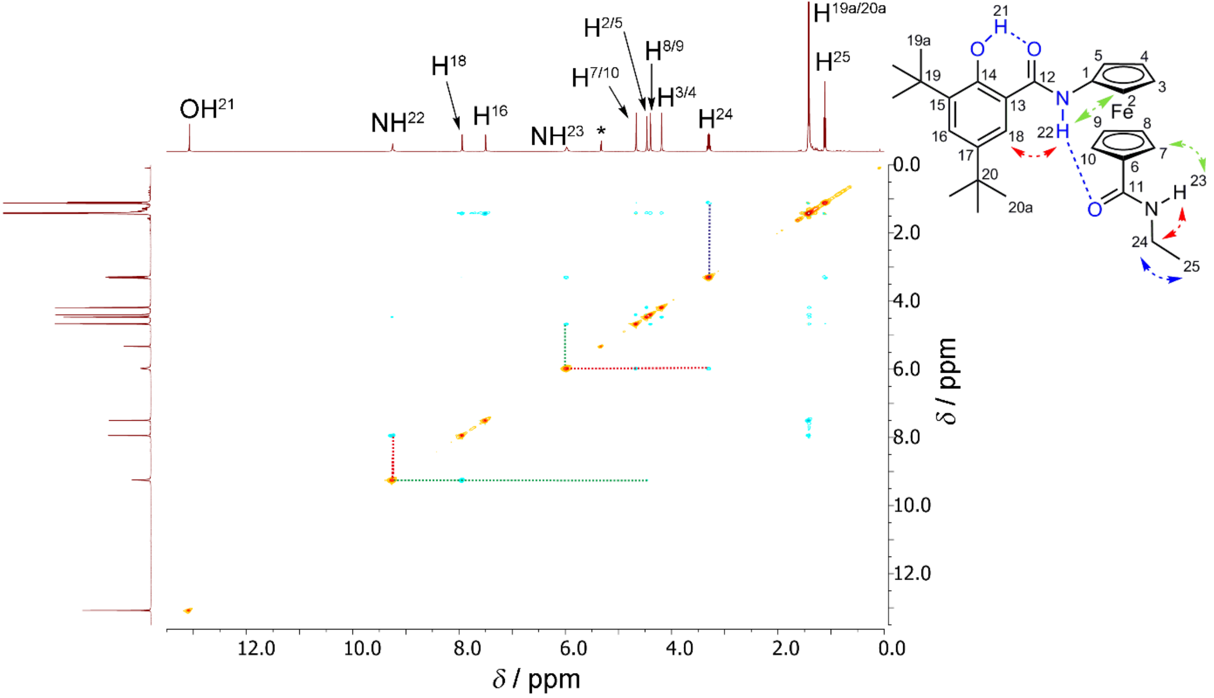

Figure S4. NOESY spectrum of $\mathbf{H\text{-}4}^{\mathbf{OHONHO\text{-}6}}$ in CD_2Cl_2 at room temperature; mixing time 1 s; solvent signal marked with an asterisk.

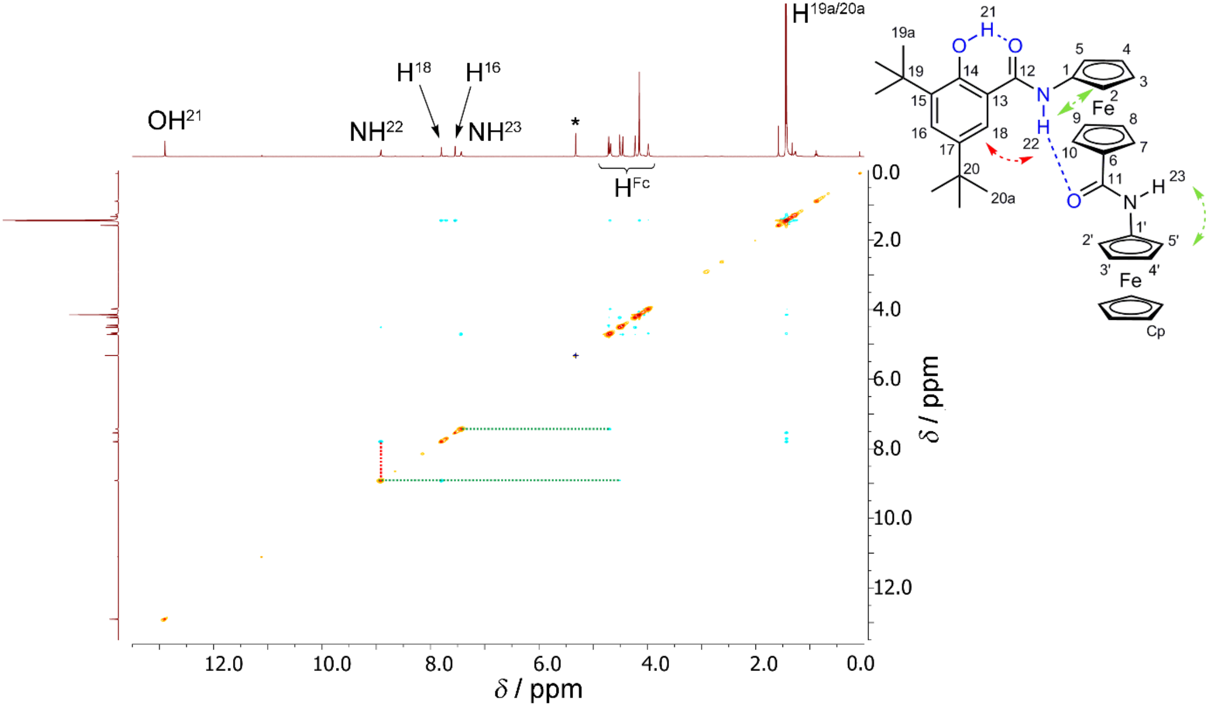

Figure S5. IR spectra of a) **H-1** (full line) and **[H-1]**$^{+\bullet}$ (dotted line), b) **H-2** (full line) and **[H-2]**$^{+\bullet}$ (dotted line), c) **H-3** (full line) and **[H-3]**$^{+\bullet}$ (dotted line), and d) **H-4** (full line), **[H-4]**$^{+\bullet}$ (dotted line) and **[H-4]**$^{2+}$ (dashed line) in CH_2Cl_2 at room temperature.

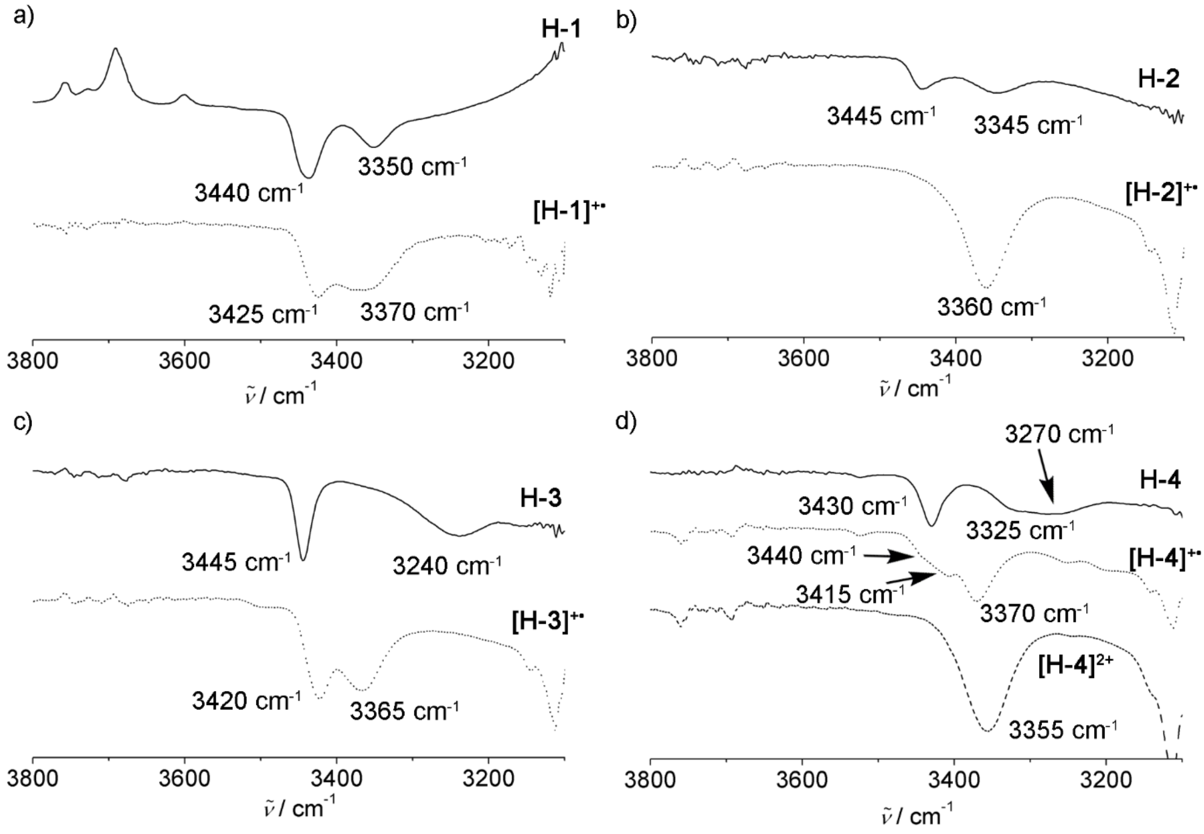

Figure S6. UV/Vis/NIR spectra of a) **H-1** (black) and **[H-1]**$^{+\bullet}$ (red), b) **[H-2]**$^{+\bullet}$, c) **[H-3]**$^{+\bullet}$, and d) **[H-4]**$^{+\bullet}$ (black) and **[H-4]**$^{2+}$ (red) in CH2Cl2 at room temperature.

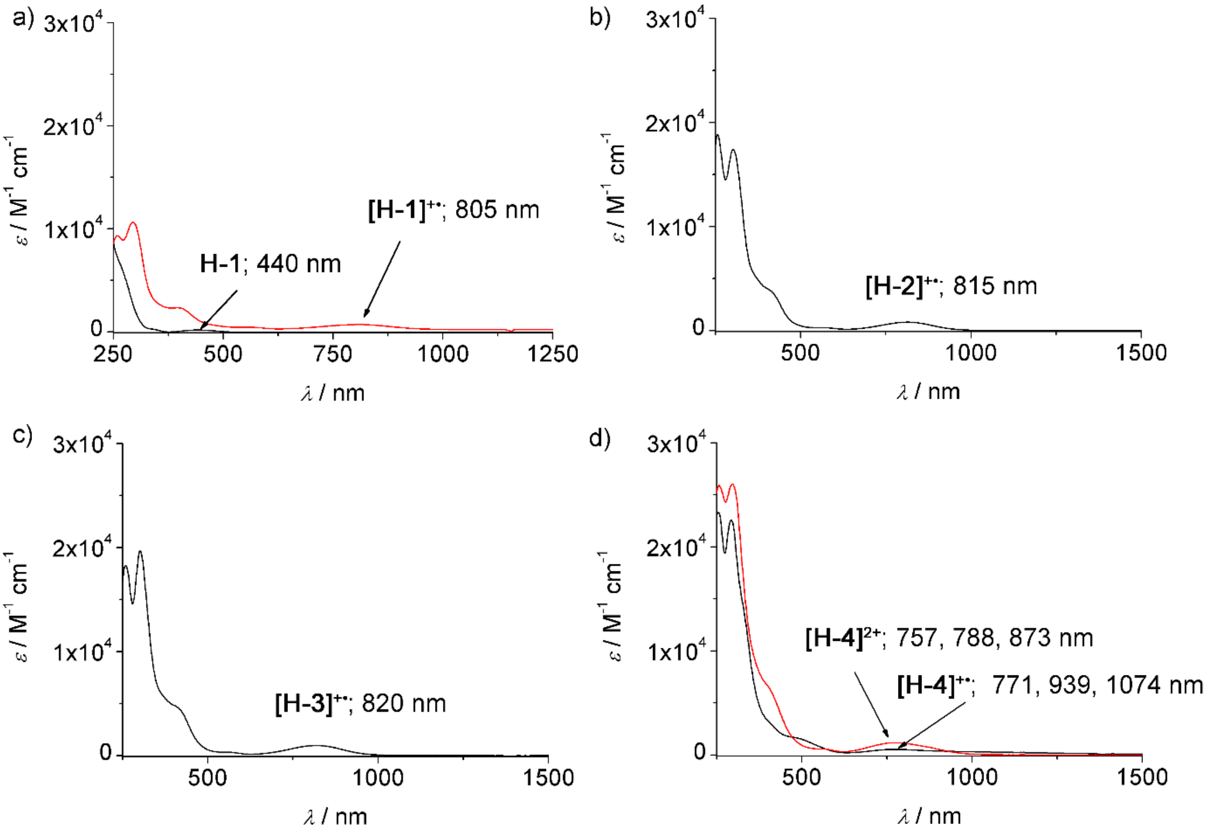

Figure S7. UV/Vis/NIR spectra of a) **H-2** and **[2]**$^{-}$, b) **H-3** and **[3]**$^{-}$, and c) **H-4** and **[4]**$^{-}$ in CH_2Cl_2 at room temperature.

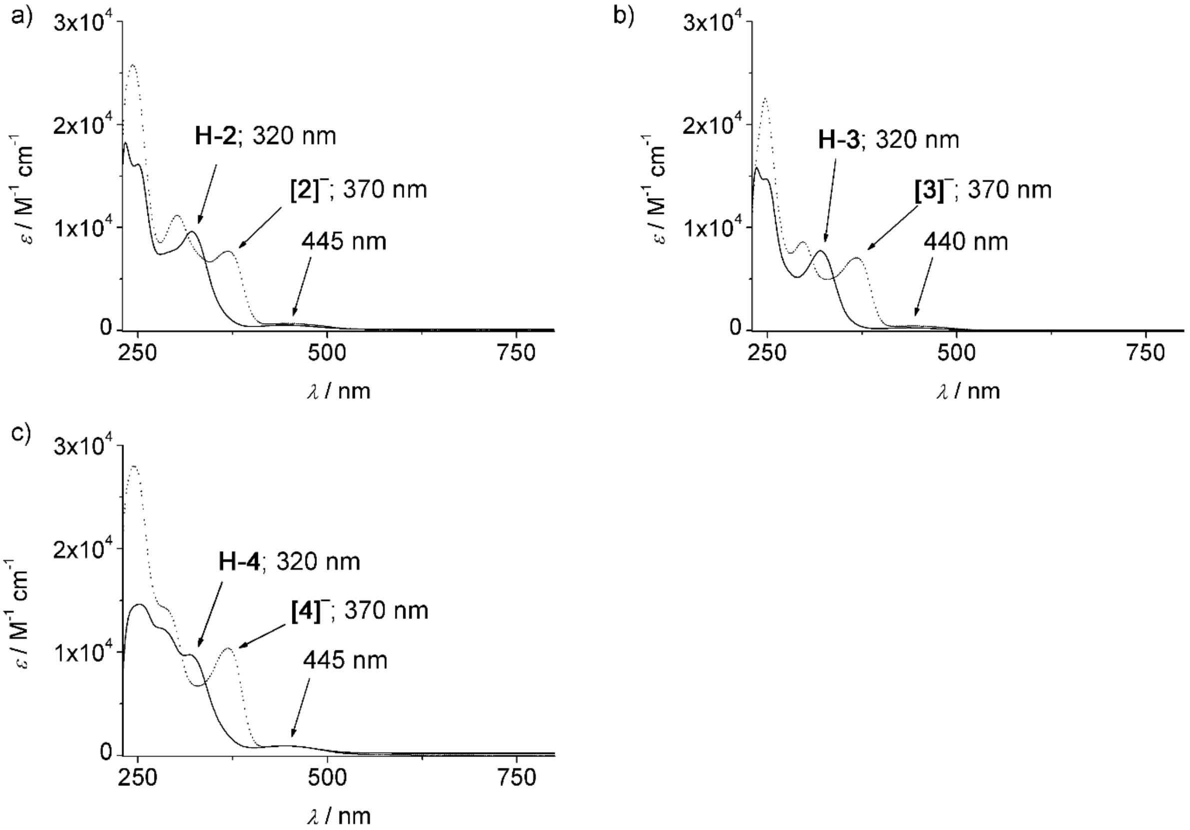

Figure S8. IR spectra of a) **H-2** and **2**⁻, b) **H-3** and **3**⁻, and c) **H-4** and **4**⁻ in CH_2Cl_2 at room temperature.

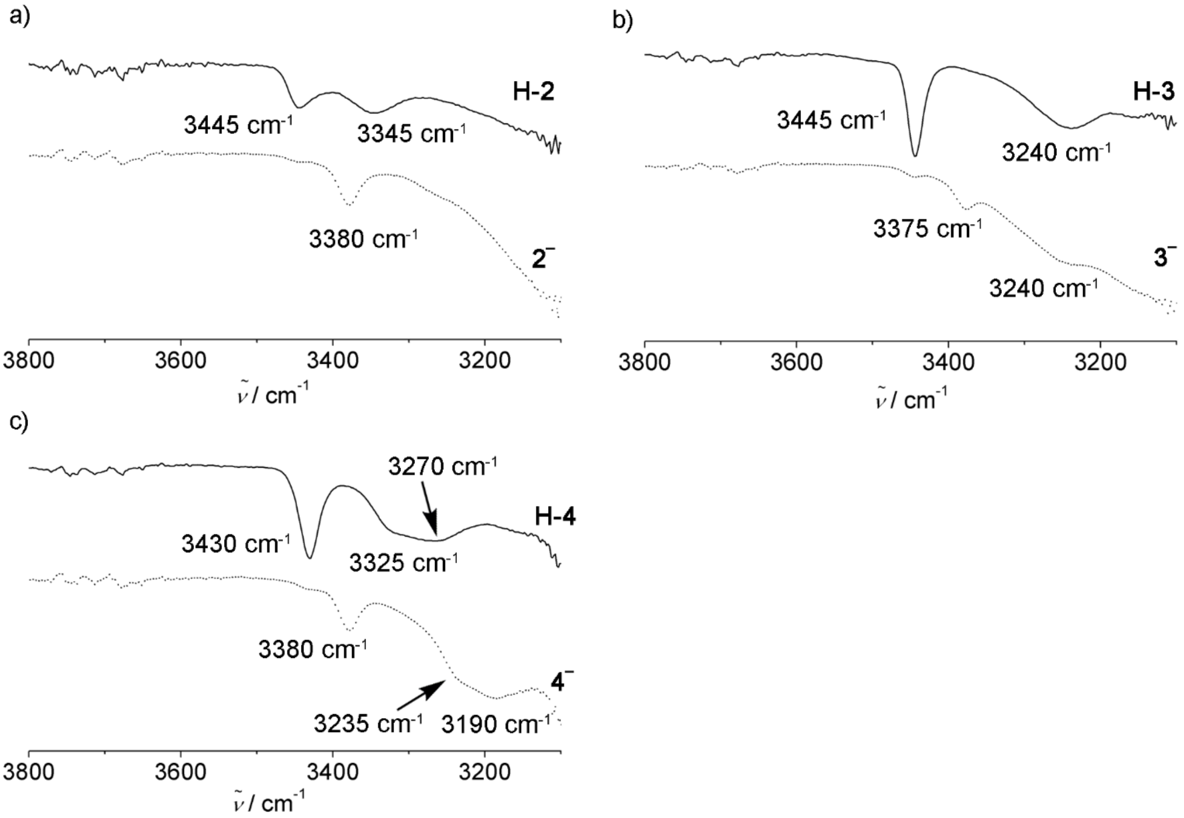

Figure S9. Cyclic voltammogram (bottom) and square wave voltammogram (top) of **H-1** in CH_2Cl_2 containing [^{n}Bu$_4$N][B(C$_6$F$_5$)$_4$] as supporting electrolyte at room temperature.

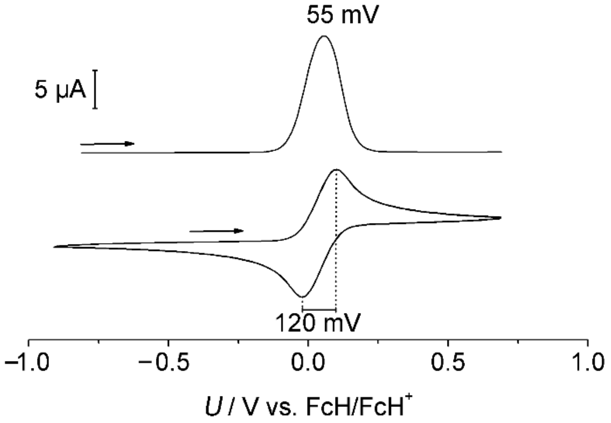

Figure S10. X-band EPR spectra and simulations of 13 mM solutions of (a) **[H-1]**$^{+\bullet}$, (b) **[H-1]**$^{+\bullet}$ + PhOH + P$_1{}^t$Bu, and (c) **[H-1]**$^{+\bullet}$ + P$_1{}^t$Bu in CH$_2$Cl$_2$ at 77 K recorded at the following parameters: sweep time = 90 s, MW attenuation = 10 dB, (a/b) field = 2999.95 G, sweep = 2998.61 G, (c) field = 2799.86 G, sweep = 3193.92 G, (a) modulation = 2000 mG and (b/c) modulation = 5000 mG.

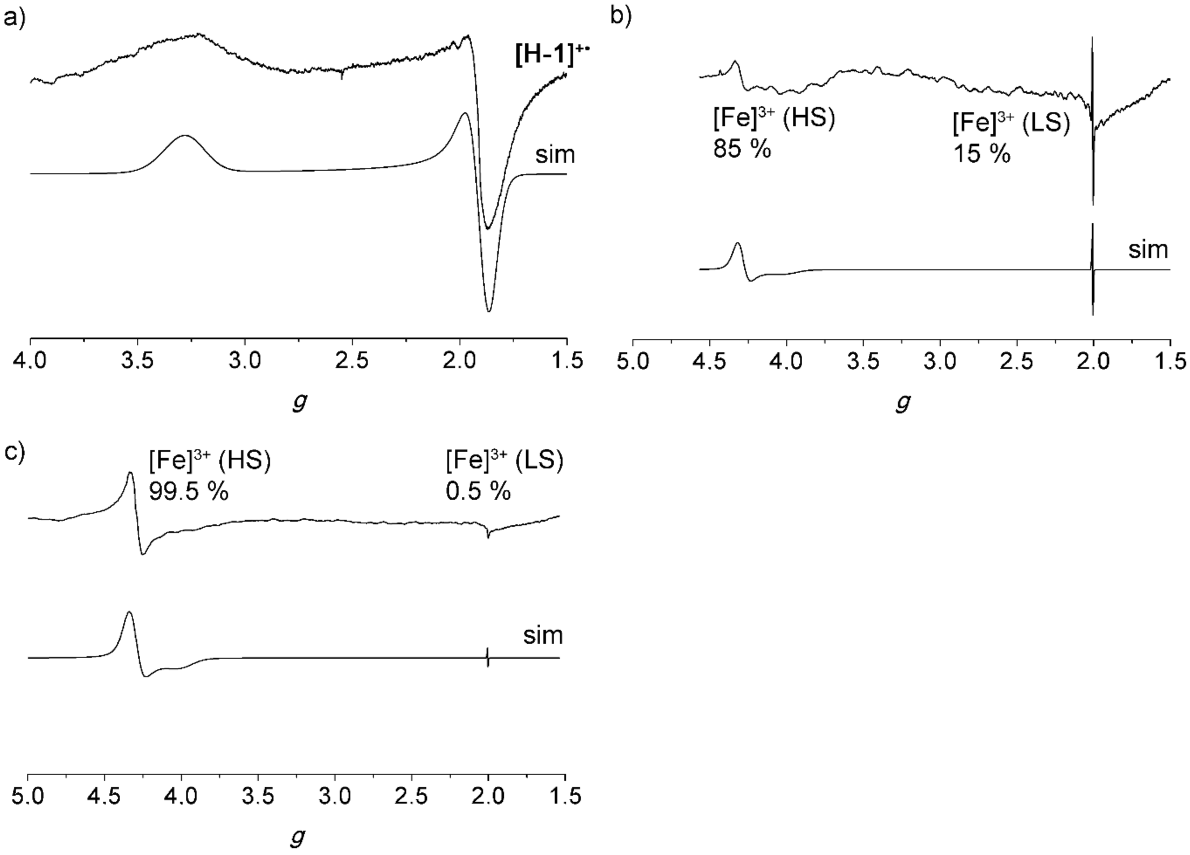

Figure S11. Vis/NIR spectra in CH_2Cl_2 at room temperature including Gaussian deconvolution of a) **[H-4]**$^{+\bullet}$ and b) **[H-4]**$^{2+}$.

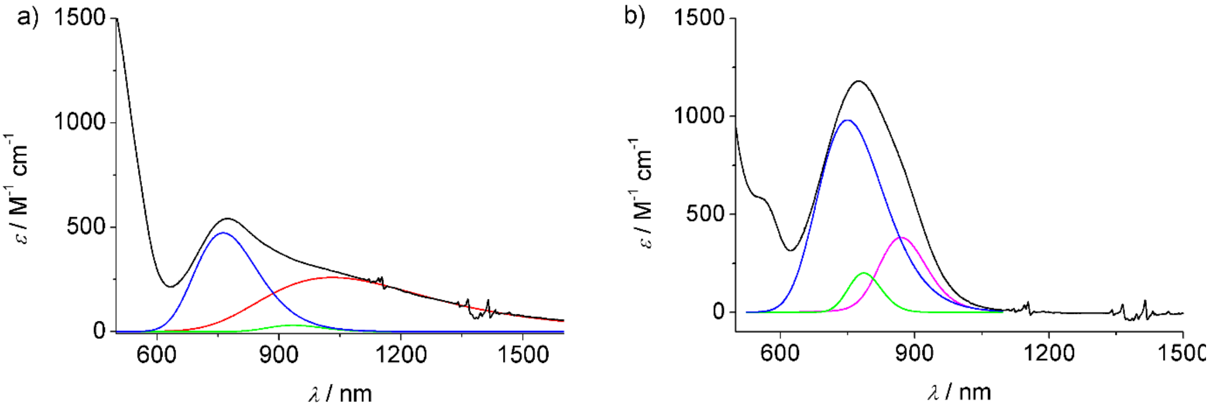

IVCT: $\tilde{\nu}$ = 9310 cm^{-1}
$\Delta\tilde{\nu}$ = 4575 cm^{-1}
ε = 260 M^{-1} cm^{-1}

LMCT: $\tilde{\nu}$ = 10694 cm^{-1}
$\Delta\tilde{\nu}$ = 1780 cm^{-1}
ε = 31 M^{-1} cm^{-1}

LMCT: $\tilde{\nu}$ = 12971 cm^{-1}
$\Delta\tilde{\nu}$ = 3135 cm^{-1}
ε = 473 M^{-1} cm^{-1}

LMCT: $\tilde{\nu}$ = 11454 cm^{-1}
$\Delta\tilde{\nu}$ = 1669 cm^{-1}
ε = 382 M^{-1} cm^{-1}

LMCT: $\tilde{\nu}$ = 12691 cm^{-1}
$\Delta\tilde{\nu}$ = 1414 cm^{-1}
ε = 200 M^{-1} cm^{-1}

LMCT: $\tilde{\nu}$ = 13206 cm^{-1}
$\Delta\tilde{\nu}$ = 3081 cm^{-1}
ε = 981 M^{-1} cm^{-1}

Figure S12. Cyclic voltammograms (bottom) and square wave voltammograms (top) of a) **[2]**$^-$, b) **[3]**$^-$, and c) **[4]**$^-$ in CH_2Cl_2 containing $[^nBu_4N][B(C_6F_5)_4]$ as supporting electrolyte at room temperature.

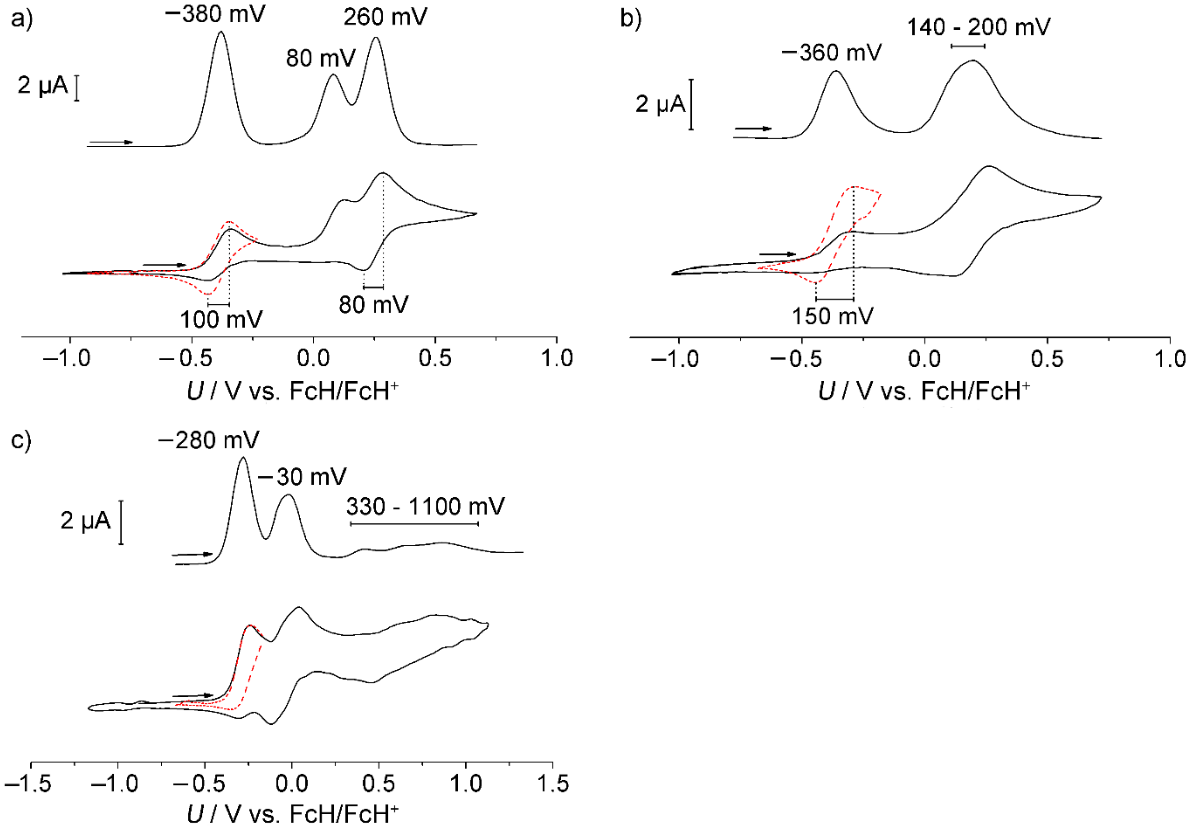

Figure S13. X-band EPR spectrum and simulation of a 13 mM solution of $[Fc\text{-}COOMe]^{+\bullet}$ + PhOH + $P_1{}^tBu$ in CH_2Cl_2 at 77 K recorded at the following parameters: field = 2799.86 G, sweep = 3193.92 G, modulation = 5000 mG, sweep time = 90 s, MW attenuation = 7 dB.

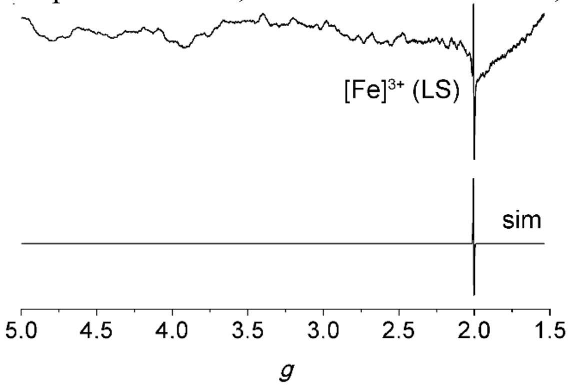

Scheme S1. Lewis structures and relative energies obtained by DFT calculations (B3LYP/SV(P)/COSMO:CH_2Cl_2) for conformers of **H-2**, **H-3**, and **H-4**. Hydrogen bonds are colored in blue.

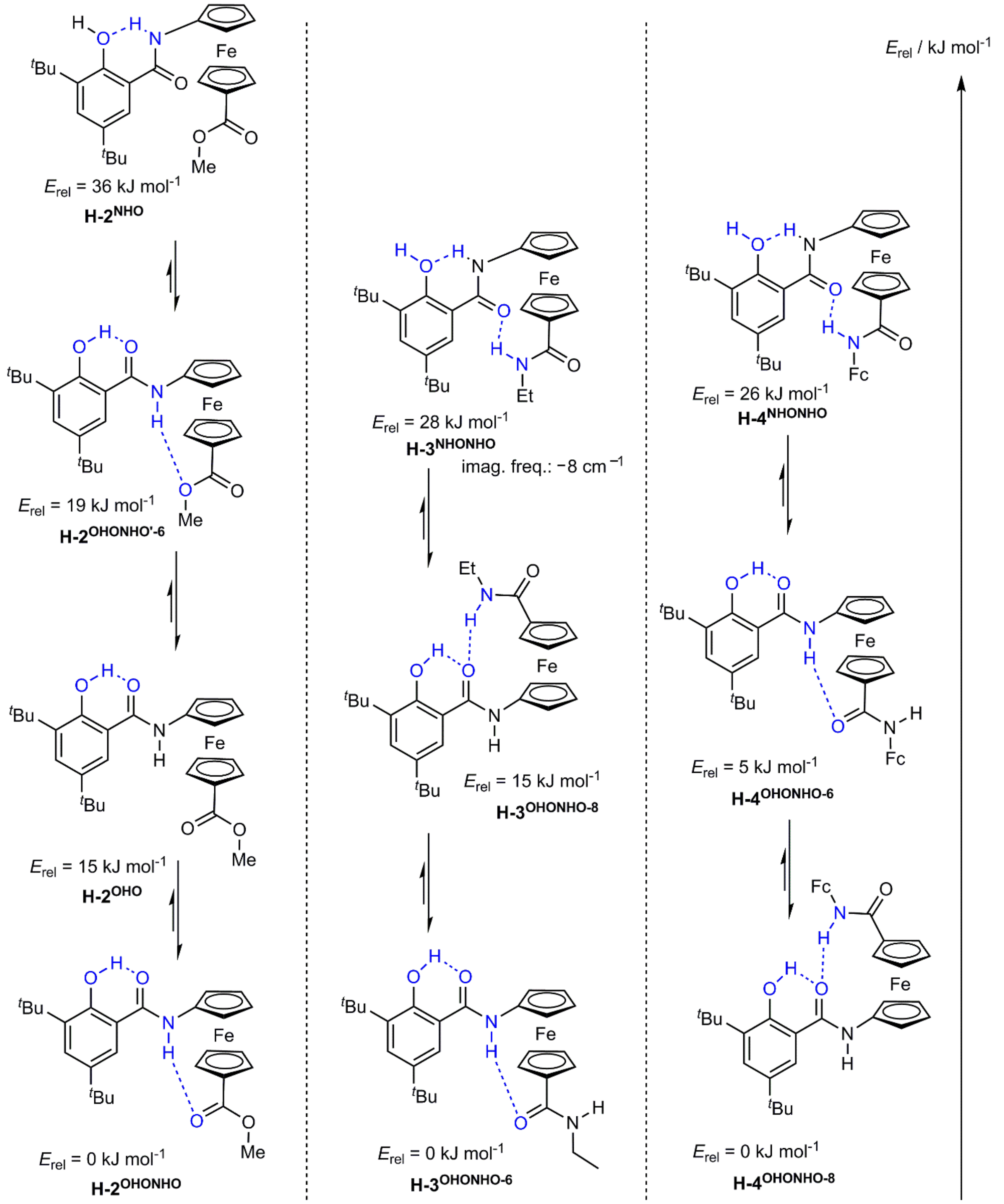

Scheme S2. Lewis structures of the conjugate bases of ferrocenyl phenol **H-2** and relative energies obtained by DFT calculations (B3LYP/SV(P)/COSMO:CH_2Cl_2). Hydrogen bonds are colored in blue.

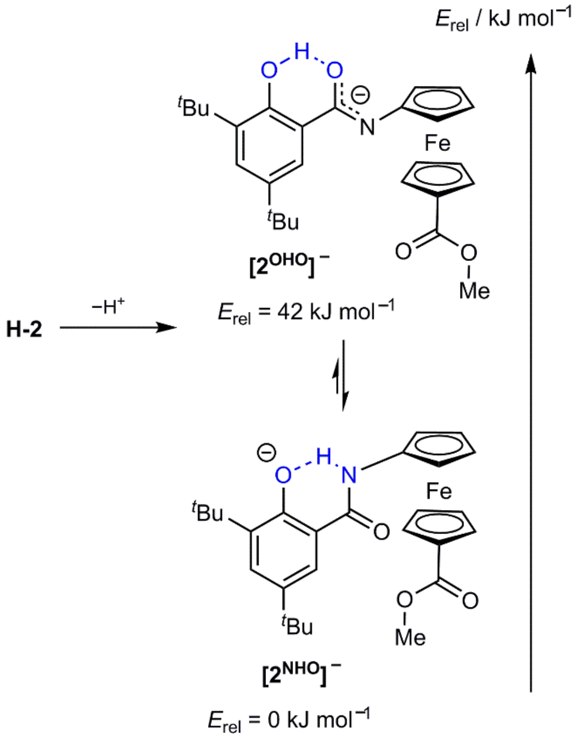

Scheme S3. Lewis structures of the conjugate bases of ferrocenyl phenols **H-3** and **H-4** and relative energies obtained by DFT calculations (B3LYP/SV(P)/COSMO:CH_2Cl_2). Hydrogen bonds are colored in blue.

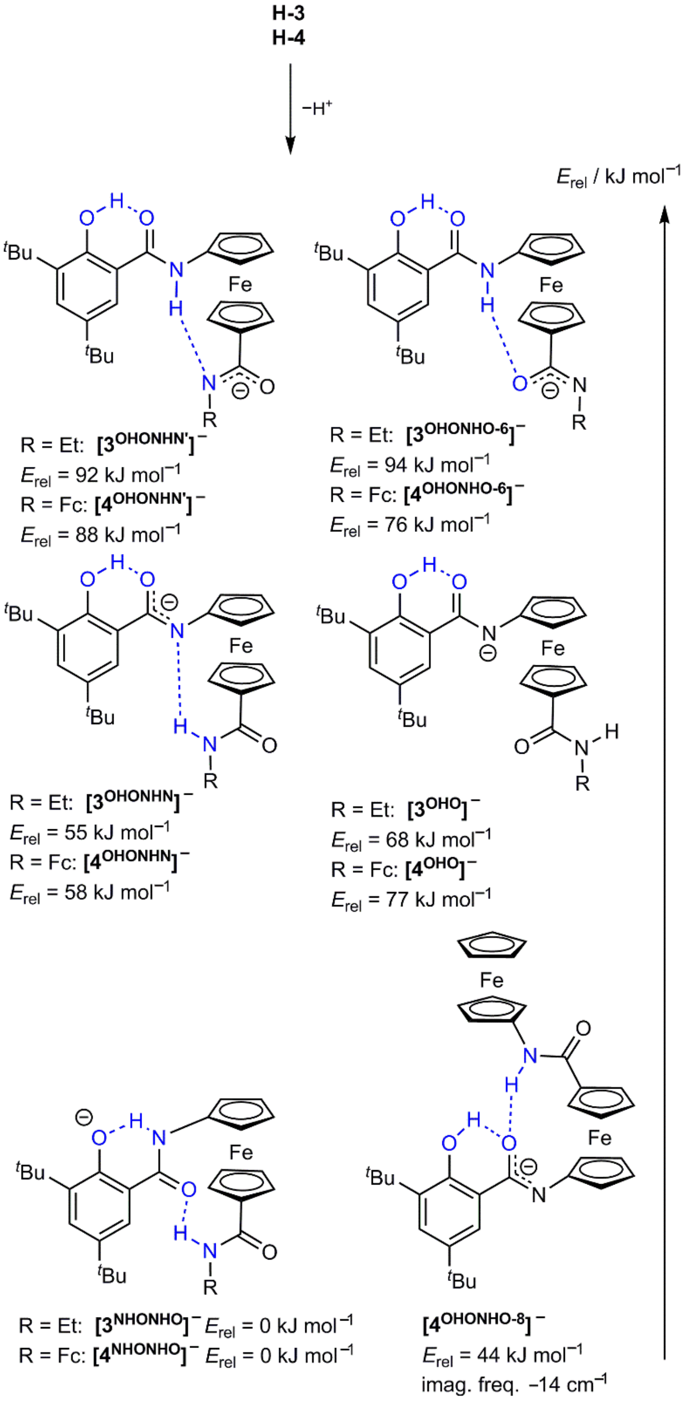

Scheme S4. Lewis structures of separated ion pairs and contact ion pairs **[H-1][SbF$_6$]** and relative energies obtained by DFT calculations (B3LYP/SV(P)/COSMO:CH$_2$Cl$_2$). Hydrogen bonds are colored in blue. The conformer **[H-1$^{\text{NHONHF-8}}$][SbF$_6$]** only converged to an electronically excited state and is thus shown without relative energy.

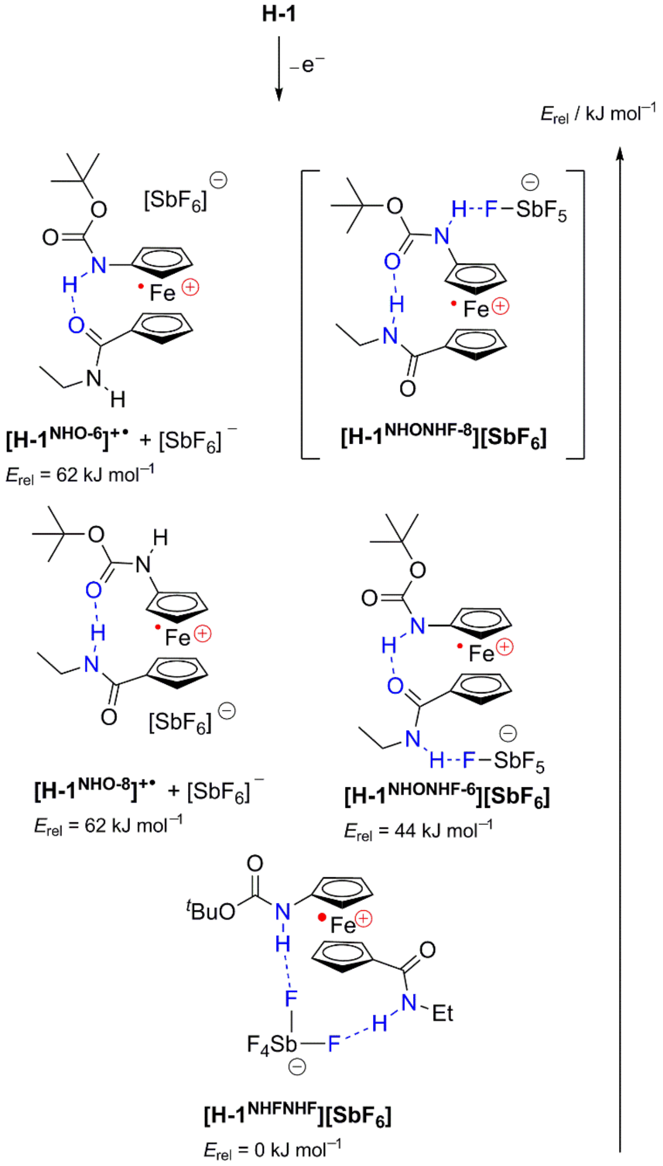

Scheme S5. Lewis structures of separated ion pairs and contact ion pairs **[H-2][SbF$_6$]** and relative energies obtained by DFT calculations (B3LYP/SV(P)/COSMO:CH$_2$Cl$_2$). Hydrogen bonds are colored in blue.

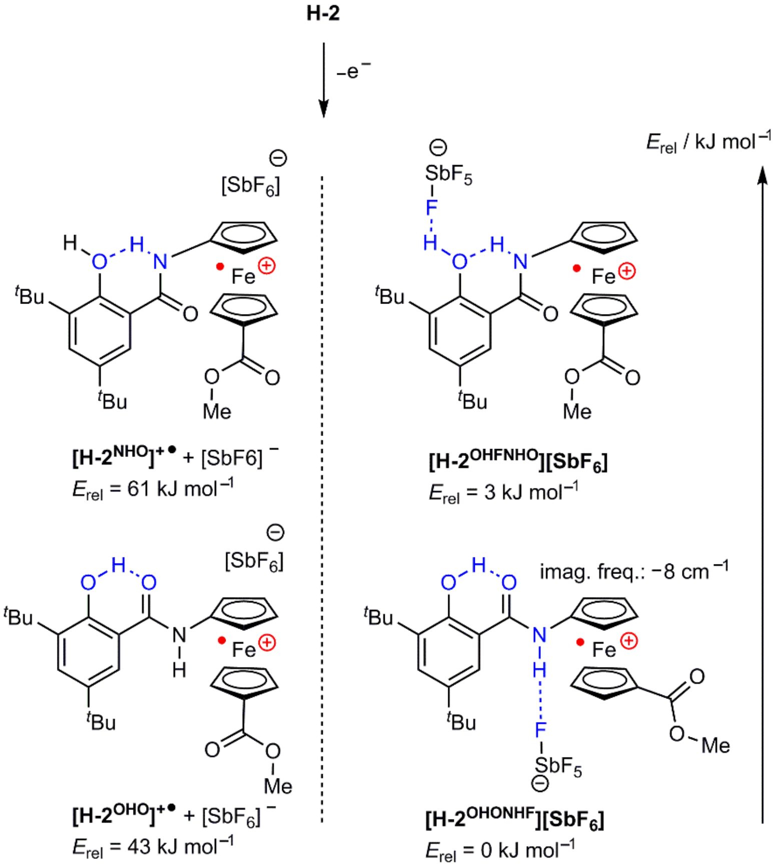

Scheme S6. Lewis structures of separated ion pairs and contact ion pairs **[H-3][SbF$_6$]** and relative energies obtained by DFT calculations (B3LYP/SV(P)/COSMO:CH$_2$Cl$_2$). Hydrogen bonds are colored in blue.

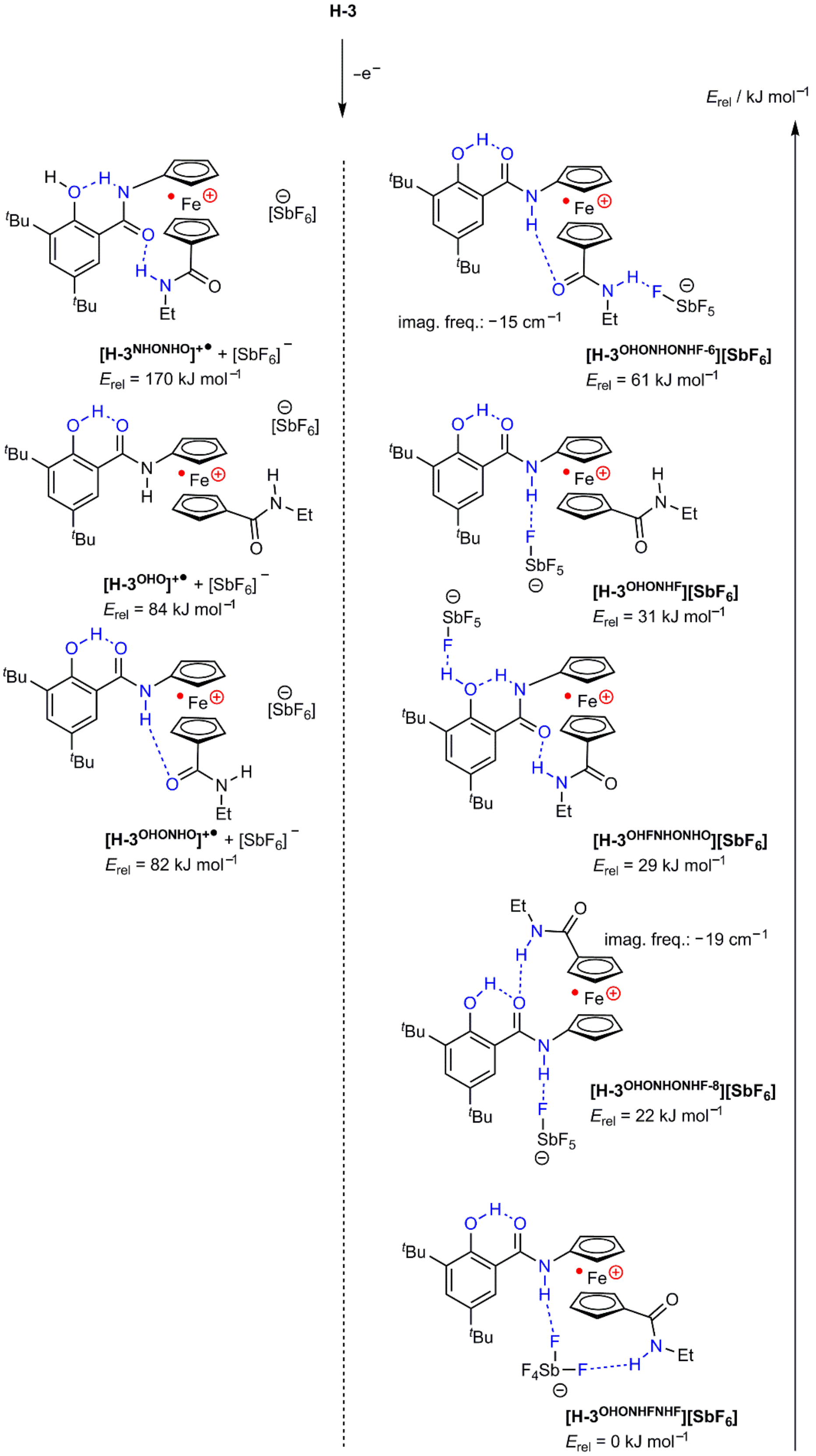

Scheme S7. Lewis structures of separated ion pairs and contact ion pairs of **[H-4][SbF$_6$]** and relative energies obtained by DFT calculations (B3LYP/SV(P)/COSMO:CH$_2$Cl$_2$). Hydrogen bonds are colored in blue. The conformer **[H-4$^{\mathrm{OHONHONHF\text{-}8}}$][SbF$_6$]** only converged to an electronically excited state and is thus shown without relative energy.

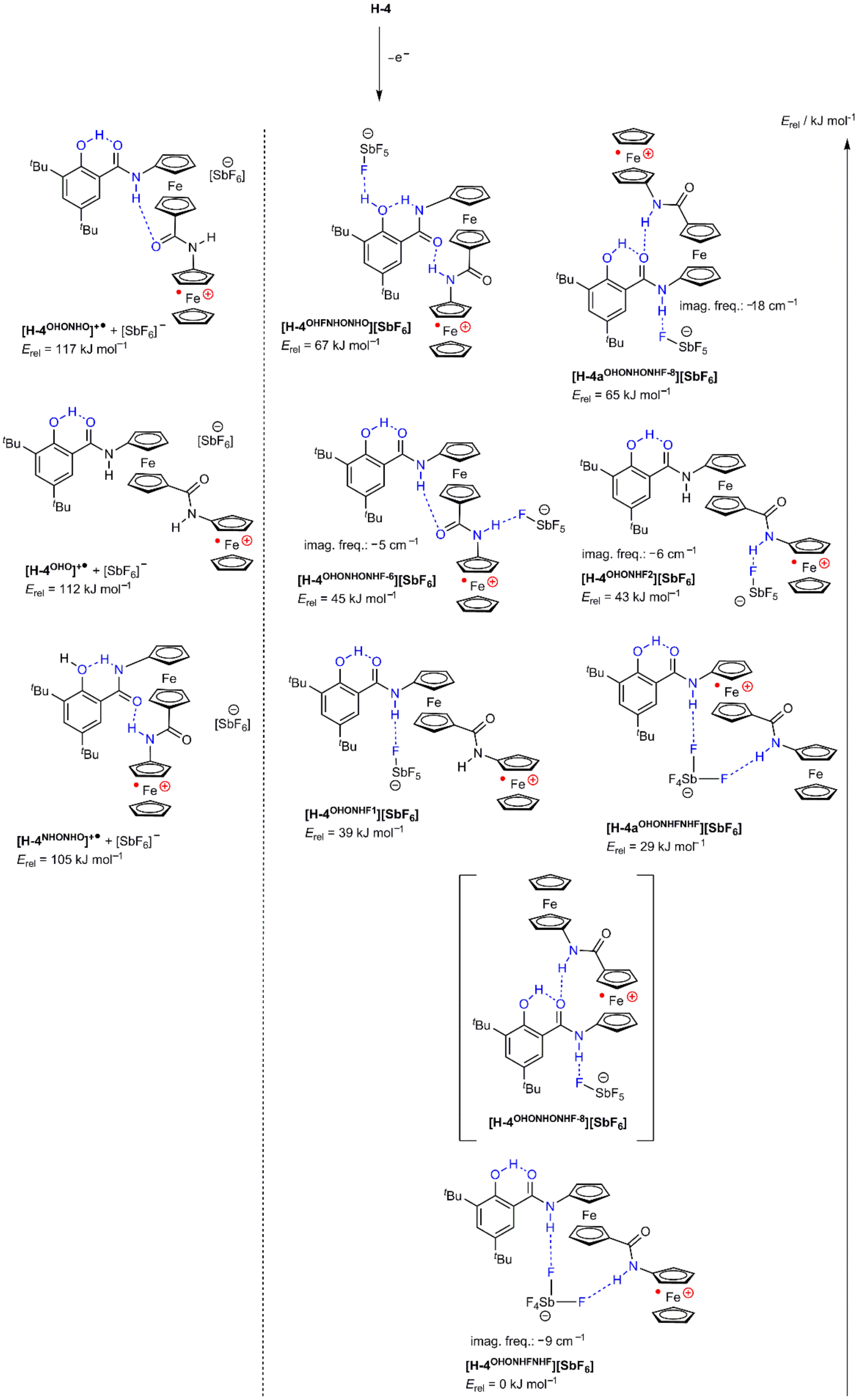

Scheme S8. Lewis structures of separated ion pairs and contact ion pairs of **[H-4][SbF$_6$]$_2$** and relative energies obtained by DFT calculations (B3LYP/SV(P)/COSMO:CH$_2$Cl$_2$). Hydrogen bonds are colored in blue.

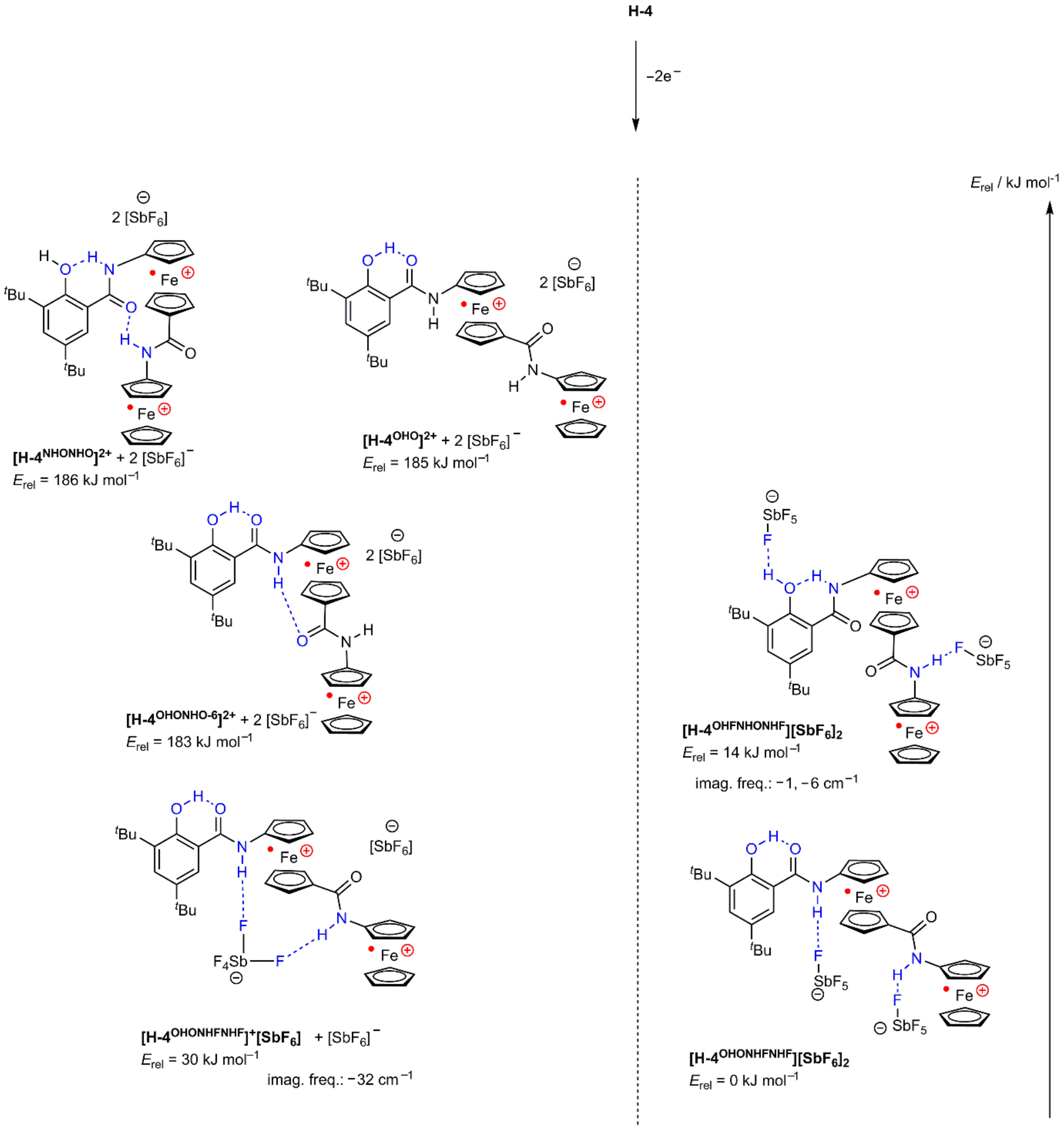

Scheme S9. Lewis structures of conformers of **[3]**$^\bullet$. Hydrogen bonds are colored in blue.

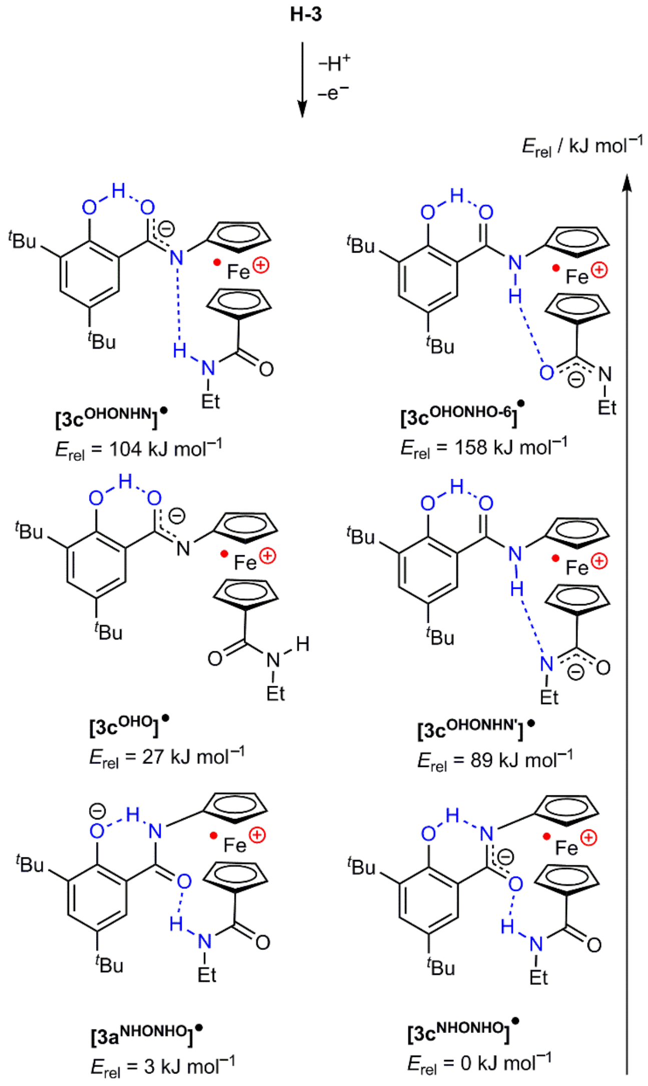

Scheme S10. Lewis structures of conformers of **[4]**$^{\bullet}$. Hydrogen bonds are colored in blue. The conformer **[4a$^{\mathrm{NHONHO}}$]**$^{\bullet}$ only converged to an electronically excited state. Therefore, not relative energy is given for this structure.

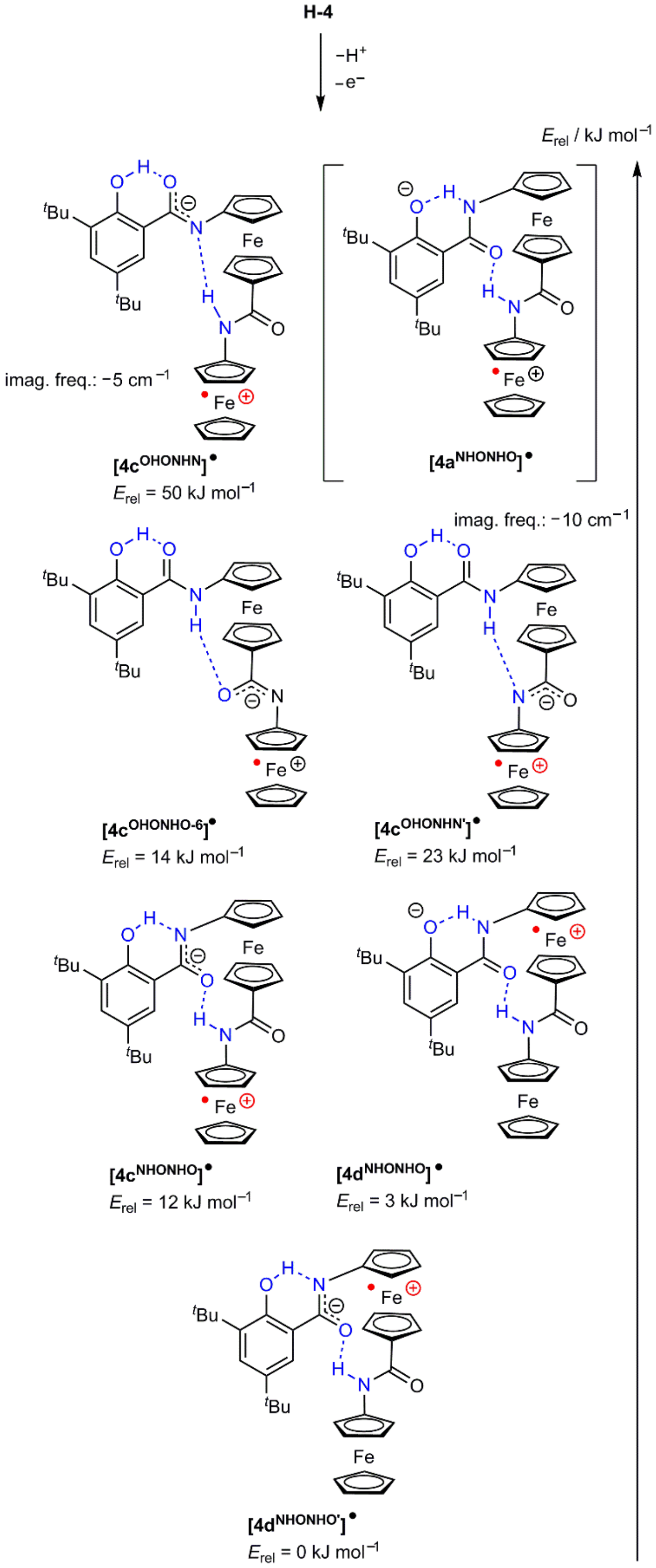

For Cartesian coordinates of DFT optimizations see electronic supporting information.

6 ACKNOWLEGDMENTS

[redacted]

[redacted]

[redacted]

[redacted]

[redacted]

[redacted]

[redacted]

[redacted]

[redacted]

[redacted]

[redacted]

[redacted]

[redacted]

[redacted]

[redacted]

[redacted]

[redacted]

[redacted]

[redacted]

[redacted]

[redacted]

[redacted]

[redacted]

[redacted]

[redacted]

[redacted]

[redacted]

[redacted]

[redacted]

[redacted]

[redacted]

7 LIST OF PUBLICATIONS

Publications:

A. Neidlinger, C. Förster, K. Heinze: „ *Conformational Switching of Responsive Ferrocenyl-Phenol Conjugates*", to be submitted.

A. Neidlinger, C. Förster, K. Heinze: „*How Hydrogen Bonds Affect Reactivity and Intervalence Charge Transfer in Ferrocenium-Phenolate Radicals*", *Eur. J. Inorg. Chem.* **2016**, in print.

A. Neidlinger, T. Kienz, K. Heinze: „*Spin-Trapping of Carbon-Centered Ferrocenyl Radicals with Nitrosobenzene*", *Organometallics*, **2015**, *34*, 5310−5320 (DOI: 10.1021/acs.organomet.5b00778).

A. Neidlinger, V. Ksenofontov, K. Heinze: „*Proton Coupled Electron Transfer in Ferrocenium-Phenolate Radicals*", *Organometallics* **2013**, *32*, 5955−5965 (DOI: 10.1021/om400498h).

Oral Presentations:

A. Neidlinger, K. Heinze: "*Proton coupled electron transfer in a ferrocene-phenol conjugate: solvent matters*"; oral presentation at the 11th Ferrocene Colloquium, 6. – 8. February 2013, Hannover.

A. Neidlinger, K. Heinze: "*Oxidation of N-ferrocenyl salicylamidate – phenoxyl or ferrocenium radical?*"; oral presentation at the *10th Ferrocene Colloquium*, 15. – 17. February 2012, Braunschweig.

Poster Presentations:

A. Neidlinger, K. Heinze: “*Spin-Trapping in Ferrocenium-Phenolate Conjugates*”; poster presented at the 13th Ferrocene Colloquium, 22. – 24. February 2015, Leipzig.

A. Neidlinger, K. Heinze: “*Effects of hydrogen bonding on intervalence charge transfer reactions in ferrocene-phenolate conjugates*”; poster presented at the 12th Ferrocene Colloquium, 17. – 19. February 2014, Innsbruck and at the 16. JCF-Frühjahrssymposium, 26. – 29. March 2014, Jena.

A. Neidlinger, K. Heinze: “*Valence isomeric phenoxyl ferrocenyl radicals*”; poster presented at the *16. Vortragstagung der Wöhler-Vereinigung*, 26. – 28. September 2012, Göttingen about and at the *15. JCF-Frühjahrssymposium*, 6. – 9. March 2013, Berlin.